ROLE OF METALLIFEROUS MUDSTONES AND GRAPHITIC SHALES IN THE LOCATION, GENESIS, AND PALEOENVIRONMENT OF VOLCANOGENIC MASSIVE SULPHIDE DEPOSITS OF THE TALLY POND VOLCANIC BELT, CENTRAL NEWFOUNDLAND, CANADA

by

© Stefanie Lode

A thesis submitted to the

School of Graduate Studies

in partial fulfillment of the requirements for the degree of

Doctor of Philosophy

Department of Earth Sciences

Memorial University of Newfoundland

April, 2016

St. John's Newfoundland and Labrador

ABSTRACT

The Cambrian Tally Pond volcanic belt in central Newfoundland contains numerous volcanogenic massive sulphide (VMS) deposits, prospects, and showings that are locally associated with metalliferous mudstones and/or graphitic shales. Deposits in the belt are bimodal felsic-type VMS that are both base metal- (e.g., Duck Pond, Boundary) and precious metal-enriched (e.g., Lemarchant). At the Lemarchant deposit metalliferous mudstones are genetically and spatially associated with mineralization, whereas the relationship of other mudstones and shales to massive sulphide mineralization is more intricate and remains not fully understood.

Metalliferous mudstones represent a hiatus in the volcanic activity where the deposition of hydrothermal products dominated over the abiogenic background sedimentation and/or dilution by volcaniclastic-epiclastic material. Lithogeochemical signatures allow one to distinguish between predominantly hydrothermally or detritally (i.e., non-hydrothermal) derived material. Metalliferous mudstones with a significant hydrothermal component, like those at Lemarchant, have elevated Fe/Al and base-metal contents, compared to detrital shales, and shale-normalized negative Ce and positive Eu anomalies, indicative of deposition from high temperature (>250°C) hydrothermal fluids within an oxygenated water column. Mudstones and shales sampled from other locations in the Tally Pond volcanic belt have more variable signatures ranging from hydrothermal (signatures as above) to non-hydrothermal (no positive Eu-anomalies, flat REE patterns), with some that have mixed (hydrothermal and detrital) signatures. Both S and Pb isotopic compositions indicate that proximal sulphides hosted in mudstones immediately associated with massive sulphide mineralization within the Lemarchant deposit contain a

higher proportion of sulphur derived from hydrothermal sources and processes, and have more juvenile lead contributions, when compared to sulphides distal (not associated with massive sulphides) from mineralization. Lead and Nd isotopic compositions of both whole rock and minerals in the Lemarchant mudstones indicate involvement of underlying crustal basement during massive sulphide formation and throughout the evolution of the Tally Pond belt.

Metalliferous mudstones precipitated early in the massive sulphide depositional history, but also have undergone syn- and post-ore-forming processes and have a larger lateral extent than the mineralization. Using lithogeochemistry, whole rock and *in situ* stable and radiogenic isotopes it is possible to distinguish prospective vent proximal (immediately associated with massive sulphide mineralization) from less prospective distal (not associated with massive sulphides) depositional environments and to reconstruct the paleotectonic setting on a deposit- to regional-scale for the Lemarchant deposit and other mudstone-associated prospects in the Tally Pond volcanic belt.

ACKNOWLEDGEMENTS

This thesis is a result of, and has benefited from, the guidance and support of many people. Most importantly, I would like to thank my supervisor Dr. Stephen Piercey for his excellent direction and encouragement throughout my PhD thesis. With his great supervision and structuring of the project I was able to complete my thesis in a timely manner, but was also motivated to pursue my own research interests. Furthermore, I would like to extend my gratitude to Dr. Graham Layne, whose experience regarding isotopic and ore forming systems greatly contributed to the progress of this thesis project. Additionally, the project benefited from discussions with my fellow graduate students of the Piercey research group, including Stefanie Brueckner, Michael Buschette, Dean Courage, Shannon Gill, Shannon Guffey, Nicolas Lachance, Conor McKinley, Hannah Mills, Jean-Luc Pilote, Inês Nobre Silva, and especially Jonathan Cloutier, who never hesitated to help with his knowledge and support. Shannon Guffey, Inês Nobre Silva, and Jonathan Cloutier are further thanked for their considerable help with editing various chapters. Furthermore, I would like to thank my committee Dr. Graham Layne and Dr. Derek Wilton for their helpful discussions.

Great support during my field work and introduction to the Lemarchant deposit was given by Dave Copeland, Christine Devine, Dianne and Charlie Fost, Alexandra Marcotte, Bryan Sparrow, and Mike Vande Guchte of Paragon Minerals Corporation (now Canadian Zinc Corporation); as well as Darren Hennessey and Gerald Squires of Teck Ltd., Duck Pond Operations (the latter now with Canadian Zinc Corporation) who introduced me to deposits, prospects, and showings of the Tally Pond belt. Dario Harazim introduced me to Bell Island and helped to choose sample locations. In-house laboratory work and organization of the field work would not have been possible without the great help from Lakmali Hewa, Keir Hiscock, Pam King, Glenn Piercey, Sherry Strong, and Anne Westhues.

Finally, I would like to thank my friends here in town and the ones from Europe, as well as family (my parents and my brother in Germany, and my cousin and her family in Ottawa) for their both scientific and non-scientific encouragement and support during the time of my PhD thesis. Moreover, I'm thankful for the company and charisma of my cats Mustikka and Koivu, who continuously provided any form of distraction possible.

Financial support was received from the project of the Canadian Mining Research Organization "Geochemistry of Shales as Vectors to Ore Deposits" CAMIRO Project 08E04 and the NSERC-CRD grant CRDPJ J-387591-09. Additional funding for research was provided by the NSERC-Altius Industrial Research Chair in Mineral Deposits, funded by NSERC, Altius Resources Inc., and the Development Corporation of Newfoundland and Labrador.

TABLE OF CONTENTS

CHAPTER 6

LIST OF TABLES

CHAPTER 2

CHAPTER 3

CHAPTER 4

CHAPTER 5

LIST OF FIGURES

CHAPTER 1

CHAPTER 2

CHAPTER 3

CHAPTER 5

LIST OF ABBREVIATIONS

Å	Ångström
A-CN-K	Al_2O_3-CaO+NaO-K_2O
A-CNK-FM	Al_2O_3-CaO+NaO+K_2O-FeO_{total}+MgO
Actlabs	Activation Laboratories Ltd.
BD	Boundary deposit
BI	Bell Island
BL	Beaver Lake prospect
BSE	Backscattered electron
BSO	Biogenic sulphide oxidation
BSR	Biogenic sulphate reduction
BW	Boundary West showing
°C	Celsius
CAMIRO	Canadian Mining Research Organization
Ce/Ce* ≤ 1	Negative Ce anomaly
CHUR	Chondritic uniform reservoir
CIA	Chemical alteration index
CLIS	Crippleback Lake Intrusive Suite
CN	Coordination number
CT	Cookstown showing
DP	Duck Pond deposit
DW	Duck West showing
ECL-based pulse-counting electronics	Emitter-coupled logic pulse-counting electronics
EMS	Exhalative mudstones immediately associated with, or that occur within five meters of, massive sulphides at contact between felsic and mafic volcanic rocks
εNd	Epsilon Neodymium
e.g.	For example
Eh	Oxidation-reduction potential
ETP 133H	Type of multiple-dynode electron multiplier for mass-spectrometry
Eu/Eu* ≥ 1	Positive Eu anomaly
FEF	Exhalative mudstones that occur within the felsic volcanic rocks
FEM	Exhalative mudstones at same stratigraphic horizon as

	EMS, but without immediate association to mineralization
FeR-1	Natural Resource Canada Standard Iron Formation-1
$f^{Sm/Nd}$	Fractional deviation of $^{147}Sm/^{144}Nd$ from CHUR
Fig.	Figure
g/t	Grams per tonne
HFSE	High field strength elements
Hg-FIMS	Flow injection mercury system
HL	Higher Levels prospect
HREE	Heavy rare earth elements
ICP-ES	Inductively coupled plasma (atomic) – emission spectroscopy
ICP-MS	Inductively coupled plasma-mass spectrometry
i.e.	id est
IFE	Interflow exhalative mudstones
km	Kilometres
KP	Keats Pond showing
LFSE	Low field strength elements
LM	Lemarchant
LREE	Light rare earth elements
m	Metre
Ma	Million years
MAF-IIC	Microanalysis Facility at Memorial University
MORB	Mid-ocean ridge basalt
Mt	Million tonnes
N	North
NE	Northeast
NM	North Moose Pond showing
ns	Nano seconds
OC	Old Camp showing
p	Pressure
PAAS	Post-Archean Australian Shale
pH	Negative of the logarithm to base 10 of the activity of the hydrogen ion
ppb	Parts per billion
ppm	Parts per million
QA/QC	Quality assurance and quality control
%	Per cent
% RD	Per cent relative difference
% RSD	Per cent relative standard deviation
REE	Rare earth elements
REY	Rare earth elements plus Yttrium
RL	Reflected light microscopy
Σ	Sum

SCO-1	USGS Standard Cody Shale
SDO-1	USGS Standard Devonian Ohio Shale
SGR-1b	USGS Standard Green River Shale
SEM	Scanning electron microscope
SEM-EDX	Scanning electron microscope – energy dispersive X-ray spectroscopy
SIMS	Secondary ion mass spectrometry
SM	South Moose Pond alteration zone
TIMS	Thermal ionization mass spectrometry
T	Temperature
TL	Transmitted light microscopy
TPB	Tally Pond belt
TSR	Thermochemical sulphate reduction
VMS	Volcanogenic massive sulphide
wt%	Weight per cent

LIST OF APPENDICES

CO-AUTHORSHIP STATEMENT

This doctoral thesis comprises six chapters. The first chapter represents the framework of the dissertation, including the problem statement and the introduction and overview of project-relevant background information. This chapter is written by the author of this thesis with editorial support. Chapters two, three, four, and five are written as individual manuscripts by the author and in collaboration with Dr. Stephen Piercey, the supervisor of this thesis, and additional co-authors. These chapters are either published, accepted, submitted, or will be submitted to international scientific journals. Information about the status of each manuscript is given as note after the title of each chapter. Chapter six summarizes the content of this thesis and outlines possible future research projects.

Chapter 2: Lode et al., 2015 (Economic Geology, v. 110, 1835-1859)

This chapter was written under the supervision of, and guidance of, Dr. Stephen Piercey as thesis supervisor. All core-logging and sample collection during fieldwork was carried out by the author, in the beginning under guidance of Christine Devine from Paragon Minerals Corporation/Canadian Zinc Corporation (now Fugro Geoconsulting, Inc.) and Dr. Stephen Piercey. The co-authors introduced the author to the Lemarchant deposit and provided initial field guidance for successful core-logging and sampling. Data

interpretation was done in collaboration with the Dr. Stephen Piercey. Laboratory work (dissolution of the samples for whole-rock lithogeochemical analyses) of the presented data was performed by the author at Memorial University, Department of Earth Sciences, with guidance from Pam King and Lakmali Hewa, and at Actlabs (Activation Laboratories Ltd.). Comments on the manuscript, other than those from the supervisor, were provided by Dr. Jonathan Cloutier (now at University of St. Andrews, Scotland), Shannon Guffey, and Dr. Inês Nobre Silva from Memorial University and Christine Devine, Michael Vande Guchte, Gerry Squires from Canadian Zinc Corporation. The manuscript was formally reviewed by external reviewers as part of the journal review process and included Dr. Paul Spry (Iowa State University, USA) and Dr. Nils Jansson (Boliden Mineral and University of Luleå, Sweden) and is published in the November 2015 issue of Economic Geology.

Chapter 3: Lode et al., in press with Mineralium Deposita

This chapter was written by the author with supervision of Dr. Stephen Piercey and Dr. Graham Layne. Both provided helpful discussions during the interpretation of the S and Pb isotopic results. Sulphur and Pb isotopic compositions were obtained using *in situ* SIMS by Glenn Piercey and by the author at the Microanalysis Facility at Memorial University (MAF-IIC). Dr. Jonathan Cloutier provided helpful discussions and support during the modelling of S isotopes. Comments on the manuscript, besides those from the co-authors, were provided by Dr. Inês Nobre Silva from Memorial University and Michael Vande Guchte and Gerry Squires from Paragon Minerals Corporation/Canadian

Zinc Corporation. The manuscript was formally reviewed by external reviewers as part of the journal review process and included Dr. David Huston (Geoscience Australia, Canberra, Australia) and Dr. Fernando Tornos (Consejo Superior de Investigaciones Cientificas, Madrid, Spain). After major revisions, this manuscript was re-submitted to the journal Mineralium Deposita on December 4th, 2015, and is currently in review.

Chapter 4: Lode, S., et al., to be submitted

This chapter was written under the supervision of, and guidance from, Dr. Stephen Piercey as thesis supervisor. Dr. Jonathan Cloutier as co-author provided helpful discussions and support during the interpretation of the isotopic data. Samarium and Nd isotopic compositions were obtained using TIMS at Memorial University by the author under the guidance of Sherri Strong and Anne Westhues. Data interpretation was performed collaboratively by the author, Dr. Stephen Piercey, and Dr. Jonathan Cloutier. The manuscript is currently in preparation for submission to an international journal.

Chapter 5: Lode et al., 2016 (Canadian Journal of Earth Sciences, v.53, p.1-39)

This chapter was written under the supervision of, and guidance from, Dr. Stephen Piercey as thesis supervisor. Gerry Squires from Teck Ltd./Canadian Zinc corporation provided an introduction to the VMS deposits, prospects, and showings associated with mudstones and shales in the Tally Pond belt. Core-logging and sampling were carried out by the author and data interpretation was done in collaboration with Dr. Piercey. Laboratory work (dissolution of the samples for whole-rock lithogeochemical analyses)

of the presented data was performed at Actlabs (Activation Laboratories Ltd.) and by the author at Memorial University, Department of Earth Sciences, with guidance from Pam King and Lakmali Hewa.

CHAPTER 1

Introduction and overview

1.1 Problem statement and study area

Metalliferous mudstones and graphitic shales are abundant in the Tally Pond volcanic belt, central Newfoundland Appalachians, and are spatially and/or genetically related to volcanogenic massive sulphide (VMS) deposits, prospects, and showings (Swinden, 1991; Squires and Moore, 2004). The study area of this PhD project is located in the Tally Pond volcanic belt, which is part of the Dunnage Zone in central Newfoundland. The Tally Pond belt belongs to the Cambrian (~513 Ma) to Permian (~275 Ma) Appalachian mountain belt, which hosts numerous VMS deposits, including the Duck Pond and Boundary mines, as well as the Lemarchant deposit (Fig. 1.1A; Williams, 1979; Swinden, 1988, 1991; Evans and Kean, 2002; Rogers et al., 2007; van Staal and Barr, 2011; Piercey et al., 2014). The Tally Pond belt volcanic rocks and related massive sulphide mineralization formed during episodes of rifting during the construction of the Cambrian to Early Ordovician Penobscot Arc (Zagorevski et al., 2010; Piercey et al., 2014). The sedimentary rocks deposited in this type of graben-/rift-related basins typically are of volcaniclastic and epiclastic nature, and locally also can contain exhalative metalliferous mudstones derived from hydrothermal plume fallout (Haymon and Kastner, 1981; Gurvich, 2006). Their depositional environment is controlled by volcanic activity and a generally active tectonic setting (Carey and Sigurdson, 1984).

The massive sulphide mineralization of the Lemarchant deposit has a known close genetic and spatial association with metalliferous mudstones and a generally well-preserved stratigraphic succession of the lithofacies (Copeland et al., 2008, 2009). Therefore, the Lemarchant deposit is an excellent location for a detailed case study to better understand the hydrothermal system that led to the formation of metalliferous mudstones that are associated with massive sulphides. The other metalliferous mudstones and graphitic shales occurring in the Tally Pond volcanic belt have less obvious spatial and/or genetic relationships to VMS-style mineralization. Thus, this PhD project provides a possibility to perform a detailed reconstruction of the hydrothermal systems that led to the formation of the Lemarchant metalliferous mudstones and massive sulphide mineralization (Chapter 2 and 3), and better understand the relationships of the Lemarchant and other metalliferous mudstones and graphitic shales to massive sulphide mineralization in the Tally Pond volcanic belt, which can be further utilized to provide insight into their paleotectonic environment of formation (Chapter 4 and 5).

The purpose of this study is to apply field, isotopic, mineralogical and lithogeochemical proxies to: 1) identify and/or confirm a hydrothermal-exhalative origin of metalliferous mudstones occurring in the Tally Pond volcanic belt (Lemarchant and others); 2) use mineral specific S isotope analyses of polymetallic sulphides in the Lemarchant mudstones (via SIMS - secondary ion mass spectrometer - microanalysis) to evaluate S sources in the mudstones and to delineate S sources within the context of the paragenesis and the multi-stage evolution of the underlying deposit; 3) determine Pb and Nd isotopic compositions of the Lemarchant mudstones to better define the tectonic environment and provenance of the Lemarchant hydrothermal system; 4) investigate a

potential spatial association of the Tally Pond belt graphitic shales with massive sulphide mineralization; and 5) better understand the depositional environment of the sedimentary rocks in the Tally Pond volcanic belt in terms of their bulk geochemical composition, the chemical composition of contributing fluids, the paleoredox conditions of the ambient seawater, and the rift basin characteristics. Upper Cambrian to Lower Ordovician black shales from Bell Island, eastern Newfoundland, were also utilized as an example of detrital shales that are not spatially and genetically associated with massive sulphide mineralization, thus providing a background dataset to compare to those from hydrothermally active volcanic basins (Fig. 1.1B). The results of this study are of significance not only for occurrences of metalliferous mudstones and graphitic shales and associated VMS deposits within the Tally Pond volcanic belt, but also have exploration implications for mudstone/shale-associated VMS districts globally.

1.2 Hydrothermal metalliferous sedimentary rocks

Metalliferous sedimentary rocks (also described as exhalites, iron formation, hydrothermal mudstones) have often a genetic and spatial association with ancient volcanogenic massive sulphide (VMS) deposits (Franklin et al., 1981; Lydon, 1984; Kalogeropoulos and Scott, 1989; Spry et al., 2000; Peter, 2003; Hannington, 2014). Since VMS deposits are small targets for exploration, it is important to identify potential ore bearing horizons, such as metalliferous mudstones and graphitic shales (Franklin et al., 1981; Gibson et al., 2007). These sediments can be used as stratigraphic marker horizon and accordingly, in the dicovery of massive sulphides (Franklin et al., 1981; Peter, 2003;

Gibson et al., 2007). The genesis of modern metalliferous deep sea sediments, which occur along active spreading centres (ocean ridges, rifted arcs, or backarc basins), and the ancient (meta-)metalliferous mudstones are principally similar in their formation (German and Von Damm, 2003; Hannington et al., 2005; Gurvich, 2006). They are interpreted to form from seafloor hydrothermal plume fallout, when hot, reduced, and metal-rich vent fluids are exhaled from hydrothermal vents and mix with the cold, oxidized, sulphate-rich ambient seawater (Haymon and Kastner, 1981; Gurvich, 2006). The hydrothermally-derived metalliferous sediments represent a hiatus in the volcanic activity, where the deposition of hydrothermal matter dominates over the abiogenic pelagic background sedimentation (Lydon, 1984). The term 'exhalites' is often used to describe such sediments and was first introduced by Ridler (1971) to describe interbedded volcaniclastic and/or detrital and chemical sedimentary rocks, but metalliferous deep-sea sediments were already documented in the reports of the Challenger Expedition 1872 to 1876 (Dekov et al., 2010). This group of hydrothermally-derived sedimentary rocks have numerous names and forms including: iron formation, tetsusekiei ('iron quartz'), tuffite, vasskis ('Weißkies' = 'white sulphide', also used for sulphidic black chert), etc. (Peter and Goodfellow, 1996; Spry et al., 2000; Peter, 2003).

These exhalative rocks are the product of deposition from hydrothermal plumes associated with seafloor vents. In general, the majority of the metals dissolved in the hydrothermal fluids emanating from the vents (≥90%) are dispersed by the buoyant and neutrally-buoyant hydrothermal plume, and subsequently precipitate as metalliferous mudstone, up to several kilometres away from the hydrothermal vent (Hannington et al., 1995; Rudnicki, 1995; Ohmoto, 1996; Gurvich, 2006). As a result, only a small portion

(≤10%) of the metals is trapped within the host rock and/or the sealing semi-permeable layer of metalliferous mudstone (Converse et al., 1984; Hekinian et al., 1993). Hydrothermal Fe precipitates occur close to the vent as Fe-sulphides and -oxyhydroxides, but can be distributed even on basin-wide scales (Resing et al., 2015). The impermeable to semi-permeable layer of unconsolidated sediment that is capping the massive sulphide lens, also likely increases the likelihood of preservation of massive sulphides (Fig. 1.2; Lydon, 1984; Hekinian et al., 1993; Hannington et al., 1995; Gurvich, 2006). Additionally, this geological membrane helps to retain more of the metal-rich hydrothermal fluids within the massive sulphide mound and decreases the amount of metals lost to the hydrothermal plume (Large, 1992; Kharaka and Hanor, 2014). Furthermore, metalliferous mudstones provide a record of processes associated with ore formation, including the relative importance of vent fluid contributions, seawater scavenging of elements by hydrothermal particles, and detrital sedimentation associated with volcanism and sedimentary activity (Hannington et al., 1995; German and Von Damm, 2003). The high temperature, reduced, and metal-rich hydrothermal vent fluids have a distinctly different chemical signature from the cold, oxidized and sulphate-rich ambient seawater (German et al., 1990; Hannington et al., 1995; German and Von Damm, 2003; Tivey, 2007). Mixing of these two fluid types creates mixed chemical patterns in the sediment precipitating from the plume (Rudnicki, 1995; Gurvich, 2006). Therefore, the bulk composition of metalliferous mudstones provides significant insight into the relative roles of hydrothermal, detrital, and scavenging processes that play an important role in the genesis of hydrothermal sedimentary rocks (de Baar et al., 1988; German and Von Damm, 2003; Peter, 2003).

1.3 A Multi-element lithogeochemical approach

1.3.1 Major elements – A method to identify hydrothermal versus detrital matter and alteration patterns

In close proximity to the hydrothermal vent site, polymetallic (Fe, Cu, Zn, Pb) sulphides and accompanying phases, such as barite, anhydrite, amorphous silica, and Al-poor clays (nontronite), co-precipitate from the buoyant plume within, or immediately after, exiting the black smoker chimney (Haymon and Kastner, 1981; Lydon, 1984; Haymon et al., 1993; Hodkinson and Cronan, 1995; Binns, 2004; Gurvich, 2006; Hannington, 2014). Detrital Al concentrations are lowest along the ridge axis and Al can be used as a tracer of detrital input (Boström et al., 1969; Gurvich, 2006). Accordingly, comparing the relative enrichments in base and transition metals, such as Fe, Mn, Cu, and Pb (exhalative), relative to Al (detrital), enables the elucidation of the relative contribution of hydrothermal and detrital components in the metalliferous sediments (Boström and Peterson, 1966; Peter, 2003). During and immediately after the precipitation of the metalliferous mudstones, hydrothermal and diagenetic alteration commences due to on-going hydrothermal activity. Since the major elements have variable mobility, with the alkali elements exhibiting considerable mobility during hydrothermal alteration and diagenetic processes, they can be compared to the immobile Al_2O_3 (Nesbitt and Young, 1982; Nesbitt, 2003). These syn- and post-depositional effects on the hydrothermal metalliferous sediments are due to the interaction of the rock with various fluids (hydrothermal, seawater, pore waters) in distinctive geochemical

environments (p, T, pH), resulting in a modified sediment with new characteristic chemical signatures (Hannington et al., 1995; Nesbitt, 2003).

1.3.2 Rare earth element and trace element bulk composition

During mixing of the hydrothermal fluids with seawater oxyanions (HPO_4^{2-}, HVO_4^{2-}, CrO_4^{2-}, $HAsO_4^{2-}$), trace elements, and rare earth elements (REE) are scavenged from seawater onto Fe-oxyhydroxides, and subsequently deposited on the mount flanks and in topographic depressions around the hydrothermal vent site in a rift-graben or caldera basin (Fig. 1.3; Rudnicki, 1995; Peter, 2003). The longer the residence time of the hydrothermal particles in the plume, the more scavenging from seawater occurs (Rudnicki, 1995; Peter 2003). Hydrothermal vent fluids have generally high temperatures (>250°C), are acidic and reduced (Von Damm, 1990; Hannington et al., 1995). Under these physicochemical conditions, dominantly divalent Eu exists in solution, and/or is bound in related complexes (Sverjensky, 1984; Bau, 1991, 1993). Europium exists in di- or trivalent form because the Eu^{2+}/Eu^{3+}-redox equilibrium is strongly temperature-dependent (Sverjensky, 1984; Bau, 1991, 1993; Peter, 2003). The Eu^{2+} is released into the hydrothermal fluid during the hydrothermal circulation in the reaction and discharge zone, when plagioclase breaks down (German and Von Damm, 2003; Peter, 2003). The divalent Eu is preferentially incorporated into the feldspar mineral structure, because of its larger ionic radius (1.25 Å) than the one from Eu^{3+} (1.066 Å). Due to the very similar ionic radii of Eu^{2+} and Sr^{2+} (1.25 Å), Eu can substitute for Sr on its specific sites in feldspars, especially Ca-plagioclase (McLennan, 1989). The other REE, except Ce, occur

in the trivalent form only. Consequently, there is no fractionation of the trivalent REE and Eu^{3+}, only with Eu^{2+}, causing a positive Eu^{2+} anomaly in the fluids and associated precipitates (German and Von Damm, 2003; Peter, 2003). This positive Eu anomaly is defined as $Eu/Eu^* = (Eu_{sample}/1.08)/ \sqrt{((Sm_{sample}/5.55)*(Gd_{sample}/4.66))}$ using the equations after McLennan (1989) and is a distinctive geochemical feature for high-T (>250°C) hydrothermal vent fluids and can indicate a hydrothermal origin of the sediment. If the hydrothermal fluids did not interact with the surrounding rocks at temperatures above 250°C, no divalent Eu is present, and thus no fractionation from the other REE^{3+} and no positive Eu anomaly will occur (Sverjensky, 1984). One caveat exists however, as detrital sediments that have no positive Eu, but strongly negative Eu anomalies when chondrite-normalized, can contaminate hydrothermal sediments and, if in sufficient abundance, can mask a positive Eu anomaly (Peter et al., 2003).

Cerium also exhibits variability in the valence state and is particularly redox sensitive in metalliferous sediments (Sverjensky, 1984; McLennan, 1989; Bau, 1991; Bau, 1993; Peter, 2003). Immediately after mixing of the reduced hydrothermal fluids with the oxidized ambient seawater, Ce^{3+} oxidizes to the less soluble Ce^{4+} (Bau and Koschinsky, 2009). This fractionates Ce^{4+} from the REE^{3+} (Peter, 2003; Bau and Koschinsky, 2009; Hannington and Monecke, 2009) and results in a negative Ce anomaly of the surrounding seawater. The Ce anomaly is defined as $Ce/Ce^* = (Ce_{sample}/79.6)/ \sqrt{((La_{sample}/38.2)*(Pr_{sample}/8.83))}$ using the equations after McLennan (1989). Fe-oxyhydroxides within metalliferous hydrothermal sediments gain their REE from the hydrothermal vent fluids, and from seawater (Elderfield and Greaves, 1981; Mills, 1995). The presence of negative Ce anomalies in the hydrothermal sediments results from

mixing of the vent fluids with Ce-depleted oxygenated seawater and scavenging of seawater REE onto Fe-oxide/-oxyhydroxide particles (German and Elderfield, 1990; Hannington and Monecke, 2009). In contrast, if there is minimal scavenging or reaction with seawater, the hydrothermal sediment will have no Ce anomalies, because of the nature of vent fluids and the lack of oxidation of Ce^{3+} to Ce^{4+} (German and Elderfield, 1990; Peter and Goodfellow, 2003). Without this oxidation, no fractionation of Ce^{3+} from other trivalent REE will take place and the hydrothermal sediments will have Ce signatures similar to the vent fluids (Mills et al., 2001; Peter, 2003; Humphris and Bach, 2005).

Similarily to Eu anomalies, caution is required in interpreting Ce anomalies as detrital sedimentary material can also affect them. In particular, the absence of negative Ce anomalies can further be caused by significant amounts of detrital input relative to the hydrothermal component (Peter and Goodfellow, 2003). Nevertheless, sediments deposited in a vent proximal environment are expected to have a more strongly pronounced hydrothermal signature, whereas in sediments that precipitated in more distal environments seawater characteristics prevail (Rudnicki, 1995; German and Von Damm, 2003). Ultimately, the hydrothermal sediments that precipitate from these paleoenvironments record prevailing redox conditions at the time of deposition.

1.3.3 Deposit scale and regional tectonic setting investigations using S, Pb, and Nd isotopes

Hydrothermal sedimentary rocks that are associated with volcanogenic massive sulphides can have S derived from various sources and processes, both inorganic and organic. Inorganic sources include: 1) thermochemical reduction of seawater sulphate (TSR); 2) magmatic contributions through leaching of S from igneous rocks or direct magmatic fluid/volatile input; and/or 3) sedimentary-diagenetic sulphides (Ohmoto and Rye, 1979; Ohmoto and Goldhaber, 1997; Seal, 2006; Shanks, 2014). Thermochemcial sulphate reduction creates and contributes hydrogen sulphide (H_2S) to the hydrothermal fluids, which are released into the ambient seawater via black smoker chimneys or as diffuse flow (Von Damm, 1990; Hannington et al., 1995; German and Von Damm, 2003. This diffuse flow is caused by hot pore waters that circulate upwards through the porous sulphide mound and the flanking metalliferous sediments and subsequently emanate onto the seafloor (Gundersen et al., 1992; Elsgaard et al., 1994; Hannington et al., 1995; German and Von Damm, 2003; Hannington, 2014). TSR generally results in sulphide minerals in VMS that are ~17-25 per mil lower than the $\delta^{34}S$ of seawater sulphate at the time of deposit formation (e.g., Sangster, 1968; Kampschulte and Strauss, 2004; Huston et al., 2010). Additionally to TSR, S can be leached from igneous sources (± direct magmatic S contributions), resulting in massive sulphides with a $\delta^{34}S$ of 0±3 ‰ (Ohmoto and Rye, 1979; Shanks et al., 1987; Campbell and Larson, 1998; Shanks, 2001).

Biogenically-derived ("organic") sulphur contributes substantially to some massive sulphide deposits and associated metalliferous mudstones. The organic S is either derived from the biogenic/microbial (bacteria and archaea) reduction of seawater sulphate (BSR), and/or from the microbial disproportionation of sulphur intermediates, with an intermediate step of biogenic/microbial sulphide oxidation (BSO) (Harrison and Thode,

1958; Elsgaard et al., 1994; Canfield, 2001; Habicht and Canfield, 2001; Shanks, 2001; Seal, 2006; Shanks, 2014). The large $\Delta^{34}S_{sulphate\text{-}H_2S}$ fractionation factors that are associated with biogenic/microbial sulphate reduction, coupled with microbial disproportionation of S intermediate compounds, result in sedimentary (and massive) sulphides with strong ^{34}S-depletion (Bak and Pfennig, 1987; Jørgensen, 1990; Jørgensen et al., 1992; Habicht and Canfield, 1997; Canfield, 2001; Habicht and Canfield, 2001). Accordingly, the S isotope compositions of polymetallic sulphides in metalliferous mudstones give insight into the various S sources that contributed to the multistage evolution of the Lemarchant hydrothermal system.

Lead isotopic compositions of sulphides (e.g., galena) provide the ability to determine the source of lead (and, by interference, other metals) within the massive sulphides and associated metalliferous mudstones, which in turn can be used to understand the tectonic setting of formation and lithological provenance (Zartman and Doe, 1981; Swinden and Thorpe, 1984; Tosdal et al., 1999; Pollock and Wilton, 2001; Ayuso et al., 2003). In VMS deposits, Pb is predominantly leached from basement rocks (Franklin and Thorpe, 1982; Swinden and Thorpe, 1984; Tosdal et al., 1999; Ayuso et al., 2003). Given the heterogeneity of the crust and mantle there can be highly variable signatures in galena in VMS deposits (e.g., Ayuso et al. 2003), with crustal sources having more radiogenic Pb values, whereas mantle-derived sources have less radiogenic, juvenile Pb (Franklin and Thorpe 1982; Swinden and Thorpe 1984).

Similar to Pb isotopes, Nd isotopes can also be utilized to understand the tectonic environment and provenance of sediments (McCulloch and Wasserburg, 1978; Creaser et

al., 1997; McDaniel et al., 1997; McLennan et al., 2003). Sm and Nd preferentially partition into different reservoirs that evolve towards characteristic Sm-Nd signatures over time, with crustal sources having evolved signatures (i.e., low $^{143}Nd/^{144}Nd$ signatures), and juvenile mantle reservoirs (with high $^{143}Nd/^{144}Nd$; McCulloch and Wasserburg, 1978; Rollinson, 1993). The epsilon Nd (εNd) values describe variations and deviations of the $^{143}Nd/^{144}Nd$ from the chondritic uniform reservoir (CHUR) value, whereby εNd > CHUR represents juvenile and εNd < CHUR evolved sources (Rollinson, 1993). εNd_t was calculated by $\varepsilon Nd_t = (^{143}Nd/^{144}Nd_{rock,t} / {}^{143}Nd/^{144}Nd_{CHUR,t}) \times 10^4$ after Rollinson (1993).

1.4 Sampling, methods, quality assurance, and quality control (QA/QC)

Metalliferous mudstones and graphitic shales were sampled from drill core from 12 deposits, prospects, and showings within the Tally Pond volcanic belt and from three locations on coastal outcrops on Bell Island. Detailed sampling procedures are given in Appendices 2.1, 3.1, 5.1 and in Chapter 4. Samples for whole-rock lithogeochemical studies were analysed for major and minor elements by lithium metaborate/tetraborate fusion followed by HNO_3 dissolution and analysis by inductively coupled plasma (atomic) – emission spectroscopy (ICP-ES). Carbon and S were obtained by infrared spectroscopy and Hg was obtained by the cold vapour flow injection mercury system (Hg-FIMS). All of the former analyses were performed by Activation Laboratories Ltd. (Actlabs) in Ancaster, Canada, which uses mild steel mills to crush, split, and pulverize the rock samples. From Actlabs returned pulps were used to analyse additional trace

elements, including rare earth elements (REE), high field strength elements (HFSE), trace metals, and many low field strength elements (LFSE), by inductively coupled plasma-mass spectrometry (ICP-MS) in the Department of Earth Sciences at Memorial University, using screw-top Teflon® bomb (Savillex®) multi-acid dissolution. The multi-acid (HNO_3, HF, HCl, H_3BO_3, and H_2O_2) whole-rock dissolution process was a modified version of that of Jenner et al. (1990) and Longerich et al. (1990) to account for the high amounts of carbonaceous material in the samples; the procedures are described in detail in Chapter 2, Appendix 2.1.

Metalliferous mudstone/exhalite types from the Lemarchant deposit were further selected for S and Pb isotopic studies including those that: 1) are immediately associated with, or occur stratigraphically within five meters of, massive sulphides (exhalative metalliferous mudstone; i.e., EMS-type) and represent the main stratigraphic marker between the felsic and mafic volcanic rocks (Bindons Pond and Lake Ambrose formations, respectively); 2) do not have an obvious relationship with mineralization, but occur along the same stratigraphic contact between the felsic and mafic volcanic rocks (felsic-exhalite-mafic; i.e., FEM-type); 3) occur as interflow exhalite mudstones within the hanging wall basalts (interflow exhalite; i.e., IFE-type). Representative samples of these three types of exhalative mudstone (EMS, FEM, and IFE) were selected for secondary ion mass spectrometer (SIMS) microanalysis based on stratigraphic, spatial, textural and paragenetic relationships as deduced from field and reflected and transmitted light microscopy. The data were obtained using a Cameca IMS 4f SIMS equipped with an ETP 133H multiple-dynode electron multiplier (em) and processed through ECL-based pulse-counting electronics with an overall dead time of 11 ns in the MAF-IIC

Microanalysis Facility at Memorial University. Detailed procedures are described in Chapter 3, Appendix 3.1.

From the Lemarchant mudstones, 12 representative samples were furthermore selected for Nd isotopic determinations. Additionally, two samples from least altered felsic and mafic volcanic rocks of the Bindons Pond and Lake Ambrose formations, respectively, were selected for analyses. Samarium and Nd isotopic compositions were measured at Memorial University using a multicollector Finnigan Mat 262 mass spectrometer. More detailed procedures are described in Chapter 4.

1.5 Manuscript format

This thesis is written in manuscript format and is a compilation of individual research manuscripts that range from being accepted by an international journal to manuscript drafts that will be submitted. Chapter 2 has been peer reviewed and was published in November 2015 in the journal Economic Geology (v. 110, p. 1835-1859). Chapter 3 has been internally and peer reviewed and is currently in review after re-submission at the journal Mineralium Deposita. The first round of revisions suggested by external reviewers from Mineralium Deposita (Drs. David Huston and Fernando Tornos) have been completed and are incorporated in this chapter. Chapter 4 has been internally reviewed and will be submitted following the thesis completion. Chapter 5 has been internally reviewed and is currently in review at the Canadian Journal of Earth Sciences. Each chapter is an individual article and repetition in the context of the thesis is, unfortunately, unavoidable.

Chapter 2 investigates the importance of hydrothermal metalliferous mudstones as stratigraphic marker horizon and vectoring tool for VMS deposits, which is well documented in the literature. However, in the Appalachian-Caledonide orogen there is minimal information on hydrothermal mudstones for the Newfoundland component of the Appalachians. In this paper we provide a detailed field, mineralogical and lithogeochemical study of stratigraphically well-constrained hydrothermal metalliferous mudstones that are intimately associated with the Cambrian precious metal-bearing Zn-Pb-Ba-Au-Ag Lemarchant VMS deposit in the Tally Pond belt, central Newfoundland. The hydrothermal mudstone samples have a wide spatial and stratigraphic distribution around the massive sulphides and this enables one to identify and quantify the hydrothermal contribution to these ancient metalliferous sediments, test certain geochemical and mineralogical proxies that can be used as proximity vectors to mineralization, and gain a better understanding of the hydrothermal system that led to the formation of the massive sulphides. Shale-hosted and/or -related mineralization not only occurs in the Canadian Appalachians, but in many other locations world-wide, e.g., Iberian Pyrite belt, and also can be related to other types of mineral deposits (e.g., the Ni-Cu-Zn-rich blackshales in Talvivaara). Thus, the results of these studies are of interest and importance to readers globally and from different economic geology backgrounds.

Chapter 3 examines the role of S and Pb isotopes of polymetallic sulphides hosted in the Lemarchant metalliferous mudstones. There are numerous S and Pb isotopic studies in VMS deposits in the literature; however, hydrothermal exhalites that are associated with VMS deposits are less represented. That is especially so for hydrothermal exhalites and associated VMS deposits located in the Newfoundland component of the

Appalachian-Caledonide orogen. In this paper we provide a detailed field, mineralogical and S and Pb isotopic study of stratigraphically well-constrained hydrothermal exhalites that are spatially and genetically associated with the Cambrian precious metal-bearing Zn-Pb-Cu-Au-Ag-Ba-Lemarchant VMS deposit in the Tally Pond belt, central Newfoundland. The hydrothermal exhalites precipitated pre-, syn, and post-mineralization and hence, provide an excellent opportunity to study the evolution of a hydrothermal system in regard to the paragenesis of the polymetallic sulphide phases present in the exhalites. Exhalites have a wide spatial and stratigraphic distribution around the massive sulphides and thus enable one to identify and quantify the varying S contributions and importance of hydrothermal fluids, seawater, and magmatic fluid inputs. Additionally, metalliferous sedimentary rocks provide the possibility to study the role of inorganic versus organic processes that contributed to the precipitates as a function of both time and in spatial relationship to mineralization. The Pb isotopic data illustrate that the exhalites have variable Pb sources (juvenile and evolved), and provide insight into the regional tectonic environment at the time of ore formation. Additionally, a combination of S and Pb isotopic systems measured on galena in the exhalites may provide a new proxy that can be used as a vector to mineralization in similar exhalative sedimentary rocks. Overall, this detailed S and Pb isotopic study on polymetallic sulphides hosted within exhalites helps to gain a better understanding of the hydrothermal system that led to the formation of the massive sulphides at Lemarchant.

Chapter 4 represents a provenance study of the Lemarchant metalliferous mudstones occurring within the Tally Pond volcanic belt, central Newfoundland, using Nd isotopic compositions of the mudstones and compares those to previously reported

whole-rock lithogeochemical and Pb isotopic data. The results of this study indicate that the detrital component of the Lemarchant mudstones were mixtures of both continental and mafic sources, likely deposited within a pericontinental rifted arc environment. The Nd isotopic compositions of the Lemarchant mudstones support the presence of crustal basement that underlies the Tally Pond volcanic rocks, which is consistent with existing results presented in the literature.

Chapter 5 is a review of metalliferous mudstone and graphitic shale occurrences within the Tally Pond volcanic belt and their spatial and/or genetic association with base metal-rich VMS-style mineralization. Lithogeochemical and petrological proxies that were studied and tested on the Lemarchant metalliferous mudstones in Chapter 2 were applied to confirm ore refute a hydrothermal origin of metalliferous mudstones (other than Lemarchant) in the Tally Pond volcanic belt, and to determine and quantify a potential proximity to massive sulphide mineralization. The study shows that, locally, VMS deposits, prospects, and showings in the Tally Pond volcanic belt are genetically and/or spatially associated with metalliferous mudstones of hydrothermal origin. However, unlike the proximal Lemarchant mudstones, it is suggested that they were predominantly deposited in a more distal depositional environment. Nevertheless, it is important that these distal metalliferous mudstones are to be identified, since they represent the stratigraphic mineralization-bearing horizon. The graphitic shales of the Tally Pond volcanic belt are proposed to be of detrital origin. However, the base of the graphitic shale sequence locally has a spatial association with mineralization and accordingly, may represent another prospective stratigraphic horizon.

Chapter 6 summarizes the major results of this study and outlines possible future research projects, such as, e.g., role of bacteria, micro - and macro? - fauna in Cambrian hydrothermal Lemarchant mudstones, and the use of hyperspectral analysis on the Lemarchant mudstones.

1.6 References

Ayuso, R. A., Wooden, J. L., Foley, N. K., Slack, J. F., Sinha, A. K., and Persing, H., 2003, Pb isotope geochemistry and U-Pb zircon (SHRIMP-RG) ages of the Bald Mountain and Mount Chase massive sulfide deposits, northern Maine; mantle and crustal contributions in the Ordovician: Economic Geology Monograph, v. 11, p. 589-609.

Bak, F., and Pfennig, N., 1987, Chemolithotrophic growth of Desulfovibrio sulfodismutans sp. nov. by disproportionation of inorganic suulfur compounds: Archives of Microbiology, v. 147, p. 184-189.

Bau, M., 1991, Rare-earth element mobility during hydrothermal and metamorphic fluid rock interaction and the significance of the oxidation-state of europium: Chemical Geology, v. 93, p. 219-230.

_____1993, Effects of syn-depositional and postdepositional processes on the rare-earth element distribution in Precambrian iron-formations: European Journal of Mineralogy, v. 5, p. 257-267.

Bau, M., and Koschinsky, A., 2009, Oxidative scavenging of cerium on hydrous Fe oxide: Evidence from the distribution of rare-earth elements and yttrium between Fe oxides and Mn oxides in hydrogenetic ferromanganese crusts: Geochemical Journal, v. 43, p. 37-47.

Binns, R. A., 2004, Eastern Manus Basin, Papua New Guinea: guides for volcanogenic massive sulphide exploration from a modern seafloor analogue, *in* McConachy, T. F., and McInnes, B. I. A., eds., CSIRO Explores, 2, p. 59-80.

Boström, K., and Peterson, M. N., 1966, Precipitates from hydrothermal exhalations on the East Pacific Rise: Economic Geology, v. 61, p. 1258-1265.

Boström, K., Peterson, M. N., Joensuu, O., and Fisher, D. E., 1969, Aluminum-poor ferromanganoan sediments on active oceanic ridges: Journal of Geophysical Research, v. 74, p. 3261-3270.

Campbell, A. R., and Larson, P. B., 1998, Introduction to stable isotope applications in hydrothermal systems., *in* Richards, J. P., and Larson, P. B., eds., Techniques in Hydrothermal Ore Deposits Geology: Reviews in Economic Geology, p. 173-193.

Canfield, D. E., 2001, Isotope fractionation by natural populations of sulfate-reducing bacteria: Geochimica et Cosmochimica Acta, v. 65, p. 1117-1124.

Carey, S., and Sigurdson, H., 1984, A model of volcanogenic sedimentation in marginal basins., *in* Kokelaar, B. P., and Howells, M. F., eds., Marginal Basin Geology: Volcanic and Associated Sedimentary and Tectonic Processes in Modern and Ancient Marginal Basins., 16(1): Geological Society Special Publication, p. 37-58.

Converse, D. R., Holland, H. D., and Edmond, J. M., 1984, Flow rates in the axial hot springs of the East Pacific Rise (21°N): Implications for the heat budget and the formation of massive sulfide deposits: Earth and Planetary Science Letters, v. 69, p. 159-175.

Copeland, D. A., McClenaghan, S. H., and Piercey, S. J., 2008, 9th year assessment report on diamond drilling, lithogeochemistry, pulse EM surveying and linecutting

on licence 8183M, South Tally Pond Property, Rogerson Lake Area, Newfoundland and Labrador, NTS 12A/10 and 12A/07: St. John's, NL, Canada, Newfoundland and Labrador Geological Survey Assessment File 012A/1459, p. 1-85.

Copeland, D. A., Toole, R. M., and Piercey, S. J., 2009, 10th year supplementary assessment report on soil sampling, linecutting, Titan 24 Geophysical Surveying, diamond drilling and petrography, licence 8183M, South Tally Pond Property, Rogerson Lake Area, Newfoundland and Labrador, NTS 12A/10 and 12A/07: St. John's, NL, Canada, Newfoundland and Labrador Geological Survey Assessment File, p. 1-56.

Creaser, R. A., Erdmer, P., Stevens, R. A., and Grant, S. L., 1997, Tectonic affinity of Nisutlin and Anvil assemblage strata from the Teslin Tectonic zone, northern Canadian Cordillera: Constraints from neodymium isotope and geochemical evidence: Tectonics, v. 16, p. 107-121.

de Baar, H. J. W., German, C. R., Elderfield, H., and van Gaans, P., 1988, Rare earth element distributions in anoxic waters of the Cariaco Trench: Geochimica et Cosmochimica Acta, v. 52, p. 1203-1219.

Dekov, V. M., Cuadros, J., Kamenov, G. D., Weiss, D., Arnold, T., Basak, C., and Rochette, P., 2010, Metalliferous sediments from the H.M.S. Challenger voyage (1872-1876): Geochimica et Cosmochimica Acta, v. 74, p. 5019-5038.

Elderfield, H., and Greaves, M. J., 1981, Negative cerium anomalies in the rare earth element patterns of oceanic ferromanganese nodules: Earth and Planetary Science Letters, v. 55, p. 163-170.

Elsgaard, L., Isaksen, M. F., Jørgensen, B. B., Alayse, A.-M., and Jannasch, H. W., 1994, Microbial sulfate reduction in deep-sea sediments at the Guaymas Basin hydrothermal vent area: Influence of temperature and substrates: Geochimica et Cosmochimica Acta, v. 58, p. 3335-3343.

Evans, D. T. W., and Kean, B. F., 2002, The Victoria Lake supergroup, central Newfoundland - its definition, setting and volcanogenic massive sulphide mineralization, Newfoundland and Labroador Department of Mines and Energy, Geological Survey, Open File NFLD/2790, p. 1-68.

Franklin, J. M., Sangster, D. M., and Lydon, J. W., 1981, Volcanic-associated massive sulfide deposits, *in* Skinner, B. J., ed., Economic Geology Seventy-Fifth Anniversary Volume, Society of Economic Geologists, p. 485-627.

Franklin, J. M., and Thorpe, R. I., 1982, Comparative metallogeny of the Superior, Slave and Churchill provinces: Special Paper - Geological Association of Canada, v. 25, p. 3-90.

German, C. R., and Elderfield, H., 1990, Application of the Ce anomaly as a paleoredox indicator: The ground rules: Paleoceanography, v. 5, p. 823-833.

German, C. R., Klinkhammer, G. P., Edmond, J. M., Mitra, A., and Elderfield, H., 1990, Hydrothermal scavenging of rare-earth elements in the ocean: Nature, v. 345, p. 516-518.

German, C. R., and Von Damm, K. L., 2003, Hydrothermal Processes, Treatise on Geochemistry: Oxford, Pergamon, p. 181-222.

Gibson, H. L., Allen, R. L., Riverin, G., and Lane, T. E., 2007, The VMS model: Advances and application to exploration targeting, *in* Milkereit, B., ed., Proceedings of Exploration 07: Fifth Decennial International Conference on Mineral Exploration: Toronto, ON, p. 717-730.

Griffith, E. M., and Paytan, A., 2012, Barite in the ocean - occurrence, geochemistry, and palaeoceanographic applications: Sedimentology, vol. 59, p. 1-19.

Gundersen, J., K., Jørgensen, B. B., Larsen, E., and Jannasch, H. W., 1992, Mats of giant sulphur bacteria on deep-sea sediments due to fluctuating hydrothermal flow: Nature, v. 360, p. 454-456.

Gurvich, E. G., 2006, Metalliferous sediments of the world ocean - Fundamental theory of deep sea hydrothermal sedimentation, Springer Berlin Heidelberg, p. 1-416.

Habicht, K. S., and Canfield, D. E., 1997, Sulfur isotope fractionation during bacterial sulfate reduction in organic-rich sediments: Geochimica et Cosmochimica Acta, v. 61, p. 5351-5361.

_____2001, Isotope fractionation by sulfate-reducing natural populations and the isotopic composition of sulfide in marine sediments: Geology, v. 29, p. 555-558.

Hannington, M., and Monecke, T., 2009, Global exploration models for polymetallic sulphides in the area: An assessment of lease block selection under the draft regulations on prospecting and exploration for polymetallic sulphides: Marine Georesources & Geotechnology, v. 27, p. 132 - 159.

Hannington, M. D., 2014, Volcanogenic massive sulfide deposits, *in* Holland, H. D., and Turekian, K.K., ed., Treatise on Geochemistry 2nd Edition, 8. Reviews in Economic Geology, Elsevier Ltd, p. 319-350.

Hannington, M. D., de Ronde, C. E. J., and Petersen, S., 2005, Sea floor tectonics and submarine hydrothermal systems, *in* Hedenquist, J. W., Thompson, J. F. H., Goldfarb, R. J., and Richards, J. P., eds., Economic Geology: One Hundredth Anniversary Volume, 1905-2005: Littleton, CO, USA, Society of Economic Geologists, p. 111-142.

Hannington, M. D., Jonasson, I. R., Herzig, P. M., and Petersen, S., 1995, Physical and chemical processes of seafloor mineralization at mid-ocean ridges: Geophysical Monograph, v. 91, p. 115-157.

Harazim, D., Callow, R. H. T., and McIlroy, D., 2013, Microbial mats implicated in the generation of intrastratal shrinkage ('synaeresis') cracks: Sedimentology, v. 6, p. 1621-1638.

Harrison, A. G., and Thode, H. G., 1958, Mechanism of the bacterial reduction of sulphate from isotope fractionation studies: Transactions Faraday Society., v. 54, p. 84-92.

Haymon, R. M., Fornari, D. J., Von Damm, K. L., Lilley, M. D., Perfit, M. R., Edmond, J. M., Shanks Iii, W. C., Lutz, R. A., Grebmeier, J. M., Carbotte, S., Wright, D., McLaughlin, E., Smith, M., Beedle, N., and Olson, E., 1993, Volcanic eruption of the mid-ocean ridge along the East Pacific Rise crest at 9°45–52′N: Direct submersible observations of seafloor phenomena associated with an eruption event in April, 1991: Earth and Planetary Science Letters, v. 119, p. 85-101.

Haymon, R. M., and Kastner, M., 1981, Hot spring deposits on the Eas Pacific Rise 21°N: preliminary description of mineralogy and genesis: Earth and Planetary Science Letters, v. 53, p. 363-381.

Hekinian, R., Hoffert, M., Larqué, P., Cheminée, J. L., Stoffers, P., and Bideau, D., 1993, Hydrothermal Fe and Si oxyhydroxide deposits from South Pacific intraplate volcanoes and East Pacific Rise axial and off-axial regions: Economic Geology, v. 88, p. 2099-2121.

Hodkinson, R. A., and Cronan, D. S., 1995, Hydrothermal sedimentation at ODP Sites 834 and 835 in relation to crustal evolution of the Lau backarck basin, *in* Parson, L. M., Walker, C. L., and Dixon, D. R., eds., Hydrothermal vents and processes., 87, Geological Society Special Publication, p. 231-248.

Humphris, S. E., and Bach, W., 2005, On the Sr isotope and REE compositions of anhydrites from the TAG seafloor hydrothermal system: Geochimica et Cosmochimica Acta, v. 69, p. 1511-1525.

Huston, D. L., Pehrsson, S., Eglington, B. M., and Zaw, K., 2010, The geology and metallogeny of volcanic-hosted massive sulfide deposits: Variations through geologic time and with tectonic setting: Economic Geology, v. 105, p. 571-591.

Jenner, G. A., Longerich, H. P., Jackson, S. E., and Fryer, B. J., 1990, ICP-MS - A powerful tool for high-precision trace element analysis in Earth sciences: Evidence from analysis of selected U.S.G.S. reference samples: Chemical Geology, v. 83, p. 133-148.

Jørgensen, B. B., 1990, A thiosulfate shunt in the sulfur cycle of marine sediments: Science, v. 249, p. 152-154.

Jørgensen, B. B., Isaksen, M. F., and Jannasch, H. W., 1992, Bacterial sulfate reduction above 100°C in deep-sea hydrothermal vent sediments: Science, v. 258, p. 1756-1757.

Kalogeropoulos, S. I., and Scott, S. D., 1989, Mineralogy and geochemistry of an Archean tuffaceous exhalite; the Main Contact Tuff, Millenbach Mine area, Noranda, Quebec: Canadian Journal of Earth Sciences = Journal Canadien des Sciences de la Terre, v. 26, p. 88-105.

Kampschulte, A., and Strauss, H., 2004, The sulfur isotopic evolution of Phanerozoic seawater based on the analysis of structurally substituted sulfate in carbonates: Chemical Geology, v. 204, p. 255-286.

Kharaka, Y. K., and Hanor, J. S., 2014, 7.14 - Deep fluids in sedimentary basins, *in* Turekian, H. D. H. K., ed., Treatise on Geochemistry (Second Edition): Oxford, Elsevier, p. 471-515.

Large, R. R., 1992, Australian volcanic-hosted massive sulfide deposits; features, styles, and genetic models: Economic Geology, v. 87, p. 471-510.

Longerich, H. P., Jenner, G. A., Fryer, B. J., and Jackson, S. E., 1990, Inductively coupled plasma-mass spectrometric analysis of geological samples: A critical evaluation based on case studies: Chemical Geology, v. 83, p. 105-118.

Lydon, J. W., 1984, Ore deposit models; 8, Volcanogenic sulphide deposits; Part I, A descriptive model: Geoscience Canada, v. 11, p. 195-202.

McCulloch, M. T., and Wasserburg, G. J., 1978, Sm-Nd and Rb-Sr chronology of continental crust formation: Science, v. 200, p. 1003-1011.

McDaniel, D. K., McLennan, S. M., and Hanson, G. N., 1997, 8. Provenance of amazon fan muds: constraints from Nd and Pb isotopes, *in* Flood, R. D., Piper, D. J. W., Klaus, A., and Peterson, L. C., eds., Proceedings of the Ocean Drilling Program, Scientific Results, 155: College Station, TX (Ocean Drilling Program).

McLennan, S. M., 1989, Rare earth elements in sedimentary rocks; influence of provenance and sedimentary processes: Reviews in Mineralogy, v. 21, p. 169-200.

McLennan, S. M., Bock, B., Hemming, S. R., Hurowitz, J. A., Lev, S. M., and McDaniel, D. K., 2003, The roles of provenance and sedimentary processes in the geochemistry of sedimentary rocks, *in* Lentz, D. R., ed., Geochemistry of Sediments and Sedimentary Rocks: Evolutionary Considerations to Mineral Deposit-Forming Environments, GEOText 4: St. John's, NL, Canada, Geological Association of Canada, p. 7-38.

Mills, R. A., 1995, Hydrothermal activity and the geochemistry of metalliferous sediment: Geophysical Monograph, v. 91, p. 392-407.

Mills, R. A., Wells, D. M., and Roberts, S., 2001, Genesis of ferromanganese crusts from the TAG hydrothermal field: Chemical Geology, v. 176, p. 283-293.

Nesbitt, H. W., 2003, Petrogenesis of siliciclastic sediments and sedimentary rocks, *in* Lentz, D. R., ed., Geochemistry of Sediments and Sedimentary Rocks: Evolutionary Considerations to Mineral Deposit-Forming Environments, GEOText 4: St. John's, NL, Canada, Geological Association of Canada, p. 39-52.

Nesbitt, H. W., and Young, G. M., 1982, Early Proterozoic climates and plate motions inferred from major element chemistry of luitites: Nature, v. 299, p. 715-717.

Ohmoto, H., 1996, Formation of volcanogenic massive sulfide deposits: The Kuroko perspective: Ore Geology Reviews, v. 10, p. 135-177.

Ohmoto, H., and Goldhaber, M. B., 1997, Sulfur and carbon isotopes, *in* Barnes, H. L., ed., Geochemistry of Hydrothermal Ore Deposits, Third Edition, John Wiley and Sons, p. 517-611.

Ohmoto, H., and Rye, R. O., 1979, Isotopes of sulfur and carbon, *in* Barnes, H. L., ed., Geochemistry of Hydrothermal Ore Deposits, Second Edition: United States, John Wiley & Sons : New York, NY, United States, p. 509-567.

Peter, J. M., 2003, Ancient iron formations: their genesis and use in the exploration for stratiform base metal sulphide deposits, with examples from the Bathurst Mining Camp, *in* Lentz, D. R., ed., Geochemistry of Sediments and Sedimentary Rocks: Secular Evolutionary Considerations to Mineral Deposit-Forming Environments, GEOtext v.4., Geological Association of Canada, p. 145-176.

Peter, J. M., Goodfellow, W. D., and Doherty, W., 2003, Hydrothermal sedimentary rocks of the Heath Steele Belt, Bathurst mining camp, New Brunswick; Part 2, Bulk and rare earth element geochemistry and implications for origin: Economic Geology Monograph, v. 11, p. 391-415.

Piercey, S. J., 2007, Volcanogenic massive sulphide (VMS) deposits of the Newfoundland Appalachians: An overview of their setting, classification, grade-tonnage data, and unresolved questions, *in* Pereira, C. P. G., and Walsh, D. G., eds., Current Research, Report 07-01: St. John's, NL, Geological Survey Branch, p. 169-178.

Piercey, S. J., 2014, Modern Analytical Facilities 2. A review of quality assurance and quality control (QA/QC) procedures for lithogeochemical data. Geoscience Canada 2014, v. 41.

Piercey, S. J., Squires, G. C., and Brace, T. D., 2014, Lithostratigraphic, hydrothermal, and tectonic setting of the Boundary volcanogenic massive sulfide deposit, Newfoundland Appalachians, Canada: Formation by subseafloor replacement in a Cambrian rifted arc: Economic Geology, v. 109, p. 661-687.

Pollock, J. C., and Wilton, D. H. C., 2001, Metallogenic studies of the Tally Pond belt, Victoria Lake Group; trace-element geochemistry and lead-isotope data from the Exploits Subzone, Newfoundland: Report - Government of Newfoundland and Labrador. Dept. of Mines and Energy, Geological Survey, Report: 2001-1, pp.247-266, Mar 2001.

Ranger, M. J., Pickerill, R. K., and Fillion, D., 1984, Lithostratigraphy of the Cambrian? - Lower Ordovician Bell Island and Wabana groups of Bell, Little Bell, and Kellys islands, Conception Bay, eastern Newfoundland: Canadian Journal of Earth Sciences, v. 21, p. 1245-1261.

Resing, J. A., Sedwick, P. N., German, C. R., Jenkins, W. J., Moffett, J. W., Sohst, B. M., and Tagliabue, A., 2015, Basin-scale transport of hydrothermal dissolved metals across the South Pacific Ocean: Nature, v. 523, p. 200-203.

Ridler, R. H., 1971, Analysis of Archean volcanic basins in the Canadian Shield using the exhalite concept: Bulletin of the Canadian Institute of Mining and Metallurgy, v. 64, p. 20.

Rogers, N., van Staal, C., Zagorevski, A., Skulski, T., Piercey, S. J., and McNicoll, V., 2007, Timing and tectonic setting of volcanogenic massive sulphide bearing terranes within the Central Mobile Belt of the Canadian Appalachians, *in* Milkereit, B., ed., Proceedings of Exploration 07: Fifth Decennial International Conference on Mineral Exploration: Toronto, ON, p. 1199-1205.

Rogers, N., van Staal, C. R., McNicoll, V., Pollock, J., Zagorevski, A., and Whalen, J., 2006, Neoproterozoic and Cambrian arc magmatism along the eastern margin of the Victoria Lake Supergroup: A remnant of Ganderian basement in central Newfoundland?: Precambrian Research, v. 147, p. 320-341.

Rollinson, H. R., 1993, Using geochemical data: evaluation, presentation, interpretation, Longman, 352 p.

Rudnicki, M. D., 1995, Particle formation, fallout and cycling within the buoyant and non-buoyant plume above the TAG vent field: Geological Society, London, Special Publication, v. 87, p. 387-396.

Sangster, D. F., 1968, Relative sulphur isotope abundances of ancient seas and strata-bound sulphide deposits: Proceedings of the Geological Association of Canada, v. 19, p. 79-91.

Seal, R. R., II, 2006, Sulfur isotope geochemistry of sulfide minerals: Reviews in Mineralogy and Geochemistry, v. 61, p. 633-677.

Shanks, W. C., 2001, Stable isotopes in seafloor hydrothermal systems: Vent fluids, hydrothermal deposits, hydrothermal alteration, and microbial processes: Reviews in Mineralogy and Geochemistry, v. 43, p. 469-525.

_____2014, 13.3 - Stable isotope geochemistry of mineral deposits, *in* Turekian, H. D. H. K., ed., Treatise on Geochemistry (Second Edition): Oxford, Elsevier, p. 59-85.

Shanks, W. C., III, Woodruff, L. G., Jilson, G. A., Jennings, D. S., Modene, J. S., and Ryan, B. D., 1987, Sulfur and lead isotope studies of stratiform Zn-Pb-Ag deposits, Anvil Range, Yukon: Basinal brine exhalation and anoxic bottom water mixing: Economic Geology, v. 82, p. 600-634.

Spry, P. G., Peter, J. M., and Slack, J. F., 2000, Meta-exhalites as exploration guides to ore, *in* Spry, P. G., Marshall, B., and Vokes, F. M., eds., Metamorphosed and metamorphogenic ore deposits, Reviews in Economic Geology 11: Littleton, CO, Society of Economic Geologists, p. 163-201.

Squires, G. C., and Moore, P. J., 2004, Volcanogenic massive sulphide environments of the Tally Pond Volcanics and adjacent area; geological, lithogeochemical and geochronological results, *in* Pereira, C. P. G., Walsh, D. G., and Kean, B. F., eds., Current Research, Report 04-1: St. John's, NL, Geological Survey Branch, p. 63-91.

Sverjensky, D. A., 1984, Europium redox equilibria in aqueous solutions: Earth and Planetary Science Letters, v. 67, p. 70-78.

Swinden, H. S., 1988, Introduction to volcanogenic sulphide deposits in Newfoundland, *in* Swinden, H. S., and Kean, B. F., eds., The volcanogenic sulphide districts of central Newfoundland, Geological Association of Canada, p. 1-26.

_____1991, Paleotectonic settings of volcanogenic massive sulphide deposits in the Dunnage Zone, Newfoundland Appalachians: Canadian Institute of Mining and Metallurgy Bulletin, v. 84, p. 59-89.

Swinden, H. S., and Thorpe, R. I., 1984, Variations in style of volcanism and massive sulfide deposition in Early to Middle Ordovician island-arc sequences of the Newfoundland Central Mobile Belt: Economic Geology, v. 79, p. 1596-1619.

Tivey, M. K., 2007, Generation of seafloor hydrothermal vent fluids and associated mineral deposits Oceanography, v. 20, p. 50-65.

Tosdal, R. M., Wooden, J. L., and Bouse, R. M., 1999, Pb isotopes, ore deposits, and metallogenic terranes: Reviews in Economic Geology, v. 12, p. 1-28.

van Staal, C. R., and Barr, S. M., 2011, Lithospheric architecture and tectonic evolution of the Canadian Appalachians and associated Atlantic margin, *in* Percival, J. A., Cook, F. A., and Clowes, R. M., eds., Chapter 2 Tectonic Styles in Canada: the LITHOPROBE Perspective, Special Paper 49, Geological Association of Canada, p. 3-55.

Von Damm, K. L., 1990, Seafloor hydrothermal activity; black smoker chemistry and chimneys: Annual Review of Earth and Planetary Sciences, v. 18, p. 173-204.

Williams, H., 1979, Appalachian Orogen in Canada: Canadian Journal of Earth Sciences, v. 16, p. 792-807.

Zagorevski, A., van Staal, C. R., Rogers, N., McNicoll, V. J., and Pollock, J., 2010, Middle Cambrian to Ordovician arc-backarc development on the leading edge of Ganderia, Newfoundland Appalachians: Geological Society of America Memoir, v. 206, p. 367-396.

Zartman, R. E., and Doe, B. R., 1981, Plumbotectonics; the model: Tectonophysics, v. 75, p. 135-162.

Fig. 1.1 A-C

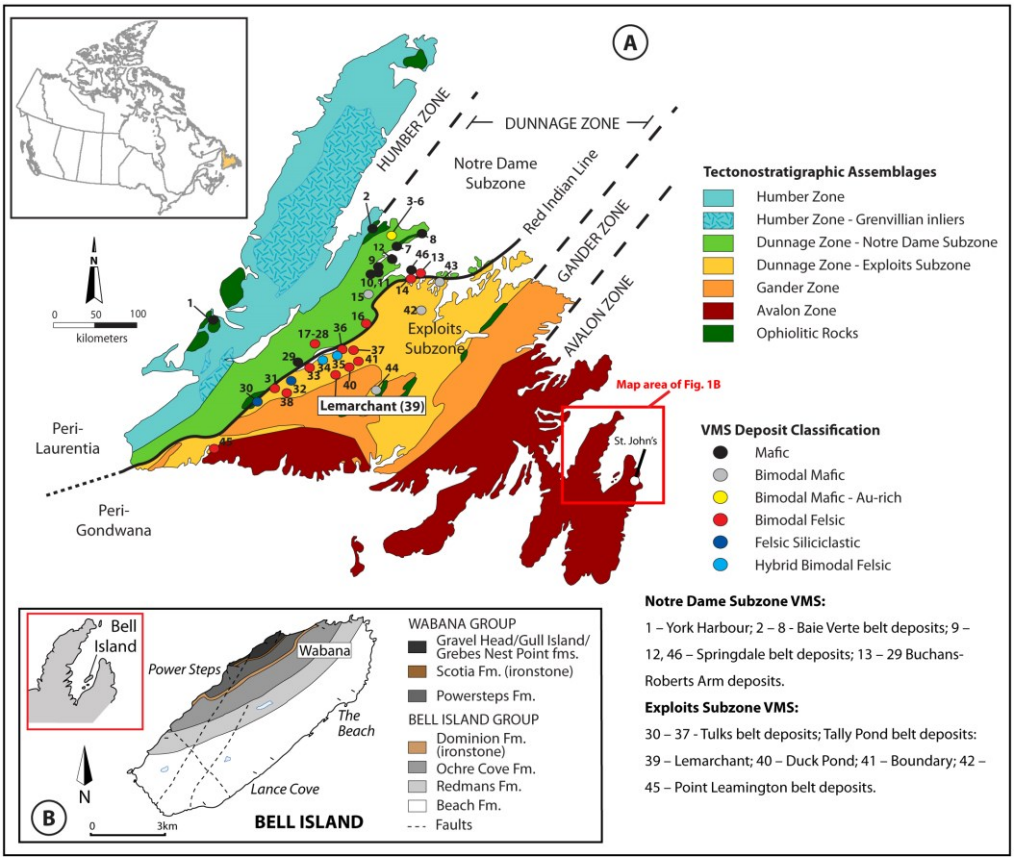

Figure 1.1 *A) Tectonostratigraphic assemblages with the main zones of the Newfoundland Appalachians (Avalon, Gander, Dunnage, and Humber zones) and VMS occurrences within the Notre Dame and Exploits subzones (modified after Swinden, 1991; Piercey, 2007). B) Overview map of the location of Bell Island. Sampled outcrops from Lance Cove, The Beach, and Powersteps (modified after Ranger et al., 1984 and Harazim et al., 2013).*

Fig. 1.2

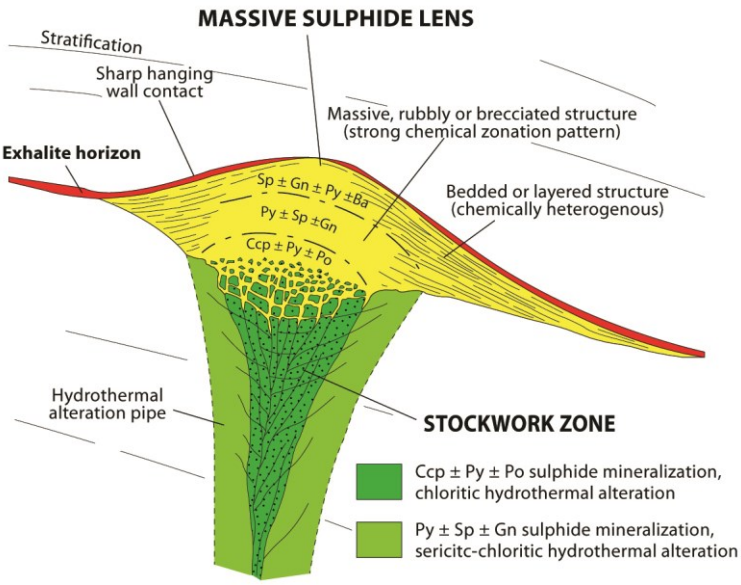

Figure 1.2 *Simplified cross-section of typical VMS deposit with capping layer of metalliferous mudstone/exhalite and discordant alteration zone beneath (modified after Lydon, 1984).*

Fig. 1.3

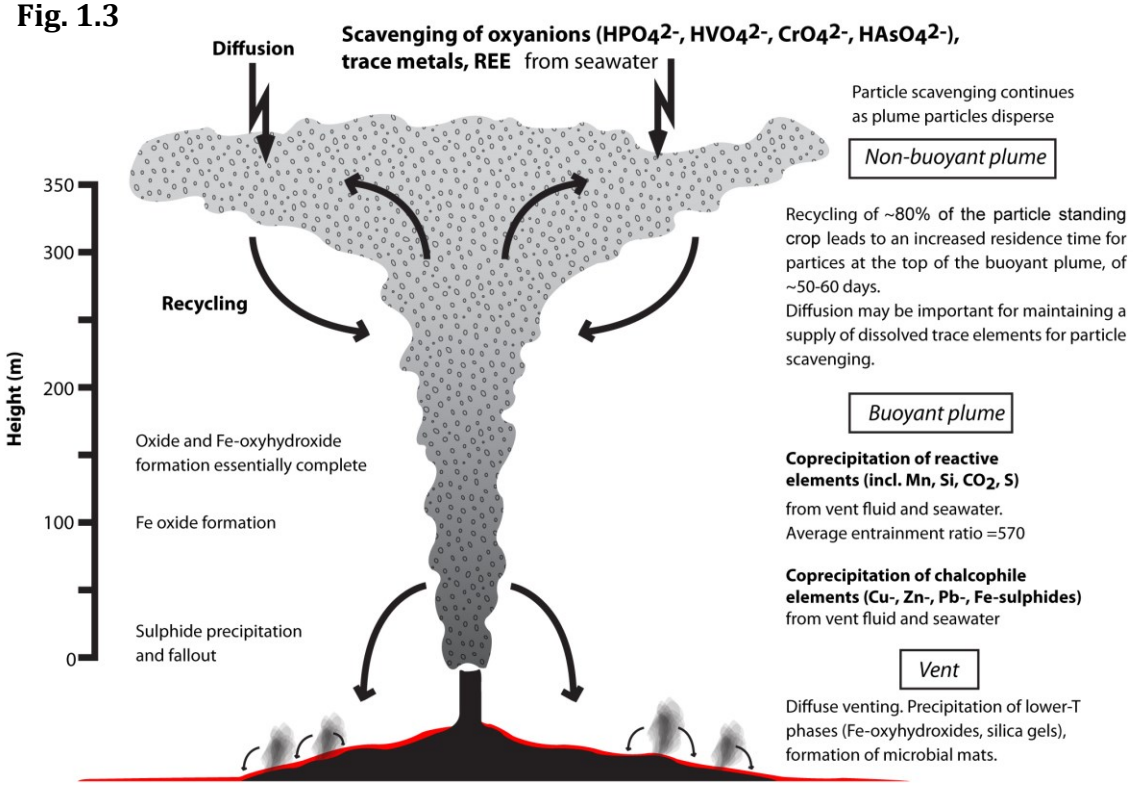

Figure 1.3 *Processes occurring in the buoyant and neutrally buoyant (non-buoyant) hydrothermal plume (modified after Rudnicki, 1995 and Peter, 2003).*

CHAPTER 2

Geology, mineralogy, and lithogeochemistry of metalliferous mudstones associated with the Lemarchant volcanogenic massive sulphide deposit, Tally Pond belt, central Newfoundland

Stefanie Lode,[1] Stephen J. Piercey,[1] and Christine A. Devine [2,3]

[1] *Department of Earth Sciences, Memorial University, 300 Prince Philip Drive, St. John's, NL, Canada, A1B 3X5*

[2] *Canadian Zinc Corporation, PO Box 1, Millertown, NL, Canada, A0H 1V0*

[3] *Fugro Geoconsulting, Inc., 6100 Hillcroft (77081), P.O. Box 740010, Houston, Texas, USA, 77274*

Status quo: Published at Economic Geology, v. 110, p. 1835-1859.

2.1 Abstract

The Cambrian Lemarchant Zn-Pb-Cu-(Au-Ag) bimodal felsic volcanogenic massive sulphide deposit, Tally Pond group, central Newfoundland, Canada, contains metalliferous mudstones that occur either immediately on top or laterally along strike from massive sulphide mineralization, or as interflow mudstones within hanging wall basaltic rocks. The mudstones are brown to black, graphite-rich, and locally have

intercalations of siliciclastic, volcaniclastic and/or amorphous chert layers, and, in some cases, fine laminae of organic matter. The main sulphide phases are pyrite (framboidal and euhedral) and pyrrhotite, with minor chalcopyrite, sphalerite, arsenopyrite and galena; barite is a common sulphate.

The metalliferous mudstones occur at various stratigraphic levels and have variable inputs of hydrothermal (high Fe/Al and base-metal values) and detrital components (lower Fe/Al and base metal values) with positive shale normalized Eu anomalies ($Eu/Eu^* \geq 1$), negative Ce anomalies ($Ce/Ce^* \leq 1$), and average Y/Ho ratio of ~28.3. These signatures suggest precipitation from reduced, high-temperature hydrothermal vent fluids in an oxygenated water column, coupled with the hydrothermal particles having a short residence time within the hydrothermal plume (i.e., a vent proximal setting). Deposition from an oxygenated water column is also supported by the presence of abundant barite in both the Lemarchant massive sulphides and the metalliferous mudstones, as well as locally preserved marcasite in the mudstones. Redox-sensitive trace elements (As, U, V, Mo, Cr, Ni, and Co) were scavenged as oxyanions onto Fe-oxyhydroxides during mudstone formation, and these elevated levels of scavenged redox-sensitive trace elements cause apparent anoxic signatures. Immobile element systematics (La-Th-Zr/10 and Th-La-Sc) indicate that the detrital component of the Lemarchant mudstones were mixtures of both continental and mafic sources, likely deposited within a pericontinental rifted arc environment. Our research illustrates that the lithogeochemistry of metalliferous mudstones can identify vent proximity and provides insights into the physiochemical conditions of the deposit formation and the ambient

environment. These results have implications for similar precious metal-bearing VMS deposits globally.

2.2 Introduction

Metalliferous mudstones (also described as exhalites, iron formation, hydrothermal mudstones) that are associated with volcanogenic massive sulphide (VMS) mineralization are interpreted to form from seafloor hydrothermal plume fallout when hot, reduced, and metal-rich vent fluids are discharged and mix with the cold, oxidized, sulphate-rich ambient seawater (Haymon and Kastner, 1981; Gurvich, 2006). Most of the particles emanating from hydrothermal vents (≥90%) are dispersed by the buoyant and neutrally-buoyant hydrothermal plume, and subsequently precipitate as metalliferous mudstone, up to several kilometres away from the hydrothermal vent (Hannington et al., 1995; Ohmoto, 1996). As a consequence, only a small fraction (≤10%) of the metals dissolved in the vent fluids are trapped within the host rock and/or the sealing semi-permeable layer of metalliferous mudstone (Hekinian et al., 1993). In close proximity to the hydrothermal vent site, polymetallic (Fe, Cu, Zn, Pb) sulphides and accompanying phases, such as barite, anhydrite, amorphous silica, and Al-poor clays (nontronite), co-precipitate from the buoyant plume within or immediately after exiting the black smoker chimney (Haymon and Kastner, 1981; Hannington, 2009). The mixing of the vent fluids and seawater causes oxidation of the metal-sulphides and formation of amorphous Fe-oxyhydroxide particles and silicagels, which deposit from the neutrally-buoyant (or non-buoyant) plume (Campbell et al., 1984; German and Von Damm, 2003). In consolidated

mudstones, as the Lemarchant metalliferous mudstones, the amorphous or only weakly crystalline Fe-oxyhydroxides are hydrothermally and diagenetically altered to Fe-sulphides (pyrite, pyrrhotite), Fe-carbonates (ferroan dolomite, ankerite ± Mg ± Mn), or Fe-chlorite, and hence, not preserved in the rock record.

The term 'exhalites' was first introduced by Ridler (1971) to describe interbedded volcaniclastic and/or detrital and chemical sedimentary rocks. The temporal and spatial association of metalliferous mudstone (exhalites) with ancient and modern VMS deposits and their use as stratigraphic marker horizons in the location of massive sulphides is well recognized (Franklin et al., 1981; Spry et al., 2000; Peter, 2003). Furthermore, metalliferous mudstones form an impermeable to semi-permeable layer capping the massive sulphide lens and therefore, likely increase the preservation probability of massive sulphides (Hannington et al., 1995; Gurvich, 2006). Additionally, this geological membrane helps to retain more of the metal-rich hydrothermal fluids within the massive sulphide mound and decreases the amount of metals lost to the hydrothermal plume (Large, 1992; Kharaka and Hanor, 2014).

In addition to capping deposits, metalliferous mudstones provide insight into, and record, processes associated with ore formation, including understanding the relative importance of vent fluid contributions, seawater scavenging of elements by hydrothermal particles, and detrital sedimentation associated with volcanism and sedimentary activity (Hannington et al., 1995; German and Von Damm, 2003). Hydrothermal metalliferous sediments represent a hiatus in this volcanic activity, where the deposition of hydrothermal matter dominates over the abiogenic pelagic background sedimentation (Lydon, 1984). Furthermore, lithogeochemistry of metalliferous mudstones can shed

insight into the relative roles of the above processes played in the genesis of these sediments (de Baar et al., 1988; Peter, 2003).

In the Tally Pond massive sulphide belt in the central Newfoundland Appalachians, sulphide-bearing mudstones are abundant and are spatially associated with numerous deposits and prospects (e.g., Swinden, 1991; McNicoll et al., 2010)(Fig. 2.1A-B). However, very few studies have been undertaken to understand their geology and lithogeochemistry, as well as the relationship of the mudstones to VMS genesis and their exploration significance. The Cambrian (~513-509 Ma) Lemarchant Zn-Pb-Cu-(Au-Ag) deposit is an ideal location to study metalliferous mudstones within the Tally Pond belt because laminated sulphide-rich mudstones are spatially and possibly genetically associated with mineralization (Fig. 2.1B). Upper Cambrian to Lower Ordovician black shales from Bell Island, eastern Newfoundland, were utilized as an example of detrital mudstones that are not spatially associated with sulphide mineralization (Fig. 2.1C). Furthermore, whereas in some cases the Lemarchant mudstones are directly associated with mineralization, they also occur at various distances from mineralization, and at various stratigraphic levels. Therefore, they provide the ability to monitor the chemical variation of the hydrothermal fluid that is a component of the mudstones as a function of stratigraphic position and spatial proximity to mineralization.

The spatial association of the Lemarchant metalliferous mudstones to massive sulphides, provides the possibility to study what kind of lithogeochemical proxies can be used to: 1) confirm and/or identify a hydrothermal origin versus, e.g., shallow basin pyrite-bearing carbonaceous black shales/mudstones (non-hydrothermal muds/shales); 2) define and better understand the depositional environment in terms of paleoredox

conditions of ambient seawater; and 3) study the chemical properties of the fluids, from which the Lemarchant mudstones precipitated. Although the results of this study are of significance to understand how the hydrothermal components of the mudstones spatially associated with the Lemarchant deposit form, they have significance for other metalliferous mudstones/shales within the Tally Pond belt, as well as VMS districts globally, and provide key insight into the evolution of VMS hydrothermal systems in ancient volcanic belts.

2.3 Regional geology

The Lemarchant Zn-Pb-Cu-Ba-(Au-Ag) VMS deposit is one of many VMS deposits within the Central Mobile Belt in central Newfoundland, Canada, that are part of the Cambrian (~515 Ma) to Permian (~275 Ma) Appalachian mountain belt (e.g., Williams, 1979; van Staal, 2007; van Staal and Barr, 2011). The Newfoundland Appalachians are divided into four tectonostratigraphic zones (from west to east): Humber, Dunnage, Gander and Avalon zones (Williams, et al. 1988; Swinden, 1988, 1991). The Dunnage Zone represents the Central Mobile Belt (Williams, 1979; Rogers et al., 2007). These zones result from and were affected by the successive accretion of three micro-continental blocks during the Early Paleozoic to Middle Paleozoic (i.e., Dashwoods, Taconic orogenesis; Ganderia, Salinic orogenesis; and Avalonia, Acadian orogenesis) and related interoceanic arcs and backarcs (Swinden, 1991; Zagorevski et al., 2010). These ribbon-shaped microcontinental blocks were located on the leading edges of Gondwana and Laurentia, forming peri-Gondwanan and peri-Laurentian terranes (Rogers

et al., 2007; van Staal and Barr, 2011). The Dunnage Zone has been subdivided into the peri-Laurentian Notre-Dame Subzone to the northwest and the peri-Gondwanan Exploits Subzone to the southeast (Fig. 2.1A; Swinden, 1988, 1991). The suture between these subzones is the Red Indian Line, a ribbon-shaped zone of a tectonic mélange, which contains remnants of Cambro-Ordovician oceanic infant arc and arc terranes that existed within the Iapetus Ocean (Williams, 1979; van Staal and Barr, 2011). Despite deformation and metamorphism, the Central Mobile Belt was only moderately affected by metamorphism (lower greenshist-facies) and deformation and internally stratigraphic relationships are well preserved (e.g., Hinchey and McNicoll, 2009; Piercey et al., 2014).

The Lemarchant VMS deposit is hosted in the lower Victoria Lake supergroup within the Exploits Subzone, which is comprised of Cambrian-Ordovician volcanic and sedimentary rocks (Dunning et al., 1991; McNicoll et al., 2010). The Victoria Lake supergroup is further subdivided into six assemblages (Zagorevski et al., 2010; Piercey et al., 2014), which are bounded by faults, and are from east to west: 1) the Tally Pond group; 2) the Long Lake group; 3) the Tulks group; 4) the Sutherlands Pond group; 5) the Pats Pond group; and 6) the Wigwam Pond group; the Tulks, Long Lake, and Tally Pond groups are known to host VMS deposits. These six tectonic assemblages yield U-Pb zircon ages ranging from ~513 to 453 Ma (Dunning et al., 1987; Evans et al., 1990; Dunning et al., 1991; Evans and Kean, 2002; Zagorevski et al., 2007; McNicoll et al., 2010). The operating Duck Pond and Boundary mines as well as the Lemarchant deposit are located within the Tally Pond group (Fig. 2.1B; e.g., Squires and Moore, 2004). The Tally Pond group (U-Pb zircon ages ranging from ~513 to 509 Ma) is divided into the felsic volcanic rock dominated Bindons Pond formation (also referred to as Boundary

Brook formation) and the mafic volcanic rock dominated Lake Ambrose formation. The latter contains island arc tholeiitic basalts (Dunning et al., 1991; Evans and Kean, 2002), whereas the former contains predominantly transitional to calc-alkalic rhyolitic rocks (Rogers et al., 2006; Piercey et al., 2014). VMS-style hydrothermal alteration and mineralization occurs in several areas within rocks of the Bindons Pond formation (Squires et al., 1991; Piercey et al., 2014). Collectively, the Tally Pond group is interpreted to represent an arc to rifted arc environment (e.g., Rogers et al., 2006).

2.4 Deposit geology

The Lemarchant deposit occurs along the contact between footwall felsic volcanic rocks of the Bindons Pond formation and hanging wall mafic volcanic rocks and metalliferous mudstones of the Lake Ambrose formation. Both formations are cross-cut by grey- to beige-bleached amygdule-rich mafic dikes. The contact between the formations is complex and commonly marked by complex intermingling of felsic and mafic volcanic rocks, with a thin (<1 to 20 m) layer of argillite, siltstone, or pyritic mudstone. This metalliferous mudstone layer is discontinuous with a short lateral extent of one to four kilometres, but similar metalliferous sediments are also found proximal to other VMS occurrences within the Tally Pond volcanic belt (Copeland et al., 2009; Fraser et al., 2012).

The Lemarchant deposit is associated with ~4,000 x 700 m hydrothermal alteration zone (Fig. 2.2B-C), with intense quartz, sericite, chlorite, and Ba-enrichment, plus anomalous disseminated and stringer-type pyrite, base-metal sulphides with lesser

amounts of pyrrhotite (Fraser et al., 2012). The mineralization occurs as semi-massive to massive sulphide within the Lemarchant Main Zone (sections 101N to 104N), and in a smaller mineralized sequence, the 24 Zone (Fig. 2.2A; Copeland et al., 2009; Fraser et al., 2012). The inferred resources for the Lemarchant Main Zone currently are 1.24 Mt at 5.38 % Zn, 0.58 % Cu, 1.19 % Pb, 1.01 g/t Au and 59.17 g/t Ag, with indicated resources of 1.34 Mt at 3.70 % Zn, 0.41 % Cu, 0.86 % Pb, 1.00 g/t Au and 50.41 g/t Ag (Fig. 2.2A-C; Fraser et al., 2012). An additional mineralized zone, the Northwest Zone (Fig. 2.2A, C), was discovered in early 2013, and has a strike length of ~100 metres, and remains open to the north and south (http://www.canadianzinc.com/images/Docs/News_Releases/CZNNR20131211.pdf). The Northwest Zone currently does not have a defined resource.

The Lemarchant Main Zone (Fig. 2.2B) is 1.7 to 30.4 m thick and consists of a barite-rich outer zone that grades into a Pb-Zn-sulphide-rich zone, and an interior zone with Zn-Cu-sulphides, which grades into stringer mineralization at depth, typical of bimodal felsic/Kuroko-style mineralization (Copeland et al., 2009; Fraser et al., 2012; Gill and Piercey, 2014). The deposit contains typical VMS sulphides (pyrite, sphalerite, galena, and chalcopyrite), but also abundant sulphosalts (e.g., tetrahedrite-tennantite), bornite, stromeyerite, electrum, bladed barite, and calcite; as well as minerals that contain enrichments in epithermal suite elements (e.g., Au, Ag, As, Hg, Sb, Bi)(Gill and Piercey, 2014). The sulphosalt-rich mineralogy, barite-calcite textures, and anomalous element suite in the ores have led to the interpretation that the Lemarchant deposit was a shallow water VMS deposit with both VMS and epithermal features (Gill and Piercey, 2014).

The massive sulphides at Lemarchant are stratigraphically overlain by metalliferous mudstones that contain many of the above minerals. The contact between

the massive sulphides and the mudstones consists of a 5 to 40 cm wide zone of Fe-rich red to purple sphalerite that grades down-dip in the drill hole into white to honey brown coloured sphalerite-dominated massive sulphides. Electrum ± Hg ± Sb also occurs in the mudstones. Due to an offset along the Lemarchant Fault at a gentle to moderate angle, a repetition of the mineralized strata and mudstone occurrences is likely (Copeland et al., 2009). The Lemarchant Fault locally cuts-off mineralization (Figs. 2.3, 2.4) and displaces the ore horizon and the mudstones. Some of the mudstones also display a foliation that is orientated parallel to the sedimentary lamination with occasional cleavage traces that cross-cut bedding.

2.5 Mudstone stratigraphy and lithofacies

The mudstones occur either immediately stratigraphically above the massive sulphides in the Bindons Pond formation, or form a layer capping volcanic rocks within the same formation (Figs. 2.3, 2.4). They laterally extend in the same stratigraphic level up to 200 m away from the mineralization in the Lemarchant Main Zone, but they are also spatially associated with the Northwest Zone, the 24 Zone, and the North Target, as well as areas west of the South Target (Fig. 2.2A). The extent of mudstones in the last three areas is difficult to determine due to the limited number of drill holes. The interflow mudstones within Lake Ambrose formation basalt occur up to 50 m above massive sulphide mineralization in stratigraphic sections that are tectonically undisturbed. Mudstones within the felsic volcanic rocks below the ore horizon are rare, and only seen in one drill hole with a thickness of ~1 m. Synsedimentary folding and faulting has

locally increased the thickness of the mudstone, but most have true thicknesses of 1 to 20 m (Figs. 2.5A, 2.6B).

The contacts between the mudstones and surrounding units (e.g., massive sulphide and basalt) range from conformable (Fig. 2.5A-B) to tectonized (Figs. 2.3, 2.4). At the contact between the mudstones and mafic volcanic rocks (flows and sills) (Fig. 2.5C) peperitic textures are locally present, whereby mafic rocks are chaotically mingled with mudstones, are interpreted as having formed by magma-wet sediment interactions and indicating contemporaneous volcanism and sedimentation (Skilling et al., 2002). Another common feature is the intermingling of the mudstones with felsic volcanic and/or volcaniclastic sedimentary material (Fig. 2.5D), which is interpreted to represent mass wasting (e.g., Füchtbauer et al., 1988).

Mudstones of various stratigraphic positions are generally brown to black, graphite-rich, finely laminated, and contain fine carbonaceous/organic matter-rich laminae that are intercalated with siliciclastic, volcaniclastic and/or amorphous kidney-shaped chert-layers (Fig. 2.5A). The sulphides occur both parallel to the bedding in the organic-rich layers, but also in later stage, stringer-like veins. Cross-cutting veins intercept the original bedding indicating diagenetic/tectonic remobilization and/or formation by intra-stratal shrinkage (synaeresis) cracks (e.g., Füchtbauer et al., 1988).

The main sulphides in the mudstones are pyrite and pyrrhotite, with minor chalcopyrite, sphalerite, arsenopyrite, marcasite, and galena, as well as rare cubanite and gersdorffite. Sphalerite commonly displays chalcopyrite disease, whereas pyrite exists as framboids and euhedral grains. The framboids occur either as scattered single spheres or in semi-massive layers (Figs. 2.6A, 2.7A). Based on the textural robustness (i.e.,

withstanding certain amounts of reworking) and $\delta^{34}S$-isotopic compositions ranging from -38.8 ‰ to +14.4 ‰ (Lode et al., *in review*), the organic-rich laminae are potentially microbial mats (Fig. 2.7F). Framboid layers are locally cross-cut by veins that are filled with later stage polymetallic sulphides including euhedral pyrite, interstitial chalcopyrite, sphalerite, and galena (Fig. 2.6B-D). These later stage veins are locally enriched in precious metals in the form of electrum ± Hg ± Sb, acanthite, pyrargyrite and stephanite (Fig. 2.6D-F). Marcasite occurs as tabular crystals or blades in euhedral or massive pyrite, or as semi-continuous layers of marcasite clusters.

Mudstones spatially associated with the massive sulphides, and interflow mudstones in the hanging wall mafic volcanic rocks, commonly have a high abundance of barium-bearing minerals, including barite, celsian, hyalophane, and witherite. Barite generally forms anhedral semi-continuous layers or occurs as bladed crystal vug-infills, whereas the Ba-feldspars (celsian and hyalophane) are later stage minerals with euhedral crystals overgrowing earlier phases such as pyrite framboids (Fig. 2.7A-E). Barite also forms in crack-and-seal type veins, cross-cutting the mudstones and Pb-Zn-Cu sulphides (Fig. 2.7E). Carbonates, quartz, sericite, Fe-Mg-chlorite, and apatite are common gangue minerals in mudstones, with accessory monazite, Y-xenotime, and rutile. Carbonates are generally Fe-bearing (e.g., ferroan dolomite and ankerite ± Mg ± minor Mn), but calcite and dolomite are also locally present (Figs. 2.6D, 2.7B, 2.7C, 2.7F).

2.6 Lithogeochemistry

2.6.1 Sampling, methods, quality assurance, and quality control (QA/QC)

Mudstone types collected from drill core include those that: 1) occur in contact with or are stratigraphically within five metres of massive sulphides and represent the main stratigraphic marker between the felsic and mafic volcanic rocks (Bindons Pond formation and Lake Ambrose formation, respectively); 2) do not have an obvious spatial and possibly genetic relation with mineralization, but occur along the same stratigraphic contact between the Bindons Pond and Lake Ambrose formations; 3) occur within the Bindons Pond felsic volcanic rocks; and 4) occur as interflow mudstones in the hanging wall Lake Ambrose basalts. Tuff is intercalated with all types of mudstones, and if the tuff had a sufficient thickness (≥5 cm) they were also sampled for whole-rock geochemical analyses.

Samples for whole-rock lithogeochemical studies were analyzed for major and minor elements by lithium metaborate/tetraborate fusion followed by HNO_3 dissolution and analysis by inductively coupled plasma (atomic) – emission spectroscopy (ICP-ES). Carbon (C) and sulphur (S) were obtained by infrared spectroscopy and mercury (Hg) was obtained by the cold vapour flow injection mercury system (Hg-FIMS). All of the former analyses were performed by Activation Laboratories Ltd. (Actlabs) in Ancaster, Canada. Additional trace elements, including rare earth elements (REE), high field strength elements (HFSE), trace metals, and many low field strength elements (LFSE) were analyzed in the Department of Earth Sciences at Memorial University, using screw-top Teflon® bomb (Savillex®) multi-acid dissolution with a finish by inductively coupled plasma-mass spectrometry (ICP-MS). The multi-acid (HNO_3, HF, HCl, H_3BO_3, and H_2O_2) whole-rock dissolution process was a modified version of that of Jenner et al.

(1990) and Longerich et al. (1990) to account for the high amounts of carbonaceous material in the samples; the procedures are described in detail in Appendix 2.1.

Precision and accuracy of the analyses were determined using duplicates and reference materials following methods described in Jenner (1996) and Piercey (2014). The reference materials utilized in the study included three different organic- and/or sulphide-rich shales (SCO-1, SDO-1 and SGR-1b) and one iron formation (FeR-1). These standards were run every twenty samples and with each analytical batch. In addition, blanks were utilized during each analytical run to test for contamination; none was detected. Precision was determined using the percent relative standard deviation (% RSD) on the replicate analyses of the reference materials, and accuracy was determined using percent relative difference (% RD) from accepted values. The detailed QA/QC protocol is given in Appendix 2.1.

2.6.2 Results

2.6.2.1 Alteration – major element systematics: The major elements have variable mobility with the alkali elements exhibiting considerable mobility during hydrothermal alteration and diagenetic processes (Nesbitt and Young, 1982; Nesbitt, 2003). Hydrothermal and diagenetic alteration starts during and immediately after the precipitation of the metalliferous mudstones due to ongoing hydrothermal activity. The alkali elements and Fe-Mg are often compared to the immobile Al_2O_3 in A-CN-K and A-CNK-FM molar diagrams (Fig. 2.8A, B; Nesbitt, 2003), which broadly mirror the chemical index of alteration (CIA) (Nesbitt and Young, 1982). The CIA describes the

degree of alteration and is calculated using the equation CIA = $100x[Al_2O_3/(Al_2O_3+CaO+Na_2O+K_2O)]$. Unaltered samples have a CIA ~50, whereas strongly altered samples yield CIA values of up to 100 (Nesbitt and Young, 1982). Most of the Lemarchant samples (95^{th} percentile) have CIA values around ~84, comparable with the average shale values of 70-80 (e.g., Nesbitt, 2003). The elevated values (max. CIA = ~94) are consistent with significant alteration, and authigenic and diagenetic clay mineral content. A smaller group of samples with higher amounts of carbonate have CIA values <25 (Table 2.1). In A-CN-K space, most mudstones lie within the sericite (illite/muscovite) and carbonate-dolomite portion of the diagram, and less so along the chlorite-smectite trend (Fig. 2.8A). Exceptions to the former are mudstones in the hanging wall mafic volcanic rocks, which have less calcite-dolomite alteration. The Bell Island black shales fall within the average shale field (Fig. 2.8A). In A-CNK-FM space mudstones plot near the FM-part of the diagram proximal to the sulphide-oxide apex, chlorite-smectite and calcite-dolomite; tuff displays trends towards muscovite/illite and feldspars. Also trending towards muscovite/illite, with only minor carbonate contribution, are the Bell Island black shales (Fig. 2.8B). A positive correlation between Al_2O_3 and TiO_2 (r^2 = 0.848; Fig. 2.8C) in the Lemarchant mudstones and tuff indicates that both were likely immobile during post-depositional processes, such as diagenesis and alteration (Barrett and MacLean, 1994a). Some of the interflow mudstones, tuff and other mudstone samples deviate from the correlation line and plot towards lower Al_2O_3/TiO_2 ratios, potentially reflecting more mafic detritus.

2.6.2.2 Hydrothermal versus detrital element signatures: Samples from Lemarchant and Bell Island have been plotted on Boström-type diagrams in Figure 2.9A and B (Boström et al., 1972; Boström, 1973). Samples from various stratigraphic levels in the Lemarchant deposit have hydrothermal signatures with Fe/Ti versus Al/(Al+Fe+Mn) systematics that suggest the hydrothermal component is between 40 and 80% (Fig. 2.9A), and lie predominantly in the hydrothermal field of Figure 2.9B, with the exception of volcanic tuff samples. In general, there are very few differences between samples that occur within five metres of mineralization, and those that are hosted within various rocks distal to mineralization (Fig. 2.9A-B). One exception is a nearly pure sulphide-rich sample consisting almost solely of layered sulphides (pyrite, Fe-sphalerite, minor galena), which falls within the same field as Red Sea metalliferous sediments (Fig. 2.9A). In comparison, the Bell Island black shales predominately consist of detrital matter and, accordingly, fall within the non-hydrothermal sediment fields (Fig. 2.9A-B). To account for the high contents of Ba and Hg in the Lemarchant hydrothermal system, a plot with Ba/Al versus (Zn+Hg)/Al was utilized, where Ba, Zn, and Hg represent hydrothermally derived components of the mineralization, and Al the detrital constituents. In this plot, proximal sediments show trends towards high Ba/Al and (Zn+Hg)/Al ratios, whereas detrital sedimentary rocks have low ratios (Fig. 2.9C).

The Lemarchant mudstones have $\Sigma FeO+Fe_2O_3$ ($Fe_{(total)}$) that ranges from 13 to 55 wt% and 2 to 42 wt% S, with mudstones that are closely associated with the massive sulphides having higher Fe and S values (average $Fe_{(total)}$ of 34.5 wt% and average S of 24.4 wt%). The Fe is hosted within Fe-sulphides, -carbonates, -oxide, and -chlorite. Tuffs generally range from 13.8 to 30.8 wt% $Fe_{(total)}$ and 4.6 to 12.9 wt% S, with two exceptions

(39.7 and 51.2 wt% $Fe_{(total)}$ and 26.5 to 24.2 wt% S), which are sulphide- and/or barite-rich proximal to massive sulphides (Fig. 2.10A). The mudstones also have elevated Zn, Pb, Co, and Cu compared to non-hydrothermal black shales, and this is particularly so for samples within five metres of mineralization (Fig. 2.10B-C).

2.6.2.3 Hydrothermal versus hydrogenous element systematics: Samples proximal to massive sulphides also have elevated Ba (up to 130,200 ppm) and Hg (up to 17,700 ppb) compared to non-hydrothermal black shales (Fig. 2.10D). One tuff sample intercalated with a proximal mudstone has a Ba content of 165,700 ppm and 543 ppb Hg. In contrast, the other tuff samples only have up to 135 ppb Hg, and the more distal mudstones up to 811 ppb. These systematics are similarly reflected by Sb and As contents (Fig. 2.10E-F), where proximal mudstones have up to 415 ppm Sb and 9,545 ppm As, whereas tuff and more distal mudstones tend to have lower values of 329 ppm Sb and 3306 ppm As, with one distal mudstone exception that has an As value of 13,671 ppm. Therefore, Zn-Pb-Cu-Co-Ba-Hg-enrichments are associated with mudstones proximal to mineralization and are lower in distal mudstones.

2.6.2.4 Rare earth element and Y (REY) signatures: The rare earth element and Y (REY) signatures of the hydrothermal mudstones and tuff from the Lemarchant deposit are shown on Figure 2.11A to E, and from Bell Island in Figure 2.11F, and normalized to post-Archean Australian shale using the data of McLennan (1989). Mudstone within five metres of mineralization has light rare earth element (LREE)-depleted normalized profiles with relatively flat heavy rare earth element (HREE) signatures (Fig. 2.11A). They have

negative Ce anomalies (Ce/Ce*<1) and positive Eu anomalies (Eu/Eu* = 1.1-3.5), and four samples with almost no or slightly negative Eu anomalies (Eu/Eu* around 0.9). Ce/Ce* and Eu/Eu* were calculated using the equations of McLennan (1989) where $Ce/Ce^* = (Ce_{sample}/79.6)/ \sqrt{((La_{sample}/38.2)*(Pr_{sample}/8.83))}$ and $Eu/Eu^* = (Eu_{sample}/1.08)/ \sqrt{((Sm_{sample}/5.55)*(Gd_{sample}/4.66))}$, respectively. A smaller group of proximal mudstones also have a slightly positive Y-anomaly (Fig. 2.11A), whereas a sulphide-rich sample, is depleted in HREEs (Fig. 2.11A). Mudstones that occur at the footwall-hanging wall interface, but are not associated with massive sulphide mineralization, and those that are in the hanging wall basaltic rocks, are broadly similar to proximal samples but have less strongly pronounced Eu anomalies (Eu/Eu* = 0.9-2.6; Fig. 2.11B-C). Tuffs intercalated with mudstones also have flat HREE patterns, a negative Ce anomaly, but either no, or only a minor positive Eu anomaly (Eu/Eu* = 0.9-1.4). One tuff that occurs in close proximity and stratigraphically above massive sulphides has a Eu/Eu* = 2.2 (Fig. 2.11D). The one sample within felsic volcanic rocks (Fig. 2.11E) has a similar REE-pattern as the mudstones shown in Figure 2.11B. The Bell Island black shales have relatively flat REE-patterns, without any significant Ce or Eu anomalies (Fig. 2.11F).

Unlike samples from the Duck Pond deposit (Piercey et al., 2012), the Lemarchant mudstones and tuff have no significant positive Y anomalies but have average Y/Ho ratios of ~28.3 that are near the chondritic ratio of 27 (Fig. 2.12A; Bau, 1996; Slack et al., 2007). In the Y/Ho-Ce/Ce* plot, the Lemarchant mudstone and tuff samples are scattered around the chondritic Y/Ho ratio of 27, with some samples tending towards lower Ce/Ce* values and higher Y/Ho ratios (trend towards the seawater value of Y/Ho > 44) (Fig.

2.12A). Three samples are outliers and plot outside of the field of the majority of the Lemarchant samples (Fig. 2.12A).

2.6.2.5 Hydrothermal versus hydrogeneous element systematics - paleoredox: Redox-sensitive elements can be used to determine the paleoredox conditions of the ambient seawater during the time of deposition of the hydrothermal sediments (Emerson and Huested, 1991; Jones et al., 2006). These redox-sensitive trace elements (U, V, Mo, Cr, and Co) have variable oxidation states and their solubility is dependent on this oxidation state and the pH of the ambient water, and, for some elements (e.g., Ni), the presence or absence of organic matter (Tribovillard et al., 2006). In Figure 2.13A and B, the Lemarchant mudstones fall within the anoxic field, whereas the Bell Island black shales plot in the oxic field. However, plots of these redox-sensitive elements have to be taken with care in hydrothermal sedimentary environments, when abundant Fe-oxyhydroxides are present.

Lemarchant mudstones and tuff that have higher P_2O_5-values (lower Fe_2O_3/P_2O_5 ratios) and exhibit a weak correlation with higher Y/Ho ratios, whereas samples with higher Fe_2O_3-values plot, around the chondritic Y/Ho value of ~27 (avg = 28.3, Fig. 2.14A). Nevertheless, this Ba versus Y/Ho plot additionally illustrates that mudstones closely associated with mineralization have higher Ba- (and Hg)-concentrations than more distal mudstones or tuff (Figs. 2.14B, 2.10D).

2.6.2.6 Immobile elements and sediment provenance: Homogenization of the detritus in sedimentary basins results in basin muds having immobile trace element patterns that reflect their source rocks (Bhatia and Crook, 1986; Nesbitt and Markovics,

1997). Ratios of immobile elements like the HFSE (e.g., Zr), the REE (e.g., La) and the compatible elements (e.g., Sc) are not significantly influenced by chemical weathering, diagenesis, hydrothermal alteration, or low-grade metamorphism and, therefore, can be used for provenance studies of sedimentary rocks, and to reconstruct the tectonic environment of deposition for sedimentary rocks (Taylor and McLennan, 1985; Kolata et al., 1996; McLennan et al., 2003).

In plots of Th-Sc-Zr/10 (Fig. 2.15A) and La-Th-Sc (Fig. 2.15B), interflow mudstones and some samples of tuff overlap fields for intraoceanic and continental arc environments, consistent with proposed tectonic models for the Tally Pond group (Dunning et al., 1991; McNicoll et al., 2010; Piercey et al., 2014). In Figure 2.15B, several samples trend towards the La-apex, particularly so for mudstones associated with massive sulphides and/or felsic volcanic rocks and suggests potential La-scavenging from seawater (e.g., Bau, 1991, 1993). The ternary Th-Sc-Zr/10 plot also shows that the Lemarchant source rocks are zirconium depleted, as previously reported by Squires and Moore (2004) and McNicoll et al. (2010) for the bimodal volcanic rocks of the Tally Pond belt (Fig. 2.15A). This Zr-depletion is also noticeable in Figure 2.15C, which indicates an upper crustal character of source rocks for mudstones associated with massive sulphides and/or felsic volcanic rocks, and trends toward more andesitic to MORB-like source rock for interflow muds and some tuff.

2.7 Discussion

2.7.1 Sediment provenance – evaluating hydrothermal, hydrogenous, and detrital components

The chemistry of metalliferous sedimentary rocks associated with the Lemarchant VMS deposit reflects the varying contribution of elements from: 1) hydrothermal exhalation; 2) detrital sedimentation; and 3) those scavenged from seawater by hydrothermal particles (e.g., Boström and Peterson, 1966; German et al., 1990; German and Von Damm, 2003). Boström and Peterson (1966) illustrated that the relative contribution of hydrothermal and detrital components in sediments can be quantified by comparing the relative enrichments in base and transition metals, such as Fe, Mn, Cu, Ni, and Pb (exhalative), relative to Al (detrital). They also illustrated that elements, such as, Ba, Zn, W, Ca, Hg, As, and S, are associated with exhalative activity and also are enriched in these sediments (Boström and Peterson, 1966, 1969). Sulphide-rich mudstones at Lemarchant contain elevated base metal and transition element contents, particularly so in those that are spatially associated with massive sulphides, and thus, consist predominantly of hydrothermal components (Figs. 2.9A-C, 2.10A-F). This is the case regardless of stratigraphic position and most mudstones have between 40-80% hydrothermal input (Fig. 2.9A, B). The elevated base and transition metal contents (Fe, Cu, Zn, Pb) reflect derivation from hydrothermal fluids as precipitated polymetallic sulphide (Jones et al., 2006), and are consistent with the sulphide mineralogy of the mudstones (Figs. 2.5, 2.6).

In addition to base metals, the samples show enrichment in metalloids. The enrichment in Ba is typical of many VMS deposits (Lydon, 1984; Large, 1992; Huston et

al., 2010), and is likely due to the formation of barite with Ba being derived from the thermochemical breakdown of feldspars in the hydrothermal reaction zone (Hannington et al. 2005; Griffith and Paytan, 2012). Reduced hydrothermal fluids transport the Ba^{2+}, which reacts with sulphate in the water column resulting in barite precipitation at or near the seafloor (Ohmoto and Goldhaber, 1997; Huston and Logan, 2004; Griffith and Paytan, 2012). The presence of barite in mudstone samples proximal to mineralization strongly favours a hydrothermal origin and a vent proximal location of deposition (Fig. 2.7). But, barite also occurs north of the Lemarchant Main Zone on section 108N, where there is no known mineralization, suggesting potential for mineralization in this location as well (Fig. 2.2A). In addition to barite, however, other Ba-minerals such as hyalophane and celsian (Fig. 2.7A-E), and witherite are present. The celsian typically overgrows pyrite-framboids to form euhedral crystals (rhombs, blades) and occurs in pyrite-chalcopyrite-rich mudstones (Fig. 2.7A-B), commonly associated with massive semi-continuous barite layers, as bladed barite in veins, or as crack-seal type barite veins that cross-cut the mudstones and sulphides (Fig. 2.7C-E). The crack-seal textures suggest that later-stage fluids must have remobilized Ba. In contrast to the vent-proximal mudstones, the basaltic interflow mudstones, or mudstones that have no close association to the mineralization show lower Ba levels, which indicates a more distal depositional environment.

Besides polymetallic sulphides and barite, the Lemarchant mineralization and mudstones have high levels Au, Ag, Hg, Sb and As compared to non-hydrothermal black shales, which are mirrored by the presence of electrum ± Hg ± Sb (Fig. 2.6D-F), as well as acanthite, pyrargyrite, stephanite, bladed barite and carbonates. The presence of

precious metals, elevated Hg-Sb-As, and bladed barite and carbonates are consistent not only with hydrothermal input, but specifically magmatic-hydrothermal (epithermal) input (e.g., Hannington and Scott, 1989), and is also found proximal to mineralization (and other areas, as e.g., section 100+00N to 101+00N, south of the Lemarchant Man Zone).

2.7.2 Anoxia versus scavenging

Fine-grained sedimentary rocks, such as black shales and hydrothermal mudstones are useful indicators of paleoceanographic conditions and basin redox. Furthermore, these units can locally shield massive sulphides from an oxic environment, thereby increasing their preservation potential (e.g., Goodfellow and McCutcheon, 2003; Peter, 2003; Sáez et al., 2011). Redox sensitive trace elements, including the transition elements/oxyanions concentrations in shales/mudstones, are particularly useful for discriminating paleoredox conditions in ancient environments (e.g., Tribovillard et al., 2006; Algeo and Tribovillard, 2009). The redox sensitive trace elements (As, U, V, Mo, Cr, Ni, and Co) are enriched in the Lemarchant mudstones and plot in the fields for deposition under anoxic bottom water conditions (Fig. 2.13A-B). Paradoxically, the presence of abundant barite coupled with negative Ce anomalies in the samples, some with high Y/Ho, suggest deposition from an oxygenated water column (de Baar et al., 1988). The presence of marcasite additionally supports an oxygenated environment (Schieber, 2011). In most cases marcasite partially replaces pyrite and it is suggested that marcasite formed paragenetically late, after the higher temperature hydrothermal system ceased, because marcasite has higher growth rates and dominates over pyrite at lower temperatures and acidic conditions (pH <5)

(Schieber, 2011). Pyrite associated with the euhedral marcasite shows corrosion textures likely due to partial re-oxidation (Schoonen and Barnes, 1991).

A basinal environment with hydrothermal activity is a unique setting associated with Fe-oxyhydroxide particles that form during turbulent mixing of hydrothermal fluids with seawater. Oxyanions, such as HPO_4^{2-}, HVO_4^{2-}, CrO_4^{2-}, $HAsO_4^{2-}$, and HPO_4^{2-} are scavenged from seawater onto the precipitated Fe-oxyhydroxide particles (Rudnicki, 1995). Accordingly, it is expected that more distally precipitated, i.e., greater residence times, hydrothermal sediments show higher contents of these oxyanions. The high abundance of Fe-oxyhydroxide particles in the buoyant, and non-buoyant hydrothermal plume also allows for increased scavenging of U, Mo, Ni and Co from seawater (e.g., German and Von Damm, 2003), compared to basin environments with non-hydrothermal black shale deposition (Morford et al., 2005). Non-hydrothermal environments do not have the excessive scavenging rates of redox-sensitive elements onto Fe-oxyhydroxide particles, but are able to retain and enrich redox sensitive elements within the sediment when reduced conditions prevail (Morford et al., 2005; Tribovillard et al., 2006). The Bell Island black shales and siltic mudstones fall within the oxic field in Figure 2.13A-B, and deposition in an oxic environment is also supported by the presence of abundant ichnofauna in the Bell Island sedimentary rocks (Harazim et al., 2013).

Enrichments in the aforementioned oxyanions in the hydrothermal sediments are therefore not a function of the anoxic character of the basin, but rather the efficiency of scavenging of these elements from seawater by upwelling hydrothermal particles in the hydrothermal plume. This ultimately results in hydrothermal sediments with an apparent (but not true) anoxic signature (e.g., Piercey et al., 2012) (Fig. 2.13A-B). Furthermore, the

longer the residence time of the hydrothermal particles in the plume, the more scavenging from seawater occurs, which will increase the apparent anoxic signature (Rudnicki, 1995; Peter et al., 2003) (Fig. 2.16). Therefore, sediments deposited in a vent proximal environment have a more strongly pronounced hydrothermal signature, whereas sediments that precipitated in more distal environments have oxyanionic features more indicative of deposition under anoxic conditions. These same sediments, however, will also have a greater seawater REE signature with a more pronounced Ce anomaly, a feature of oxic seawater, and therefore the combination of seawater-like REE signatures and oxyanion enrichment can be used to distinguished apparent from real anoxic depositional conditions in hydrothermal sediments.

2.7.3 Physiochemical conditions of hydrothermal sediment formation: insight from rare earth elements and Y (REY)

The REY in hydrothermal fluids, and by association hydrothermal sediments, provide significant insight into the physiochemical conditions of VMS formation. Unlike the other REEs, which occur in the trivalent state only, Eu and Ce have two redox states (di- and trivalent, and tri- and tetravalent, respectively) that are affected by the temperature and Eh-pH conditions of the hydrothermal fluids (Michard et al., 1983; Sverjensky, 1984; Bau, 1993). Europium is particularly useful and its behaviour in hydrothermal fluids is dependent on whether it is in its divalent or trivalent form. Furthermore, the Eu^{2+}/Eu^{3+}-redox equilibrium is strongly temperature-dependent, and under high-T (>250°C), acidic and reducing conditions as in VMS hydrothermal fluids,

divalent Eu is the predominant species in solution, and/or bound in related complexes (Sverjensky, 1984; Bau, 1999; Peter, 2003). Consequently, hydrothermal fluids and precipitates that are derived from high temperature fluids have positive Eu^{2+} anomalies (German and Von Damm, 2003; Peter et al., 2003), and given that all samples from the Lemarchant deposit, regardless of location or stratigraphic position, have positive Eu anomalies (Fig. 2.11A-C, 2.11E), it suggests deposition from fluids with temperatures greater than 250°C. In contrast, detrital sediments have no positive Eu-anomalies (Peter and Goodfellow, 2003), a pattern that is reflected in the Bell Island black shales (Fig. 2.11F). Therefore, increased mixing of hydrothermal and detrital sediments can result in a masking of a positive Eu anomaly due to input of abundant detrital material (Peter and Goodfellow, 2003). Given that all samples have positive Eu anomalies, it suggests that the latter, dilution of the anomaly by detritus, was minimal and that the Eu/Eu* values represent the hydrothermal conditions of deposition for the mudstones.

Although Eu can provide insight into the thermal conditions of the fluids, Ce provides a proxy for the prevailing redox conditions during the precipitation of metalliferous sediments (McLennan, 1989; Peter, 2003). In oxidized ambient seawater, Ce^{3+} oxidizes to the less soluble Ce^{4+} after being scavenged onto Fe-Mn-oxyhydroxides (German and Elderfield, 1990, Bau and Koschinsky, 2009). This causes fractionation of the Ce^{4+} from the REE^{3+} (Peter et al., 2003; Bau and Koschinsky, 2009; Hannington, 2009) and results in a negative Ce anomaly of the surrounding seawater. These negative Ce anomalies are also present in pelagic clays (Elderfield and Greaves, 1981) and in currently formed hydrothermal sediments (Mills and Elderfield, 1995). Fe-oxyhydroxides within metalliferous hydrothermal sediments gain their REE from the hydrothermal vent

fluids, and from seawater. The presence of the negative Ce anomalies in the hydrothermal sediments is inherited from mixing of the vent fluids with Ce-depleted oxygenated seawater (German and Elderfield, 1990; Hannington, 2009). No negative Ce anomalies are expected in reduced vent fluids, as Ce^{3+} will not oxidize to Ce^{4+} in such fluids (Mills et al., 2001; Peter and Goodfellow, 2003; Humphris and Bach, 2005), or when the shale sample is similar in composition to the shale used for normalization of the samples (e.g., post-Archean Australian shales). An absence of negative Ce anomalies can further be caused by large amounts of detrital input to the hydrothermal component (Peter and Goodfellow, 2003). Given that all of the mudstones from the Lemarchant deposit have weakly to strongly negative Ce anomalies argues very strongly that they have not been affected by significant detrital material and were deposited into an oxygenated water column.

Support for mixing with oxygenated seawater is also reinforced by the Y/Ho systematics of the hydrothermal metalliferous mudstones. Yttrium is typically enriched relative to Ho in oxygenated seawater relative to hydrothermal vent fluids (e.g., Bau, 1996; Bau and Dulski, 1999). Correspondingly, hydrothermal particles that have spent considerable residence time in an oxygenated water column will scavenge Y from the column, and inherit a high Y/Ho ratio.

Due to the general similarity of the REY-patterns between the mudstones of various stratigraphic levels (Fig. 2.11A-C, 2.11E), it is suggested here that they were all derived from the same hydrothermal fluids. There are, however, slight variations, particularly in the Y systematics and size of the Eu anomalies. In particular, interflow mudstones and those more distal to mineralization have higher Y, Y/Ho, and slightly

smaller positive Eu anomalies (Fig. 2.11B-C). Increased Y-values from seawater seem to be weakly correlated with stronger negative Ce anomalies (Fig. 2.12A), indicating more REY-scavenging from seawater due to longer residence times of the hydrothermal particles in the plume. Correspondingly, the utilization of Eu anomalies and lower Y/Ho ratios may be useful in delineating mudstones more proximal to mineralization than those distal from mineralization in similar geological environments.

2.7.4 Sediment provenance – basin setting and tectonics

Provenance-related immobile element systematics of all four types of Lemarchant metalliferous mudstones and tuff have continental to oceanic island arc signatures (Fig. 2.15A-C). This is strongly controlled, however, by local host rocks in the Lemarchant deposit. For example, the oceanic island arc signatures are found predominantly in interflow mudstones within Lake Ambrose formation basalt and in some tuff samples, whereas those hosted primarily by Bindons Pond rhyolite have more continental island arc signatures. These systematics are expected for sediments deposited in a graben/caldera basin in a rifted continental arc, or an arc proximal to continental crust, which is the suggested tectonic model for the Tally Pond belt (Rogers et al., 2006; McNicoll et al., 2010; Zagorevski et al., 2010; Piercey et al., 2014). The occurrence of mudstones with hydrothermal signatures within hanging wall mafic volcanic rocks of the Lake Ambrose formation further indicates that the Lemarchant hydrothermal system and exhalation was still active during the emplacement of the basaltic lava flows.

A rifted arc environment is also consistent with much of the mineralogy, compositions and paragenesis of the phases in the hydrothermal metalliferous sediments. It is proposed that the deposit likely formed at moderate to shallow water (~1200 m) depth in a rift/caldera setting, which is atypical for most VMS deposits (Hannington et al., 2005; de Ronde et al., 2012). Due to this relatively shallow depth, and a suggested temperature of formation of >250°C, the boiling curve for seawater can be intercepted and shifted from the one phase field (VMS-style mineralization) to the two phase (liquid and vapor) field (magmatic-epithermal input due to boiling), when depth and pressure of the depositional system decreases and/or temperature increases (Fig. 2.17). Hence, the Lemarchant hydrothermal system records both normal seafloor hydrothermal activity and magmatic-epithermal fluid contributions (e.g., Gill and Piercey, 2014). Given that the mudstones are cross-cut by younger sulphide and barite (Figs. 2.6B, C, 2.7C-E), it is proposed that they represent the first hydrothermal activity in the Lemarchant deposit. Mudstone deposition was followed by precipitation of barite and Zn-Pb sulphides, which themselves were cut by galena, electrum and sulphosalts, and subsequently replaced or cross-cut by Cu-sulphides. This type of activity could reasonably be assumed to represent an early lower temperature Zn-Pb sulphide forming event with barite precipitation, followed by fluid boiling leading to the epithermal suite minerals and electrum, and a final stage with a higher temperature Cu-rich fluid that overprinted the latter. A similar situation was described previously for the Lemarchant deposit by Copeland et al. (2009) and Gill and Piercey (2014). The late high temperature Cu-sulphide forming event was followed by an event characterized by crack-and-seal type barite veins that cross-cut the Pb-Zn- and Cu-sulphides (Fig. 2.7E).

Such a model is permissible within the proposed tectonic regime of the region. In particular, early stage Zn-Pb-epithermal activity could have occurred early in the basin's history during initial arc rifting. This shallower water environment would have allowed the hydrothermal fluids to intersect the depth to boiling curve and form epithermal suite enrichments due to phase separation (e.g., Hannington, 2009). With continued extension, the hydrothermal system would have subsided and allowed the system to get hotter (i.e., >300°C), enabled the fluids to carry Cu, and led to the formation of higher-temperature Cu-Zn stringer mineralization and interstitial chalcopyrite typical of VMS deposits. This later stage chalcopyrite phase is recorded within the mudstones as well as in the massive sulphides at Lemarchant (Gill and Piercey, 2014). However, chalcopyrite predominantly occurs as stringer type, and not as massive sulphide ore. This suggests that temperatures between >300°C to 350°C were not sustained over a long period of time. At T>350°C hydrothermal fluids are undersaturated in metals, and leaching of chalcopyrite will occur (Large, 1992), a feature which is not observed at Lemarchant. Accordingly, the Lemarchant mineral assemblages provide some evidence of water depth, the presence of positive Eu anomalies (T > 250°C) and the lack of massive chalcopyrite ore (T < 325°C), as well as evidence for boiling and an epithermal element suite, suggests that the deposit formed between 250° and 325°C (Fig. 2.17). This broadly coincides with measurements of modern arc-related hydrothermal systems (Hannington et al., 2005), which are similar to the inferred environment of formation of the Lemarchant deposit.

2.8 Conclusions

The Lemarchant deposit provides for an understanding of the relationship of hydrothermal metalliferous mudstones to mineralization in bimodal felsic environments. Exploration criteria to delineate potentially productive from less prospective mudstones from this study include: 1) the hydrothermal mudstones have high Fe and base metals, and plot within the hydrothermal fields on Boström-type plots; 2) an enrichment in base metal sulphides, barite, and epithermal suite elements, namely Hg-Sb-As that is unique to the Lemarchant deposit in the Tally Pond belt, but similar to other VMS-epithermal hybrids in comparable settings, and which enables potentially prospective mudstones using a Ba-Hg diagram to be identified; and 3) REY systematics that are indicative of deposition from high temperature fluids (i.e., Eu/Eu*>1), and that are rock buffered (i.e., Y/Ho~27 and not like seawater with Y/Ho>44), with or without evidence for mixing with oxygenated seawater (Ce/Ce*<1). Additionally, due to processes occurring within the hydrothermal plume, i.e., mixing of hydrothermal fluids with seawater and scavenging of hydrogenous elements, metalliferous sediments can record paleoredox conditions at the time of precipitation. Redox-sensitive proxies, such as occurrences of barite and marcasite, and the presence of positive Ce anomalies, are indicative of deposition of the metalliferous Lemarchant exhalites from an oxygenated water column. Even though V-Cr-Ni-Co-Mo-U characteristics suggest an anoxic depositional environment, enhanced scavenging of oxyanions onto Fe-oxyhydroxides possibly creates this apparent anoxic environment.

These geochemical and mineralogical signatures are useful for the Tally Pond belt and likely similar environments globally. The results herein, however, require further

testing and this can only be achieved via increased drill hole density and 2D and 3D sampling coupled with a sound understanding of the basin geology and architecture.

2.9 Acknowledgements

This research was funded by the Canadian Mining Research Organization (CAMIRO) and an NSERC CRD grant. Kind support was provided by Christine Devine, Dianne and Charlie Fost, Michael Vande Guchte, Alexandria Marcotte, and Bryan Sparrow from Paragon Minerals Corporation (now Canadian Zinc Corporation. Research was also funded by the NSERC-Altius Industrial Research Chair in Mineral Deposits, funded by NSERC, Altius Resources Inc., and the Development Corporation of Newfoundland and Labrador. Furthermore, the help and support from the technical staff, Lakmali Hewa, Keir Hiscock, and Pam King, as well as the Piercey research group, and especially from Michael Buschette, Jonathan Cloutier, Shannon Gill, Shannon Guffey, Dario Harazim, Hannah Mills, Inês Nobre Silva, and Jean-Luc Pilote are greatly appreciated. Additionally, we thank John Hinchey from the Geological Survey of Newfoundland for his help and support. Also very much appreciated are the reviews and recommendations of *Economic Geology* reviewers, Paul Spry and Nils Jansson, which greatly improved the manuscript.

2.10 References

Algeo, T. J., and Tribovillard, N., 2009, Environmental analysis of paleoceanographic systems based on molybdenum-uranium covariation: Chemical Geology, v. 268, p. 211-225.

Barrett, T. J., and MacLean, W. H., 1994, Chemostratigraphy and hydrothermal alteration in exploration for VHMS deposits in greenstones and younger rocks, *in* Lentz, D. R., ed., Alteration and Alteration Processes Associated with Ore-Forming Systems, Short Course Notes Volume 11, Geological Association of Canada, p. 433-467.

Bau, M., 1991, Rare-earth element mobility during hydrothermal and metamorphic fluid rock interaction and the significance of the oxidation-state of europium: Chemical Geology, v. 93, p. 219-230.

_____1993, Effects of syn-depositional and postdepositional processes on the rare-earth element distribution in Precambrian iron-formations: European Journal of Mineralogy, v. 5, p. 257-267.

_____1996, Controls on the fractionation of isovalent trace elements in magmatic and aqueous systems: Evidence from Y/Ho, Zr/Hf, and lanthanide tetrad effect: Contributions to Mineralogy and Petrology, v. 123, p. 323-333.

_____1999, Scavenging of dissolved yttrium and rare earths by precipitating iron oxyhydroxide; experimental evidence for Ce oxidation, Y-Ho fractionation, and lanthanide tetrad effect: Geochimica et Cosmochimica Acta, v. 63, p. 67-77.

Bau, M., and Dulski, P., 1999, Comparing yttrium and rare earths in hydrothermal fluids from the Mid-Atlantic Ridge; implications for Y and REE behaviour during near-vent mixing and for the Y/Ho ratio of Proterozoic seawater: Chemical Geology, v. 155, p. 77-90.

Bau, M., and Koschinsky, A., 2009, Oxidative scavenging of cerium on hydrous Fe oxide: Evidence from the distribution of rare earth elements and yttrium between Fe oxides and Mn oxides in hydrogenetic ferromanganese crusts: Geochemical Journal, v. 43, p. 37-47.

Bhatia, M. R., and Crook, K. A. W., 1986, Trace element characteristics of graywackes and tectonic setting discrimination of sedimentary basins: Contributions to Mineralogy and Petrology, v. 92, p. 181-193.

Boström, K., 1973, The origin and fate of ferromanganoan active ridge sediments: Stockholm Contributions in Geology, v. 27, p. 147-243.

Boström, K., Joensuu, O., Valdés, S., and Riera, M., 1972, Geochemical history of south Atlantic Ocean sediments since Late Cretaceous: Marine Geology, v. 12, p. 85-121.

Boström, K., and Peterson, M. N., 1966, Precipitates from hydrothermal exhalations on the East Pacific Rise: Economic Geology, v. 61, p. 1258-1265.

_____1969, The origin of aluminum-poor ferromanganoan sediments in areas of high heat flow on the East Pacific Rise: Marine Geology, v. 7, p. 427-447.

Campbell, I. H., Lesher, C. M., Coad, P., Franklin, J. M., Gorton, M. P., and Thurston, P. C., 1984, Rare-earth element mobility in alteration pipes below massive Cu-Zn sulfide deposits: Chemical Geology, v. 45, p. 181-202.

Copeland, D. A., Toole, R. M., and Piercey, S. J., 2009, 10th Year supplementary assessment report on soil sampling, linecutting, Titan 24 geophysical surveying, diamond drilling and petrography, licence 8183M, South Tally Pond property, Rogerson Lake area, Newfoundland and Labrador, NTS 12A/10 and 12A/07: St.

John's, NL, Canada, Newfoundland and Labrador Geological Survey Assessment File, p. 56.

de Baar, H. J. W., German, C. R., Elderfield, H., and van Gaans, P., 1988, Rare earth element distributions in anoxic waters of the Cariaco Trench: Geochimica et Cosmochimica Acta, v. 52, p. 1203-1219.

de Ronde, C.E.J., Butterfield, D.A., and Leybourne, M.I., 2012, Metallogenesis and mineralization of intraoceanic arcs I: Kermadec Arc—introduction: Economic Geology, v. 107, p. 1521-1525.

Dunning, G. R., Thurlow, J.G., Kean, B. F., and Swinden, H. S., 1987, Geochronology of the Buchans, Roberts Arm, and Victoria Lake groups and Mansfield Cove Complex, Newfoundland: Canadian Journal of Earth Sciences, v. 24, p. 1175-1184.

Dunning, G. R., Swinden, H. S., Kean, B. F., Evans, D. T. W., and Jenner, G. A., 1991, A Cambrian island arc in Iapetus; geochronology and geochemistry of the Lake Ambrose volcanic belt, Newfoundland Appalachians: Geological Magazine, v. 128, p. 1-17.

Elderfield, H. and Greaves, M.J., 1981, Negative cerium anomalies in the rare earth element patterns of oceanic ferromanganese nodules: Earth and Planetary Science Letters, v. 55, p. 163-170.

Emerson, S. R., and Huested, S. S., 1991, Ocean anoxia and the concentrations of molybdenum and vanadium in seawater: Marine Chemistry, v. 34, p. 177-196.

Evans, D. T. W., and Kean, B. F., 2002, The Victoria Lake supergroup, central Newfoundland - its definition, setting and volcanogenic massive sulphide mineralization, Newfoundland and Labrador Department of Mines and Energy, Geological Survey, Open File NFLD/2790, p. 1-68.

Evans, D. T. W., Kean, B. F., and Dunning, G. R., 1990, Geological studies, Victoria Lake Group, Central Newfoundland Current Research Report, Geological Survey Branch, Report: 90-1, p. 131-144.

Franklin, J. M., Lydon, J. W., and Sangster, D. F., 1981, Volcanic-associated massive sulfide deposits: Economic Geology 75th Anniversary Volume, p. 485-627.

Fraser, D., Giroux, G. A., Copeland, D. A., and Devine, C. A., 2012, NI-43-101 Technical report and mineral resource estimate on the Lemarchant deposit, South Tally Pond VMS project, central Newfoundland, Canada for Paragon Minerals Corporation, National Instrument 43-101 Technical Report: Toronto, ON, Canada, National Instrument 43-101 Technical Report, p. 1-132.

Füchtbauer, H., Heling, D., Müller, G., Richter, D. K., Schmincke, H.-U., Schneider, H.-J., Valeton, I., Walther, H. W., and Wolf, M., 1988, Sedimente und Sedimentgesteine - Sedimentpetrologie, Teil II: Stuttgart, p. 1-1141.

German, C.R. and Elderfield, H., 1990, Application of the Ce anomaly as a paleoredox indicator: The ground rules: Paleoceanography, v. 5, p. 823-833.

German, C. R., and Von Damm, K. L., 2003, Hydrothermal processes: Treatise on Geochemistry, Volume 6, Elsevier, 2003, p. 181-222.

Gill, S. B., and Piercey, S. J., 2014, Preliminary mineralogy of barite-associated sulphide mineralization in the Ordovician Zn-Pb-Cu-Ag-Au Lemarchant volcanogenic

massive sulphide deposit, Newfoundland and Labrador: Current Research - Geological Survey of Canada, v. 2013-17, p. 1-15.

Goodfellow, W. D., and McCutcheon, S. R., 2003, Geologic and genetic attributes of volcanic sediment-hosted massive sulfide deposits of the Bathurst mining camp, northern New Brunswick; a synthesis: Economic Geology Monographs, v. 11, p. 245-301.

Griffith, E. M., and Paytan, A., 2012, Barite in the ocean - occurrence, geochemistry, and palaeoceanographic applications: Sedimentology, v. 59, p. 1817-1835.

Gurvich, E. G., 2006, Metalliferous sediments of the World Ocean - Fundamental theory of deep sea hydrothermal sedimentation: Springer Berlin Heidelberg, p. 1-416.

Hannington, M. D., 2009, Modern submarine hydrothermal systems - a global perspective on distribution, size, and tectonic settings, *in* Cousens, B. L., and Piercey, S. J., eds., Submarine volcanism and mineralization: Modern through ancient, Short Course 29-30 May 2008, Geological Association of Canada, p. 91-148.

_____2014, Volcanogenic massive sulfide deposits, *in* Holland, H. D., and Turekian, K.K., ed., Treatise on Geochemistry 2nd Edition, 8. Reviews in Economic Geology, Elsevier, p. 319-350.

Hannington, M. D., and Scott, S. D., 1989, Sulfidation equilibria as guides to gold mineralization in volcanogenic massive sulfides; evidence from sulfide mineralogy and the composition of sphalerite: Economic Geology, v. 84, p. 1978-1995.

Hannington, M. D., de Ronde, C. E. J., and Petersen, S., 2005, Sea floor tectonics and submarine hydrothermal systems, Economic Geology 100th Anniversary Volume, p. 111-142.

Hannington, M. D., Jonasson, I. R., Herzig, P. M., and Petersen, S., 1995, Physical and chemical processes of seafloor mineralization at mid-ocean ridges: Geophysical Monograph, v. 91, p. 115-157.

Harazim, D., Callow, R. H. T., and McIlroy, D., 2013, Microbial mats implicated in the generation of intrastratal shrinkage ('synaeresis') cracks: Sedimentology, v. 6, p. 1621-1638.

Haymon, R. M., and Kastner, M., 1981, Hot spring deposits on the East Pacific Rise 21°N: preliminary description of mineralogy and genesis: Earth and Planetary Science Letters, v. 53, p. 363-381.

Hekinian, R., Hoffert, M., Larqué, P., Cheminée, J. L., Stoffers, P., and Bideau, D., 1993, Hydrothermal Fe and Si oxyhydroxide deposits from South Pacific intraplate volcanoes and East Pacific Rise axial and off-axial regions: Economic Geology, v. 88, p. 2099-2121.

Hinchey, J. G., and McNicoll, V., 2009, Tectonostratigraphic architecture and VMS mineralization of the southern Tulks Volcanic Belt: New insights from U-Pb geochronology and lithogeochemistry, *in* Pereira, C. P. G., and Walsh, D. G., eds., Current Research, Report 09-01: St. John's, NL, Canada, Geological Survey Branch, p. 13-42.

Humphris, S. E., and Bach, W., 2005, On the Sr isotope and REE compositions of anhydrites from the TAG seafloor hydrothermal system: Geochimica et Cosmochimica Acta, v. 69, p. 1511-1525.

Huston, D. L., and Logan, G. A., 2004, Barite, BIFs and bugs; evidence for the evolution of the Earth's early hydrosphere: Earth and Planetary Science Letters, v. 220, p. 41-55.

Huston, D. L., Pehrsson, S., Eglington, B. M., and Zaw, K., 2010, The geology and metallogeny of volcanic-hosted massive sulfide deposits: variations through geologic time and with tectonic setting: Economic Geology, v. 105, p. 571-591.

Jenner, G. A., 1996, Trace element geochemistry of igneous rocks: Geochemical nomenclature and analytical geochemistry, *in* Wyman, D. A., ed., Trace element geochemistry of volcanic rocks: Applications for massive sulfide exploration, 12: Geological Association of Canada, Short Course Notes, p. 51-77.

Jenner, G. A., Longerich, H. P., Jackson, S. E., and Fryer, B. J., 1990, ICP-MS - A powerful tool for high-precision trace element analysis in Earth sciences: Evidence from analysis of selected U.S.G.S. reference samples: Chemical Geology, v. 83, p. 133-148.

Jones, S., Gemmell, J. B., and Davidson, G. J., 2006, Petrographic, geochemical, and fluid inclusion evidence for the origin of siliceous cap rocks above volcanic-hosted massive sulfide deposits at Myra Falls, Vancouver Island, British Columbia, Canada: ECONOMIC GEOLOGY, v. 101, p. 555-584.

Kharaka, Y. K., and Hanor, J. S., 2014, Deep fluids in sedimentary basins, *in* Turekian, H. D. H. K., ed., Treatise on geochemistry (Second Edition): Oxford, Elsevier, v. 7, p. 471-515.

Kolata, D. R., Huff, W. D., and Bergström, S. M., 1996, Ordovician K-bentonites of eastern North America: Geological Society of America Special Paper, v. 313, p. 1-89.

Large, R. R., 1992, Australian volcanic-hosted massive sulfide deposits; features, styles, and genetic models: Economic Geology, v. 87, p. 471-510.

Lode, S., Piercey, S. J., Layne, G. D., Piercey, G., and Devine, C. A., 2014, Sulfur isotopic studies of poly-metallic sulfides hosted within hydrothermal mudstones associated with the Cambrian Lemarchant volcanogenic massive sulfide (VMS) deposit, Newfoundland, Canada [abs.]: Conference Abstract, SEG 2014, Keystone.

Lode, S., Piercey, S. J., Layne, G. D., Piercey, G., and Cloutier, J., in review, Multiple sulphur and lead sources recorded in hydrothermal exhalites associated with the Lemarchant volcanogenic massive sulphide deposit, central Newfoundland, Canada: Mineralium Deposita.

Longerich, H. P., Jenner, G. A., Fryer, B. J., and Jackson, S. E., 1990, Inductively coupled plasma-mass spectrometric analysis of geological samples: A critical evaluation based on case studies: Chemical Geology, v. 83, p. 105-118.

Lydon, J. W., 1984, Ore deposit models; 8, Volcanogenic sulphide deposits; Part I, A descriptive model: Geoscience Canada, v. 11, p. 195-202.

McLennan, S. M., 1989, Rare earth elements in sedimentary rocks; influence of provenance and sedimentary processes: Reviews in Mineralogy, v. 21, p. 169-200.

McLennan, S. M., Bock, B., Hemming, S. R., Hurowitz, J. A., Lev, S. M., and McDaniel, D. K., 2003, The roles of provenance and sedimentary processes in the geochemistry of sedimentary rocks, *in* Lentz, D. R., ed., Geochemistry of

sediments and sedimentary rocks: Evolutionary considerations to mineral deposit-forming environments, GEOText 4: St. John's, NL, Canada, Geological Association of Canada, p. 7-38.

McNicoll, V., Squires, G., Kerr, A., and Moore, P., 2010, The Duck Pond and Boundary Cu-Zn deposits, Newfoundland: new insights into the ages of host rocks and the timing of VHMS mineralization: Canadian Journal of Earth Sciences, v. 47, p. 1481-1506.

Michard, A., Albarède, F., Michard, G., Minster, J. F., and Charlou, J. L., 1983, Rare-earth elements and uranium in high-temperature solutions from East Pacific Rise hydrothermal vent field (13 degrees N): Nature, v. 303, p. 795-797.

Mills, R.A. and Elderfield, H., 1995, Rare earth element geochemistry of hydrothermal deposits from the active TAG Mound, 26°N Mid-Atlantic Ridge: Geochimica et Cosmochimica Acta, v. 59, p. 3511-3524.

Mills, R. A., Wells, D. M., and Roberts, S., 2001, Genesis of ferromanganese crusts from the TAG hydrothermal field: Chemical Geology, v. 176, p. 283-293.

Morford, J. L., Emerson, S. R., Breckel, E. J., and Kim, S. H., 2005, Diagenesis of oxyanions (V, U, Re, and Mo) in pore waters and sediments from a continental margin: Geochimica et Cosmochimica Acta, v. 69, p. 5021-5032.

Nesbitt, H. W., 2003, Petrogenesis of siliciclastic sediments and sedimentary rocks, *in* Lentz, D. R., ed., Geochemistry of Sediments and Sedimentary Rocks: Evolutionary Considerations to Mineral Deposit-Forming Environments, GEOText 4: St. John's, NL, Canada, Geological Association of Canada, p. 39-52.

Nesbitt, H. W., and Markovics, G., 1997, Weathering of granodioritic crust, long-term storage of elements in weathering profiles, and petrogenesis of siliciclastic sediments: Geochimica et Cosmochimica Acta, v. 61, p. 1653-1670.

Nesbitt, H. W., and Young, G. M., 1982, Early Proterozoic climates and plate motions inferred from major element chemistry of lutites: Nature, v. 299, p. 715-717.

Ohmoto, H., 1996, Formation of volcanogenic massive sulfide deposits: The Kuroko perspective: Ore Geology Reviews, v. 10, p. 135-177.

Ohmoto, H., and Goldhaber 1997, Sulfur and carbon isotopes, in Barnes, H.L., ed., Geochimistry of hydrothermal ore deposits, 3rd edition: New York, John Wiley & Sons: New York, p. 517-611.

Peter, J. M., 2003, Ancient iron formations: their genesis and use in the exploration for stratiform base metal sulphide deposits, with examples from the Bathurst Mining Camp, *in* Lentz, D. R., ed., Geochemistry of sediments and sedimentary rocks: Secular evolutionary considerations to mineral deposit-forming environments, GEOtext v. 4, Geological Association of Canada, p. 145-176.

Peter, J. M., and Goodfellow, W. D., 2003, Hydrothermal sedimentary rocks of the Heath Steele Belt, Bathurst mining camp, New Brunswick; Part 3, Application of mineralogy and mineral and bulk compositions to massive sulfide exploration: Economic Geology Monograph, v. 11, p. 417-433.

Peter, J. M., Goodfellow, W. D., and Doherty, W., 2003, Hydrothermal sedimentary rocks of the Heath Steele Belt, Bathurst mining camp, New Brunswick; Part 2, Bulk and rare earth element geochemistry and implications for origin: Economic Geology Monographs, v. 11, p. 391-415.

Piercey, S.J. 2007. Volcanogenic Massive Sulphide (VMS) Deposits of the Newfoundland Appalachians, Canada: An Overview of their Setting, Classification, Grade-Tonnage Data, and Unresolved Questions. Digging Deeper, Vols. 1 and 2: 931-934.

Piercey, S. J., 2014, Modern Analytical Facilities 2. A Review of quality assurance and quality control (QA/QC) procedures for lithogeochemical data: Geoscience Canada, v. 41, p. 75-88.

Piercey, S. J., Squires, G. C., Brace, T., and Lode, S., 2012, Initial report: Hydrothermal mudstones from the Duck Pond volcanogenic massive sulfide (VMS) deposit, Central Mobile Belt Newfoundland and Labrador, Canada: Part 1 – Geology and Lithogeochemistry, CAMIRO Project 08E04 2012 Annual Report, The geochemistry of shales as vectors to ore deposits, p. 1-41.

Piercey, S. J., Squires, G. C., and Brace, T. D., 2014, Lithostratigraphic, hydrothermal, and tectonic setting of the Boundary volcanogenic massive sulfide deposit, Newfoundland Appalachians, Canada: Formation by subseafloor replacement in a Cambrian rifted arc: Economic Geology, v. 109, p. 661-687.

Ridler, R. H., 1971, Analysis of Archean volcanic basins in the Canadian Shield using the exhalite concept: Bulletin of the Canadian Institute of Mining and Metallurgy, v. 64, p. 20.

Rogers, N., van Staal, C. R., McNicoll, V., Pollock, J., Zagorevski, A., and Whalen, J., 2006, Neoproterozoic and Cambrian arc magmatism along the eastern margin of the Victoria Lake supergroup: A remnant of Ganderian basement in central Newfoundland?: Precambrian Research, v. 147, p. 320-341.

Rogers, N., van Staal, C., Zagorevski, A., Skulski, T., Piercey, S. J., and McNicoll, V., 2007, Timing and tectonic setting of volcanogenic massive sulphide bearing terranes within the Central Mobile Belt of the Canadian Appalachians, *in* Milkereit, B., ed., Proceedings of Exploration 07: Fifth Decennial International Conference on Mineral Exploration: Toronto, ON, p. 1199-1205.

Rudnicki, M. D., 1995, Particle formation, fallout and cycling within the buoyant and non-buoyant plume above the TAG vent field: Geological Society, London, Special Publications, v. 87, p. 387-396.

Sáez, R., Moreno, C., González, F., and Almodóvar, G., 2011, Black shales and massive sulfide deposits: causal or casual relationships? Insights from Rammelsberg, Tharsis, and Draa Sfar: Mineralium Deposita, v. 46, p. 585-614.

Schieber, J., 2011, Marcasite in black shales - a mineral proxy for oxygenated bottom waters and intermittent oxidation of carbonaceous muds: Journal of Sedimentary Research, v. 81, p. 447-458.

Schoonen, M. A. A., and Barnes, H. L., 1991, Reactions forming pyrite and marcasite from solution: II. Via FeS precursors below 100°C: Geochimica et Cosmochimica Acta, v. 55, p. 1505-1514.

Skilling, I. P., White, J. D. L., and McPhie, J., 2002, Peperite: A review of magma-sediment mingling: Journal of Volcanology and Geothermal Research, v. 114, p. 1-17.

Slack, J. F., Grenne, T., Bekker, A., Rouxel, O. J., and Lindberg, P. A., 2007, Suboxic deep seawater in the late Paleoproterozoic: Evidence from hematitic chert and iron

formation related to seafloor-hydrothermal sulfide deposits, central Arizona, USA: Earth and Planetary Science Letters, v. 255, p. 243-256.

Spry, P. G., Peter, J. M., and Slack, J. F., 2000, Meta-exhalites as exploration guides to ore: Reviews in Economic Geology , v. 11, p. 163-201.

Squires, G. C., MacKenzie, A. C., and MacInnis, D., 1991, Geology and genesis of the Duck Pond volcanogenic massive sulfide deposit, *in* Swinden, H. S., Evans, D. T. W., and Kean, B. F., eds., Metallogenic framework of base and precious metal deposits, central and western Newfoundland: Geological Survey of Canada Open File 2156: Ottawa, ON, Canada, Geological Survey of Canada, p. 56-64.

Squires, G. C., and Moore, P. J., 2004, Volcanogenic massive sulphide environments of the Tally Pond Volcanics and adjacent area; geological, lithogeochemical and geochronological results, *in* Pereira, C. P. G., Walsh, D. G., and Kean, B. F., eds., Current Research, Report 04-1: St. John's, NL, Geological Survey Branch, p. 63-91.

Sverjensky, D. A., 1984, Europium redox equilibria in aqueous-solution: Earth and Planetary Science Letters, v. 67, p. 70-78.

Swinden, H. S., 1988, Introduction to volcanogenic sulphide deposits in Newfoundland, *in* Swinden, H. S., and Kean, B. F., eds., The volcanogenic sulphide districts of central Newfoundland, Geological Association of Canada, p. 1-26.

_____1991, Paleotectonic settings of volcanogenic massive sulphide deposits in the Dunnage Zone, Newfoundland Appalachians: Canadian Institute of Mining and Metallurgy Bulletin, v. 84, p. 59-89.

Taylor, S. R., and McLennan, S. M., 1985, The continental crust: its composition and evolution: Oxford, Blackwell Scientific Publications, 312 p.

Tribovillard, N., Algeo, T. J., Lyons, T., and Riboulleau, A., 2006, Trace metals as paleoredox and paleoproductivity proxies: An update: Chemical Geology, v. 232, p. 12-32.

van Staal, C. R., 2007, Pre-Carboniferous tectonic evolution and metallogeny of the Canadian Appalachians, *in* Goodfellow, W. D., ed., Mineral deposits of Canada: A synthesis of major deposit-types, district metallogeny, the evolution of geological provinces, and exploration methods, Special Publication 5, Mineral Deposits Division, Geological Association of Canada, p. 793-818.

van Staal, C. R., and Barr, S. M., 2011, Lithospheric architecture and tectonic evolution of the Canadian Appalachians and associated Atlantic margin, *in* Percival, J. A., Cook, F. A., and Clowes, R. M., eds., Chapter 2 Tectonic styles in Canada: the LITHOPROBE Perspective, Special Paper 49, Geological Association of Canada, p. 3-55.

Webb, G. E., and Kamber, B. S., 2000, Rare earth elements in Holocene reefal microbialites; a new shallow seawater proxy: Geochimica et Cosmochimica Acta, v. 64, p. 1557-1565.

Williams, H., 1979, Appalachian Orogen in Canada: Canadian Journal of Earth Sciences, v. 16, p. 792-807.

_____1995, Geology of the Appalachian-Caledonian Orogen in Canada and Greenland: Geology of Canada, v. 6, p. 1-944.

Williams, H., Colman-Sadd, S. P., and Swinden, H. S., 1988, Tectonostratigraphic subdivisions of central Newfoundland., Current Research, Part B, Paper 88-1B: Ottawa, ON, Canada, Geological Survey of Canada, p. 91-98.

Zagorevski, A., van Staal, C. R., McNicoll, V. J., and Rogers, N., 2007, Upper Cambrian to Upper Ordovician peri-Gondwanan island arc activity in the Victoria Lake supergroup, central Newfoundland; tectonic development of the northern Ganderian margin: American Journal of Science, v. 307, p. 339-370.

Zagorevski, A., van Staal, C. R., Rogers, N., McNicoll, V. J., and Pollock, J., 2010, Middle Cambrian to Ordovician arc-backarc development on the leading edge of Ganderia, Newfoundland Appalachians: Geological Society of America Memoir, v. 206, p. 367-396.

Table 2.1

Whole-rock lithogeochemical data for the Lemarchant mudstones and tuffs

Sample #			**CNF25074**	**CNF25075**	**CNF25062b**	**CNF25063**	**CNF25064**	**CNF25065**	**CNF25066**	**CNF25067**	**CNF38438**	**CNF30955**	**CNF38437**	**CNF30954**	**CNF38436**
Drill Hole			LM13-78	LM13-78	LM13-76	LM13-76	LM13-77	LM13-77	LM13-77	LM13-77	LM07-13	LM07-13	LM07-13	LM07-13	LM07-13
Section N			99+75N	99+75N	100+50N	100+50N	100+50N	100+50N	100+50N	100+50N	101N	101N	101N	101N	101N
Northing (UTM)			5374477	5374477	5374537	5374537	5374537	5374537	5374537	5374537	5374599.93	5374599.93	5374599.93	5374599.93	5374599.93
Easting (UTM)			520956	520956	521049	521049	521049	521049	521049	521049	521111.73	521111.73	521111.73	521111.73	521111.73
Sample Drill Hole Depth (m)			119.74	121.05	163.78	172.28	139.56	140	142.1	142.76	164.2	165.32	164.5	164.67	423.96
Description			T	FEM	FEM	T	T	T	FEM	FEM	EMS	EMS	EMS	EMS	IFE
$C_{(total)}$	%	IR	1.70	3.16	0.20	3.41	0.23	3.06	0.78	0.03	0.16	0.02	0.16	0.10	0.60
$S_{(total)}$	%	IR	8.23	27.20	25.50	6.84	26.50	4.57	21.10	21.80	21.80	16.60	33.60	33.10	17.60
Hg	ppb	FIMS	57.00	42.00	160.00	10.00	112.00	11.00	175.00	701.00	111.00	195.00	122.00	186.00	279.00
SiO_2	%	ICP-ES	22.82	18.04	36.88	40.08	31.86	45.92	26.32	32.06	45.60	39.80	14.57	21.16	45.16
Al_2O_3	%	ICP-ES	17.71	5.26	5.89	5.73	4.21	6.78	9.20	12.69	4.28	8.33	4.14	5.44	9.87
$Fe_{(total)}$[1]	%	ICP-ES	25.81	53.02	32.23	13.79	39.71	14.15	37.01	29.20	29.70	23.63	48.59	44.07	22.75
MnO	%	ICP-ES	1.06	0.10	0.05	0.32	0.05	0.61	0.14	0.04	0.07	0.03	0.08	0.07	0.02
MgO	%	ICP-ES	5.51	1.79	1.23	2.77	0.70	2.00	1.47	1.04	1.90	0.89	2.34	2.36	0.66
CaO	%	ICP-ES	7.16	0.32	1.16	16.78	0.38	14.35	1.20	1.11	1.02	1.18	2.10	1.04	2.21
Na_2O	%	ICP-ES	0.31	0.05	0.05	0.38	0.06	0.08	0.08	0.15	0.06	0.05	0.03	0.02	0.96
K_2O	%	ICP-ES	2.60	0.74	1.02	0.19	0.64	0.81	1.27	2.80	0.47	0.51	0.25	0.40	2.20
TiO_2	%	ICP-ES	1.17	0.27	0.26	0.42	0.18	0.29	0.32	0.44	0.27	0.32	0.34	0.27	0.41
P_2O_5	%	ICP-ES	0.17	0.33	0.31	1.15	0.30	0.92	0.06	0.84	0.73	0.80	1.54	0.70	0.94
LOI	%	ICP-ES	10.37	16.98	17.61	9.42	16.89	7.97	17.68	15.34	14.44	11.16	23.85	22.70	13.03
Total	%	ICP-ES	94.68	96.89	96.69	91.03	94.98	93.89	94.75	95.73	98.54	86.70	97.83	98.23	98.21
Ba	ppm	ICP-ES	517.00	323.00	1067.00	372.00	2074.00	2612.00	5859.00	11480.00	1544.00	50540.00	6037.00	17540.00	649.00
Sc	ppm	ICP-ES	33.00	6.00	8.00	12.00	5.00	8.00	12.00	16.00	13.00	9.00	7.00	7.00	12.00
Be	ppm	ICP-ES	2.00	1.00	0.50	0.50	0.50	0.50	2.00	2.00	0.50	2.00	0.50	1.00	0.50
V	ppm	ICP-ES	830.00	635.00	393.00	237.00	688.00	414.00	896.00	1825.00	267.00	962.00	342.00	543.00	1811.00
Li	ppm	ICP-MS	15.47	4.38	3.28	7.13	2.04	4.78	4.72	2.97	2.34	13.87	4.63	6.66	2.16
Sr	ppm	ICP-MS	158.75	19.54	16.41	157.08	11.45	118.99	15.38	24.88	17.27	83.47	50.47	64.93	58.45
Y	ppm	ICP-MS	12.83	12.16	8.26	26.36	7.54	28.87	8.31	16.25	13.69	15.52	20.77	13.75	17.77
Zr	ppm	ICP-MS	85.88	55.70	52.61	32.40	36.88	56.31	56.57	77.11	26.53	62.17	42.40	46.72	90.15
Nb	ppm	ICP-MS	0.64	2.23	1.85	0.95	1.49	1.09	1.71	3.74	0.82	3.86	2.79	1.89	8.81
Cs	ppm	ICP-MS	0.53	0.37	0.51	0.13	0.34	0.27	0.61	1.09	0.19	1.58	0.23	0.55	1.59
Ba_2	ppm	ICP-MS	531.97	327.29	895.70	354.06	1605.68	2708.12	3769.95	2399.92	1049.16	41616.33	3781.31	18100.32	718.07
La	ppm	ICP-MS	6.73	15.12	13.67	15.04	7.39	26.54	11.12	20.09	16.19	19.84	18.78	14.97	19.23
Ce	ppm	ICP-MS	7.64	19.66	21.23	21.05	11.11	29.89	16.88	31.16	28.27	28.95	25.21	18.38	33.24
Pr	ppm	ICP-MS	1.78	3.75	3.75	3.76	2.12	5.99	2.95	6.17	4.21	5.32	4.93	3.54	6.14
Nd	ppm	ICP-MS	7.15	14.65	14.91	17.02	8.86	23.41	11.35	25.65	18.97	22.64	21.92	14.40	26.49
Sm	ppm	ICP-MS	1.74	2.86	3.45	4.55	1.80	5.09	2.29	5.81	4.59	4.89	4.84	3.07	6.17
Eu	ppm	ICP-MS	0.42	0.64	0.90	1.64	0.48	1.55	0.74	1.55	1.15	1.54	1.51	0.95	1.58
Gd	ppm	ICP-MS	2.05	2.75	2.83	5.70	1.68	5.41	1.92	5.47	4.76	4.18	5.19	2.92	5.74
Tb	ppm	ICP-MS	0.33	0.40	0.38	0.78	0.25	0.76	0.30	0.69	0.61	0.54	0.71	0.41	0.74
Dy	ppm	ICP-MS	2.13	2.34	1.88	4.56	1.47	4.62	1.85	3.58	3.16	2.98	3.79	2.21	3.89
Ho	ppm	ICP-MS	0.48	0.48	0.33	0.86	0.28	0.92	0.34	0.65	0.53	0.54	0.70	0.43	0.70
Er	ppm	ICP-MS	1.63	1.41	0.98	2.32	0.79	2.64	1.10	1.80	1.31	1.50	1.70	1.25	1.85
Tm	ppm	ICP-MS	0.29	0.25	0.16	0.33	0.15	0.40	0.22	0.30	0.17	0.24	0.27	0.22	0.30
Yb	ppm	ICP-MS	2.32	1.50	1.05	1.75	0.91	2.47	1.48	1.96	1.00	1.49	1.58	1.15	2.03
Lu	ppm	ICP-MS	0.42	0.25	0.20	0.27	0.15	0.42	0.25	0.33	0.15	0.26	0.23	0.20	0.33
Hf	ppm	ICP-MS	8.11	2.64	3.17	1.74	1.47	4.67	2.71	3.47	0.78	1.71	1.07	1.22	2.22
Ta	ppm	ICP-MS	0.06	0.19	0.14	0.06	0.13	0.09	0.16	0.31	0.08	0.21	0.12	0.10	0.54
Tl	ppm	ICP-MS	1.68	2.19	0.89	0.31	1.93	0.72	3.72	7.50	1.44	1.88	1.36	2.51	3.61
Pb	ppm	ICP-MS	14.96	806.81	761.86	163.42	600.82	21.80	1184.86	761.00	433.14	211.40	754.27	896.90	581.51
Bi	ppm	ICP-MS	0.10	0.91	0.86	0.22	0.32	0.18	0.70	0.62	0.45	0.23	0.54	0.43	0.62
Th	ppm	ICP-MS	2.51	5.39	5.20	1.44	3.50	3.65	5.00	6.14	1.66	4.45	2.16	2.60	6.58
U	ppm	ICP-MS	1.69	30.61	25.12	5.18	16.34	4.88	61.36	55.88	5.26	39.31	13.98	12.42	66.85
Cr	ppm	ICP-MS	40.57	34.91	52.99	27.04	35.99	40.61	38.25	112.37	20.03	94.42	56.99	38.66	129.01
Fe	ppm	ICP-MS	137854.65	281694.38	214167.90	94744.28	242710.05	101344.44	196517.28	152849.46	192603.54	150078.55	311549.80	276654.66	146492.75
Mn	ppm	ICP-MS	5504.84	620.96	389.02	2410.25	363.82	4621.34	837.17	225.87	524.38	210.48	529.20	496.99	131.50
Co	ppm	ICP-MS	8.39	31.54	19.58	28.98	110.24	14.04	75.72	38.29	53.15	16.65	73.90	14.49	18.53
Ni	ppm	ICP-MS	105.09	457.01	182.26	82.76	251.92	76.28	339.26	479.49	142.97	276.51	165.71	191.41	570.12
Cu	ppm	ICP-MS	145.19	522.21	502.75	120.92	216.82	101.81	508.56	392.37	219.71	56188.59	605.33	233.46	263.95
Zn	ppm	ICP-MS	625.34	907.06	540.16	295.46	234.19	203.07	108.36	66.28	94.17	3659.78	214.03	263.79	919.90
As	ppm	ICP-MS	14.48	203.00	216.07	41.63	3305.98	139.88	2069.99	1302.14	376.72	394.79	9545.16	1201.81	682.75
Se	ppm	ICP-MS	6.05	21.84	7.62	2.46	9.91	5.86	17.93	24.09	4.62	6.98	9.60	12.55	35.35
Br	ppm	ICP-MS	91.59	87.20	87.25	95.81	88.72	99.32	103.90	92.51	114.06	140.06	123.14	143.13	141.08
Mo	ppm	ICP-MS	6.80	125.95	108.39	20.45	113.42	26.16	263.83	213.91	34.35	136.51	33.74	86.16	151.28
Ag	ppm	ICP-MS	0.78	12.05	19.06	1.16	29.09	1.22	30.80	31.65	4.28	116.09	31.04	36.54	11.87
Cd	ppm	ICP-MS	2.74	6.65	8.19	1.09	4.05	1.00	0.62	0.59	1.26	19.18	1.11	0.26	11.08
Sn	ppm	ICP-MS	3.19	3.08	2.82	2.89	3.16	3.00	3.44	3.60	1.43	3.62	1.54	1.76	2.74
Sb	ppm	ICP-MS	1.87	140.36	23.23	2.92	51.32	1.12	49.20	81.32	71.78	26.74	111.10	120.42	61.73
Te	ppm	ICP-MS	0.10	0.73	0.96	0.55	0.82	0.10	1.70	0.89	1.71	1.87	2.44	3.71	1.13
I	ppm	ICP-MS	1.59	1.59	1.59	1.59	1.59	1.59	1.22	1.59	8.98	5.35	8.98	1.36	8.98
W	ppm	ICP-MS	4.41	6.19	1.47	2.13	2.52	1.81	2.60	6.34	2.45	14.08	6.86	5.02	4.54
CIA			63.75	82.57	72.54	24.83	79.58	30.79	78.30	75.76	73.41	82.72	63.50	78.84	64.76
Ce/Ce*			0.51	0.60	0.68	0.65	0.65	0.55	0.68	0.65	0.79	0.65	0.60	0.58	0.71
Eu/Eu*			1.05	1.08	1.36	1.52	1.29	1.39	1.67	1.29	1.16	1.60	1.42	1.50	1.25
Y/Ho			26.51	25.59	24.85	30.79	27.28	31.32	24.42	25.16	25.80	28.66	29.77	31.79	25.42

[1]Fe(total) = (Fe_2O_3+FeO)

EMS: Exhalite[2] associated with massive sulfides (within 5m)

FEM: Exhalite associated with felsic and mafic volcanic rocks, no massive sulfides

FEF: Exhalite within felsic volcanic rocks, no massive sulfides

IFE: Interflow exhalite

T: Tuff

[2]The term exhalite represents the Lemarchant metalliferous mudstones and was chosen to simplify the abbreviations.

Sample #			**CNF25100**	**CNF30979**	**CNF30980**	**CNF30981**	**CNF30982**	**CNF30983**	**CNF30984**	**CNF30985**	**CNF30986**	**CNF30987b**	**CNF30988**	**CNF25072**	**CNF25069**
Drill Hole			LM10-46	LM11-65	LM11-65	LM11-65	LM11-65	LM11-65	LM11-72	LM11-72	LM11-72	LM11-72	LM11-72	LM13-79	LM13-79
Section N			101N	101N	101N	101N	101N	101N	101+25N	101+25N	101+25N	101+25N	101+25N	101+25N	101+25N
Northing (UTM)			5374599.93	5374599.585	5374599.585	5374599.585	5374599.585	5374599.585	5374625.355	5374625.355	5374625.355	5374625.355	5374625.355	5374625.36	5374625.36
Easting (UTM)			521111.73	521114.134	521114.134	521114.134	521114.134	521114.134	521114.59	521114.59	521114.59	521114.59	521114.59	521114.59	521114.59
Sample Drill Hole Depth (m)			174.85	148.97	154.82	157.11	157.7	160.74	160.42	168.46	168.78	172.22	173	169.01	181.92
Description			EMS	IFE	EMS	EMS	EMS	EMS	IFE	IFE	IFE	EMS	EMS	IFE	EMS
$C_{(total)}$	%	IR	0.07	0.15	0.27	2.45	0.14	0.33	0.69	1.60	0.47	3.12	0.02	0.11	1.20
$S_{(total)}$	%	IR	34.00	29.90	28.60	8.55	19.50	17.50	9.49	8.65	24.80	4.48	38.00	33.20	38.80
Hg	ppb	FIMS	268.00	199.00	238.00	13.00	263.00	304.00	56.00	2.50	12.00	2.50	251.00	101.00	211.00
SiO_2	%	ICP-ES	16.18	28.23	27.85	35.69	28.52	38.09	63.07	52.50	31.28	35.81	14.60	14.76	16.07
Al_2O_3	%	ICP-ES	3.84	5.37	6.34	8.13	8.21	7.88	1.76	4.23	6.07	7.88	5.35	5.08	5.03
$Fe_{(total)}$ [1]	%	ICP-ES	50.71	35.40	40.40	23.60	28.97	21.68	14.61	24.53	38.16	20.47	47.50	49.87	46.32
MnO	%	ICP-ES	0.13	0.02	0.07	0.45	0.06	0.05	0.11	0.36	0.12	1.10	0.04	0.11	0.04
MgO	%	ICP-ES	1.91	0.44	1.34	4.62	2.05	0.53	0.82	1.51	2.29	2.46	1.45	1.52	0.63
CaO	%	ICP-ES	0.53	2.29	0.19	6.71	1.06	2.81	7.18	3.21	1.08	14.64	0.20	1.86	0.03
Na_2O	%	ICP-ES	0.01	0.05	0.05	0.05	0.07	0.03	0.02	0.05	0.04	0.03	0.04	0.01	0.04
K_2O	%	ICP-ES	0.11	0.65	0.94	0.68	0.49	0.12	0.03	0.52	0.72	0.37	0.56	0.10	1.12
TiO_2	%	ICP-ES	0.16	0.25	0.27	0.52	0.46	0.34	0.05	0.20	0.28	0.36	0.28	0.28	0.23
P_2O_5	%	ICP-ES	0.30	1.35	0.09	1.05	0.74	1.54	3.27	1.83	0.77	2.00	0.15	1.45	0.08
LOI	%	ICP-ES	24.74	19.34	20.39	15.69	12.79	11.42	9.01	11.54	18.43	9.30	24.84	22.83	25.93
Total	%	ICP-ES	98.63	93.40	97.93	97.18	83.41	84.50	99.93	100.50	99.25	94.40	95.01	97.87	95.52
Ba	ppm	ICP-ES	691.00	38510.00	7057.00	6617.00	54200.00	90110.00	615.00	3194.00	3665.00	3413.00	35230.00	239.00	7930.00
Sc	ppm	ICP-ES	5.00	9.00	8.00	12.00	12.00	18.00	2.00	6.00	9.00	10.00	8.00	7.00	6.00
Be	ppm	ICP-ES	0.50	0.50	1.00	0.50	3.00	9.00	0.50	0.50	0.50	0.50	3.00	0.50	3.00
V	ppm	ICP-ES	461.00	546.00	797.00	333.00	1985.00	1516.00	252.00	336.00	561.00	330.00	854.00	644.00	538.00
Li	ppm	ICP-MS	2.03	2.35	4.22	6.20	3.67	0.33	3.11	3.06	3.87	3.23	3.79	2.91	1.53
Sr	ppm	ICP-MS	12.48	84.25	14.88	72.72	132.73	117.40	111.99	72.77	34.25	265.13	42.26	23.75	8.75
Y	ppm	ICP-MS	6.90	30.60	7.46	26.27	16.44	35.53	49.79	32.55	16.10	39.74	8.77	27.26	10.45
Zr	ppm	ICP-MS	35.35	55.68	55.18	70.89	82.69	76.49	15.46	41.38	56.76	65.24	58.14	49.15	53.26
Nb	ppm	ICP-MS	2.23	4.63	5.09	4.39	9.58	7.33	1.18	3.73	4.04	3.43	4.88	3.28	2.96
Cs	ppm	ICP-MS	0.08	0.61	0.39	0.23	0.38	0.11	0.03	0.22	0.34	0.14	0.48	0.10	0.59
Ba_2	ppm	ICP-MS	616.39	20027.21	6713.10	7026.47	37836.30	41843.28	573.00	2471.87	3008.77	3288.17	19239.16	250.40	617.38
La	ppm	ICP-MS	8.21	12.60	15.23	35.22	28.37	28.45	33.11	28.33	15.53	40.57	14.22	17.09	15.61
Ce	ppm	ICP-MS	8.85	20.04	22.67	50.73	35.67	41.73	33.62	33.96	21.73	48.94	19.97	19.17	20.36
Pr	ppm	ICP-MS	1.76	4.62	3.70	8.76	6.60	8.47	6.54	6.38	3.78	9.19	3.63	4.50	4.26
Nd	ppm	ICP-MS	6.94	21.58	15.20	35.73	25.72	37.22	27.92	27.17	15.67	37.91	14.32	19.05	16.79
Sm	ppm	ICP-MS	1.39	6.00	2.83	7.48	4.76	8.44	6.70	5.88	3.16	7.80	2.89	4.25	3.08
Eu	ppm	ICP-MS	0.54	2.11	0.71	2.18	1.66	2.61	4.14	2.40	1.17	2.52	0.61	0.58	0.52
Gd	ppm	ICP-MS	1.35	6.85	2.15	7.45	3.92	8.49	8.04	6.56	3.34	8.06	1.86	4.77	2.31
Tb	ppm	ICP-MS	0.18	1.06	0.27	0.96	0.51	1.11	1.10	0.94	0.47	1.17	0.26	0.66	0.30
Dy	ppm	ICP-MS	1.20	5.76	1.55	5.40	2.98	6.32	6.31	5.13	2.57	6.78	1.45	4.12	1.73
Ho	ppm	ICP-MS	0.26	1.07	0.31	1.04	0.59	1.17	1.26	0.99	0.52	1.27	0.30	0.86	0.36
Er	ppm	ICP-MS	0.79	2.77	0.97	2.85	1.78	3.31	3.31	2.70	1.49	3.53	1.03	2.46	1.08
Tm	ppm	ICP-MS	0.12	0.39	0.21	0.42	0.31	0.50	0.45	0.42	0.25	0.50	0.21	0.36	0.20
Yb	ppm	ICP-MS	0.83	2.21	1.31	2.82	1.98	3.06	2.37	2.34	1.54	3.06	1.20	2.02	1.31
Lu	ppm	ICP-MS	0.14	0.33	0.20	0.43	0.30	0.47	0.31	0.34	0.21	0.48	0.19	0.31	0.23
Hf	ppm	ICP-MS	2.34	1.35	1.34	2.09	2.16	1.75	0.35	0.99	1.31	1.95	1.42	1.88	2.68
Ta	ppm	ICP-MS	0.23	0.28	0.32	0.28	0.54	0.40	0.05	0.19	0.21	0.24	0.27	0.26	0.24
Tl	ppm	ICP-MS	2.19	1.70	2.99	1.17	2.73	1.82	0.22	1.10	1.28	0.81	4.76	1.06	14.00
Pb	ppm	ICP-MS	609.09	710.10	1711.80	45.47	932.17	271.67	93.51	522.51	546.19	20.62	1353.01	390.82	929.21
Bi	ppm	ICP-MS	0.63	0.59	1.01	0.29	0.57	0.74	0.20	0.97	0.64	0.38	0.46	1.04	0.53
Th	ppm	ICP-MS	3.33	3.55	4.60	3.22	7.06	5.26	0.85	2.81	3.43	3.44	4.27	3.75	5.09
U	ppm	ICP-MS	6.90	11.51	45.42	4.02	49.24	38.23	8.61	5.90	11.58	2.81	26.74	12.63	13.08
Cr	ppm	ICP-MS	31.32	46.33	39.54	65.78	94.63	149.47	32.67	35.88	57.84	51.20	41.77	40.41	38.13
Fe	ppm	ICP-MS	260737.66	221865.50	269635.56	153536.64	176987.02	137191.41	97749.98	152256.19	245019.13	142422.68	304407.29	262046.45	247792.14
Mn	ppm	ICP-MS	873.28	115.92	462.01	3221.42	403.50	325.01	768.46	2533.94	848.32	8728.13	277.77	644.69	223.71
Co	ppm	ICP-MS	22.93	24.15	48.86	10.24	25.43	17.85	11.71	16.69	57.50	17.77	16.60	34.01	16.84
Ni	ppm	ICP-MS	318.38	214.00	456.10	180.48	182.67	708.34	83.98	73.26	188.79	86.47	231.89	149.73	182.92
Cu	ppm	ICP-MS	162.18	608.07	511.02	6126.92	65884.04	22067.18	610.75	165.27	286.26	449.04	1095.19	131.38	263.64
Zn	ppm	ICP-MS	409.15	424.71	467.29	104.14	1711.11	2287.67	77.95	39.99	251.18	299.14	132.01	172.26	1105.17
As	ppm	ICP-MS	978.30	358.87	720.72	250.06	431.22	1034.65	289.11	6.09	18.03	6.23	906.89	344.95	1069.23
Se	ppm	ICP-MS	12.04	11.50	21.49	11.50	31.08	26.42	11.50	10.81	2.84	5.35	11.50	13.18	9.87
Br	ppm	ICP-MS	103.46	113.89	136.45	136.91	133.38	158.99	140.36	149.90	129.78	138.33	120.59	95.67	89.48
Mo	ppm	ICP-MS	42.70	55.72	331.10	11.89	215.48	128.80	12.76	25.35	66.09	3.63	123.98	43.95	75.58
Ag	ppm	ICP-MS	30.20	27.03	24.65	8.91	157.06	59.89	3.16	1.66	2.42	0.27	36.37	5.90	26.84
Cd	ppm	ICP-MS	2.59	4.47	7.47	0.80	21.18	29.84	1.11	0.54	7.87	0.38	0.54	0.85	8.73
Sn	ppm	ICP-MS	2.27	1.89	1.90	1.93	2.86	3.38	1.81	1.55	2.04	2.03	2.51	2.65	2.75
Sb	ppm	ICP-MS	59.43	61.00	120.00	2.67	40.62	38.07	15.67	2.25	2.85	0.55	150.96	43.14	152.19
Te	ppm	ICP-MS	1.03	0.99	3.71	3.71	2.48	4.70	3.71	3.71	1.48	0.08	3.71	0.98	0.37
I	ppm	ICP-MS	1.62	5.35	5.35	5.35	5.35	5.35	5.35	5.35	5.35	5.35	5.35	1.59	1.59
W	ppm	ICP-MS	0.81	3.84	6.72	9.12	24.82	2.20	4.09	3.02	4.72	0.99	22.26	1.54	7.66
CIA			85.52	64.23	84.31	52.22	83.52	72.69	19.58	52.81	76.74	34.38	86.99	72.06	80.87
Ce/Ce*			0.54	0.61	0.70	0.67	0.60	0.62	0.53	0.58	0.65	0.58	0.64	0.50	0.58
Eu/Eu*			1.84	1.55	1.36	1.37	1.81	1.45	2.66	1.82	1.70	1.50	1.24	0.61	0.91
Y/Ho			26.69	28.71	24.34	25.31	27.91	30.37	39.46	32.84	30.83	31.33	28.87	31.66	29.09

[1] Fe(total) = (Fe_2O_3+FeO)

EMS: Exhalite[2] associated with massive sulfides (within 5m)

FEM: Exhalite associated with felsic and mafic volcanic rocks, no massive sulfides

FEF: Exhalite within felsic volcanic rocks, no massive sulfides

IFE: Interflow exhalite

T: Tuff

[2] The term exhalite represents the Lemarchant metalliferous mudstones and was chosen to simplify the abbreviations.

Sample #			CNF25070b	CNF38435	CNF38433	CNF20955	CNF30990	CNF30991	CNF30992	CNF30993	CNF38404	CNF25096	CNF20976	CNF20990	CNF20991
Drill Hole			LM13-79	LM07-14	LM07-14	LM08-32	LM11-67	LM11-68	LM11-68	LM11-68	LM08-34	LM11-63	LM10-43	LM11-52	LM11-52
Section N			101+25N	102N	102N	102N	102N	102N	102N	102N	102+12.5N	102+50N	102+50N	102+70N	102+70N
Northing (UTM)			5374625.36	5374697.64	5374697.204	5374699.945	5374699.232	5374699.274	5374699.274	5374699.274	5374724.548	5374749.78	5374724.548	5374749.616	5374749.616
Easting (UTM)			521114.59	521111.75	521114.681	521063.845	521065.915	521065.518	521065.518	521065.518	520918.507	521062.35	520918.507	521062.781	521062.781
Sample Drill Hole Depth (m)			182.75	201.2	503.51	207.93	158.48	196.2	196.47	196.95	156.5	206.71	202.29	210.42	210.6
Description			EMS	EMS	IFE	EMS	IFE	EMS	EMS	EMS	FEM	EMS	EMS	EMS	EMS
$C_{(total)}$	%	IR	1.17	0.32	0.98	0.23	0.07	0.58	2.89	0.23	5.94	0.58	0.91	0.44	2.94
$S_{(total)}$	%	IR	30.70	21.40	19.50	41.60	17.00	25.10	14.30	28.50	20.50	28.70	32.10	33.40	11.90
Hg	ppb	FIMS	286.00	141.00	13.00	171.00	111.00	147.00	30.00	300.00	101.00	345.00	309.00	155.00	2.50
SiO_2	%	ICP-ES	21.61	44.31	39.27	10.61	32.54	27.76	26.32	16.66	15.07	20.25	19.27	22.78	19.32
Al_2O_3	%	ICP-ES	9.99	3.35	2.73	3.53	11.67	6.36	8.39	9.79	2.84	7.42	4.48	2.74	9.33
$Fe_{(total)}$ [1]	%	ICP-ES	38.07	25.43	43.09	55.04	30.52	30.48	17.32	33.71	26.95	35.70	40.48	44.80	29.59
MnO	%	ICP-ES	0.05	0.06	0.05	0.04	0.13	0.08	0.50	0.05	0.24	0.10	0.10	0.09	1.76
MgO	%	ICP-ES	0.99	0.96	1.16	0.41	4.67	0.51	2.32	0.36	1.78	0.74	0.93	0.13	2.29
CaO	%	ICP-ES	0.01	5.26	2.22	0.13	2.09	5.33	11.55	2.05	19.20	3.07	3.91	0.39	7.03
Na_2O	%	ICP-ES	0.08	0.05	0.06	0.04	0.06	0.04	0.06	0.04	0.12	0.04	0.07	0.07	0.10
K_2O	%	ICP-ES	2.34	0.80	0.33	0.84	1.94	0.85	0.55	0.33	0.45	0.21	1.10	0.05	0.15
TiO_2	%	ICP-ES	0.39	0.13	0.14	0.15	0.54	0.49	0.38	0.44	0.13	0.26	0.21	0.14	0.44
P_2O_5	%	ICP-ES	0.06	3.61	0.06	0.04	1.39	2.37	1.64	1.14	3.15	1.45	1.26	0.16	0.70
LOI	%	ICP-ES	21.81	14.12	9.51	28.49	13.81	18.51	12.89	18.53	16.79	19.81	24.62	23.80	10.17
Total	%	ICP-ES	95.40	98.08	98.62	99.31	99.36	92.79	81.90	83.09	86.72	89.05	96.45	95.15	80.88
Ba	ppm	ICP-ES	15720.00	4830.00	207.00	3750.00	4626.00	46020.00	89320.00	130200.00	2001.00	80760.00	8511.00	34250.00	112300.00
Sc	ppm	ICP-ES	14.00	5.00	6.00	5.00	19.00	11.00	10.00	14.00	4.00	4.00	5.00	3.00	11.00
Be	ppm	ICP-ES	4.00	0.50	0.50	0.50	3.00	2.00	2.00	6.00	0.50	0.50	1.00	0.50	1.00
V	ppm	ICP-ES	819.00	357.00	197.00	410.00	641.00	477.00	689.00	2204.00	332.00	666.00	528.00	274.00	419.00
Li	ppm	ICP-MS	2.72	2.67	2.98	2.78	9.37	1.68	0.43	0.37	1.22	0.17	7.66	2.22	2.54
Sr	ppm	ICP-MS	11.96	181.23	27.23	5.63	47.33	150.28	467.99	128.88	276.44	106.34	77.31	337.03	362.72
Y	ppm	ICP-MS	10.23	56.41	3.26	5.15	28.32	38.85	32.19	23.68	41.19	18.84	18.77	34.32	35.96
Zr	ppm	ICP-MS	53.89	32.23	27.29	30.82	79.10	44.66	79.40	79.77	29.01	73.70	66.06	76.79	76.75
Nb	ppm	ICP-MS	2.59	0.95	0.62	2.45	1.68	2.71	6.88	7.35	1.36	4.49	4.97	7.03	7.00
Cs	ppm	ICP-MS	0.97	0.37	0.22	0.44	0.63	0.31	0.22	0.18	0.33	0.10	0.80	0.18	0.21
Ba_2	ppm	ICP-MS	1365.42	4527.81	198.21	3480.74	3362.42	24182.56	46708.88	37473.24	1228.75	7985.29	3513.82	59359.87	63821.79
La	ppm	ICP-MS	16.81	41.99	4.36	26.70	27.49	27.61	42.54	27.56	22.47	10.62	21.17	33.12	33.54
Ce	ppm	ICP-MS	22.34	42.23	7.28	23.78	52.17	44.65	55.14	38.11	27.54	18.62	36.06	51.18	52.19
Pr	ppm	ICP-MS	4.03	6.99	1.21	4.01	8.08	8.10	11.15	7.87	5.60	3.51	5.32	9.11	9.15
Nd	ppm	ICP-MS	15.26	28.23	5.26	13.48	37.00	37.64	47.63	32.57	25.37	14.96	22.42	37.94	39.13
Sm	ppm	ICP-MS	2.90	6.29	1.15	1.92	9.08	8.95	9.49	6.98	6.20	3.25	5.15	7.89	8.26
Eu	ppm	ICP-MS	0.57	5.07	0.33	0.32	1.98	3.08	2.47	2.43	2.64	0.91	1.44	2.23	2.53
Gd	ppm	ICP-MS	2.18	7.58	0.97	1.12	9.42	9.35	8.93	5.87	7.18	3.51	5.10	7.10	7.10
Tb	ppm	ICP-MS	0.31	1.16	0.13	0.15	1.21	1.33	1.11	0.75	1.05	0.52	0.78	1.09	1.09
Dy	ppm	ICP-MS	1.87	7.00	0.78	0.84	5.92	7.35	6.06	4.09	6.02	3.27	4.28	6.41	6.24
Ho	ppm	ICP-MS	0.40	1.36	0.14	0.20	1.00	1.26	1.14	0.81	1.19	0.67	0.77	1.32	1.27
Er	ppm	ICP-MS	1.29	3.75	0.50	0.60	2.53	3.02	2.98	2.35	2.94	1.93	2.08	3.78	3.72
Tm	ppm	ICP-MS	0.23	0.51	0.09	0.10	0.40	0.39	0.49	0.40	0.43	0.28	0.32	0.61	0.59
Yb	ppm	ICP-MS	1.49	2.74	0.58	0.68	2.20	2.44	2.75	2.53	2.48	1.96	2.27	3.98	3.99
Lu	ppm	ICP-MS	0.25	0.36	0.09	0.13	0.33	0.35	0.46	0.40	0.35	0.32	0.36	0.59	0.56
Hf	ppm	ICP-MS	2.55	0.84	0.64	0.76	2.60	1.32	1.99	2.14	0.69	4.65	1.78	2.02	1.94
Ta	ppm	ICP-MS	0.20	0.06	0.04	0.14	0.11	0.13	0.39	0.50	0.08	0.73	0.28	0.42	0.41
Tl	ppm	ICP-MS	17.47	2.45	0.44	2.43	2.65	2.67	1.40	2.54	3.21	3.36	1.41	0.86	0.85
Pb	ppm	ICP-MS	830.36	377.51	1312.17	749.60	389.95	388.68	139.48	630.46	516.60	644.31	678.66	27.01	28.00
Bi	ppm	ICP-MS	0.74	0.23	4.17	0.35	0.68	0.19	0.30	0.65	0.29	0.43	0.66	0.10	0.11
Th	ppm	ICP-MS	4.85	1.66	2.05	2.48	3.20	2.05	4.99	5.75	1.82	4.18	3.73	5.78	5.78
U	ppm	ICP-MS	72.79	9.11	6.37	3.63	10.38	18.30	10.65	53.10	16.96	35.31	37.61	2.72	2.69
Cr	ppm	ICP-MS	28.99	91.34	17.04	75.97	58.83	31.73	70.70	134.07	33.19	31.13	57.89	77.92	67.18
Fe	ppm	ICP-MS	199240.13	170020.93	287946.41	190864.68	200410.66	212043.18	115310.07	217169.95	176411.85	210863.26	178136.09	183238.51	160384.16
Mn	ppm	ICP-MS	289.85	427.56	353.53	1143.92	946.83	569.76	3438.19	338.33	1844.57	695.17	1524.40	15631.22	13736.94
Co	ppm	ICP-MS	20.52	11.00	96.77	32.67	20.64	66.38	12.98	23.62	16.29	14.93	21.17	1.60	1.34
Ni	ppm	ICP-MS	263.29	134.66	332.21	711.98	139.99	103.47	62.58	746.08	221.10	120.76	373.19	85.50	73.61
Cu	ppm	ICP-MS	244.81	274.71	1152.91	553.31	292.87	134.11	81.39	1369.91	210.08	601.06	783.48	1042.87	909.55
Zn	ppm	ICP-MS	833.24	290.81	46.32	2828.05	230.91	287.31	252.36	4561.69	4604.88	527.50	1042.95	305.76	242.48
As	ppm	ICP-MS	1055.06	517.16	0.76	390.02	293.30	519.93	186.67	952.24	488.55	504.48	451.58	12.33	3.08
Se	ppm	ICP-MS	10.93	12.03	21.25	26.98	11.01	11.50	1.34	13.37	24.22	5.05	15.89	9.60	0.83
Br	ppm	ICP-MS	94.79	138.57	157.50	125.44	108.19	121.78	125.18	169.22	173.35	124.93	143.83	137.77	124.92
Mo	ppm	ICP-MS	189.81	37.43	62.28	117.36	71.17	24.19	4.65	185.94	92.96	209.20	142.89	3.63	1.50
Ag	ppm	ICP-MS	21.96	13.17	12.15	4.50	14.39	9.94	1.32	17.53	23.88	17.22	5.19	0.95	0.41
Cd	ppm	ICP-MS	5.95	1.94	0.01	21.22	0.90	1.35	0.60	23.30	30.78	3.58	3.36	4.76	0.14
Sn	ppm	ICP-MS	3.46	1.88	0.78	3.21	2.13	2.45	2.14	2.26	0.98	2.44	1.79	2.40	2.25
Sb	ppm	ICP-MS	157.73	26.38	38.51	16.39	37.65	37.40	6.07	38.99	119.51	61.03	7.29	0.55	0.20
Te	ppm	ICP-MS	1.84	0.03	4.76	0.41	0.23	2.87	0.41	6.67	2.44	2.42	0.69	2.44	0.86
I	ppm	ICP-MS	1.59	8.98	0.31	8.98	5.35	5.35	5.35	2.67	5.62	1.62	8.98	8.98	8.98
W	ppm	ICP-MS	10.28	3.69	0.52	1.38	3.24	13.97	18.29	2.39	4.30	2.53	8.91	11.51	10.64
CIA			80.47	35.41	51.12	77.75	74.05	50.56	40.83	80.18	12.56	69.09	46.86	84.31	56.17
Ce/Ce*			0.63	0.57	0.73	0.53	0.81	0.69	0.58	0.60	0.57	0.70	0.78	0.68	0.69
Eu/Eu*			1.07	3.46	1.49	1.04	1.01	1.58	1.27	1.79	1.87	1.26	1.32	1.40	1.56
Y/Ho			25.58	41.50	22.89	25.50	28.20	30.84	28.23	29.20	34.52	28.00	24.24	25.92	28.36

[1] Fe(total) = (Fe_2O_3+FeO)

EMS: Exhalite[2] associated with massive sulfides (within 5m)

FEM: Exhalite associated with felsic and mafic volcanic rocks, no massive sulfides

FEF: Exhalite within felsic volcanic rocks, no massive sulfides

IFE: Interflow exhalite

T: Tuff

[2] The term exhalite represents the Lemarchant metalliferous mudstones and was chosen to simplify the abbreviations.

Sample #			CNF25074	CNF25075	CNF25062b	CNF25063	CNF25064	CNF25065	CNF25066	CNF25067	CNF38438	CNF30955	CNF38437	CNF30954	CNF38436
Drill Hole			LM13-78	LM13-78	LM13-76	LM13-76	LM13-77	LM13-77	LM13-77	LM13-77	LM07-13	LM07-13	LM07-13	LM07-13	LM07-13
Section N			99+75N	99+75N	100+50N	100+50N	100+50N	100+50N	100+50N	100+50N	101N	101N	101N	101N	101N
Northing (UTM)			5374477	5374477	5374537	5374537	5374537	5374537	5374537	5374537	5374599.93	5374599.93	5374599.93	5374599.93	5374599.93
Easting (UTM)			520956	520956	521049	521049	521049	521049	521049	521049	521111.73	521111.73	521111.73	521111.73	521111.73
Sample Drill Hole Depth (m)			119.74	121.05	163.78	172.28	139.56	140	142.1	142.76	164.2	165.32	164.5	164.67	423.96
Description			T	FEM	FEM	T	T	T	FEM	FEM	EMS	EMS	EMS	EMS	IFE
$C_{(total)}$	%	IR	1.70	3.16	0.20	3.41	0.23	3.06	0.78	0.03	0.16	0.02	0.16	0.10	0.60
$S_{(total)}$	%	IR	8.23	27.20	25.50	6.84	26.50	4.57	21.10	21.80	21.80	16.60	33.60	33.10	17.60
Hg	ppb	FIMS	57.00	42.00	160.00	10.00	112.00	11.00	175.00	701.00	111.00	195.00	122.00	186.00	279.00
SiO_2	%	ICP-ES	22.82	18.04	36.88	40.08	31.86	45.92	26.32	32.06	45.60	39.80	14.57	21.16	45.16
Al_2O_3	%	ICP-ES	17.71	5.26	5.89	5.73	4.21	6.78	9.20	12.69	4.28	8.33	4.14	5.44	9.87
$Fe_{(total)}$ [1]	%	ICP-ES	25.81	53.02	32.23	13.79	39.71	14.15	37.01	29.20	29.70	23.63	48.59	44.07	22.75
MnO	%	ICP-ES	1.06	0.10	0.05	0.32	0.05	0.61	0.14	0.04	0.07	0.03	0.08	0.07	0.02
MgO	%	ICP-ES	5.51	1.79	1.23	2.77	0.70	2.00	1.47	1.04	1.90	0.89	2.34	2.36	0.66
CaO	%	ICP-ES	7.16	0.32	1.16	16.78	0.38	14.35	1.20	1.11	1.02	1.18	2.10	1.04	2.21
Na_2O	%	ICP-ES	0.31	0.05	0.05	0.38	0.06	0.08	0.08	0.15	0.06	0.05	0.03	0.02	0.96
K_2O	%	ICP-ES	2.60	0.74	1.02	0.19	0.64	0.81	1.27	2.80	0.47	0.51	0.25	0.40	2.20
TiO_2	%	ICP-ES	1.17	0.27	0.26	0.42	0.18	0.29	0.32	0.44	0.27	0.32	0.34	0.27	0.41
P_2O_5	%	ICP-ES	0.17	0.33	0.31	1.15	0.30	0.92	0.06	0.84	0.73	0.80	1.54	0.70	0.94
LOI	%	ICP-ES	10.37	16.98	17.61	9.42	16.89	7.97	17.68	15.34	14.44	11.16	23.85	22.70	13.03
Total	%	ICP-ES	94.68	96.89	96.69	91.03	94.98	93.89	94.75	95.73	98.54	86.70	97.83	98.23	98.21
Ba	ppm	ICP-ES	517.00	323.00	1067.00	372.00	2074.00	2612.00	5859.00	11480.00	1544.00	50540.00	6037.00	17540.00	649.00
Sc	ppm	ICP-ES	33.00	6.00	8.00	12.00	5.00	8.00	12.00	16.00	13.00	9.00	7.00	7.00	12.00
Be	ppm	ICP-ES	2.00	1.00	0.50	0.50	0.50	0.50	2.00	2.00	0.50	2.00	0.50	1.00	0.50
V	ppm	ICP-ES	830.00	635.00	393.00	237.00	688.00	414.00	896.00	1825.00	267.00	962.00	342.00	543.00	1811.00
Li	ppm	ICP-MS	15.47	4.38	3.28	7.13	2.04	4.78	4.72	2.97	2.34	13.87	4.63	6.66	2.16
Sr	ppm	ICP-MS	158.75	19.54	16.41	157.08	11.45	118.99	15.38	24.88	17.27	83.47	50.47	64.93	58.45
Y	ppm	ICP-MS	12.83	12.16	8.26	26.36	7.54	28.87	8.31	16.25	13.69	15.52	20.77	13.75	17.77
Zr	ppm	ICP-MS	85.88	55.70	52.61	32.40	36.88	56.31	56.57	77.11	26.53	62.17	42.40	46.72	90.15
Nb	ppm	ICP-MS	0.64	2.23	1.85	0.95	1.49	1.09	1.71	3.74	0.82	3.86	2.79	1.89	8.81
Cs	ppm	ICP-MS	0.53	0.37	0.51	0.13	0.34	0.27	0.61	1.09	0.19	1.58	0.23	0.55	1.59
Ba_2	ppm	ICP-MS	531.97	327.29	895.70	354.06	1605.68	2708.12	3769.95	2399.92	1049.16	41616.33	3781.31	18100.32	718.07
La	ppm	ICP-MS	6.73	15.12	13.67	15.04	7.39	26.54	11.12	20.09	16.19	19.84	18.78	14.97	19.23
Ce	ppm	ICP-MS	7.64	19.66	21.23	21.05	11.11	29.89	16.88	31.16	28.27	28.95	25.21	18.38	33.24
Pr	ppm	ICP-MS	1.78	3.75	3.75	3.76	2.12	5.99	2.95	6.17	4.21	5.32	4.93	3.54	6.14
Nd	ppm	ICP-MS	7.15	14.65	14.91	17.02	8.86	23.41	11.35	25.65	18.97	22.64	21.92	14.40	26.49
Sm	ppm	ICP-MS	1.74	2.86	3.45	4.55	1.80	5.09	2.29	5.81	4.59	4.89	4.84	3.07	6.17
Eu	ppm	ICP-MS	0.42	0.64	0.90	1.64	0.48	1.55	0.74	1.55	1.15	1.54	1.51	0.95	1.58
Gd	ppm	ICP-MS	2.05	2.75	2.83	5.70	1.68	5.41	1.92	5.47	4.76	4.18	5.19	2.92	5.74
Tb	ppm	ICP-MS	0.33	0.40	0.38	0.78	0.25	0.76	0.30	0.69	0.61	0.54	0.71	0.41	0.74
Dy	ppm	ICP-MS	2.13	2.34	1.88	4.56	1.47	4.62	1.85	3.58	3.16	2.98	3.79	2.21	3.89
Ho	ppm	ICP-MS	0.48	0.48	0.33	0.86	0.28	0.92	0.34	0.65	0.53	0.54	0.70	0.43	0.70
Er	ppm	ICP-MS	1.63	1.41	0.98	2.32	0.79	2.64	1.10	1.80	1.31	1.50	1.70	1.25	1.85
Tm	ppm	ICP-MS	0.29	0.25	0.16	0.33	0.15	0.40	0.22	0.30	0.17	0.24	0.27	0.22	0.30
Yb	ppm	ICP-MS	2.32	1.50	1.05	1.75	0.91	2.47	1.48	1.96	1.00	1.49	1.58	1.15	2.03
Lu	ppm	ICP-MS	0.42	0.25	0.20	0.27	0.15	0.42	0.25	0.33	0.15	0.26	0.23	0.20	0.33
Hf	ppm	ICP-MS	8.11	2.64	3.17	1.74	1.47	4.67	2.71	3.47	0.78	1.71	1.07	1.22	2.22
Ta	ppm	ICP-MS	0.06	0.19	0.14	0.06	0.13	0.09	0.16	0.31	0.08	0.21	0.12	0.10	0.54
Tl	ppm	ICP-MS	1.68	2.19	0.89	0.31	1.93	0.72	3.72	7.50	1.44	1.88	1.36	2.51	3.61
Pb	ppm	ICP-MS	14.96	806.81	761.86	163.42	600.82	21.80	1184.86	761.00	433.14	211.40	754.27	896.90	581.51
Bi	ppm	ICP-MS	0.10	0.91	0.86	0.22	0.32	0.18	0.70	0.62	0.45	0.23	0.54	0.43	0.62
Th	ppm	ICP-MS	2.51	5.39	5.20	1.44	3.50	3.65	5.00	6.14	1.66	4.45	2.16	2.60	6.58
U	ppm	ICP-MS	1.69	30.61	25.12	5.18	16.34	4.88	61.36	55.88	5.26	39.31	13.98	12.42	66.85
Cr	ppm	ICP-MS	40.57	34.91	52.99	27.04	35.99	40.61	38.25	112.37	20.03	94.42	56.99	38.66	129.01
Fe	ppm	ICP-MS	137854.65	281694.38	214167.90	94744.28	242710.05	101344.44	196517.28	152849.46	192603.54	150078.55	311549.80	276654.66	146492.75
Mn	ppm	ICP-MS	5504.84	620.96	389.02	2410.25	363.82	4621.34	837.17	225.87	524.38	210.48	529.20	496.99	131.50
Co	ppm	ICP-MS	8.39	31.54	19.58	28.98	110.24	14.04	75.72	38.29	53.15	16.65	73.90	14.49	18.53
Ni	ppm	ICP-MS	105.09	457.01	182.26	82.76	251.92	76.28	339.26	479.49	142.97	276.51	165.71	191.41	570.12
Cu	ppm	ICP-MS	145.19	522.21	502.75	120.92	216.82	101.81	508.56	392.37	219.71	56188.59	605.33	233.46	263.95
Zn	ppm	ICP-MS	625.34	907.06	540.16	295.46	234.19	203.07	108.36	66.28	94.17	3659.78	214.03	263.79	919.90
As	ppm	ICP-MS	14.48	203.00	216.07	41.63	3305.98	139.88	2069.99	1302.14	376.72	394.79	9545.16	1201.81	682.75
Se	ppm	ICP-MS	6.05	21.84	7.62	2.46	9.91	5.86	17.93	24.09	4.62	6.98	9.60	12.55	35.35
Br	ppm	ICP-MS	91.59	87.20	87.25	95.81	88.72	99.32	103.90	92.51	114.06	140.06	123.14	143.13	141.08
Mo	ppm	ICP-MS	6.80	125.95	108.39	20.45	113.42	26.16	263.83	213.91	34.35	136.51	33.74	86.16	151.28
Ag	ppm	ICP-MS	0.78	12.05	19.06	1.16	29.09	1.22	30.80	31.65	4.28	116.09	31.04	36.54	11.87
Cd	ppm	ICP-MS	2.74	6.65	8.19	1.09	4.05	1.00	0.62	0.59	1.26	19.18	1.11	0.26	11.08
Sn	ppm	ICP-MS	3.19	3.08	2.82	2.89	3.16	3.00	3.44	3.60	1.43	3.62	1.54	1.76	2.74
Sb	ppm	ICP-MS	1.87	140.36	23.23	2.92	51.32	1.12	49.20	81.32	71.78	26.74	111.10	120.42	61.73
Te	ppm	ICP-MS	0.10	0.73	0.96	0.55	0.82	0.10	1.70	0.89	1.71	1.87	2.44	3.71	1.13
I	ppm	ICP-MS	1.59	1.59	1.59	1.59	1.59	1.59	1.22	1.59	8.98	5.35	8.98	1.36	8.98
W	ppm	ICP-MS	4.41	6.19	1.47	2.13	2.52	1.81	2.60	6.34	2.45	14.08	6.86	5.02	4.54
CIA			63.75	82.57	72.54	24.83	79.58	30.79	78.30	75.76	73.41	82.72	63.50	78.84	64.76
Ce/Ce*			0.51	0.60	0.68	0.65	0.65	0.55	0.68	0.65	0.79	0.65	0.60	0.58	0.71
Eu/Eu*			1.05	1.08	1.36	1.52	1.29	1.39	1.67	1.29	1.16	1.60	1.42	1.50	1.25
Y/Ho			26.51	25.59	24.85	30.79	27.28	31.32	24.42	25.16	25.80	28.66	29.77	31.79	25.42

[1] Fe(total) = (Fe_2O_3+FeO)

EMS: Exhalite[2] associated with massive sulfides (within 5m)

FEM: Exhalite associated with felsic and mafic volcanic rocks, no massive sulfides

FEF: Exhalite within felsic volcanic rocks, no massive sulfides

IFE: Interflow exhalite

T: Tuff

[2] The term exhalite represents the Lemarchant metalliferous mudstones and was chosen to simplify the abbreviations.

Sample #			CNF25074	CNF25075	CNF25062b	CNF25063	CNF25064	CNF25065	CNF25066	CNF25067	CNF38438	CNF30955	CNF38437	CNF30954	CNF38436
Drill Hole			LM13-78	LM13-78	LM13-76	LM13-76	LM13-77	LM13-77	LM13-77	LM13-77	LM07-13	LM07-13	LM07-13	LM07-13	LM07-13
Section N			99+75N	99+75N	100+50N	100+50N	100+50N	100+50N	100+50N	100+50N	101N	101N	101N	101N	101N
Northing (UTM)			5374477	5374477	5374537	5374537	5374537	5374537	5374537	5374537	5374599.93	5374599.93	5374599.93	5374599.93	5374599.93
Easting (UTM)			520956	520956	521049	521049	521049	521049	521049	521049	521111.73	521111.73	521111.73	521111.73	521111.73
Sample Drill Hole Depth (m)			119.74	121.05	163.78	172.28	139.56	140	142.1	142.76	164.2	165.32	164.5	164.67	423.96
Description			T	FEM	FEM	T	T	T	FEM	FEM	EMS	EMS	EMS	EMS	IFE
$C_{(total)}$	%	IR	1.70	3.16	0.20	3.41	0.23	3.06	0.78	0.03	0.16	0.02	0.16	0.10	0.60
$S_{(total)}$	%	IR	8.23	27.20	25.50	6.84	26.50	4.57	21.10	21.80	21.80	16.60	33.60	33.10	17.60
Hg	ppb	FIMS	57.00	42.00	160.00	10.00	112.00	11.00	175.00	701.00	111.00	195.00	122.00	186.00	279.00
SiO_2	%	ICP-ES	22.82	18.04	36.88	40.08	31.86	45.92	26.32	32.06	45.60	39.80	14.57	21.16	45.16
Al_2O_3	%	ICP-ES	17.71	5.26	5.89	5.73	4.21	6.78	9.20	12.69	4.28	8.33	4.14	5.44	9.87
$Fe_{(total)}$ [1]	%	ICP-ES	25.81	53.02	32.23	13.79	39.71	14.15	37.01	29.20	29.70	23.63	48.59	44.07	22.75
MnO	%	ICP-ES	1.06	0.10	0.05	0.32	0.05	0.61	0.14	0.04	0.07	0.03	0.08	0.07	0.02
MgO	%	ICP-ES	5.51	1.79	1.23	2.77	0.70	2.00	1.47	1.04	1.90	0.89	2.34	2.36	0.66
CaO	%	ICP-ES	7.16	0.32	1.16	16.78	0.38	14.35	1.20	1.11	1.02	1.18	2.10	1.04	2.21
Na_2O	%	ICP-ES	0.31	0.05	0.05	0.38	0.06	0.08	0.08	0.15	0.06	0.05	0.03	0.02	0.96
K_2O	%	ICP-ES	2.60	0.74	1.02	0.19	0.64	0.81	1.27	2.80	0.47	0.51	0.25	0.40	2.20
TiO_2	%	ICP-ES	1.17	0.27	0.26	0.42	0.18	0.29	0.32	0.44	0.27	0.32	0.34	0.27	0.41
P_2O_5	%	ICP-ES	0.17	0.33	0.31	1.15	0.30	0.92	0.06	0.84	0.73	0.80	1.54	0.70	0.94
LOI	%	ICP-ES	10.37	16.98	17.61	9.42	16.89	7.97	17.68	15.34	14.44	11.16	23.85	22.70	13.03
Total	%	ICP-ES	94.68	96.89	96.69	91.03	94.98	93.89	94.75	95.73	98.54	86.70	97.83	98.23	98.21
Ba	ppm	ICP-ES	517.00	323.00	1067.00	372.00	2074.00	2612.00	5859.00	11480.00	1544.00	50540.00	6037.00	17540.00	649.00
Sc	ppm	ICP-ES	33.00	6.00	8.00	12.00	5.00	8.00	12.00	16.00	13.00	9.00	7.00	7.00	12.00
Be	ppm	ICP-ES	2.00	1.00	0.50	0.50	0.50	0.50	2.00	2.00	0.50	2.00	0.50	1.00	0.50
V	ppm	ICP-ES	830.00	635.00	393.00	237.00	688.00	414.00	896.00	1825.00	267.00	962.00	342.00	543.00	1811.00
Li	ppm	ICP-MS	15.47	4.38	3.28	7.13	2.04	4.78	4.72	2.97	2.34	13.87	4.63	6.66	2.16
Sr	ppm	ICP-MS	158.75	19.54	16.41	157.08	11.45	118.99	15.38	24.88	17.27	83.47	50.47	64.93	58.45
Y	ppm	ICP-MS	12.83	12.16	8.26	26.36	7.54	28.87	8.31	16.25	13.69	15.52	20.77	13.75	17.77
Zr	ppm	ICP-MS	85.88	55.70	52.61	32.40	36.88	56.31	56.57	77.11	26.53	62.17	42.40	46.72	90.15
Nb	ppm	ICP-MS	0.64	2.23	1.85	0.95	1.49	1.09	1.71	3.74	0.82	3.86	2.79	1.89	8.81
Cs	ppm	ICP-MS	0.53	0.37	0.51	0.13	0.34	0.27	0.61	1.09	0.19	1.58	0.23	0.55	1.59
Ba_2	ppm	ICP-MS	531.97	327.29	895.70	354.06	1605.68	2708.12	3769.95	2399.92	1049.16	41616.33	3781.31	18100.32	718.07
La	ppm	ICP-MS	6.73	15.12	13.67	15.04	7.39	26.54	11.12	20.09	16.19	19.84	18.78	14.97	19.23
Ce	ppm	ICP-MS	7.64	19.66	21.23	21.05	11.11	29.89	16.88	31.16	28.27	28.95	25.21	18.38	33.24
Pr	ppm	ICP-MS	1.78	3.75	3.75	3.76	2.12	5.99	2.95	6.17	4.21	5.32	4.93	3.54	6.14
Nd	ppm	ICP-MS	7.15	14.65	14.91	17.02	8.86	23.41	11.35	25.65	18.97	22.64	21.92	14.40	26.49
Sm	ppm	ICP-MS	1.74	2.86	3.45	4.55	1.80	5.09	2.29	5.81	4.59	4.89	4.84	3.07	6.17
Eu	ppm	ICP-MS	0.42	0.64	0.90	1.64	0.48	1.55	0.74	1.55	1.15	1.54	1.51	0.95	1.58
Gd	ppm	ICP-MS	2.05	2.75	2.83	5.70	1.68	5.41	1.92	5.47	4.76	4.18	5.19	2.92	5.74
Tb	ppm	ICP-MS	0.33	0.40	0.38	0.78	0.25	0.76	0.30	0.69	0.61	0.54	0.71	0.41	0.74
Dy	ppm	ICP-MS	2.13	2.34	1.88	4.56	1.47	4.62	1.85	3.58	3.16	2.98	3.79	2.21	3.89
Ho	ppm	ICP-MS	0.48	0.48	0.33	0.86	0.28	0.92	0.34	0.65	0.53	0.54	0.70	0.43	0.70
Er	ppm	ICP-MS	1.63	1.41	0.98	2.32	0.79	2.64	1.10	1.80	1.31	1.50	1.70	1.25	1.85
Tm	ppm	ICP-MS	0.29	0.25	0.16	0.33	0.15	0.40	0.22	0.30	0.17	0.24	0.27	0.22	0.30
Yb	ppm	ICP-MS	2.32	1.50	1.05	1.75	0.91	2.47	1.48	1.96	1.00	1.49	1.58	1.15	2.03
Lu	ppm	ICP-MS	0.42	0.25	0.20	0.27	0.15	0.42	0.25	0.33	0.15	0.26	0.23	0.20	0.33
Hf	ppm	ICP-MS	8.11	2.64	3.17	1.74	1.47	4.67	2.71	3.47	0.78	1.71	1.07	1.22	2.22
Ta	ppm	ICP-MS	0.06	0.19	0.14	0.06	0.13	0.09	0.16	0.31	0.08	0.21	0.12	0.10	0.54
Tl	ppm	ICP-MS	1.68	2.19	0.89	0.31	1.93	0.72	3.72	7.50	1.44	1.88	1.36	2.51	3.61
Pb	ppm	ICP-MS	14.96	806.81	761.86	163.42	600.82	21.80	1184.86	761.00	433.14	211.40	754.27	896.90	581.51
Bi	ppm	ICP-MS	0.10	0.91	0.86	0.22	0.32	0.18	0.70	0.62	0.45	0.23	0.54	0.43	0.62
Th	ppm	ICP-MS	2.51	5.39	5.20	1.44	3.50	3.65	5.00	6.14	1.66	4.45	2.16	2.60	6.58
U	ppm	ICP-MS	1.69	30.61	25.12	5.18	16.34	4.88	61.36	55.88	5.26	39.31	13.98	12.42	66.85
Cr	ppm	ICP-MS	40.57	34.91	52.99	27.04	35.99	40.61	38.25	112.37	20.03	94.42	56.99	38.66	129.01
Fe	ppm	ICP-MS	137854.65	281694.38	214167.90	94744.28	242710.05	101344.44	196517.28	152849.46	192603.54	150078.55	311549.80	276654.66	146492.75
Mn	ppm	ICP-MS	5504.84	620.96	389.02	2410.25	363.82	4621.34	837.17	225.87	524.38	210.48	529.20	496.99	131.50
Co	ppm	ICP-MS	8.39	31.54	19.58	28.98	110.24	14.04	75.72	38.29	53.15	16.65	73.90	14.49	18.53
Ni	ppm	ICP-MS	105.09	457.01	182.26	82.76	251.92	76.28	339.26	479.49	142.97	276.51	165.71	191.41	570.12
Cu	ppm	ICP-MS	145.19	522.21	502.75	120.92	216.82	101.81	508.56	392.37	219.71	56188.59	605.33	233.46	263.95
Zn	ppm	ICP-MS	625.34	907.06	540.16	295.46	234.19	203.07	108.36	66.28	94.17	3659.78	214.03	263.79	919.90
As	ppm	ICP-MS	14.48	203.00	216.07	41.63	3305.98	139.88	2069.99	1302.14	376.72	394.79	9545.16	1201.81	682.75
Se	ppm	ICP-MS	6.05	21.84	7.62	2.46	9.91	5.86	17.93	24.09	4.62	6.98	9.60	12.55	35.35
Br	ppm	ICP-MS	91.59	87.20	87.25	95.81	88.72	99.32	103.90	92.51	114.06	140.06	123.14	143.13	141.08
Mo	ppm	ICP-MS	6.80	125.95	108.39	20.45	113.42	26.16	263.83	213.91	34.35	136.51	33.74	86.16	151.28
Ag	ppm	ICP-MS	0.78	12.05	19.06	1.16	29.09	1.22	30.80	31.65	4.28	116.09	31.04	36.54	11.87
Cd	ppm	ICP-MS	2.74	6.65	8.19	1.09	4.05	1.00	0.62	0.59	1.26	19.18	1.11	0.26	11.08
Sn	ppm	ICP-MS	3.19	3.08	2.82	2.89	3.16	3.00	3.44	3.60	1.43	3.62	1.54	1.76	2.74
Sb	ppm	ICP-MS	1.87	140.36	23.23	2.92	51.32	1.12	49.20	81.32	71.78	26.74	111.10	120.42	61.73
Te	ppm	ICP-MS	0.10	0.73	0.96	0.55	0.82	0.10	1.70	0.89	1.71	1.87	2.44	3.71	1.13
I	ppm	ICP-MS	1.59	1.59	1.59	1.59	1.59	1.59	1.22	1.59	8.98	5.35	8.98	1.36	8.98
W	ppm	ICP-MS	4.41	6.19	1.47	2.13	2.52	1.81	2.60	6.34	2.45	14.08	6.86	5.02	4.54
CIA			63.75	82.57	72.54	24.83	79.58	30.79	78.30	75.76	73.41	82.72	63.50	78.84	64.76
Ce/Ce*			0.51	0.60	0.68	0.65	0.65	0.55	0.68	0.65	0.79	0.65	0.60	0.58	0.71
Eu/Eu*			1.05	1.08	1.36	1.52	1.29	1.39	1.67	1.29	1.16	1.60	1.42	1.50	1.25
Y/Ho			26.51	25.59	24.85	30.79	27.28	31.32	24.42	25.16	25.80	28.66	29.77	31.79	25.42

[1] Fe(total) = (Fe_2O_3+FeO)

EMS: Exhalite[2] associated with massive sulfides (within 5m)

FEM: Exhalite associated with felsic and mafic volcanic rocks, no massive sulfides

FEF: Exhalite within felsic volcanic rocks, no massive sulfides

IFE: Interflow exhalite

T: Tuff

[2] The term exhalite represents the Lemarchant metalliferous mudstones and was chosen to simplify the abbreviations.

Sample #			CNF25074	CNF25075	CNF25062b	CNF25063	CNF25064	CNF25065	CNF25066	CNF25067	CNF38438	CNF30955	CNF38437	CNF30954	CNF38436
Drill Hole			LM13-78	LM13-78	LM13-76	LM13-76	LM13-77	LM13-77	LM13-77	LM13-77	LM07-13	LM07-13	LM07-13	LM07-13	LM07-13
Section N			99+75N	99+75N	100+50N	100+50N	100+50N	100+50N	100+50N	100+50N	101N	101N	101N	101N	101N
Northing (UTM)			5374477	5374477	5374537	5374537	5374537	5374537	5374537	5374537	5374599.93	5374599.93	5374599.93	5374599.93	5374599.93
Easting (UTM)			520956	520956	521049	521049	521049	521049	521049	521049	521111.73	521111.73	521111.73	521111.73	521111.73
Sample Drill Hole Depth (m)			119.74	121.05	163.78	172.28	139.56	140	142.1	142.76	164.2	165.32	164.5	164.67	423.96
Description			T	FEM	FEM	T	T	T	FEM	FEM	EMS	EMS	EMS	EMS	IFE
$C_{(total)}$	%	IR	1.70	3.16	0.20	3.41	0.23	3.06	0.78	0.03	0.16	0.02	0.16	0.10	0.60
$S_{(total)}$	%	IR	8.23	27.20	25.50	6.84	26.50	4.57	21.10	21.80	21.80	16.60	33.60	33.10	17.60
Hg	ppb	FIMS	57.00	42.00	160.00	10.00	112.00	11.00	175.00	701.00	111.00	195.00	122.00	186.00	279.00
SiO_2	%	ICP-ES	22.82	18.04	36.88	40.08	31.86	45.92	26.32	32.06	45.60	39.80	14.57	21.16	45.16
Al_2O_3	%	ICP-ES	17.71	5.26	5.89	5.73	4.21	6.78	9.20	12.69	4.28	8.33	4.14	5.44	9.87
$Fe_{(total)}$ [1]	%	ICP-ES	25.81	53.02	32.23	13.79	39.71	14.15	37.01	29.20	29.70	23.63	48.59	44.07	22.75
MnO	%	ICP-ES	1.06	0.10	0.05	0.32	0.05	0.61	0.14	0.04	0.07	0.03	0.08	0.07	0.02
MgO	%	ICP-ES	5.51	1.79	1.23	2.77	0.70	2.00	1.47	1.04	1.90	0.89	2.34	2.36	0.66
CaO	%	ICP-ES	7.16	0.32	1.16	16.78	0.38	14.35	1.20	1.11	1.02	1.18	2.10	1.04	2.21
Na_2O	%	ICP-ES	0.31	0.05	0.05	0.38	0.06	0.08	0.08	0.15	0.06	0.05	0.03	0.02	0.96
K_2O	%	ICP-ES	2.60	0.74	1.02	0.19	0.64	0.81	1.27	2.80	0.47	0.51	0.25	0.40	2.20
TiO_2	%	ICP-ES	1.17	0.27	0.26	0.42	0.18	0.29	0.32	0.44	0.27	0.32	0.34	0.27	0.41
P_2O_5	%	ICP-ES	0.17	0.33	0.31	1.15	0.30	0.92	0.06	0.84	0.73	0.80	1.54	0.70	0.94
LOI	%	ICP-ES	10.37	16.98	17.61	9.42	16.89	7.97	17.68	15.34	14.44	11.16	23.85	22.70	13.03
Total	%	ICP-ES	94.68	96.89	96.69	91.03	94.98	93.89	94.75	95.73	98.54	86.70	97.83	98.23	98.21
Ba	ppm	ICP-ES	517.00	323.00	1067.00	372.00	2074.00	2612.00	5859.00	11480.00	1544.00	50540.00	6037.00	17540.00	649.00
Sc	ppm	ICP-ES	33.00	6.00	8.00	12.00	5.00	8.00	12.00	16.00	13.00	9.00	7.00	7.00	12.00
Be	ppm	ICP-ES	2.00	1.00	0.50	0.50	0.50	0.50	2.00	2.00	0.50	2.00	0.50	1.00	0.50
V	ppm	ICP-ES	830.00	635.00	393.00	237.00	688.00	414.00	896.00	1825.00	267.00	962.00	342.00	543.00	1811.00
Li	ppm	ICP-MS	15.47	4.38	3.28	7.13	2.04	4.78	4.72	2.97	2.34	13.87	4.63	6.66	2.16
Sr	ppm	ICP-MS	158.75	19.54	16.41	157.08	11.45	118.99	15.38	24.88	17.27	83.47	50.47	64.93	58.45
Y	ppm	ICP-MS	12.83	12.16	8.26	26.36	7.54	28.87	8.31	16.25	13.69	15.52	20.77	13.75	17.77
Zr	ppm	ICP-MS	85.88	55.70	52.61	32.40	36.88	56.31	56.57	77.11	26.53	62.17	42.40	46.72	90.15
Nb	ppm	ICP-MS	0.64	2.23	1.85	0.95	1.49	1.09	1.71	3.74	0.82	3.86	2.79	1.89	8.81
Cs	ppm	ICP-MS	0.53	0.37	0.51	0.13	0.34	0.27	0.61	1.09	0.19	1.58	0.23	0.55	1.59
Ba_2	ppm	ICP-MS	531.97	327.29	895.70	354.06	1605.68	2708.12	3769.95	2399.92	1049.16	41616.33	3781.31	18100.32	718.07
La	ppm	ICP-MS	6.73	15.12	13.67	15.04	7.39	26.54	11.12	20.09	16.19	19.84	18.78	14.97	19.23
Ce	ppm	ICP-MS	7.64	19.66	21.23	21.05	11.11	29.89	16.88	31.16	28.27	28.95	25.21	18.38	33.24
Pr	ppm	ICP-MS	1.78	3.75	3.75	3.76	2.12	5.99	2.95	6.17	4.21	5.32	4.93	3.54	6.14
Nd	ppm	ICP-MS	7.15	14.65	14.91	17.02	8.86	23.41	11.35	25.65	18.97	22.64	21.92	14.40	26.49
Sm	ppm	ICP-MS	1.74	2.86	3.45	4.55	1.80	5.09	2.29	5.81	4.59	4.89	4.84	3.07	6.17
Eu	ppm	ICP-MS	0.42	0.64	0.90	1.64	0.48	1.55	0.74	1.55	1.15	1.54	1.51	0.95	1.58
Gd	ppm	ICP-MS	2.05	2.75	2.83	5.70	1.68	5.41	1.92	5.47	4.76	4.18	5.19	2.92	5.74
Tb	ppm	ICP-MS	0.33	0.40	0.38	0.78	0.25	0.76	0.30	0.69	0.61	0.54	0.71	0.41	0.74
Dy	ppm	ICP-MS	2.13	2.34	1.88	4.56	1.47	4.62	1.85	3.58	3.16	2.98	3.79	2.21	3.89
Ho	ppm	ICP-MS	0.48	0.48	0.33	0.86	0.28	0.92	0.34	0.65	0.53	0.54	0.70	0.43	0.70
Er	ppm	ICP-MS	1.63	1.41	0.98	2.32	0.79	2.64	1.10	1.80	1.31	1.50	1.70	1.25	1.85
Tm	ppm	ICP-MS	0.29	0.25	0.16	0.33	0.15	0.40	0.22	0.30	0.17	0.24	0.27	0.22	0.30
Yb	ppm	ICP-MS	2.32	1.50	1.05	1.75	0.91	2.47	1.48	1.96	1.00	1.49	1.58	1.15	2.03
Lu	ppm	ICP-MS	0.42	0.25	0.20	0.27	0.15	0.42	0.25	0.33	0.15	0.26	0.23	0.20	0.33
Hf	ppm	ICP-MS	8.11	2.64	3.17	1.74	1.47	4.67	2.71	3.47	0.78	1.71	1.07	1.22	2.22
Ta	ppm	ICP-MS	0.06	0.19	0.14	0.06	0.13	0.09	0.16	0.31	0.08	0.21	0.12	0.10	0.54
Tl	ppm	ICP-MS	1.68	2.19	0.89	0.31	1.93	0.72	3.72	7.50	1.44	1.88	1.36	2.51	3.61
Pb	ppm	ICP-MS	14.96	806.81	761.86	163.42	600.82	21.80	1184.86	761.00	433.14	211.40	754.27	896.90	581.51
Bi	ppm	ICP-MS	0.10	0.91	0.86	0.22	0.32	0.18	0.70	0.62	0.45	0.23	0.54	0.43	0.62
Th	ppm	ICP-MS	2.51	5.39	5.20	1.44	3.50	3.65	5.00	6.14	1.66	4.45	2.16	2.60	6.58
U	ppm	ICP-MS	1.69	30.61	25.12	5.18	16.34	4.88	61.36	55.88	5.26	39.31	13.98	12.42	66.85
Cr	ppm	ICP-MS	40.57	34.91	52.99	27.04	35.99	40.61	38.25	112.37	20.03	94.42	56.99	38.66	129.01
Fe	ppm	ICP-MS	137854.65	281694.38	214167.90	94744.28	242710.05	101344.44	196517.28	152849.46	192603.54	150078.55	311549.80	276654.66	146492.75
Mn	ppm	ICP-MS	5504.84	620.96	389.02	2410.25	363.82	4621.34	837.17	225.87	524.38	210.48	529.20	496.99	131.50
Co	ppm	ICP-MS	8.39	31.54	19.58	28.98	110.24	14.04	75.72	38.29	53.15	16.65	73.90	14.49	18.53
Ni	ppm	ICP-MS	105.09	457.01	182.26	82.76	251.92	76.28	339.26	479.49	142.97	276.51	165.71	191.41	570.12
Cu	ppm	ICP-MS	145.19	522.21	502.75	120.92	216.82	101.81	508.56	392.37	219.71	56188.59	605.33	233.46	263.95
Zn	ppm	ICP-MS	625.34	907.06	540.16	295.46	234.19	203.07	108.36	66.28	94.17	3659.78	214.03	263.79	919.90
As	ppm	ICP-MS	14.48	203.00	216.07	41.63	3305.98	139.88	2069.99	1302.14	376.72	394.79	9545.16	1201.81	682.75
Se	ppm	ICP-MS	6.05	21.84	7.62	2.46	9.91	5.86	17.93	24.09	4.62	6.98	9.60	12.55	35.35
Br	ppm	ICP-MS	91.59	87.20	87.25	95.81	88.72	99.32	103.90	92.51	114.06	140.06	123.14	143.13	141.08
Mo	ppm	ICP-MS	6.80	125.95	108.39	20.45	113.42	26.16	263.83	213.91	34.35	136.51	33.74	86.16	151.28
Ag	ppm	ICP-MS	0.78	12.05	19.06	1.16	29.09	1.22	30.80	31.65	4.28	116.09	31.04	36.54	11.87
Cd	ppm	ICP-MS	2.74	6.65	8.19	1.09	4.05	1.00	0.62	0.59	1.26	19.18	1.11	0.26	11.08
Sn	ppm	ICP-MS	3.19	3.08	2.82	2.89	3.16	3.00	3.44	3.60	1.43	3.62	1.54	1.76	2.74
Sb	ppm	ICP-MS	1.87	140.36	23.23	2.92	51.32	1.12	49.20	81.32	71.78	26.74	111.10	120.42	61.73
Te	ppm	ICP-MS	0.10	0.73	0.96	0.55	0.82	0.10	1.70	0.89	1.71	1.87	2.44	3.71	1.13
I	ppm	ICP-MS	1.59	1.59	1.59	1.59	1.59	1.59	1.22	1.59	8.98	5.35	8.98	1.36	8.98
W	ppm	ICP-MS	4.41	6.19	1.47	2.13	2.52	1.81	2.60	6.34	2.45	14.08	6.86	5.02	4.54
CIA			63.75	82.57	72.54	24.83	79.58	30.79	78.30	75.76	73.41	82.72	63.50	78.84	64.76
Ce/Ce*			0.51	0.60	0.68	0.65	0.65	0.55	0.68	0.65	0.79	0.65	0.60	0.58	0.71
Eu/Eu*			1.05	1.08	1.36	1.52	1.29	1.39	1.67	1.29	1.16	1.60	1.42	1.50	1.25
Y/Ho			26.51	25.59	24.85	30.79	27.28	31.32	24.42	25.16	25.80	28.66	29.77	31.79	25.42

[1] Fe(total) = (Fe_2O_3+FeO)

EMS: Exhalite[2] associated with massive sulfides (within 5m)

FEM: Exhalite associated with felsic and mafic volcanic rocks, no massive sulfides

FEF: Exhalite within felsic volcanic rocks, no massive sulfides

IFE: Interflow exhalite

T: Tuff

[2] The term exhalite represents the Lemarchant metalliferous mudstones and was chosen to simplify the abbreviations.

Sample #			CNF25074	CNF25075	CNF25062b	CNF25063	CNF25064	CNF25065	CNF25066	CNF25067	CNF38438	CNF30955	CNF38437	CNF30954	CNF38436
Drill Hole			LM13-78	LM13-78	LM13-76	LM13-76	LM13-77	LM13-77	LM13-77	LM13-77	LM07-13	LM07-13	LM07-13	LM07-13	LM07-13
Section N			99+75N	99+75N	100+50N	100+50N	100+50N	100+50N	100+50N	100+50N	101N	101N	101N	101N	101N
Northing (UTM)			5374477	5374477	5374537	5374537	5374537	5374537	5374537	5374537	5374599.93	5374599.93	5374599.93	5374599.93	5374599.93
Easting (UTM)			520956	520956	521049	521049	521049	521049	521049	521049	521111.73	521111.73	521111.73	521111.73	521111.73
Sample Drill Hole Depth (m)			119.74	121.05	163.78	172.28	139.56	140	142.1	142.76	164.2	165.32	164.5	164.67	423.96
Description			T	FEM	FEM	T	T	T	FEM	FEM	EMS	EMS	EMS	EMS	IFE
$C_{(total)}$	%	IR	1.70	3.16	0.20	3.41	0.23	3.06	0.78	0.03	0.16	0.02	0.16	0.10	0.60
$S_{(total)}$	%	IR	8.23	27.20	25.50	6.84	26.50	4.57	21.10	21.80	21.80	16.60	33.60	33.10	17.60
Hg	ppb	FIMS	57.00	42.00	160.00	10.00	112.00	11.00	175.00	701.00	111.00	195.00	122.00	186.00	279.00
SiO_2	%	ICP-ES	22.82	18.04	36.88	40.08	31.86	45.92	26.32	32.06	45.60	39.80	14.57	21.16	45.16
Al_2O_3	%	ICP-ES	17.71	5.26	5.89	5.73	4.21	6.78	9.20	12.69	4.28	8.33	4.14	5.44	9.87
$Fe_{(total)}$ [1]	%	ICP-ES	25.81	53.02	32.23	13.79	39.71	14.15	37.01	29.20	29.70	23.63	48.59	44.07	22.75
MnO	%	ICP-ES	1.06	0.10	0.05	0.32	0.05	0.61	0.14	0.04	0.07	0.03	0.08	0.07	0.02
MgO	%	ICP-ES	5.51	1.79	1.23	2.77	0.70	2.00	1.47	1.04	1.90	0.89	2.34	2.36	0.66
CaO	%	ICP-ES	7.16	0.32	1.16	16.78	0.38	14.35	1.20	1.11	1.02	1.18	2.10	1.04	2.21
Na_2O	%	ICP-ES	0.31	0.05	0.05	0.38	0.06	0.08	0.08	0.15	0.06	0.05	0.03	0.02	0.96
K_2O	%	ICP-ES	2.60	0.74	1.02	0.19	0.64	0.81	1.27	2.80	0.47	0.51	0.25	0.40	2.20
TiO_2	%	ICP-ES	1.17	0.27	0.26	0.42	0.18	0.29	0.32	0.44	0.27	0.32	0.34	0.27	0.41
P_2O_5	%	ICP-ES	0.17	0.33	0.31	1.15	0.30	0.92	0.06	0.84	0.73	0.80	1.54	0.70	0.94
LOI	%	ICP-ES	10.37	16.98	17.61	9.42	16.89	7.97	17.68	15.34	14.44	11.16	23.85	22.70	13.03
Total	%	ICP-ES	94.68	96.89	96.69	91.03	94.98	93.89	94.75	95.73	98.54	86.70	97.83	98.23	98.21
Ba	ppm	ICP-ES	517.00	323.00	1067.00	372.00	2074.00	2612.00	5859.00	11480.00	1544.00	50540.00	6037.00	17540.00	649.00
Sc	ppm	ICP-ES	33.00	6.00	8.00	12.00	5.00	8.00	12.00	16.00	13.00	9.00	7.00	7.00	12.00
Be	ppm	ICP-ES	2.00	1.00	0.50	0.50	0.50	0.50	2.00	2.00	0.50	2.00	0.50	1.00	0.50
V	ppm	ICP-ES	830.00	635.00	393.00	237.00	688.00	414.00	896.00	1825.00	267.00	962.00	342.00	543.00	1811.00
Li	ppm	ICP-MS	15.47	4.38	3.28	7.13	2.04	4.78	4.72	2.97	2.34	13.87	4.63	6.66	2.16
Sr	ppm	ICP-MS	158.75	19.54	16.41	157.08	11.45	118.99	15.38	24.88	17.27	83.47	50.47	64.93	58.45
Y	ppm	ICP-MS	12.83	12.16	8.26	26.36	7.54	28.87	8.31	16.25	13.69	15.52	20.77	13.75	17.77
Zr	ppm	ICP-MS	85.88	55.70	52.61	32.40	36.88	56.31	56.57	77.11	26.53	62.17	42.40	46.72	90.15
Nb	ppm	ICP-MS	0.64	2.23	1.85	0.95	1.49	1.09	1.71	3.74	0.82	3.86	2.79	1.89	8.81
Cs	ppm	ICP-MS	0.53	0.37	0.51	0.13	0.34	0.27	0.61	1.09	0.19	1.58	0.23	0.55	1.59
Ba_2	ppm	ICP-MS	531.97	327.29	895.70	354.06	1605.68	2708.12	3769.95	2399.92	1049.16	41616.33	3781.31	18100.32	718.07
La	ppm	ICP-MS	6.73	15.12	13.67	15.04	7.39	26.54	11.12	20.09	16.19	19.84	18.78	14.97	19.23
Ce	ppm	ICP-MS	7.64	19.66	21.23	21.05	11.11	29.89	16.88	31.16	28.27	28.95	25.21	18.38	33.24
Pr	ppm	ICP-MS	1.78	3.75	3.75	3.76	2.12	5.99	2.95	6.17	4.21	5.32	4.93	3.54	6.14
Nd	ppm	ICP-MS	7.15	14.65	14.91	17.02	8.86	23.41	11.35	25.65	18.97	22.64	21.92	14.40	26.49
Sm	ppm	ICP-MS	1.74	2.86	3.45	4.55	1.80	5.09	2.29	5.81	4.59	4.89	4.84	3.07	6.17
Eu	ppm	ICP-MS	0.42	0.64	0.90	1.64	0.48	1.55	0.74	1.55	1.15	1.54	1.51	0.95	1.58
Gd	ppm	ICP-MS	2.05	2.75	2.83	5.70	1.68	5.41	1.92	5.47	4.76	4.18	5.19	2.92	5.74
Tb	ppm	ICP-MS	0.33	0.40	0.38	0.78	0.25	0.76	0.30	0.69	0.61	0.54	0.71	0.41	0.74
Dy	ppm	ICP-MS	2.13	2.34	1.88	4.56	1.47	4.62	1.85	3.58	3.16	2.98	3.79	2.21	3.89
Ho	ppm	ICP-MS	0.48	0.48	0.33	0.86	0.28	0.92	0.34	0.65	0.53	0.54	0.70	0.43	0.70
Er	ppm	ICP-MS	1.63	1.41	0.98	2.32	0.79	2.64	1.10	1.80	1.31	1.50	1.70	1.25	1.85
Tm	ppm	ICP-MS	0.29	0.25	0.16	0.33	0.15	0.40	0.22	0.30	0.17	0.24	0.27	0.22	0.30
Yb	ppm	ICP-MS	2.32	1.50	1.05	1.75	0.91	2.47	1.48	1.96	1.00	1.49	1.58	1.15	2.03
Lu	ppm	ICP-MS	0.42	0.25	0.20	0.27	0.15	0.42	0.25	0.33	0.15	0.26	0.23	0.20	0.33
Hf	ppm	ICP-MS	8.11	2.64	3.17	1.74	1.47	4.67	2.71	3.47	0.78	1.71	1.07	1.22	2.22
Ta	ppm	ICP-MS	0.06	0.19	0.14	0.06	0.13	0.09	0.16	0.31	0.08	0.21	0.12	0.10	0.54
Tl	ppm	ICP-MS	1.68	2.19	0.89	0.31	1.93	0.72	3.72	7.50	1.44	1.88	1.36	2.51	3.61
Pb	ppm	ICP-MS	14.96	806.81	761.86	163.42	600.82	21.80	1184.86	761.00	433.14	211.40	754.27	896.90	581.51
Bi	ppm	ICP-MS	0.10	0.91	0.86	0.22	0.32	0.18	0.70	0.62	0.45	0.23	0.54	0.43	0.62
Th	ppm	ICP-MS	2.51	5.39	5.20	1.44	3.50	3.65	5.00	6.14	1.66	4.45	2.16	2.60	6.58
U	ppm	ICP-MS	1.69	30.61	25.12	5.18	16.34	4.88	61.36	55.88	5.26	39.31	13.98	12.42	66.85
Cr	ppm	ICP-MS	40.57	34.91	52.99	27.04	35.99	40.61	38.25	112.37	20.03	94.42	56.99	38.66	129.01
Fe	ppm	ICP-MS	137854.65	281694.38	214167.90	94744.28	242710.05	101344.44	196517.28	152849.46	192603.54	150078.55	311549.80	276654.66	146492.75
Mn	ppm	ICP-MS	5504.84	620.96	389.02	2410.25	363.82	4621.34	837.17	225.87	524.38	210.48	529.20	496.99	131.50
Co	ppm	ICP-MS	8.39	31.54	19.58	28.98	110.24	14.04	75.72	38.29	53.15	16.65	73.90	14.49	18.53
Ni	ppm	ICP-MS	105.09	457.01	182.26	82.76	251.92	76.28	339.26	479.49	142.97	276.51	165.71	191.41	570.12
Cu	ppm	ICP-MS	145.19	522.21	502.75	120.92	216.82	101.81	508.56	392.37	219.71	56188.59	605.33	233.46	263.95
Zn	ppm	ICP-MS	625.34	907.06	540.16	295.46	234.19	203.07	108.36	66.28	94.17	3659.78	214.03	263.79	919.90
As	ppm	ICP-MS	14.48	203.00	216.07	41.63	3305.98	139.88	2069.99	1302.14	376.72	394.79	9545.16	1201.81	682.75
Se	ppm	ICP-MS	6.05	21.84	7.62	2.46	9.91	5.86	17.93	24.09	4.62	6.98	9.60	12.55	35.35
Br	ppm	ICP-MS	91.59	87.20	87.25	95.81	88.72	99.32	103.90	92.51	114.06	140.06	123.14	143.13	141.08
Mo	ppm	ICP-MS	6.80	125.95	108.39	20.45	113.42	26.16	263.83	213.91	34.35	136.51	33.74	86.16	151.28
Ag	ppm	ICP-MS	0.78	12.05	19.06	1.16	29.09	1.22	30.80	31.65	4.28	116.09	31.04	36.54	11.87
Cd	ppm	ICP-MS	2.74	6.65	8.19	1.09	4.05	1.00	0.62	0.59	1.26	19.18	1.11	0.26	11.08
Sn	ppm	ICP-MS	3.19	3.08	2.82	2.89	3.16	3.00	3.44	3.60	1.43	3.62	1.54	1.76	2.74
Sb	ppm	ICP-MS	1.87	140.36	23.23	2.92	51.32	1.12	49.20	81.32	71.78	26.74	111.10	120.42	61.73
Te	ppm	ICP-MS	0.10	0.73	0.96	0.55	0.82	0.10	1.70	0.89	1.71	1.87	2.44	3.71	1.13
I	ppm	ICP-MS	1.59	1.59	1.59	1.59	1.59	1.59	1.22	1.59	8.98	5.35	8.98	1.36	8.98
W	ppm	ICP-MS	4.41	6.19	1.47	2.13	2.52	1.81	2.60	6.34	2.45	14.08	6.86	5.02	4.54
CIA			63.75	82.57	72.54	24.83	79.58	30.79	78.30	75.76	73.41	82.72	63.50	78.84	64.76
Ce/Ce*			0.51	0.60	0.68	0.65	0.65	0.55	0.68	0.65	0.79	0.65	0.60	0.58	0.71
Eu/Eu*			1.05	1.08	1.36	1.52	1.29	1.39	1.67	1.29	1.16	1.60	1.42	1.50	1.25
Y/Ho			26.51	25.59	24.85	30.79	27.28	31.32	24.42	25.16	25.80	28.66	29.77	31.79	25.42

[1] Fe(total) = (Fe_2O_3+FeO)

EMS: Exhalite[2] associated with massive sulfides (within 5m)

FEM: Exhalite associated with felsic and mafic volcanic rocks, no massive sulfides

FEF: Exhalite within felsic volcanic rocks, no massive sulfides

IFE: Interflow exhalite

T: Tuff

[2] The term exhalite represents the Lemarchant metalliferous mudstones and was chosen to simplify the abbreviations.

Sample #			CNF25074	CNF25075	CNF25062b	CNF25063	CNF25064	CNF25065	CNF25066	CNF25067	CNF38438	CNF30955	CNF38437	CNF30954	CNF38436
Drill Hole			LM13-78	LM13-78	LM13-76	LM13-76	LM13-77	LM13-77	LM13-77	LM13-77	LM07-13	LM07-13	LM07-13	LM07-13	LM07-13
Section N			99+75N	99+75N	100+50N	100+50N	100+50N	100+50N	100+50N	100+50N	101N	101N	101N	101N	101N
Northing (UTM)			5374477	5374477	5374537	5374537	5374537	5374537	5374537	5374537	5374599.93	5374599.93	5374599.93	5374599.93	5374599.93
Easting (UTM)			520956	520956	521049	521049	521049	521049	521049	521049	521111.73	521111.73	521111.73	521111.73	521111.73
Sample Drill Hole Depth (m)			119.74	121.05	163.78	172.28	139.56	140	142.1	142.76	164.2	165.32	164.5	164.67	423.96
Description			T	FEM	FEM	T	T	T	FEM	FEM	EMS	EMS	EMS	EMS	IFE
$C_{(total)}$	%	IR	1.70	3.16	0.20	3.41	0.23	3.06	0.78	0.03	0.16	0.02	0.16	0.10	0.60
$S_{(total)}$	%	IR	8.23	27.20	25.50	6.84	26.50	4.57	21.10	21.80	21.80	16.60	33.60	33.10	17.60
Hg	ppb	FIMS	57.00	42.00	160.00	10.00	112.00	11.00	175.00	701.00	111.00	195.00	122.00	186.00	279.00
SiO_2	%	ICP-ES	22.82	18.04	36.88	40.08	31.86	45.92	26.32	32.06	45.60	39.80	14.57	21.16	45.16
Al_2O_3	%	ICP-ES	17.71	5.26	5.89	5.73	4.21	6.78	9.20	12.69	4.28	8.33	4.14	5.44	9.87
$Fe_{(total)}$ [1]	%	ICP-ES	25.81	53.02	32.23	13.79	39.71	14.15	37.01	29.20	29.70	23.63	48.59	44.07	22.75
MnO	%	ICP-ES	1.06	0.10	0.05	0.32	0.05	0.61	0.14	0.04	0.07	0.03	0.08	0.07	0.02
MgO	%	ICP-ES	5.51	1.79	1.23	2.77	0.70	2.00	1.47	1.04	1.90	0.89	2.34	2.36	0.66
CaO	%	ICP-ES	7.16	0.32	1.16	16.78	0.38	14.35	1.20	1.11	1.02	1.18	2.10	1.04	2.21
Na_2O	%	ICP-ES	0.31	0.05	0.05	0.38	0.06	0.08	0.08	0.15	0.06	0.05	0.03	0.02	0.96
K_2O	%	ICP-ES	2.60	0.74	1.02	0.19	0.64	0.81	1.27	2.80	0.47	0.51	0.25	0.40	2.20
TiO_2	%	ICP-ES	1.17	0.27	0.26	0.42	0.18	0.29	0.32	0.44	0.27	0.32	0.34	0.27	0.41
P_2O_5	%	ICP-ES	0.17	0.33	0.31	1.15	0.30	0.92	0.06	0.84	0.73	0.80	1.54	0.70	0.94
LOI	%	ICP-ES	10.37	16.98	17.61	9.42	16.89	7.97	17.68	15.34	14.44	11.16	23.85	22.70	13.03
Total	%	ICP-ES	94.68	96.89	96.69	91.03	94.98	93.89	94.75	95.73	98.54	86.70	97.83	98.23	98.21
Ba	ppm	ICP-ES	517.00	323.00	1067.00	372.00	2074.00	2612.00	5859.00	11480.00	1544.00	50540.00	6037.00	17540.00	649.00
Sc	ppm	ICP-ES	33.00	6.00	8.00	12.00	5.00	8.00	12.00	16.00	13.00	9.00	7.00	7.00	12.00
Be	ppm	ICP-ES	2.00	1.00	0.50	0.50	0.50	0.50	2.00	2.00	0.50	2.00	0.50	1.00	0.50
V	ppm	ICP-ES	830.00	635.00	393.00	237.00	688.00	414.00	896.00	1825.00	267.00	962.00	342.00	543.00	1811.00
Li	ppm	ICP-MS	15.47	4.38	3.28	7.13	2.04	4.78	4.72	2.97	2.34	13.87	4.63	6.66	2.16
Sr	ppm	ICP-MS	158.75	19.54	16.41	157.08	11.45	118.99	15.38	24.88	17.27	83.47	50.47	64.93	58.45
Y	ppm	ICP-MS	12.83	12.16	8.26	26.36	7.54	28.87	8.31	16.25	13.69	15.52	20.77	13.75	17.77
Zr	ppm	ICP-MS	85.88	55.70	52.61	32.40	36.88	56.31	56.57	77.11	26.53	62.17	42.40	46.72	90.15
Nb	ppm	ICP-MS	0.64	2.23	1.85	0.95	1.49	1.09	1.71	3.74	0.82	3.86	2.79	1.89	8.81
Cs	ppm	ICP-MS	0.53	0.37	0.51	0.13	0.34	0.27	0.61	1.09	0.19	1.58	0.23	0.55	1.59
Ba_2	ppm	ICP-MS	531.97	327.29	895.70	354.06	1605.68	2708.12	3769.95	2399.92	1049.16	41616.33	3781.31	18100.32	718.07
La	ppm	ICP-MS	6.73	15.12	13.67	15.04	7.39	26.54	11.12	20.09	16.19	19.84	18.78	14.97	19.23
Ce	ppm	ICP-MS	7.64	19.66	21.23	21.05	11.11	29.89	16.88	31.16	28.27	28.95	25.21	18.38	33.24
Pr	ppm	ICP-MS	1.78	3.75	3.75	3.76	2.12	5.99	2.95	6.17	4.21	5.32	4.93	3.54	6.14
Nd	ppm	ICP-MS	7.15	14.65	14.91	17.02	8.86	23.41	11.35	25.65	18.97	22.64	21.92	14.40	26.49
Sm	ppm	ICP-MS	1.74	2.86	3.45	4.55	1.80	5.09	2.29	5.81	4.59	4.89	4.84	3.07	6.17
Eu	ppm	ICP-MS	0.42	0.64	0.90	1.64	0.48	1.55	0.74	1.55	1.15	1.54	1.51	0.95	1.58
Gd	ppm	ICP-MS	2.05	2.75	2.83	5.70	1.68	5.41	1.92	5.47	4.76	4.18	5.19	2.92	5.74
Tb	ppm	ICP-MS	0.33	0.40	0.38	0.78	0.25	0.76	0.30	0.69	0.61	0.54	0.71	0.41	0.74
Dy	ppm	ICP-MS	2.13	2.34	1.88	4.56	1.47	4.62	1.85	3.58	3.16	2.98	3.79	2.21	3.89
Ho	ppm	ICP-MS	0.48	0.48	0.33	0.86	0.28	0.92	0.34	0.65	0.53	0.54	0.70	0.43	0.70
Er	ppm	ICP-MS	1.63	1.41	0.98	2.32	0.79	2.64	1.10	1.80	1.31	1.50	1.70	1.25	1.85
Tm	ppm	ICP-MS	0.29	0.25	0.16	0.33	0.15	0.40	0.22	0.30	0.17	0.24	0.27	0.22	0.30
Yb	ppm	ICP-MS	2.32	1.50	1.05	1.75	0.91	2.47	1.48	1.96	1.00	1.49	1.58	1.15	2.03
Lu	ppm	ICP-MS	0.42	0.25	0.20	0.27	0.15	0.42	0.25	0.33	0.15	0.26	0.23	0.20	0.33
Hf	ppm	ICP-MS	8.11	2.64	3.17	1.74	1.47	4.67	2.71	3.47	0.78	1.71	1.07	1.22	2.22
Ta	ppm	ICP-MS	0.06	0.19	0.14	0.06	0.13	0.09	0.16	0.31	0.08	0.21	0.12	0.10	0.54
Tl	ppm	ICP-MS	1.68	2.19	0.89	0.31	1.93	0.72	3.72	7.50	1.44	1.88	1.36	2.51	3.61
Pb	ppm	ICP-MS	14.96	806.81	761.86	163.42	600.82	21.80	1184.86	761.00	433.14	211.40	754.27	896.90	581.51
Bi	ppm	ICP-MS	0.10	0.91	0.86	0.22	0.32	0.18	0.70	0.62	0.45	0.23	0.54	0.43	0.62
Th	ppm	ICP-MS	2.51	5.39	5.20	1.44	3.50	3.65	5.00	6.14	1.66	4.45	2.16	2.60	6.58
U	ppm	ICP-MS	1.69	30.61	25.12	5.18	16.34	4.88	61.36	55.88	5.26	39.31	13.98	12.42	66.85
Cr	ppm	ICP-MS	40.57	34.91	52.99	27.04	35.99	40.61	38.25	112.37	20.03	94.42	56.99	38.66	129.01
Fe	ppm	ICP-MS	137854.65	281694.38	214167.90	94744.28	242710.05	101344.44	196517.28	152849.46	192603.54	150078.55	311549.80	276654.66	146492.75
Mn	ppm	ICP-MS	5504.84	620.96	389.02	2410.25	363.82	4621.34	837.17	225.87	524.38	210.48	529.20	496.99	131.50
Co	ppm	ICP-MS	8.39	31.54	19.58	28.98	110.24	14.04	75.72	38.29	53.15	16.65	73.90	14.49	18.53
Ni	ppm	ICP-MS	105.09	457.01	182.26	82.76	251.92	76.28	339.26	479.49	142.97	276.51	165.71	191.41	570.12
Cu	ppm	ICP-MS	145.19	522.21	502.75	120.92	216.82	101.81	508.56	392.37	219.71	56188.59	605.33	233.46	263.95
Zn	ppm	ICP-MS	625.34	907.06	540.16	295.46	234.19	203.07	108.36	66.28	94.17	3659.78	214.03	263.79	919.90
As	ppm	ICP-MS	14.48	203.00	216.07	41.63	3305.98	139.88	2069.99	1302.14	376.72	394.79	9545.16	1201.81	682.75
Se	ppm	ICP-MS	6.05	21.84	7.62	2.46	9.91	5.86	17.93	24.09	4.62	6.98	9.60	12.55	35.35
Br	ppm	ICP-MS	91.59	87.20	87.25	95.81	88.72	99.32	103.90	92.51	114.06	140.06	123.14	143.13	141.08
Mo	ppm	ICP-MS	6.80	125.95	108.39	20.45	113.42	26.16	263.83	213.91	34.35	136.51	33.74	86.16	151.28
Ag	ppm	ICP-MS	0.78	12.05	19.06	1.16	29.09	1.22	30.80	31.65	4.28	116.09	31.04	36.54	11.87
Cd	ppm	ICP-MS	2.74	6.65	8.19	1.09	4.05	1.00	0.62	0.59	1.26	19.18	1.11	0.26	11.08
Sn	ppm	ICP-MS	3.19	3.08	2.82	2.89	3.16	3.00	3.44	3.60	1.43	3.62	1.54	1.76	2.74
Sb	ppm	ICP-MS	1.87	140.36	23.23	2.92	51.32	1.12	49.20	81.32	71.78	26.74	111.10	120.42	61.73
Te	ppm	ICP-MS	0.10	0.73	0.96	0.55	0.82	0.10	1.70	0.89	1.71	1.87	2.44	3.71	1.13
I	ppm	ICP-MS	1.59	1.59	1.59	1.59	1.59	1.59	1.22	1.59	8.98	5.35	8.98	1.36	8.98
W	ppm	ICP-MS	4.41	6.19	1.47	2.13	2.52	1.81	2.60	6.34	2.45	14.08	6.86	5.02	4.54
CIA			63.75	82.57	72.54	24.83	79.58	30.79	78.30	75.76	73.41	82.72	63.50	78.84	64.76
Ce/Ce*			0.51	0.60	0.68	0.65	0.65	0.55	0.68	0.65	0.79	0.65	0.60	0.58	0.71
Eu/Eu*			1.05	1.08	1.36	1.52	1.29	1.39	1.67	1.29	1.16	1.60	1.42	1.50	1.25
Y/Ho			26.51	25.59	24.85	30.79	27.28	31.32	24.42	25.16	25.80	28.66	29.77	31.79	25.42

[1] Fe(total) = (Fe_2O_3+FeO)

EMS: Exhalite[2] associated with massive sulfides (within 5m)

FEM: Exhalite associated with felsic and mafic volcanic rocks, no massive sulfides

FEF: Exhalite within felsic volcanic rocks, no massive sulfides

IFE: Interflow exhalite

T: Tuff

[2] The term exhalite represents the Lemarchant metalliferous mudstones and was chosen to simplify the abbreviations.

Sample #			CNF25074	CNF25075	CNF25062b	CNF25063	CNF25064	CNF25065	CNF25066	CNF25067	CNF38438	CNF30955	CNF38437	CNF30954	CNF38436
Drill Hole			LM13-78	LM13-78	LM13-76	LM13-76	LM13-77	LM13-77	LM13-77	LM13-77	LM07-13	LM07-13	LM07-13	LM07-13	LM07-13
Section N			99+75N	99+75N	100+50N	100+50N	100+50N	100+50N	100+50N	100+50N	101N	101N	101N	101N	101N
Northing (UTM)			5374477	5374477	5374537	5374537	5374537	5374537	5374537	5374537	5374599.93	5374599.93	5374599.93	5374599.93	5374599.93
Easting (UTM)			520956	520956	521049	521049	521049	521049	521049	521049	521111.73	521111.73	521111.73	521111.73	521111.73
Sample Drill Hole Depth (m)			119.74	121.05	163.78	172.28	139.56	140	142.1	142.76	164.2	165.32	164.5	164.67	423.96
Description			T	FEM	FEM	T	T	T	FEM	FEM	EMS	EMS	EMS	EMS	IFE
$C_{(total)}$	%	IR	1.70	3.16	0.20	3.41	0.23	3.06	0.78	0.03	0.16	0.02	0.16	0.10	0.60
$S_{(total)}$	%	IR	8.23	27.20	25.50	6.84	26.50	4.57	21.10	21.80	21.80	16.60	33.60	33.10	17.60
Hg	ppb	FIMS	57.00	42.00	160.00	10.00	112.00	11.00	175.00	701.00	111.00	195.00	122.00	186.00	279.00
SiO_2	%	ICP-ES	22.82	18.04	36.88	40.08	31.86	45.92	26.32	32.06	45.60	39.80	14.57	21.16	45.16
Al_2O_3	%	ICP-ES	17.71	5.26	5.89	5.73	4.21	6.78	9.20	12.69	4.28	8.33	4.14	5.44	9.87
$Fe_{(total)}$ [1]	%	ICP-ES	25.81	53.02	32.23	13.79	39.71	14.15	37.01	29.20	29.70	23.63	48.59	44.07	22.75
MnO	%	ICP-ES	1.06	0.10	0.05	0.32	0.05	0.61	0.14	0.04	0.07	0.03	0.08	0.07	0.02
MgO	%	ICP-ES	5.51	1.79	1.23	2.77	0.70	2.00	1.47	1.04	1.90	0.89	2.34	2.36	0.66
CaO	%	ICP-ES	7.16	0.32	1.16	16.78	0.38	14.35	1.20	1.11	1.02	1.18	2.10	1.04	2.21
Na_2O	%	ICP-ES	0.31	0.05	0.05	0.38	0.06	0.08	0.08	0.15	0.06	0.05	0.03	0.02	0.96
K_2O	%	ICP-ES	2.60	0.74	1.02	0.19	0.64	0.81	1.27	2.80	0.47	0.51	0.25	0.40	2.20
TiO_2	%	ICP-ES	1.17	0.27	0.26	0.42	0.18	0.29	0.32	0.44	0.27	0.32	0.34	0.27	0.41
P_2O_5	%	ICP-ES	0.17	0.33	0.31	1.15	0.30	0.92	0.06	0.84	0.73	0.80	1.54	0.70	0.94
LOI	%	ICP-ES	10.37	16.98	17.61	9.42	16.89	7.97	17.68	15.34	14.44	11.16	23.85	22.70	13.03
Total	%	ICP-ES	94.68	96.89	96.69	91.03	94.98	93.89	94.75	95.73	98.54	86.70	97.83	98.23	98.21
Ba	ppm	ICP-ES	517.00	323.00	1067.00	372.00	2074.00	2612.00	5859.00	11480.00	1544.00	50540.00	6037.00	17540.00	649.00
Sc	ppm	ICP-ES	33.00	6.00	8.00	12.00	5.00	8.00	12.00	16.00	13.00	9.00	7.00	7.00	12.00
Be	ppm	ICP-ES	2.00	1.00	0.50	0.50	0.50	0.50	2.00	2.00	0.50	2.00	0.50	1.00	0.50
V	ppm	ICP-ES	830.00	635.00	393.00	237.00	688.00	414.00	896.00	1825.00	267.00	962.00	342.00	543.00	1811.00
Li	ppm	ICP-MS	15.47	4.38	3.28	7.13	2.04	4.78	4.72	2.97	2.34	13.87	4.63	6.66	2.16
Sr	ppm	ICP-MS	158.75	19.54	16.41	157.08	11.45	118.99	15.38	24.88	17.27	83.47	50.47	64.93	58.45
Y	ppm	ICP-MS	12.83	12.16	8.26	26.36	7.54	28.87	8.31	16.25	13.69	15.52	20.77	13.75	17.77
Zr	ppm	ICP-MS	85.88	55.70	52.61	32.40	36.88	56.31	56.57	77.11	26.53	62.17	42.40	46.72	90.15
Nb	ppm	ICP-MS	0.64	2.23	1.85	0.95	1.49	1.09	1.71	3.74	0.82	3.86	2.79	1.89	8.81
Cs	ppm	ICP-MS	0.53	0.37	0.51	0.13	0.34	0.27	0.61	1.09	0.19	1.58	0.23	0.55	1.59
Ba_2	ppm	ICP-MS	531.97	327.29	895.70	354.06	1605.68	2708.12	3769.95	2399.92	1049.16	41616.33	3781.31	18100.32	718.07
La	ppm	ICP-MS	6.73	15.12	13.67	15.04	7.39	26.54	11.12	20.09	16.19	19.84	18.78	14.97	19.23
Ce	ppm	ICP-MS	7.64	19.66	21.23	21.05	11.11	29.89	16.88	31.16	28.27	28.95	25.21	18.38	33.24
Pr	ppm	ICP-MS	1.78	3.75	3.75	3.76	2.12	5.99	2.95	6.17	4.21	5.32	4.93	3.54	6.14
Nd	ppm	ICP-MS	7.15	14.65	14.91	17.02	8.86	23.41	11.35	25.65	18.97	22.64	21.92	14.40	26.49
Sm	ppm	ICP-MS	1.74	2.86	3.45	4.55	1.80	5.09	2.29	5.81	4.59	4.89	4.84	3.07	6.17
Eu	ppm	ICP-MS	0.42	0.64	0.90	1.64	0.48	1.55	0.74	1.55	1.15	1.54	1.51	0.95	1.58
Gd	ppm	ICP-MS	2.05	2.75	2.83	5.70	1.68	5.41	1.92	5.47	4.76	4.18	5.19	2.92	5.74
Tb	ppm	ICP-MS	0.33	0.40	0.38	0.78	0.25	0.76	0.30	0.69	0.61	0.54	0.71	0.41	0.74
Dy	ppm	ICP-MS	2.13	2.34	1.88	4.56	1.47	4.62	1.85	3.58	3.16	2.98	3.79	2.21	3.89
Ho	ppm	ICP-MS	0.48	0.48	0.33	0.86	0.28	0.92	0.34	0.65	0.53	0.54	0.70	0.43	0.70
Er	ppm	ICP-MS	1.63	1.41	0.98	2.32	0.79	2.64	1.10	1.80	1.31	1.50	1.70	1.25	1.85
Tm	ppm	ICP-MS	0.29	0.25	0.16	0.33	0.15	0.40	0.22	0.30	0.17	0.24	0.27	0.22	0.30
Yb	ppm	ICP-MS	2.32	1.50	1.05	1.75	0.91	2.47	1.48	1.96	1.00	1.49	1.58	1.15	2.03
Lu	ppm	ICP-MS	0.42	0.25	0.20	0.27	0.15	0.42	0.25	0.33	0.15	0.26	0.23	0.20	0.33
Hf	ppm	ICP-MS	8.11	2.64	3.17	1.74	1.47	4.67	2.71	3.47	0.78	1.71	1.07	1.22	2.22
Ta	ppm	ICP-MS	0.06	0.19	0.14	0.06	0.13	0.09	0.16	0.31	0.08	0.21	0.12	0.10	0.54
Tl	ppm	ICP-MS	1.68	2.19	0.89	0.31	1.93	0.72	3.72	7.50	1.44	1.88	1.36	2.51	3.61
Pb	ppm	ICP-MS	14.96	806.81	761.86	163.42	600.82	21.80	1184.86	761.00	433.14	211.40	754.27	896.90	581.51
Bi	ppm	ICP-MS	0.10	0.91	0.86	0.22	0.32	0.18	0.70	0.62	0.45	0.23	0.54	0.43	0.62
Th	ppm	ICP-MS	2.51	5.39	5.20	1.44	3.50	3.65	5.00	6.14	1.66	4.45	2.16	2.60	6.58
U	ppm	ICP-MS	1.69	30.61	25.12	5.18	16.34	4.88	61.36	55.88	5.26	39.31	13.98	12.42	66.85
Cr	ppm	ICP-MS	40.57	34.91	52.99	27.04	35.99	40.61	38.25	112.37	20.03	94.42	56.99	38.66	129.01
Fe	ppm	ICP-MS	137854.65	281694.38	214167.90	94744.28	242710.05	101344.44	196517.28	152849.46	192603.54	150078.55	311549.80	276654.66	146492.75
Mn	ppm	ICP-MS	5504.84	620.96	389.02	2410.25	363.82	4621.34	837.17	225.87	524.38	210.48	529.20	496.99	131.50
Co	ppm	ICP-MS	8.39	31.54	19.58	28.98	110.24	14.04	75.72	38.29	53.15	16.65	73.90	14.49	18.53
Ni	ppm	ICP-MS	105.09	457.01	182.26	82.76	251.92	76.28	339.26	479.49	142.97	276.51	165.71	191.41	570.12
Cu	ppm	ICP-MS	145.19	522.21	502.75	120.92	216.82	101.81	508.56	392.37	219.71	56188.59	605.33	233.46	263.95
Zn	ppm	ICP-MS	625.34	907.06	540.16	295.46	234.19	203.07	108.36	66.28	94.17	3659.78	214.03	263.79	919.90
As	ppm	ICP-MS	14.48	203.00	216.07	41.63	3305.98	139.88	2069.99	1302.14	376.72	394.79	9545.16	1201.81	682.75
Se	ppm	ICP-MS	6.05	21.84	7.62	2.46	9.91	5.86	17.93	24.09	4.62	6.98	9.60	12.55	35.35
Br	ppm	ICP-MS	91.59	87.20	87.25	95.81	88.72	99.32	103.90	92.51	114.06	140.06	123.14	143.13	141.08
Mo	ppm	ICP-MS	6.80	125.95	108.39	20.45	113.42	26.16	263.83	213.91	34.35	136.51	33.74	86.16	151.28
Ag	ppm	ICP-MS	0.78	12.05	19.06	1.16	29.09	1.22	30.80	31.65	4.28	116.09	31.04	36.54	11.87
Cd	ppm	ICP-MS	2.74	6.65	8.19	1.09	4.05	1.00	0.62	0.59	1.26	19.18	1.11	0.26	11.08
Sn	ppm	ICP-MS	3.19	3.08	2.82	2.89	3.16	3.00	3.44	3.60	1.43	3.62	1.54	1.76	2.74
Sb	ppm	ICP-MS	1.87	140.36	23.23	2.92	51.32	1.12	49.20	81.32	71.78	26.74	111.10	120.42	61.73
Te	ppm	ICP-MS	0.10	0.73	0.96	0.55	0.82	0.10	1.70	0.89	1.71	1.87	2.44	3.71	1.13
I	ppm	ICP-MS	1.59	1.59	1.59	1.59	1.59	1.59	1.22	1.59	8.98	5.35	8.98	1.36	8.98
W	ppm	ICP-MS	4.41	6.19	1.47	2.13	2.52	1.81	2.60	6.34	2.45	14.08	6.86	5.02	4.54
CIA			63.75	82.57	72.54	24.83	79.58	30.79	78.30	75.76	73.41	82.72	63.50	78.84	64.76
Ce/Ce*			0.51	0.60	0.68	0.65	0.65	0.55	0.68	0.65	0.79	0.65	0.60	0.58	0.71
Eu/Eu*			1.05	1.08	1.36	1.52	1.29	1.39	1.67	1.29	1.16	1.60	1.42	1.50	1.25
Y/Ho			26.51	25.59	24.85	30.79	27.28	31.32	24.42	25.16	25.80	28.66	29.77	31.79	25.42

[1] Fe(total) = (Fe_2O_3+FeO)

EMS: Exhalite[2] associated with massive sulfides (within 5m)

FEM: Exhalite associated with felsic and mafic volcanic rocks, no massive sulfides

FEF: Exhalite within felsic volcanic rocks, no massive sulfides

IFE: Interflow exhalite

T: Tuff

[2] The term exhalite represents the Lemarchant metalliferous mudstones and was chosen to simplify the abbreviations.

Sample #			CNF25074	CNF25075	CNF25062b	CNF25063	CNF25064	CNF25065	CNF25066	CNF25067	CNF38438	CNF30955	CNF38437	CNF30954	CNF38436
Drill Hole			LM13-78	LM13-78	LM13-76	LM13-76	LM13-77	LM13-77	LM13-77	LM13-77	LM07-13	LM07-13	LM07-13	LM07-13	LM07-13
Section N			99+75N	99+75N	100+50N	100+50N	100+50N	100+50N	100+50N	100+50N	101N	101N	101N	101N	101N
Northing (UTM)			5374477	5374477	5374537	5374537	5374537	5374537	5374537	5374537	5374599.93	5374599.93	5374599.93	5374599.93	5374599.93
Easting (UTM)			520956	520956	521049	521049	521049	521049	521049	521049	521111.73	521111.73	521111.73	521111.73	521111.73
Sample Drill Hole Depth (m)			119.74	121.05	163.78	172.28	139.56	140	142.1	142.76	164.2	165.32	164.5	164.67	423.96
Description			T	FEM	FEM	T	T	T	FEM	FEM	EMS	EMS	EMS	EMS	IFE
$C_{(total)}$	%	IR	1.70	3.16	0.20	3.41	0.23	3.06	0.78	0.03	0.16	0.02	0.16	0.10	0.60
$S_{(total)}$	%	IR	8.23	27.20	25.50	6.84	26.50	4.57	21.10	21.80	21.80	16.60	33.60	33.10	17.60
Hg	ppb	FIMS	57.00	42.00	160.00	10.00	112.00	11.00	175.00	701.00	111.00	195.00	122.00	186.00	279.00
SiO_2	%	ICP-ES	22.82	18.04	36.88	40.08	31.86	45.92	26.32	32.06	45.60	39.80	14.57	21.16	45.16
Al_2O_3	%	ICP-ES	17.71	5.26	5.89	5.73	4.21	6.78	9.20	12.69	4.28	8.33	4.14	5.44	9.87
$Fe_{(total)}$ [1]	%	ICP-ES	25.81	53.02	32.23	13.79	39.71	14.15	37.01	29.20	29.70	23.63	48.59	44.07	22.75
MnO	%	ICP-ES	1.06	0.10	0.05	0.32	0.05	0.61	0.14	0.04	0.07	0.03	0.08	0.07	0.02
MgO	%	ICP-ES	5.51	1.79	1.23	2.77	0.70	2.00	1.47	1.04	1.90	0.89	2.34	2.36	0.66
CaO	%	ICP-ES	7.16	0.32	1.16	16.78	0.38	14.35	1.20	1.11	1.02	1.18	2.10	1.04	2.21
Na_2O	%	ICP-ES	0.31	0.05	0.05	0.38	0.06	0.08	0.08	0.15	0.06	0.05	0.03	0.02	0.96
K_2O	%	ICP-ES	2.60	0.74	1.02	0.19	0.64	0.81	1.27	2.80	0.47	0.51	0.25	0.40	2.20
TiO_2	%	ICP-ES	1.17	0.27	0.26	0.42	0.18	0.29	0.32	0.44	0.27	0.32	0.34	0.27	0.41
P_2O_5	%	ICP-ES	0.17	0.33	0.31	1.15	0.30	0.92	0.06	0.84	0.73	0.80	1.54	0.70	0.94
LOI	%	ICP-ES	10.37	16.98	17.61	9.42	16.89	7.97	17.68	15.34	14.44	11.16	23.85	22.70	13.03
Total	%	ICP-ES	94.68	96.89	96.69	91.03	94.98	93.89	94.75	95.73	98.54	86.70	97.83	98.23	98.21
Ba	ppm	ICP-ES	517.00	323.00	1067.00	372.00	2074.00	2612.00	5859.00	11480.00	1544.00	50540.00	6037.00	17540.00	649.00
Sc	ppm	ICP-ES	33.00	6.00	8.00	12.00	5.00	8.00	12.00	16.00	13.00	9.00	7.00	7.00	12.00
Be	ppm	ICP-ES	2.00	1.00	0.50	0.50	0.50	0.50	2.00	2.00	0.50	2.00	0.50	1.00	0.50
V	ppm	ICP-ES	830.00	635.00	393.00	237.00	688.00	414.00	896.00	1825.00	267.00	962.00	342.00	543.00	1811.00
Li	ppm	ICP-MS	15.47	4.38	3.28	7.13	2.04	4.78	4.72	2.97	2.34	13.87	4.63	6.66	2.16
Sr	ppm	ICP-MS	158.75	19.54	16.41	157.08	11.45	118.99	15.38	24.88	17.27	83.47	50.47	64.93	58.45
Y	ppm	ICP-MS	12.83	12.16	8.26	26.36	7.54	28.87	8.31	16.25	13.69	15.52	20.77	13.75	17.77
Zr	ppm	ICP-MS	85.88	55.70	52.61	32.40	36.88	56.31	56.57	77.11	26.53	62.17	42.40	46.72	90.15
Nb	ppm	ICP-MS	0.64	2.23	1.85	0.95	1.49	1.09	1.71	3.74	0.82	3.86	2.79	1.89	8.81
Cs	ppm	ICP-MS	0.53	0.37	0.51	0.13	0.34	0.27	0.61	1.09	0.19	1.58	0.23	0.55	1.59
Ba_2	ppm	ICP-MS	531.97	327.29	895.70	354.06	1605.68	2708.12	3769.95	2399.92	1049.16	41616.33	3781.31	18100.32	718.07
La	ppm	ICP-MS	6.73	15.12	13.67	15.04	7.39	26.54	11.12	20.09	16.19	19.84	18.78	14.97	19.23
Ce	ppm	ICP-MS	7.64	19.66	21.23	21.05	11.11	29.89	16.88	31.16	28.27	28.95	25.21	18.38	33.24
Pr	ppm	ICP-MS	1.78	3.75	3.75	3.76	2.12	5.99	2.95	6.17	4.21	5.32	4.93	3.54	6.14
Nd	ppm	ICP-MS	7.15	14.65	14.91	17.02	8.86	23.41	11.35	25.65	18.97	22.64	21.92	14.40	26.49
Sm	ppm	ICP-MS	1.74	2.86	3.45	4.55	1.80	5.09	2.29	5.81	4.59	4.89	4.84	3.07	6.17
Eu	ppm	ICP-MS	0.42	0.64	0.90	1.64	0.48	1.55	0.74	1.55	1.15	1.54	1.51	0.95	1.58
Gd	ppm	ICP-MS	2.05	2.75	2.83	5.70	1.68	5.41	1.92	5.47	4.76	4.18	5.19	2.92	5.74
Tb	ppm	ICP-MS	0.33	0.40	0.38	0.78	0.25	0.76	0.30	0.69	0.61	0.54	0.71	0.41	0.74
Dy	ppm	ICP-MS	2.13	2.34	1.88	4.56	1.47	4.62	1.85	3.58	3.16	2.98	3.79	2.21	3.89
Ho	ppm	ICP-MS	0.48	0.48	0.33	0.86	0.28	0.92	0.34	0.65	0.53	0.54	0.70	0.43	0.70
Er	ppm	ICP-MS	1.63	1.41	0.98	2.32	0.79	2.64	1.10	1.80	1.31	1.50	1.70	1.25	1.85
Tm	ppm	ICP-MS	0.29	0.25	0.16	0.33	0.15	0.40	0.22	0.30	0.17	0.24	0.27	0.22	0.30
Yb	ppm	ICP-MS	2.32	1.50	1.05	1.75	0.91	2.47	1.48	1.96	1.00	1.49	1.58	1.15	2.03
Lu	ppm	ICP-MS	0.42	0.25	0.20	0.27	0.15	0.42	0.25	0.33	0.15	0.26	0.23	0.20	0.33
Hf	ppm	ICP-MS	8.11	2.64	3.17	1.74	1.47	4.67	2.71	3.47	0.78	1.71	1.07	1.22	2.22
Ta	ppm	ICP-MS	0.06	0.19	0.14	0.06	0.13	0.09	0.16	0.31	0.08	0.21	0.12	0.10	0.54
Tl	ppm	ICP-MS	1.68	2.19	0.89	0.31	1.93	0.72	3.72	7.50	1.44	1.88	1.36	2.51	3.61
Pb	ppm	ICP-MS	14.96	806.81	761.86	163.42	600.82	21.80	1184.86	761.00	433.14	211.40	754.27	896.90	581.51
Bi	ppm	ICP-MS	0.10	0.91	0.86	0.22	0.32	0.18	0.70	0.62	0.45	0.23	0.54	0.43	0.62
Th	ppm	ICP-MS	2.51	5.39	5.20	1.44	3.50	3.65	5.00	6.14	1.66	4.45	2.16	2.60	6.58
U	ppm	ICP-MS	1.69	30.61	25.12	5.18	16.34	4.88	61.36	55.88	5.26	39.31	13.98	12.42	66.85
Cr	ppm	ICP-MS	40.57	34.91	52.99	27.04	35.99	40.61	38.25	112.37	20.03	94.42	56.99	38.66	129.01
Fe	ppm	ICP-MS	137854.65	281694.38	214167.90	94744.28	242710.05	101344.44	196517.28	152849.46	192603.54	150078.55	311549.80	276654.66	146492.75
Mn	ppm	ICP-MS	5504.84	620.96	389.02	2410.25	363.82	4621.34	837.17	225.87	524.38	210.48	529.20	496.99	131.50
Co	ppm	ICP-MS	8.39	31.54	19.58	28.98	110.24	14.04	75.72	38.29	53.15	16.65	73.90	14.49	18.53
Ni	ppm	ICP-MS	105.09	457.01	182.26	82.76	251.92	76.28	339.26	479.49	142.97	276.51	165.71	191.41	570.12
Cu	ppm	ICP-MS	145.19	522.21	502.75	120.92	216.82	101.81	508.56	392.37	219.71	56188.59	605.33	233.46	263.95
Zn	ppm	ICP-MS	625.34	907.06	540.16	295.46	234.19	203.07	108.36	66.28	94.17	3659.78	214.03	263.79	919.90
As	ppm	ICP-MS	14.48	203.00	216.07	41.63	3305.98	139.88	2069.99	1302.14	376.72	394.79	9545.16	1201.81	682.75
Se	ppm	ICP-MS	6.05	21.84	7.62	2.46	9.91	5.86	17.93	24.09	4.62	6.98	9.60	12.55	35.35
Br	ppm	ICP-MS	91.59	87.20	87.25	95.81	88.72	99.32	103.90	92.51	114.06	140.06	123.14	143.13	141.08
Mo	ppm	ICP-MS	6.80	125.95	108.39	20.45	113.42	26.16	263.83	213.91	34.35	136.51	33.74	86.16	151.28
Ag	ppm	ICP-MS	0.78	12.05	19.06	1.16	29.09	1.22	30.80	31.65	4.28	116.09	31.04	36.54	11.87
Cd	ppm	ICP-MS	2.74	6.65	8.19	1.09	4.05	1.00	0.62	0.59	1.26	19.18	1.11	0.26	11.08
Sn	ppm	ICP-MS	3.19	3.08	2.82	2.89	3.16	3.00	3.44	3.60	1.43	3.62	1.54	1.76	2.74
Sb	ppm	ICP-MS	1.87	140.36	23.23	2.92	51.32	1.12	49.20	81.32	71.78	26.74	111.10	120.42	61.73
Te	ppm	ICP-MS	0.10	0.73	0.96	0.55	0.82	0.10	1.70	0.89	1.71	1.87	2.44	3.71	1.13
I	ppm	ICP-MS	1.59	1.59	1.59	1.59	1.59	1.59	1.22	1.59	8.98	5.35	8.98	1.36	8.98
W	ppm	ICP-MS	4.41	6.19	1.47	2.13	2.52	1.81	2.60	6.34	2.45	14.08	6.86	5.02	4.54
CIA			63.75	82.57	72.54	24.83	79.58	30.79	78.30	75.76	73.41	82.72	63.50	78.84	64.76
Ce/Ce*			0.51	0.60	0.68	0.65	0.65	0.55	0.68	0.65	0.79	0.65	0.60	0.58	0.71
Eu/Eu*			1.05	1.08	1.36	1.52	1.29	1.39	1.67	1.29	1.16	1.60	1.42	1.50	1.25
Y/Ho			26.51	25.59	24.85	30.79	27.28	31.32	24.42	25.16	25.80	28.66	29.77	31.79	25.42

[1] Fe(total) = (Fe_2O_3+FeO)

EMS: Exhalite[2] associated with massive sulfides (within 5m)

FEM: Exhalite associated with felsic and mafic volcanic rocks, no massive sulfides

FEF: Exhalite within felsic volcanic rocks, no massive sulfides

IFE: Interflow exhalite

T: Tuff

[2] The term exhalite represents the Lemarchant metalliferous mudstones and was chosen to simplify the abbreviations.

Sample #			CNF25074	CNF25075	CNF25062b	CNF25063	CNF25064	CNF25065	CNF25066	CNF25067	CNF38438	CNF30955	CNF38437	CNF30954	CNF38436
Drill Hole			LM13-78	LM13-78	LM13-76	LM13-76	LM13-77	LM13-77	LM13-77	LM13-77	LM07-13	LM07-13	LM07-13	LM07-13	LM07-13
Section N			99+75N	99+75N	100+50N	100+50N	100+50N	100+50N	100+50N	100+50N	101N	101N	101N	101N	101N
Northing (UTM)			5374477	5374477	5374537	5374537	5374537	5374537	5374537	5374537	5374599.93	5374599.93	5374599.93	5374599.93	5374599.93
Easting (UTM)			520956	520956	521049	521049	521049	521049	521049	521049	521111.73	521111.73	521111.73	521111.73	521111.73
Sample Drill Hole Depth (m)			119.74	121.05	163.78	172.28	139.56	140	142.1	142.76	164.2	165.32	164.5	164.67	423.96
Description			T	FEM	FEM	T	T	T	FEM	FEM	EMS	EMS	EMS	EMS	IFE
$C_{(total)}$	%	IR	1.70	3.16	0.20	3.41	0.23	3.06	0.78	0.03	0.16	0.02	0.16	0.10	0.60
$S_{(total)}$	%	IR	8.23	27.20	25.50	6.84	26.50	4.57	21.10	21.80	21.80	16.60	33.60	33.10	17.60
Hg	ppb	FIMS	57.00	42.00	160.00	10.00	112.00	11.00	175.00	701.00	111.00	195.00	122.00	186.00	279.00
SiO_2	%	ICP-ES	22.82	18.04	36.88	40.08	31.86	45.92	26.32	32.06	45.60	39.80	14.57	21.16	45.16
Al_2O_3	%	ICP-ES	17.71	5.26	5.89	5.73	4.21	6.78	9.20	12.69	4.28	8.33	4.14	5.44	9.87
$Fe_{(total)}$ [1]	%	ICP-ES	25.81	53.02	32.23	13.79	39.71	14.15	37.01	29.20	29.70	23.63	48.59	44.07	22.75
MnO	%	ICP-ES	1.06	0.10	0.05	0.32	0.05	0.61	0.14	0.04	0.07	0.03	0.08	0.07	0.02
MgO	%	ICP-ES	5.51	1.79	1.23	2.77	0.70	2.00	1.47	1.04	1.90	0.89	2.34	2.36	0.66
CaO	%	ICP-ES	7.16	0.32	1.16	16.78	0.38	14.35	1.20	1.11	1.02	1.18	2.10	1.04	2.21
Na_2O	%	ICP-ES	0.31	0.05	0.05	0.38	0.06	0.08	0.08	0.15	0.06	0.05	0.03	0.02	0.96
K_2O	%	ICP-ES	2.60	0.74	1.02	0.19	0.64	0.81	1.27	2.80	0.47	0.51	0.25	0.40	2.20
TiO_2	%	ICP-ES	1.17	0.27	0.26	0.42	0.18	0.29	0.32	0.44	0.27	0.32	0.34	0.27	0.41
P_2O_5	%	ICP-ES	0.17	0.33	0.31	1.15	0.30	0.92	0.06	0.84	0.73	0.80	1.54	0.70	0.94
LOI	%	ICP-ES	10.37	16.98	17.61	9.42	16.89	7.97	17.68	15.34	14.44	11.16	23.85	22.70	13.03
Total	%	ICP-ES	94.68	96.89	96.69	91.03	94.98	93.89	94.75	95.73	98.54	86.70	97.83	98.23	98.21
Ba	ppm	ICP-ES	517.00	323.00	1067.00	372.00	2074.00	2612.00	5859.00	11480.00	1544.00	50540.00	6037.00	17540.00	649.00
Sc	ppm	ICP-ES	33.00	6.00	8.00	12.00	5.00	8.00	12.00	16.00	13.00	9.00	7.00	7.00	12.00
Be	ppm	ICP-ES	2.00	1.00	0.50	0.50	0.50	0.50	2.00	2.00	0.50	2.00	0.50	1.00	0.50
V	ppm	ICP-ES	830.00	635.00	393.00	237.00	688.00	414.00	896.00	1825.00	267.00	962.00	342.00	543.00	1811.00
Li	ppm	ICP-MS	15.47	4.38	3.28	7.13	2.04	4.78	4.72	2.97	2.34	13.87	4.63	6.66	2.16
Sr	ppm	ICP-MS	158.75	19.54	16.41	157.08	11.45	118.99	15.38	24.88	17.27	83.47	50.47	64.93	58.45
Y	ppm	ICP-MS	12.83	12.16	8.26	26.36	7.54	28.87	8.31	16.25	13.69	15.52	20.77	13.75	17.77
Zr	ppm	ICP-MS	85.88	55.70	52.61	32.40	36.88	56.31	56.57	77.11	26.53	62.17	42.40	46.72	90.15
Nb	ppm	ICP-MS	0.64	2.23	1.85	0.95	1.49	1.09	1.71	3.74	0.82	3.86	2.79	1.89	8.81
Cs	ppm	ICP-MS	0.53	0.37	0.51	0.13	0.34	0.27	0.61	1.09	0.19	1.58	0.23	0.55	1.59
Ba_2	ppm	ICP-MS	531.97	327.29	895.70	354.06	1605.68	2708.12	3769.95	2399.92	1049.16	41616.33	3781.31	18100.32	718.07
La	ppm	ICP-MS	6.73	15.12	13.67	15.04	7.39	26.54	11.12	20.09	16.19	19.84	18.78	14.97	19.23
Ce	ppm	ICP-MS	7.64	19.66	21.23	21.05	11.11	29.89	16.88	31.16	28.27	28.95	25.21	18.38	33.24
Pr	ppm	ICP-MS	1.78	3.75	3.75	3.76	2.12	5.99	2.95	6.17	4.21	5.32	4.93	3.54	6.14
Nd	ppm	ICP-MS	7.15	14.65	14.91	17.02	8.86	23.41	11.35	25.65	18.97	22.64	21.92	14.40	26.49
Sm	ppm	ICP-MS	1.74	2.86	3.45	4.55	1.80	5.09	2.29	5.81	4.59	4.89	4.84	3.07	6.17
Eu	ppm	ICP-MS	0.42	0.64	0.90	1.64	0.48	1.55	0.74	1.55	1.15	1.54	1.51	0.95	1.58
Gd	ppm	ICP-MS	2.05	2.75	2.83	5.70	1.68	5.41	1.92	5.47	4.76	4.18	5.19	2.92	5.74
Tb	ppm	ICP-MS	0.33	0.40	0.38	0.78	0.25	0.76	0.30	0.69	0.61	0.54	0.71	0.41	0.74
Dy	ppm	ICP-MS	2.13	2.34	1.88	4.56	1.47	4.62	1.85	3.58	3.16	2.98	3.79	2.21	3.89
Ho	ppm	ICP-MS	0.48	0.48	0.33	0.86	0.28	0.92	0.34	0.65	0.53	0.54	0.70	0.43	0.70
Er	ppm	ICP-MS	1.63	1.41	0.98	2.32	0.79	2.64	1.10	1.80	1.31	1.50	1.70	1.25	1.85
Tm	ppm	ICP-MS	0.29	0.25	0.16	0.33	0.15	0.40	0.22	0.30	0.17	0.24	0.27	0.22	0.30
Yb	ppm	ICP-MS	2.32	1.50	1.05	1.75	0.91	2.47	1.48	1.96	1.00	1.49	1.58	1.15	2.03
Lu	ppm	ICP-MS	0.42	0.25	0.20	0.27	0.15	0.42	0.25	0.33	0.15	0.26	0.23	0.20	0.33
Hf	ppm	ICP-MS	8.11	2.64	3.17	1.74	1.47	4.67	2.71	3.47	0.78	1.71	1.07	1.22	2.22
Ta	ppm	ICP-MS	0.06	0.19	0.14	0.06	0.13	0.09	0.16	0.31	0.08	0.21	0.12	0.10	0.54
Tl	ppm	ICP-MS	1.68	2.19	0.89	0.31	1.93	0.72	3.72	7.50	1.44	1.88	1.36	2.51	3.61
Pb	ppm	ICP-MS	14.96	806.81	761.86	163.42	600.82	21.80	1184.86	761.00	433.14	211.40	754.27	896.90	581.51
Bi	ppm	ICP-MS	0.10	0.91	0.86	0.22	0.32	0.18	0.70	0.62	0.45	0.23	0.54	0.43	0.62
Th	ppm	ICP-MS	2.51	5.39	5.20	1.44	3.50	3.65	5.00	6.14	1.66	4.45	2.16	2.60	6.58
U	ppm	ICP-MS	1.69	30.61	25.12	5.18	16.34	4.88	61.36	55.88	5.26	39.31	13.98	12.42	66.85
Cr	ppm	ICP-MS	40.57	34.91	52.99	27.04	35.99	40.61	38.25	112.37	20.03	94.42	56.99	38.66	129.01
Fe	ppm	ICP-MS	137854.65	281694.38	214167.90	94744.28	242710.05	101344.44	196517.28	152849.46	192603.54	150078.55	311549.80	276654.66	146492.75
Mn	ppm	ICP-MS	5504.84	620.96	389.02	2410.25	363.82	4621.34	837.17	225.87	524.38	210.48	529.20	496.99	131.50
Co	ppm	ICP-MS	8.39	31.54	19.58	28.98	110.24	14.04	75.72	38.29	53.15	16.65	73.90	14.49	18.53
Ni	ppm	ICP-MS	105.09	457.01	182.26	82.76	251.92	76.28	339.26	479.49	142.97	276.51	165.71	191.41	570.12
Cu	ppm	ICP-MS	145.19	522.21	502.75	120.92	216.82	101.81	508.56	392.37	219.71	56188.59	605.33	233.46	263.95
Zn	ppm	ICP-MS	625.34	907.06	540.16	295.46	234.19	203.07	108.36	66.28	94.17	3659.78	214.03	263.79	919.90
As	ppm	ICP-MS	14.48	203.00	216.07	41.63	3305.98	139.88	2069.99	1302.14	376.72	394.79	9545.16	1201.81	682.75
Se	ppm	ICP-MS	6.05	21.84	7.62	2.46	9.91	5.86	17.93	24.09	4.62	6.98	9.60	12.55	35.35
Br	ppm	ICP-MS	91.59	87.20	87.25	95.81	88.72	99.32	103.90	92.51	114.06	140.06	123.14	143.13	141.08
Mo	ppm	ICP-MS	6.80	125.95	108.39	20.45	113.42	26.16	263.83	213.91	34.35	136.51	33.74	86.16	151.28
Ag	ppm	ICP-MS	0.78	12.05	19.06	1.16	29.09	1.22	30.80	31.65	4.28	116.09	31.04	36.54	11.87
Cd	ppm	ICP-MS	2.74	6.65	8.19	1.09	4.05	1.00	0.62	0.59	1.26	19.18	1.11	0.26	11.08
Sn	ppm	ICP-MS	3.19	3.08	2.82	2.89	3.16	3.00	3.44	3.60	1.43	3.62	1.54	1.76	2.74
Sb	ppm	ICP-MS	1.87	140.36	23.23	2.92	51.32	1.12	49.20	81.32	71.78	26.74	111.10	120.42	61.73
Te	ppm	ICP-MS	0.10	0.73	0.96	0.55	0.82	0.10	1.70	0.89	1.71	1.87	2.44	3.71	1.13
I	ppm	ICP-MS	1.59	1.59	1.59	1.59	1.59	1.59	1.22	1.59	8.98	5.35	8.98	1.36	8.98
W	ppm	ICP-MS	4.41	6.19	1.47	2.13	2.52	1.81	2.60	6.34	2.45	14.08	6.86	5.02	4.54
CIA			63.75	82.57	72.54	24.83	79.58	30.79	78.30	75.76	73.41	82.72	63.50	78.84	64.76
Ce/Ce*			0.51	0.60	0.68	0.65	0.65	0.55	0.68	0.65	0.79	0.65	0.60	0.58	0.71
Eu/Eu*			1.05	1.08	1.36	1.52	1.29	1.39	1.67	1.29	1.16	1.60	1.42	1.50	1.25
Y/Ho			26.51	25.59	24.85	30.79	27.28	31.32	24.42	25.16	25.80	28.66	29.77	31.79	25.42

[1] Fe(total) = (Fe_2O_3+FeO)

EMS: Exhalite[2] associated with massive sulfides (within 5m)

FEM: Exhalite associated with felsic and mafic volcanic rocks, no massive sulfides

FEF: Exhalite within felsic volcanic rocks, no massive sulfides

IFE: Interflow exhalite

T: Tuff

[2] The term exhalite represents the Lemarchant metalliferous mudstones and was chosen to simplify the abbreviations.

Sample #			CNF25074	CNF25075	CNF25062b	CNF25063	CNF25064	CNF25065	CNF25066	CNF25067	CNF38438	CNF30955	CNF38437	CNF30954	CNF38436
Drill Hole			LM13-78	LM13-78	LM13-76	LM13-76	LM13-77	LM13-77	LM13-77	LM13-77	LM07-13	LM07-13	LM07-13	LM07-13	LM07-13
Section N			99+75N	99+75N	100+50N	100+50N	100+50N	100+50N	100+50N	100+50N	101N	101N	101N	101N	101N
Northing (UTM)			5374477	5374477	5374537	5374537	5374537	5374537	5374537	5374537	5374599.93	5374599.93	5374599.93	5374599.93	5374599.93
Easting (UTM)			520956	520956	521049	521049	521049	521049	521049	521049	521111.73	521111.73	521111.73	521111.73	521111.73
Sample Drill Hole Depth (m)			119.74	121.05	163.78	172.28	139.56	140	142.1	142.76	164.2	165.32	164.5	164.67	423.96
Description			T	FEM	FEM	T	T	T	FEM	FEM	EMS	EMS	EMS	EMS	IFE
$C_{(total)}$	%	IR	1.70	3.16	0.20	3.41	0.23	3.06	0.78	0.03	0.16	0.02	0.16	0.10	0.60
$S_{(total)}$	%	IR	8.23	27.20	25.50	6.84	26.50	4.57	21.10	21.80	21.80	16.60	33.60	33.10	17.60
Hg	ppb	FIMS	57.00	42.00	160.00	10.00	112.00	11.00	175.00	701.00	111.00	195.00	122.00	186.00	279.00
SiO_2	%	ICP-ES	22.82	18.04	36.88	40.08	31.86	45.92	26.32	32.06	45.60	39.80	14.57	21.16	45.16
Al_2O_3	%	ICP-ES	17.71	5.26	5.89	5.73	4.21	6.78	9.20	12.69	4.28	8.33	4.14	5.44	9.87
$Fe_{(total)}$ [1]	%	ICP-ES	25.81	53.02	32.23	13.79	39.71	14.15	37.01	29.20	29.70	23.63	48.59	44.07	22.75
MnO	%	ICP-ES	1.06	0.10	0.05	0.32	0.05	0.61	0.14	0.04	0.07	0.03	0.08	0.07	0.02
MgO	%	ICP-ES	5.51	1.79	1.23	2.77	0.70	2.00	1.47	1.04	1.90	0.89	2.34	2.36	0.66
CaO	%	ICP-ES	7.16	0.32	1.16	16.78	0.38	14.35	1.20	1.11	1.02	1.18	2.10	1.04	2.21
Na_2O	%	ICP-ES	0.31	0.05	0.05	0.38	0.06	0.08	0.08	0.15	0.06	0.05	0.03	0.02	0.96
K_2O	%	ICP-ES	2.60	0.74	1.02	0.19	0.64	0.81	1.27	2.80	0.47	0.51	0.25	0.40	2.20
TiO_2	%	ICP-ES	1.17	0.27	0.26	0.42	0.18	0.29	0.32	0.44	0.27	0.32	0.34	0.27	0.41
P_2O_5	%	ICP-ES	0.17	0.33	0.31	1.15	0.30	0.92	0.06	0.84	0.73	0.80	1.54	0.70	0.94
LOI	%	ICP-ES	10.37	16.98	17.61	9.42	16.89	7.97	17.68	15.34	14.44	11.16	23.85	22.70	13.03
Total	%	ICP-ES	94.68	96.89	96.69	91.03	94.98	93.89	94.75	95.73	98.54	86.70	97.83	98.23	98.21
Ba	ppm	ICP-ES	517.00	323.00	1067.00	372.00	2074.00	2612.00	5859.00	11480.00	1544.00	50540.00	6037.00	17540.00	649.00
Sc	ppm	ICP-ES	33.00	6.00	8.00	12.00	5.00	8.00	12.00	16.00	13.00	9.00	7.00	7.00	12.00
Be	ppm	ICP-ES	2.00	1.00	0.50	0.50	0.50	0.50	2.00	2.00	0.50	2.00	0.50	1.00	0.50
V	ppm	ICP-ES	830.00	635.00	393.00	237.00	688.00	414.00	896.00	1825.00	267.00	962.00	342.00	543.00	1811.00
Li	ppm	ICP-MS	15.47	4.38	3.28	7.13	2.04	4.78	4.72	2.97	2.34	13.87	4.63	6.66	2.16
Sr	ppm	ICP-MS	158.75	19.54	16.41	157.08	11.45	118.99	15.38	24.88	17.27	83.47	50.47	64.93	58.45
Y	ppm	ICP-MS	12.83	12.16	8.26	26.36	7.54	28.87	8.31	16.25	13.69	15.52	20.77	13.75	17.77
Zr	ppm	ICP-MS	85.88	55.70	52.61	32.40	36.88	56.31	56.57	77.11	26.53	62.17	42.40	46.72	90.15
Nb	ppm	ICP-MS	0.64	2.23	1.85	0.95	1.49	1.09	1.71	3.74	0.82	3.86	2.79	1.89	8.81
Cs	ppm	ICP-MS	0.53	0.37	0.51	0.13	0.34	0.27	0.61	1.09	0.19	1.58	0.23	0.55	1.59
Ba_2	ppm	ICP-MS	531.97	327.29	895.70	354.06	1605.68	2708.12	3769.95	2399.92	1049.16	41616.33	3781.31	18100.32	718.07
La	ppm	ICP-MS	6.73	15.12	13.67	15.04	7.39	26.54	11.12	20.09	16.19	19.84	18.78	14.97	19.23
Ce	ppm	ICP-MS	7.64	19.66	21.23	21.05	11.11	29.89	16.88	31.16	28.27	28.95	25.21	18.38	33.24
Pr	ppm	ICP-MS	1.78	3.75	3.75	3.76	2.12	5.99	2.95	6.17	4.21	5.32	4.93	3.54	6.14
Nd	ppm	ICP-MS	7.15	14.65	14.91	17.02	8.86	23.41	11.35	25.65	18.97	22.64	21.92	14.40	26.49
Sm	ppm	ICP-MS	1.74	2.86	3.45	4.55	1.80	5.09	2.29	5.81	4.59	4.89	4.84	3.07	6.17
Eu	ppm	ICP-MS	0.42	0.64	0.90	1.64	0.48	1.55	0.74	1.55	1.15	1.54	1.51	0.95	1.58
Gd	ppm	ICP-MS	2.05	2.75	2.83	5.70	1.68	5.41	1.92	5.47	4.76	4.18	5.19	2.92	5.74
Tb	ppm	ICP-MS	0.33	0.40	0.38	0.78	0.25	0.76	0.30	0.69	0.61	0.54	0.71	0.41	0.74
Dy	ppm	ICP-MS	2.13	2.34	1.88	4.56	1.47	4.62	1.85	3.58	3.16	2.98	3.79	2.21	3.89
Ho	ppm	ICP-MS	0.48	0.48	0.33	0.86	0.28	0.92	0.34	0.65	0.53	0.54	0.70	0.43	0.70
Er	ppm	ICP-MS	1.63	1.41	0.98	2.32	0.79	2.64	1.10	1.80	1.31	1.50	1.70	1.25	1.85
Tm	ppm	ICP-MS	0.29	0.25	0.16	0.33	0.15	0.40	0.22	0.30	0.17	0.24	0.27	0.22	0.30
Yb	ppm	ICP-MS	2.32	1.50	1.05	1.75	0.91	2.47	1.48	1.96	1.00	1.49	1.58	1.15	2.03
Lu	ppm	ICP-MS	0.42	0.25	0.20	0.27	0.15	0.42	0.25	0.33	0.15	0.26	0.23	0.20	0.33
Hf	ppm	ICP-MS	8.11	2.64	3.17	1.74	1.47	4.67	2.71	3.47	0.78	1.71	1.07	1.22	2.22
Ta	ppm	ICP-MS	0.06	0.19	0.14	0.06	0.13	0.09	0.16	0.31	0.08	0.21	0.12	0.10	0.54
Tl	ppm	ICP-MS	1.68	2.19	0.89	0.31	1.93	0.72	3.72	7.50	1.44	1.88	1.36	2.51	3.61
Pb	ppm	ICP-MS	14.96	806.81	761.86	163.42	600.82	21.80	1184.86	761.00	433.14	211.40	754.27	896.90	581.51
Bi	ppm	ICP-MS	0.10	0.91	0.86	0.22	0.32	0.18	0.70	0.62	0.45	0.23	0.54	0.43	0.62
Th	ppm	ICP-MS	2.51	5.39	5.20	1.44	3.50	3.65	5.00	6.14	1.66	4.45	2.16	2.60	6.58
U	ppm	ICP-MS	1.69	30.61	25.12	5.18	16.34	4.88	61.36	55.88	5.26	39.31	13.98	12.42	66.85
Cr	ppm	ICP-MS	40.57	34.91	52.99	27.04	35.99	40.61	38.25	112.37	20.03	94.42	56.99	38.66	129.01
Fe	ppm	ICP-MS	137854.65	281694.38	214167.90	94744.28	242710.05	101344.44	196517.28	152849.46	192603.54	150078.55	311549.80	276654.66	146492.75
Mn	ppm	ICP-MS	5504.84	620.96	389.02	2410.25	363.82	4621.34	837.17	225.87	524.38	210.48	529.20	496.99	131.50
Co	ppm	ICP-MS	8.39	31.54	19.58	28.98	110.24	14.04	75.72	38.29	53.15	16.65	73.90	14.49	18.53
Ni	ppm	ICP-MS	105.09	457.01	182.26	82.76	251.92	76.28	339.26	479.49	142.97	276.51	165.71	191.41	570.12
Cu	ppm	ICP-MS	145.19	522.21	502.75	120.92	216.82	101.81	508.56	392.37	219.71	56188.59	605.33	233.46	263.95
Zn	ppm	ICP-MS	625.34	907.06	540.16	295.46	234.19	203.07	108.36	66.28	94.17	3659.78	214.03	263.79	919.90
As	ppm	ICP-MS	14.48	203.00	216.07	41.63	3305.98	139.88	2069.99	1302.14	376.72	394.79	9545.16	1201.81	682.75
Se	ppm	ICP-MS	6.05	21.84	7.62	2.46	9.91	5.86	17.93	24.09	4.62	6.98	9.60	12.55	35.35
Br	ppm	ICP-MS	91.59	87.20	87.25	95.81	88.72	99.32	103.90	92.51	114.06	140.06	123.14	143.13	141.08
Mo	ppm	ICP-MS	6.80	125.95	108.39	20.45	113.42	26.16	263.83	213.91	34.35	136.51	33.74	86.16	151.28
Ag	ppm	ICP-MS	0.78	12.05	19.06	1.16	29.09	1.22	30.80	31.65	4.28	116.09	31.04	36.54	11.87
Cd	ppm	ICP-MS	2.74	6.65	8.19	1.09	4.05	1.00	0.62	0.59	1.26	19.18	1.11	0.26	11.08
Sn	ppm	ICP-MS	3.19	3.08	2.82	2.89	3.16	3.00	3.44	3.60	1.43	3.62	1.54	1.76	2.74
Sb	ppm	ICP-MS	1.87	140.36	23.23	2.92	51.32	1.12	49.20	81.32	71.78	26.74	111.10	120.42	61.73
Te	ppm	ICP-MS	0.10	0.73	0.96	0.55	0.82	0.10	1.70	0.89	1.71	1.87	2.44	3.71	1.13
I	ppm	ICP-MS	1.59	1.59	1.59	1.59	1.59	1.59	1.22	1.59	8.98	5.35	8.98	1.36	8.98
W	ppm	ICP-MS	4.41	6.19	1.47	2.13	2.52	1.81	2.60	6.34	2.45	14.08	6.86	5.02	4.54
CIA			63.75	82.57	72.54	24.83	79.58	30.79	78.30	75.76	73.41	82.72	63.50	78.84	64.76
Ce/Ce*			0.51	0.60	0.68	0.65	0.65	0.55	0.68	0.65	0.79	0.65	0.60	0.58	0.71
Eu/Eu*			1.05	1.08	1.36	1.52	1.29	1.39	1.67	1.29	1.16	1.60	1.42	1.50	1.25
Y/Ho			26.51	25.59	24.85	30.79	27.28	31.32	24.42	25.16	25.80	28.66	29.77	31.79	25.42

[1] Fe(total) = (Fe_2O_3+FeO)

EMS: Exhalite[2] associated with massive sulfides (within 5m)

FEM: Exhalite associated with felsic and mafic volcanic rocks, no massive sulfides

FEF: Exhalite within felsic volcanic rocks, no massive sulfides

IFE: Interflow exhalite

T: Tuff

[2] The term exhalite represents the Lemarchant metalliferous mudstones and was chosen to simplify the abbreviations.

Fig. 2.1 A-C

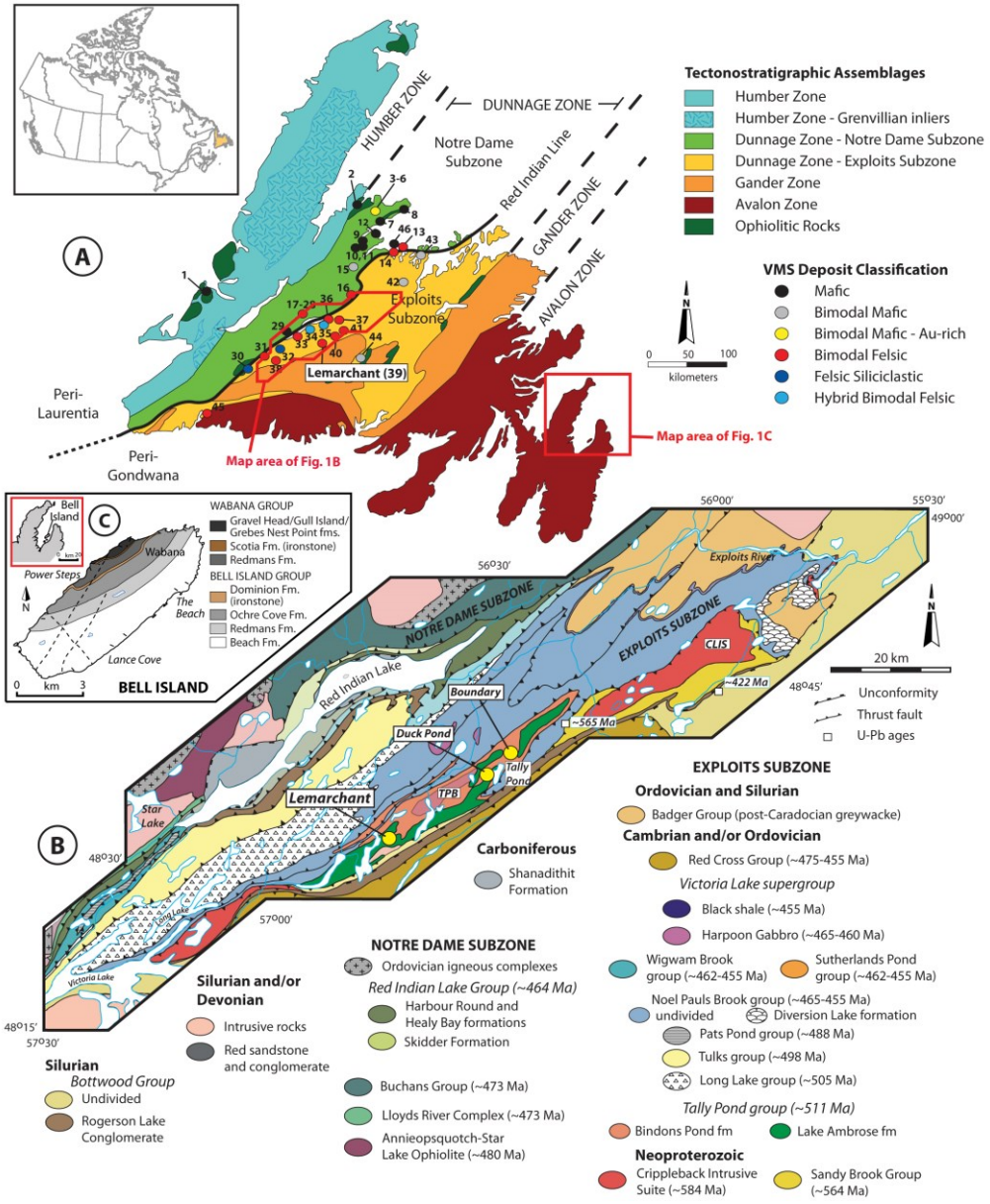

Figure 2.1 *A: Tectonostratigraphic assemblages with the main zones of the Newfoundland Appalachians (Avalon, Gander, Dunnage, and Humber zones) and VMS occurrences within the Notre Dame and Exploits subzones (modified after Swinden 1991; Piercey, 2007). Notre Dame Subzone VMS: 1 – York Harbour; 2 – 8 - Baie Verte belt deposits; 9 – 12, 46 – Springdale belt deposits; 13 – 29 Buchans-Roberts Arm deposits.*
Exploits Subzone VMS: 30 – 37 - Tulks belt deposits; Tally Pond belt deposits: 39 – Lemarchant; 40 – Duck Pond; 41 – Boundary; 42 – 45 – Point Leamington belt deposits. B)
Geological setting of the Victoria Lake supergroup, including the Tally Pond and Tulks volcanic belts. The Tally Pond group hosts the Lemarchant deposit and the Duck Pond and Boundary mines. Diagram after Piercey et al. (2014). TPB = Tally Pond belt, CLIS = Crippleback intrusive suite. C) Overview map of the location of Bell Island. Sampled outcrops from Lance Cove, The Beach, and Powersteps.

Fig. 2.2 A

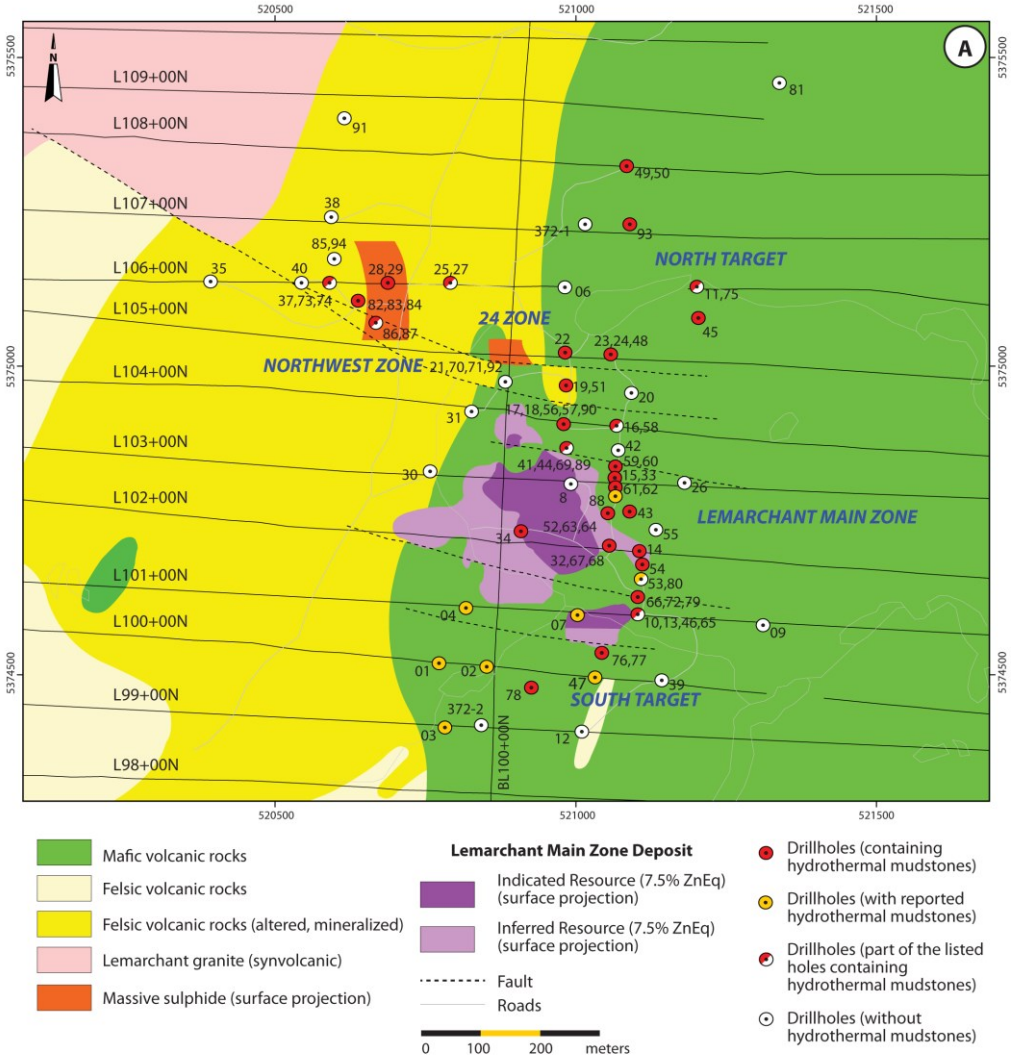

Figure 2.2 *A) Resource map with indicated (purple) and inferred (lilac) resources suggesting that the Lemarchant Main Zone is open along strike. Massive sulphides are projected to the surface. The Northwest and 24 zones are displayed in red colours. Rose coloured in the upper left corner is the Lemarchant microgranite. Drill holes with metalliferous mudstones are displayed as red (if logged) and orange circles (if not logged). White circles display drill holes that do not contain mudstones. Half-coloured circles indicate that some of the listed holes have mudstone (modified from the resource map of Canadian Zinc Corporation). B) Cross-section of the moderately east dipping Lemarchant Main Zone along section 103N. C) Cross-section of the moderately west dipping Northwest Zone along section 106N.*

Fig. 2.2 B-C

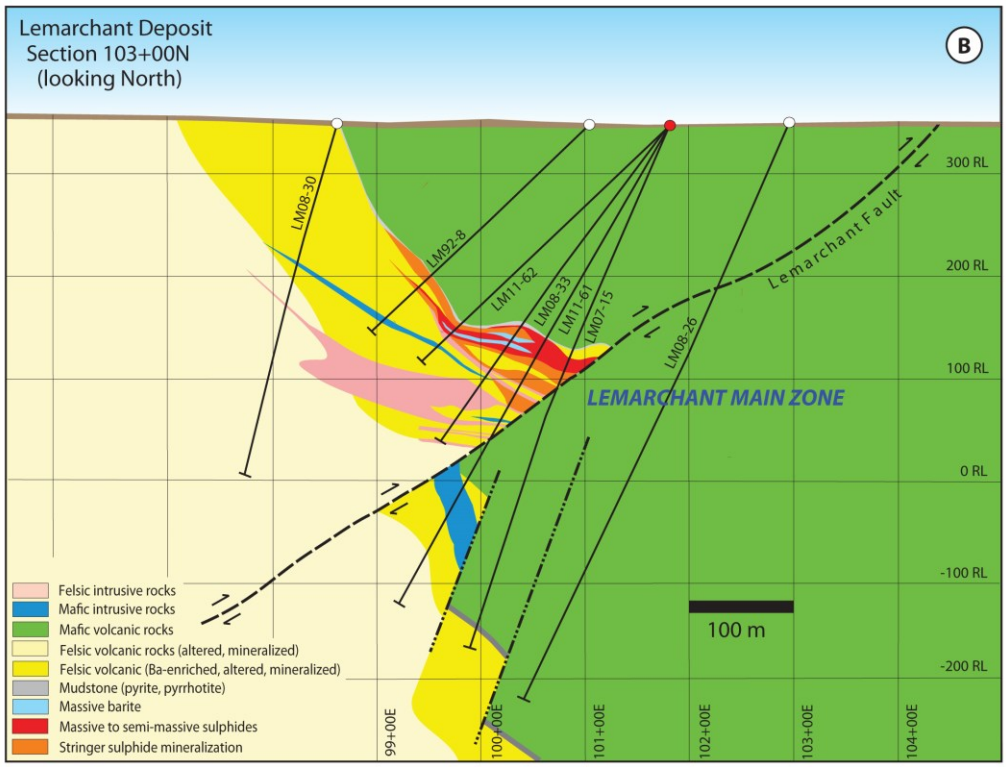
Lemarchant Deposit
Section 103+00N
(looking North)
B
LM08-30
LM92-8
LM11-62
LM08-33
LM11-61
LM07-15
LM08-26
Lemarchant Fault
LEMARCHANT MAIN ZONE
300 RL
200 RL
100 RL
0 RL
-100 RL
-200 RL
100 m
99+00E
100+00E
101+00E
102+00E
103+00E
104+00E
Felsic intrusive rocks
Mafic intrusive rocks
Mafic volcanic rocks
Felsic volcanic rocks (altered, mineralized)
Felsic volcanic (Ba-enriched, altered, mineralized)
Mudstone (pyrite, pyrrhotite)
Massive barite
Massive to semi-massive sulphides
Stringer sulphide mineralization

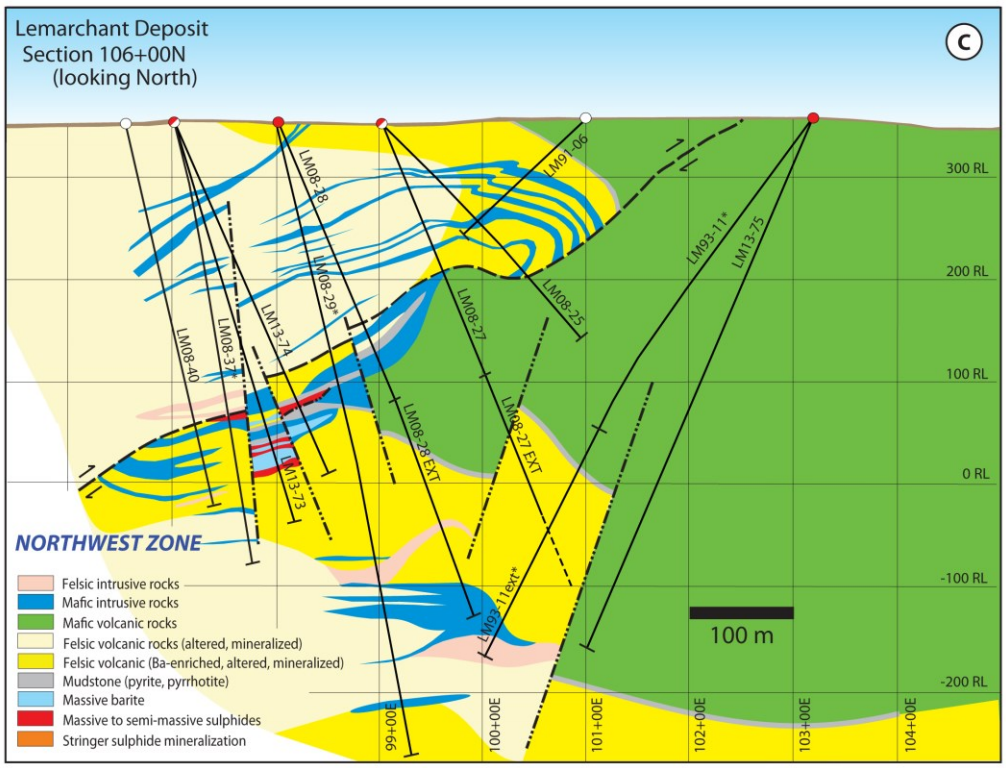
Lemarchant Deposit
Section 106+00N
(looking North)
C
LM08-38
LM91-06
LM08-29*
LM93-11*
LM13-75
LM13-74
LM08-37*
LM08-40
LM08-27
LM08-25
LM08-28 EXT
LM08-27 EXT
LM13-73
LM93-11ext*
NORTHWEST ZONE
300 RL
200 RL
100 RL
0 RL
-100 RL
-200 RL
100 m
99+00E
100+00E
101+00E
102+00E
103+00E
104+00E
Felsic intrusive rocks
Mafic intrusive rocks
Mafic volcanic rocks
Felsic volcanic rocks (altered, mineralized)
Felsic volcanic (Ba-enriched, altered, mineralized)
Mudstone (pyrite, pyrrhotite)
Massive barite
Massive to semi-massive sulphides
Stringer sulphide mineralization

Fig. 2.3

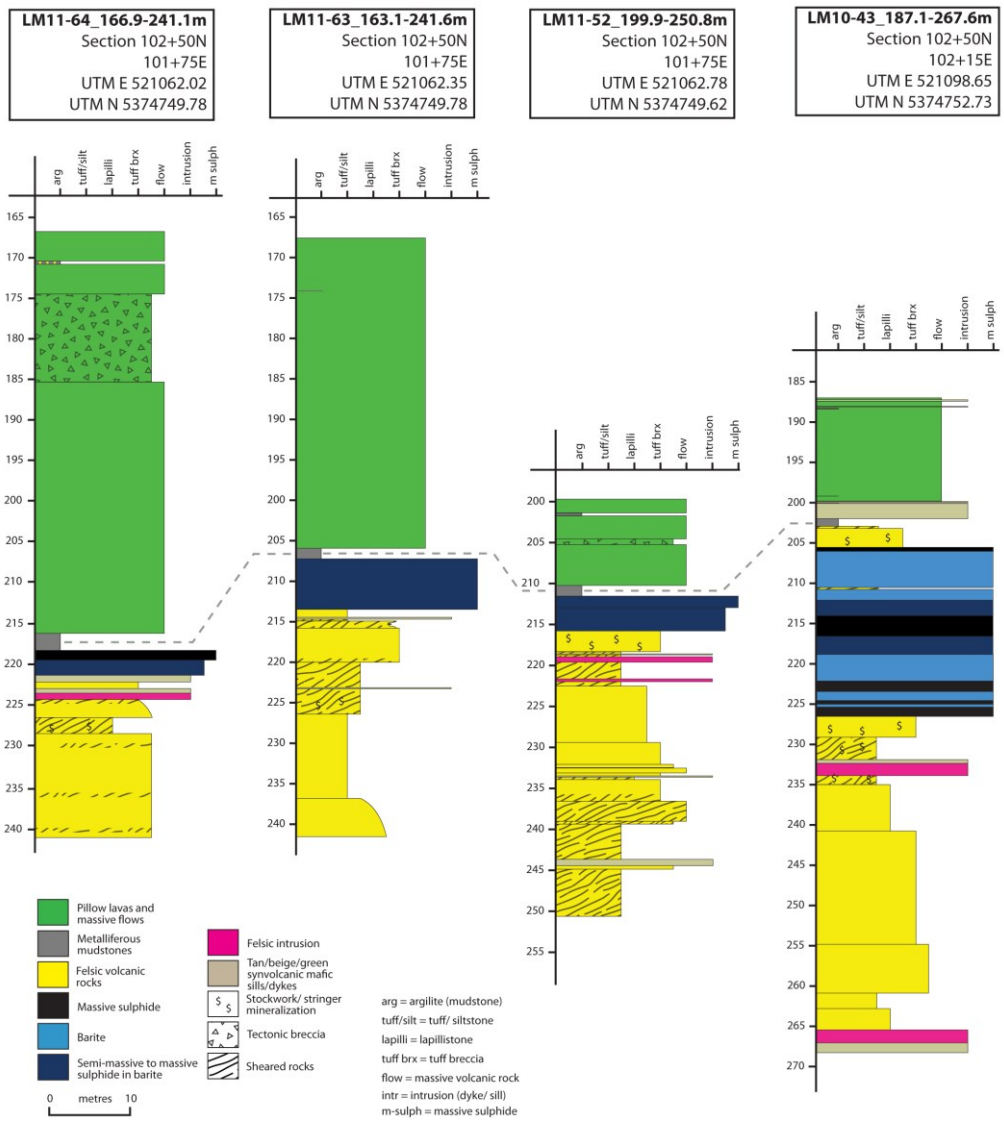

Figure 2.3 *Lithostratigraphic columns at section 102+50N, from 101+75E to 102+15E, intercepting the Lemarchant Main Zone. The lithofacies, including the mudstones, are shown in true thickness. The selected drill holes are shown in Figure 2.2A. Metalliferous mudstones occur in close association with mineralization, at or close to the contact between the felsic and mafic hanging wall volcanic rocks, and also as interflow mudstones.*

Fig. 2.4

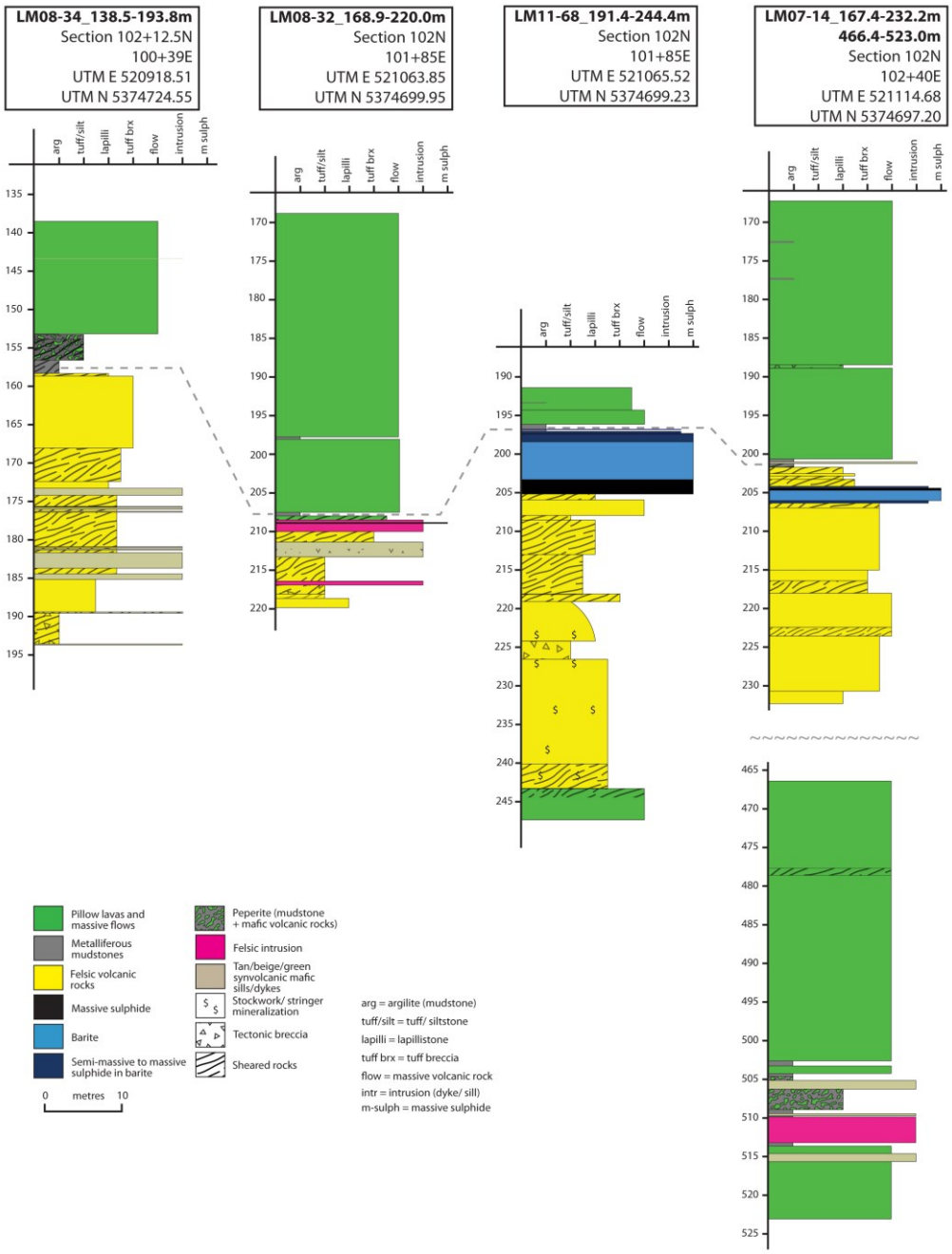

Figure 2.4 *Lithostratigraphic columns at section 102N to 102+12.5N, from 100+39E to 102E, intercepting the Lemarchant Main Zone in holes LM11-68 and LM07-14. Shearing associated with felsic dykes partially cut-off the main sulphide lens, LM08-32. Drill hole LM08-34 is located ~150 m west of the main sulphide lens and does not intercept mineralization. Metalliferous mudstones occur at the contact between felsic and mafic volcanic rocks and can be correlated to the other drill holes (LM11-64, LM11-63, LM11-52, LM10-43, LM08-32, LM11-68, and LM07-14) shown in Figures 2.3 and 2.4, since the main sulphide lens dips to the east. Hence, mudstones are expected to occur in shallower levels further west. In drill hole LM07-14 interflow mudstones were also intercepted within mafic volcanic rocks of the lower mafic block. The various lithofacies, including the mudstones are shown in true thickness. The locations of the drill holes are shown in Figure 2.2A.*

Fig. 2.5 A-D

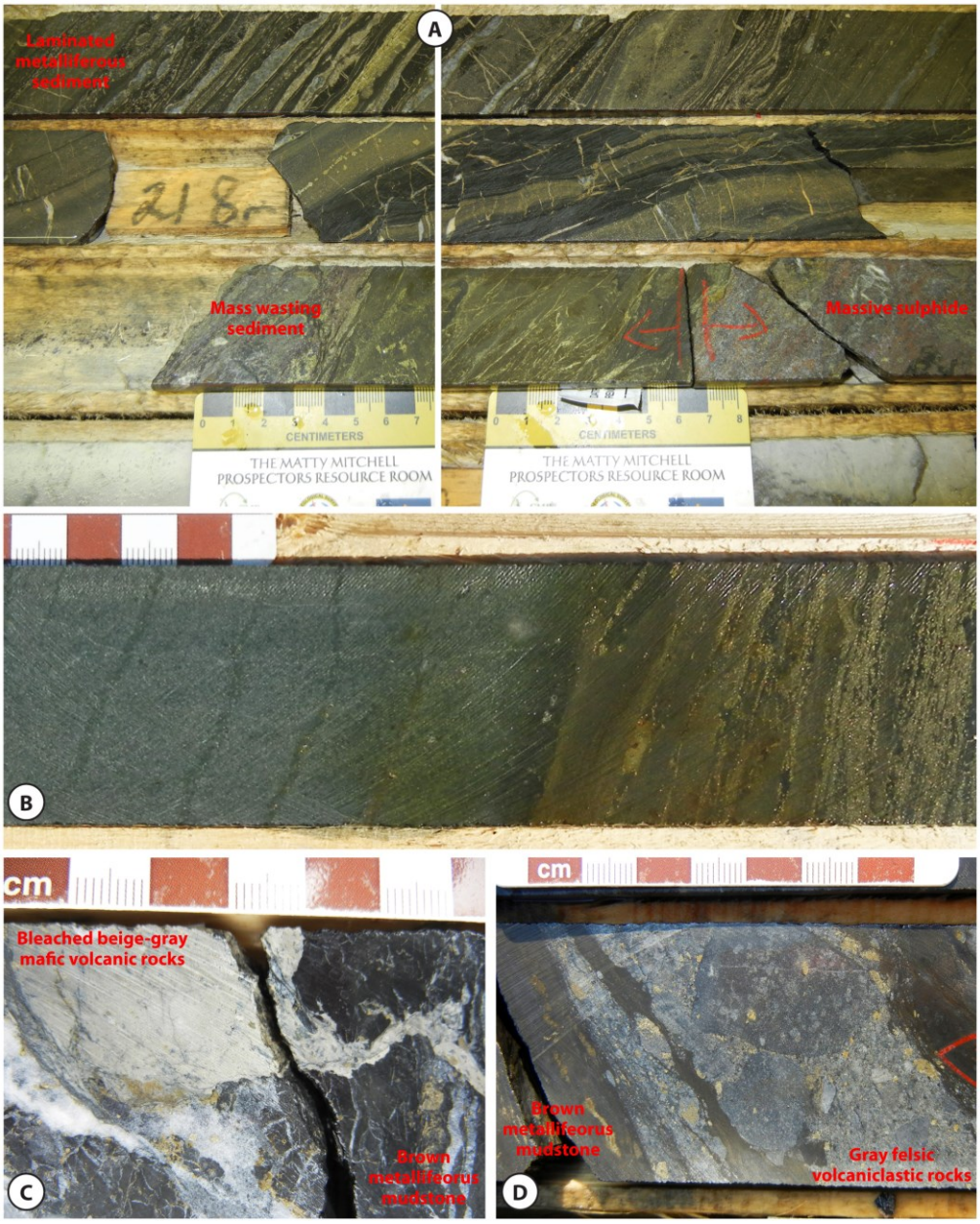
A
Laminated metalliferous sediment
Mass wasting sediment
Massive sulphide
CENTIMETERS
THE MATTY MITCHELL PROSPECTORS RESOURCE ROOM
B
cm
Bleached beige-gray mafic volcanic rocks
Brown metalliferous mudstone
C
cm
Brown metalliferous mudstone
Gray felsic volcaniclastic rocks
D

Figure 2.5 *A) Dark-brown to black graphite- and sulphide-rich metalliferous mudstone immediately above massive sulphides (lower right corner) of the Lemarchant Main Zone. The mudstones show planar lamination, roughly parallel to massive sulphides mineralization. Mass wasting and reworking of mudstones occurs in a section above the massive sulphides with incorporated felsic volcaniclastic rocks (lower left corner), followed by a section with bedding subparallel to the core due to reworking and folding (middle row). Sulphide-rich layers alternate with graphite-rich layers. Lamination is interrupted by syn-sedimentary faulting; drill hole LM08-33. Section 103N. Top to the left B) Laminated, sulphide-rich mudstones are conformably overlain by flow banded hanging wall basalts; drill hole LM08-32, section 102N; top to the left. C) Synvolcanic peperitic texture: hydrothermal mud intermingled with beige-grey-bleached mafic dykes; LM11-49, section 108N. D) Mass-wasting sediment: grey felsic lapilli-tuff reworked into dark brown metalliferous sediment; drill hole LM11-56, section 104N.*

Figure 2.6 *A) Back-scattered electron image of layered framboidal-rich mudstone. Non-sulphidic matrix consists mostly of quartz, chlorite ± carbonaceous material. LM08-24ext, section 105N, CNF20983. Top is towards the upper left. B) Possible syn-sedimentary slump structure in framboidal-rich mudstone. Void space within slump structure filled with later-stage polymetallic sulphides and ferroan dolomite ± Mg ± Mn. LM11-59, section 103+25N, CNF30959. C) Reflected light microscope image from a thin-section of layers of laminated framboidal-rich mudstone that is cross-cut by a vein filled with later-stage polymetallic sulphides (euhedral pyrite, interstitial chalcopyrite and sphalerite), and minor electrum. LM13-76, section 100+50N, CNF25062b. D) Reflected light image from a polished epoxy puck with electrum (light yellow) in sample shown in 2.7C, associated with chalcopyrite (cpy, yellow) and galena (gal, grey), occurring interstitially between euhedral pyrite (py, dominant mineral) with ankerite (ank), Fe-Mg-chlorite (Fe-Mg-chlor), and quartz (qtz) gangue (black). LM13-76, section 100+50N, CNF25062b. E) SEM-BSE image of interstitial Hg-bearing electrum and galena (gal) between euhedral arsenopyrite (aspy) in a pyrrhotite (po) layer, with minor pyrite (py). LM13-77, section 100+50N, CNF25064. F) Reflected light image of chalcopyrite (cpy), galena (gal), and pyrargyrite with quartz (qtz) gangue. LM11-69, section 103+50N, CNF30994.*

Figure 2.7 *A) SEM-BSE image of euhedral celsian (Ba-feldspar) overgrowing pyrite framboids. LM10-43, section 102N, CNF20978. B) SEM-BSE image of euhedral overgrowths of celsian (cels, Ba-feldspar) on pyrite (py), and barite (bar), apatite (apat), ferroan dolomite (Fe-dol), and quartz (qtz) as gangue. LM11-59, section 103+25N, CNF30959. C) SEM-BSE image of a vein filled with bladed barite (bar) and calcite (calc), and euhedral celsian (cels) rhombs in the pyrite-framboid-rich mudstone. LM13-79, section 101+25N, CNF25071. D) SEM-BSE image of massive barite (bar) with kaolinite (kaol) in a mudstone with chalcopyrite (cpy), pyrite (py), and galena (gal). LM07-17, section 104N, CNF30953. E) SEM-BSE image from a thin-section showing a barite vein cross-cutting chalcopyrite-pyrite-sphalerite-celsian-rich mudstone. LM07-13, section 101N, CNF30955. F) Reflected light image with chalcopyrite (cpy), euhedral pyrite (py), and a framboidal pyrite layer (possibly microbial mat) with Fe-Mg-chlorite (Fe-Mg-chlor) and ferroan dolomite (Fe-dol) gangue. LM07-16, section 104N, CNF30951.*
) in a pyrrhotite (po) layer, with minor pyrite (py). LM13-77, section 100+50N, CNF25064. F) Reflected light image of chalcopyrite (cpy), galena (gal), and pyrargyrite with quartz (qtz) gangue. LM11-69, section 103+50N, CNF30994.

Fig. 2.6 A-F

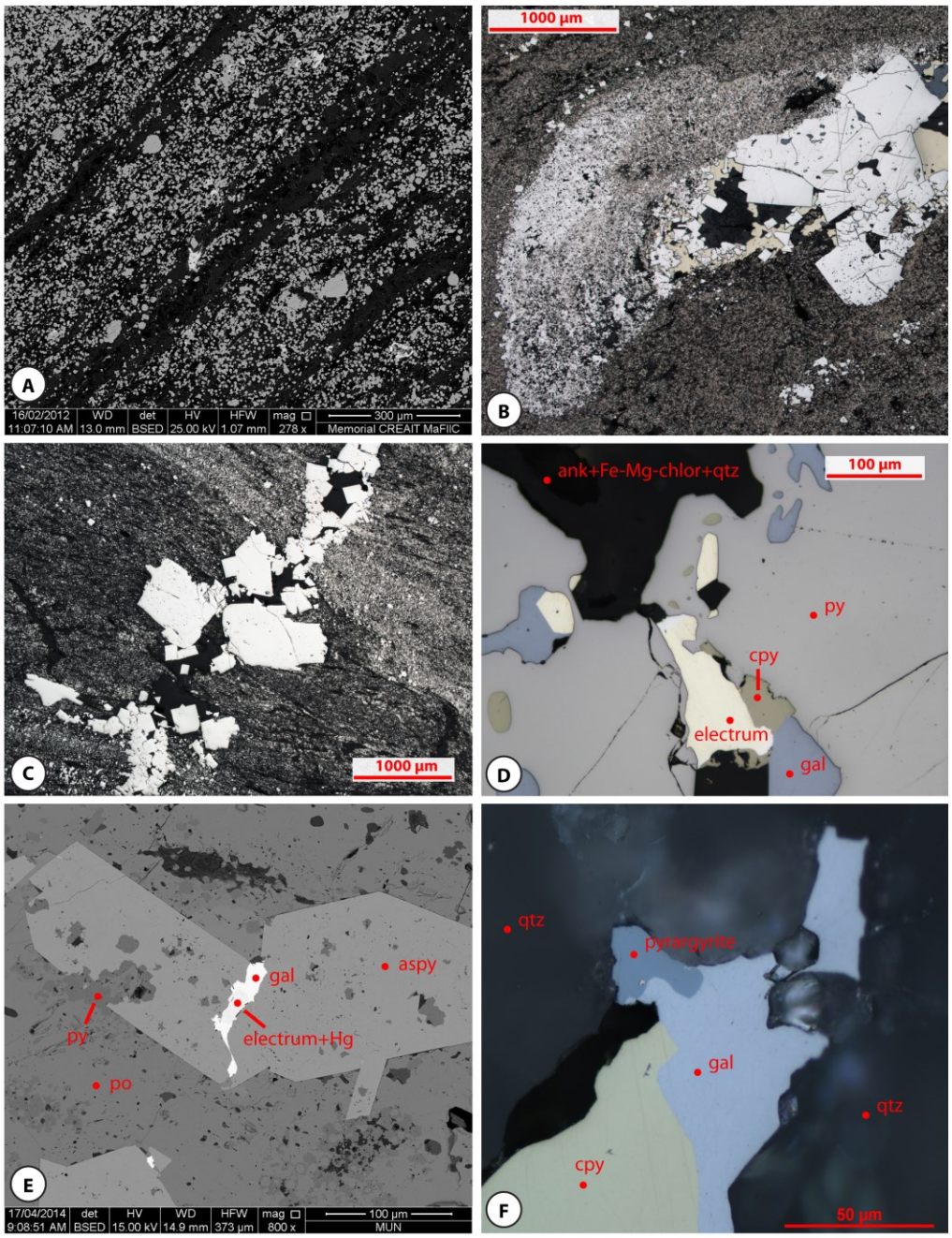
A
16/02/2012 | WD | det | HV | HFW | mag | 300 µm
11:07:10 AM | 13.0 mm | BSED | 25.00 kV | 1.07 mm | 278 x | Memorial CREAIT MaFIIC
B
1000 µm
C
1000 µm
D
ank+Fe-Mg-chlor+qtz
100 µm
py
cpy
electrum
gal
E
gal
aspy
py
electrum+Hg
po
17/04/2014 | det | HV | WD | HFW | mag | 100 µm
9:08:51 AM | BSED | 15.00 kV | 14.9 mm | 373 µm | 800 x | MUN
F
qtz
pyrargyrite
gal
qtz
cpy
50 µm

Fig. 2.7 A-F

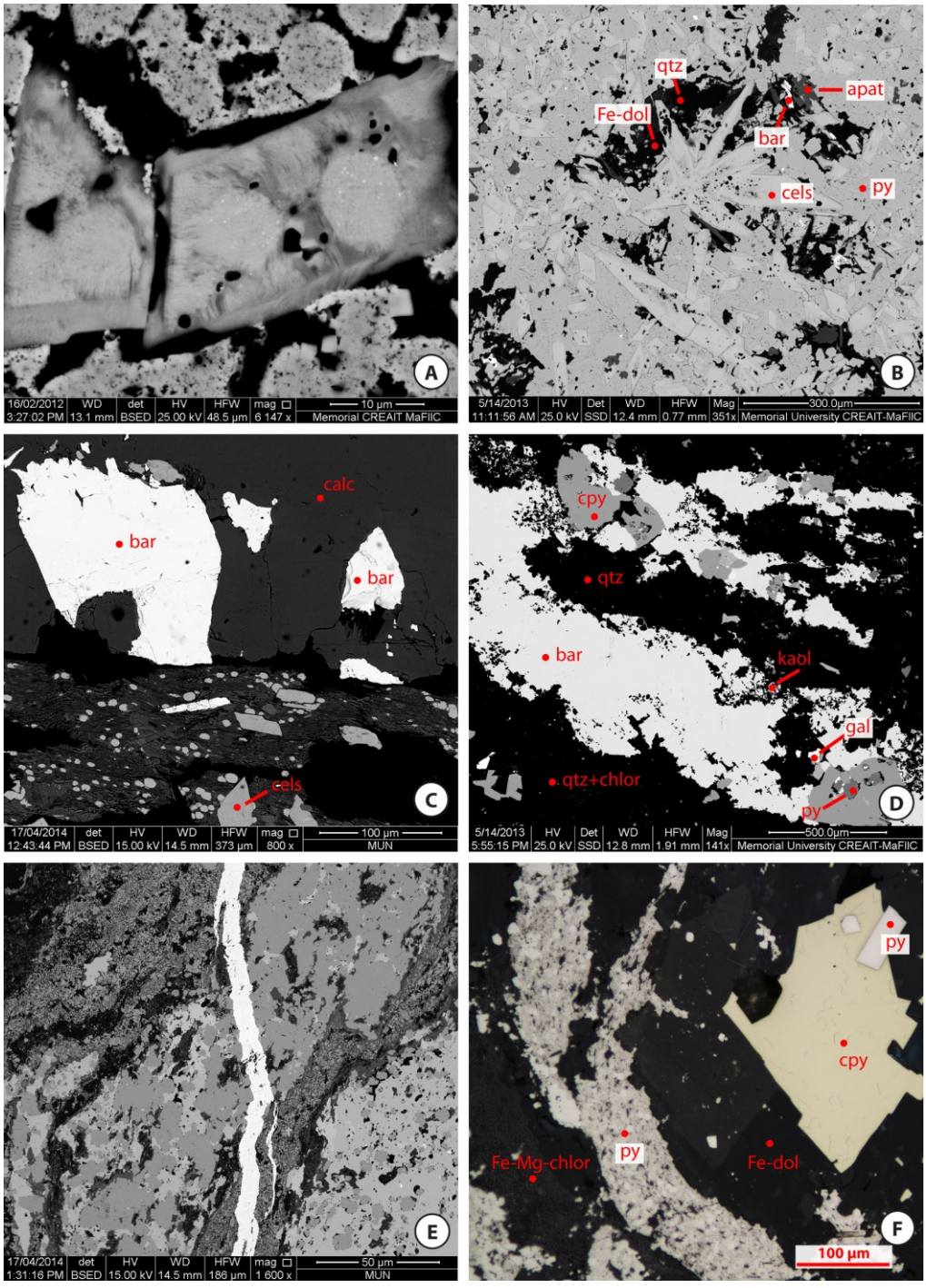
A
16/02/2012 | WD | det | HV | HFW | mag | 10 µm
3:27:02 PM | 13.1 mm | BSED | 25.00 kV | 48.5 µm | 6 147 x | Memorial CREAIT MaFIIC
B
qtz
apat
Fe-dol
bar
cels
py
5/14/2013 | HV | Det | WD | HFW | Mag | 300.0µm
11:11:56 AM | 25.0 kV | SSD | 12.4 mm | 0.77 mm | 351x | Memorial University CREAIT-MaFIIC
C
calc
bar
bar
cels
17/04/2014 | det | HV | WD | HFW | mag | 100 µm
12:43:44 PM | BSED | 15.00 kV | 14.5 mm | 373 µm | 800 x | MUN
D
cpy
qtz
bar
kaol
gal
qtz+chlor
py
5/14/2013 | HV | Det | WD | HFW | Mag | 500.0µm
5:55:15 PM | 25.0 kV | SSD | 12.8 mm | 1.91 mm | 141x | Memorial University CREAIT-MaFIIC
E
17/04/2014 | det | HV | WD | HFW | mag | 50 µm
1:31:16 PM | BSED | 15.00 kV | 14.5 mm | 186 µm | 1 600 x | MUN
F
py
cpy
Fe-Mg-chlor
py
Fe-dol
100 µm

Fig. 2.8 A-C

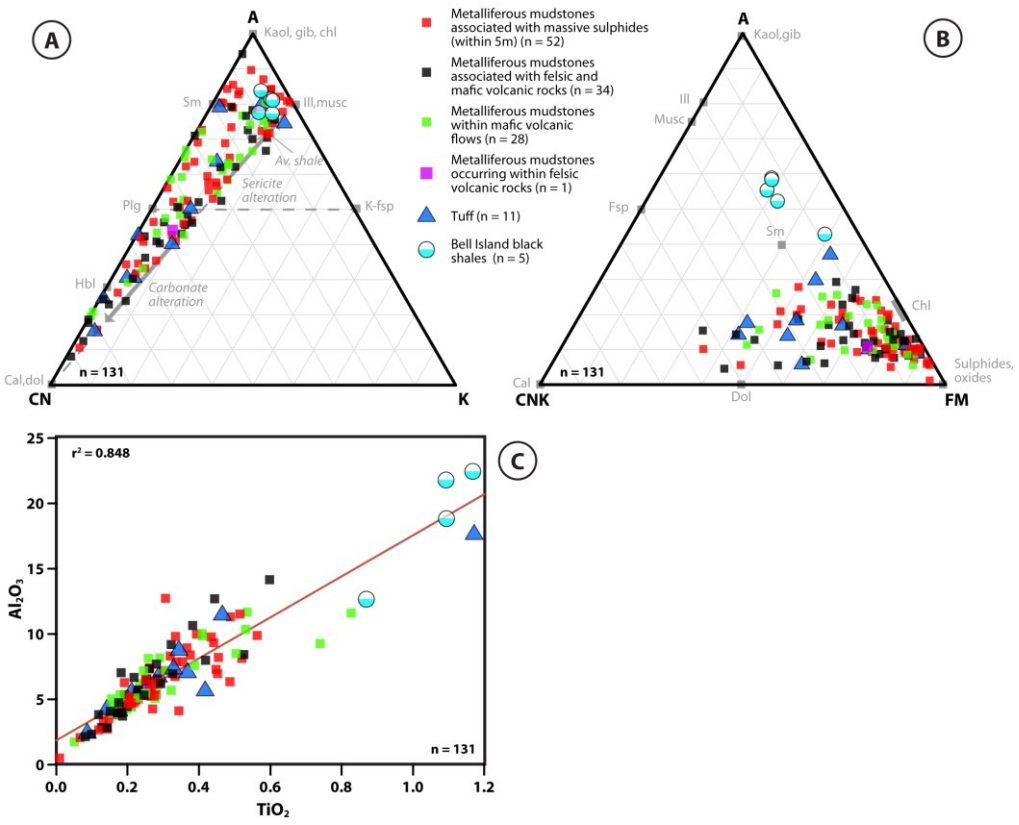

Figure 2.8 *A) A) Ternary A-CN-K diagram A = Al_2O_3, CN = $CaO+Na_2O$, and K = K_2O,B) Ternary A-CNK-FM diagram. A = Al_2O_3, CNK = $CaO+Na_2O+K_2O$, and FM = $(FeO+Fe_2O_3)+MgO$, C) Al_2O_3 versus TiO_2. Diagrams A) and B) are after Nesbitt (2003), and C) after Barrett and MacLean (1994).*

Fig. 2.9 A-C

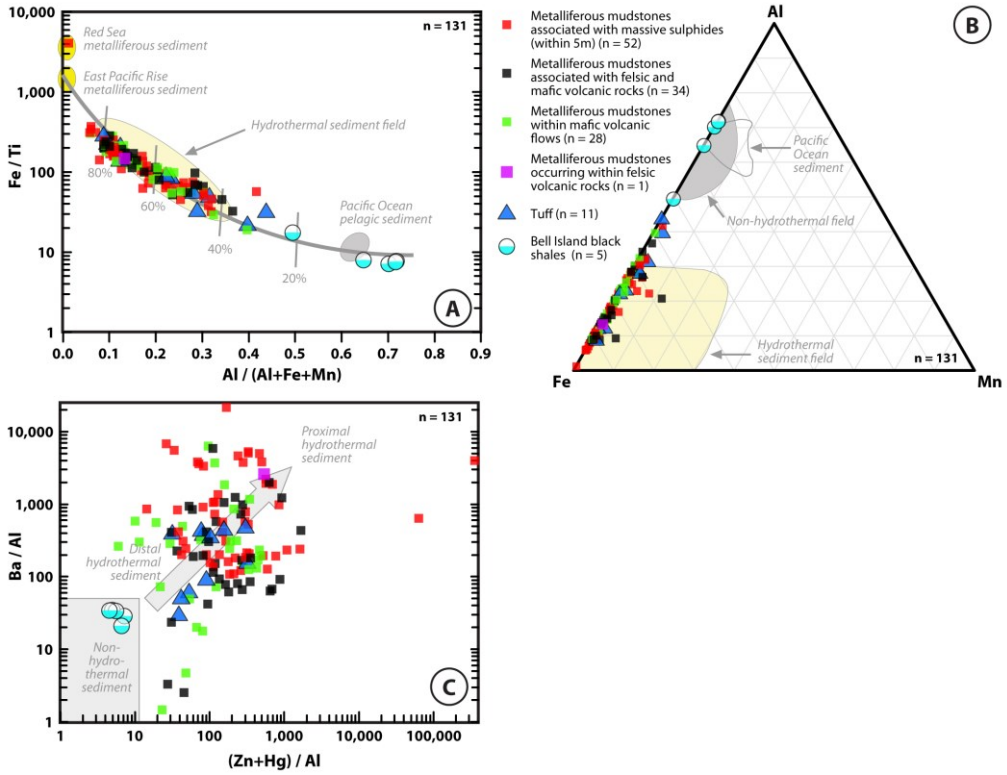

Figure 2.9 *Fe-Ti/Al-Fe-Mn (A) and Fe-Al-Mn (B) discrimination diagrams indicating a hydrothermal origin for the Lemarchant mudstones. According to their higher Al-contents, tuff samples plot towards the right hand side of the diagram, partially outside of the hydrothermal field. Diagrams after Boström et al. (1972). C) Ba/Al versus (Zn+Hg)/Al, where Ba, Zn, and Hg represent the hydrothermally derived components of the mineralization, and Al is a detrital constituent.*

Fig. 2.10 A-F

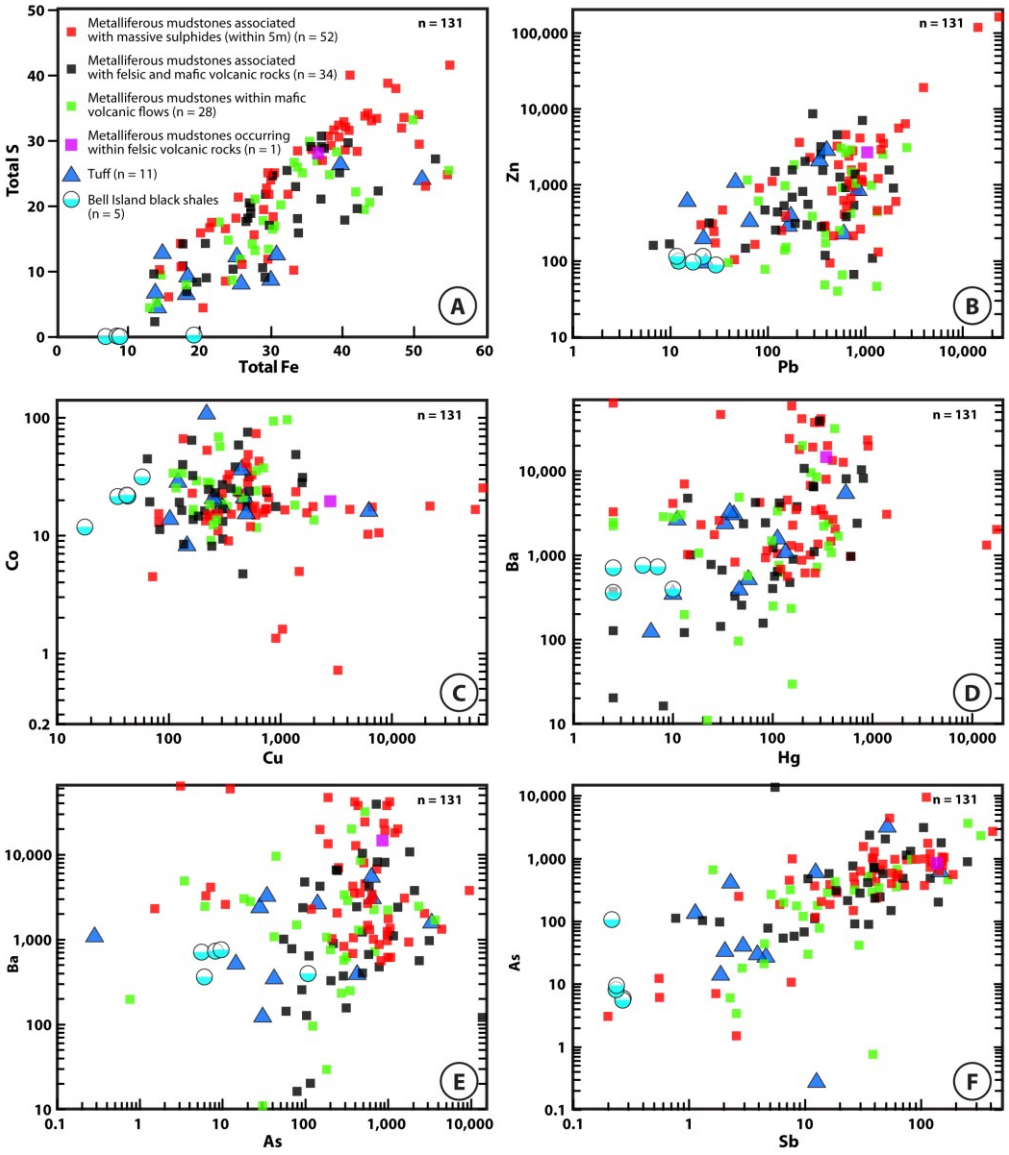

Figure 2.10 *Selected base metal, transition element, and hydrothermal element plots: A) Total S versus Fe_2O_3 (T), B) Zn versus Pb, C) Co versus Cu, and D) Ba versus Hg (after Piercey et al., 2012), E) Ba versus As, and F) Ba versus Sb.*

Fig. 2.11 A-F

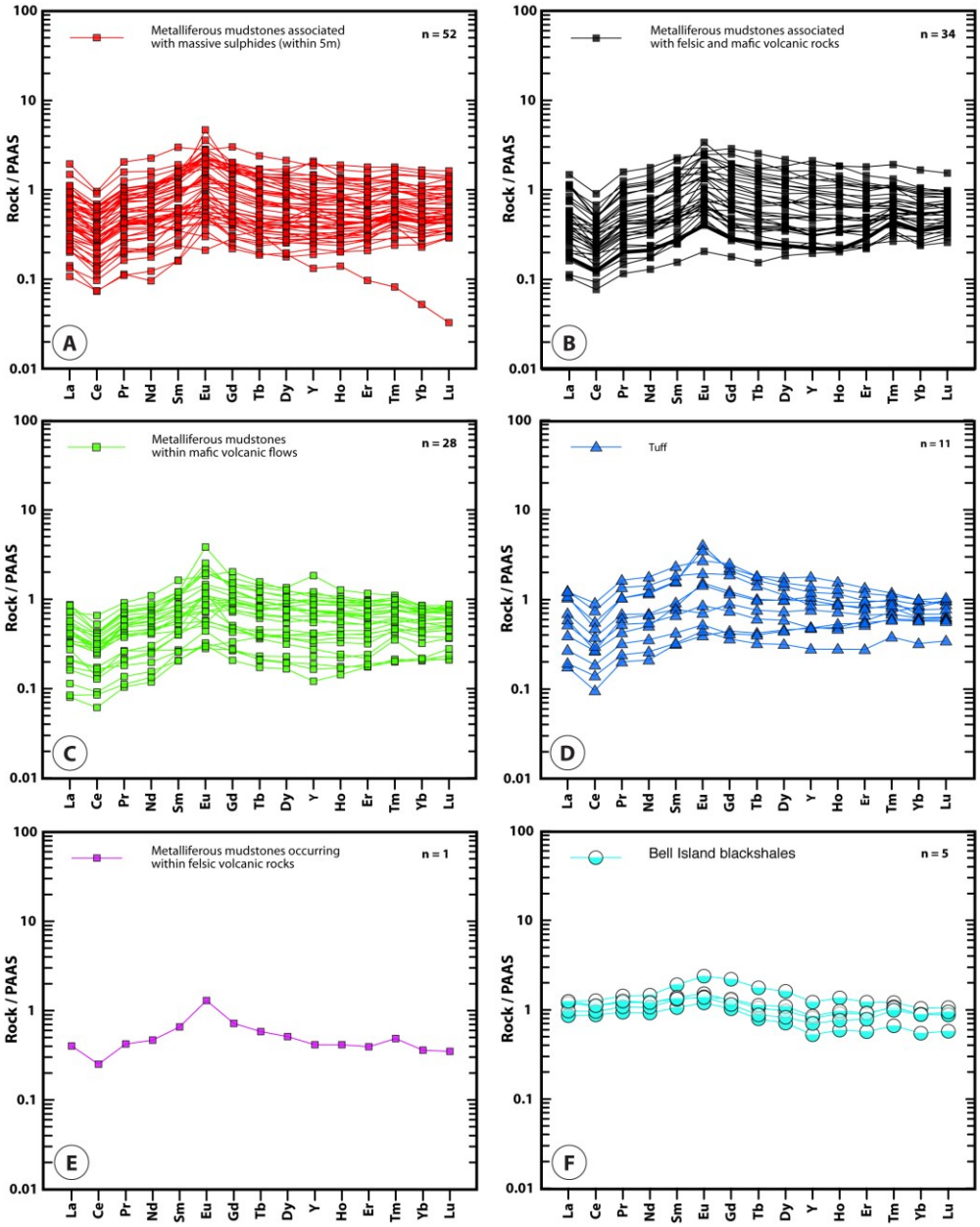

Figure 2.11 *REE plus Y geospider plots of Lemarchant mudstones and tuff of various stratigraphic levels: A) Mudstones that are closely associated with massive sulphides (within five meters), B) Mudstones at the contact between felsic and mafic volcanic rocks, C) Interflow mudstones within the hanging wall mafic volcanic rocks, D) Tuff samples that are intercalated with mudstones from various stratigraphic levels. E) Mudstone occurring within felsic volcanic rocks, and F) Bell Island samples. All samples are normalized to the post-Archean Australian shale of McLennan (1989).*

Fig. 2.12 A-B

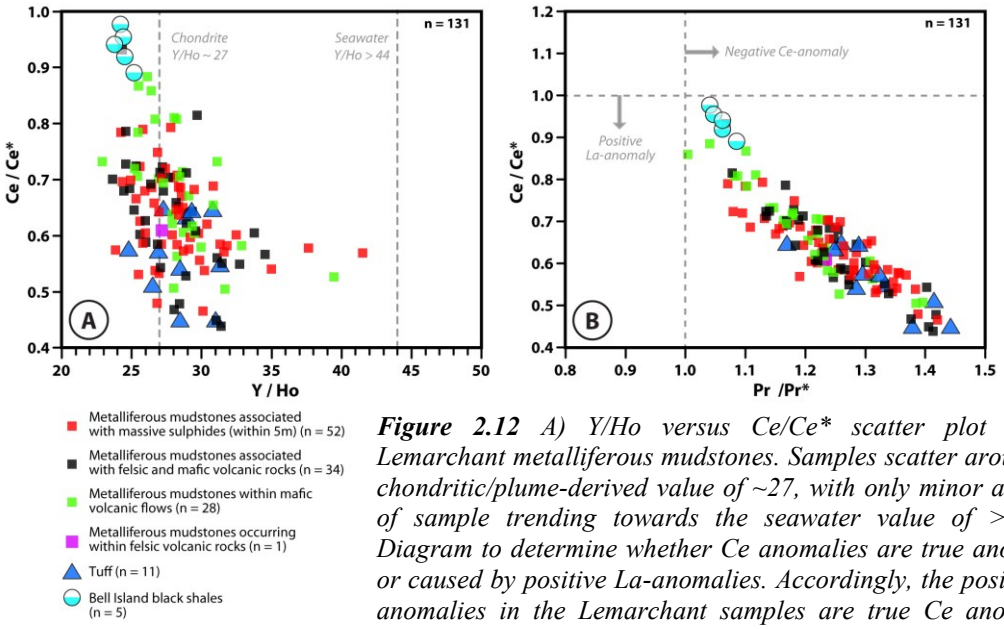

Figure 2.12 *A) Y/Ho versus Ce/Ce* scatter plot of the Lemarchant metalliferous mudstones. Samples scatter around the chondritic/plume-derived value of ~27, with only minor amounts of sample trending towards the seawater value of >44. B) Diagram to determine whether Ce anomalies are true anomalies or caused by positive La-anomalies. Accordingly, the positive Ce anomalies in the Lemarchant samples are true Ce anomalies. Ce/Ce* and Pr/Pr* values are calculated based on McLennan (1989) and the equation* $Pr/Pr^* = (Pr_{sample}/8.83)/SQRT((Ce_{sample}/79.6)*(Nd_{sample}/3.39))$. *Diagrams are after Bau (1996), Webb and Kamber (2000), and Slack et al. (2007).*

Fig. 2.13 A-B

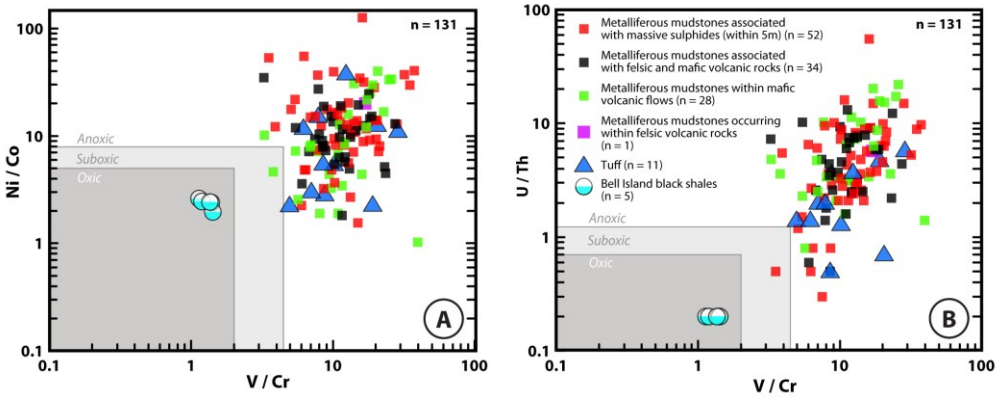

Figure 2.13 *Diagrams of redox-sensitive trace elements: A) Ni/Co versus V/Cr, B) U-Th versus V/Cr. Diagrams after Algeo and Tribovillard (2009).*

Fig. 2.14 A-B

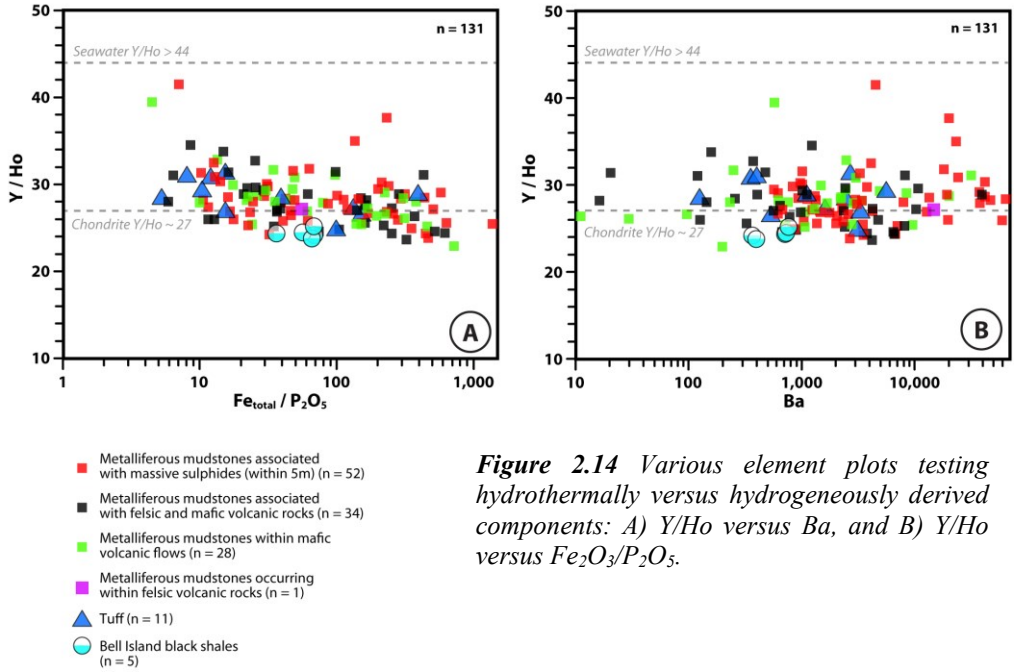

Figure 2.14 *Various element plots testing hydrothermally versus hydrogeneously derived components: A) Y/Ho versus Ba, and B) Y/Ho versus* Fe_2O_3/P_2O_5.

Fig. 2.15 A-B

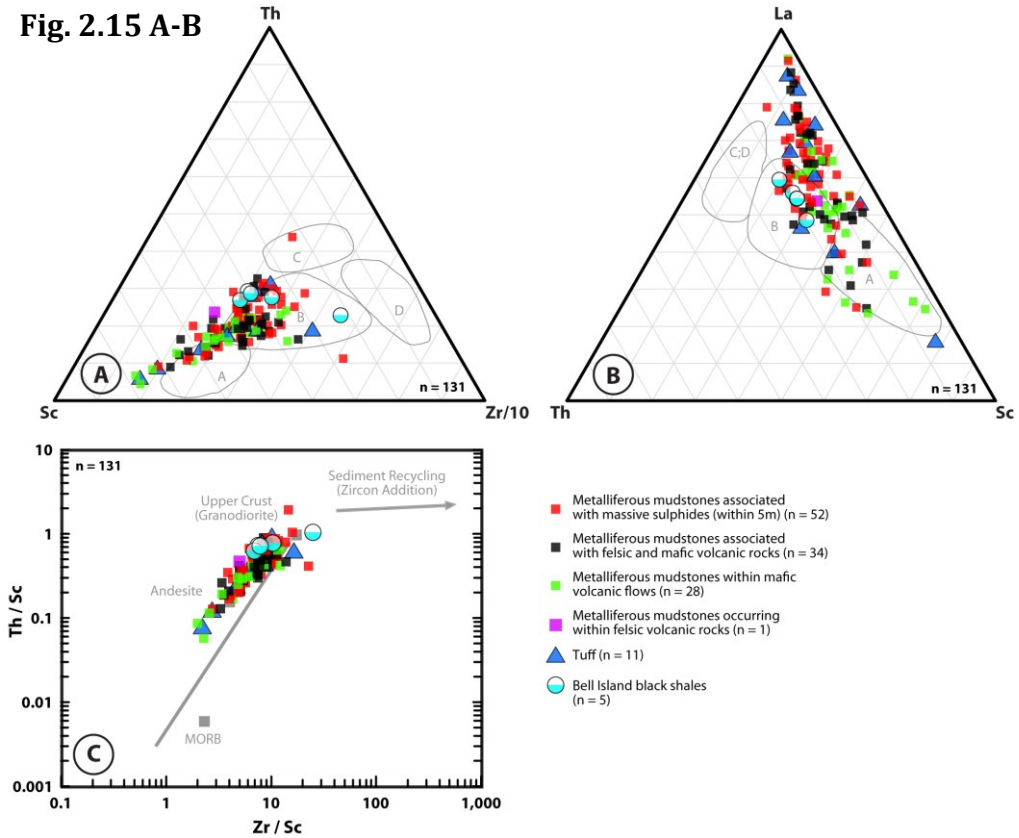

Figure 2.15 *A) Th-Sc-Zr/10 and B) La-Th-Sc plots: Both show that Lemarchant mudstones and tuff were derived from continental island arc settings with oceanic island arc characteristics. Interflow mudstones (green squares) and some tuff (blue triangle) show an association with mafic basaltic (oceanic island arc type) rocks, mudstones associated with massive sulphides (red squares) and/or felsic volcanic rocks show more continental arc source rock character. Th-Sc-Zr/10 plot (A) also shows that the Lemarchant source rocks are zircon depleted. In the La-Th-Sc diagram (B), Lemarchant mudstones that are associated with massive sulphides and/or felsic volcanic rocks trend towards the La apex due to La-scavenging from seawater. La-enrichment is caused when the hydrothermal fluids mix with seawater. A) and B) Fields: 'A' Oceanic island arc, 'B' Continental island arc, 'C' Active continental margin, and 'D' Passive margins. C) The Th/Sc versus Zr/Sc diagram shows upper crustal character of source rocks for mudstones associated with massive sulphides and/or felsic volcanic rocks, and trends towards more andesitic to MORB like source rocks for interflow muds and some of the tuff. The Zr-depletion is noticable as well, indicating a lack of Zr-recycling due to the overall nil to small influence of detrital sedimentary rocks. Immobile element plots after Bhatia and Crook (1986).*

Figure 2.16 *Figure showing the processes occurring within the buoyant and neutrally-buoyant (non-buoyant) hydrothermal plume associated with the formation of the Lemarchant deposit (modified after Rudnicki,1995; Peter, 2003).*

Figure 2.17 *Diagram of the two-phase curve for seawater and areas of maximum vent temperatures for modern hydrothermal systems with conditions for the Lemarchant hydrothermal system. Red dashed outlined area: depth-temperature ranges of maximum vent temperatures for selected ridge-related hydrothermal systems (Indian Ocean, East Pacific Rise, Mid-Atlantic Ridge, and NE Pacific ridges, and sediment covered ridges). Orange dashed outlined area: depth-temperature ranges of maximum vent temperatures for selected arc-related hydrothermal systems (backarc, arc volcano). Green stripe: possible temperature/water depth range for the Lemarchant hydrothermal system in a rifted arc setting. Modified after Hannington et al. (2005).*

Fig. 2.16

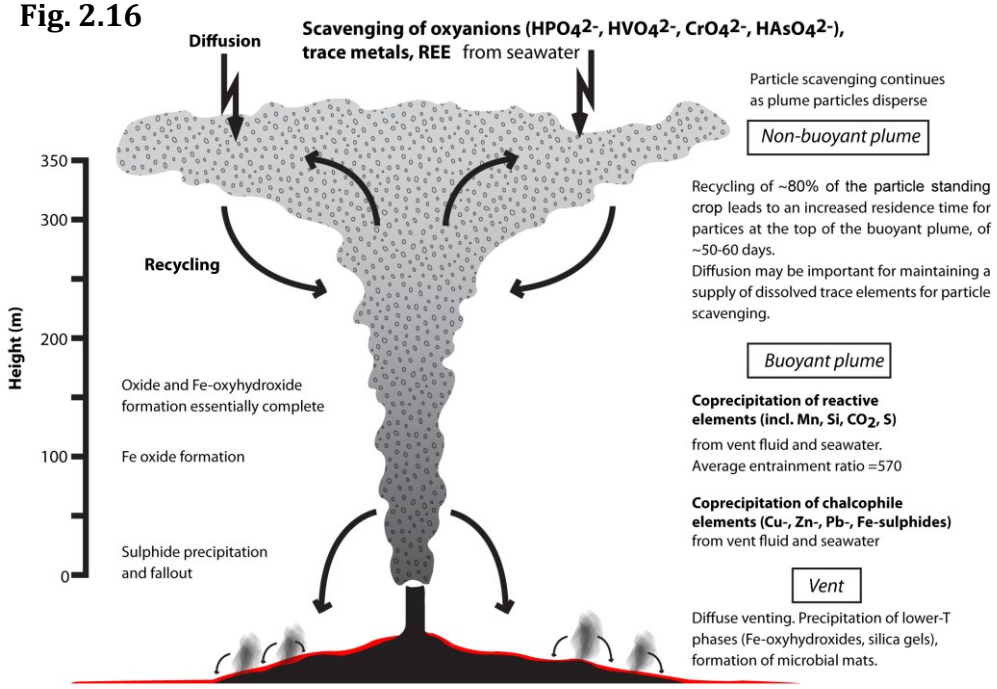

Fig. 2.17

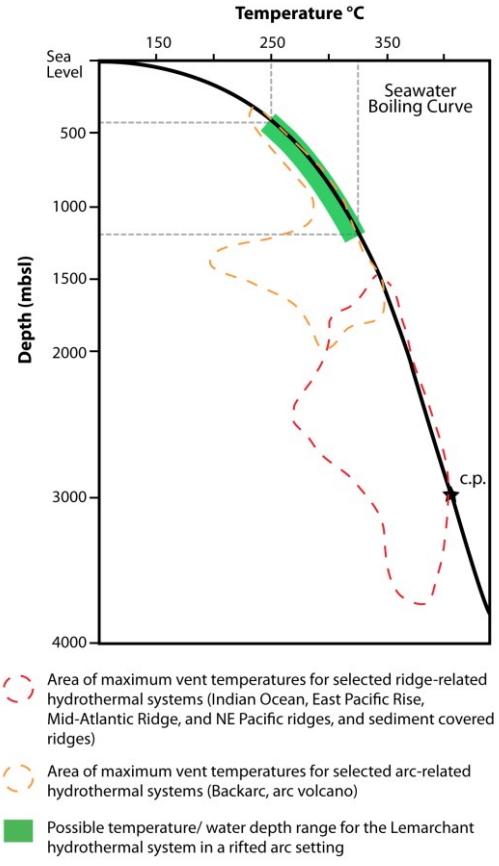

Appendix 2.1

2.1.1 Lithogeochemistry methods

During the fieldwork drill holes that contain metalliferous mudstones were logged and selected mudstones sampled for thin-section preparation and whole-rock analyses. Petrographic studies were undertaken on 184 thin-sections, which predominantly represent various mudstone types, tuff and surrounding lithological mafic and felsic volcanic units. High resolution backscattered electron (BSE) images were obtained using a FEI Quanta 400 scanning electron microscope (SEM) at Memorial University, which is equipped with an energy dispersive x-ray (EDX) analytical system from Bruker. Samples for whole-rock lithogeochemical studies (n = 126) were analyzed for major and minor elements by lithium metaborate/tetraborate fusion followed by HNO_3 dissolution and analysis by inductively coupled plasma (atomic) – emission spectroscopy (ICP-ES). Carbon (C) and sulphur (S) were obtained by infrared spectroscopy and mercury (Hg) was obtained by the cold vapour flow injection mercury system (Hg-FIMS). All of the former analyses were obtained at Activation Laboratories Ltd. (Actlabs) in Ancaster, Canada. Additional trace elements, including rare earth elements (REE), high field strength elements (HFSE), trace metals, and many low field strength elements (LFSE) were analyzed in the Department of Earth Sciences at Memorial University, using screw-top Teflon® bomb (Savillex®) multi-acid dissolution with a finish by inductively coupled plasma-mass spectrometry (ICP-MS). The whole-rock dissolution process was a modified version of that of Jenner et al. (1990) and Longerich et al. (1990) to account for the high amounts of carbonaceous material in the samples, as outlined below.

Powdered sample equivalent to 0.1000 g was put into a clean and dry screw-top Teflon® bomb (Savillex®) with 2 ml of 8N nitric acid (HNO_3) and 1 ml of hydrofluoric acid (HF) and placed on a hot plate at ~70 °C for three days. If the sample was not completely dissolved after that time, the cap was carefully removed and the condensed sample liquid on the cap rinsed into the jar with 8N HNO_3, and the bomb was left uncovered on the hot plate at about 80-100 °C to evaporate until dry. When dry, another 2 ml of 8N HNO_3 and 2 ml of hydrochloric acid (HCl) were added, the lid closed, and the sample left for a further day on a hot plate to reflux at ~70°C. After this additional step, or if the sample was already completely dissolved after the initial three days, the sample was evaporated until dry. When dry, 2 ml of 8N HNO_3 and 1 ml of boric acid (0.453M) were added to the sample liquid and then evaporated to dryness. To the dried sample a further 2 ml of 8N HNO_3 and 2 ml HCl were added, the cap was placed back on the jar and the sample left for 2 hours on the hot plate at ~70°C. After 2 hours, the cap was removed and the sample liquid evaporated to dryness. When dry, 2 ml of 8N HNO_3 and 1.3 ml oxalic acid (0.22M) were added, the cap placed back on, and the sample left for 2 hours on the hot plate at ~70°C. Subsequently, an additional 1 ml of H_2O_2 was added, the cap placed back on again, and the sample left for another 2 hours on the hot plate at ~70°C. Since many of the samples contain abundant carbonaceous material it is noted that each additional 1 ml of HCl and 1 ml of H_2O_2 added above reduced the amount of visible residual carbonaceous material quite significantly.

Solution material from the latter step above was transferred into 120 ml snap seal container. For this, the caps are rinsed with nanopure water into the snap seal jar, 0.665 ml HF/boric solution (0.113M HF/ 0.453 boric acid) is added, and the weight made up to

a final weight of 60 g with nanopure water. If visible residues still remained, the sample was filtered before the final sample dissolution preparation.

Two tubes were prepared for the ICP-MS, one with the sample dissolution and one with the sample dissolution plus a trace spike solution. To each 11 ml test tubes 0.5 g of sample solution were added with one tube having 9.5 g of 0.2N HNO_3 added, whereas the second tube contained 4.5 g of 0.2N HNO_3 and 5 g of trace spike solution; both tubes were capped, shaken and mixed prior to analysis by ICP-MS.

The residues left behind in the filter paper were checked at Memorial University via scanning electron microscope - energy dispersive X-ray spectroscopy (SEM-EDX) to ascertain that no elements of interest, particularly the HFSE and REE, remained. For this, the residues were mounted on a holder with double-sided carbon tape and semi-quantitatively analyzed by EDX under low-vacuum conditions to avoid carbon-coating. The analyses of the residues yielded, with one exception, purely carbonaceous material, and hence, no important trace elements were present in the residues. One residue consisted of predominantly carbonaceous material with traces of barite. Accordingly, to avoid interferences of organic matter with Ba, Ba-values of the fusion method (ICP-ES) were used, instead of ICP-MS. To correct for a possible mass spectral interference of the isobaric phases $^{135}Ba^{16}O$ and ^{151}Eu, two standard solutions were utilized and the interference factor calculated accordingly (Jenner et al, 1990).

2.1.2 Quality assurance and quality control (QA/QC)

Precision and accuracy of the analyses were determined using duplicates and reference materials following methods described in Jenner (1996) and Piercey (2014).

The reference materials utilized in the study included three different organic- and/or sulphide-rich shales (SCO-1, SDO-1 and SGR-1b) and one iron formation (FeR-1). These standards were run every twenty samples and with each analytical batch. In addition, blanks were utilized during each analytical run to test contamination; none was detected. Precision was determined using the percent relative standard deviation (% RSD) on the replicate analyses of the reference materials, and accuracy was determined using percent relative difference (% RD) from accepted values. Analyses from Actlabs of the major and some minor elements, and C, S, and Hg have following % RSD values: major elements range between 0.6-1.6% and 7.9%; P_2O_5. Ba, Sr, Y, Zr, Sc, Be, V have % RSD values between 0-2.6% RSD; and 0.3-0.5% RSD for C and S with one S-outlier of 6.7% RSD. Replicate Hg measurements have an average % RSD of 4.6% (range = 0-9.6%). Accuracy of the Actlabs analyzed major and minor elements ranges from 0.1-12.5% RD, from 0.2-5.6% RD for C and S, and 0.9-8.8% RD for Hg.

Analytical precision calculated for samples analyzed at Memorial University yielded the following values: low field strength elements (LFSE) range between 3.8-8.8% RSD (except Li, Rb), and HFSE had 3.7-4.4% RSD for high field strength elements. The REE (La to Lu) % RSD values range from 2.8-8.4 and base and transitional metals (except Ti and V) have a precision between 2.5-5.3% RSD.

Determination of accuracy is dependent on and limited to the quality and amount of published and certified values. For many sediment-rich samples the range of certified values is limited and/or results were obtained by methods not utilized in this study (e.g., Instrumental Neutron Activation Analysis - INAA). Therefore, accuracy values in the analyses outlined below are provided for where published data were available. Accuracies

for elements in standard FeR-1 range from 0.8-9.0% RD for most of the REE and Cu, Zn and Pb. Gd, Tm and Lu yield less accurate values between 10.9-15.1% RD. The standard SCO-1 has an accuracy of 0.4-8.1% RD for La, Pr and Nd, 13.4% RD for Ce, and 0.1% RD for Pb. Accuracies for standard SDO-1 range from 1.9-12.4% RD for La, Pr, Nd, Sm, Eu, Gd, Tm, and Pb, Co, Ni, Zn, and Fe. Ce, Tb, Dy, Ho, Er, Yb and Lu have accuracy values ranging between 12.0-25.9% RD. SGR-1b yields accuracy values between 4.9-9.4% RD for Pb, Co, Ni, Fe, and 16.4% RD for Cu and Zn. La, Ce, Gd, Tm range from 5.6-11.4% RD, and Nd, Sm, Eu, Dy, Ho, Er, Yb from 12.1-24.6% RD.

CHAPTER 3

Multiple sulphur and lead sources recorded in hydrothermal exhalites associated with the Lemarchant volcanogenic massive sulphide deposit, central Newfoundland, Canada

Stefanie Lode[1*], Stephen J. Piercey[1], Graham D. Layne[1], Glenn Piercey[2], and Jonathan Cloutier[1,3]

[1]*Department of Earth Sciences, Memorial University, 300 Prince Philip Drive, St. John's, NL, Canada, A1B 3X5*

[2]*MAF-IIC SIMS Facility, Memorial University, St. John's, NL, Canada, A1B 3X5*

[3]*Department of Earth Sciences, University of St. Andrews, St. Andrews, Scotland, UK, KY16 9AL*

Status quo: Published at Mineralium Deposita, 2016, *in press*.

3.1 Abstract

Metalliferous sedimentary rocks (mudstones, exhalites) associated with the Cambrian precious metal-bearing Lemarchant Zn-Pb-Cu-Au-Ag-Ba volcanogenic massive sulphide (VMS) deposit, Tally Pond volcanic belt, precipitated both before and after VMS mineralization. Sulphur and Pb isotopic studies of sulphides within the

Lemarchant exhalites provide insight into the sources of S and Pb in the exhalites as a function of paragenesis and evolution of the deposit, and subsequent post-depositional modification. *In situ* S isotope microanalyses of polymetallic sulphides (euhedral and framboidal pyrite, anhedral chalcopyrite, pyrrhotite, galena, and euhedral arsenopyrite) by secondary ion mass spectrometry (SIMS) yield $\delta^{34}S$ values ranging from -38.8‰ to +14.4‰, with an average of ~-12.8‰. The $\delta^{34}S$ systematics indicate sulphur was predominantly biogenically-derived via microbial sulphate reduction of seawater sulphate, microbial sulphide oxidation, and microbial disproportionation of intermediate S compounds. These biogenic processes are coupled and occur within layers of microbial mats consisting of different bacterial/archaeal species, i.e., sulphate reducers, sulphide oxidizers, and those that disproportionate sulphur compounds. Inorganic processes or sources (i.e., thermochemical sulphate reduction of seawater sulphate, leached or direct igneous sulphur) also contributed to the S budget in the hydrothermal exhalites, and are more pronounced in exhalites that are immediately associated with massive sulphides.

Galena Pb isotopic compositions (also from SIMS microanalysis) suggest derivation of evolved Pb from underlying crustal basement (e.g., felsic volcanic rocks of Sandy Brook Group) and less radiogenic Pb derived from juvenile sources (leached from mafic volcanic rocks of, e.g., the Sandy Brook Group and/or Tally Pond group). This indicates that the hydrothermal fluid interacted with juvenile and evolved crust during hydrothermal circulation, consistent with the existing tectonic model that suggests a formation of the Tally Pond belt volcanic rocks and associated VMS deposits in a rifted arc environment upon crustal basement of the Ediacaran age Sandy Brook Group and Crippleback Intrusive Suite. Combined S and Pb isotope data illustrate that sulphides

within the ore deposit that occur proximal to the vent, contain a higher proportion of sulphur derived from thermochemical sulphate reduction (TSR), because hydrothermal fluids are enriched in H_2S derived from TSR. They also have lower radiogenic Pb contributions than sulphides occurring distal from mineralization. Hence, such data may provide an exploration vector in exhalites associated with similar VMS environments globally.

3.2 Introduction

Metalliferous sedimentary rocks (exhalites, mudstones) are commonly associated with volcanogenic massive sulphide (VMS) deposits (Franklin et al., 1981; Lydon, 1984; Kalogeropoulos and Scott, 1989; Spry et al., 2000; Peter, 2003; Hannington, 2014). Metalliferous sediments can pre- or post-date massive sulphide mineralization. They precipitate as hydrothermal plume fallout proximal to the hydrothermal vent, but also occur as thin layers up to several kilometres away from the vent site (e.g., Haymon and Kastner, 1981; Lydon, 1984; Haymon et al., 1993; Hodkinson and Cronan, 1995; Binns, 2004; Gurvich, 2006; Hannington, 2014). Iron, Zn, Pb, and Cu sulphides co-precipitate with sulphates (barite, anhydrite), and other phases (e.g. amorphous silica and Fe-oxyhydroxides), from the buoyant to neutrally-buoyant hydrothermal plume after mixing with the ambient seawater (Haymon and Kastner, 1981; Campbell et al., 1984; Hodkinson and Cronan, 1995; German and Von Damm, 2003; Binns, 2004; Dias et al., 2008; Hannington, 2009; Hekinian et al., 1993). These exhalites consist of hydrothermal, seawater, and detrital components that are reflected in their sediment mineralogy,

chemistry, and S and Pb isotopic compositions (Boström and Peterson, 1966; Boström et al., 1969; Shanks, 2001; German and Von Damm, 2003; Dias et al., 2008; Shanks, 2014).

Reduced sulphur in volcanogenic massive sulphide and associated hydrothermal sedimentary rocks can be derived from various sources and processes, both inorganic and organic. Inorganic sources include: 1) thermochemical reduction of seawater sulphate (TSR); 2) magmatic contributions through leaching of sulphur from igneous rocks or direct magmatic fluid/volatile input; and/or 3) sedimentary-diagenetic sulphides (Ohmoto and Rye, 1979; Ohmoto and Goldhaber, 1997; Seal, 2006; Shanks, 2014). Hydrogen sulphide (H_2S), a product of TSR is present in the buoyant plume when the hydrothermal fluids exit the seafloor via black smokers, but also in hot pore waters that circulate upwards through the porous sulphide mound and flanking sediments and subsequently emanate as diffuse hydrothermal flow into the ambient seawater column (Von Damm, 1990; Gundersen et al., 1992; Elsgaard et al., 1994; Hannington et al., 1995; German and Von Damm, 2003; Hannington, 2014). Additionally, H_2S can be incorporated into the hydrothermal fluids by direct degassing of magmas (Hannington et al., 1999). In some massive sulphide deposits, and associated metalliferous mudstones, biogenically-derived ("organic") sulphide plays a substantial role in their sulphur budget - with organic sulphur derived from the biogenic/microbial (bacterial and archaeal) reduction of seawater sulphate (BSR), and the microbial disproportionation of sulphur intermediates, with an intermediate step of biogenic sulphide oxidation (Harrison and Thode, 1958; Elsgaard et al., 1994; Canfield, 2001b; Habicht and Canfield, 2001; Shanks, 2001; Seal, 2006; Shanks, 2014). Microbial sulphate reduction, coupled with microbial disproportionation

of sulphur intermediate compounds produces large $\Delta^{34}S_{sulphate\text{-}H_2S}$ fractionation factors, which results in sedimentary (and massive) sulphides with strong ^{34}S-depletion (Bak and Pfennig, 1987; Jørgensen, 1990; Jørgensen et al., 1992; Canfield, 2001b; Habicht and Canfield, 2001; Habicht and Canfield, 1997). The mineral specific S isotope systematics of polymetallic sulphides in metalliferous exhalites (via SIMS microanalysis) thus provides the opportunity to evaluate sulphur sources in the exhalites, and allows delineation of sulphur sources as a function of paragenesis and the multi-stage evolution of the underlying deposit.

Similarly, Pb isotopes provide insight into the source of Pb (and, by interference, other metals) within massive sulphides and other ore deposits and their lithological provenance (Swinden and Thorpe, 1984; Zartman and Doe, 1981; Tosdal et al., 1999; Ayuso et al., 2003). In VMS deposits, Pb is predominantly leached from basement rocks, which can have varying Pb isotope signatures if Pb was derived from different reservoirs, (Franklin and Thorpe, 1982; Swinden and Thorpe, 1984; Tosdal et al., 1999; Ayuso et al., 2003). A contribution of Pb derived from crustal sources results in more radiogenic Pb values, whereas mantle-derived sources are characterized by less radiogenic, juvenile Pb (Franklin and Thorpe, 1982; Swinden and Thorpe, 1984). Determining Pb isotopic ratios in galena hosted in the Lemarchant metalliferous exhalites therefore provides a possibility to identify sources of Pb that contributed to the Lemarchant exhalites and hence, helps to better understand its tectonic environment.

The Cambrian precious metal-bearing Lemarchant Pb-Zn-Cu VMS deposit provides an ideal location to study the S and Pb sources in metalliferous mudstones

associated with massive sulphide mineralization. In this deposit metalliferous mudstones are located immediately atop massive sulphides and are also located at a considerable distance from mineralization, along strike as well as in different stratigraphic horizons. A hydrothermal origin for these metalliferous mudstones has been shown (Lode et al., 2015), and these mudstones can be considered as exhalites (e.g., Ridler, 1971; Peter and Goodfellow, 2003; Galley et al., 2007). Furthermore, the Lemarchant exhalites have exquisite textural and paragenetic preservation, thus providing an opportunity to evaluate changing sources of S and Pb in both space, and as a function of deposit evolution. These data also contribute to understanding the tectonic environment, ore genesis, and paleoceanographic environment of formation for the Lemarchant deposit. Finally, the data presented herein have implications for utilizing S and Pb in hydrothermal sedimentary rocks as a potential vector for VMS deposits in similar geological environments.

3.3 Regional and deposit geology

The Zn-Pb-Cu-Ba-Au-Ag-bearing Lemarchant deposit is hosted within the Central Mobile Belt, Newfoundland, part of the Cambrian (~515 Ma) to Permian (~275 Ma) Appalachian mountain belt (Fig. 3.1A; Williams, 1979; Swinden, 1988; Swinden, 1991; Squires and Moore, 2004; Franklin et al., 2005; Piercey, 2007; Rogers et al., 2007; Copeland et al., 2009; McNicoll et al., 2010; van Staal and Barr, 2011). The Central Mobile Belt hosts numerous VMS deposits and was only moderately affected by metamorphism (lower greenschist-facies) and deformation during the three Late Cambrian to Late Ordovician (495-450 Ma) Taconic orogenic cycles and the Early

Silurian (440-423 Ma) Salinic orogeny (Swinden, 1991; Squires and Moore, 2004; van Staal and Barr, 2011). As such, the internal stratigraphic and textural relationships are well preserved, both regionally, and within the VMS deposits (Hinchey and McNicoll, 2009; Zagorevski et al., 2010; van Staal and Barr, 2011; Piercey et al., 2014).

The Newfoundland Appalachians are divided into four tectonostratigraphic zones: Humber, Dunnage, Gander and Avalon zones (Fig. 3.1A). These zones result from, and were affected by, the successive accretion of three micro-continental blocks and related interoceanic arcs and backarcs during the Early Paleozoic to Middle Paleozoic (Swinden, 1991; Rogers et al., 2007; van Staal, 2007; Zagorevski et al., 2010; van Staal and Barr, 2011). These ribbon-shaped micro-continental blocks were located on the leading edges of Gondwana and Laurentia, forming peri-Gondwanan and peri-Laurentian terranes (Rogers et al., 2007; Zagorevski et al., 2010; van Staal and Barr, 2011). The Dunnage Zone (~Central Mobile Belt; Williams, 1979; Williams et al., 1988; Swinden, 1991; Squires and Moore, 2004) has been subdivided into the peri-Laurentian Notre-Dame and the peri-Gondwanan Exploits subzones (Swinden, 1988; Swinden, 1991; Pollock and Wilton, 2001)(Fig. 3.1A). The Exploits Subzone is comprised of Cambrian-Ordovician volcanic and sedimentary rocks (Dunning et al., 1991; Rogers et al., 2007; van Staal and Barr, 2011; McNicoll et al., 2010) and includes the Victoria Lake supergroup. The Lemarchant deposit and the Duck Pond and Boundary mines are located within the Tally Pond group, one of the six tectonic assemblages within the Victoria Lake supergroup that yield U-Pb zircon ages ranging from ~513 to 453 Ma (Dunning et al., 1987; Dunning et al., 1991; Evans and Kean, 2002; Rogers et al., 2007; Zagorevski et al., 2007; McNicoll et al., 2010; Zagorevski et al., 2010; Piercey et al., 2014). The Tally Pond group (~513-509

Ma) is further divided into the Bindons Pond and Lake Ambrose formations (Fig. 3.1B) and is interpreted to have been formed in an arc to rifted arc setting upon crustal basement rocks of the Sandy Brook Group and Cripppleback Intrusive Suite (Rogers et al., 2006; McNicoll et al., 2010; Zagorevski et al., 2010; Piercey et al., 2014). The Cripppleback Intrusive Suite comprises the Cripppleback Lake Pluton, which includes a quartz-monzonite that yielded a 563 Ma U-Pb zircon age, as well as the Valentine Lake and Lemottes Lake plutons (Rogers et al., 2006). The penecontemporaneous Sandy Brook Group consists of mafic and felsic volcanic rocks with continental arc characteristics (Rogers et al., 2006). The Bindons Pond formation is dominated by felsic volcanic rocks (dacite to rhyolite), whereas the Lake Ambrose formation is dominated by mafic volcanic rocks (basalt, basaltic andesite, andesite) (Dunning et al., 1991; Evans and Kean, 2002; Rogers et al., 2006; McNicoll et al., 2010; Piercey et al., 2014). Volcanogenic massive sulphide mineralization and related hydrothermal alteration occurs within the Bindons Pond formation at the Duck Pond, Boundary, and Lemarchant deposits, as well as in several other areas within this formation (Squires et al., 1991; Squires and Moore, 2004; McNicoll et al., 2010; Zagorevski et al., 2010; Piercey et al., 2014).

The Lemarchant deposit is hosted in the felsic volcanic rocks of the Bindons Pond formation near the hanging wall mafic volcanic rocks of the Lake Ambrose formation (Figs. 3.1B, 3.2A). The contact between the formations is complex and often marked by intricate intermingling of felsic and mafic volcanic rocks, with a thin (<1 to 20 m) layer of metalliferous mudstone (Fig. 3.2B-C). Most commonly, this exhalite layer occurs between the felsic and mafic volcanic rocks, either capping the massive sulphides, or at the same stratigraphic position, but distal from mineralization (Figs. 3.3A-C, 3.4A-C,

respectively). Equally common are interflow mudstones occurring within the hanging wall basalts (Fig. 3.5A-C). The distribution of these metalliferous sedimentary rocks is discontinuous over one to four kilometres from the deposit (Copeland et al., 2009; Fraser et al., 2012).

Alteration at the Lemarchant deposit includes intense quartz, sericite and chlorite alteration (Fig. 3.2B-C), Ba-enrichment, anomalous disseminated and stringer-type pyrite, and base-metal sulphides with lesser amounts of pyrrhotite (Fraser et al., 2012). The majority of mineralization occurs as semi-massive to massive sulphide within the Lemarchant Main Zone and the smaller 24 Zone (sections 101N to 104N)(Copeland et al., 2009; Fraser et al., 2012); an additional mineralized zone, the Northwest Zone, with a strike length of 100 meters (Fig. 3.2A, C), was discovered in early 2013. Both, the Lemarchant Main and Northwest zones, remain open in north and south directions (http://www.canadianzinc.com/images/Docs/News_Releases/CZNNR20131211.pdf). The indicated resources for the Lemarchant Main Zone currently are 1.24 Mt at 5.38 % Zn, 0.58 % Cu, 1.19 % Pb, 1.01 g/t Au and 59.17 g/t Ag, with inferred resources of 1.34 Mt at 3.70 % Zn, 0.41 % Cu, 0.86 % Pb, 1.00 g/t Au and 50.41 g/t Ag (Fraser et al., 2012)(Fig. 3.2A). The recently defined Northwest Zone is not included in the published resource estimates, and represents potential additional resources.

The Lemarchant Main Zone (Fig. 3.2A-C) is 1.7 to 30.4 m thick and consists of a barite-rich outer zone that grades into a Pb-Zn-sulphide-rich zone, and an interior zone with Zn-Cu-sulphides that grades into stringer mineralization at depth (Copeland et al., 2009; Fraser et al., 2012; Gill and Piercey, 2014; Gill, 2015). In addition to typical VMS sulphides (pyrite, sphalerite, galena, and chalcopyrite), the massive sulphides also contain

abundant sulphosalts (e.g., tetrahedrite-tennantite), bornite, stromeyerite, and electrum) (Copeland et al., 2009; Gill, 2015). The trace elements and minor and major element mineral compositions of polymetallic sulphides, sulphosalts, bornite, electrum, as well as barite, were studied in detail using LA-ICPMS (laser ablation-inductively coupled plasma mass spectometry) and EMPA (electron microprobe analysis) resulting in the detection of enrichments in 'epithermal suite elements' (e.g., Au, Ag, As, Hg ± Sb, Bi, Te)(Mercier-Langevin et al., 2011; Gill and Piercey, 2014; Gill, 2015). These epithermal suite elements are commonly recognized in precious metal-enriched VMS (Hannington et al., 1999; Mercier-Langevin et al., 2011). Additionally, bladed barite and calcite/Ca-Fe-Mg-Mn-carbonate and potassium feldspar alteration are common features in the deposit (Gill and Piercey, 2014; Gill, 2015). Collectively, these petrological and lithogeochemical characteristics have led to the interpretation that the Lemarchant deposit was a shallow water VMS deposit, with both VMS and epithermal features (Gill and Piercey, 2014; Gill et al., 2015; Lode et al., 2015). The Lemarchant exhalites also contain many of the above main sulphide and other mineral phases, including bladed barite and calcite/Ca-Fe-Mg-Mn-carbonate, electrum ±Hg ±Sb, as well as acanthite and the Ag-Sb sulphosalts pyrargyrite and stephanite and also commonly display potassium feldspar alteration (Lode et al., 2015).

3.4 Exhalite stratigraphy and lithofacies

The Lemarchant exhalites occur either immediately on top of massive sulphide mineralization between the felsic and mafic volcanic rocks (exhalite-massive sulphide

(EMS)-type; Fig. 3.3A-C); extending laterally outwards from mineralization, but at the same stratigraphic level and without immediate association with mineralization (felsic-exhalite-mafic (FEM)-type; Fig. 3.4A-C); or as interflow mudstones within the hanging wall basaltic rocks (interflow exhalite (IFE)-type; Fig. 3.5A-C). Interflow mudstones occur more commonly within 15 metres above the massive sulphide mineralization, but are present up to 70 meters above the ore horizon. Exhalites within the felsic volcanic rocks (FEF) below the ore horizon are rare, and only present in one drill hole (LM13-87, 283.4 m), where it is intermingled with felsic volcanic rocks. These four exhalite types most commonly occur proximal and up to 200 m away from the mineralization of the Lemarchant Main Zone, but are also associated with the Northwest Zone, and in the area of the North target (Fig. 3.2A).

The exhalites, independent of their stratigraphic positions, are brown to black, graphite-rich, finely laminated, and contain fine carbonaceous/organic-rich laminae that are intercalated with siliciclastic, volcaniclastic and/or amorphous kidney-shaped chert±apatite layers (Figs. 3.3A, 3.4A, 3.5A). The main sulphide phases are pyrite (framboidal, massive and euhedral)(Fig. 3.6E-F) and pyrrhotite, with minor marcasite (Fig. 3.6F), chalcopyrite, sphalerite, arsenopyrite and galena (Fig. 3.6F-H). Contents of chalcopyrite, sphalerite, and galena increase proximal to mineralization (Fig. 3.7A-B). The sulphides occur both parallel to bedding, and in later stage, stringer-like veins (Figs. 3.3A, 3.4A, 3.5A, 3.7C-D). Locally, veins that cross-cut the original lamination, indicate diagenetic/tectonic remobilization and/or formation by intra-stratal shrinkage (synaeresis) cracks (e.g., de-watering structures)(Füchtbauer et al., 1988; Harazim et al., 2013). Furthermore, stringer-type later stage veins have precious metal minerals including

electrum ± Hg ± Sb (Fig. 3.7D-E) as well as acanthite, pyrargyrite and stephanite and are suggested to represent the epithermal stage that overprinted the VMS-style mineral assemblage. Electrum, acanthite (Fig. 3.7D-F), pyrargyrite, stephanite, gersdorffite, cubanite, and digenite are rare, occurring as inclusions in pyrite, or interstitial to other sulphide phases. Electrum also occurs associated with pyrrhotite, arsenopyrite, chalcopyrite and galena (Fig. 3.7E). All four types of exhalites have a high abundance of Ba-containing minerals, including barite, celsian, hyalophane (Fig. 3.7G-H), and witherite (Ba-carbonate).

3.5 Mudstone sulphide and sulphate mineralogy

Sulphide and sulphate minerals were characterized by optical microscopy on polished thin-sections and/or polished epoxy mounts. Pyrite occurs as euhedral grains, as framboids, or as massive aggregates. The framboids are present as scattered single larger spheres (20-100 μm), as flocks of framboids, or as semi-massive framboid layers, consisting of small framboidal pyrite grains (1-10 μm). Dense layers of very fine-grained pyrite framboids commonly occur within the finely laminated mudstones. Pyrite tubes oriented parallel to lamination are also present in finely laminated carbonaceous exhalites. These pyritic tubes are partially overgrown by euhedral pyrite and arsenopyrite, and interstices between tubes are locally filled with chalcopyrite and sphalerite (Fig. 3.6g). Marcasite occurs as tabular crystals or blades in euhedral or massive pyrite (Fig. 3.6F), or as semi-continuous layers of marcasite clusters. In most cases, marcasite partially replaces pyrite and it is suggested that marcasite formed paragenetically late, after the

higher temperature hydrothermal system ceased, because marcasite has higher growth rates and dominates over pyrite at lower temperatures and acidic conditions (pH <5)(Murowchick and Barnes, 1986; Schoonen and Barnes, 1991; Schieber, 2011). Pyrite associated with the euhedral marcasite locally shows corrosion textures that are likely due to partial re-oxidation (Schieber, 2011). This partial oxidation of pyrite is caused by the oxygenated ambient waters and creates conditions that favour marcasite precipitation (Schieber, 2011). Chalcopyrite occurs predominantly as interstitial grains between euhedral or framboidal pyrite and as a paragenetically late-stage phase in sulphide-rich layers parallel to the sedimentary lamination, or in cross-cutting veins (Figs. 3.6B, F-H, 3.7A-E). It is commonly associated with pyrrhotite, galena, sphalerite, and/or electrum. Chalcopyrite also forms pseudomorphs after euhedral pyrite and occurs as chalcopyrite-disease in sphalerite. Immediately proximal (<10 cm) to massive sulphides the sphalerite content increases significantly (Fig. 3.7A-B). Sphalerite on the contact between the massive sulphides and the exhalites (5-70 cm wide zone) is Fe-rich (up to ~8 wt% Fe) red to purple sphalerite that grades down-stratigraphy into Fe-poor (<1 wt% Fe) white to honey brown sphalerite-dominated massive sulphides (Fig. 3.3A). Galena occurs as inclusions in, or interstitial to, euhedral pyrite, and is associated with chalcopyrite, sphalerite, electrum and, locally, pyrrhotite (Figs. 3.6H, 3.7B, D-E). In EMS-type exhalites galena is a major phase and is associated with sphalerite and euhedral or massive pyrite (Fig. 3.7B). Pyrrhotite occurs as disseminated patches in sulphide-poor mudstones or tuff, or as (semi-)continuous layers parallel to or cross-cutting mudstone laminations. Pyrrhotite is commonly associated with euhedral arsenopyrite and chalcopyrite, and locally with electrum (Fig. 3.7E). Ba-mineral phases include barite

($BaSO_4$), the Ba-rich feldspar celsian ($BaAl_2Si_2O_8$), and a barian K-feldspar with <2wt% Ba (hyalophane or barian adularia $(K,Ba)Al(Si,Al)_3O_8$). Barite forms anhedral (semi-)continuous layers or occurs as bladed crystals in vugs or veins, which are commonly associated with bladed Ca-Fe-Mg-Mn-carbonates. Barite-filled veins generally occur as crack-and-seal type veins that cross-cut the exhalites and Pb-Zn-Cu sulphides (Fig. 3.7G-H). The Ba-feldspars are commonly present as paragenetically late minerals, with euhedral crystals overgrowing earlier phases such as pyrite framboids or barite (Fig. 3.7G-H). The Ba-carbonate witherite also occurs in the exhalites, but is less common than the other Ba-phases.

3.6 Sulphur and Pb isotopes

3.6.1 Sampling, methods, quality assurance, and quality control (QA/QC)

Samples were obtained during stratigraphic mapping and logging of drill core. Representative exhalites were sampled for thin-section preparation and whole-rock analyses. Petrographic studies were undertaken on 184 thin-sections, which predominantly represented various exhalite types, but also crystal lithic vitric tuff that is intercalated with the exhalites, and surrounding mafic and felsic volcanic lithologies. High resolution backscattered electron (BSE) images were obtained using a FEI Quanta 400 scanning electron microscope (SEM) at Memorial University, which is equipped with a Bruker energy dispersive x-ray (EDX) analytical system. Exhalite types further selected for S and Pb isotopic studies included those that: 1) are immediately associated with, or occur stratigraphically within five meters of, massive sulphides (EMS-type) and represent

the main stratigraphic marker between the felsic and mafic volcanic rocks (Bindons Pond and Lake Ambrose formations, respectively); 2) do not have an obvious relationship with mineralization, but occur along the same stratigraphic contact between the felsic volcanic rocks of the Bindons Pond and mafic volcanic rocks of the Lake Ambrose formations (FEM-type); and 3) occur as interflow exhalites within the hanging wall Lake Ambrose formation basalts (IFE-type).

Representative samples of these three types of exhalites (EMS, FEM, and IFE) were selected for secondary ion mass spectrometer (SIMS) microanalysis based on stratigraphic, spatial, textural and paragenetic relationships as deduced from field relationships, reflected and transmitted light microscopy, and SEM. Samples were collected from the Lemarchant Main and Northwest zones of the deposit, as well as from the North target (Fig. 3.2A). Secondary ion mass spectrometry was chosen because of the high spatial resolution (15 μm spot size for S and 25 μm spot size for Pb), and because it allows *in situ* determination of S and Pb isotopic compositions of neighbouring phases within the polymetallic sulphides as a function of texture and paragenesis.

Pyrite (euhedral, massive, framboidal, spherical, and tube-like pyrite textures), pyrrhotite, chalcopyrite, arsenopyrite, and galena were analysed *in situ* for S isotopes using SIMS. Sulphide grains chosen for analysis were selected based on associated mineral assemblages, grain size, shape, and paragenesis. Overall, 210 $\delta^{34}S$ spot analyses of sulphides in 26 samples were measured, covering drill hole depths ranging from 9 m to 511 m and sections from 100+50N to 108+00N (Fig. 3.2A). To correct for instrumental mass fractionation (IMF) the following sulphide in-house standards were used: 1) pyrite – UL9 ($\delta^{34}S$ = +15.8‰) and KH87 ($\delta^{34}S$ = +0.2‰); 2) chalcopyrite – Norilsk ($\delta^{34}S$ =

+8.3‰); 3) pyrrhotite – PoW1 ($\delta^{34}S$ = +2.3‰); 4) arsenopyrite – Arspy57 ($\delta^{34}S$ = +2.8‰); and 5) galena – HT10 ($\delta^{34}S$ = +14.2‰). Internal precision of individual $\delta^{34}S$ measurements was generally better than ±0.25‰ (1σ), with ±0.35‰ for the overall reproducibility.

Lead isotopes were analysed *in situ* by SIMS on galena that were inclusion free and larger than >25 μm. Six samples met these criteria and $^{206}Pb/^{204}Pb$, $^{207}Pb/^{204}Pb$, and $^{208}Pb/^{204}Pb$ were obtained in 38 spot analyses; spots for Pb isotope analyses were selected preferentially from the subset of samples that were previously analysed for S-isotopes. Seven data points were rejected based on poor data quality based on analysis of the data and the quality of the post-analysis SIMS pit left in the sample. Two in-house galena standards (F19 and JMBH) were used to correct for instrumental mass fractionation (IMF). 15 cycle analyses accumulated in 9 min routinely yield internal precisions (standard error of the mean) on $^{204}Pb/^{206}Pb$, $^{207}Pb/^{206}Pb$ and $^{208}Pb/^{206}Pb$ determinations of better than ±0.05 to 0.10 % (1σ), while producing sputter craters only a few μm deep. Overall reproducibility, based on replicate analyses of the secondary standard JMBH, is typically better than ±0.10 – 0.15% for these same ratios. Samples were prepared and analysed following the methods described in detail in Brueckner et al. (2015) and Gill (2015) and described in Appendix 3.1.

3.6.2 Results

3.6.2.1 Sulphur isotopes: Sulphur isotope determinations are summarized in Table 3.1. Pyrite has the widest range in $\delta^{34}S$ values; from -38.9‰ to +14.4‰. In detail, $\delta^{34}S$

analyses of euhedral pyrite (Figs. 3.6G-H, 3.7A-E) have values between -26.1‰ and +14.4‰ (n = 70), with three distinct populations: a) values ranging from -20‰ to -10‰; b) from -2‰ to +6‰; and c) from +10.0‰ to +14.4‰ (Fig. 3.8). Pyrite framboids (Figs. 3.7C, 3.9A) have very negative $\delta^{34}S$ signatures, with values ranging from -38.9‰ to -11.0‰ (n = 24), except one analysis with $\delta^{34}S$ of +12.2‰. Mats consisting of fine framboidal pyrite have $\delta^{34}S$ values that range from -16.9‰ to -5.7‰ (n = 6). Tube-like pyrite that occurs in two distinct laminae in brown, finely laminated sulphide-rich exhalite, (Fig. 3.6C, G) have $\delta^{34}S$ signatures between -30.5‰ and -20.1‰ (n = 2). The three marcasite samples, including framboidal and euhedral marcasite (Fig. 3.6F), have a very restricted $\delta^{34}S$ of between -13.1‰ to -12.4‰. Arsenopyrite (Figs. 3.6G, 7E) and pyrrhotite (Fig. 3.7E) have similar $\delta^{34}S$ signatures, ranging from -24.4‰ to -10.5‰ (n = 11) and -23.7‰ to -8.1‰ (n = 24), respectively. Chalcopyrite has $\delta^{34}S$ that ranges from -22.8‰ to +3.2‰ (n = 43) (Figs. 3.6A-H, 3.7A-C, E), and galena has values from -20.0‰ to +12.0‰ (n = 26) (Figs. 3.6E, 3.7B, D). Both chalcopyrite and galena have two distinctive distributions: at -20‰ to -10‰ and -2‰ to +6‰ (Fig. 3.8). Notably, euhedral pyrite, chalcopyrite, and galena in exhalites proximal to Main Zone mineralization tend towards positive $\delta^{34}S$ signatures (Fig. 3.10B, Table 3.1). In contrast, pyrite framboids, arsenopyrite, and pyrrhotite do not show distinct spatial variations in $\delta^{34}S$ (Fig. 3.9A-C). Exhalites closely related to massive sulphides (EMS-type) have more positive $\delta^{34}S$ values than interflow exhalites (IFE-type); FEM-type exhalites have intermediate values between the EMS- and IFE-type exhalites (Fig. 3.10A-B).

3.6.2.2 Lead isotopes: Galena lead isotope data are summarized in Table 3.2. Overall, the data form constrained clusters, yielding average ratios of $^{206}Pb/^{204}Pb$ = 18.11 ±0.13, $^{207}Pb/^{204}Pb$ = 15.53 ±0.16, and $^{208}Pb/^{204}Pb$ = 37.70 ±0.17, respectively, and overall ranges of $^{206}Pb/^{204}Pb$ = 18.03-18.23, $^{207}Pb/^{204}Pb$ = 15.40-15.81, and $^{208}Pb/^{204}Pb$ = 37.35-39.01, respectively. Nevertheless, in EMS-type exhalites small variations in $^{206}Pb/^{204}Pb$ are discernable, and the $^{207}Pb/^{204}Pb$ and $^{208}Pb/^{204}Pb$ ratios are more highly variable. EMS-type mudstones have less radiogenic $^{206}Pb/^{204}Pb$ ratios than those exhalites that have no immediate association with massive sulphides (FEM); and both groups lie on subparallel trends with distinctive $^{206}Pb/^{204}Pb$ (Fig. 3.11A-B).

EMS-type exhalites yield average $^{206}Pb/^{204}Pb$, $^{207}Pb/^{204}Pb$, and $^{208}Pb/^{204}Pb$ ratios of 18.09 ±0.12, 15.53 ±0.15, and 37.67 ±0.16, respectively, and range from 18.03-18.19, 15.40-15.62, and 37.35-38.05, respectively. These values overlap, for the most part, with the results for bulk galena samples in the Lemarchant massive sulphides (Gill, 2015; Pollock and Wilton, 2001)(Fig. 3.11A-B).

FEM-type exhalites have slightly more radiogenic $^{206}Pb/^{204}Pb$ ratios relative to the EMS-type, with an average of 18.16 ±0.14, but similar $^{207}Pb/^{204}Pb$ and $^{208}Pb/^{204}Pb$ ratios with averages of 15.54 ±0.18 and 37.76 ±0.20, respectively. The FEM-type exhalites have $^{206}Pb/^{204}Pb$, $^{207}Pb/^{204}Pb$, and $^{208}Pb/^{204}Pb$ that range from 18.03-18.23, 15.45-16.61, and 37.65-37.93, respectively. These FEM-type samples plot along a trend towards the more radiogenic Duck Pond hydrothermal metalliferous mudstones (Fig. 3.11A-B; data from Piercey *unpublished data*). One FEM-galena outlier plots at the least radiogenic end of the $^{207}Pb/^{204}Pb$ and $^{208}Pb/^{204}Pb$ cluster, but the analytical errors are larger than those of the other samples and, therefore, the significance of this analysis is uncertain. Overall, the

EMS- and FEM-type mudstones have similar $^{207}Pb/^{204}Pb$ and $^{208}Pb/^{204}Pb$ and the $^{206}Pb/^{204}Pb$ values overlap within analytical error; however 2σ error ellipses calculated with Isoplot 3.75 suggest that the $^{206}Pb/^{204}Pb$ of the EMS- and FEM-mudstones form two distinct clusters (Fig. 3.11A-B).

Calculated Stacey-Kramers model ages and μ values for all Lemarchant exhalite galena samples are listed in Online Resource 2 and range from 130 to 430 Ma (μ-values: 9.12 to 9.88) and have an average of 249 Ma (μ-value: 9.47), with one sample that has a model age of 0 Ma (μ-value: 8.87). These ages are significantly younger than the reported U-Pb zircon age for the host rocks to the Lemarchant deposit (513 ±2 Ma) (Dunning et al., 1991). However, they correlate with Stacey-Kramers model ages and μ values reported by Gill (2015) for the Lemarchant massive sulphides, which range from 163 Ma to 578 Ma with μ values between 9.22 and 10.20. A similar model age of 411 Ma is reported from a Tally Pond belt sample by Swinden and Thorpe (1984) and model ages of 305 and 325 Ma are reported for Lemarchant samples reported by Pollock and Wilton (2001). The cluster of the Lemarchant mudstones measured from this study as well as the massive sulphide data indicate an interception with the young upper crust curve (0.5 Ga) modelled after Kramers and Tolstikhin (1997), which correlates with the general tectonic environment of the Tally Pond volcanic belt (Rogers et al., 2006; McNicoll et al., 2010; Piercey et al., 2014).

3.6.2.3 Sulphur and Pb isotope correlations: From the 31 analysed Pb isotope spots measured on galena, 25 (from 6 samples) were also measured for sulphur isotopic compositions (15 EMS-type; 10 in the FEM-type). Notably, the majority of galena

samples in EMS-type exhalites have predominantly positive $\delta^{34}S$ isotopic signatures (-1.2‰ to +5.9‰) and are associated with lower (less radiogenic) $^{206}Pb/^{204}Pb$ isotopic signatures (Fig. 3.12A-C). In contrast, FEM-type exhalites have negative $\delta^{34}S$ values (-18.0‰ to -14.5‰) and have more radiogenic $^{206}Pb/^{204}Pb$ isotopic ratios (Fig. 3.12A-C). The $^{207}Pb/^{204}Pb$ and $^{208}Pb/^{204}Pb$ ratios show less distinction between EMS- and FEM-type mudstones. Two galena Pb isotope analyses of the EMS-type exhalites have very negative $\delta^{34}S$ (-14.7‰) but have Pb isotope ratios that fall within the ranges of the other EMS galena Pb values (Fig. 3.12A-C).

3.7 Discussion

3.7.1 Sulphur isotopic composition of exhalites and the role of bacteria/archea

A hydrothermal origin and formation from black smoker plume fallout of the sulphide-bearing exhalites of the Lemarchant deposit was confirmed by lithogeochemistry (Lode et al., 2015). Hydrothermal exhalites, including those from Lemarchant, have similar sulphur sources to the associated massive sulphides, including sulphur derived from both inorganic processes and organic processes (Ohmoto and Rye, 1979; Ohmoto and Goldhaber, 1997; Huston, 1999; Seal, 2006; Alt and Shanks, 2011). Below we evaluate these various sources.

In VMS deposits the main sources of inorganic sulphur are thermochemical sulphate reduction (TSR) of seawater sulphate, and sulphur leached from igneous and/or sedimentary rocks (+/- direct magmatic sulphur contributions). TSR-derived H_2S forms during hydrothermal circulation via the reaction of heated seawater sulphate ($T>150^oC$)

with ferrous silicates and oxides within the wallrock (Ohmoto and Rye, 1979; Shanks et al., 1981; Ohmoto and Goldhaber, 1997; Shanks, 2001; German and Von Damm, 2003; Seal, 2006; Tivey, 2007; Huston et al., 2011):

$$SO_4^{2-} + 8Fe^{2+} + 10H+ \Rightarrow H_2S + 8Fe^{2+} + 4H_2O \qquad (1).$$

Pyrite-rich polymetallic sulphides in Phanerozoic VMS deposits have $\delta^{34}S$ values in sulphides that are ~18‰ to 25‰ lower than the $\delta^{34}S$ of seawater at the time of formation (Sangster, 1968; Ohmoto and Goldhaber, 1997; Huston, 1999; Seal, 2006). In contrast, igneous sources are much more restricted, and high temperature (~350°C) leaching of sulphides from basement rocks generally yields massive sulphides with $\delta^{34}S$ values of 0±3‰, (Ohmoto and Rye, 1979; Shanks et al., 1987; Campbell and Larson, 1998; Shanks, 2001). Magmatic sulphur from degassing of magmatic volatiles also yields sulphur isotopes in sulphides with $\delta^{34}S$ ~0‰. However, significant $\delta^{34}S$ variations can occur due to magmatic disproportionation of SO_2 in magmatic volatiles, yielding sulphides with substantially more variable $\delta^{34}S$ (e.g., Woodruff and Shanks, 1988; Shanks, 2001; Seal, 2006).

To predict the expected range of $\delta^{34}S$ for TSR-derived sulphur isotopes in pyrite, pyrrhotite, chalcopyrite, and galena in the Lemarchant exhalites, modelling was undertaken following modified methods described in Brueckner et al. (2015) and Cloutier et al. (2015), using formulas described in Ohmoto and Rye (1979), Ohmoto and Goldhaber (1997) and Seal (2006). Due to a lack of reliable experimental fractionation data for arsenopyrite, no modelling was undertaken on arsenopyrite. For the modelling of pyrite, pyrrhotite, chalcopyrite, and galena, an estimated $\delta^{34}S$ of +34.5‰ was used for

Cambrian seawater (Kampschulte and Strauss, 2004; Seal, 2006), and TSR was modelled over the range of 250°C to 350°C, a typical temperature range for VMS-related TSR (Shanks et al., 1981). Based on this modelling, expected $\delta^{34}S$ values for pyrite, pyrrhotite, chalcopyrite, and galena are shown in Figures 3.13A-D and 3.14A-D, and show that some Lemarchant exhalites have a component of TSR-derived sulphur. However, TSR cannot explain the entire range $\delta^{34}S$ observed. For example, pyrite with 100‰ TSR-derived sulphur at a temperature range of 250°C to 350°C is expected to yield $\delta^{34}S$ values from +11.1‰ to +16.6% (Figs. 3.13A, 3.14A). However, mixing with biogenically-derived sulphur sources can dilute these $\delta^{34}S$ values significantly. $\delta^{34}S$ values from -22.4‰ to +14.4% in the measured pyrites have contributions of TSR-sulphur from >0 to 100%, respectively, to the biogenically-derived sulphur. According to the modelling, values below -22.4‰ have no TSR-contributions at all, which indicates to biogenically-derived sulphur only (Fig. 3.14A).

Accordingly, the Lemarchant exhalites show evidence for significant biogenically-derived sulphur. In general, the main source of organic H_2S is expected to be from microbial/biogenic (bacteria and archaea) reduction of seawater sulphate (BSR) at temperatures <120°C (Thode et al., 1951; Kaplan and Rittenberg, 1964; Shanks et al., 1981; Canfield, 2001a; Canfield, 2001b; Shanks, 2001; Seal, 2006; Konhauser, 2007; Alt and Shanks, 2011). The currently known and measured upper limit of temperature for the growth of organisms is achieved by Archea with 121°C, and by hyperthermophile sulphate-reducing bacteria with 110°C that live in hot sediments around deep-sea hydrothermal vents (Gottschal and Prins, 1991; Jørgensen et al., 1992; Elsgaard et al., 1994; Konhauser, 2007).

BSR is a kinetic and mass dependent process, which results in hydrogen sulphide (H_2S) that is enriched in ^{32}S and depleted in ^{34}S (Harrison and Thode, 1957; Harrison and Thode, 1958; Kaplan and Rittenberg, 1964; Canfield, 2001b). BSR follows the principle of Rayleigh distillation processes, because Rayleigh models define isotopic variations, such as the precipitation of minerals from solutions, but also the biogenic reduction of sulphate to sulphide (Shanks et al., 1981; Ohmoto and Goldhaber, 1997; Seal, 2006; Shanks, 2014). Maximum fractionation of ~40 to 45‰ from the $\delta^{34}S$ of the SO_4^{2-} reservoir being reduced were obtained from natural microbial populations and laboratory cultures (Kemp and Thode, 1968; Habicht and Canfield, 1997; Canfield, 2001a; Habicht and Canfield, 2001). This process commonly occurs in semi-permeable sediments, near the interface with the oxygenated ambient seawater, and can take place as long as there is an SO_4^{2-} supply, sufficient organic matter, and temperatures remain <120°C (Habicht and Canfield, 1997; Habicht and Canfield, 2001; Seal, 2006).

Pyrite-framboids are a common by-product of BSR-related processes. However, biogenically-produced H_2S can be fixed into sulphides with any kind of metals (or metalloid) present in the pore-fluids, not only Fe^{2+}, but also including hydrothermally derived Cu^{+}, Zn^{2+}, Pb^{2+}, and As. Both pyrite framboids, and these base metal-sulphides, are expected to yield negative $\delta^{34}S$ values, characteristic of biogenically-derived sulphur. On the other hand, positive $\delta^{34}S$ values only do not exclude the presence of microbial sulphate reduction. If hydrothermal fluids with TSR-derived H_2S contribute to the pore-fluids in the hydrothermal exhalites, as shown above, the precipitated sediment-hosted sulphides will have mixed sulphur-signatures with $\delta^{34}S$ ranging from negative to positive values.

The Lemarchant exhalites display mixed sulphur isotope signatures consistent with both TSR- and biogenically-derived sulphur components (Fig. 3.10A). The preponderance of negative $\delta^{34}S$ values in the exhalites indicates the presence of significant microbial H_2S in the sulphides. There is a variation within this BSR signature, with exhalites distal from mineralization having lower $\delta^{34}S$ than those proximal (EMS-type) with a greater input from hydrothermal TSR (or direct or leached magmatic S) (Figs. 3.9A, C, and 3.10B). Similar variation in the $\delta^{34}S$ signatures were reported by Roth (2002) from carbonaceous and metalliferous argillites of the Eskay Creek deposit, British Columbia, Canada.

To quantify the relative roles of BSR and TSR, a two component mixing model is used. The modelling was undertaken using modified methods described by Ohmoto and Rye (1979), Ohmoto and Goldhaber (1997), Seal (2006), Brueckner et al. (2015), and Cloutier et al. (2015). The models were used for the sulphur isotope data for pyrite, pyrrhotite, chalcopyrite, and galena. For these calculations the biogenic sulphur reservoir was assumed to have an average $\delta^{34}S$ of -25‰, which is reflected by the lower end of the bulk of the polymetallic sulphide data (Fig. 3.10A). The same estimate of $\delta^{34}S$ of +34.5‰ for Cambrian seawater (Kampschulte and Strauss, 2004) was used, as well as a temperature of 300°C for producing TSR-derived H_2S. The temperature of 300°C for the TSR-derived H_2S reflects the assumption that the Lemarchant hydrothermal system likely did not reach much higher temperatures than 300°C, based on the lack of abundant chalcopyrite in the massive Pb-Zn-sulphides. For BSR-derived H_2S, temperatures of 0°C, 50°C, 100°C, and 120°C were chosen to calculate the mixing lines, bracketing the known temperature ranges at which bacteria/archaea can thrive and BSR occurs (Jørgensen et al.,

1992; Elsgaard et al., 1994; Ohmoto and Goldhaber, 1997). Results of the mixing calculations illustrate that pyrrhotite samples contain 0 % to 48 % TSR-derived sulphur (Fig. 3.14B). The close spatial association of arsenopyrite with pyrrhotite, and its low $\delta^{34}S$ (Figs. 3.9A, 3.10B), suggest both minerals are predominantly co-genetically formed, when reactions with organic matter causes low fO_2 and conditions favouring arsenopyrite and pyrrhotite precipitation (biogenic-diagenetic origin) (Hannington et al., 1995). In contrast, chalcopyrite and galena have between ~5 % and 82 %, and ~20 % to 100 % of TSR-derived sulphur, respectively, indicating a greater hydrothermal sulphur input into their genesis (Fig. 3.14C-D). The variability of pyrite $\delta^{34}S$ also indicates TSR-BSR mixing, with euhedral pyrite having a greater TSR sulphur component. Conversely, the pyrite-framboids have BSR-only, or BSR-dominated, sulphur (Fig. 3.9A).

For EMS-type exhalites, however (Fig. 3.8A-B), those proximal to massive sulphide mineralization have values that are lower than those typically expected simply from TSR of Cambrian seawater (Kampschulte and Strauss, 2004). As these depleted values could be attributed to BSR, there is potential that they have contributions from igneous sources. This is possible, because the igneous-like signatures occur in euhedral pyrite, chalcopyrite, and galena, proximal to massive sulphide mineralization (Fig. 3.7A-B), which are also associated with electrum ± Hg ± Sb (Fig. 3.7D-E) as well as acanthite (Fig. 3.7F), pyrargyrite, stephanite, and that have epithermal suite element enrichments (Lode et al., 2015). These near zero $\delta^{34}S$ values are similar to values expected from igneous sources; however, the nature of the igneous source (i.e., leaching from basement vs. magmatic fluids) is difficult to determine unequivocally with sulphur isotopes alone.

Nevertheless, the more negative $\delta^{34}S$ values are potentially more closely affiliated with magmatic fluids, as magmatic disproportionation and subsequent SO_2 condensation is known to produce H_2S and sulphides with $\delta^{34}S<0$ (Rye, 1993; Huston et al., 2011). Such a sulphur source is also consistent with observed mineral associations, enrichments of epithermal suite elements, and the sulphosalt-rich mineralogy of the underlying massive sulphides in the Lemarchant deposit (Gill and Piercey, 2014; Gill et al., 2015; Lode et al., 2015). Precious metal enrichment and post-VMS mineralization potassium feldspar alteration further support the previous interpretations that there was a magmatic-epithermal input into the Lemarchant VMS system in a shallow water tectonic setting that enabled boiling (Hannington et al., 1999; Mercier-Langevin et al., 2011; Gill and Piercey, 2014; Gill et al., 2015; Lode et al., 2015). Precious metal bearing VMS-epithermal hybrid deposits are known to occur in shallow water environments associated with arc rifting (Sillitoe et al., 1996; Hannington et al., 1999; Mercier-Langevin, 2011); a tectonic environment which is suggested for the Lemarchant deposit and the Tally Pond belt (Piercey et al., 2014; Lode et al., 2015).

In addition to near zero $\delta^{34}S$ values, there are also some extremely negative values in pyrite (i.e., $\delta^{34}S < -25‰$), which are much lower than can be reasonably explained by BSR only, using fractionation factors of ~45‰ (Habicht and Canfield, 1997; Canfield, 2001a; Habicht and Canfield, 2001). Even if seawater sulphate showed substantial variation in the Cambrian (e.g., $\delta^{34}S$ = +28.8‰ to 34.5‰; Sangster, 1968; Kampschulte and Strauss, 2004), this would only yield values $\delta^{34}S$ values from BSR from -16.2‰ to -10.5 (Habicht and Canfield, 1997; Canfield, 2001a; Habicht and Canfield, 2001). Accordingly, another process for ^{34}S depletion in the sulphur isotopic system is required

to create the large implied fractionation factors of $\Delta^{34}S_{Seawater\ sulphate\text{-}H_2S}$ = 73.3‰ (Fig. 3.10A) in these samples, and we propose that these extremely low values are due to sulphide-oxidizing bacteria and microbial disproportionation of sulphur intermediates. However, large fractionation factors up to 72‰ for single-step microbial sulphate reduction is reported by Wortmann et al. (2001) from deep (>20 m below seawater surface) pore-waters in a carbonate ramp. This process may represent another possibility to create large fractionation factors (Wortmann et al., 2001); however, this deep brine poor water environment in carbonate rocks is exceptional settings and their microbial communities likely are different from those occurring in microbial mats at the sediment-water interface (Wortmann et al., 2001).

Sulphide oxidizing bacteria (e.g., microbial mats of *Beggiatoa* sp.) are known to occur in ridge environments as surface films on sulphidic sediments associated with sulphate reducers, create some of the largest fractionation rates reported (Kaplan and Rittenberg, 1964; Jørgensen, 1990; Elsgaard et al., 1994, Frank et al., 2013). These *Beggiatoa* sp. mats occur around hydrothermally active sites, e.g., in the Guaymas Basin (Elsgaard et al., 1994). The biogenic oxidation (BSO) involves non-phototrophic oxidation of reduced sulphur compounds (H_2S, S_0) and is coupled to the microbial disproportionation of sulphur intermediate compounds (Canfield, 2001b). These biologically-mediated processes fractionate sulphur isotopes towards more negative values, and, more importantly, the products of microbial fermentation and thermal degradation of organic matter provide the substrate that is required for microbial/biogenic SO_4^{2-} reduction (BSR) (Kaplan and Rittenberg, 1964; Jørgensen, 1990; Elsgard et al.,

1994, Canfield, 2001b). Thereby, fermentative microbes decompose dead microbial biomass, which stimulates BSR (Elsgard et al., 1994). These diverse microbial communities (chemolithotrophic bacteria/archaea) also commonly occur around hydrothermal vent sites and in areas of diffuse venting, as in exhalites (Gottschal and Prins, 1991; Elsgaard et al., 1994; Hannington et al., 1995; Canfield, 2001a; Canfield, 2001b; Frank et al., 2013), which would be consistent with their presence in the Lemarchant exhalites. Furthermore, the very common finely laminated texture (e.g., Fig. 3.6A-D), stromatolite-like bulbous layers in finely laminated mudstone and chert (Konhauser, 2007) (Fig. 3.IA-B, Appendix 3.2), and bands in the mudstones containing tubes of pyrite with interstitial chalcopyrite and sphalerite with a general textural robustness, are all features consistent with them originally being microbial mats (Berkenbosch et al., 2012; Schieber, J. *pers. comm.* (Fig. 3.6C, G).

Microbial mats can serve as the nucleus for mineral growth, and microbially mediated changes in pH and fO_2 can induce local sulphide precipitation, which can influence the isotopic compositions of the mineralizing sulphides and sulphates (Jørgensen et al., 1992). Chemolithoautotrophic microbial mat-forming bacterial and archaeal communities consist not only of sulphate-reducers and -oxidizers, but also of microbial species that gain the energy necessary for their metabolism via microbial disproportionation of sulphur intermediate compounds, such as elemental sulphur (S^0), thiosulphate ($S_2O_3^{2-}$), and sulphite (SO_3^{2-}) (Figs. 3.15, 3.16B) (Bak and Pfennig, 1987; Jørgensen, 1990; Jørgensen et al., 1992; Canfield, 2001b; Konhauser, 2007). The SO_4^{2-} produced via microbial disproportionation can thus then be further utilized for BSR,

resulting in a cyclic process involving various species of sulphur. Microbial disproportionation of sulphur intermediate compounds is a process that can cause further ^{34}S depletion in the produced sulphide of up to ~6‰ and can be described with following reactions (Bak and Pfennig, 1987; Jørgensen, 1990; Habicht and Canfield, 1997; Canfield, 2001a):

$$S_2O_3^{2-} + H_2O \Rightarrow H_2S + SO_4^{2-} \quad (2)$$

$$4SO_3^{2-} + 2H^+ \Rightarrow H_2S + 3SO_4^{2-} \quad (3)$$

$$4S^0 + 4H_2O \Rightarrow 3H_2S + SO_4^{2-} + 2H^+ \quad (4)$$

Reaction (2) does not require an electron donor or acceptor, and is biologically catalysed. However, in the presence of Fe-oxyhydroxides and organic matter, which are both common in hydrothermal sediments, microbes can utilize these phases as electron acceptor and donor, respectively (Jørgensen, 1990):

$$S_2O_3^{2-} + CH_3COO^- + H^+ \Rightarrow 2HS^- + 2CO_2 + H_2O \quad (5)$$

$$S_2O_3^{2-} + 8FeOOH + 14H^+ \Rightarrow 2SO_4^{2-} + 8Fe^{2+} + 11H_2O \quad (6)$$

The FEM-type exhalite sample (CNF20927) shown in Figure 3.6C, G contains two ~1 mm thick bands of sulphide in a finely laminated carbonaceous exhalite. These bands consist of pyrite tubes with interstitial chalcopyrite and sphalerite, as well as arsenopyrite. The sulphur isotopic analysis of one these tubes yielded a $\delta^{34}S$ of -30.5‰, which implies additional biogenic sulphur sources other than BSR, e.g., BSO and microbial disproportionation. Therefore, it is suggested that the tubes are microbial in origin, and that the two ~1 mm thick bands are sulphidized mats of microbial filaments. The interstitial chalcopyrite, sphalerite, and arsenopyrite - which display mixed,

biogenically- and TSR-derived sulphur sources - were precipitated from later-stage metalliferous fluids overprinting earlier formed tubes. Similar microbial tubes are reported related to modern black smoker chimneys of the Brothers submarine volcanoes in the Kermadec Arc (Berkenbosch et al., 2012).

Figure 3.15 delineates the process pathway for sulphur isotopic compositions occurring in sedimentary sulphides. In this scheme, initial sulphate reduction (BSR and/or TSR) is followed by an intermediate step of sulphide oxidation. Subsequent microbial disproportionation of sulphur intermediate compounds creates H_2S that is further depleted in ^{34}S, and SO_4^{2-} that can be further utilized in the reduction processes (Canfield, 2001a). A combination of cycling and cumulative ^{34}S depletion during these microbial processes (BSR, BSO, microbial disproportionation), provides a plausible explanation of the large fractionation factors (>45‰) observed in hydrothermal sedimentary sulphides in general, and, in particular, the Lemarchant exhalite pyrite.

3.7.2 Open versus closed system conditions

Microbial sulphate reduction, and the isotopic composition of precipitated BSR-related sulphides, depend on whether there is a limited (closed) or unlimited (open) source of seawater SO_4^{2-} (Kemp and Thode, 1968; Ohmoto and Goldhaber, 1997). In many ore deposits, whether the system is open or closed depends on whether more SO_4^{2-} is available for reduction than SO_4^{2-} is reduced, which in turn can have influence on the nature, preservation and processes of sulphide deposition (e.g., Goodfellow and Peter, 1996). When the water column is oxygenated there is generally an effectively infinite

supply of seawater sulphate, such that the H_2S generated, and subsequently fixed as sedimentary sulphides, has strongly negative $\delta^{34}S$ values with relatively constant fractionation factors $\Delta^{34}S_{sulphide\text{-}sulphate}$ relative to the seawater reservoir (Ohmoto and Goldhaber, 1997; Huston, 1999; Canfield, 2001b; Seal, 2006). In anoxic, closed environments there is commonly a stratified water column, which if euxinic, is dominated by H_2S, and the supply of SO_4^{2-} is finite and the re-oxidation of H_2S is limited. In these environments, lighter $^{32}SO_4^{2-}$ is preferentially utilized in the early microbially-formed sulphides, resulting in initially negative sulphide $\delta^{34}S$ values (Bottrell and Newton, 2006). However, in a persistently closed system without a supply of fresh sulphate, the microbes eventually metabolize $^{34}SO_4^{2-}$ resulting in sulphate-recycling and $\delta^{34}S$ values that gradually shift towards progressively heavier values (e.g. Ohmoto and Goldhaber, 1997).

Seal et al. (2000) and Seal (2006) produced model histograms of $\delta^{34}S$ distribution for sedimentary sulphides as a function of whether the environment was open or closed to seawater sulphate. Narrow, restricted ranges in $\delta^{34}S$ represent open system conditions, whereas wide ranging $\delta^{34}S$ reflects near closed-system conditions. Transitional patterns represent partially closed and open system conditions (Seal, 2000; Seal, 2006). The distribution of $\delta^{34}S$ in the Lemarchant exhalites suggests deposition under open to partially closed conditions (Fig. 3.8). However, the presence of abundant barite at Lemarchant, and the rare-earth element patterns in the Lemarchant exhalites, are consistent with deposition from an oxygenated water column (Lode et al., 2015). Therefore, the widely distributed $\delta^{34}S$ values in the frequency histograms for Lemarchant hydrothermal mudstone sulphides (Fig. 3.8) are interpreted to result from mixing between

hydrothermal, inorganically TSR-derived sulphur and biogenic sulphur on the flanks of the sulphide mound.

3.7.3 Lead isotopic composition of hydrothermal exhalites

Lead isotopes in sulphides are a proxy for the sources of Pb (and, by interference, other metals) in massive sulphide deposits and associated metalliferous sediments (Zartman and Doe, 1981; Swinden and Thorpe, 1984; Kramers and Tolstikhin, 1997; Tosdal et al., 1999, Ayuso et al., 2003). The Pb sources in VMS are derived predominantly from leached basement rocks, which can have varying Pb isotope signatures and may contain Pb from different reservoirs, depending on their origin (Franklin et al., 1981; Swinden and Thorpe, 1984; Tosdal et al., 1999; Ayuso et al., 2003). Lead isotopes in the Lemarchant exhalites were measured *in situ* on galena, which is used as a proxy for the Pb in other sulphide phases. This is supported by both paragenetic relationships and S isotopic data. For example, galena is paragenetically and spatially associated with chalcopyrite and has similar $\delta^{34}S$ (Fig. 3.9C), suggesting deposition from the same hydrothermal fluid.

Overall, the Pb isotopic compositions of the Lemarchant exhalite overlap values present in various massive sulphide deposits in the Tally Pond Belt, including the Lemarchant massive sulphides (Fig. 3.11A-B; Swinden and Thorpe, 1984; Pollock and Wilton, 2001; Gill, 2015; Piercey, *unpublished data*). The observed variations in Pb isotope ratios require derivation from juvenile to more evolved crustal sources (Fig. 3.11A-B). Leaching of basement rocks could explain the Pb isotope variations, as the

underlying stratigraphy of the Sandy Brook Group is bimodal, with mafic to felsic rocks that have varying isotopic signatures (Rogers et al., 2006). Further, the entire Victoria Lake supergroup is of peri-Gondwanan affinity and has a peri-continental character (Rogers et al., 2006; Zagorevski et al., 2010). Thus, variations from more continental to juvenile are expected (e.g., Swinden and Thorpe, 1984; Rogers et al., 2006; Zagorevski et al., 2010). The overlapping clusters of the EMS-type exhalites and the massive sulphides of the Lemarchant deposit suggest that they have the same, by leaching homogenized, Pb source.

While leaching of basement can explain the absolute variation in exhalite Pb isotope geochemistry, the presence of more evolved Pb isotope signatures in distal FEM-type exhalites relative to the more juvenile signatures in EMS-type exhalites proximal from mineralization cannot be explained by leaching alone. This suggests a more radiogenic and evolved (possibly detritally- or seawater-derived) Pb source contributing to the FEM-type exhalites (Gale et al., 1981; Spooner and Gale, 1982; Mills and Elderfield, 1995), which is not, or only minimally, shared with the proximal mudstones and massive sulphides at Lemarchant. Interestingly, the FEM-type exhalites with more radiogenic $^{206}Pb/^{204}Pb$ also yield $\delta^{34}S$ values that indicate to the presence of less TSR-derived hydrothermal sulphur, whereas proximal EMS exhalites have a lower, more juvenile $^{206}Pb/^{204}Pb$ and a stronger hydrothermal signature (Fig. 3.12A). This correspondence of low $\delta^{34}S$ and more juvenile Pb isotopic signatures may also serve as a vector towards mineralization in proximal environments in other metalliferous mudstones in the Lemarchant deposit area, the Tally Pond belt, and globally.

3.8 Conclusions

The Lemarchant hydrothermal exhalites record different S sources and processes and precipitated prior to, during, and after the formation of massive sulphide mineralization. The majority of the sulphides hosted in the Lemarchant exhalites have mixed inorganic and organic sources and processes, including: 1) sulphur derived from thermochemical reduction of seawater sulphate TSR; 2) biogenic sulphur; and 3) potential magmatic contributions by either leaching of crustal rocks and/or direct magmatic fluid/volatile input. The biogenic processes (bacterial/archaeal) involved in the sulphur isotope fractionation in the Lemarchant exhalites include: 1) the biogenic/microbial reduction of seawater sulphate (BSR); 2) the microbial disproportionation of sulphur intermediates; and 3) an intermediate step of biogenic sulphide oxidation (BSO). These organic processes occurred within microbial mats that covered the sulphide-rich metalliferous sediment, which may have also helped to consolidate the exhalites, enhancing sulphide precipitation. Despite the presence of abundant negative $\delta^{34}S$ values and the importance of biogenic processes, exhalites closely associated with massive sulphides have a greater proportion of TSR-derived S (+/- igneous/magmatic S) than interflow exhalites and exhalites that have no immediate association with mineralization.

Lead isotopes in galena from the Lemarchant exhalites suggest they have both juvenile and more evolved Pb sources. The mixed Pb is consistent with derivation from underlying basement rocks. In exhalites proximal to mineralization, however, there is a correspondence between lower $^{206}Pb/^{204}Pb$ ratios and more positive $\delta^{34}S$ values within the range of TSR, suggesting that these exhalites have a greater hydrothermal component

with potential contributions from magmatic S sources and juvenile Pb derived from leaching of mafic volcanic basement rocks. The correspondence of juvenile Pb and hydrothermal $\delta^{34}S$ derived from TSR may be a useful vector for proximity to mineralization in hydrothermal exhalites, and in other VMS hydrothermal systems in similar exhalative environments globally.

3.9 Acknowledgements

This research is funded by the Canadian Mining Research Organization (CAMIRO) and an NSERC CRD grant. Kind support was provided by Dianne and Charlie Fost, Michael Vande Guchte, Alexandria Marcotte, and Gerry Squires from Paragon Minerals Corporation (now Canadian Zinc Corporation). Research is also funded by the NSERC-Altius Industrial Research Chair in Mineral Deposits, funded by NSERC, Altius Resources Inc., and the Development Corporation of Newfoundland and Labrador. The authors would like to thank for the help and support from Keir Hiscock, Pam King, Michael Buschette, Shannon Gill, Shannon Guffey, Dario Harazim, and Inês Nobre Silva. Also very much appreciated are the reviews and suggestions of the *Mineralium Deposita* reviewers, David Huston and Fernando Tornos, which greatly improved the manuscript.

3.10 References

Alt, J. C., and Shanks, W. C., 2011, Microbial sulfate reduction and the sulfur budget for a complete section of altered oceanic basalts, IODP Hole 1256D (eastern Pacific): Earth and Planetary Science Letters, v. 310, p. 73-83.

Ayuso, R. A., Wooden, J. L., Foley, N. K., Slack, J. F., Sinha, A. K., and Persing, H., 2003, Pb isotope geochemistry and U-Pb zircon (SHRIMP-RG) ages of the Bald Mountain and Mount Chase massive sulfide deposits, northern Maine; mantle and

crustal contributions in the Ordovician: Economic Geology Monograph, v. 11, p. 589-609.

Bak, F., and Pfennig, N., 1987, Chemolithotrophic growth of Desulfovibrio sulfodismutans sp. nov. by disproportionation of inorganic sulfur compounds: Arch Microbiology, v. 147, p. 184-189.

Berkenbosch, H. A., de Ronde, C. E. J., Gemmell, J. B., McNeill, A. W., and Goemann, K., 2012, Mineralogy and Formation of Black Smoker Chimneys from Brothers Submarine Volcano, Kermadec Arc: Economic Geology, v. 107, p. 1613-1633.

Binns, R. A., 2004, Eastern Manus Basin, Papua New Guinea: guides for volcanogenic massive sulphide exploration from a modern seafloor analogue, *in* McConachy, T. F., and McInnes, B. I. A., eds., CSIRO Explores, 2, p. 59-80.

Boström, K., and Peterson, M. N., 1966, Precipitates from hydrothermal exhalations on the East Pacific Rise: Economic Geology, v. 61, p. 1258-1265.

Boström, K., Peterson, M. N., Joensuu, O., and Fisher, D. E., 1969, Aluminum-poor ferromanganoan sediments on active oceanic ridges: Journal of Geophysical Research, v. 74, p. 3261-3270.

Bottrell, S. H., and Newton, R. J., 2006, Reconstruction of changes in global sulfur cycling from marine sulfate isotopes: Earth-Sciences Reviews, v. 75, p. 59-83.

Brueckner, S. M., Piercey, S. J., Layne, G. D., Piercey, G., and Sylvester, P. J., 2015, Variations of sulphur isotope signatures in sulphides from the metamorphosed Ming Cu(-Au) volcanogenic massive sulphide deposit, Newfoundland Appalachians, Canada: Mineralium Deposita, v. 50, p. 619-640.

Campbell, A. R., and Larson, P. B., 1998, Introduction to stable isotope applications in hydrothermal systems., *in* Richards, J. P., and Larson, P. B., eds., Techniques in Hydrothermal Ore Deposits Geology: Reviews in Economic Geology, p. 173-193.

Campbell, I. H., Lesher, C. M., Coad, P., Franklin, J. M., Gorton, M. P., and Thurston, P. C., 1984, Rare-earth element mobility in alteration pipes below massive Cu-Zn sulfide deposits: Chemical Geology, v. 45, p. 181-202.

Canadian Zinc Corporation Press Release December 11, 2013 available at:
www.canadianzinc.com/images/Docs/News_Releases/CZNNR20131211.pdf
www.sedar.com/DisplayCompanyDocuments.do?lang=EN&issuerNo=00002753

Canfield, D. E., 2001a, Biogeochemistry of Sulfur Isotopes: Reviews in Mineralogy and Geochemistry, v. 43, p. 607-636.

_____2001b, Isotope fractionation by natural populations of sulfate-reducing bacteria: Geochimica et Cosmochimica Acta, v. 65, p. 1117-1124.

Cloutier, J., Piercey, S. J., Layne, G. D., Heslop, J. B., and Hussey, A. M., in press, Styles, Textural Evolution and Sulfur Isotope Systematics of Cu-rich Sulfides from the Cambrian Whalesback Volcanogenic Massive Sulfide (VMS) Deposit, Central Newfoundland, Canada: Economic Geology.

Copeland, D. A., 2009, Assessment Report on Prospecting, Lithogeochemical Sampling and Data Interpretation on the Harpoon Property (Licenses 7695M, 10461M, 10464M, 10465M, 10607M, 12357M, 12885M, 13583M, 13448M, 13449M and 13667M) and the South Tally Pond Property (Licences 8183M, 9569M and 14158M) Lake Ambrose Area, Newfoundland and Labrador. NTS 12A/10 and 12A/07, Paragon Minerals Corporation.

Copeland, D. A., Toole, R. M., and Piercey, S. J., 2009, 10th Year Supplementary Assessment Report on Soil Sampling, Linecutting, Titan 24 Geophysical Surveying, Diamond Drilling and Petrography, Licence 8183M, South Tally Pond Property, Rogerson Lake Area, Newfoundland and Labrador, NTS 12A/10 and 12A/07: St. John's, NL, Canada, Newfoundland and Labrador Geological Survey Assessment File, p. 56.

Dias, A. S., Mills, R. A., Taylor, R. N., Ferreira, P., and Barriga, F. J. A. S., 2008, Geochemistry of a sediment push-core from the Lucky Strike hydrothermal field, Mid-Atlantic Ridge: Chemical Geology, v. 247, p. 339-351.

Dunning, G. R., Kean, B. F., Thurlow, J. G., and Swinden, H. S., 1987, Geochronology of the Buchans, Roberts Arm, and Victoria Lake groups and Mansfield Cove Complex, Newfoundland: Canadian Journal of Earth Sciences, v. 24, p. 1175-1184.

Dunning, G. R., Swinden, H. S., Kean, B. F., Evans, D. T. W., and Jenner, G. A., 1991, A Cambrian island arc in Iapetus; geochronology and geochemistry of the Lake Ambrose volcanic belt, Newfoundland Appalachians: Geological Magazine, v. 128, p. 1-17.

Elsgaard, L., Isaksen, M. F., Jørgensen, B. B., Alayse, A.-M., and Jannasch, H. W., 1994, Microbial sulfate reduction in deep-sea sediments at the Guaymas Basin hydrothermal vent area: Influence of temperature and substrates: Geochimica et Cosmochimica Acta, v. 58, p. 3335-3343.

Evans, D. T. W., and Kean, B. F., 2002, The Victoria Lake Supergroup, central Newfoundland - its definition, setting and volcanogenic massive sulphide mineralization, Newfoundland and Labroador Department of Mines and Energy, Geological Survey, Open File NFLD/2790, p. 68.

Frank, K. L., Rogers, D. R., Olins, H. C., Vidoudez, C., and Girguis, P. R., 2013, Characterizing the distribution and rates of microbial sulfate reduction at Middle Valley hydrothermal vents: International Society for Microbial Ecology, v. 7, p. 1391-1401.

Franklin, J. M., Gibson, H. L., Galley, A. G., and Jonasson, I. R., 2005, Volcanogenic Massive Sulfide Deposits, *in* Hedenquist, J. W., Thompson, J. F. H., Goldfarb, R. J., and Richards, J. P., eds., Economic Geology 100th Anniversary Volume: Littleton, CO, Society of Economic Geologists, p. 523-560.

Franklin, J. M., Sangster, D. M., and Lydon, J. W., 1981, Volcanic-associated massive sulfide deposits, *in* Skinner, B. J., ed., Economic Geology Seventy-Fifth Anniversary Volume, Society of Economic Geologists, p. 485-627.

Franklin, J. M., and Thorpe, R. I., 1982, Comparative metallogeny of the Superior, Slave and Churchill provinces: Special Paper - Geological Association of Canada, v. 25, p. 3-90.

Fraser, D., Giroux, G. A., Copeland, D. A., and Devine, C. A., 2012, NI-43-101 Technical Report and Mineral Resource Estimate on the Lemarchant Deposit, South Tally Pond VMS Project, central Newfoundland, Canada for Paragon Minerals Corporation, National Instrument 43-101 Technical Report: Toronto, ON, Canada, National Instrument 43-101 Technical Report, p. 137.

Füchtbauer, H., Heling, D., Müller, G., Richter, D. K., Schmincke, H.-U., Schneider, H.-J., Valeton, I., Walther, H. W., and Wolf, M., 1988, Sedimente und Sedimentgesteine - Sedimentpetrologie, Teil II: Stuttgart.

Gale, N. H., Spooner, E. T., and Potts, P. J., 1981, The lead and strontium isotope geochemistry of metalliferous sediments associated with Upper Cretaceous ophiolitic rocks in Cyprus, Syria, and the Sultanate of Oman: Canadian Journal of Earth Sciences = Journal Canadien des Sciences de la Terre, v. 18, p. 1290-1302.

Galley, A. G., Hannington, M., and Jonasson, I., 2007, Volcanogenic massive sulphide deposits, *in* Goodfellow, W. D., ed., Mineral Deposits of Canada: A Synthesis of Major Deposit-types, District Metallogeny, the Evolution of Geological Provinces, and Exploration Methods, Special Publication 5, Mineral Deposits Division, Geological Association of Canada, p. 141-161.

German, C. R., and Von Damm, K. L., 2003, Hydrothermal Processes, Treatise on Geochemistry: Oxford, Pergamon, p. 181-222.

Gill, S. B., 2015, Mineralogy, metal zoning, and genesis of the Zn-Pb-Ba-Ag-Au Lemarchant volcanogenic massive sulfide (VMS) deposit, Memorial University of Newfoundland.

Gill, S. B., and Piercey, S. J., 2014, Preliminary mineralogy of barite-associated sulphide mineralization in the Ordovician Zn-Pb-Cu-Ag-Au Lemarchant volcanogenic massive sulphide deposit, Newfoundland and Labrador: Current Research - Geological Survey of Canada, v. 2013-17, p. 15.

Goodfellow, W. D., and Peter, J. M., 1996, Sulfur isotope composition of the Brunswick No. 12 massive sulfide deposit, Bathurst Mining Camp, New Brunswick: implications for ambient environment, sulfur source and ore genesis: Canadian Journal of Earth Sciences, v. 33, p. 231-251.

Gottschal, J. C., and Prins, R. A., 1991, Thermophiles: A life at elevated temperatures: Trends in Ecology and Evolution, v. 6, p. 157-162.

Gundersen, J., K., Jørgensen, B. B., Larsen, E., and Jannasch, H. W., 1992, Mats of giant sulphur bacteria on deep-sea sediments due to fluctuating hydrothermal flow: Nature, v. 360, p. 454-456.

Gurvich, E. G., 2006, Metalliferous sediments of the World Ocean - Fundamental theory of deep sea hydrothermal sedimentation: Berlin Heidelberg, Springer.

Habicht, K. S., and Canfield, D. E., 1997, Sulfur isotope fractionation during bacterial sulfate reduction in organic-rich sediments: Geochimica et Cosmochimica Acta, v. 61, p. 5351-5361.

_____2001, Isotope fractionation by sulfate-reducing natural populations and the isotopic composition of sulfide in marine sediments: Geology, v. 29, p. 555-558.

Hannington, M. D., 2009, Modern submarine hydrothermal systems - a global perspective on distribution, size, and tectonic settings, *in* Cousens, B. L., and Piercey, S. J., eds., Submarine Volcanism and Mineralization: Modern through Ancient, Shourt Course 29-30 May 2008, Geological Association of Canada, p. 91-148.

_____2014, Volcanogenic massive sulfide deposits, *in* Holland, H. D., and Turekian, K.K., ed., Treatise on Geochemistry 2nd Edition, 8. Reviews in Economic Geology, Elsevier Ltd, p. 319-350.

Hannington, M. D., Jonasson, I. R., Herzig, P. M., and Petersen, S., 1995, Physical and chemical processes of seafloor mineralization at mid-ocean ridges, *in* Humphris, S. E., Zierenberg, R. A., mullineaux, L. S., and Thomson, R. S., eds., Seafloor Hydrothermal Systems: Physical, Chemical, Biological and Geological Interactions, American Geophysical Union Monograph 91, p. 115-157.

Hannington, M. D., Poulsen, K. H., Thompson, J. F. H., and Sillitoe, R. H., 1999, Volcanogenic gold in the massive sulfide environment, *in* Barrie, C. T., and Hannington, M. D., eds., Volcanic-Associated Massive Sulfide Deposits: Processes and Examples in Modern and Ancient Settings, Reviews in Economic Geology 8: Littleton, CO, USA, Society of Economic Geologists, p. 325-356.

Harazim, D., Callow, R. H. T., and McIlroy, D., 2013, Microbial mats implicated in the generation of intrastratal shrinkage ('synaeresis') cracks: Sedimentology, v. 6, p. 1621-1638.

Harrison, A. G., and Thode, H. G., 1957, The kinetic isotope effect in the chemical reduction of sulphate: Trans. Faraday Society, v. 53, p. 1648-1651.

_____1958, Mechanism of the bacterial reduction of sulphate from isotope fractionation studies: Trans. Faraday Soc., v. 54, p. 84-92.

Haymon, R. M., Fornari, D. J., Von Damm, K. L., Lilley, M. D., Perfit, M. R., Edmond, J. M., Shanks Iii, W. C., Lutz, R. A., Grebmeier, J. M., Carbotte, S., Wright, D., McLaughlin, E., Smith, M., Beedle, N., and Olson, E., 1993, Volcanic eruption of the mid-ocean ridge along the East Pacific Rise crest at 9°45–52′N: Direct submersible observations of seafloor phenomena associated with an eruption event in April, 1991: Earth and Planetary Science Letters, v. 119, p. 85-101.

Haymon, R. M., and Kastner, M., 1981, Hot spring deposits on the East Pacific Rise at 21°N: preliminary description of mineralogy and genesis: Earth and Planetary Science Letters, v. 53, p. 363-381.

Hekinian, R., Hoffert, M., Larqué, P., Cheminée, J. L., Stoffers, P., and Bideau, D., 1993, Hydrothermal Fe and Si oxyhydroxide deposits from South Pacific intraplate volcanoes and East Pacific Rise axial and off-axial regions: Economic Geology, v. 88, p. 2099-2121.

Hinchey, J. G., and McNicoll, V., 2009, Tectonostratigraphic architecture and VMS mineralization of the southern Tulks Volcanic Belt: New insights from U-Pb geochronology and lithogeochemistry, *in* Pereira, C. P. G., and Walsh, D. G., eds., Current Research, Report 09-01: St. John's, NL, Canada, Geological Survey Branch, p. 13-42.

Hodkinson, R. A., and Cronan, D. S., 1995, Hydrothermal sedimentation at ODP Sites 834 and 835 in relation to crustal evolution of the Lau backarck basin, *in* Parson, L. M., Walker, C. L., and Dixon, D. R., eds., Hydrothermal vents and processes., 87, Geological Society Special Publication, p. 231-248.

Huston, D., Relvas, J., Gemmell, J., and Drieberg, S., 2011, The role of granites in volcanic-hosted massive sulphide ore-forming systems: an assessment of magmatic–hydrothermal contributions: Mineralium Deposita, v. 46, p. 473-507.

Huston, D. L., 1999, Stable isotopes and their significance for understanding the genesis of volcanic-hosted massive sulfide deposits; a review: Reviews in Economic Geology, v. 8, p. 157-179.

Jørgensen, B. B., 1990, A thiosulfate shunt in the sulfur cycle of marine sediments: Science, v. 249, p. 152-154.
Jørgensen, B. B., Isaksen, M. F., and Jannasch, H. W., 1992, Bacterial sulfate reduction above 100°C in deep-sea hydrothermal vent sediments: Science, v. 258, p. 1756-1757.
Kalogeropoulos, S. I., and Scott, S. D., 1989, Mineralogy and geochemistry of an Archean tuffaceous exhalite; the Main Contact Tuff, Millenbach Mine area, Noranda, Quebec: Canadian Journal of Earth Sciences, v. 26, p. 88-105.
Kampschulte, A., and Strauss, H., 2004, The sulfur isotopic evolution of Phanerozoic seawater based on the analysis of structurally substituted sulfate in carbonates: Chemical Geology, v. 204, p. 255-286.
Kaplan, I. R., and Rittenberg, S. C., 1964, Microbiological Fractionation of Sulphur Isotopes: Journal of General Microbiology, v. 34, p. 195-212.
Kemp, A. L. W., and Thode, H. G., 1968, The mechanism of the bacterial reduction of sulphate and of sulphite from isotope fractionation studies: Geochimica et Cosmochimica Acta, v. 32, p. 71-91.
Konhauser, K. O., 2007, Introduction to Geomicrobiology, Blackwell Publishing Ltd, 440 p.
Kramers, J. D., and Tolstikhin, I. N., 1997, Two terrestrial lead isotope paradoxes, forward transport modelling, core formation and the history of the continental crust: Chemical Geology, v. 139, p. 75-110.
Lode, S., Piercey, J. S., and Devine, C. A., 2015, Geology, mineralogy, and lithogeochemistry of metalliferous mudstones associated with the Lemarchant volcanogenic massive sulfide deposit, Tally Pond belt, central Newfoundland: Economic Geology, v. 110, p. 1835-1859.
Lydon, J. W., 1984, Ore deposit models; 8, Volcanogenic sulphide deposits; Part I, A descriptive model: Geoscience Canada, v. 11, p. 195-202.
McNicoll, V., Squires, G., Kerr, A., and Moore, P., 2010, The Duck Pond and Boundary Cu-Zn deposits, Newfoundland: new insights into the ages of host rocks and the timing of VHMS mineralization: Canadian Journal of Earth Sciences, v. 47, p. 1481-1506.
Mercier-Langevin, P., Hannington, M., Dubé, B., and Bécu, V., 2011, The gold content of volcanogenic massive sulfide deposits: Mineralium Deposita, v. 46, p. 509-539.
Mills, R. A., and Elderfield, H., 1995, Hydrothermal activity and the geochemistry of metallliferous sediment: Geophysical Monograph, v. 91, p. 392-407.
Murowchick, J. B., and Barnes, H. L., 1986, Marcasite precipitation from hydrothermal solutions: Geochimica et Cosmochimica Acta, v. 50, p. 2615-2629.
Ohmoto, H., and Goldhaber, M. B., 1997, Sulfur and Carbon Isotopes, *in* Barnes, H. L., ed., Geochemistry of Hydrothermal Ore Deposits, Third Edition, John Wiley and Sons, p. 517-611.
Ohmoto, H., and Rye, R. O., 1979, Isotopes of sulfur and carbon, *in* Barnes, H. L., ed., Geochemistry of Hydrothermal Ore Deposits, Second Edition: United States, John Wiley & Sons : New York, NY, United States, p. 509-567.
Peter, J. M., 2003, Ancient iron formations: their genesis and use in the exploration for stratiform base metal sulphide deposits, with examples from the Bathurst Mining

Camp, *in* Lentz, D. R., ed., Geochemistry of Sediments and Sedimentary Rocks: Secular Evolutionary Considerations to Mineral Deposit-Forming Environments, GEOtext v.4., Geological Association of Canada, p. 145-176.

Peter, J. M., and Goodfellow, W. D., 2003, Hydrothermal sedimentary rocks of the Heath Steele Belt, Bathurst mining camp, New Brunswick; Part 3, Application of mineralogy and mineral and bulk compositions to massive sulfide exploration: Economic Geology Monographs, v. 11, p. 417-433.

Piercey, S. J., 2007, Volcanogenic massive sulphide (VMS) deposits of the Newfoundland Appalachians: An overview of their setting, classification, grade-tonnage data, and unresolved questions, *in* Pereira, C. P. G., and Walsh, D. G., eds., Current Research, Report 07-01: St. John's, NL, Geological Survey Branch, p. 169-178.

Piercey, S. J., Squires, G. C., and Brace, T. D., 2014, Lithostratigraphic, hydrothermal, and tectonic setting of the Boundary volcanogenic massive sulfide deposit, Newfoundland Appalachians, Canada: Formation by subseafloor replacement in a Cambrian rifted arc: Economic Geology, v. 109, p. 661-687.

Pollock, J. C., and Wilton, D. H. C., 2001, Metallogenic studies of the Tally Pond Belt, Victoria Lake Group; trace-element geochemistry and lead-isotope data from the Exploits Subzone, Newfoundland: Report - Government of Newfoundland and Labrador. Dept. of Mines and Energy, Geological Survey, Report: 2001-1, pp.247-266, Mar 2001.

Ridler, R. H., 1971, Analysis of Archean volcanic basins in the Canadian Shield using the exhalite concept: Bulletin of the Canadian Institute of Mining and Metallurgy, v. 64.

Rogers, N., van Staal, C., Zagorevski, A., Skulski, T., Piercey, S. J., and McNicoll, V., 2007, Timing and tectonic setting of volcanogenic massive sulphide bearing terranes within the Central Mobile Belt of the Canadian Appalachians, *in* Milkereit, B., ed., Proceedings of Exploration '07: Fifth Decennial International Conference on Mineral Exploration: Toronto, ON, p. 1199-1205.

Rogers, N., van Staal, C. R., McNicoll, V., Pollock, J., Zagorevski, A., and Whalen, J., 2006, Neoproterozoic and Cambrian arc magmatism along the eastern margin of the Victoria Lake Supergroup: A remnant of Ganderian basement in central Newfoundland?: Precambrian Research, v. 147, p. 320-341.

Roth, T., 2002, Physical and chemical constraints on mineralization in the Eskay Creek deposit, northwestern British Columbia: Evidence from petrography, mineral chemistry, and sulfur isotopes: Unpublished Ph.D. thesis, University of British Columbia, 401 p.

Rye, R. O., 1993, The evolution of magmatic fluids in the epithermal environment; the stable isotope perspective: Economic Geology, v. 88, p. 733-752.

Sangster, D. F., 1968, Relative sulphur isotope abundances of ancient seas and strata-bound sulphide deposits: Proceedings of the the Geological Association of Canada, v. 19, p. 79-91.

Schieber, J., 2011, Marcasite in black shales-a mineral proxy for oxygenated bottom waters and intermittent oxidation of carbonaceous muds: Journal of Sedimentary Research, v. 81, p. 447-458.

Schoonen, M. A. A., and Barnes, H. L., 1991, Reactions forming pyrite and marcasite from solution: II. Via FeS precursors below 100°C: Geochimica et Cosmochimica Acta, v. 55, p. 1505-1514.

Seal, R. R., II, 2006, Sulfur isotope geochemistry of sulfide minerals: Reviews in Mineralogy and Geochemistry, v. 61, p. 633-677.

Seal, R. R., II, Alpers, C. N., and Rye, R. O., 2000, Stable isotope systematics of sulfate minerals: Reviews in Mineralogy and Geochemistry, v. 40, p. 541-602.

Shanks, W. C., 2001, Stable isotopes in seafloor hydrothermal systems: Vent fluids, hydrothermal deposits, hydrothermal alteration, and microbial processes: Reviews in Mineralogy and Geochemistry, v. 43, p. 469-525.

_____2014, 13.3 - Stable isotope geochemistry of mineral deposits, *in* Turekian, H. D. H. K., ed., Treatise on Geochemistry (Second Edition): Oxford, Elsevier, p. 59-85.

Shanks, W. C., Bischoff, J. L., and Rosenbauer, R. J., 1981, Seawater sulfate reduction and sulfur isotope fractionation in basaltic systems: Interaction of seawater with fayalite and magnetite at 200-350°C: Geochimica et Cosmochimica Acta, v. 45, p. 1977-1995.

Shanks, W. C., III, Woodruff, L. G., Jilson, G. A., Jennings, D. S., Modene, J. S., and Ryan, B. D., 1987, Sulfur and lead isotope studies of stratiform Zn-Pb-Ag deposits, Anvil Range, Yukon; basinal brine exhalation and anoxic bottom-water mixing: Economic Geology, v. 82, p. 600-634.

Sillitoe, R. H., Hannington, M. D., and Thompson, J. F. H., 1996, High sulfidation deposits in the volcanogenic massive sulfide environment: Economic Geology, v. 91, p. 204-212.

Spooner, E. T. C., and Gale, N. H., 1982, Pb isotopic composition of ophiolitic volcanogenic sulphide deposits, Troodos Complex, Cyprus: Nature (London), v. 296, p. 239-242.

Spry, P. G., Peter, J. M., and Slack, J. F., 2000, Meta-exhalites as exploration guides to ore, *in* Spry, P. G., Marshall, B., and Vokes, F. M., eds., Metamorphosed and metamorphogenic ore deposits, Reviews in Economic Geology 11: Littleton, CO, Society of Economic Geologists, p. 163-201.

Squires, G. C., and Hinchey, J. G., 2006, Geology of the Tally Pond Volcanic Belt and Adjacent Areas (parts of NTS 12A/09 & 12A/10). Map 2006-01, Government of Newfoundland and Labrador, Department of Natural Resources, Geological Survey, Map 2006-01, Open File 012A/1202.

Squires, G. C., MacKenzie, A. C., and MacInnis, D., 1991, Geology and genesis of the Duck Pond volcanogenic massive sulfide deposit, *in* Swinden, H. S., Evans, D. T. W., and Kean, B. F., eds., Metallogenic Framework of Base and Precious Metal Deposits, Central and Western Newfoundland, Geological Survey of Canada Open File 2156: Ottawa, ON, Canada, Geological Survey of Canada, p. 56-64.

Squires, G. C., and Moore, P. J., 2004, Volcanogenic massive sulphide environments of the Tally Pond Volcanics and adjacent area; geological, lithogeochemical and geochronological results, *in* Pereira, C. P. G., Walsh, D. G., and Kean, B. F., eds., Current Research, Report 04-1: St. John's, NL, Geological Survey Branch, p. 63-91.

Swinden, H. S., 1988, Introduction to volcanogenic sulphide deposits in Newfoundland, *in* Swinden, H. S., and Kean, B. F., eds., The volcanogenic sulphide districts of central Newfoundland, Geological Association of Canada, p. 1-26.

_____1991, Paleotectonic settings of volcanogenic massive sulphide deposits in the Dunnage Zone, Newfoundland Appalachians: Canadian Institute of Mining and Metallurgy Bulletin, v. 84, p. 59-89.

Swinden, H. S., and Thorpe, R. I., 1984, Variations in style of volcanism and massive sulfide deposition in Early to Middle Ordovician island-arc sequences of the Newfoundland Central Mobile Belt: Economic Geology, v. 79, p. 1596-1619.

Thode, H. G., Kleerekoper, H., and McElcheran, D., 1951, Isotope fractionation in the bacterial reduction of sulphate: Research (London), v. 4, p. 581-582.

Tivey, M. K., 2007, Generation of seafloor hydrothermal vent fluids and associated mineral deposits Oceanography, v. 20, p. 50-65.

Tosdal, R. M., Wooden, J. L., and Bouse, R. M., 1999, Pb isotopes, ore deposits, and metallogenic terranes: Reviews in Economic Geology, v. 12, p. 1-28.

van Staal, C. R., and Barr, S. M., 2011, Lithospheric architecture and tectonic evolution of the Canadian Appalachians and associated Atlantic margin, *in* Percival, J. A., Cook, F. A., and Clowes, R. M., eds., Chapter 2 Tectonic Styles in Canada: the LITHOPROBE Perspective, Special Paper 49, Geological Association of Canada, p. 3-55.

van Staal, C. R., 2007, Pre-Carboniferous tectonic evolution and metallogeny of the Canadian Appalachians, *in* Goodfellow, W. D., ed., Mineral Deposits of Canada: A Synthesis of Major Deposit-types, District Metallogeny, the Evolution of Geological Provinces, and Exploration Methods, Special Publication 5, Mineral Deposits Division, Geological Association of Canada, p. 793-818.

Von Damm, K. L., 1990, Seafloor hydrothermal activity; black smoker chemistry and chimneys: Annual Review of Earth and Planetary Sciences, v. 18, p. 173-204.

Williams, H., 1979, Appalachian Orogen in Canada: Canadian Journal of Earth Sciences, v. 16, p. 792-807.

Williams, H., Colman-Sadd, S. P., and Swinden, H. S., 1988, Tectonostratigraphic subdivisions of central Newfoundland., Current Research, Part B, Paper 88-1B: Ottawa, ON, Canada, Geological Survey of Canada, p. 91-98.

Woodruff, L. G., and Shanks, W. C., 1988, Sulfur isotope study of chimney minerals and vent fluids from 21°N, East Pacific Rise: Hydrothermal sulfur sources and disequilibrium sulfate reduction: Journal of Geophysical Research: Solid Earth, v. 93, p. 4562-4572.

Wortmann, U. G., Bernasconi, S. M., and Böttcher, M. E., 2001, Hypersulfidic deep biosphere indicates extreme sulfur isotope fractionation during single-step microbial sulfate reduction: Geology, v. 29, p. 647-650.

York, D., 1969, Least-squares fit of a straight line with correlated errors: Earth and Planetary Science Letters, v. 5, p. 320-324.

Zagorevski, A., van Staal, C. R., and McNicoll, V. J., 2007, Distinct Taconic, Salinic, and Acadian deformation along the Iapetus suture zone, Newfoundland Appalachians: Canadian Journal of Earth Sciences, v. 44, p. 1567-1585.

Zagorevski, A., van Staal, C. R., Rogers, N., McNicoll, V. J., and Pollock, J., 2010, Middle Cambrian to Ordovician arc-backarc development on the leading edge of Ganderia, Newfoundland Appalachians: Geological Society of America Memoir, v. 206, p. 367-396.

Zartman, R. E., and Doe, B. R., 1981, Plumbotectonics; the model: Tectonophysics, v. 75, p. 135-162.

Table 3.1

Sulphur isotope data for pyrite, chalcopyrite, pyrrhotite, arsenopyrite, and galena hosted in the Lemarchant exhalites

Sulphur isotope data for pyrite, chalcopyrite, pyrrhotite, arsenopyrite, and galena hosted in the Lemarchant exhalites

Sample #	Drill hole	Section	UTM NAD27 Z21 - East	UTM NAD27 Z21 - North	Depth	Exhalite type	Sulphide description	$\delta^{34}S$ [VCDT]	1 σ
CNF25062b Py1	LM13-76	10050	521049	5374537	163.78	FEM	Py-euh in vein	-20.9	0.21
CNF25062b Py2	LM13-76	10050	521049	5374537	163.78	FEM	Py-euh	-19.1	0.25
CNF25062b Py3	LM13-76	10050	521049	5374537	163.78	FEM	Py-framb.	-18.2	0.29
CNF25062b Py4	LM13-76	10050	521049	5374537	163.78	FEM	Py-euh in vein with Ccp	-21.5	0.23
CNF25062b Py5	LM13-76	10050	521049	5374537	163.78	FEM	Py-euh in vein with Gn	-19.0	0.24
CNF25062b Py6	LM13-76	10050	521049	5374537	163.78	FEM	Py-euh in vein with electrum-Ccp-Gn	-19.9	0.22
CNF25064 Py1	LM13-77	10050	521049	5374537	139.56	FEM	Py-framb. cluster with Py-euh	-19.0	0.39
CNF25064 Py2	LM13-77	10050	521049	5374537	139.56	FEM	Py-euh with Py-framb. and Po	-20.3	0.28
CNF25067 Py1	LM13-77	10050	521049	5374537	142.76	FEM	Py-euh	-17.4	0.19
CNF25067 Py2	LM13-77	10050	521049	5374537	142.76	FEM	Py-framb.	12.2	0.24
CNF25067 Py3	LM13-77	10050	521049	5374537	142.76	FEM	Py-euh	-17.1	0.18
CNF25067 Py4	LM13-77	10050	521049	5374537	142.76	FEM	Py-euh with Gn	-17.6	0.21
CNF30982 Py1 (marc.)	LM11-65	10100	521114.13	5374599.59	157.7	EMS	Marcasite cluster	-12.4	0.26
CNF30982 Py2	LM11-65	10100	521114.13	5374599.59	157.7	EMS	Py-framb.	-16.6	0.25
CNF30982 Py3	LM11-65	10100	521114.13	5374599.59	157.7	EMS	Py-euh with marcasite	-12.0	0.19
CNF30982 Py4 (marc.)	LM11-65	10100	521114.13	5374599.59	157.7	EMS	Marcasite cluster	-13.1	0.24
CNF30982 Py5	LM11-65	10100	521114.13	5374599.59	157.7	EMS	Py-euh with Ccp	-11.1	0.23
CNF30982 Py6	LM11-65	10100	521114.13	5374599.59	157.7	EMS	Py-massive with marcasite	-11.3	0.20
CNF30982 Py7 (marc.)	LM11-65	10100	521114.13	5374599.59	157.7	EMS	Marcasite in Py-massive	-12.6	0.19
CNF30982 Py8	LM11-65	10100	521114.13	5374599.59	157.7	EMS	Py-euh with Ccp	-11.5	0.20
CNF30982 Py9	LM11-65	10100	521114.13	5374599.59	157.7	EMS	Py-framb. cluster	-34.3	0.23
CNF30982 Py10	LM11-65	10100	521114.13	5374599.59	157.7	EMS	Py-euh with Ccp-Gn	-13.6	0.19
CNF30982 Py11	LM11-65	10100	521114.13	5374599.59	157.7	EMS	Py-euh with Ccp	-12.2	0.32
CNF25071a Py1	LM13-79	10125	521114.59	5374625.36	186.56	EMS	Py-euh with Sp	11.1	0.23
CNF25071a Py2	LM13-79	10125	521114.59	5374625.36	186.56	EMS	Py-massive with Sp-Gn	11.8	0.32
CNF25071a Py3	LM13-79	10125	521114.59	5374625.36	186.56	EMS	Py-euh with Gn-Sp	11.9	0.25
CNF25071a Py4	LM13-79	10125	521114.59	5374625.36	186.56	EMS	Py-euh with Gn-Sp-Ccp	10.3	0.23
CNF25071a Py5	LM13-79	10125	521114.59	5374625.36	186.56	EMS	Py-euh with Gn-Sp-Ccp	12.6	0.42
CNF25071b Py1	LM13-79	10125	521114.59	5374625.36	186.56	EMS	Py-euh with Ccp-Gn	5.2	0.32
CNF25071b Py2	LM13-79	10125	521114.59	5374625.36	186.56	EMS	Py-massive with Ccp-Gn	8.2	0.23

Gn = Galena, Ccp = chalcopyrite, Sp = Sphalerite, Po = Pyrrhotite, Apy = arsenopyrite, Py = Pyrite, euh = euhedral, framb. = framboid

Sample #	Drill hole	Section (N)	UTM NAD27 Z21 - East	UTM NAD27 Z21 - North	Depth	Exhalite type	Sulphide description	$\delta^{34}S$ [VCDT]	1 σ
CNF25071b Py3	LM13-79	10125	521114.59	5374625.36	186.56	EMS	Py-euh with Py-framb. Sp-Ccp-Gn	10.3	0.27
CNF25071b Py4	LM13-79	10125	521114.59	5374625.36	186.56	EMS	Py-euh with Ccp-Gn	9.5	0.23
CNF20978 Py1	LM10-43	10250	521098.653	5374752.731	199.8	IFE	Py-euh overgrowing framb.	-16.0	0.22
CNF20978 Py2	LM10-43	10250	521098.653	5374752.731	199.8	IFE	Py-euh with framb.	-14.3	0.23
CNF20978 Py3	LM10-43	10250	521098.653	5374752.731	199.8	IFE	Py-framb.	-17.6	0.27
CNF20978 Py4	LM10-43	10250	521098.653	5374752.731	199.8	IFE	Py-massive	-17.6	0.27
CNF20995 Py1	LM07-15	10300	521072.261	5374803.855	398.86	IFE	Py-framb. with Py overgrowth	-38.8	0.38
CNF20995 Py2	LM07-15	10300	521072.261	5374803.855	398.86	IFE	Py-framb./mat	-33.6	0.23
CNF20995 Py3	LM07-15	10300	521072.261	5374803.855	398.86	IFE	Py-euh with Po	-20.5	0.27
CNF20995 Py4	LM07-15	10300	521072.261	5374803.855	398.86	IFE	Py-euh with Po	-20.6	0.22
CNF20995 Py5	LM07-15	10300	521072.261	5374803.855	398.86	IFE	Py-euh with Po	-20.9	0.24
CNF30998 Py1	LM11-59	10325	521077.866	5374828.815	194.17	FEM	Py-euh, overgrowing framb.	-18.7	0.32
CNF30998 Py2	LM11-59	10325	521077.866	5374828.815	194.17	FEM	Py-framb.	-16.1	0.20
CNF30998 Py3	LM11-59	10325	521077.866	5374828.815	194.17	FEM	Py-massive w Ccp	-8.4	0.34
CNF30998 Py4	LM11-59	10325	521077.866	5374828.815	194.17	FEM	Py-euh with Ccp	-10.1	0.19
CNF30998 Py5	LM11-59	10325	521077.866	5374828.815	194.17	FEM	Py-massive with Po	-12.0	0.23
CNF30998 Py6	LM11-59	10325	521077.866	5374828.815	194.17	FEM	Py-euh, with Py-massive	8.2	0.21
CNF30994 Py1	LM11-69	10350	520993.337	5374860.131	178.24	EMS	Py-euh	-3.8	0.21
CNF30994 Py2	LM11-69	10350	520993.337	5374860.131	178.24	EMS	Py-euh	-0.3	0.20
CNF30994 Py3	LM11-69	10350	520993.337	5374860.131	178.24	EMS	Py-massive with Ccp-Gn	1.1	0.21
CNF30994 Py6	LM11-69	10350	520993.337	5374860.131	178.24	EMS	Py-massive with Ccp-Gn	4.0	0.34
CNF30994 Py7	LM11-69	10350	520993.337	5374860.131	178.24	EMS	Py-euh with Ccp-Gn	3.6	0.16
CNF30994 Py8	LM11-69	10350	520993.337	5374860.131	178.24	EMS	Py-Speres with Gn	5.8	0.16
CNF30951 Py1	LM07-16	10400	521080.229	5374900.176	284.48	FEM	Py-mat	-15.7	0.38
CNF30951 Py2	LM07-16	10400	521080.229	5374900.176	284.48	FEM	Py-euh	2.5	0.20
CNF30951 Py3	LM07-16	10400	521080.229	5374900.176	284.48	FEM	Py-mat	-13.6	0.20
CNF30951 Py4	LM07-16	10400	521080.229	5374900.176	284.48	FEM	Py-framb.	-18.9	0.31
CNF30951 Py5	LM07-16	10400	521080.229	5374900.176	284.48	FEM	Py-mat with small Py-euh	-8.2	0.21
CNF30951 Py6	LM07-16	10400	521080.229	5374900.176	284.48	FEM	Py-mat with small Py-euh	-5.7	0.21
CNF30951 Py7	LM07-16	10400	521080.229	5374900.176	284.48	FEM	Py-mat	-16.9	0.23

Gn = Galena, Ccp = chalcopyrite, Sp = Sphalerite, Po = Pyrrhotite, Apy = arsenopyrite, Py = Pyrite, euh = euhedral, framb. = framboid

Sample #	Drill hole	Section (N)	UTM NAD27 Z21 - East	UTM NAD27 Z21 - North	Depth	Exhalite type	Sulphide description	$\delta^{34}S$ [VCDT]	1 σ
CNF30951 Py8	LM07-16	10400	521080.229	5374900.176	284.48	FEM	Py-euh	-0.8	0.16
CNF30951 Py9	LM07-16	10400	521080.229	5374900.176	284.48	FEM	Py-mat	-12.7	0.21
CNF30953 Py2	LM07-17	10400	520989.959	5374908.512	238.38	EMS	Py-euh	0.5	0.23
CNF30953 Py3	LM07-17	10400	520989.959	5374908.512	238.38	EMS	Py-mat with small Py-euh	14.4	0.31
CNF30953 Py4	LM07-17	10400	520989.959	5374908.512	238.38	EMS	Py-euh	1.0	0.23
CNF36560 Py1	LM11-57	10400	520989.644	5374908.55	511.19	FEM	Py-euh with Po	-21.2	0.20
CNF36560 Py2	LM11-57	10400	520989.644	5374908.55	511.19	FEM	Py-euh with Po	-21.1	0.34
CNF38406 Py1	LM08-22	10500	520992.886	5375012.591	9.24	IFE	Py-massive-framb. cluster with Apy	-25.4	0.27
CNF38406 Py2	LM08-22	10500	520992.886	5375012.591	9.24	IFE	Py-massive-framb. cluster with Ccp	-25.4	0.21
CNF38406 Py3	LM08-22	10500	520992.886	5375012.591	9.24	IFE	Py-euh with Py-framb.	-26.1	0.27
CNF38406 Py4	LM08-22	10500	520992.886	5375012.591	9.24	IFE	Py-framb.	-29.3	0.21
CNF38410 Py1	LM08-23	10500	521066.364	5375010.736	65.63	FEM	Py-euh with Py-framb.	-18.8	0.23
CNF38410 Py2	LM08-23	10500	521066.364	5375010.736	65.63	FEM	Py-framb.-cluster	-24.2	0.32
CNF20983 Py1	LM08-24ext	10500	521067.705	5375010.664	432.76	EMS	Py-euh	-8.6	0.27
CNF20983 Py2	LM08-24ext	10500	521067.705	5375010.664	432.76	EMS	Py-framb.	-25.2	0.27
CNF20983 Py3	LM08-24ext	10500	521067.705	5375010.664	432.76	EMS	Py-framb.	-16.1	0.24
CNF20983 Py4	LM08-24ext	10500	521067.705	5375010.664	432.76	EMS	Py-framb.	-18.6	0.26
CNF38401 Py1	LM08-28	10600	520698.947	5375123.515	242.12	FEM	Py-euh overgrowing framb.	-15.1	0.22
CNF38401 Py2	LM08-28	10600	520698.947	5375123.515	242.12	FEM	Py-framb.-cluster	-23.4	0.25
CNF38401 Py3	LM08-28	10600	520698.947	5375123.515	242.12	FEM	Py-euh overgrowing framb.	-16.4	0.23
CNF38401 Py4	LM08-28	10600	520698.947	5375123.515	242.12	FEM	Py-framb.	-18.2	0.25
CNF25005a Py1	LM13-74	10600	520599.3	5375124	306.2	EMS	Py-euh overgrowing framb.	-13.3	0.27
CNF25005a Py2	LM13-74	10600	520599.3	5375124	306.2	EMS	Py-euh	-12.5	0.22
CNF25005b Py1	LM13-74	10600	520599.3	5375124	306.2	EMS	Py-euh overgrowing framb.	-12.1	0.24
CNF25005b Py2	LM13-74	10600	520599.3	5375124	306.2	EMS	Py-euh overgrowing framb.	-11.5	0.20
CNF25005a Py3	LM13-74	10600	520599.3	5375124	306.2	EMS	Py-framb. cluster with Apy-Gn	-12.8	0.20
CNF25005a Py4	LM13-74	10600	520599.3	5375124	306.2	EMS	Py-massive with Gn	-12.9	0.19
CNF25005a Py5	LM13-74	10600	520599.3	5375124	306.2	EMS	Py-framb. cluster	-11.0	0.28
CNF20911 Py1	LM11-49	10800	521092.545	5375314.262	158.7	IFE	Py-euh	-21.1	0.18
CNF20911 Py2	LM11-49	10800	521092.545	5375314.262	158.7	IFE	Py-framb.	-28.6	0.22

Gn = Galena, Ccp = chalcopyrite, Sp = Sphalerite, Po = Pyrrhotite, Apy = arsenopyrite, Py = Pyrite, euh = euhedral, framb. = framboid

Sample #	Drill hole	Section (N)	UTM NAD27 Z21 - East	UTM NAD27 Z21 - North	Depth	Exhalite type	Sulphide description	$\delta^{34}S$ [VCDT]	1 σ
CNF20911 Py3	LM11-49	10800	521092.545	5375314.262	158.7	IFE	Py-euh	-20.4	0.34
CNF20911 Py4	LM11-49	10800	521092.545	5375314.262	158.7	IFE	Py-framb.	-27.0	0.23
CNF20914 Py1	LM11-49	10800	521092.545	5375314.262	447.3	FEM	Py-euh	-18.2	0.21
CNF20915 Py1	LM11-49	10800	521092.545	5375314.262	447.44	FEM	Py-euh with Ccp-Po	-17.1	0.49
CNF20915 Py2	LM11-49	10800	521092.545	5375314.262	447.44	FEM	Py-euh with Ccp-Po	-16.0	0.28
CNF20927 Py1	LM11-50	10800	521093.252	5375314.302	114.58	FEM	Py-framb.	-34.5	0.27
CNF20927 Py2	LM11-50	10800	521093.252	5375314.302	114.58	FEM	Py-euh	-16.4	0.21
CNF20927 Py3	LM11-50	10800	521093.252	5375314.302	114.58	FEM	Py-euh- with tubes	-15.9	0.23
CNF20927 Py4	LM11-50	10800	521093.252	5375314.302	114.58	FEM	Py-tubes	-30.5	0.38
CNF20927 Py5	LM11-50	10800	521093.252	5375314.302	114.58	FEM	Py-massive - biogenic?	-20.0	0.29
CNF20927 Py6	LM11-50	10800	521093.252	5375314.302	114.58	FEM	Py-massive quench texture	-13.0	0.29
CNF20932 Py1	LM11-50	10800	521093.252	5375314.302	143.57	IFE	Py-euh with Py-framb.	-19.7	0.17
CNF20932 Py2	LM11-50	10800	521093.252	5375314.302	143.57	IFE	Py-framb.	-14.9	0.22
CNF20932 Py3	LM11-50	10800	521093.252	5375314.302	143.57	IFE	Py-euh with Gn-Ccp-Po	-19.8	0.21
CNF25062b Ccp1	LM13-76	10050	521049	5374537	163.78	FEM	Ccp in Py	-22.5	0.53
CNF25064 Ccp1	LM13-77	10050	521049	5374537	139.56	FEM	Ccp with Gn-electrum-Po-Apy	-18.7	0.23
CNF25064 Ccp2	LM13-77	10050	521049	5374537	139.56	FEM	Ccp with Po	-19.1	0.23
CNF25064 Ccp3	LM13-77	10050	521049	5374537	139.56	FEM	Ccp with Po-electrum-Py	-19.0	0.21
CNF25067 Ccp1	LM13-77	10050	521049	5374537	142.76	FEM	Ccp with Py-euh-Gn (Py overgr. framb.)	-20.1	0.31
CNF25067 Ccp2	LM13-77	10050	521049	5374537	142.76	FEM	Ccp with Py-euh-Gn (Py overgr. framb.)	-18.2	0.58
CNF30982 Ccp1	LM11-65	10100	521114.134	5374599.585	157.7	EMS	Ccp with Gn in vein in Py-framb-cluster	-10.4	0.40
CNF30982 Ccp2	LM11-65	10100	521114.134	5374599.585	157.7	EMS	Ccp with Py-euh with marcasite	-11.0	0.34
CNF30982 Ccp3	LM11-65	10100	521114.134	5374599.585	157.7	EMS	Ccp with Py-euh and Po	-12.6	0.21
CNF30982 Ccp4	LM11-65	10100	521114.134	5374599.585	157.7	EMS	Ccp with Py-euh and Po	-11.4	0.22
CNF30982 Ccp5	LM11-65	10100	521114.134	5374599.585	157.7	EMS	Ccp with Py-euh and Po	-12.0	0.19
CNF25071a Ccp1	LM13-79	10125	521114.59	5374625.36	186.56	EMS	Ccp massive	2.5	0.24
CNF25071a Ccp2	LM13-79	10125	521114.59	5374625.36	186.56	EMS	Ccp with Gn-Sp-Py-euh	1.6	0.23
CNF25071b Ccp1	LM13-79	10125	521114.59	5374625.36	186.56	EMS	Ccp with Py-euh-Gn	2.3	0.31
CNF25071b Ccp2	LM13-79	10125	521114.59	5374625.36	186.56	EMS	Ccp with Py-euh-Gn-Sp	1.7	0.31
CNF25071b Ccp3	LM13-79	10125	521114.59	5374625.36	186.56	EMS	Ccp with Py-euh-Gn-Sp	3.0	0.30

Gn = Galena, Ccp = chalcopyrite, Sp = Sphalerite, Po = Pyrrhotite, Apy = arsenopyrite, Py = Pyrite, euh = euhedral, framb. = framboid

Sample #	Drill hole	Section (N)	UTM NAD27 Z21 - East	UTM NAD27 Z21 - North	Depth	Exhalite type	Sulphide description	$\delta^{34}S$ [VCDT]	1 σ
CNF25071b Ccp4	LM13-79	10125	521114.59	5374625.36	186.56	EMS	Ccp with Py-euh-Gn-Sp	1.6	0.39
CNF25071b Ccp5	LM13-79	10125	521114.59	5374625.36	186.56	EMS	Ccp with Py-euh-Gn-Sp	2.5	0.23
CNF25071b Ccp6	LM13-79	10125	521114.59	5374625.36	186.56	EMS	Ccp with Py-euh-Gn	3.2	0.27
CNF20945 Ccp2	LM07-14	10200	521114.681	5374697.204	504.68	IFE	Ccp with Po	-16.3	0.31
CNF30998 Ccp2	LM11-59	10325	521077.866	5374828.815	194.17	FEM	Ccp ithw Py-euh-framb.-cluster and Po	-11.6	0.29
CNF30994 Ccp1	LM11-69	10350	520993.337	5374860.131	178.24	EMS	Ccp with Gn in Py	-0.3	0.29
CNF30994 Ccp2	LM11-69	10350	520993.337	5374860.131	178.24	EMS	Ccp in Py-Spere	-2.2	0.26
CNF30994 Ccp3	LM11-69	10350	520993.337	5374860.131	178.24	EMS	Ccp with Gn-Sp	-2.1	0.37
CNF30951 Ccp1	LM07-16	10400	521080.229	5374900.176	284.48	FEM	Ccp with Py-euh	-0.6	0.28
CNF30951 Ccp2	LM07-16	10400	521080.229	5374900.176	284.48	FEM	Ccp with Py-framb. cluster/mat	-6.0	0.36
CNF30951 Ccp3	LM07-16	10400	521080.229	5374900.176	284.48	FEM	Ccp with Py-euh	-3.3	0.21
CNF30953 Ccp1	LM07-17	10400	520989.959	5374908.512	238.38	EMS	Ccp with gal-Sp	-2.2	0.28
CNF30953 Ccp2	LM07-17	10400	520989.959	5374908.512	238.38	EMS	Ccp with Sp	-1.6	0.21
CNF20983 Ccp1	LM08-24ext	10500	521067.705	5375010.664	432.76	EMS	Ccp with Po-Py-euh	-10.1	0.20
CNF20983 Ccp2	LM08-24ext	10500	521067.705	5375010.664	432.76	EMS	Ccp with Po-Py-euh	-9.9	0.17
CNF38401 Ccp1	LM08-28	10600	520698.947	5375123.515	242.12	FEM	Ccp-repl Py-euh with Sp and Py-framb.	-9.7	0.19
CNF25005a Ccp1	LM13-74	10600	520599.3	5375124	306.2	EMS	Ccp with Py-massive	-12.9	0.27
CNF25005a Ccp2	LM13-74	10600	520599.3	5375124	306.2	EMS	Ccp with Gn-Py-euh and Sp-mantle	-11.8	0.30
CNF25005a Ccp3	LM13-74	10600	520599.3	5375124	306.2	EMS	Ccp with Py-Po	-14.1	0.24
CNF25005a Ccp4	LM13-74	10600	520599.3	5375124	306.2	EMS	Ccp with Py-Po	-13.1	0.32
CNF20911 Ccp1	LM11-49	10800	521092.545	5375314.262	158.7	IFE	Ccp with Py-euh	-22.8	0.30
CNF20915 Ccp1	LM11-49	10800	521092.545	5375314.262	447.44	FEM	Ccp with Py-euh-Po	-17.5	0.50
CNF20915 Ccp2	LM11-49	10800	521092.545	5375314.262	447.44	FEM	Ccp with Py-euh-Po	-16.6	0.34
CNF20927 Ccp1	LM11-50	10800	521093.252	5375314.302	114.58	FEM	Ccp with Apy in Py-tubes	-15.8	0.21
CNF20927 Ccp2	LM11-50	10800	521093.252	5375314.302	114.58	FEM	Ccp with Apy in Py-tubes	-15.7	0.20
CNF20932 Ccp1	LM11-50	10800	521093.252	5375314.302	143.57	IFE	Ccp with Py-euh-Po	-19.9	0.29
CNF25064 Po1	LM13-77	10050	521049	5374537	139.56	FEM	Po with Ccp-electrum-Py	-19.4	0.22
CNF25064 Po2	LM13-77	10050	521049	5374537	139.56	FEM	Po with Py-Apy-Gn-electrum	-19.6	0.20
CNF25064 Po3	LM13-77	10050	521049	5374537	139.56	FEM	Po with Ccp-Py-Apy-electrum	-19.8	0.21
CNF30982 Po2	LM11-65	10100	521114.134	5374599.585	157.7	EMS	Po with Ccp and Po	-12.6	0.27

Gn = Galena, Ccp = chalcopyrite, Sp = Sphalerite, Po = Pyrrhotite, Apy = arsenopyrite, Py = Pyrite, euh = euhedral, framb. = framboid

Sample #	Drill hole	Section (N)	UTM NAD27 Z21 - East	UTM NAD27 Z21 - North	Depth	Exhalite type	Sulphide description	$\delta^{34}S$ [VCDT]	1 σ
CNF20945 Po1	LM07-14	10200	521114.681	5374697.204	504.68	IFE	Po with Ccp	-23.7	0.27
CNF20945 Po2	LM07-14	10200	521114.681	5374697.204	504.68	IFE	Po with Ccp	-16.5	0.26
CNF20945 Po3	LM07-14	10200	521114.681	5374697.204	504.68	IFE	Po with Ccp	-17.2	0.22
CNF20995 Po1	LM07-15	10300	521072.261	5374803.855	398.86	IFE	Po with Py-euh	-21.0	0.28
CNF20995 Po2	LM07-15	10300	521072.261	5374803.855	398.86	IFE	Po with Py-euh	-19.8	0.30
CNF30998 Po1	LM11-59	10325	521077.866	5374828.815	194.17	FEM	Po with Ccp-Sp	-11.8	0.23
CNF30998 Po2	LM11-59	10325	521077.866	5374828.815	194.17	FEM	Po with Py-massive	-11.3	0.18
CNF36560 Po1	LM11-57	10400	520989.644	5374908.55	511.19	FEM	Po with Py-euh	-21.6	0.26
CNF36560 Po2	LM11-57	10400	520989.644	5374908.55	511.19	FEM	Po with Py-euh	-22.3	0.35
CNF20983 Po1	LM08-24ext	10500	521067.705	5375010.664	432.76	EMS	Po with Py-euh-Ccp	-8.1	0.20
CNF20983 Po2	LM08-24ext	10500	521067.705	5375010.664	432.76	EMS	Po with Py in cross-cutting vein	-11.3	0.29
CNF25005a Po1	LM13-74	10600	520599.3	5375124	306.2	EMS	Po with Ccp-Py	-12.1	0.17
CNF25005a Po2	LM13-74	10600	520599.3	5375124	306.2	EMS	Po with Ccp-Py	-13.0	0.21
CNF20914 Po1	LM11-49	10800	521092.545	5375314.262	447.3	FEM	Po with carbonate	-20.4	0.22
CNF20914 Po2	LM11-49	10800	521092.545	5375314.262	447.3	FEM	Po with Py-euh	-19.8	0.18
CNF20915 Po1	LM11-49	10800	521092.545	5375314.262	447.44	FEM	Po with Py-euh-Ccp	-17.0	0.30
CNF20915 Po2	LM11-49	10800	521092.545	5375314.262	447.44	FEM	Po with Py-euh-Ccp	-17.2	0.18
CNF20932 Po1	LM11-50	10800	521093.252	5375314.302	143.57	IFE	Po with Ccp-Gn-Py-euh	-20.6	0.34
CNF20932 Po2	LM11-50	10800	521093.252	5375314.302	143.57	IFE	Po with Gn	-21.0	0.38
CNF25064 Apy1	LM13-77	10050	521049	5374537	139.56	FEM	Apy with Po-Gn-Ccp-electrum	-15.9	0.44
CNF25064 Apy2	LM13-77	10050	521049	5374537	139.56	FEM	Apy with electrum-Gn	-16.9	0.37
CNF25064 Apy3	LM13-77	10050	521049	5374537	139.56	FEM	Apy with electrum-Gn	-17.3	0.70
CNF38406 Apy1	LM08-22	10500	520992.886	5375012.591	9.24	IFE	Apy with Py	-24.4	0.60
CNF25005a Apy1	LM13-74	10600	520599.3	5375124	306.2	EMS	Apy with Py-Gn	-11.6	0.38
CNF25005a Apy2	LM13-74	10600	520599.3	5375124	306.2	EMS	Apy with Py-Gn	-11.1	0.36
CNF25005b Apy1	LM13-74	10600	520599.3	5375124	306.2	EMS	Apy with Py-Gn-Sp	-10.5	0.77
CNF20927 Apy4	LM11-50	10800	521093.252	5375314.302	114.58	FEM	Apy with Ccp in Py-tubes	-16.4	0.26
CNF20927 Apy1	LM11-50	10800	521093.252	5375314.302	114.58	FEM	Apy with Ccp in Py-tubes	-15.5	0.31
CNF20927 Apy2	LM11-50	10800	521093.252	5375314.302	114.58	FEM	Apy with Py	-15.5	0.35
CNF20927 Apy3	LM11-50	10800	521093.252	5375314.302	114.58	FEM	Apy with Py	-16.8	0.31

Gn = Galena, Ccp = chalcopyrite, Sp = Sphalerite, Po = Pyrrhotite, Apy = arsenopyrite, Py = Pyrite, euh = euhedral, framb. = framboid

Sample #	Drill hole	Section (N)	UTM NAD27 Z21 - East	UTM NAD27 Z21 - North	Depth	Exhalite type	Sulphide description	$\delta^{34}S$ [VCDT]	1 σ
CNF25067 Gn1	LM13-77	10050	521049	5374537	142.76	FEM	Gn with Py-euh	-17.5	0.24
CNF30982 Gn1	LM11-65	10100	521114.134	5374599.585	157.7	EMS	Gn with Ccp-Py	-11.1	0.29
CNF30982 Gn2	LM11-65	10100	521114.134	5374599.585	157.7	EMS	Gn in Py-euh	-14.7	0.25
CNF25071a Gn1	LM13-79	10125	521114.59	5374625.36	186.56	EMS	Gn with Ccp-Sp-Py-euh	3.0	0.19
CNF25071a Gn3	LM13-79	10125	521114.59	5374625.36	186.56	EMS	Gn in Sp w Py-euh-Ccp	5.1	0.24
CNF25071b Gn1	LM13-79	10125	521114.59	5374625.36	186.56	EMS	Gn with Ccp-Sp-Py-euh	2.6	0.20
CNF25071b Gn2	LM13-79	10125	521114.59	5374625.36	186.56	EMS	Gn with Ccp-Sp-Py-euh	3.0	0.22
CNF25071b Gn3	LM13-79	10125	521114.59	5374625.36	186.56	EMS	Gn with Ccp-Sp-Py-euh	5.9	0.24
CNF25071b Gn4	LM13-79	10125	521114.59	5374625.36	186.56	EMS	Gn with Ccp-Py	-1.2	0.23
CNF25071b Gn5	LM13-79	10125	521114.59	5374625.36	186.56	EMS	Gn with Ccp-Py	2.4	0.23
CNF30998 Gn1	LM11-59	10325	521077.866	5374828.815	194.17	FEM	Gn in Py-euh	12.0	0.22
CNF30994 Gn1	LM11-69	10350	520993.337	5374860.131	178.24	EMS	Gn with Ccp-Py	-3.8	0.22
CNF30994 Gn2	LM11-69	10350	520993.337	5374860.131	178.24	EMS	Gn with Sp-Py-euh	-2.9	0.20
CNF30994 Gn3	LM11-69	10350	520993.337	5374860.131	178.24	EMS	Gn with Sp-Py-euh	-2.9	0.19
CNF30994 Gn4	LM11-69	10350	520993.337	5374860.131	178.24	EMS	Gn with Sp-Py-euh	-2.4	0.17
CNF30994 Gn5	LM11-69	10350	520993.337	5374860.131	178.24	EMS	Gn with Sp-Ccp	-3.2	0.26
CNF30994 Gn6	LM11-69	10350	520993.337	5374860.131	178.24	EMS	Gn in Py-Speres	1.8	0.28
CNF30953 Gn1	LM07-17	10400	520989.959	5374908.512	238.38	EMS	Gn with Ccp-Py	-2.3	0.21
CNF30953 Gn2	LM07-17	10400	520989.959	5374908.512	238.38	EMS	Gn with Sp-Ccp	-1.7	0.32
CNF30953 Gn3	LM07-17	10400	520989.959	5374908.512	238.38	EMS	Gn in Py	-0.7	0.22
CNF20932 Gn1	LM11-50	10800	521093.252	5375314.302	143.57	IFE	Gn with Ccp-Po-Py-euh	-16.3	0.27
CNF20932 Gn2	LM11-50	10800	521093.252	5375314.302	143.57	IFE	Gn with Ccp-Py-euh	-20.0	0.34
CNF20932 Gn3	LM11-50	10800	521093.252	5375314.302	143.57	IFE	Gn with Po	-16.9	0.23

Gn = Galena, Ccp = chalcopyrite, Sp = Sphalerite, Po = Pyrrhotite, Apy = arsenopyrite, Py = Pyrite, euh = euhedral, framb. = framboid

Table 3.2

Lead isotope data for galena hosted in the Lemarchant exhalites

Lead isotope data for galena hosted in the Lemarchant exhalites

Sample #	Drill hole	Section	UTM NAD27 Z21 - East	UTM NAD27 Z21 - North	Depth	Exhalite type	Galena description	$^{206}Pb/^{204}Pb$	% SEM	$^{207}Pb/^{204}Pb$	% SEM	$^{208}Pb/^{204}Pb$	% SEM
CNF25005b Pb1	LM13-74	10600	520599.3	5375124	306.2	EMS	Gn Sp in Py-massive	18.107	0.104	15.610	0.135	38.009	0.176
CNF25005b Pb2	LM13-74	10600	520599.3	5375124	306.2	EMS	Gn Sp in Py-massive	18.086	0.110	15.544	0.123	37.749	0.128
CNF25062b Pb1	LM13-76	10050	521049	5374537	163.8	FEM	Gn with electrum in vein	18.164	0.105	15.549	0.118	37.724	0.128
CNF25062b Pb2	LM13-76	10050	521049	5374537	163.8	FEM	Gn in Py-euh in vein	18.156	0.081	15.544	0.099	37.777	0.089
CNF25062b Pb3	LM13-76	10050	521049	5374537	163.8	FEM	Gn in Py-euh in vein	18.226	0.134	15.610	0.141	37.933	0.159
CNF25062b Pb4	LM13-76	10050	521049	5374537	163.8	FEM	Gn in Py-euh in vein	18.205	0.125	15.582	0.143	37.826	0.157
CNF25062b Pb5	LM13-76	10050	521049	5374537	163.8	FEM	Gn with Ccp-Py-euh in vein	18.181	0.121	15.538	0.134	37.727	0.148
CNF25067 Pb1	LM13-77	10050	521049	5374537	142.8	FEM	Gn in Py-euh in vein	18.172	0.120	15.536	0.129	37.735	0.136
CNF25067 Pb3	LM13-77	10050	521049	5374537	142.8	FEM	Gn with Ccp-Py-euh in vein	18.171	0.080	15.529	0.094	37.654	0.105
CNF25067 Pb5	LM13-77	10050	521049	5374537	142.8	FEM	Gn in Py-euh in vein	18.162	0.115	15.516	0.212	37.674	0.309
CNF25067 Pb7	LM13-77	10050	521049	5374537	142.8	FEM	Gn in Py-euh in vein	18.169	0.156	15.520	0.228	37.793	0.286
CNF25067 Pb8	LM13-77	10050	521049	5374537	142.8	FEM	Gn with Ccp-Py-euh in vein	18.033	0.389	15.451	0.478	37.772	0.470
CNF25005a Pb1	LM13-74	10600	520599.3	5375124	306.2	EMS	Gn in Py-massive	18.194	0.089	15.624	0.112	38.051	0.131
CNF25005a Pb2	LM13-74	10600	520599.3	5375124	306.2	EMS	Gn in Py-massive	18.132	0.157	15.625	0.180	37.943	0.181
CNF25005a Pb3	LM13-74	10600	520599.3	5375124	306.2	EMS	Gn in Py-massive	18.104	0.138	15.581	0.160	37.844	0.166
CNF25005a Pb4	LM13-74	10600	520599.3	5375124	306.2	EMS	Gn in Py-massive	18.026	0.120	15.399	0.277	37.352	0.294
CNF25071a Pb1	LM13-79	10125	521114.59	5374625.36	186.6	EMS	Gn with Sp-Ccp-Py-euh	18.058	0.123	15.469	0.135	37.465	0.137
CNF25071a Pb2	LM13-79	10125	521114.59	5374625.36	186.6	EMS	Gn with Sp-Ccp-Py-euh	18.073	0.167	15.479	0.174	37.487	0.179
CNF25071a Pb3	LM13-79	10125	521114.59	5374625.36	186.6	EMS	Gn with Sp	18.090	0.146	15.565	0.153	37.785	0.160
CNF25071a Pb4	LM13-79	10125	521114.59	5374625.36	186.6	EMS	Gn with Sp-Py-euh	18.116	0.160	15.503	0.221	37.563	0.248
CNF25071a Pb5	LM13-79	10125	521114.59	5374625.36	186.6	EMS	Gn with Sp-Py-euh	18.133	0.066	15.563	0.075	37.708	0.083
CNF25071a Pb6	LM13-79	10125	521114.59	5374625.36	186.6	EMS	Gn with Sp	18.065	0.111	15.500	0.131	37.496	0.134
CNF25071a Pb7	LM13-79	10125	521114.59	5374625.36	186.6	EMS	Gn with Sp-Py-massive	18.100	0.072	15.543	0.109	37.679	0.115
CNF25071a Pb8	LM13-79	10125	521114.59	5374625.36	186.6	EMS	Gn with Sp-Py-euh	18.084	0.150	15.487	0.164	37.527	0.181
CNF25071a Pb9	LM13-79	10125	521114.59	5374625.36	186.6	EMS	Gn with Sp-Py-euh	18.072	0.138	15.488	0.147	37.499	0.146
CNF25071a Pb11	LM13-79	10125	521114.59	5374625.36	186.6	EMS	Gn with Sp-Ccp-Py-mass.	18.094	0.122	15.523	0.144	37.657	0.150
CNF25071b Pb1	LM13-79	10125	521114.59	5374625.36	186.6	EMS	Gn with Ccp-Py-euh	18.083	0.068	15.516	0.090	37.597	0.089
CNF25071b Pb2	LM13-79	10125	521114.59	5374625.36	186.6	EMS	Gn with Ccp-Py-euh	18.042	0.164	15.484	0.182	37.613	0.197
CNF25071b Pb4	LM13-79	10125	521114.59	5374625.36	186.6	EMS	Gn with Sp-Ccp-Py-euh	18.047	0.084	15.473	0.090	37.504	0.102
CNF25071b Pb5	LM13-79	10125	521114.59	5374625.36	186.6	EMS	Gn with Sp-Ccp-Py-euh	18.073	0.104	15.520	0.119	37.649	0.121
CNF25071b Pb6	LM13-79	10125	521114.59	5374625.36	186.6	EMS	Gn with Sp-Ccp-Py-euh	18.129	0.127	15.558	0.151	37.801	0.145
DP87116 Gn11	Duck Pond Hydrothermal Mud - Upper Block							18.307	0.075	15.641	0.083	37.929	0.095
DP87116 Gn12	Duck Pond Hydrothermal Mud - Upper Block							18.289	0.078	15.648	0.088	37.971	0.101

Gn = Galena, Ccp = chalcopyrite, Sp = Sphalerite, Py = Pyrite, euh = euhedral

Fig. 3.1 A-B

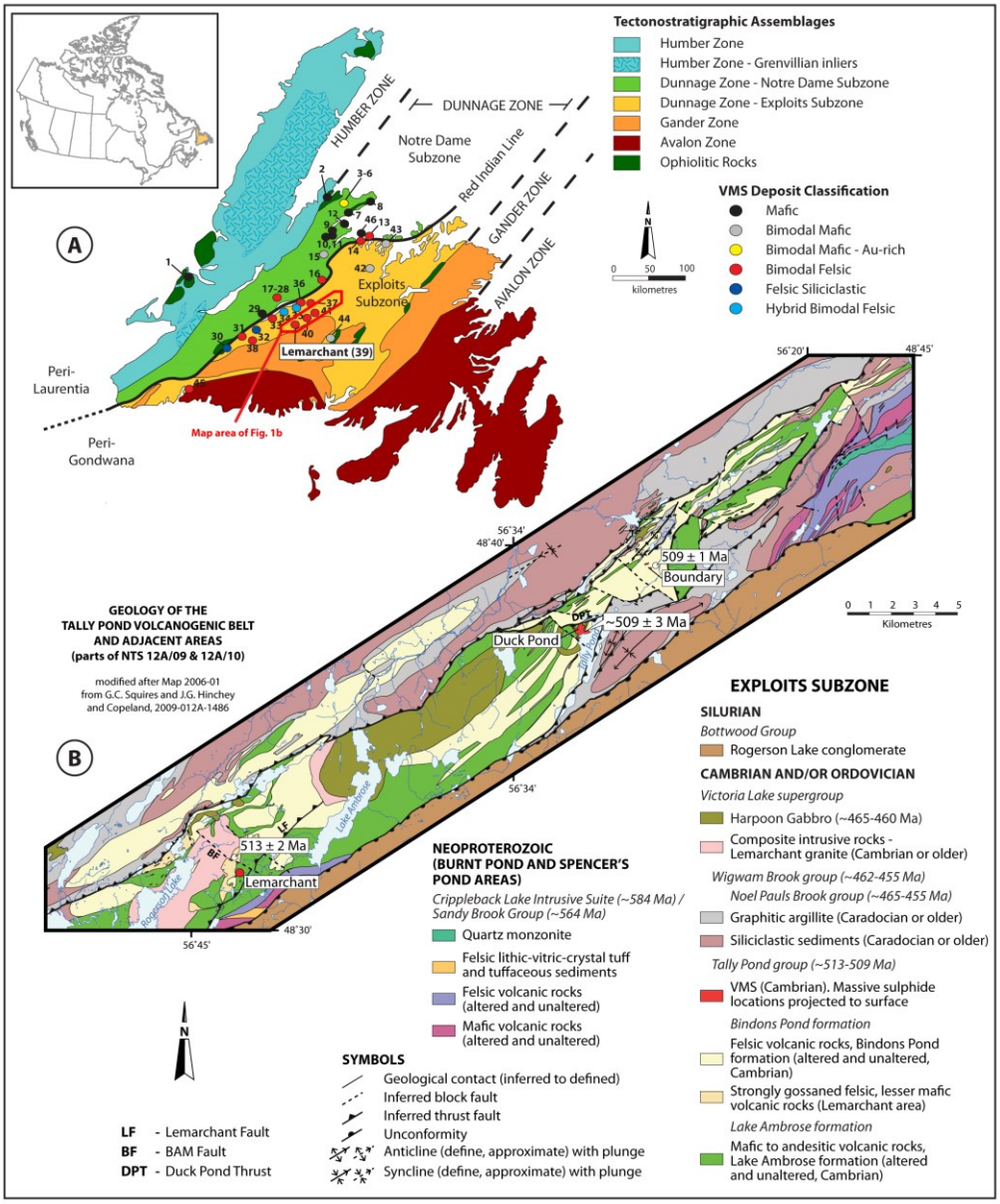

Figure 3.1 *A) Tectonostratigraphic assemblages with the main zones of the Newfoundland Appalachians (Avalon, Gander, Dunnage, and Humber zones) and VMS occurrences within the Notre Dame and Exploits subzones. Notre Dame Subzone VMS: 1 – York Harbour; 2 – 8 - Baie Verte Belt Deposits; 9 – 12, 46 – Springdale Belt Deposits; 13 – 29 Buchans-Roberts Arm Deposits. Exploits Subzone VMS: 30 – 37 - Tulks Belt Deposits; Tally Pond Belt Deposits: 39 – Lemarchant; 40 – Duck Pond; 41 – Boundary; 42 – 45 – Point Leamington Belt Deposits. Modified after (Swinden, 1991) and Piercey (2007). B) Geological map of the Tally Pond volcanic belt. The Tally Pond group comprises the Lemarchant deposit and the Duck Pond and Boundary mines. Figure after (Copeland 2009) and Map 2006-01 from Squires and Hinchey (2006).*

Fig. 3.2 A

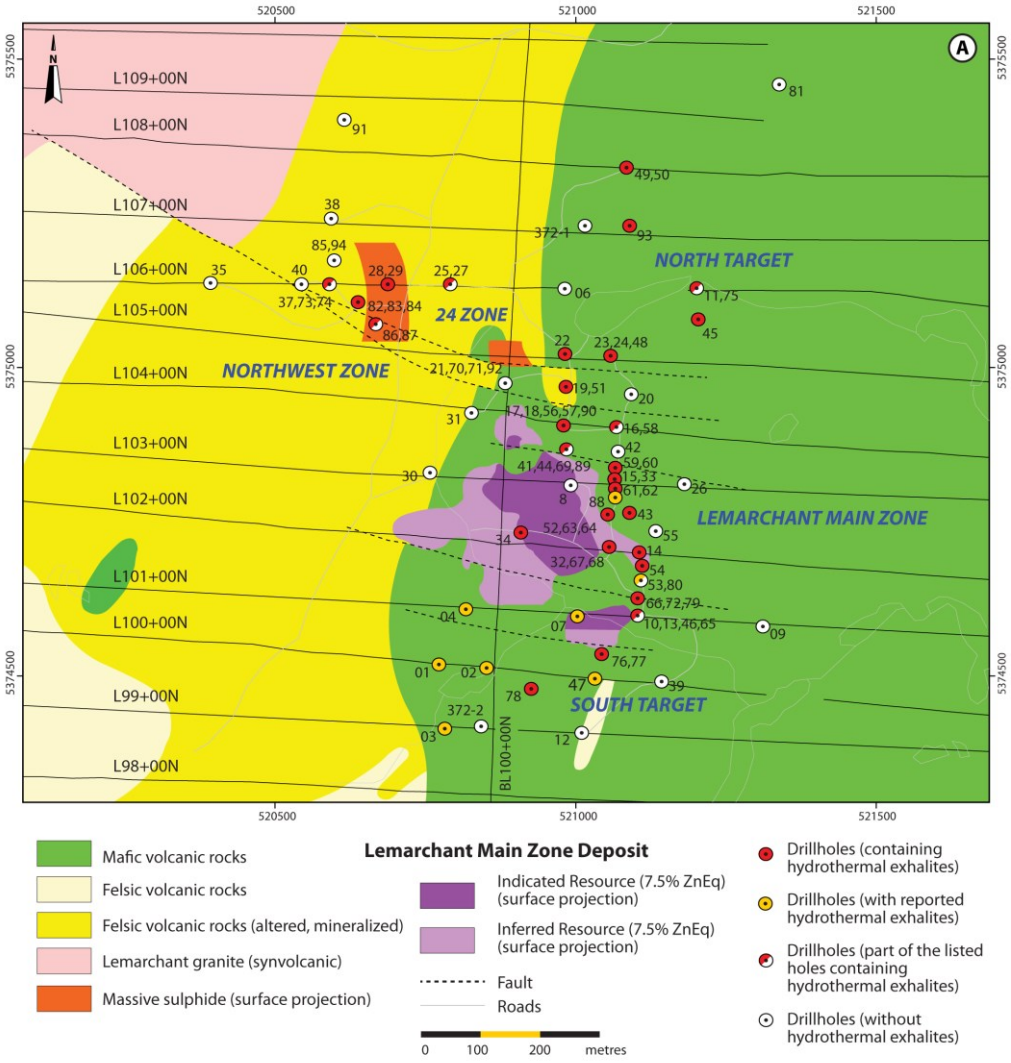

Figure 3.2 *A) Resource map of the massive sulphides of the Lemarchant Main, 24 Zone, and Northwest Zone. Massive sulphides are projected to the surface. Drill holes with exhalites are displayed as red circles, if logged, and as orange circle if not logged, because holes were either not accessible or not drilled yet during the field sessions. White circles display drill holes that do not contain exhalites. Half-coloured circles indicate that some of the listed holes have exhalites (modified from the resource map of Canadian Zinc Corporation). B) Cross-section of the moderately east dipping Lemarchant Main Zone along section 103N. C) Cross-section of the moderately west dipping Northwest Zone along section 106N.*

Fig. 3.2 B-C

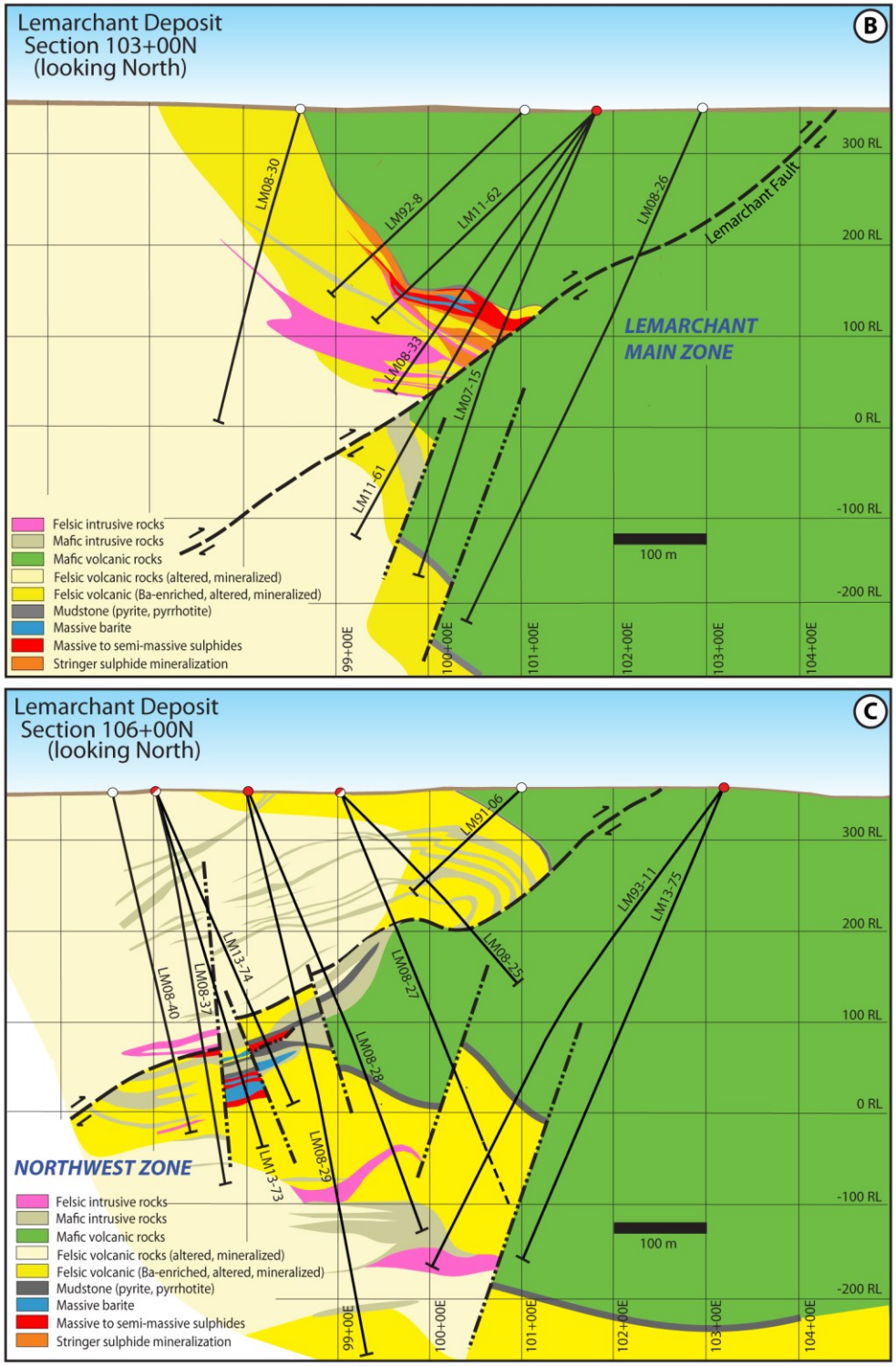
Lemarchant Deposit
Section 103+00N
(looking North)
B
LM08-30
LM92-8
LM11-62
LM08-26
Lemarchant Fault
LM08-33
LM07-15
LM11-61
LEMARCHANT
MAIN ZONE
300 RL
200 RL
100 RL
0 RL
-100 RL
-200 RL
100 m
99+00E
100+00E
101+00E
102+00E
103+00E
104+00E
Felsic intrusive rocks
Mafic intrusive rocks
Mafic volcanic rocks
Felsic volcanic rocks (altered, mineralized)
Felsic volcanic (Ba-enriched, altered, mineralized)
Mudstone (pyrite, pyrrhotite)
Massive barite
Massive to semi-massive sulphides
Stringer sulphide mineralization
Lemarchant Deposit
Section 106+00N
(looking North)
C
LM91-06
LM93-11
LM13-75
LM13-74
LM08-40
LM08-37
LM08-25
LM08-27
LM08-28
LM08-29
LM13-73
NORTHWEST ZONE
300 RL
200 RL
100 RL
0 RL
-100 RL
-200 RL
100 m
99+00E
100+00E
101+00E
102+00E
103+00E
104+00E
Felsic intrusive rocks
Mafic intrusive rocks
Mafic volcanic rocks
Felsic volcanic rocks (altered, mineralized)
Felsic volcanic (Ba-enriched, altered, mineralized)
Mudstone (pyrite, pyrrhotite)
Massive barite
Massive to semi-massive sulphides
Stringer sulphide mineralization

Fig. 3.3 A-C

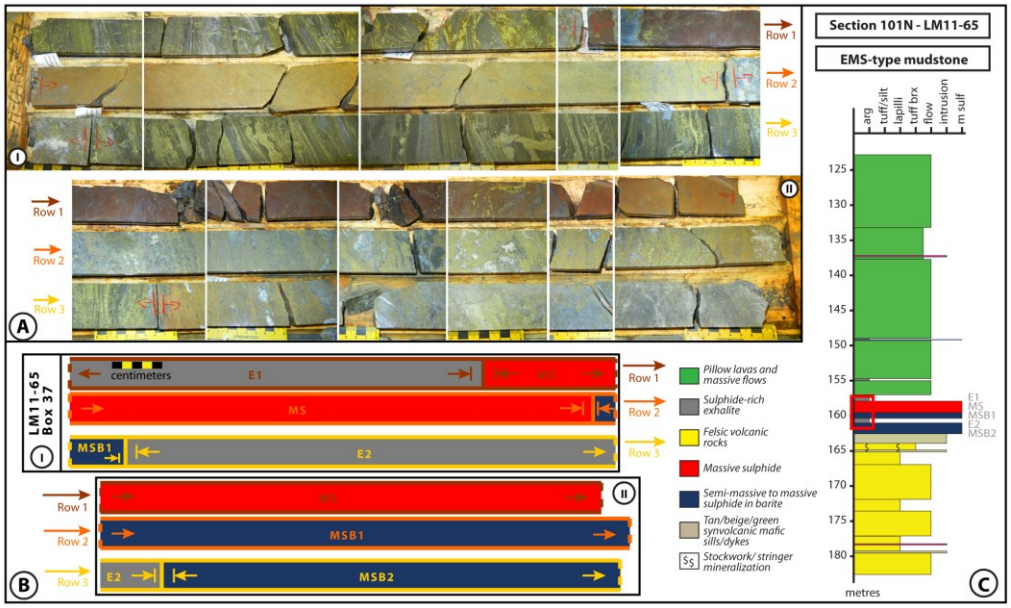

Figure 3.3 *Section 101N, LM11-65. A) EMS-type mudstone. Photograph of core box 37, 157.4 - 161.6 m, rows 1-3 (I), which continue in (II). Sequence of exhalite (E1), massive sulphide (MS), massive sulphide+barite (MSB1), exhalite (E2), massive sulphide+barite (MSB2). B) Digitized version of A. C) Digitized version of a detailed logged drill hole section. Sequence of A and B represented by red square. Sequence includes finely laminated to reworked, sulphide- and Ba-rich (pyrite, chalcopyrite, barite, celsian) exhalites (E1), which conformably overlie Fe-rich red massive sphalerite ore (MS). Fe-content decreases downhole, i.e., red sphalerite-dominated massive sulphides grade into orange to honeybrown-dominated sphalerite. Honeybrown sphalerite ore grades downhole into barite-rich massive sulphides (MSB1). The latter conformably overlies finely laminated to partly reworked, sulphide- and Ba-rich (pyrite, chalcopyrite, barite, celsian) exhalites (E2) that are intercalated with chert-apatite layers. These exhalites (II) conformably overlie barite-rich massive sulphides (MSB2).*

Fig. 3.4 A-C

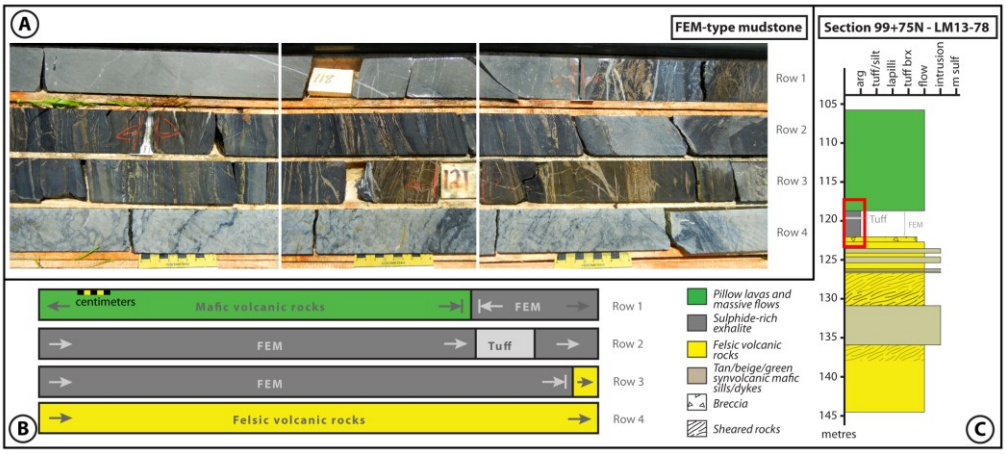

Figure 3.4 *Section 99+75N, LM13-78. A) FEM-type mudstone. Photograph of a section of core box rows of a sequence of felsic volcanic rocks (massive to brecciated rhyolite), which are conformably overlain by FEM-type exhalites. Exhalites are finely laminated to reworked, sulphide-rich (pyrite, pyrrhotite, minor chalcopyrite), and intercalated by a 8 cm thick mineralized micaceous tuff layer. Sulphides occur parallel to the lamination and in cross-cutting veins. The exhalites are conformably overlain by the hanging wall basalts. B) Digitized version of A. C - Digitized version of a detailed logged drill hole section. Sequence of A and B represented by red square.*

Fig. 3.5 A-C

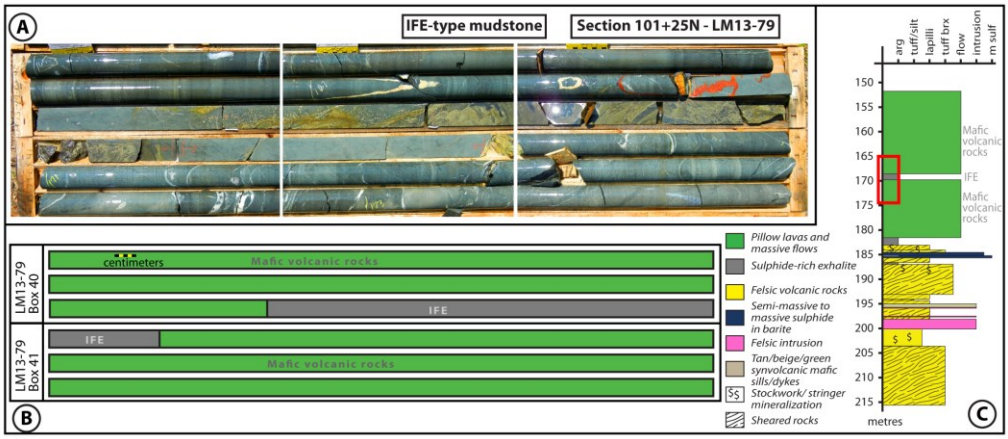

Figure 3.5 *Section 101+25N, LM13-79. A) IFE-type mudstone. Photograph of two core box rows of interflow exhalites occurring within hanging wall mafic volcanic rocks. Exhalites are sulphide-rich (fine-disseminated pyrite plus recrystallized pyrite), and intercalated by chert. B) Digitized version of A. C) Digitized version of a detailed logged drill hole section. Sequence of A and B represented by red square.*

Fig. 3.6 A-H

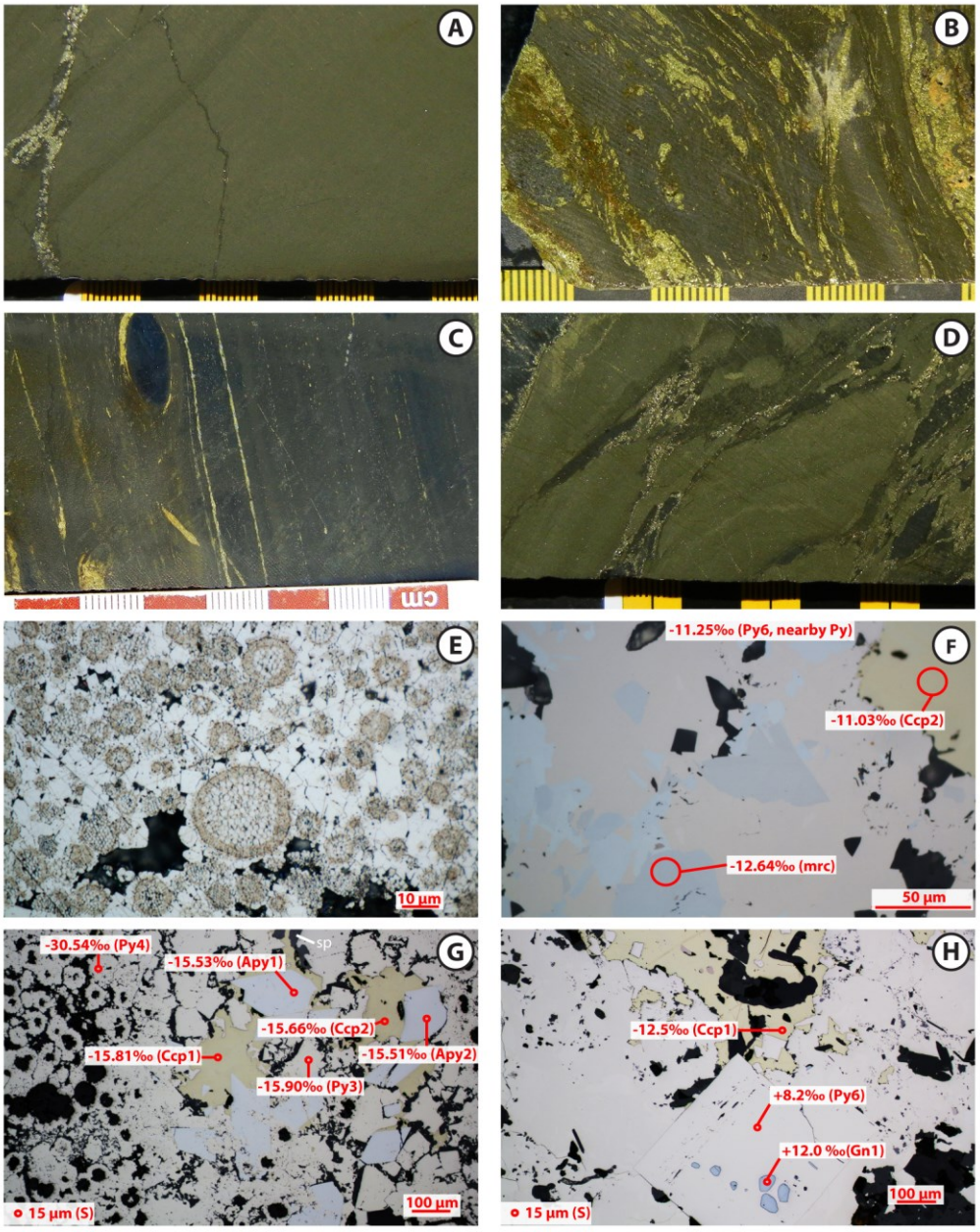
A
B
C
cm
D
E
10 µm
-11.25‰ (Py6, nearby Py)
F
-11.03‰ (Ccp2)
-12.64‰ (mrc)
50 µm
-30.54‰ (Py4)
-15.53‰ (Apy1)
G
-15.66‰ (Ccp2)
-15.81‰ (Ccp1)
-15.51‰ (Apy2)
-15.90‰ (Py3)
15 µm (S)
100 µm
H
-12.5‰ (Ccp1)
+8.2‰ (Py6)
+12.0 ‰(Gn1)
15 µm (S)
100 µm

Figure 3.6 *A) A) Section 101+25N, LM13-79, 181.9 m. EMS-type exhalite, sample CNF25069. Photograph of a finely laminated mudstone, which is cross-cut by veins with polymetallic sulphides. B) Section 101N, LM11-65, 157.7 m. EMS-type exhalite, sample CNF30982. Photograph of a reworked finely laminated pyrite-chalcopyrite-rich exhalite. C) Section 108N, LM11-50, 114.6 m. FEM-type exhalite, sample CNF20927. Photograph of a carbonaceous finely laminated exhalite with a black chert-apatite nodule. Two ~1 mm thick bands contain pyrite tubes. D) Section 101+25N, LM13-79, 169.0 m. IFE-type exhalite, sample CNF25072. Photograph of a reworked, possibly bioturbated carbonaceous pyrite-rich interflow exhalite. E) Section 102+70N, LM11-52, 210.4 m. EMS-type exhalite, sample CNF20990. Photomicrograph (reflected light, RL) of a framboid-cluster. Pyrite framboids are overgrown by euhedral pyrite. Tan rims on framboids show 'hairy' texture, which may reflect fossilized bacterial or archaeal textures. F) Section 101N, LM11-65, 157.7 m. EMS-type exhalite, sample CNF30982. Photomicrograph (RL) of euhedral marcasite (Mrc) in massive pyrite (Py) associated with chalcopyrite (Ccp) and sulphur isotopic results of spot analyses on these mineral phases. G) Section 108N, LM11-50, 114.6 m. FEM-type exhalite, sample CNF20927. RL microscope image of microbial pyrite (Py) tubes and later stage euhedral pyrite, arsenopyrite (Apy), sphalerite (Sp), with chalcopyrite disease, and chalcopyrite (Ccp) and sulphur isotopic results of spot analyses. H) Section 103+25N, LM11-59, 194.2 m. FEM-type exhalite, sample CNF30998. Photomicrograph (RL) of euhedral and massive pyrite (Py) with galena (Gn) inclusions and associated interstitial chalcopyrite (Ccp) and pyrrhotite and sulphur isotopic results of spot analyses.*

Figure 3.7 *A) Section 101+25N, LM13-79, 186.6 m. EMS-type exhalite, sample CNF25071b. Photomicrograph (RL) of a rock chip embedded in epoxy (epoxy puck) with Pb-Zn-massive sulphides grading into a chalcopyrite-, sphalerite-, and pyrite-rich exhalite. Contact is conformable, but reworked. Spot analyses of detailed S- and Pb-analyses are marked in red and blue, respectively. B) Section 101+25N, LM13-79, 186.6 m. EMS-type exhalite, sample CNF25071b. Detailed photomicrograph (RL) of Figure 7a with euhedral pyrite (Py), sphalerite (Sp) with chalcopyrite-disease, galena (Gn), and chalcopyrite (Ccp) S- and Pb-spot analyses. C) Section 105N, LM08-24ext, 432.8 m. EMS-type exhalite, sample CNF20983. Photomicrograph (RL) of a framboids-rich exhalite with a sulphide-rich vein parallel lamination. Vein sulphides consist of euhedral pyrite (Py), interstitial chalcopyrite (Ccp), and pyrrhotite (Po) and were analysed for S-isotopes. D) Section 100+50N, LM13-76, 163.8 m. FEM-type exhalite, sample CNF25062b. Photomicrograph (RL) microscope image of a framboid-rich exhalite with a sulphide-rich vein cross-cutting lamination. Vein sulphides consist of euhedral pyrite (Py), interstitial chalcopyrite (Ccp), and galena (Gn) and were analysed for S- and Pb-isotopes. E) Section 100+50N, LM13-77, 139.6 m. FEM-type exhalite, sample CNF25064. Photomicrograph (RL) microscope image of pyrrhotite (Po) associated with chalcopyrite (Ccp), galena (Gn), and electrum (El) and S- and Pb-spot analyses. F) Section 101N, LM07-13, 165.5 m. EMS-type exhalite, sample CNF30955. Scanning electron microscope (SEM) image in back-scattered electron (BSE) mode of a sulphide-rich and Ba-bearing exhalite with high precious-metal contents. Acanthite (Aca) is associated with euhedral pyrite (Py), chalcopyrite (Ccp), Fe-rich sphalerite (Fe-Sp), barite, and Fe-rich chlorite (Fe-Chl). G) and H) Section 101N, LM07-13, 165.5 m. EMS-type exhalite, sample CNF30955. Photomicrograph (transmitted light, TL, II nicols) and SEM-BSE image of a barite-(Brt)vein cross-cutting a celsian-(Cls)rich exhalite. Other mineral phases are pyrite (py), chalcopyrite (Ccp), quartz (Qz), and hyalophane (hyal).*

Fig. 3.7 A-H

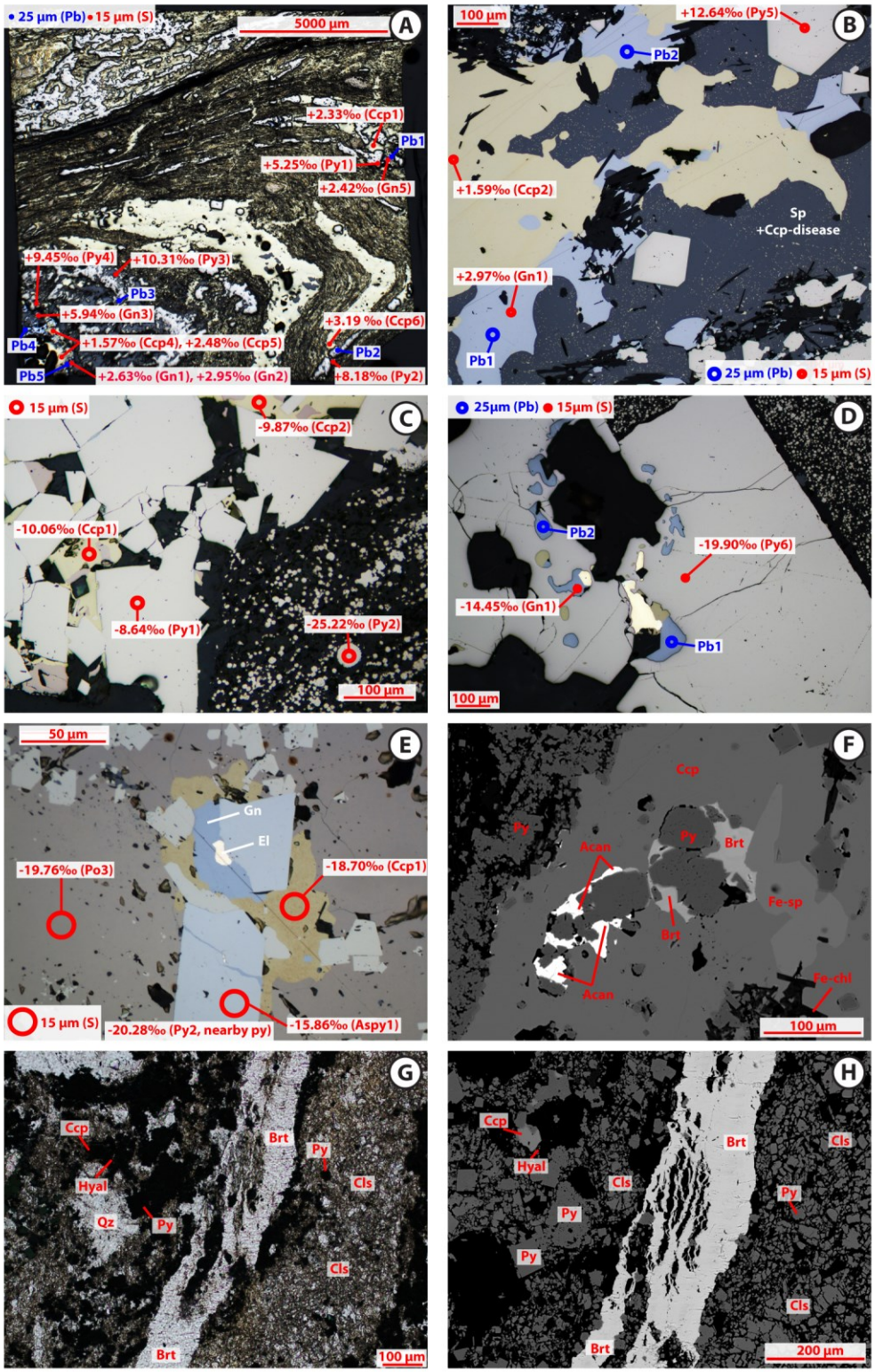
• 25 µm (Pb) • 15 µm (S)
5000 µm
A
+2.33‰ (Ccp1)
Pb1
+5.25‰ (Py1)
+2.42‰ (Gn5)
+9.45‰ (Py4)
+10.31‰ (Py3)
Pb3
+5.94‰ (Gn3)
+3.19 ‰ (Ccp6)
Pb4
+1.57‰ (Ccp4), +2.48‰ (Ccp5)
Pb2
Pb5
+2.63‰ (Gn1), +2.95‰ (Gn2)
+8.18‰ (Py2)
100 µm
+12.64‰ (Py5)
B
Pb2
+1.59‰ (Ccp2)
Sp
+Ccp-disease
+2.97‰ (Gn1)
Pb1
25 µm (Pb) 15 µm (S)
15 µm (S)
-9.87‰ (Ccp2)
C
-10.06‰ (Ccp1)
-8.64‰ (Py1)
-25.22‰ (Py2)
100 µm
25µm (Pb) 15µm (S)
D
Pb2
-19.90‰ (Py6)
-14.45‰ (Gn1)
Pb1
100 µm
50 µm
E
Gn
El
-19.76‰ (Po3)
-18.70‰ (Ccp1)
15 µm (S)
-20.28‰ (Py2, nearby py)
-15.86‰ (Aspy1)
Ccp
F
Py
Py
Acan
Brt
Fe-sp
Brt
Acan
Fe-chl
100 µm
G
Ccp
Brt
Py
Hyal
Cls
Qz
Py
Cls
Brt
100 µm
H
Ccp
Brt
Cls
Hyal
Cls
Py
Py
Py
Cls
Brt
200 µm

Fig. 3.8

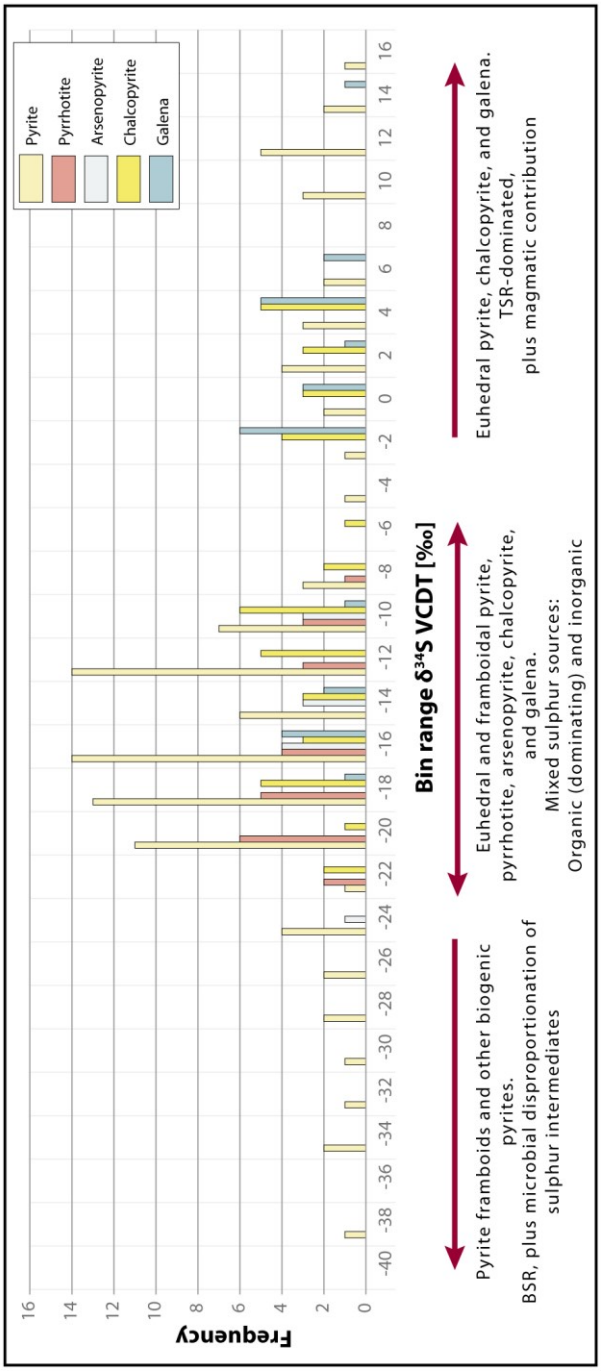

Figure 3.8 *Frequency histogram for polymetallic sulphides (pyrite, pyrrhotite, arsenopyrite, chalcopyrite, and galena) hosted within the Lemarchant exhalites. $\delta^{34}S$ values range from -38.8‰ to +14.4‰ with a total number of analyses of n = 210. Bin width = 2‰. All values in ‰ based on the sulphur standard VCDT.*

Fig. 3.9 A-C

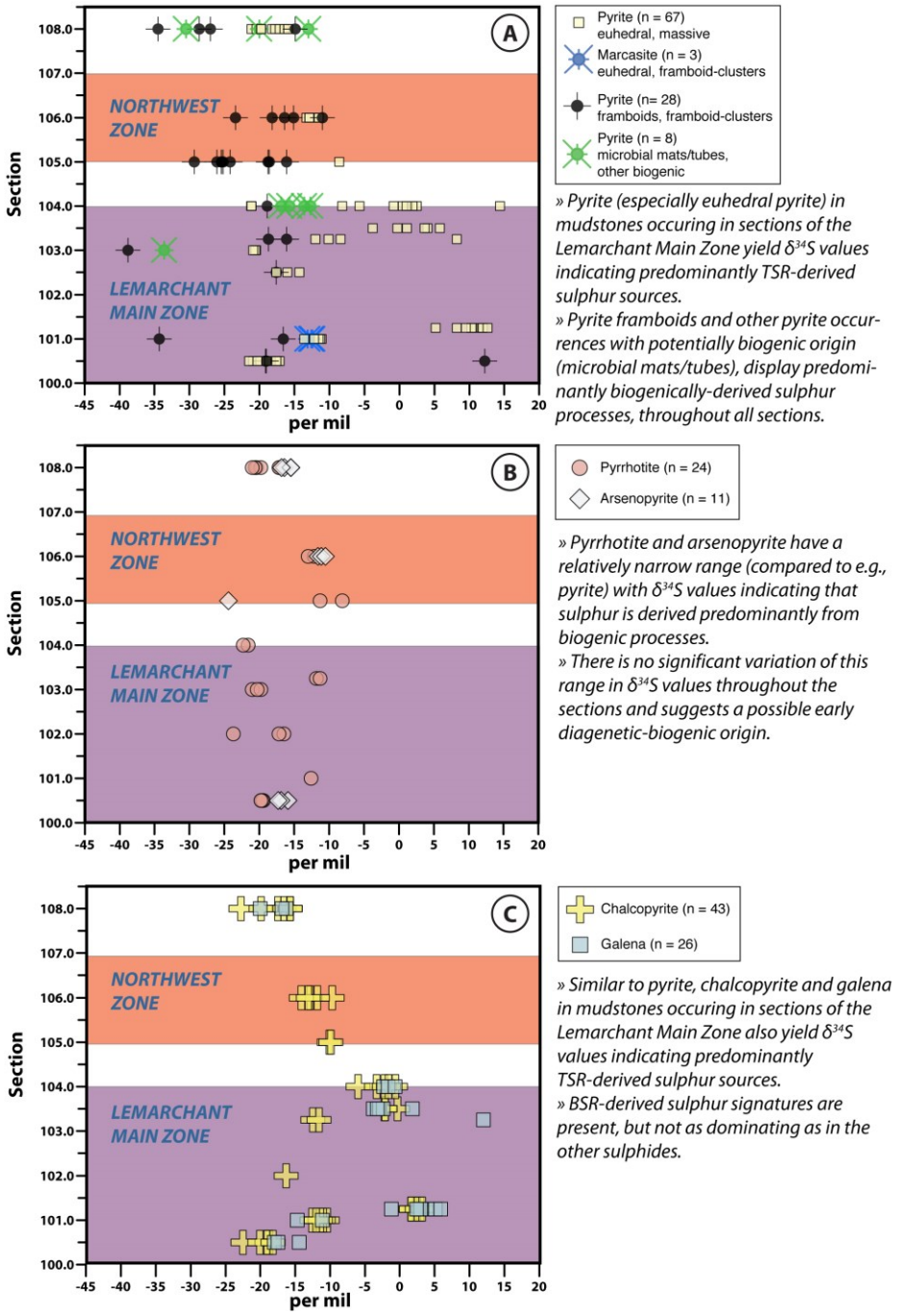

Figure 3.9 *Diagram showing the spatial distribution in respect to the mineralization of the Lemarchant Main and Northwest zones and the $\delta^{34}S$ values for A) euhedral and framboidal pyrite, marcasite, and other biogenic textures, B) pyrrhotite and arsenopyrite, and C) chalcopyrite and galena.*

Fig. 3.10 A-B

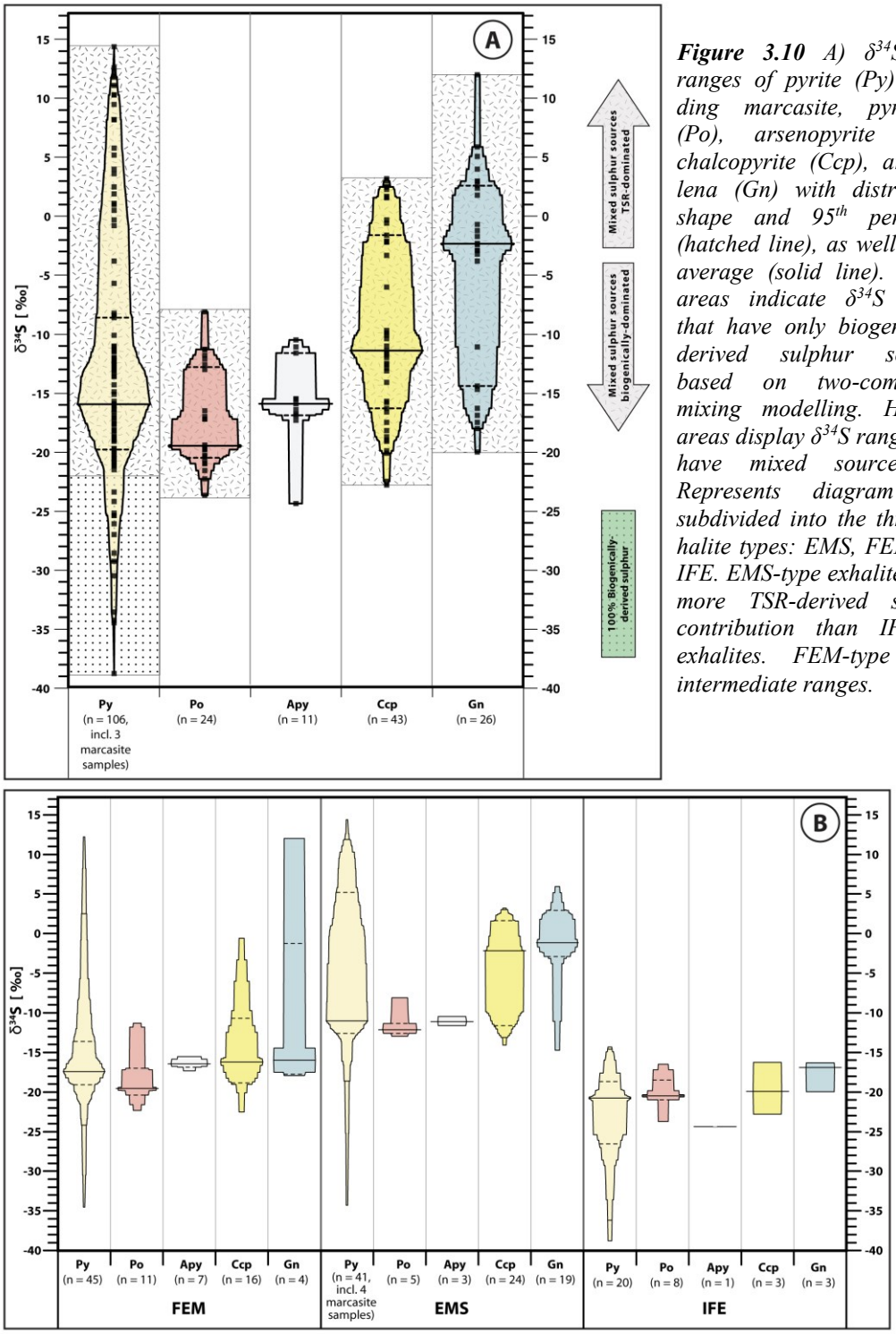

Figure 3.10 *A) $\delta^{34}S$ data ranges of pyrite (Py) including marcasite, pyrrhotite (Po), arsenopyrite (Apy), chalcopyrite (Ccp), and galena (Gn) with distribution shape and 95th percentile (hatched line), as well as the average (solid line). Dotted areas indicate $\delta^{34}S$ values that have only biogenically-derived sulphur sources, based on two-component mixing modelling. Hatched areas display $\delta^{34}S$ ranges that have mixed sources. B) Represents diagram 14A subdivided into the three exhalite types: EMS, FEM, and IFE. EMS-type exhalites have more TSR-derived sulphur contribution than IFE-type exhalites. FEM-type show intermediate ranges.*

Fig. 3.11 A-B

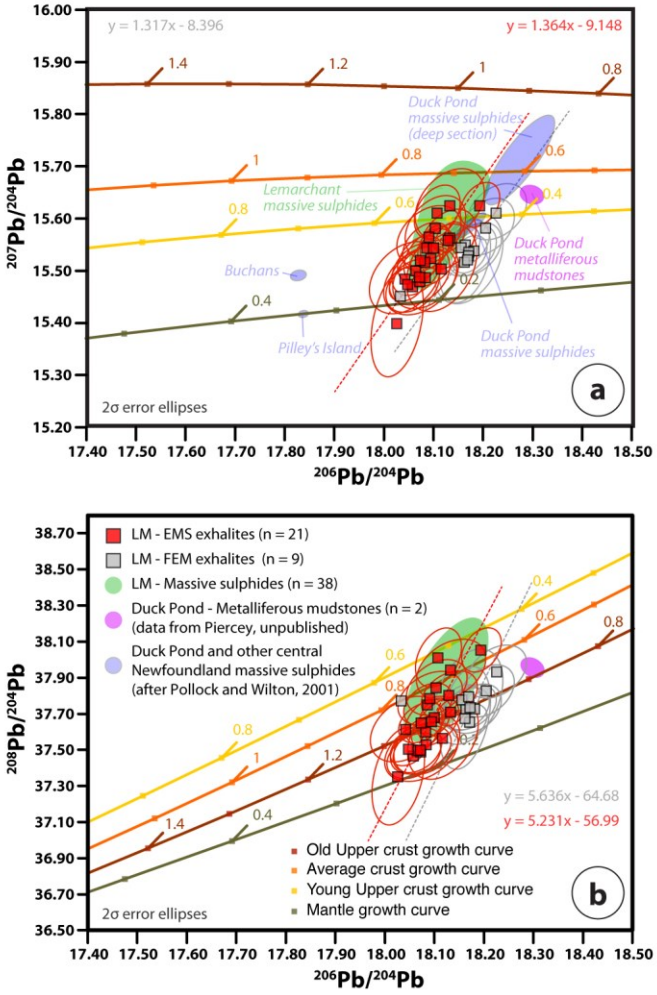

Figure 3.11 *A) $^{207}Pb/^{204}Pb$ versus $^{206}Pb/^{204}Pb$ space for in situ SIMS measurements on galena hosted in EMS- and FEM-type Lemarchant exhalites. For comparison analyses measured on galena from the Lemarchant massive sulphides (Gill 2015) (green field) and from Duck Pond metalliferous mudstones (Piercey, unpublished data) (purple field) were included, as well as representative fields for other massive sulphide deposits in central Newfoundland (Pollock and Wilton 2001) (blue fields). Growth curves were modelled after data from Kramers and Tolstikhin (1997) representing the different reservoirs Old Upper Crust, Average Crust, Young Upper Crust, and Mantle. The trendlines are York (1969) regressions and error ellipses are calculated using Isoplot 3.75. B) $^{208}Pb/^{204}Pb$ versus $^{206}Pb/^{204}Pb$ space for the same data as in 3.11A.*

Fig. 3.12 A-C

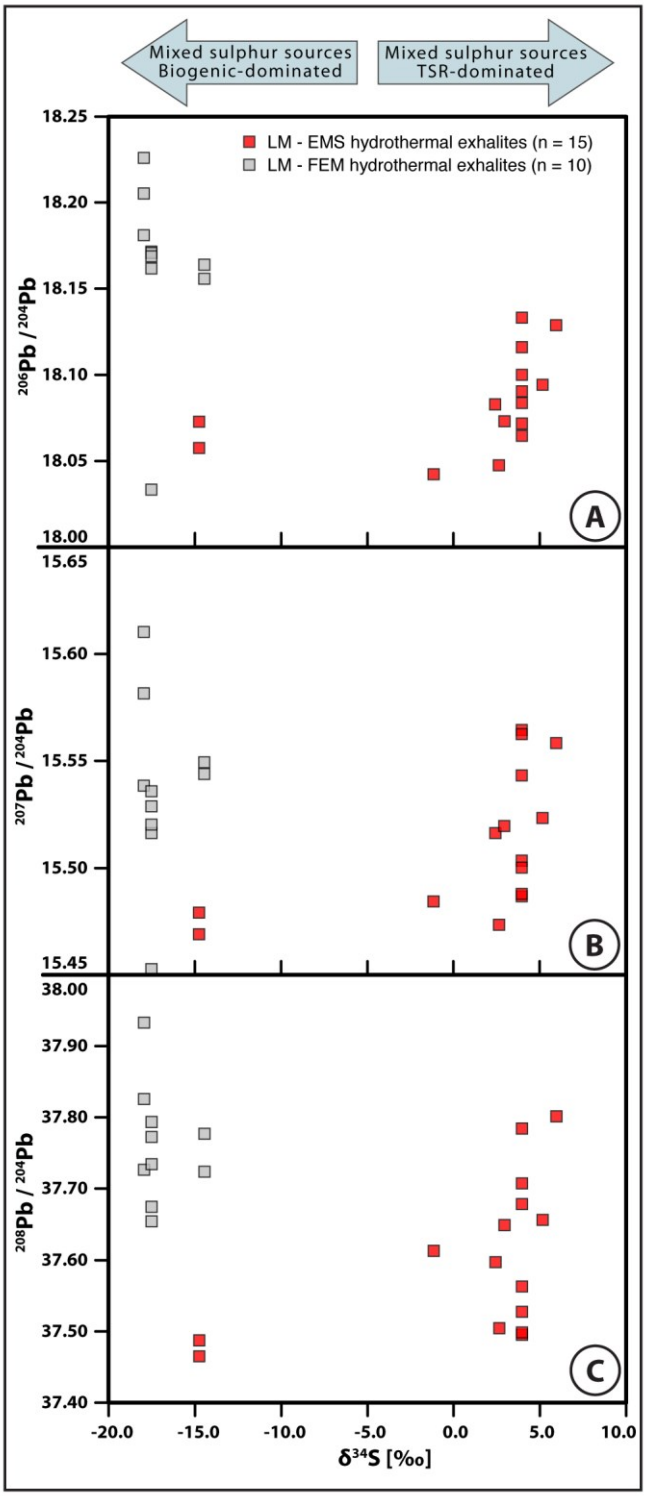

Figure 3.12 *$^{206}Pb/^{204}Pb$, $^{207}Pb/^{204}Pb$, and $^{208}Pb/^{204}Pb$ versus $\delta^{34}S$ for analyses measured on the same galena of the EMS- and FEM-type exhalites. EMS-type preferentially have TSR-dominated sulphur sources and less radiogenic Pb isotopic signatures, whereas FEM-type exhalites have more biogenic sulphur contribution, and more radiogenic Pb isotopic compositions.*

Fig. 3.13 A-D

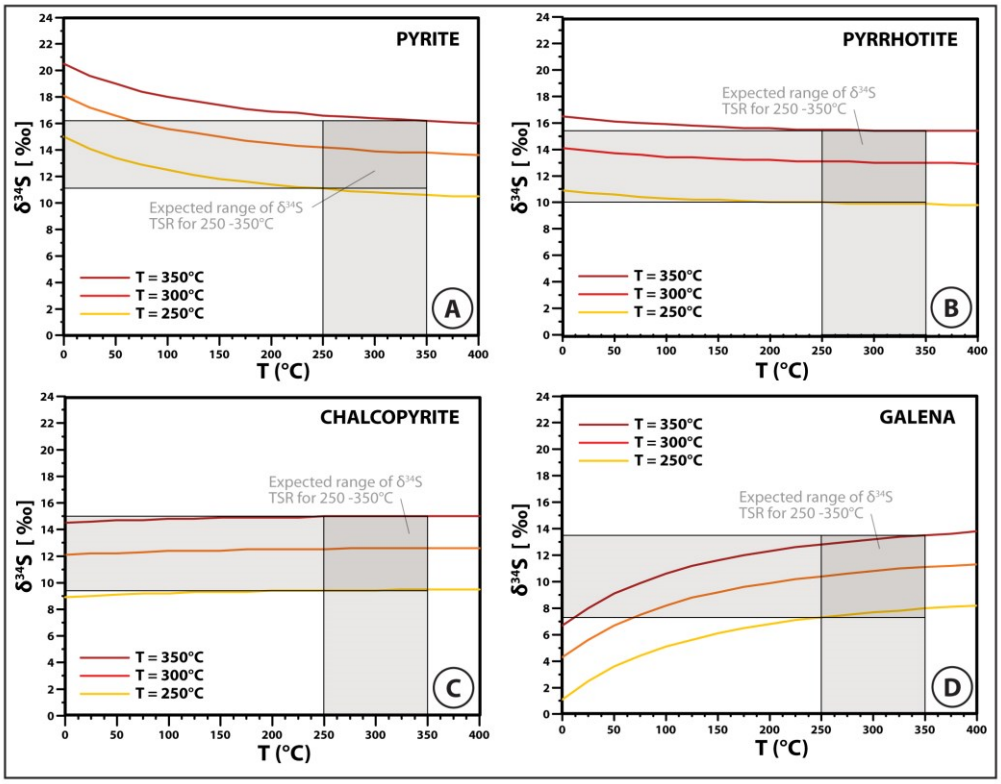

Figure 3.13 *Modelled range of sulphur isotopes for sulphides with TSR-derived sulphur at 250°C, 300°C, and 350°C for A) pyrite, B) pyrrhotite, C) chalcopyrite, and D) galena, and the range of $\delta^{34}S$ values for the Lemarchant exhalite sulphides. Due to a lack of reliable fractionation data for arsenopyrite, no modelling was undertaken.*

Fig. 3.14 A-D

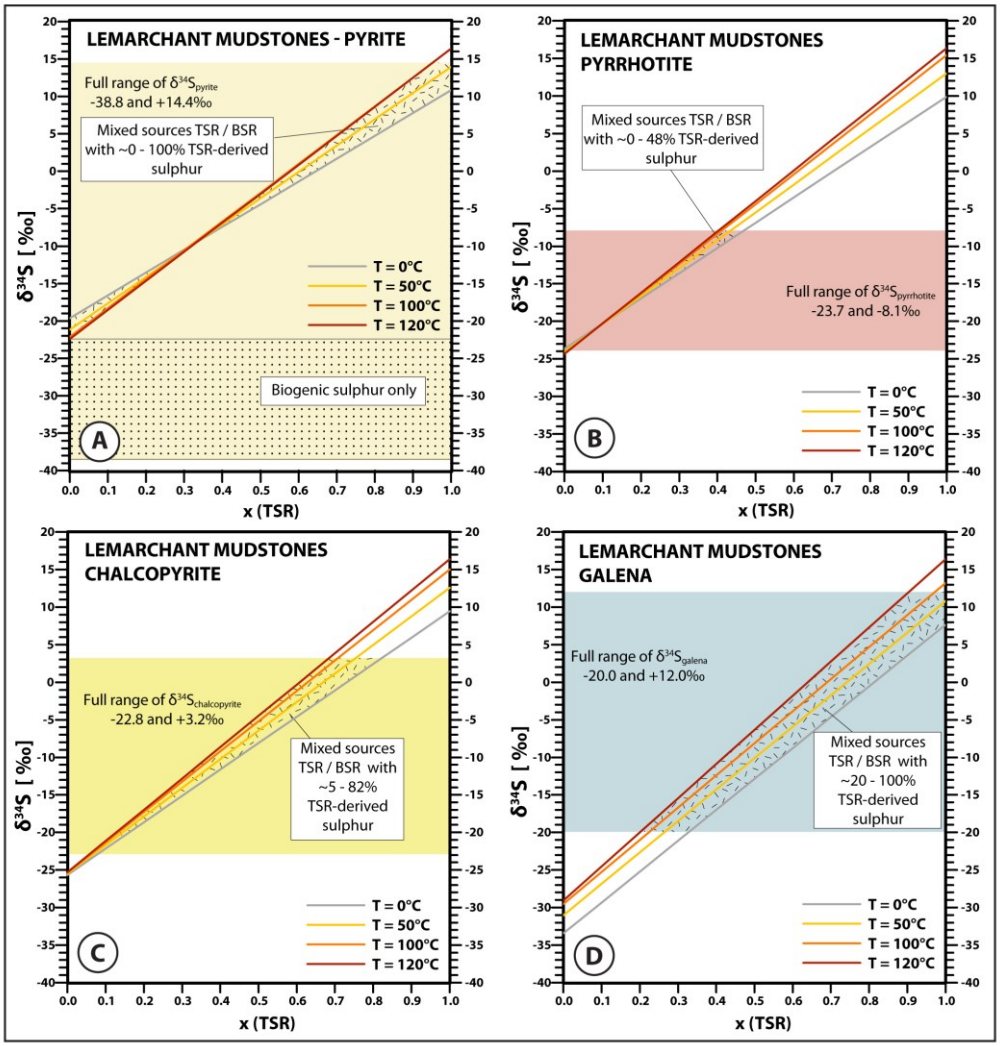

Figure 3.14 *Mixing models between TSR- and BSR-derived sulphur for the sulphides: A) pyrite, B) pyrrhotite, C) chalcopyrite, and D) galena. The mixing lines are calculated based on BSR-derived H_2S at each T = 0°C, 50°C, 100°C, and 120°C, with TSR-H_2S at T = 300°C. The interception of the range of $\delta^{34}S$ values for each sulphide measured in this study (highlighted in its respective colour) and the BSR-TSR mixing lines are highlighted in hatched fields and represent the proportion of TSR-derived sulphur in the sulphides precipitating under those parameters. $\delta^{34}S$ values of pyrite below -22.4‰ have no TSR-derived sulphur contribution, hence, have biogenically-derived sulphur only (BSR and microbial disproportionation). For modelling purpose an average $\delta^{34}S_{BSR}$ of -25‰, and $\delta^{34}S_{Cambrian\ seawater}$ of +34.5‰ is used.*

Fig. 3.15

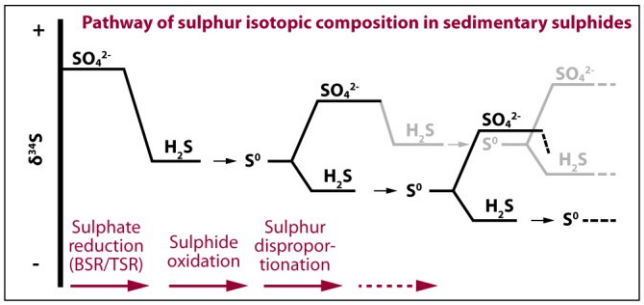

Figure 3.15 *Pathway of sulphur isotopic composition explaining the large fractionation factors present in hydrothermal sedimentary sulphides. Initial sulphate reduction, either inorganic or organic, is followed by an intermediate step of microbial sulphide oxidation and followed by microbial disproportionation of sulphur intermediate compounds (thiosulphate, sulphite, and elemental sulphur) represented by* S_0*. Modified after Canfield (2001b).*

Figure 3.16 *Polymetallic sulphides in the Lemarchant exhalites have organic and inorganic sulphur sources. Inorganic sulphur sources are more prominent in euhedral pyrite, chalcopyrite, and galena hosted in exhalites proximal to vent (and massive sulphide mineralization) than in more distally precipitates exhalites. TSR = Thermochemical sulphate reduction, BSR = bacterial sulphate reduction, BSO = biogenic/microbial sulphide oxidation. A) A synvolcanic intrusion (possibly Lemarchant microgranite) provides the heat to drive hydrothermal circulation, and adds magmatic/epithermal fluids and volatiles to seawater-derived hydrothermal fluid cells. Hot hydrothermal fluids are focused along synvolcanic faults and discharged via black and white smoker into the ambient seawater. B) Close-up cartoon of exhalites with microbial mats on rock-water-interface (green rectangle). Exhalites with microbial mats are deposited around the vent site and form a semi-permeable cover layer. Hot hydrothermal fluids circulate upwards through semi-permeable exhalites and exit via diffuse venting onto the seafloor. The hydrothermal fluids mix with cold seawater within the sediment and after emanating from the hydrothermal plume into the ambient seawater. Thermophile and hyperthermophile bacteria and archaea (sulphide-oxidizing and sulphate-reducing) form laminae of microbial mats. Modified after Gundersen et al. (1992).*

Fig. 3.16 A-B

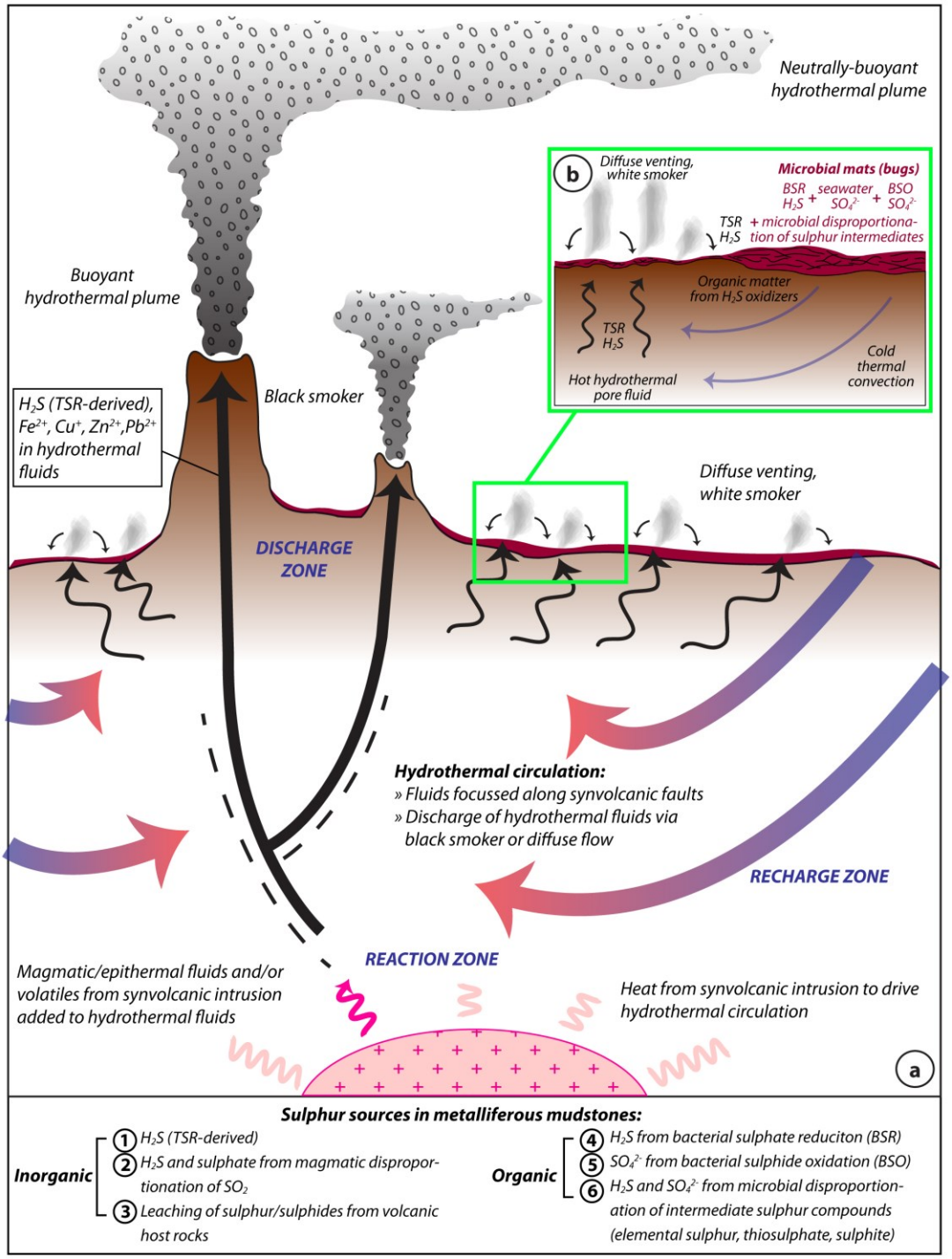
Neutrally-buoyant hydrothermal plume
Buoyant hydrothermal plume
Black smoker
H_2S (TSR-derived), Fe^{2+}, Cu^{+}, Zn^{2+}, Pb^{2+} in hydrothermal fluids
b
Diffuse venting, white smoker
Microbial mats (bugs)
BSR H_2S + seawater SO_4^{2-} + BSO SO_4^{2-}
TSR H_2S + microbial disproportionation of sulphur intermediates
Organic matter from H_2S oxidizers
TSR H_2S
Cold thermal convection
Hot hydrothermal pore fluid
Diffuse venting, white smoker
DISCHARGE ZONE
Hydrothermal circulation:
» Fluids focussed along synvolcanic faults
» Discharge of hydrothermal fluids via black smoker or diffuse flow
RECHARGE ZONE
REACTION ZONE
Magmatic/epithermal fluids and/or volatiles from synvolcanic intrusion added to hydrothermal fluids
Heat from synvolcanic intrusion to drive hydrothermal circulation
a
Sulphur sources in metalliferous mudstones:
Inorganic
1 H_2S (TSR-derived)
2 H_2S and sulphate from magmatic disproportionation of SO_2
3 Leaching of sulphur/sulphides from volcanic host rocks
Organic
4 H_2S from bacterial sulphate reduciton (BSR)
5 SO_4^{2-} from bacterial sulphide oxidation (BSO)
6 H_2S and SO_4^{2-} from microbial disproportionation of intermediate sulphur compounds (elemental sulphur, thiosulphate, sulphite)

Appendix 3.1

3.1.1 SIMS analytical methods for S and Pb isotopes

Blocks of sample (thin section cut-offs) were embedded in epoxy in 25 mm aluminium rings and polished using standard lapidary procedures. Samples were coated with 300 Å of Au, and then analysed using a Cameca IMS 4f SIMS equipped with an ETP 133H multiple-dynode electron multiplier (em) and processed through ECL-based pulse-counting electronics with an overall dead time of 11 ns in the MAF-IIC Microanalysis Facility at Memorial University.

$\delta^{34}S$ spot analyses were performed by bombardment of the sample with a primary ion microbeam of 0.60 to 1.00 nano-amps (nA) of Cs, with current adjusted to provide optimal counting rates on each sulphide phase (750K – 900K cps). The primary beam was accelerated through a nominal 10 keV potential, and focused into a spot of 10-15 μm diameter. For sulphur isotope analyses, samples were pre-sputtered for 120-180 s with a 25 μm square raster, to remove surface contamination before analysis, followed by 200 s of data accumulation using the 10-15 μm beam diameter for the spot analysis.

Negatively charged sputtered ions were accelerated into the mass spectrometer through a nominal potential of 4.5 keV. To sufficiently discriminate $^{33}SH^-$ (and $^{32}SH_2^-$) from $^{34}S^-$ a mass resolving power (MRP of ~2,975), with additional energy filtering (sample offset of 60 eV and energy window of 40 eV) applied to effectively eliminate other minor isobaric interferences. Cyclical magnetic peak switching (80 cycles) was used to obtain signals for $^{32}S^-$ and $^{34}S^-$ and a 31.67 Dalton (Da) background position, with standard counting times of 0.5 s at background position, 2.0 s on $^{32}S^-$, and 6.0 s on $^{34}S^-$.

Magnet settling was assured by inserting waiting times of 0.25 s before each peak counting. These procedures resulted in a 15 minutes acquisition time per analysis, including pre-sputtering. Sulphur isotope results are reported using the standard $\delta^{34}S$ notation with units in per mil [‰] relative to the international Vienna Cañon Diablo Troilite (VCDT) standard. To correct for instrumental mass fractionation (IMF) the following sulphide in-house standards were used: 1) pyrite – UL9 ($\delta^{34}S$ = +15.8‰) and KH87 ($\delta^{34}S$ = +0.2‰); 2) chalcopyrite – Norilsk ($\delta^{34}S$ = +8.3‰); 3) pyrrhotite – PoW1 ($\delta^{34}S$ = +2.3‰); 4) arsenopyrite – Arspy57 ($\delta^{34}S$ = +2.8‰); and 5) galena – HT10 ($\delta^{34}S$ = +14.2‰). Internal precision of individual $\delta^{34}S$ measurements with analytical runs of 12 min (excluding pre-sputtering) was generally better than ±0.25‰ (1σ), with ±0.35‰ for the overall reproducibility.

Samples for lead isotope microanalyses, samples were pre-sputtered for 120-180 s with a 25 μm square raster, followed by 75 s with the spot beam, to remove surface contamination before analysis. Spot analyses for Pb isotopes were performed by bombardment of the sample with a primary ion microbeam of 14 to 16 nano-amps (nA) of O^-. The primary beam was accelerated through a nominal 10 keV potential, and focused into a 20-25 μm diameter spot. Positively charged sputtered ions were accelerated into the mass spectrometer of the instrument through a nominal potential of 4.5 keV. The mass spectrometer was operated with a minimal mass resolving power (MRP 300) and energy filtering (sample offset of 60 eV and energy window of 60 eV) was applied to effectively eliminate minor isobaric interferences. Cyclical magnetic peak switching (15 cycles) was used to obtain signals for $^{204}Pb^+$, $^{206}Pb^+$, $^{207}Pb^+$, and $^{208}Pb^+$, and a 203.67 Dalton (Da) background position, with standard counting times of 1.0 s at background position, 8.0 s

on $^{204}Pb^{+}$, and 4.0 s on $^{206}Pb^{+}$, $^{207}Pb^{+}$, and $^{208}Pb^{+}$. Magnet settling was achieved by inserting waiting times of 0.5 s before each was peak counted. These procedures resulted in a 12 minutes acquisition time per analysis, including pre-sputtering. Any change in overall peak intensities with time - which is typically monotonic in homogeneous lead-rich sulphide mineral phases (and thus quantitatively minor in its effect on measured Pb ratios) - was compensated for using a standard double interpolation ratio algorithm (an approach adopted from TIMS analysis), with each $^{204,207,208}Pb^{+}$ peak ratioed to the time-corrected interpolation of the two immediately adjacent $^{206}Pb^{+}$ peaks. Two in-house galena standards (F19 and JMBH) were used to correct for instrumental mass fractionation (IMF). In press values for these reference materials were: F19 $^{204}Pb/^{206}Pb$ = 0.05896, $^{207}Pb/^{206}Pb$ = 0.9160, and $^{208}Pb/^{206}Pb$ = 2.154 and standard JMBH $^{204}Pb/^{206}Pb$ = 0.06248, $^{207}Pb/^{206}Pb$ = 0.9616, and $^{208}Pb/^{206}Pb$ = 2.228. 15 cycle analyses accumulated in 9 min routinely yield internal precisions (standard error of the mean) on $^{204}Pb/^{206}Pb$, $^{207}Pb/^{206}Pb$ and $^{208}Pb/^{206}Pb$ determinations of better than ±0.05 to 0.10 % (1σ), while producing sputter craters only a few μm deep. Overall reproducibility, based on replicate analyses of the secondary standard JMBH, is typically better than ±0.10 – 0.15% for these same ratios.

Appendix 3.2: Supplementary Figure

Appendix Fig. 3.2.1 A-B

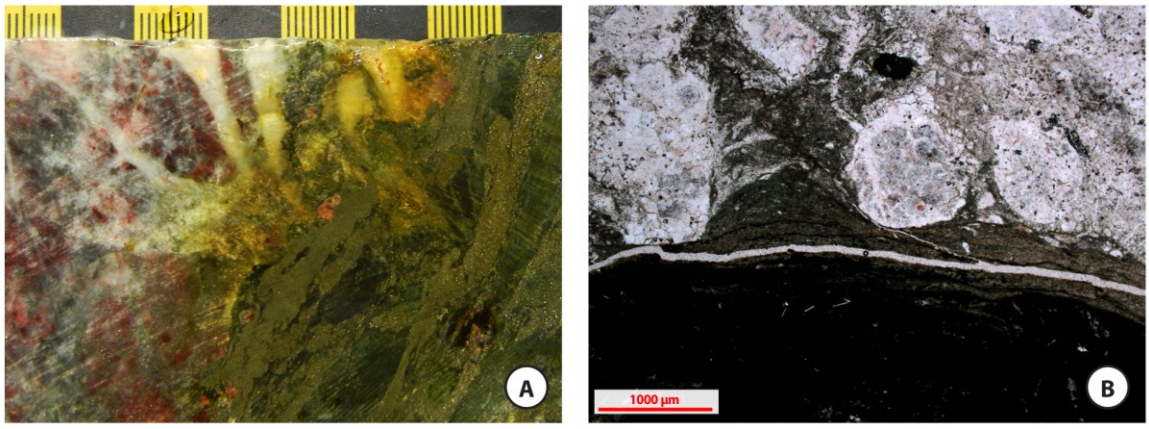

Appendix Figure 3.2.1 *A) Section 104+51N, LM08-19, 98.9 m. EMS-type exhalite, sample CNF30957. Core-photograph of a sulphide-rich, partially reworked exhalite that is conformably overlain by a chert-jasper layer. B) TS-II microscope image of the contact between the exhalite and jasper, which is marked by carbonaceous and cherty layer of suggested paleo-microbial mats.*

CHAPTER 4

Lithogeochemical and Nd isotopic provenance studies of metalliferous mudstones associated with the Lemarchant volcanogenic massive sulphide deposit, central Newfoundland, Canada

Stefanie Lode[1*], Stephen J. Piercey[1], and Jonathan Cloutier[1,2]

[1]*Department of Earth Sciences, Memorial University, 300 Prince Philip Drive, St. John's, NL, Canada, A1B 3X5*

[2]*Department of Earth Sciences, University of St. Andrews, St. Andrews, Scotland, UK, KY16 9AL*

Status quo: Preliminary draft for a paper that will be finalized for submission ~early 2016

4.1 Abstract

Neodymium isotopic and geochemical data in combination with *in situ* Pb isotopic data on metalliferous mudstones and tuffs associated with the Cambrian Lemarchant Zn-Pb-Cu-Ba-(Au-Ag) VMS deposit provide insights into the tectonic environment and metallogenic evolution of the Tally Pond volcanic belt, northern Appalachians. The Tally Pond belt represents the oldest (~513-509 Ma) magmatism associated with the construction of the Cambrian to Ordovician Penobscot Arc, and is built upon crustal

basement of the Ediacaran age Cripplebback Intrusive Suite and the coeval Sandy Brook Group and possibly Mesoproterozoic Ganderian basement. The Lemarchant metalliferous mudstones and tuffs yield εNd_{513} between -6.0 and -1.8, whereas the associated Tally Pond belt felsic and mafic volcanic rocks have more juvenile εNd_{513} of +0.4 and +1.4, respectively. The latter are similar to previously reported values for volcanic rocks of the Tally Pond belt. The more evolved values of the exhalative sediments have not been reported previously in this belt; however, they overlap the documented range of εNd for the underlying Neoproterozoic Sandy Brook Group rhyolite ($\square Nd_t$ = -6.5 to -1.9), and the Cripplebback Intrusive Suite ($\square Nd_t$ = -5.9 to -5.2). Accordingly, it is suggested that the exhalative metalliferous mudstones that precipitated from hydrothermal fluids, represent mixed Nd sources with Nd inherited from the Tally Pond volcanic rocks as well as from the evolved crustal basement sources. Combined with lithogeochemical provenance data it is proposed that the Lemarchant sedimentary rocks were deposited in a volcanic basin/caldera setting in a peri-continental rifted arc environment, with evolved continental and juvenile mafic sources, which is consistent with previously reported tectonic environment of formation for the Tally Pond volcanic belt.

4.2 Introduction

Metalliferous mudstones are abundant in the Tally Pond volcanic belt, central Newfoundland Appalachians, and are locally genetically associated with volcanogenic massive sulphide (VMS) deposits (Swinden, 1991; Squires and Moore, 2004). The Tally Pond volcanic belt, which is part of the Dunnage Zone in central Newfoundland, belongs

to the Cambrian (~515 Ma) to Permian (~275 Ma) Appalachian mountain belt and hosts numerous VMS deposits, including the economically significant Duck Pond and Boundary mines, as well as the Lemarchant deposit (Fig. 4.1A-B; Williams, 1979; Swinden, 1988, 1991; Evans and Kean, 2002; Rogers et al., 2007; van Staal and Barr, 2011; Piercey et al., 2014). The Tally Pond belt (~513-509 Ma) volcanic rocks and related massive sulphide mineralization formed during episodes of rifting throughout the construction of the Cambrian to Early Ordovician Penobscot Arc, which is built upon Late Precambrian (~563 Ma) crustal basement of the Cripplebback Intrusive Suite and the coeval Sandy Brook Group (Pollock et al., 2002; Zagorevski et al., 2007; Zagorevski et al., 2010; Piercey et al., 2014). Volcanogenic massive sulphide (VMS) mineralization and associated hydrothermal sedimentary rocks in the Tally Pond group formed during the ~513-509 Ma rifting within the Penobscot Arc (Rogers et al., 2006; Copeland et al., 2009; Zagorevski et al., 2010). The sedimentary rocks deposited in this type of graben-/rift-related basins typically are of volcaniclastic and epiclastic nature, and locally also can contain exhalative metalliferous mudstones. Their depositional environment is controlled by volcanic activity and a generally active tectonic setting (Carey and Sigurdson, 1984). Exhalative hydrothermal sedimentary rocks associated with modern VMS deposits form from the deposition of hydrothermal precipitates that formed in buoyant hydrothermal plumes upon fluid venting from black smokers (Hekinian et al., 1993; Hannington et al., 1995; German and Von Damm, 2003). These black smokers and associated hydrothermal sedimentary rocks occur in close proximity to sites where hydrothermal fluids are focused along deep synvolcanic faults in extensional settings, e.g. ocean ridges, rifted arcs, or backarc basin spreading centres (Fig. 4.2; Lydon, 1984; Hannington et al., 2005; Gibson

et al., 2007). The hydrothermal fluids are modified seawater, which is entrained through oceanic or rift-related continental crust, and are variably metal-bearing with Fe, Mn, Cu, Pb, and Zn, as well as reduced sulphur and Si (Von Damm, 1990; German and Von Damm, 2003; Galley et al., 2007; Tivey, 2007; Huston et al., 2010). The metals and other ligands are generally derived from: seawater (S), leached from host rocks (e.g., metals, Si ±S), and depending on the depth of the hydrothermal circulation, the fluids may contain additional inputs from magmatic fluids/volatiles from underlying magmatic intrusions (Fig. 4.2; Hannington et al., 2005; Huston et al., 2011).

By using various isotopic tracers, and in particular the Nd isotopic system, it is possible to decipher the potential sources of various components in hydrothermal sediments. The Nd isotopic system is specifically useful for understanding the relative roles of evolved versus juvenile crust, and provides further insight into tectonic environment and provenance of the metalliferous mudstones, as it is robust and not significantly modified by diagenetic, hydrothermal, and metamorphic processes (McCulloch and Wasserburg, 1978; McLennan et al., 2003). In addition, the separation of Sm-Nd in Earth's reservoirs is particularly useful in delineating juvenile versus evolved crust and the time-integrated sources of materials in Earth materials (McCulloch and Wasserburg, 1978; Rollinson, 1993; McLennan et al., 2003). Sm and Nd preferentially partition into different reservoirs that evolve towards characteristic Sm-Nd signatures over time, with crustal sources having evolved signatures (i.e., low $^{143}Nd/^{144}Nd$ signatures), and juvenile mantle reservoirs (with high $^{143}Nd/^{144}Nd$; McCulloch and Wasserburg, 1978; Rollinson, 1993). The epsilon Nd (εNd) values describe variations and deviations of the $^{143}Nd/^{144}Nd$ from the chondritic uniform reservoir (CHUR) value,

whereby εNd > CHUR represents juvenile and εNd < CHUR evolved sources (Rollinson, 1993). εNd_t was calculated by $\varepsilon Nd_t = (^{143}Nd/^{144}Nd_{rock,t} / {}^{143}Nd/^{144}Nd_{CHUR,t}) \times 10^4$ after Rollinson (1993).

The Tally Pond belt formed in a rifted arc environment and has juvenile εNd signatures between +1.8 and +3.1 (Rogers et al., 2006; Piercey et al., 2014; Zagorevski et al., 2010), whereas the underlying crustal basement rocks of the Cripplebacк Intrusive Suite and the Sandy Brook Group show more evolved εNd characteristics: between -3.90 to -4.60 and -0.67 to -5.18, respectively (Rogers et al., 2006; McNicoll et al., 2010; Piercey et al., 2014). Correspondingly, the Nd isotopic signatures of the mudstones may be useful in elucidating potential contributions to their provenance components.

The stratigraphy of the lithofacies at Lemarchant is generally well preserved and accordingly, the Lemarchant deposit, including the metalliferous mudstones, is an excellent location to understand the provenance of hydrothermal mudstones in ancient rifted arcs (Copeland et al., 2008; Copeland et al., 2009). The purpose of this study is to 1) determine the sources of Nd in the metalliferous mudstones and massive sulphides of the Lemarchant deposit; and 2) because the Tally Pond volcanic belt is formed upon Late Precambrian crustal basement rocks, to evaluate the relative roles of mantle and crustal inputs that contributed to the Lemarchant hydrothermal system using the Nd isotope compositions measured on metalliferous mudstones.

4.3 Regional geology

The Newfoundland Appalachians are divided into four tectonostratigraphic zones (from west to east): Humber, Dunnage, Gander and Avalon zones (Fig. 4.1A; Williams, 1979; Swinden, 1988, 1991). The Dunnage Zone represents the Central Mobile Belt (Williams et al., 1988; Swinden, 1991; Rogers et al., 2007). These zones result from, and were affected by, the successive accretion of three micro-continental blocks during the Early Paleozoic to Middle Paleozoic (i.e., Dashwoods, Taconic orogenesis; Ganderia, Salinic orogenesis; and Avalonia, Acadian orogenesis) and related interoceanic arcs and backarcs (Swinden, 1991; Zagorevski et al., 2010). These ribbon-shaped micro-continental blocks were located on the leading edges of Gondwana and Laurentia, forming peri-Gondwanan and peri-Laurentian terranes (Rogers et al., 2007; Zagorevski et al., 2010; van Staal and Barr, 2011). The suture between the peri-Laurentian Notre-Dame Subzone and the peri-Gondwanan Exploits Subzone is represented by the Red Indian Line, and corresponds to a ribbon-shaped zone of a tectonic mélange, which contains remnants of Cambro-Ordovician oceanic infant arc and arc terranes that existed within the Iapetus Ocean (Williams, 1979; Zagorevski et al., 2010; van Staal and Barr, 2011). The Exploits Subzone represents two phases of arc-backarc formation, the Cambrian to Early Ordovician Penobscot Arc and the Early to Middle Ordovician Victoria Arc (Zagorevski et al., 2010). Massive sulphide formation is associated with the evolution and rifting of the Penobscot Arc (Swinden et al., 1989; Rogers et al., 2007; Zagorevski et al., 2010). The Tally Pond volcanic belt and its VMS deposits (Duck Pond and Boundary mines, and the Lemarchant deposit, Fig. 4.1B) are hosted in the lower Victoria Lake supergroup within the Exploits Subzone, which is comprised of Cambrian to Ordovician volcanic and sedimentary rocks (Dunning et al., 1991; Rogers et al., 2007; McNicoll et al., 2010; van

Staal and Barr, 2011). The Tally Pond group (U-Pb zircon ages ranging from ~513 to 509 Ma) is the oldest of six fault-bounded tectonic assemblages that together, form the Victoria Lake supergroup (Dunning et al., 1987; Dunning et al., 1991; Evans and Kean, 2002; McNicoll et al., 2010; Zagorevski et al., 2010; Piercey et al., 2014). The Tally Pond group is informally subdivided into the felsic volcanic rock dominated Bindons Pond formation (also referred to as Boundary Brook formation) and the mafic volcanic rock dominated Lake Ambrose formation (Pollock et al., 2002; Copeland et al., 2009). The latter contains island arc tholeiitic basalts to andesites with εNd_{511} of +3.1 (Dunning et al., 1991; Evans and Kean, 2002; Rogers et al., 2006), whereas the former contains predominantly transitional to calc-alkalic rhyolitic to dacitic rocks with εNd_{511} of +1.8 to 2.6 (Rogers et al., 2006; Piercey et al., 2014). Metalliferous mudstones predominantly occur at the contact between the Bindons Pond and the Lake Ambrose formations, and commonly are associated with massive sulphide deposits, e.g., the Lemarchant VMS deposit (Copeland et al., 2008; Lode et al., 2015). Collectively, the Tally Pond group is interpreted to represent an arc to rifted arc environment built upon basement consisting of the ~563 Ma (U-Pb; zircon) Cripplebeck Intrusive Suite and the Sandy Brook Group (Pollock et al., 2002; Rogers et al., 2006; McNicoll et al., 2010; Zagorevski et al., 2010; Piercey et al., 2014).

4.4 Deposit geology and lithofacies

The Lemarchant VMS deposit is hosted within the Bindons Pond formation and is capped by a <1 to 20 m thick layer of metalliferous mudstones occurring at the contact

between the Bindons Pond and Lake Ambrose formations (Fig. 4.3, 4.4A; Copeland et al., 2009; Fraser et al., 2012). These sulphide-rich metalliferous mudstones extend discontinuously around the massive sulphides for one to four kilometres (Copeland et al., 2009; Fraser et al., 2012). The massive sulphides of the Lemarchant Main Zone are 1.7 to 30.4 m thick and consist of a barite-rich outer zone that grades into a Pb-Zn-sulphide-rich zone, and a Zn-Cu-sulphide core, which grades into stringer mineralization at depth, typical of bimodal felsic/Kuroko-style mineralization (Copeland et al., 2009; Fraser et al., 2012; Gill, 2015). The deposit contains typical VMS sulphides (pyrite, sphalerite, galena, and chalcopyrite), but also abundant sulphosalts (e.g., tetrahedrite-tennantite), bornite, stromeyerite, electrum, bladed barite, and calcite; and is enriched in epithermal suite elements (e.g., Au, Ag, As, Hg, Sb, Bi) (Gill and Piercey, 2014; Gill, 2015). The Lemarchant mudstones also contain many of the above minerals, including bladed barite and calcite/Ca-Fe-Mg-Mn-carbonate, electrum ±Hg ±Sb, as well as acanthite and the Ag-Sb sulphosalts pyrargyrite and stephanite (Lode et al., 2015). The sulphosalt-rich mineralogy, barite-calcite textures, and anomalous element suite in the ores and mudstones indicate that the Lemarchant deposit formed in a shallow water environment with both VMS and epithermal features (Gill and Piercey, 2014; Gill, 2015; Lode et al., 2015).

Three main types of exhalative mudstones occur at the Lemarchant deposit: 1) mudstones immediately on top of massive sulphide mineralization between the felsic and mafic volcanic rocks (exhalative mudstone-massive sulphide (EMS)-type; Fig. 4.4A-C, G-H); 2) mudstones extending laterally outwards from mineralization, but at the same stratigraphic level and not directly associated with mineralization (felsic-exhalative

mudstone-mafic (FEM)-type; Fig. 4.4D); and 3) interflow mudstones within the hanging wall basaltic rocks (interflow exhalative mudstone (IFE)-type; Fig. 4.4E). Interflow mudstones occur commonly within 15 meters above the massive sulphide mineralization, but are present up to 70 meters above the ore horizon (Fig. 4.3). Independent of their stratigraphic positions, the mudstones are brown to black, graphite-rich, finely laminated, and contain fine carbonaceous/organic-rich laminae that are intercalated with siliciclastic, volcaniclastic and/or amorphous kidney-shaped chert±apatite layers (Fig. 4.4C, F). The main sulphides are pyrite (framboidal, massive and euhedral) and pyrrhotite, with minor marcasite, chalcopyrite, sphalerite, arsenopyrite and galena. Contents of chalcopyrite, sphalerite, and galena increase with increasing proximity to mineralization. The sulphides occur both parallel to bedding, and in later stage, stringer-like veins (Fig. 4.4A, D-E).

4.5 Methodology

4.5.1 Sampling, methods, quality assurance, and quality control (QA/QC)

Samples were collected during stratigraphic mapping and drill core logging of the Lemarchant deposit from drill holes that have metalliferous mudstones and include the Lemarchant Main Zone, the Northwest and 24 zones, as well as the North and South targets (Fig. 4.3, 4.6B), from drill hole depths ranging from 9 m to 511 m. Samples for petrographic studies were collected from representative exhalative mudstone types (EMS, FEM, and IFE), tuff, and surrounding mafic and felsic volcanic host rocks. The results of the whole rock lithogeochemical studies of the Lemarchant exhaltive mudstones and a

detailed description of the used methods as well as the QA/QC protocol can be found in Lode et al. (2015), and are reproduced here only to compare to Nd isotope results.

4.5.2 Neodymium isotopic technique

Twelve representative samples were selected from the Lemarchant mudstones for Nd isotopic determinations from the three mudstone types and tuffs that are intercalated with the mudstones. These samples were chosen to cover both the horizontal and vertical distributions of all mudstones types and tuff occurring in the Lemarchant area. Additionally, one least altered sample from each of the felsic and mafic volcanic rocks of the Bindons Pond and Lake Ambrose formations, respectively (Fig. 4.4G-H) was selected for analyses. Samarium and Nd isotopic compositions were measured at Memorial University using a multicollector Finnigan Mat 262 thermal ionization mass spectrometer in static and dynamic acquiring modes. Samples for Nd analyses were prepared from whole-rock powders using a multi-acid (HF, HNO_3, and HCl) dissolution-evaporation process following methods described in Fisher et al. (2011). Separation of Sm and Nd was obtained using conventional two-step column chemistry methods (Fisher et al., 2011).

Accuracy and precision for the Nd analyses were determined using the standards JNdi-1 and BCR-2 as reference materials following methods described in Fisher et al. (2011). The JNdi-1 and BCR-2 standards have the following reported values: $^{143}Nd/^{144}Nd = 0.512115$ and $^{143}Nd/^{144}Nd = 0.512633$, respectively (Tanaka et al., 2000; Raczek et al., 2003). Standards were run every 11 samples within each analytical batch. Additionally,

blanks were utilized during each analytical run to test for contamination; none was detected. Precision was determined using the percent relative standard deviation (% RSD) on the replicate analyses of the reference materials, and accuracy was determined using percent relative difference (% RD) from accepted values. Analyses for the Lemarchant samples have an average 0.0013 %RSD for $^{143}Nd/^{144}Nd$ and 0.00055 %RD for $^{143}Nd/^{144}Nd$.

The results are presented using the epsilon notation (εNd) and calculated for a formation age of 513 Ma, as reported by Dunning et al. (1991), and presented in Table 4.1 and Figures 4.5A-B and 4.6A-B. εNd_{513} was calculated by $\varepsilon Nd_t = (^{143}Nd/^{144}Nd_{rock,t} / ^{143}Nd/^{144}Nd_{CHUR,t}) \times 10^4$ after Rollinson (1993) and $f^{Sm/Nd} = [(^{147}Sm/^{144}Nd_{sample,t}) / (^{147}Sm/^{144}Nd_{CHUR,t}) - 1]$ after McLennan et al. (1990). Depleted mantle model ages (T_{DM}) were calculated using depleted mantle values of $^{144}Nd/^{144}Nd = 0.513163$ and $^{147}Sm/^{144}Nd = 0.2137$, and a decay constant of $\lambda = 6.54 \times 10^{-12}$.

4.5.3 Results

4.5.3.1 Neodymium isotopic systematics: The Lemarchant mudstones (n = 10), have εNd_{513} = -6.0 to -1.8 and T_{DM} = 1.63-3.05 Ga (Table 4.1). Overall, the three types of Lemarchant mudstones (EMS = proximal; FEM = distal; IFE = interflow) have similar εNd_{513} values; however, the EMS-type have slightly lower εNd_{513} values and range from -5.6 to -4.1 with an average of -4.8, the FEM-type are less evolved and range from εNd_{513} = -4.0 to -3.2 with an average of -3.7, and the IFE-type has the widest range of εNd_{513} = -6.0 to -1.8 and average of -3.9 (Table 4.1; Fig. 4.5A-B, 4.6A-B). The Lemarchant tuff

samples (n = 2) have εNd_{513} = -5.7 to -4.7 with an average of -5.2 and T_{DM} = 1.75-1.81 Ga. The εNd versus Th/Sc space for sedimentary rocks describes potential source rocks in terms of their relative age (εNd) and bulk composition (Th/Sc) (McLennan et al., 1993). The Lemarchant mudstones and tuff have Th/Sc ratios of 0.06 to 1.93 and fall between the arc andesite fields, and samples with greater Th/Sc and likely felsic component have lower εNd like the upper crust (Fig. 4.5A). These more evolved samples also trend towards the field of the 563 Ma Crippleback Intrusive Suite and Sandy Brook Group crustal basement rocks. For direct comparison, the Nd values for these basement rocks reported by Rogers et al. (2006) were recalculated for 513 Ma (Fig. 4.5A). The Lemarchant felsic volcanic rock measured in this study (n = 1) has εNd_{513} = +0.4 and a T_{DM} = 1.47 Ga, and the Lemarchant mafic volcanic rock measured in this study (n = 1) has a more juvenile value of εNd_{513} = +1.4 and a T_{DM} = 1.74 Ga and plot in the field for arc rocks (Table 4.1, Fig. 4.5B). These values for the Lemarchant volcanic rocks correspond to values reported by Rogers et al. (2006) and McNicoll et al. (2010) for felsic and mafic volcanic rocks of the Tally Pond volcanic belt, including samples from the Upper and the Mineralized blocks of the Duck Pond deposit (Fig. 4.5B).

The $f^{Sm/Nd}$ reflects the deviation of $^{147}Sm/^{144}Nd$ from CHUR in parts per 10^4 and monitors igneous differentiation processes and the overall extent of differentiation (McDaniel et al., 1997; McLennan et al., 2003). Accordingly, in $f^{Sm/Nd}$ - εNd space (Fig. 4.5B) the Lemarchant mudstone and tuff samples have more evolved εNd_{513} values than the Lemarchant volcanic rocks, and overall are comparable in εNd to values reported by Rogers et al. (2006) for the Neoproterozoic Crippleback quartz-monzonite and Sandy Brook Group rhyolite (εNd re-calculated for 513 Ma). However, in regard to the $f^{Sm/Nd}$

ratios, the Lemarchant mudstone and tuff samples are higher than the Neoproterozoic Crippleback quartz-monzonite and Sandy Brook Group rhyolite and trend towards those of the volcanic rocks of Lemarchant and other volcanic rock samples from the Tally Pond volcanic belt; these Tally Pond belt volcanic rocks overlap with the field for arc rocks (Fig. 4.5B; McLennan et al., 2003). The εNd values of the Lemarchant mudstone and tuff samples do not show any spatial variations throughout the sections and/or with depth in the stratigraphy in the Lemarchant area (Fig. 4.6 A-B). The T_{DM} = 1.63-3.05 Ga of the Lemarchant mudstones are older than reported values for the coeval felsic volcanic rocks of the Upper Block at Duck Pond of 1.1 and 1.4 Ga (McNicoll et al., 2010) and are also older than those of the Crippleback Intrusive Suite (1.3 and 1.4 Ga) and the Sandy Brook Group (1.2-1.3 Ga) (Rogers et al., 2006). This may be a result of breakdown of volcaniclastic component in the hydrothermal sediments, which can cause, especially in mud-sized sediments, differences in the Nd isotopic composition (McLennan et al., 1989).

4.5.3.2 Immobile element systematics: The major elements have variable mobility with the alkali elements exhibiting considerable mobility during hydrothermal alteration and diagenetic processes (Nesbitt and Young, 1982; Nesbitt, 2003). Accordingly, a Zr/Ti-Nb/Y projection after Winchester and Floyd (1977) and Pearce (1996) permits the discrimination between, and identification of, rock types, independently from the degree of alteration. The volcanic rocks (sampled as felsic and mafic volcanic rocks) of the Lemarchant deposit are subalkaline basaltic andesites, with the ‘felsic’ rocks trending towards the dacite boundary, and the ‘mafic’ rocks trending towards the basalt boundary

(Fig. 4.7A). Because of the limited sample number for volcanic rocks from this study, fields from Cloutier et al. (*unpublished data)* were added for felsic, intermediate, and mafic volcanic rocks from the Lemarchant deposit. Additionally, samples for Tally Pond belt felsic and mafic volcanic rocks, as well as for Sandy Brook Group rhyolite and basalt and Crippleback quartz-monzonite were added for comparison from Rogers (2004) and Rogers et al. (2006). The volcanic rocks of Lemarchant show a wide compositional range, with felsic-dominated rhyolite-dacite of the Bindons Pond formation as well as intermediate andesite-basaltic andesite and mafic rocks of the Lake Ambrose formation (Cloutier et al., *unpublished data*). The Nb-Y diagram of Pearce et al. (1996), which discriminates the general tectonic settings and is relatively unaffected by hydrothermal alteration, shows that the Tally Pond belt volcanic rocks plot predominantly in the volcanic arc field (Fig. 4.7B).

4.6 Discussion

4.6.1 Evaluation of provenance, tectonic setting, and the role of crustal input

The Tally Pond volcanic belt represents the oldest magmatism of the Penobscot Arc and formed during phases of arc rifting at the leading edge of the Ganderian margin (Rogers et al., 2006; Zagorevski et al., 2010; Piercey et al., 2014). The volcanic rocks of the Tally Pond belt were built directly on Ganderian crustal rocks, which are represented by the Ediacaran age (563 Ma) Crippleback Intrusive Suite and coeval Sandy Brook Group (Rogers et al., 2006; Rogers et al., 2007; Zagorevski et al., 2010). Volcanic rocks that host massive sulphide deposits are the products of melting and re-melting processes,

and can give insights into the tectonic environment in which they were formed (Lentz, 1998; Gibson et al., 1999; Piercey, 2011). The Tally Pond group, with felsic-dominated rhyolite-dacite of the Bindons Pond formation as well as intermediate basaltic andesite and basalt of the Lake Ambrose formation, have trace element signatures consistent with formation in a volcanic arc environment (Fig. 4.7A; Rogers et al., 2006; Zagorevski et al., 2010; Piercey et al., 2014). Furthermore, the provenance-related immobile element systematics of all types of metalliferous mudstones and tuff at Lemarchant have continental to oceanic island arc signatures (Lode et al., 2015). Collectively, these data are consistent with formation in a graben/caldera in a rifted continental arc, or an arc proximal to continental crust, consistent with existing tectonic models for the Tally Pond belt (Rogers et al., 2006; McNicoll et al., 2010; Zagorevski et al., 2010; Piercey et al., 2014).

The εNd values of samples from the Lake Ambrose and Bindons Pond formations of this study (εNd = +1.4 and +0.4, respectively) are comparable with values that were previously reported for volcanic rocks of the Tally Pond volcanic belt (Fig. 4.5B; Rogers et al., 2006; Zagorevski et al., 2010). These indicate that the Lake Ambrose formation basalts have predominantly juvenile signatures (εNd_{511} around +3), which are characteristic of tholeiitic basaltic to andesitic flows. In contrast, the rhyolite and dacites of the Bindons Pond formation have less juvenile values (εNd_{511} of +1.8 and +2.6) (Rogers et al., 2006; Zagorevski et al., 2010). The Lemarchant mudstones, regardless of type, and the tuffs have $f^{Sm/Nd}$ ratios similar to those of the Tally Pond belt volcanic rocks (Fig. 4.5B), implying that the Lemarchant mudstones and tuffs have derived Nd from the bounding volcanic rocks. However, there is a noticeable difference in εNd_{513} values

between the sedimentary and volcanic rocks of the Lemarchant deposit. Unlike the volcanic rocks, which have slightly positive values (εNd = +1.4 and +0.4), the mudstones and tuffs have lower εNd_{513} values between -6.0 and -1.8 (Fig. 4.5B). These values are similar to those of the Sandy Brook Group rhyolite $\varepsilon Nd_{\text{corrected for 513}}$ = -6.5 to -1.9, as well as those of the Cripplebeck Intrusive Suite $\varepsilon Nd_{\text{corrected for 513}}$ = -5.9 to -5.2 (Rogers et al., 2006). Moreover, the Lemarchant mudstones have similar εNd_{513} values throughout the sections of the Lemarchant Main Zone, the Northwest and 24 zones, and the North Target (Fig. 4.6A-B), but proximal EMS-type Lemarchant mudstones have more evolved εNd_{513} values than the more distal FEM-type mudstones (Fig. 4.6A-B). The REE, including Nd, are considered immobile under most settings of hydrothermal activity and thus, Nd is negligibly mobilized in hydrothermal fluids (Rollinson, 1993), unless orthomagmatic fluids contribute to the hydrothermal fluids (Wood and Williams-Jones, 1994). However, it is more plausible that the evolved Nd is derived from weathered Cripplebeck/Sandy Group Group basement, which was exposed during arc rifting and formation of the Tally Pond belt volcanic rocks, including the Lemarchant massive sulphides and metalliferous mudstones. Exposure of this crustal basement would have brought crustally-derived evolved Nd into the ambient seawater, which subsequently was adsorbed onto hydrothermally-derived particles, such as Fe-oxyhydroxides (Wood and Williams-Jones, 1994; Mills and Elderfield, 1995; Rudnicki, 1995; Chavagnac et al., 2005). This process can explain the evolved Nd signatures in the hydrothermal sediments, which are not present in the more juvenile Tally Pond volcanic rocks (Fig. 4.5B). More sampling is required, however, to determine whether the slightly more evolved signature in the EMS-type mudstones (compared to the slightly less evolved FEM-type) is universally

representative or due to insufficient data density (Fig. 4.6A). Involvement of Mesoproterozoic Ganderian basement has not been reported yet for the Tally Pond belt; however, the evolved Nd signatures present in the Lemarchant mudstones may indicate contribution of evolved Nd not only from the Ediacaran age Cripplebacк/Sandy Brook Group basement, but also from the underlying Mesoproterozoic Ganderian basement (e.g., Zagorevski et al., 2007). The presence of this Mesoproterozoic Ganderian basement is supported by inherited zircons with U-Pb ages of 0.9 – 1.2 Ga in the Pats Pond group, which occurs in the Victoria Arc that was built upon the Penobscot Arc (e.g., Zagorevski et al., 2007). Significant input from evolved crustal material is also supported by the Pb isotopic data of the Lemarchant deposit and other massive sulphide occurrences in the Tally Pond belt (Swinden and Thorpe, 1984; Pollock and Wilton, 2001; Gill, 2015; Lode et al., in press), and together, the isotopic data support that basement plays a role in hydrothermal activity, either through direct leaching (Pb) or via adsorption/deposition (Nd) from the water column.

4.7 Conclusions

We propose that the volcanogenic massive sulphides of the Lemarchant deposit and related exhalative metalliferous mudstones that are associated with felsic, intermediate, and mafic volcanic rocks formed from fluids that ascended along deep synvolcanic faults. These hydrothermal sediments precipitated in a rift-related graben/caldera setting, where crustal basement of the Cripplebacк Intrusive Suite and the Sandy Brook Group was exposed and eroded, which contributed evolved crustal Nd to the

ambient seawater. Hydrothermally-derived Fe-oxyhydroxides efficiently scavenged REE, including Nd, and record the evolved εNd signature in the sediments. As a result, the hydrothermal sediments have more evolved εNd values than the genetically associated Tally Pond belt volcanic rocks. Overall, the Nd isotopic compositions, as well as the lithogeochemical provenance studies, of the Lemarchant metalliferous mudstones and tuffs collectively support a rifted arc environment built upon Ganderian crustal basement for the formation of Tally Pond belt, consistent with existing models for the Tally Pond group.

4.8 Acknowledgements

This research is funded by the Canadian Mining Research Organization (CAMIRO) and an NSERC CRD grant. Kind support was provided by Dianne and Charlie Fost, Michael Vande Guchte, Alexandria Marcotte, and Gerry Squires from Paragon Minerals Corporation (now Canadian Zinc Corporation). Research was also funded by the NSERC-Altius Industrial Research Chair in Mineral Deposits, funded by NSERC, Altius Resources Inc., and the Research and Development Corporation of Newfoundland and Labrador. We thank Keir Hiscock, Pam King, Sherry Strong, Anne Westhues, as well as Inês Nobre Silva for help and support.

4.9 References

Carey, S., and Sigurdson, H., 1984, A model of volcanogenic sedimentation in marginal basins., *in* Kokelaar, B. P., and Howells, M. F., eds., Marginal Basin Geology: Volcanic and Associated Sedimentary and Tectonic Processes in Modern and

Ancient Marginal Basins., 16(1): Geological Society Special Publication, p. 37-58.

Chavagnac, V., German, C. R., Milton, J. A., and Palmer, M. R., 2005, Sources of REE in sediment cores from the Rainbow vent site (36°14′N, MAR): Chemical Geology, v. 216, p. 329-352.

Copeland, D. A., McClenaghan, S. H., and Piercey, S. J., 2008, 9th year Assessment Report on Diamond Drilling, Lithogeochemistry, Pulse EM Surveying and Linecutting on Licence 8183M, South Tally Pond Property, Rogerson Lake Area, Newfoundland and Labrador, NTS 12A/10 and 12A/07: St. John's, NL, Canada, Newfoundland and Labrador Geological Survey Assessment File 012A/1459, p. 85.

Copeland, D. A., Toole, R. M., and Piercey, S. J., 2009, 10th Year Supplementary Assessment Report on Soil Sampling, Linecutting, Titan 24 Geophysical Surveying, Diamond Drilling and Petrography, Licence 8183M, South Tally Pond Property, Rogerson Lake Area, Newfoundland and Labrador, NTS 12A/10 and 12A/07: St. John's, NL, Canada, Newfoundland and Labrador Geological Survey Assessment File, p. 56.

Dunning, G. R., Kean, B. F., Thurlow, J. G., and Swinden, H. S., 1987, Geochronology of the Buchans, Roberts Arm, and Victoria Lake groups and Mansfield Cove Complex, Newfoundland: Canadian Journal of Earth Sciences, v. 24, p. 1175-1184.

Dunning, G. R., Swinden, H. S., Kean, B. F., Evans, D. T. W., and Jenner, G. A., 1991, A Cambrian island arc in Iapetus; geochronology and geochemistry of the Lake Ambrose volcanic belt, Newfoundland Appalachians: Geological Magazine, v. 128, p. 1-17.

Evans, D. T. W., and Kean, B. F., 2002, The Victoria Lake Supergroup, central Newfoundland - its definition, setting and volcanogenic massive sulphide mineralization, Newfoundland and Labroador Department of Mines and Energy, Geological Survey, Open File NFLD/2790, p. 68.

Fisher, C. M., McFarlane, C. R. M., Hanchar, J. M., Schmitz, M. D., Sylvester, P. J., Lam, R., and Longerich, H. P., 2011, Sm-Nd isotope systematics by laser ablation-multicollector-inductively coupled plasma mass spectrometry: Methods and potential natural and synthetic reference materials: Chemical Geology, v. 284, p. 1-20.

Fraser, D., Giroux, G. A., Copeland, D. A., and Devine, C. A., 2012, NI-43-101 Technical Report and Mineral Resource Estimate on the Lemarchant Deposit, South Tally Pond VMS Project, central Newfoundland, Canada for Paragon Minerals Corporation, National Instrument 43-101 Technical Report: Toronto, ON, Canada, National Instrument 43-101 Technical Report, p. 137.

Gale, A., Langmuir, C. H., and Dalton, C. A., 2014, The global systematics of Ocean Ridge Basalts and their origin: Journal of Petrology, v. 55, p. 1051-1082.

Galley, A. G., Hannington, M., and Jonasson, I., 2007, Volcanogenic massive sulphide deposits, *in* Goodfellow, W. D., ed., Mineral Deposits of Canada: A Synthesis of Major Deposit-types, District Metallogeny, the Evolution of Geological

Provinces, and Exploration Methods, Special Publication 5, Mineral Deposits Division, Geological Association of Canada, p. 141-161.

German, C. R., and Von Damm, K. L., 2003, Hydrothermal Processes, Treatise on Geochemistry: Oxford, Pergamon, p. 181-222.

Gibson, H. L., Allen, R. L., Riverin, G., and Lane, T. E., 2007, The VMS model: Advances and application to exploration targeting, *in* Milkereit, B., ed., Proceedings of Exploration '07: Fifth Decennial International Conference on Mineral Exploration: Toronto, ON, p. 717-730.

Gibson, H. L., Morton, R. L., and Hudak, G. J., 1999, Submarine volcanic processes, deposits, and environments favorable for the location of volcanic-associated massive sulfide deposits, *in* Barrie, C. T., and Hannington, M. D., eds., Volcanic-Associated Massive Sulfide Deposits: Processes and Examples in Modern and Ancient Environments, Reviews in Economic Geology v.8, p. 13-51.

Gill, S. B., 2015, Mineralogy, metal zoning, and genesis of the Zn-Pb-Ba-Ag-Au Lemarchant volcanogenic massive sulfide (VMS) deposit, Memorial University of Newfoundland.

Gill, S. B., and Piercey, S. J., 2014, Preliminary mineralogy of barite-associated sulphide mineralization in the Ordovician Zn-Pb-Cu-Ag-Au Lemarchant volcanogenic massive sulphide deposit, Newfoundland and Labrador: Current Research - Geological Survey of Canada, v. 2013-17, p. 15.

Goldstein, S. L., O'Nions, R. K., and Hamilton, P. J., 1984, A Sm-Nd isotopic study of atmospheric dusts and particulates from major river systems: Earth and Planetary Science Letters, v. 70, p. 221-237.

Hannington, M. D., de Ronde, C. E. J., and Petersen, S., 2005, Sea floor tectonics and submarine hydrothermal systems, *in* Hedenquist, J. W., Thompson, J. F. H., Goldfarb, R. J., and Richards, J. P., eds., Economic Geology: One Hundredth Anniversary Volume, 1905-2005: Littleton, CO, USA, Society of Economic Geologists, p. 111-142.

Hannington, M. D., Jonasson, I. R., Herzig, P. M., and Petersen, S., 1995, Physical and chemical processes of seafloor mineralization at mid-ocean ridges: Geophysical Monograph, v. 91, p. 115-157.

Hawkesworth, C. J., Norry, M. J., Baker, R. P. E., Francis, P. W., and Thorpe, R. S., 1979, $^{143}Nd/^{144}Nd$, $^{87}Sr/^{86}Sr$, and incompatible element variations in calc-alkaline andesites and plateau lavas from South America: Earth and Planetary Science Letters, v. 42, p. 45-57.

Hekinian, R., Hoffert, M., Larqué, P., Cheminée, J. L., Stoffers, P., and Bideau, D., 1993, Hydrothermal Fe and Si oxyhydroxide deposits from South Pacific intraplate volcanoes and East Pacific Rise axial and off-axial regions: Economic Geology, v. 88, p. 2099-2121.

Huston, D., Relvas, J., Gemmell, J., and Drieberg, S., 2011, The role of granites in volcanic-hosted massive sulphide ore-forming systems: an assessment of magmatic–hydrothermal contributions: Mineralium Deposita, v. 46, p. 473-507.

Huston, D. L., Pehrsson, S., Eglington, B. M., and Zaw, K., 2010, The geology and metallogeny of volcanic-hosted massive sulfide deposits: Variations through geologic time and with tectonic setting: Economic Geology, v. 105, p. 571-591.

Ickert, R. B., 2013, Algorithms for estimating uncertainties in initial radiogenic isotope ratios and model ages: Chemical Geology, v. 340, p. 131-138.

Lentz, D. R., 1998, Petrogenetic evolution of felsic volcanic sequences associated with Phanerozoic volcanic-hosted massive sulfide systems: the role of extensional geodynamics: Ore Geology Reviews, v. 12, p. 289-327.

Lode, S., Piercey, J. S., and Devine, C. A., 2015, Geology, mineralogy, and lithogeochemistry of metalliferous mudstones associated with the Lemarchant volcanogenic massive sulfide deposit, Tally Pond belt, Central Newfoundland: Economic Geology, v. 110, p. 1835-1859.

Lode, S., Piercey, S. J., Layne, G. D., Piercey, G., and Cloutier, J., in press, Multiple sulphur and lead sources recorded in hydrothermal exhalites associated with the Lemarchant volcanogenic massive sulphide deposit, central Newfoundland, Canada: Mineralium Deposita.

Lydon, J. W., 1984, Ore deposit models; 8, Volcanogenic sulphide deposits; Part I, A descriptive model: Geoscience Canada, v. 11, p. 195-202.

McCulloch, M. T., and Wasserburg, G. J., 1978, Sm-Nd and Rb-Sr chronology of continental crust formation: Science, v. 200, p. 1003-1011.

McDaniel, D. K., McLennan, S. M., Hanson, G. N., Flood, R. D., Piper, D. J. W., Klaus, A., Burns, S. J., Busch, W. H., Cisowski, S. M., Cramp, A., Damuth, J. E., Goni, M. A., Haberle, S. G., Hall, F. R., Hinrichs, K.-U., Hiscott, R. N., Kowsmann, R. O., Kronen, J. D., Jr., Long, D., Lopez, M., McDaniel, D. K., Manley, P. L., Maslin, M. A., Mikkelsen, N., Nanayama, F., Normark, W. R., Pirmez, C., dos Santos, J. R., Schneider, R. R., Showers, W. J., Soh, W., and Thibal, J., 1997, Provenance of Amazon Fan muds; constraints from Nd and Pb isotopes: Proceedings of the Ocean Drilling Program, Scientific Results, v. 155, p. 169-176.

McLennan, S. M., Bock, B., Hemming, S. R., Hurowitz, J. A., Lev, S. M., and McDaniel, D. K., 2003, The roles of provenance and sedimentary processes in the geochemistry of sedimentary rocks, *in* Lentz, D. R., ed., Geochemistry of Sediments and Sedimentary Rocks: Evolutionary Considerations to Mineral Deposit-Forming Environments, GEOText 4: St. John's, NL, Canada, Geological Association of Canada, p. 7-38.

McLennan, S. M., Hemming, S., McDaniel, D. K., and Hanson, G. N., 1993, Geochemical approaches to sedimentation, provenance, and tectonics: Special Paper Geological Society of America, v. 284, p. 21-40.

McLennan, S. M., McCulloch, M. T., Taylor, S. R., and Maynard, J. B., 1989, Effects of sedimentary sorting on neodymium isotopes in deep-sea turbidites: Nature (London), v. 337, p. 547-549.

McLennan, S. M., Taylor, S. R., McCulloch, M. T., and Maynard, J. B., 1990, Geochemical and Nd-Sr isotopic composition of deep-sea turbidites; crustal evolution and plate tectonic associations: Geochimica et Cosmochimica Acta, v. 54, p. 2015-2050.

McNicoll, V., Squires, G., Kerr, A., and Moore, P., 2010, The Duck Pond and Boundary Cu-Zn deposits, Newfoundland: new insights into the ages of host rocks and the timing of VHMS mineralization: Canadian Journal of Earth Sciences, v. 47, p. 1481-1506.

Mills, R. A., and Elderfield, H., 1995, Hydrothermal activity and the geochemistry of metallliferous sediment: Geophysical Monograph, v. 91, p. 392-407.

Nesbitt, H. W., and Young, G. M., 1982, Early Proterozoic climates and plate motions inferred from major element chemistry of luitites: Nature, v. 299, p. 715-717.

Nesbitt, H. W., 2003, Petrogenesis of siliciclastic sediments and sedimentary rocks, *in* Lentz, D. R., ed., Geochemistry of Sediments and Sedimentary Rocks: Evolutionary Considerations to Mineral Deposit-Forming Environments, GEOText 4: St. John's, NL, Canada, Geological Association of Canada, p. 39-52.

Pearce, J. A., 1996, A user's guide to basalt discrimination diagrams, *in* Wyman, D. A., ed., Trace element geochemistry of volcanic rocks: Applications for massive sulphide exploration, Short Course Notes, Volume 12, Geological Association of Canada, p. 79-113.

Piercey, S. J., 2007, Volcanogenic massive sulphide (VMS) deposits of the Newfoundland Appalachians: An overview of their setting, classification, grade-tonnage data, and unresolved questions, *in* Pereira, C. P. G., and Walsh, D. G., eds., Current Research, Report 07-01: St. John's, NL, Geological Survey Branch, p. 169-178.

Piercey, S., 2011, The setting, style, and role of magmatism in the formation of volcanogenic massive sulfide deposits: Mineralium Deposita, v. 46, p. 449-471.

Piercey, S. J., Squires, G. C., and Brace, T. D., 2014, Lithostratigraphic, hydrothermal, and tectonic setting of the Boundary volcanogenic massive sulfide deposit, Newfoundland Appalachians, Canada: Formation by subseafloor replacement in a Cambrian rifted arc: Economic Geology, v. 109, p. 661-687.

Pollock, J. C., and Wilton, D. H. C., 2001, Metallogenic studies of the Tally Pond Belt, Victoria Lake Group; trace-element geochemistry and lead-isotope data from the Exploits Subzone, Newfoundland: Report - Government of Newfoundland and Labrador. Dept. of Mines and Energy, Geological Survey, Report: 2001-1, pp.247-266, Mar 2001.

Pollock, J. C., Wilton, D. H. C., and van Staal, C. R., 2002, Geological studies and definition of the Tally Pond Group, Victoria Lake Supergroup, Exploits Subzone, Newfoundland Appalachians: Current Research - Newfoundland. Geological Survey Branch, Report: 02-1, pp.155-167, Mar 2002.

Raczek, I., Jochum, K. P., and Hofmann, A. W., 2003, Neodymium and strontium isotope data for USGS reference materials BCR-1, BCR-2, BHVO-1, BHVO-2, AGV-1, AGV-2, GSP-1, GSP-2 and eight MPI-DING reference glasses: The Journal of Geostandards and Geoanalysis, v. 27, p. 173-179.

Rogers, N., 2004, Geochemical database, Red Indian Line project, central Newfoundland, *in* Canada, Geological Survey of Newfoundland: Open File 4605.

Rogers, N., van Staal, C., Zagorevski, A., Skulski, T., Piercey, S. J., and McNicoll, V., 2007, Timing and tectonic setting of volcanogenic massive sulphide bearing terranes within the Central Mobile Belt of the Canadian Appalachians, *in* Milkereit, B., ed., Proceedings of Exploration ‘07: Fifth Decennial International Conference on Mineral Exploration: Toronto, ON, p. 1199-1205.

Rogers, N., van Staal, C. R., McNicoll, V., Pollock, J., Zagorevski, A., and Whalen, J., 2006, Neoproterozoic and Cambrian arc magmatism along the eastern margin of

the Victoria Lake Supergroup: A remnant of Ganderian basement in central Newfoundland?: Precambrian Research, v. 147, p. 320-341.

Rollinson, H. R., 1993, Using geochemical data: evaluation, presentation, interpretation, Longman, 352 p.

Rudnicki, M. D., 1995, Particle formation, fallout and cycling within the buoyant and non-buoyant plume above the TAG vent field: Geological Society, London, Special Publication, v. 87, p. 387-396.

Squires, G. C., and Hinchey, J. G., 2006, Geology of the Tally Pond Volcanic Belt and Adjacent Areas (parts of NTS 12A/09 & 12A/10). Map 2006-01, Government of Newfoundland and Labrador, Department of Natural Resources, Geological Survey, Map 2006-01, Open File 012A/1202.

Squires, G. C., and Moore, P. J., 2004, Volcanogenic massive sulphide environments of the Tally Pond Volcanics and adjacent area; geological, lithogeochemical and geochronological results, *in* Pereira, C. P. G., Walsh, D. G., and Kean, B. F., eds., Current Research, Report 04-1: St. John's, NL, Geological Survey Branch, p. 63-91.

Swinden, H. S., 1988, Introduction to volcanogenic sulphide deposits in Newfoundland, *in* Swinden, H. S., and Kean, B. F., eds., The volcanogenic sulphide districts of central Newfoundland, Geological Association of Canada, p. 1-26.

_____1991, Paleotectonic settings of volcanogenic massive sulphide deposits in the Dunnage Zone, Newfoundland Appalachians: Canadian Institute of Mining and Metallurgy Bulletin, v. 84, p. 59-89.

Swinden, H. S., Jenner, G. A., Kean, B. F., and Evans, D. T. W., 1989, Volcanic rock geochemistry as a guide for massive sulphide exploration in central Newfoundland, Current Research, Report 89-1, Newfoundland Department of Mines, p. 201-219.

Swinden, H. S., and Thorpe, R. I., 1984, Variations in style of volcanism and massive sulfide deposition in Early to Middle Ordovician island-arc sequences of the Newfoundland Central Mobile Belt: Economic Geology, v. 79, p. 1596-1619.

Tanaka, T., Togashi, S., Kamioka, H., Amakawa, H., Kagami, H., Hamamoto, T., Yuhara, M., Orihashi, Y., Shigekazu, Y., Shimuzu, H., Kunimaru, T., Takahashi, K., Yanagi, T., Nakano, T., Fujimaki, H., Shinjo, R., Asahara, Y., Tanimizu, M., and Dragusanu, C., 2000, JNdi-1: a neodymium isotopic reference in consistency with LaJolla neodymium: Chemical Geology, v. 168, p. 279-281.

Tivey, M. K., 2007, Generation of seafloor hydrothermal vent fluids and associated mineral deposits Oceanography, v. 20, p. 50-65.

van Staal, C. R., and Barr, S. M., 2011, Lithospheric architecture and tectonic evolution of the Canadian Appalachians and associated Atlantic margin, *in* Percival, J. A., Cook, F. A., and Clowes, R. M., eds., Chapter 2 Tectonic Styles in Canada: the LITHOPROBE Perspective, Special Paper 49, Geological Association of Canada, p. 3-55.

Von Damm, K. L., 1990, Seafloor hydrothermal activity; black smoker chemistry and chimneys: Annual Review of Earth and Planetary Sciences, v. 18, p. 173-204.

Williams, H., 1979, Appalachian Orogen in Canada: Canadian Journal of Earth Sciences, v. 16, p. 792-807.

Williams, H., Colman-Sadd, S. P., and Swinden, H. S., 1988, Tectonostratigraphic subdivisions of central Newfoundland., Current Research, Part B, Paper 88-1B: Ottawa, ON, Canada, Geological Survey of Canada, p. 91-98.

Winchester, J. A., and Floyd, P. A., 1977, Geochemical discrimination of different magma series and their differentiation products using immobile elements: Chemical Geology, v. 20, p. 325-343.

Wood, S. A., and Williams-Jones, A. E., 1994, The aqueous geochemistry of rare-earth elements and yttrium. Part 4. Monazite solubility and REE mobility in exhalative massive sulfide-depositing environments: Chemical Geology, v. 115, p. 135-162.

Zagorevski, A., van Staal, C. R., McNicoll, V. J., and Rogers, N., 2007, Upper Cambrian to Upper Ordovician peri-Gondwanan island arc activity in the Victoria Lake Supergroup, central Newfoundland; tectonic development of the northern Ganderian margin: American Journal of Science, v. 307, p. 339-370.

Zagorevski, A., van Staal, C. R., Rogers, N., McNicoll, V. J., and Pollock, J., 2010, Middle Cambrian to Ordovician arc-backarc development on the leading edge of Ganderia, Newfoundland Appalachians: Geological Society of America Memoir, v. 206, p. 367-396.

Table 4.1

Neodymium isotope data for the Lemarchant metalliferous mudstones

Sm-Nd isotope data for Lemarchant exhalites and bimodal volcanic rocks

Sample #	Drill hole	Section (N)	UTM NAD27 Z21 - East	UTM NAD27 Z21 - North	Depth	Rock type	$^{143}Nd/^{144}Nd$ Rock t_0*	$^{147}Sm/^{144}Nd$ Rock t_0	$^{143}Nd/^{144}Nd$ Rock t_{513}	εNd_{513}	2σ***	fSm/Nd	T_{DM} [Ma]**
CNF-25062b	LM13-76	10050	5374537.00	521049.00	163.8	FEM	0.512206	0.129000	0.511772	-4.001	0.283	-0.344	1717.9
CNF-25065	LM13-77	10050	5374537.00	521049.00	140.0	Tuff	0.512161	0.126400	0.511736	-4.709	0.293	-0.357	1624.5
CNF-30982	LM11-65	10100	5374599.59	521114.13	157.7	EMS	0.512065	0.110900	0.511692	-5.567	0.286	-0.436	1809.6
CNF-38435	LM07-14	10200	5374697.64	521111.75	201.2	EMS	0.512213	0.133900	0.511763	-4.186	0.294	-0.319	1742.9
CNF-38433	LM07-14	10200	5374697.20	521114.68	503.5	IFE	0.512372	0.144700	0.511886	-1.789	0.278	-0.264	1702.6
CNF-20976	LM10-43	10250	5374724.55	520918.51	202.3	EMS	0.512134	0.121800	0.511725	-4.935	0.271	-0.380	1634.2
CNF-20995	LM07-15	10300	5374803.86	521072.26	174.0	IFE	0.512038	0.109000	0.511672	-5.970	0.317	-0.446	3047.8
CNF-30998	LM11-59	10325	5374828.82	521077.87	194.2	FEM	0.512404	0.176000	0.511813	-3.219	0.290	-0.105	2163.7
CNF-30953	LM07-17	10400	5374908.51	520989.96	238.4	EMS	0.512278	0.151600	0.511769	-4.078	0.278	-0.229	1698.4
CNF-20983	LM08-24	10500	5375010.66	521067.71	432.8	EMS	0.512122	0.120500	0.511717	-5.084	0.280	-0.387	1813.0
CNF-25002A	LM13-74	10600	5375124.00	520599.30	294.2	Tuff	0.512105	0.125000	0.511685	-5.711	0.288	-0.364	1816.2
CNF-20914	LM11-49	10800	5375314.26	521092.55	158.7	FEM	0.512231	0.135700	0.511775	-3.953	0.281	-0.310	1745.0
CNF-20910	LM11-49	10800	5375314.26	521092.55	144.6	Felsic	0.512477	0.142800	0.511997	0.386	0.293	-0.274	1472.3
CNF-20913	LM11-49	10800	5375314.26	521092.55	422.9	Mafic	0.512600	0.164400	0.512048	1.371	0.308	-0.164	1736.3

EMS = Exhalative mudstone immediately associated with massive sulphides (within 5m) and felsic and mafic volcanic rocks; FEM = Exhalative mudstone associated with felsic and mafic volcanic rocks; mantle reservoir (Goldstein et al.1984)

IFE = Interflow mudstone within mafic volcanic rocks.

*Calculated using $^{143}Nd/^{144}Nd$ of chondrite uniform reservoir (CHUR) = 0.512638 and $^{147}Sm/^{144}Nd$ CHUR today = 0.1967 from Rollinson (1993)

**Calculated using the values of $^{143}Nd/^{144}Nd$ = 0.513163 and $^{147}Sm/^{144}Nd$ = 0.2137 for the depleted

***2σ calculated using the algorithm after Ickert (2013)

Fig. 4.1 A-B

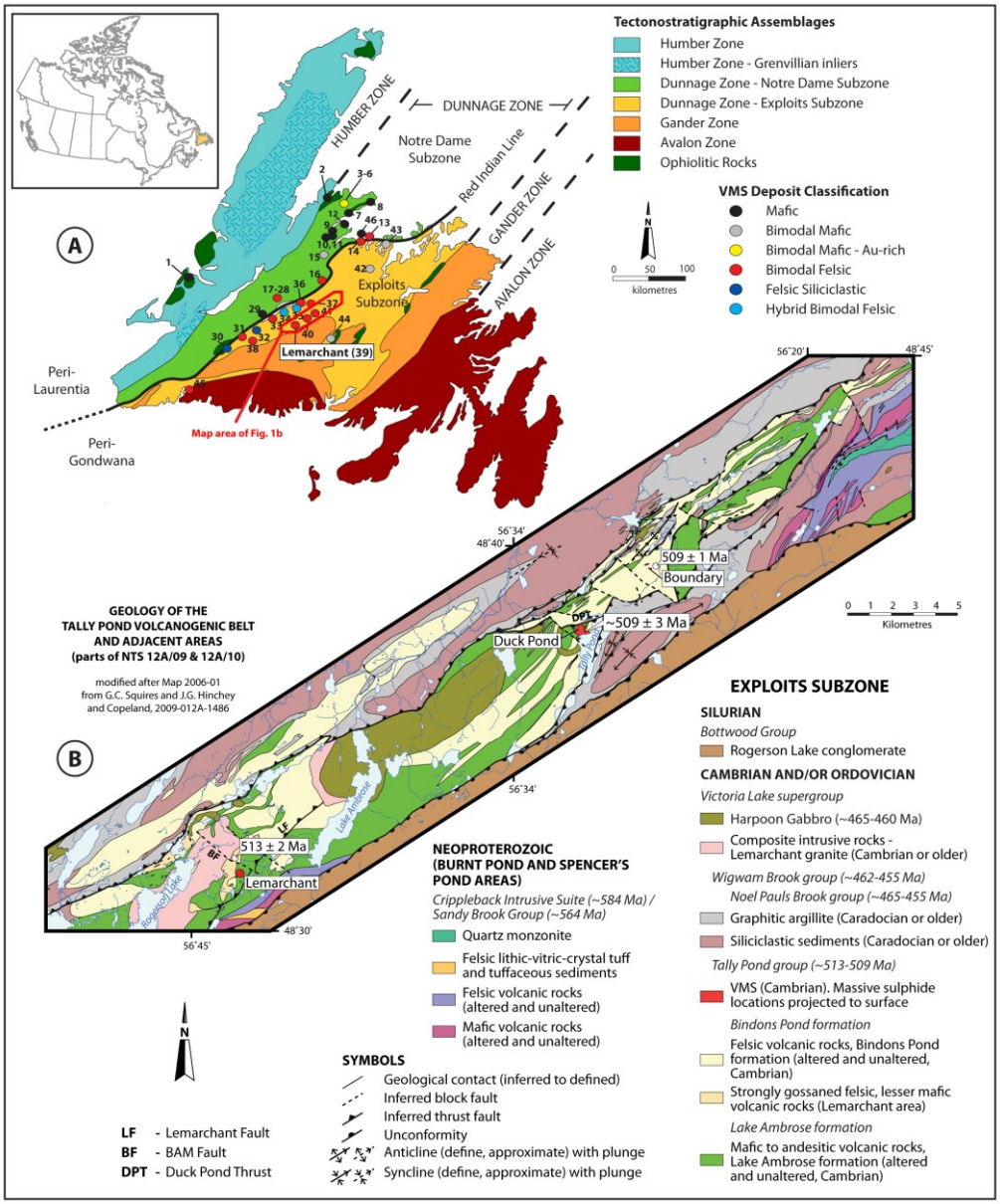

Figure 4.1 *A) Tectonostratigraphic assemblages with the main zones of the Newfoundland Appalachians (Avalon, Gander, Dunnage, and Humber zones) and VMS occurrences within the Notre Dame and Exploits subzones. Notre Dame Subzone VMS: 1 – York Harbour; 2 – 8 - Baie Verte Belt Deposits; 9 – 12, 46 – Springdale Belt Deposits; 13 – 29 Buchans-Roberts Arm Deposits. Exploits Subzone VMS: 30 – 37 - Tulks Belt Deposits; Tally Pond Belt Deposits: 39 – Lemarchant; 40 – Duck Pond; 41 – Boundary; 42 – 45 – Point Leamington Belt Deposits. Modified after (Swinden, 1991) and Piercey (2007). B) Geological map of the Tally Pond volcanic belt. The Tally Pond group comprises the Lemarchant deposit and the Duck Pond and Boundary mines. Figure after (Copeland 2009) and Map 2006-01 from Squires and Hinchey (2006).*

Fig. 4.2

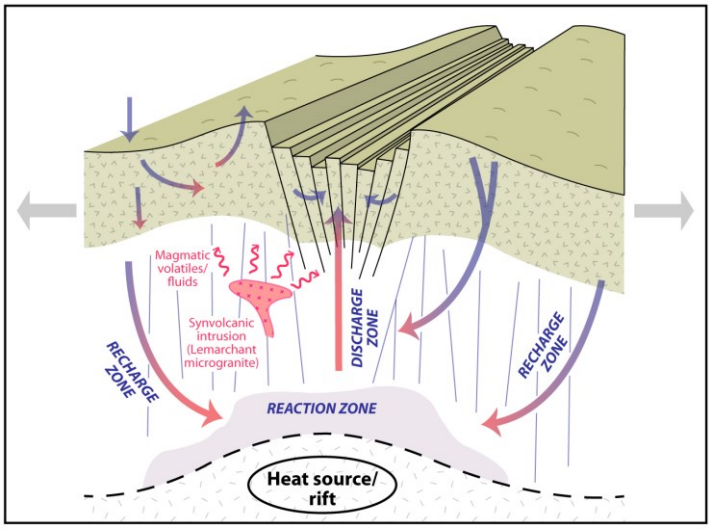

Figure 4.2 *Schematic illustration of the main aspects of hydrothermal circulation in extensional tectonic environments. In the recharge zone seawater is entrained through crustal and progressively heated during downward migration. Water-rock interactions lead to loss of* Mg^{2+}, SO_4^{2-}, *and* OH^- *and generation of* H_2S. *These reactions produce* H^+ *and create acidic fluids that leach metals out of rocks. In the reaction zone the highest temperatures are reached and the hydrothermal fluids gain their geochemical signatures. The hot fluids rise buoyantly up along synvolcanic faults and are expelled via hydrothermal plume into the ambient seawater. Figure modified after German and Von Damm (2003) and Gibson et al. (2007).*

Fig. 4.3

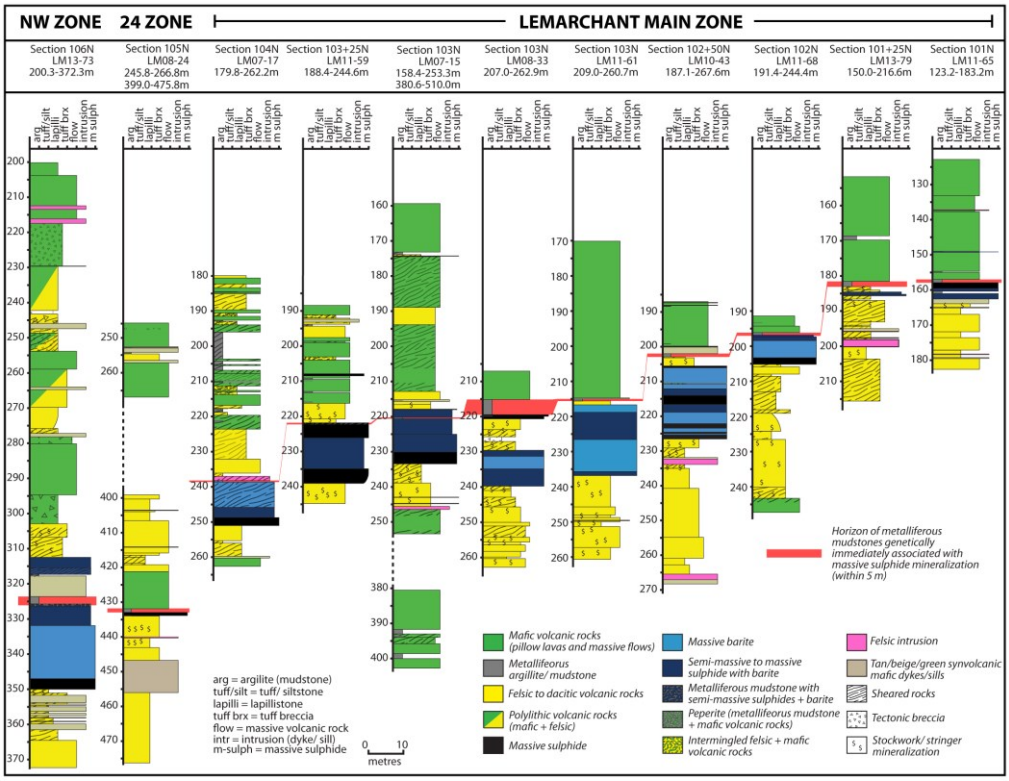

Figure 4.3 *North-south long-section with graphic logs of the Lemarchant deposit and its three mineralized zones: the Lemarchant Main Zone, the 24 Zone, and the Northwest Zone.*

Figure 4.4 *Core photographs of the main Lemarchant mudstone types, tuff, and associated felsic and mafic volcanic rocks of the Bindons Pond and Lake Ambrose formations, respectively. A) Finely laminated sulphide-rich EMS-type metalliferous mudstone with cross-cutting stringer type veins and overlying massive sulphide mineralization. Section 101N, LM11-65, mudstone sample CNF30983, 160.7 m B) Proximal EMS-type metalliferous mudstone associated with the Lemarchant Main Zone. Section 102+50N, LM10-43, CNF20976, 202.3 m. C) Proximal EMS-type metalliferous mudstone with intercalated chert-apatite layers. Section 101N, LM07-13, CNF30954, 164.7 m. D) FEM-type mudstone associated with the Northwest Zone. Section 106N, LM08-28, CNF20986, 240.6 m. E) Sulphide-rich exhalative interflow mudstone. Section 101+25N, LM13-79, CNF25072, 169.0 m. F) Lithic crystal vitric tuff that is intercalated with FEM-type mudstone. Section 99+75N, LM13-78, CNF25074, 119.8 m. G) Felsic to intermediate volcanic rock of the Bindons Pond formation located in the North target. Section 108N, LM11-49, 144.6 m. H) Mafic to intermediate volcanic rock of the Lake Ambrose formation located in the North target. Section 108N, LM11-49, 422.9 m.*

Fig. 4.4 A-H

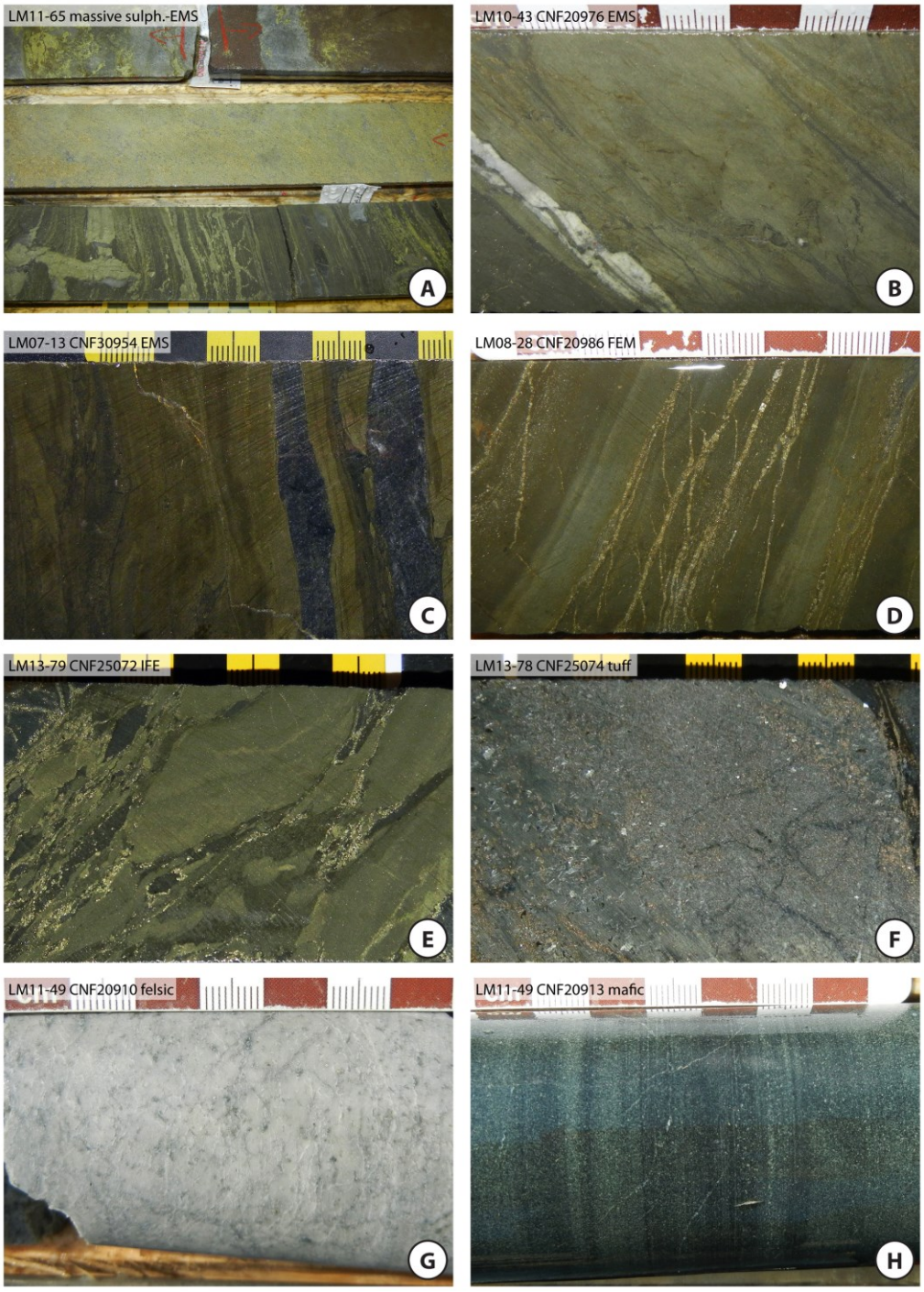
LM11-65 massive sulph.-EMS
A
LM10-43 CNF20976 EMS
B
LM07-13 CNF30954 EMS
C
LM08-28 CNF20986 FEM
D
LM13-79 CNF25072 IFE
E
LM13-78 CNF25074 tuff
F
LM11-49 CNF20910 felsic
G
LM11-49 CNF20913 mafic
H

Fig. 4.5 A-B

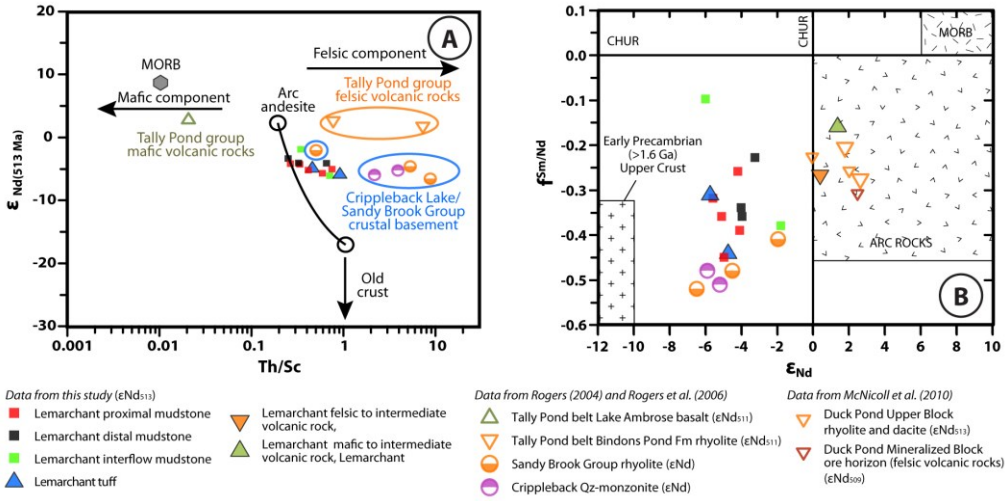

Figure 4.5 *A) Diagram of εNd versus Th/Sc ratio for the three main types of Lemarchant mudstones (EMS, FEM, and IFE) and tuff. Also plotted are data from Rogers et al. (2006) for felsic and mafic volcanic rocks of the Tally Pond belt and the Crippleback/Sandy Brook Group crustal basement rocks. Mid Ocean Ridge Basalt (MORB) field from data from Gale et al. (2014). Arc andesite field from data from Hawkeswoth et al. (1979). All data recalculated for* εNd_{513}*. Diagram modified after McLennan et al. (1993). B) Plot of* $f^{Sm/Nd}$ *versus εNd for the EMS-, FEM-, and IFE-type mudstones and tuff, as well as the Lemarchant felsic and mafic volcanic rock from this study. Also plotted are data from Rogers (2004) and Rogers et al. (2006) for felsic and mafic volcanic rocks of the Tally Pond belt, a felsic volcanic rock samples from the unmineralized Upper Block at Duck Pond and a sample from the Mineralized Block at Duck Pond from data from McNicoll et al. (2010), and the Crippleback/Sandy Brook Group crustal basement rocks. Diagram modified after McLennan et al. (1993).*

Fig. 4.6 A-B

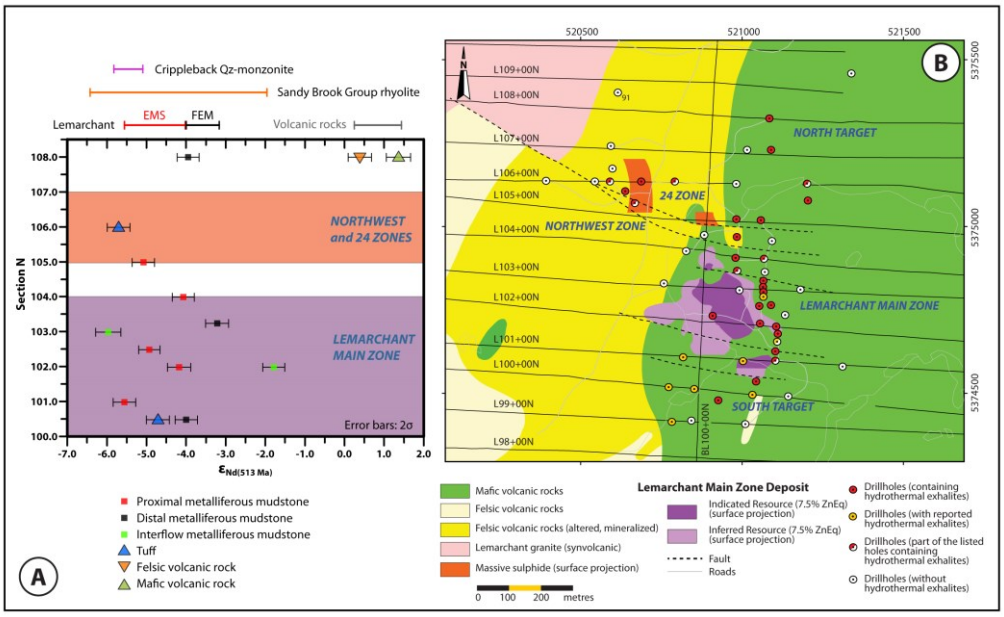

Figure 4.6 *A) Spatial distribution of εNd for the EMS-, FEM-, and IFE-type mudstones and tuff, as well as the Lemarchant felsic and mafic volcanic rock from this study. Sample data do not show any spatial variations throughout the sections and/or with depth in the stratigraphy in the Lemarchant area. 2σ error bars calculated after algorithm from Ickert (2013) B) Resource map of the massive sulphides of the Lemarchant Main, 24 Zone, and Northwest Zone. Massive sulphides are projected to the surface. Modified from the resource map of Canadian Zinc Corporation.*

Fig. 4.7 A-B

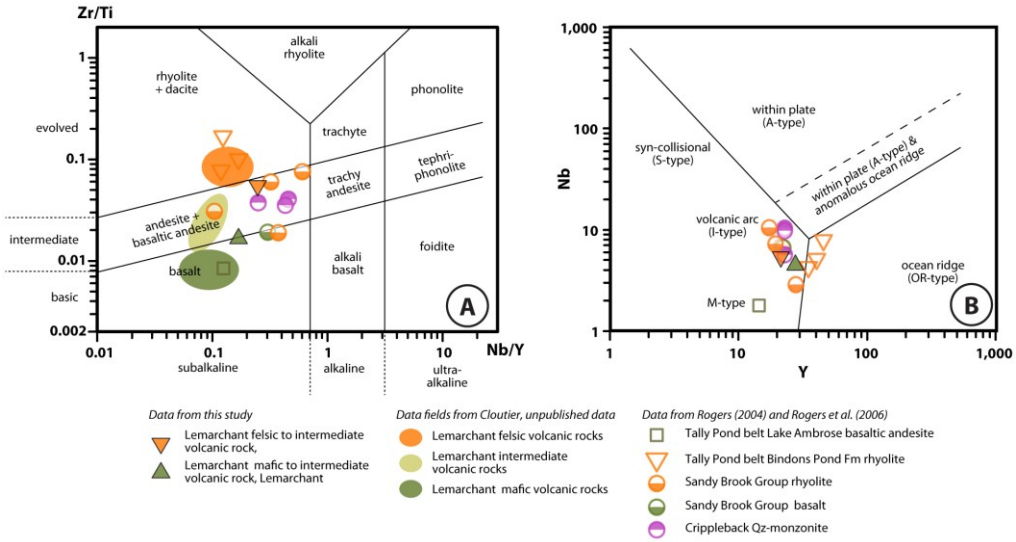

Figure 4.7 *A) and B) Zr/Ti versus Nb/Y and Nb versus Y discrimination diagrams for volcanic rocks after Winchester and Floyd (1977) and Pearce (1996) for the Lemarchant felsic and mafic volcanic rocks from this study and from data from Rogers (2004) and Rogers et al. (2006). Additionally, data fields for felsic, intermediate, and mafic volcanic rocks were added (Cloutier, unpublished data). Data from Rogers (2004) and Rogers et al. (2006) was also used to plot the Crippleback Lake/Sandy Brook Group crustal basement rocks.*

CHAPTER 5

Role of metalliferous mudstones and graphitic shales in the localization, genesis, and paleoenvironment of volcanogenic massive sulphide deposits of the Tally Pond volcanic belt, central Newfoundland, Canada.

Stefanie Lode[1*], Stephen J. Piercey[1], and Gerald C. Squires[2,3]

[1]Department of Earth Sciences, Memorial University, 300 Prince Philip Drive, St. John's, NL, Canada, A1B 3X5

[2]Formerly, Teck Resources Ltd., P.O. Box 9, Millertown, NL, Canada, A0H 1V0

[3]Present address - Canadian Zinc Corporation, PO Box 1, Millertown, NL, Canada, A0H 1V0

Status quo: Published at the Canadian Journal of Earth Sciences, 2016, v. 53, p. 1-39

5.1 Abstract

The Cambrian Tally Pond volcanic belt in central Newfoundland hosts numerous volcanogenic massive sulphide (VMS) deposits and prospects associated with exhalative metalliferous mudstones. Deposits in the belt are bimodal felsic type VMS deposits that are both base metal- (e.g., Duck Pond, Boundary), as well as base metal- and precious

metal-rich (Lemarchant). At the Lemarchant deposit, metalliferous mudstones are stratigraphically and spatially associated with mineralization: they cap the mineralization, are interlayered with exhalative barite, underlain by rhyolite domes and/or breccias, and occur within syn- and post-mineralization pillow flows. In the remainder of the Tally Pond belt, detrital graphitic shales occur predominantly in the northeastern part of the belt (mostly as unrelated mid-Ordovician structural blocks) in the upper sections of the Cambrian volcanic stratigraphy, but locally also are intercalated with exhalative metalliferous mudstones. The relationships of these Tally Pond belt shales and mudstones to massive sulphides is less obvious, with many spatially, but perhaps not genetically related to mineralization. Metalliferous mudstones at Boundary West and Old Camp predominantly occur at, or adjacent to, the contact of the footwall felsic and the hanging wall mafic volcanic rocks and represent a slightly stratigraphically higher distal equivalent to the mineralized horizon at Boundary. These suggest a long-lived, or re-occurring, character of the hydrothermal system. Other investigated Tally Pond belt prospects and showings include Keats Pond, South Moose Pond, North Moose Pond, Duck West, Cookstown, Higher Levels, and Beaver Lake, which also have occurrences of metalliferous mudstones and graphitic shales associated with either felsic and/or mafic volcanic units. Upper Cambrian to Lower Ordovician black shales from Bell Island, which represent pelagic sedimentation not associated with hydrothermal activity and volcanism, are compared to the Tally Pond belt mudstones and shales.

The metalliferous mudstones of the Tally Pond belt represent hiatuses in the volcanic activity, where the deposition of hydrothermal matter dominated over abiogenic background pelagic sedimentation. Hydrothermal exhalative mudstones, like those at

Lemarchant, have elevated Fe/Al ratios and base-metal contents, and have shale normalized negative Ce and positive Eu anomalies, indicative of deposition from high temperature (>250ºC) hydrothermal fluids within an oxygenated water column. Oxygenated conditions are also supported by the presence of barite in the mudstones and massive sulphides, suggesting SO_4^{2-} in the water column. Mudstones and shales sampled from other Tally Pond prospects have more variable signatures, ranging from hydrothermal (signatures as above) to non-hydrothermal black shales (no positive Eu-anomalies, flat REE-patterns, low Fe/Al ratios and base metal contents), to those that have mixed signatures. Accordingly, mudstones from those areas with a Lemarchant-like hydrothermal and vent-proximal character are more attractive exploration targets than mudstones and shales with predominantly detrital signatures.

5.2 Introduction

Exhalative metalliferous mudstones and detrital graphitic shales are abundant in the Tally Pond volcanic belt, central Newfoundland Appalachians, and are spatially and/or genetically associated with numerous massive sulphide deposits, prospects, and showings (Swinden, 1991; Squires and Moore, 2004). The Tally Pond belt volcanic rocks and related massive sulphide mineralization were formed during with episodes of rifting during the construction of the Cambrian to Early Ordovician Penobscot arc (Dunning et al., 1991; Rogers et al., 2007; Zagorevski et al., 2010; Piercey et al., 2014). The sedimentary rocks deposited in graben/rift-related basins typically are of volcaniclastic and epiclastic nature, and locally also can contain exhalative metalliferous mudstones.

Their depositional environment is controlled by volcanic activity and an active tectonic environment (Carey and Sigurdson, 1984), with metalliferous mudstones spatially and genetically associated with volcanism and related massive sulphide deposits (Haymon and Kastner, 1981; Gurvich, 2006; Hannington, 2014). Metalliferous mudstones form from black smoker plume fallout during a hiatus in volcanic activity, resulting in the deposition of hydrothermal precipitates that dominate over the detrital, abiogenic pelagic background sedimentation (Lydon, 1984; German and Von Damm, 2003). The hydrothermal precipitates can be diluted by volcanic and/or sedimentary detritus, resulting in sequences of hydrothermal sedimentary rocks that are intercalated with and/or overlain by volcaniclastic and epiclastic rocks, as well as black shales (Peter and Goodfellow, 2003; Sáez et al., 2011).

Metalliferous mudstones in the Lemarchant area have a hydrothermal-exhalative origin (Copeland et al., 2008; Lode et al., 2015). Hence, the term 'metalliferous mudstone' is used for Lemarchant-like sulphide-rich mudstones with a known or proposed hydrothermal origin and a genetic association with massive sulphide mineralization. The term 'graphitic shale' is utilized to describe non-exhalative black shales that occur predominantly in the northeastern parts of the Tally Pond volcanic belt. These graphitic shales are interpreted to have no genetic relationship to mineralization, but they locally are spatially associated with massive sulphides (Pollock, 2004; Squires and Moore, 2004). Since volcanogenic massive sulphide (VMS) deposits are small targets for exploration, it is important to identify potential ore bearing horizons, and delineate metalliferous mudstones from less prospective graphitic shales (Franklin et al., 1981; Gibson et al., 2007).

The purpose of this study is to apply geological and lithogeochemical proxies to: 1) identify and test a hydrothermal-exhalative origin of metalliferous mudstones occurring in the Tally Pond volcanic belt; 2) to better understand the relationships of the Lemarchant and other metalliferous mudstones and detrital shales to massive sulphide mineralization; and to 3) define the depositional environment of the metalliferous mudstones and detrital shales in terms of provenance, geochemistry of contributing fluids, the paleoredox conditions of ambient seawater, and the rift basin characteristics at the time of formation. The results of this study are of significance not only for occurrences of metalliferous mudstones and graphitic shales and associated VMS deposits within the Tally Pond belt, but also have exploration implications for mudstone/shale-associated VMS districts globally.

5.3 Regional geology

The Tally Pond volcanic belt is located within the Central Mobile Belt, Newfoundland, Canada, which is part of the Cambrian (~515 Ma) to Permian (~275 Ma) Appalachian mountain belt (Williams, 1979; Swinden, 1988; Rogers et al., 2007; van Staal and Barr, 2011). The Newfoundland Appalachians are divided into four tectonostratigraphic zones (from west to east): Humber, Dunnage, Gander and Avalon zones (Fig 5.1A)(Williams, 1979; Swinden and Kean, 1988; Swinden, 1991). The Dunnage Zone represents the Central Mobile Belt (Williams et al., 1988; Swinden, 1991; Rogers et al., 2007). These zones result from and were affected by the successive accretion of three micro-continental blocks during the Early Paleozoic to Middle

Paleozoic (i.e., Dashwoods, Taconic orogenesis; Ganderia, Salinic orogenesis; and Avalonia, Acadian orogenesis) and related interoceanic arcs and backarcs (Swinden, 1991; Zagorevski et al., 2010). These ribbon-shaped micro-continental blocks were located on the leading edges of Gondwana and Laurentia, forming peri-Gondwanan and peri-Laurentian terranes (Rogers et al., 2007; Zagorevski et al., 2010; van Staal and Barr, 2011). The Dunnage Zone has been subdivided into the peri-Laurentian Notre-Dame Subzone to the northwest and the peri-Gondwanan Exploits Subzone to the southeast (Fig. 5.1A; Swinden and Kean, 1988; Swinden, 1991). The suture between the subzones is called the Red Indian Line, and represents a ribbon-shaped zone of tectonic mélange, which contains remnants of Cambro-Ordovician oceanic infant arc and arc terranes that existed within the Iapetus Ocean (Williams, 1979; Zagorevski et al., 2010; van Staal and Barr, 2011). The Exploits Subzone represents two phases of arc-backarc formation, the Cambrian to Early Ordovician Penobscot arc and the Early to Middle Ordovician Victoria arc (Zagorevski et al., 2010). Despite deformation and metamorphism, the Central Mobile Belt was only moderately affected by metamorphism (lower greenshist-facies) and deformation and thus, internal stratigraphic relationships are well preserved (e.g., Hinchey and McNicoll, 2009; Zagorevski et al., 2010; van Staal and Barr, 2011; Piercey et al., 2014). Massive sulphide formation is associated with the evolution and rifting of the Cambrian to Ordovician Penobscot arc (Swinden et al., 1989; Rogers et al., 2007; Zagorevski et al., 2010). The Duck Pond and Boundary mines, the Lemarchant deposit, and numerous other prospects and showings also occur within the Tally Pond volcanic belt (Fig. 5.1B) (Dunning et al., 1991; Evans and Kean, 2002; Rogers et al., 2007; McNicoll et al., 2010).

The Tally Pond volcanic belt and its volcanogenic massive sulphide deposits are hosted in the lower Victoria Lake supergroup within the Exploits Subzone, which is comprised of Cambrian to Ordovician volcanic and sedimentary rocks (Dunning et al., 1991; Rogers et al., 2007; McNicoll et al., 2010; van Staal and Barr, 2011). The Victoria Lake supergroup is further subdivided into six fault bounded assemblages (Zagorevski et al., 2010; Piercey et al., 2014), which are from east to west: 1) the Tally Pond group (Fig. 5.1B); 2) the Long Lake group; 3) the Tulks group; 4) the Sutherlands Pond group; 5) the Pats Pond group; and 6) the Wigwam Pond group. The Tulks, Long Lake, and Tally Pond groups are known to host VMS deposits (Squires and Moore, 2004; Rogers et al., 2006; Zagorevski et al., 2010; Hinchey, 2011; Piercey et al., 2014). These six tectonic assemblages yield U-Pb zircon ages ranging from ~513 to 453 Ma (Dunning et al., 1987; Evans et al., 1990; Dunning et al., 1991; Evans and Kean, 2002; McNicoll et al., 2010; Zagorevski et al., 2007). The Tally Pond group (U-Pb zircon ages ranging from ~513 to 509 Ma) is informally divided into the felsic volcanic rock dominated Bindons Pond formation (also referred to as Boundary Brook formation) and the mafic volcanic rock-dominated Lake Ambrose formation (Pollock et al., 2002; Copeland et al., 2009). The latter contains island arc tholeiitic basalts to andesites (Dunning et al., 1991; Evans and Kean, 2002; Rogers et al., 2006), whereas the former contains predominantly transitional to calc-alkalic rhyolitic to dacitic rocks (Rogers et al., 2006; Piercey et al., 2014). The bimodal volcanic sequence of the Tally Pond group is unconformably overlain by a thick unit of graphitic argillaceous shales, as well as volcaniclastic, epiclastic, and turbiditic rocks of the Wigwam Pond group/Noel Paul's Brook group (Squires et al., 1991; Evans and Kean, 2002; Squires and Moore, 2004). These volcaniclastic sedimentary rocks and

graphitic shales occur either as sequences with undisturbed lamination and bedding, or are strongly reworked and sheared; the latter is also known as ‘black shale mélange’ (Pollock, 2004; Copeland, 2009a). The contact between the volcanic and volcaniclastic sedimentary rocks is considered to be tectonic in nature and is marked by a thrust fault, e.g., the Trout Brook Fault (Fig. 5.1B; Squires et al., 1991; Pollock, 2004; Squires and Moore, 2004). This black shale mélange contains pebble- to block-sized fragments of rhyolite, felsic volcaniclastic rocks, which locally are mineralized, and is commonly intruded by andesitic to mafic volcanic dykes/sills (Pollock, 2004; Copeland et al., 2009). Rare fossil data in the graphitic black shales indicates a Middle Ordovician (Sandbian to Katian/Caradocian) age (Zagorevski et al., 2010), but locally shales occur also intercalated with volcanic rocks of the Cambrian Bindons Pond and Lake Ambrose formations, as well as with metalliferous mudstone (Copeland et al., 2009). The metalliferous mudstones as well as the graphitic shales are graphite-rich (i.e., contain abundant finely disseminated or subhedral graphite), or are carbonaceous (i.e., have organic matter in the form of microbial/algal mat fragments). Metalliferous mudstones occur predominantly at the contact between the Bindons Pond and the Lake Ambrose formations, and are commonly associated with massive sulphide deposits, e.g., the Lemarchant VMS deposit (Copeland et al., 2008; Lode et al., 2015). Collectively, the Tally Pond group is interpreted to represent an arc to rifted arc environment (Rogers et al., 2006; McNicoll et al., 2010; Zagorevski et al., 2010; Piercey et al., 2014).

5.4 Massive sulphide mineralization associated with hydrothermal mudstones and graphitic black shales

Twelve deposits, prospects, and showings occurring in the Tally Pond volcanic belt contain metalliferous mudstones and graphitic black shales with known to unknown relationships to VMS mineralization. The deposits, prospects, and showings described in this section include (broadly from west to east): the Lemarchant deposit, the Cookstown showing, the Higher Levels, Beaver Lake, and Duck West prospects, the Duck Pond and Boundary deposits, and the Boundary West, Old Camp, Keats Pond, North Moose Pond, and South Moose Pond showings (Fig. 5.1B) and are summarized in Table 5.1. These prospects and showings range from single-hole intercepts with elevated base metal contents (compared to non-hydrothermal black shales) to the Duck Pond and Boundary mines. Upper Cambrian to Lower Ordovician black shales from Bell Island, eastern Newfoundland, were utilized for comparison as an example of detrital shales that are not spatially and/or genetically associated with massive sulphide mineralization (Fig. 5.1C).

Lemarchant deposit

The Cambrian Lemarchant Zn-Pb-Cu-Ba-(Au-Ag) VMS deposit has metalliferous mudstones both immediately associated with, and distal from, mineralization (Fig. 5.1B). The inferred resources for the Lemarchant Main Zone currently are 1.24 Mt at 5.38 % Zn, 0.58 % Cu, 1.19 % Pb, 1.01 g/t Au and 59.17 g/t Ag, with indicated resources of 1.34 Mt at 3.70 % Zn, 0.41 % Cu, 0.86 % Pb, 1.00 g/t Au and 50.41 g/t Ag (Fraser et al., 2012). Additional mineralized zones are the 24 Zone and the Northwest Zone (Fig. 5.2). A

quartz-phyric tuff in the general vicinity of the Lemarchant deposit yielded a U-Pb zircon age of 513 ± 2 Ma (Dunning et al., 1991).

The main metalliferous mudstone horizon at Lemarchant occurs in all mineralized zones (the Main Zone, the 24 Zone, and the Northwest Zone), stratigraphically immediately above the massive sulphides in the Bindons Pond formation and at the contact with the hanging wall mafic volcanic rocks of the Lake Ambrose formation (Fig. 5.3). The mudstone horizon extends laterally west of the Lemarchant Main Zone, at the same stratigraphic level but not in immediate contact with massive sulphides, up to 200 m away from the mineralization. Metalliferous mudstones also occur as interflow mudstones within Lake Ambrose formation basalt, up to 50 m above the massive sulphide mineralization. Locally, barite-rich metalliferous mudstones occur in areas of the North and South targets (Lode et al., 2015). Due to an offset along the gently west-dipping Lemarchant Fault, a repetition of the mineralized strata and mudstone occurrences is likely (Squires and Moore, 2004; Copeland et al., 2009).

Cookstown showing

The Cookstown showing (Fig. 5.1B) was discovered in 2005 by Rubicon Minerals during a short trenching program that targeted EM conductors and weak historic till anomalies. Trenching exposed sulphide-rich, graphitic shales associated with felsic and mafic volcanic rocks (Collins, 1989; Sparkes, 2005; Copeland, 2009b). The graphitic shales occur within a bimodal succession of volcanic and volcaniclastic rocks, where felsic volcanic rocks of the Bindons Pond formation are intercalated with mafic volcanic

rocks of the Lake Ambrose formation. This bimodal sequence is intruded by synvolcanic mafic dykes/sills and feldspar-phyric felsic dykes (Fig. 5.3A).

Higher Levels prospect

The base metal mineralization of the Higher Levels prospect (Fig. 5.1B) consists of pyrite, chalcopyrite, sphalerite, minor pyrrhotite and galena, hosted in laminated metalliferous mudstones that are intercalated with graphitic shales. These sedimentary rocks occur within mafic volcanic flows of the Lake Ambrose formation that overly the felsic volcanic rocks of the Bindons Pond formation (Squires and Moore, 2004). The stratigraphy is noted to be folded where the sedimentary rocks are present in the core of a syncline (Fig. 5.3B; Squires and Moore, 2004). Both, the felsic and mafic volcanic rocks locally have VMS-style alteration and stringer mineralization (Squires and Moore, 2004).

Beaver Lake prospect

The Beaver Lake prospect (Fig. 5.1B) is a three-kilometer-long, VMS-style sericite-chlorite-silica alteration zone in felsic volcanic rocks that was found via anomalous base metal values in till samples (Copeland, 2009a). In 2011, Paragon Minerals Corporation (now Canadian Zinc Corporation) drilled three holes (BL11-01, BL11-02, and BL11-03) intercepting a felsic-dominated bimodal volcanic sequence (felsic volcanic rocks of the Bindons Pond formation and mafic volcanic rocks of the Lake Ambrose formation), locally with stringer mineralization and VMS-style alteration. The volcanic rocks and mineralization are intercalated with metalliferous mudstones and graphitic shales (Fig. 5.3C).

Duck West showing

The Duck West showing is hosted by VMS-style altered felsic volcanic rocks (Fig. 5.1B). The stratigraphy of the felsic volcanic rocks of the Duck West alteration zone correlates with the 'Mineralized Block' that hosts the Duck Pond massive sulphide deposit (Figs. 5.4-5.5) (Squires and Moore, 2004; Copeland, 2009a). The felsic volcanic rocks consist of massive to jigsaw-fit quartz-chlorite-sericite altered felsic volcanic rocks that are intercalated with locally reworked graphitic shales and mineralized tuff.

Duck Pond deposit

The Duck Pond deposit (Fig. 5.1B) and was discovered by Noranda in 1985 (McNicoll et al., 2010). The deposit consists of the structurally dismembered Upper Duck lens, which holds the majority of the ore, the Lower Duck lens, and the Sleeper Zones. The Cu-Zn-massive sulphides are hosted by aphyric and quartz-phyric felsic tuffs and "fragmentals" (mineralized sequence), and were formed by pervasive subseafloor hydrothermal replacement of the originally permeable volcaniclastic host rocks (McNicoll et al., 2010; Piercey et al., 2012; Piercey et al., 2014). The mineralized sequence overlies a thick succession of hydrothermally altered footwall aphyric felsic flows (Fig. 5.5; Squires and Moore, 2004). Together they represent the 'Mineralized Block', which predominantly yielded U-Pb zircon ages of 509 ± 3 Ma (McNicoll et al., 2010). The 'Upper Block' is structurally juxtaposed along the Duck Pond thrust on top of the Mineralized Block and consists of an unaltered bimodal volcanic sequence with metalliferous mudstones in the Duck Pond area at the contact between the felsic volcanic rocks of the Bindons Pond formation and mafic volcanic rocks of the Lake Ambrose

formation (Squires and Moore, 2004; Piercey et al., 2012). Felsic volcanic rocks in the Upper Block at Duck Pond yield U-Pb zircon ages of 513 ± 2 Ma, and ~563 Ma for inherited zircons from underlying rocks (Dunning et al., 1991; McNicoll et al., 2010). Combined resources of the Duck Pond and Boundary (see below) deposits are 4.1 Mt @ 3.3% Cu, 5.7% Zn, 0.9% Pb, 59.3 g/t Ag, and 0.9 g/t Au) (Aur Resources, 2007; Piercey et al., 2014). Production of the Upper Duck lens started in May 2007 (McNicoll et al., 2010) and ended permanently in mid-2015 (Teck Resources Ltd, Q1_2015 report).

Boundary deposit

The Boundary deposit is located ~4.5 kilometers northeast of the Duck Pond deposit and was also discovered by Noranda, in 1979-1980. The Boundary deposit consists of three shallow lenses; the North, South, and Southeast zones (Figs. 5.1B, 5.6; Squires and Moore, 2004; Piercey et al., 2014). The North and South zones are a structural offset of a once single lens via the Wagner fault (Wagner, 1993; Piercey et al., 2014). The mineralization at the Boundary lenses is predominantly comprised of Fe-, Cu-, and Zn-sulphides that are hosted by aphyric felsic tuff, flows, and autobreccias at, and below, the contact with quartz-phyric hanging wall felsic flows and tuff (Piercey et al., 2014). Laterally extending from the massive sulphide lens is the tuffaceous exhalative Boundary horizon that is intercalated locally with metalliferous mudstones (Fig. 5.7A). In the Boundary area the Mineralized Block is outcropping, whereas the Upper Block is likely eroded (Squires and Moore, 2004; McNicoll et al., 2010; Piercey et al., 2014). The mineralized sequences in the Mineralized Block of the Boundary and Duck Pond deposits are correlative in regard to mineralization and alteration style, in host rock type, and in

age (509 ± 3 Ma) (Squires and Moore, 2004; McNicoll et al., 2010; Piercey et al., 2014). The most recent resource estimates for the Boundary deposits are ~ 0.5 Mt @ 3.5% Cu, 4% Zn, 1% Pb, 34.0 g/t Ag (Piercey et al., 2014). However, at the cessation of mining at Boundary, a total of 750,000 tonnes of "ore grade" material was sent through the mill (Greg Tucker, senior engineer, *pers. comm.*, 2015), including disseminated and stockwork wallrock mineralization.

Boundary West showing

The Boundary West showing (Figs. 5.1B, 5.6) was discovered by Noranda by testing EM conductors that subsequently resulted in the intersection of 8 metres of stringer mineralized felsic quartz-crystal tuff in hole 374-60 (deepened as hole TP88-01). The felsic tuffs are spatially associated with cherty to metalliferous mudstones that are overlain by locally peperitic mafic flows that are preserved in a 45° NE-plunging synclinal structure (Fig. 5.7B-C; Squires and Moore, 2004). Graphitic shales are intercalated with the felsic volcanic rocks and the metalliferous mudstones. The mineralized Boundary West crystal tuffs correlate with the mineralized sequence hanging wall quartz-phyric volcanic rocks that immediately overlie the Boundary North deposit, occurring at a slightly higher stratigraphic level (Squires and Moore, 2004).

Old Camp showing

The original Old Camp showing (Figs. 5.1B, 5.8) comprises a weakly Zn-enriched pyritic and graphitic metalliferous mudstone over an interval of 6.4 m intersected in drill hole TP88-58. Several metalliferous mudstones occur at, or up to 200 m below, the

contact between chloritized, quartz-phyric felsic volcanic flows and tuffs, and mafic volcanic rocks (Fig. 5.8B) interpreted to be stratigraphically slightly above the Boundary deposit. The mineralized sequence of the Boundary deposit occurs stratigraphically ~100 m deeper, but nevertheless is correlated with the mineralized Old Camp sequence (Squires and Moore, 2004). The bimodal volcanic succession of the Old Camp area is structurally overlain by graphitic shales and siltstones of the Wigwam Pond group/Noel Paul's Brook group via the Overview thrust (Fig. 5.8B; Squires and Moore, 2004; Piercey et al., 2014).

Keats Pond showing

The Keats Pond showing (Fig. 5.1B) consists of 30 to 50 vol% chlorite-altered fragmental rhyolite that underlies a sequence of reworked and sheared graphitic shale to polymictic conglomerate interpreted to be VMS-related. Locally, the sedimentary rocks are intercalated with metalliferous mudstones and intruded by andesitic intrusive volcanic rocks (Fig. 5.9A).

North Moose Pond showing

The North Moose Pond showing (Fig. 5.1B) contains an area of float containing intense chlorite alteration and chalcopyrite stringers underlain by a bimodal volcanic sequence that has anomalous base metal contents (Squires and Moore, 2004). This bimodal succession is spatially associated with metalliferous mudstones and structurally overlain by graphitic shales and volcaniclastic turbidites. The contact between the sedimentary and volcanic rocks is marked by the Trout Brook fault (Fig. 5.9B; Squires

and Moore, 2004). The graphitic shales are locally intruded by andesitic dykes. Based on drill core logging, the stratigraphy in drill hole NM00-01 is overturned, and in NM01-05 is inferred to be overturned (Fig. 5.9C). Carbonaceous material that possibly represents a graptolite fragment in a volcaniclastic turbidite/tuff sequence that overlies metalliferous mudstones, tentatively suggests a Late Cambrian/Early Ordovician age (E. Burden, *pers. comm.* 2015).

South Moose Pond alteration zone

The South Moose Pond alteration zone (Fig. 5.1B) contains an area (the "NW flank") of about 2 x 1 km with stringer and disseminated pyrite, sphalerite, chalcopyrite, and galena in felsic and mafic flows, but overall well-stratified units are lacking (Squires and Moore, 2004). Metalliferous mudstones occur as interflow mudstones in mafic volcanic rocks in drill hole SM97-08. Graphitic shales in drill hole SM97-06 structurally overlie, via the Overview thrust, the mafic volcanic rocks (Fig. 5.9B-C).

Bell Island

Bell Island is located ~25 km west-northwest of St John's in Conception Bay (Fig. 5.1C). The island consists of an interbedded succession of "non-hydrothermal" sandstones, shales, siltstones, and oolitic ironstones of Upper Cambrian to Middle Ordovician age that presumably unconformably lie upon Precambrian Gondwanan continental crust. Shale samples were taken from two coastal outcrops from the Lower Ordovician Beach Formation/Bell Island Group (The Beach, Lance Cove), and from one

outcrop along the coast from the Middle Ordovician Powersteps Formation/Wabana Group (Powersteps)(Fig. 5.1C).

5.5 Mudstone stratigraphy, lithofacies, and mineralogy

Lemarchant deposit

The Lemarchant metalliferous mudstones, independently of their stratigraphic position, are finely laminated, brown to black, graphite-rich, and carbonaceous, and have a thickness of <1 m to 20 m (Fig. 5.10A). The main sulphide phases are pyrite (framboidal and euhedral) and pyrrhotite, with minor chalcopyrite, sphalerite, arsenopyrite and galena. These sulphide phases occur parallel to lamination or as cross-cutting polymetallic veins (Fig. 5.10B). Barium-minerals include massive and bladed barite, the Ba-feldspars celsian and hyalophane, and the Ba-carbonate witherite. Precious metals occur in the form of electrum, which is predominantly associated with chalcopyrite and galena in the later-stage polymetallic veins (Fig. 5.10B). Detailed geological, mineralogical, and lithogeochemical studies have shown these metalliferous mudstones have a hydrothermal origin (Lode et al., 2015).

Cookstown showing

In the Cookstown drill hole CT11-01, laminated to reworked dark-grey to black cherty mudstones range from 0.2 to 5 metres in thickness and are locally intercalated with fine-grained crystal (feldspar) lithic tuff. The main sulphide phase is pyrrhotite with minor chalcopyrite and traces of galena. Pyrrhotite occurs as semi-continuous layers

parallel to lamination, in cross-cutting veins, as patches (Fig. 5.10C-D), or as pseudomorphs after euhedral pyrite. Locally, pyrrhotite veins show pyrrhotite halos that extend into the generally sulphide-poor matrix (Fig. 5.10E). Calcite is present as gangue in sulphide-rich veins. The mudstone matrix predominantly consists of clay, chlorite, and quartz, with carbonaceous and/or graphitic material present as laminae or finely disseminated in the matrix.

Higher Levels prospect

The sedimentary rocks at the Higher Levels prospect consist predominantly of metalliferous mudstones and lesser graphitic shales that reach a drilled thickness of ~18 m in the core of a syncline. The mudstones are finely laminated, carbonaceous and graphite-rich. The main sulphide phases are pyrite, chalcopyrite, sphalerite, minor pyrrhotite, and galena. Pyrite occurs predominantly as abundant framboids in the mudstone matrix and as euhedral crystals in cross-cutting veins (Fig. 5.10F-G). Chalcopyrite and sphalerite are mainly present interstitially between euhedral pyrite in these veins. Sphalerite locally displays chalcopyrite disease and also forms pseudomorphs after pyrite framboids. Pyrrhotite and galena are minor phases and are present as inclusions in pyrite. Covellite locally forms supergene rims around chalcopyrite (Fig. 5.10G). Gangue minerals in these veins consist of ferroan dolomite to Mg-Mn-bearing ankerite, quartz, and subhedral to euhedral graphite that is associated with sulphides and the other gangue minerals (Fig. 5.10H). The mudstone matrix consists of quartz, chlorite, sericite, carbonates, and carbonaceous material. Accessory minerals include apatite, monazite, rutile, and gersdorffite.

Beaver Lake prospect

The Beaver Lake prospect contains metalliferous mudstones that locally are intercalated with graphitic shale beds up to 5 m thick. The metalliferous mudstones are finely laminated, graphite- and sulphide-rich, with sulphides predominantly finely disseminated and paralleling lamination (Fig. 5.10I), but also in veins that cross-cut the lamination. The matrix is rich in framboidal pyrite and fine-disseminated graphite. Subhedral to euhedral graphite occurs in veins associated with pyrite, sphalerite, chalcopyrite, and gersdorffite, and carbonates. Sphalerite locally displays chalcopyrite-disease. Cross-cutting veins consist predominantly of euhedral pyrite, sphalerite, chalcopyrite, and the gangue minerals quartz, ankerite, dolomite, and chlorite (Fig. 5.10J). Mass-wasting textures, whereby felsic volcanic detritus is intermingled with metalliferous mudstones, are present in the drill holes BL11-01 and BL11-02. Shearing, strong foliation, and tectonic cataclastic brecciation of the volcanic and sedimentary rocks is common (Fig. 5.3C). Small-scale parasitic buckle folds are observed in the drill holes BL11-01 and BL11-03, with cleavage developed parallel to the axial plane of the fold (T. Calon, *pers. comm.*, 2015).

Duck West showing

The altered felsic rocks of the Duck West showing are interbedded with about 6 m of graphitic shale (Fig. 5.11A) that overlies mineralized tuff. The sedimentary rocks are silty shales, locally with finely disseminated and euhedral pyrite and strong carbonate alteration. The mineralized tuff is sulphide-rich, consisting predominantly of colloform to euhedral pyrite and minor sphalerite with a matrix of recrystallized quartz.

Duck Pond deposit area

Laminated sulphide-rich (pyrite, pyrrhotite) mudstones occur in 10 to 30 cm thick beds in the unmineralized Duck Pond Upper Block (~514 ± 2 Ma, U-Pb zircon age), as interflow mudstones in mafic pillow lavas of the Lake Ambrose formation, or at the contact between the Lake Ambrose formation mafic volcanic rocks and the felsic rhyolite flows and volcaniclastic rocks of the Bindons Pond formation (Piercey et al., 2012). The Upper Block is structurally juxtaposed upon the 5 Ma younger Duck Pond Mineralized Block, and metalliferous mudstones occurring in this Upper Block are genetically not related to massive sulphide mineralization present in the Mineralized Block. The main sulphide phases in the Upper Block mudstones are pyrrhotite, framboidal pyrite, chalcopyrite, and sphalerite, with apatite and carbonates as common gangue minerals (Piercey et al., 2012). Graphitic shales from the Cambrian Serendipity zone horizon are structurally incorporated into the Duck Pond thrust and are locally tectonically intermingled with mineralized tuff fragments of the Duck Pond mineralized sequence (Fig. 5.5; Squires and Moore, 2004).

Boundary deposit

Metalliferous mudstones occur at the fringes of the Boundary South Zone and reach up to 4 m in thickness. They are commonly interbedded with mineralized tuff of varying thickness and grain size (mm to dm scale). They are brown to black, finely laminated with sulphides occurring predominantly parallel to lamination. In proximity to the massive sulphides, the mudstones are intercalated with beds of mineralized lapilli tuff (replacement-style mineralization)(e.g., drill hole BD00-169; Figs. 5.7A, 5.11B). The

grain size and thickness of the tuff beds intercalated with the mudstones decreases with increasing distance from mineralization (e.g., drill hole BD10-009; Figs. 5.7A, 5.11B-C). The finely laminated metalliferous mudstones are framboid-rich with euhedral pyrite overgrowing the framboids, and chalcopyrite and sphalerite occurring interstitially between the framboids (Fig. 5.11D).

Boundary West showing

The Boundary West showing has metalliferous mudstones that occur at the upper contact of the Boundary deposit hanging wall quartz-phyric to aphyric felsic volcanic flows to volcaniclastic rocks and overlying mafic volcanic flows (Fig. 5.7B-C). The metalliferous mudstones are up to ~4 m thick, are locally reworked, intercalated with lapilli tuff layers, and exhibit peperitic textures with the pillowed mafic volcanic rocks; the peperite forms up to a ~12 m thick sequence. Felsic volcaniclastic rocks that are intermingled with metalliferous mudstone (up to 4 m thick) are interpreted to represent mass wasting deposits. The main sulphide phases are framboidal pyrite, which forms a finely disseminated sulphide matrix, euhedral pyrite that is overgrowing the framboids, and interstitial chalcopyrite and sphalerite (Fig. 5.11E-F). The latter commonly displays chalcopyrite disease.

Old Camp showing

The metalliferous mudstones associated with the Old Camp showing are up to ~5 m thick and occur at three stratigraphic levels in the Boundary deposit quartz-phyric hanging wall that extends laterally to the Old Camp area. They are finely laminated, dark-

brown, graphite- and sulphide-rich mudstones (Fig. 5.11G) that are locally reworked and/or intercalated with cherty layers. Framboidal pyrite is abundant in the matrix and occasionally overgrown by euhedral pyrite. Sphalerite, chalcopyrite, and euhedral pyrite are associated with ankerite-dolomite-chlorite-quartz-gangue in veins (Fig. 5.11H). Structurally juxtaposed mid-Ordovician sedimentary rocks of up to 130 m drill-intersected thickness occur primarily in the upper section of the stratigraphy and consist of tectonized dark gray to black graphite-rich silty shales, volcaniclastic turbidites, and polymictic pebble- to cobble-sized conglomerates within a shaly matrix (Figs. 5.8B, 5.11I). These sedimentary rocks are strongly sheared and reworked, contain mylonitized mafic volcanic "rafts", and are locally intruded by mafic dykes. Fragments of metalliferous mudstones are occasionally incorporated into shales and volcaniclastic rocks associated by faulting (Fig. 5.11J).

Keats Pond showing

The Keats Pond showing consists of a sequence of graphitic, volcaniclastic-rich shales to polymictic conglomerates with a shaly matrix that overlie altered felsic volcanic rocks. These shales and conglomerates locally contain clasts of mineralized tuff and a thin horizon of metalliferous mudstones. The metalliferous mudstones are finely laminated, dark brown to grey with finely disseminated sulphides parallel to lamination. The sulphides consist of finely disseminated framboidal and euhedral pyrite, which also occurs in cross-cutting veins (Fig. 5.12A). The contact between the metalliferous mudstone horizon and the graphitic shale is sheared but is interpreted to be conformable.

North Moose Pond showing

Metalliferous mudstones at the North Moose Pond showing stratigraphically overlie stringer mineralized felsic volcanic rocks and reach a thickness of up to 3 m. They grade into, and are progressively diluted by, shard-rich volcaniclastic turbiditic rocks. The metalliferous mudstones are finely laminated with sulphides occurring predominantly parallel to lamination and in minor cross-cutting veins (Fig. 5.12B). The main sulphide phases are framboidal pyrite in the matrix, and euhedral pyrite that is associated with interstitial sphalerite and chalcopyrite. Sphalerite displays chalcopyrite disease (Fig. 5.12C). In drill hole NM01-05 mafic volcanic rocks contain interflow mudstones, which locally are peperitic. Sheared graphitic shales tectonically overlie the mafic volcanic rocks, are (tectonically) intercalated with felsic volcanic rocks, and intruded by mafic volcanic dykes. A metalliferous mudstone horizon occurs within the graphitic shale in spatial proximity to the mafic volcanic rocks. Based on sedimentary textures (dewatering structures) the stratigraphy is likely overturned (Fig. 5.12D); accordingly, stratigraphic up is down-hole (Fig. 5.9C). The North Moose Pond volcaniclastic rocks (fine-grained to coarse-grained tuff) and graphitic shales that occur stratigraphically above the volcanic rocks and metalliferous mudstones have planar and continuous bedding, are locally graded, which indicates a deposition from turbidity currents and suspension during a quiescent episode during bimodal volcanism (McPhie et al., 1993).

South Moose Pond alteration zone

The South Moose Pond showing is comprised of strongly sheared graphitic shales to polymictic pebble to cobble conglomerate that locally contain mineralized clasts of

felsic tuff and the sequence overlies mafic volcanic rocks. The graphitic shales are intercalated with reworked laminated dark brown metalliferous mudstones (Fig. 5.12E). Metalliferous mudstones also occur as interflow mudstones within variably sheared mafic volcanic rocks. The matrix of the metalliferous mudstones contains framboidal and euhedral pyrite and minor chalcopyrite and galena. Quartz-carbonate (ankerite-dolomite)-chlorite veins are commonly associated with euhedral pyrite and chalcopyrite. Tight parasitic folds in tuff layers and overall strong shearing indicate a complex stratigraphy in the South Moose Pond area.

Bell Island

The Bell Island black shales were deposited in tidal-influenced to subtidal offshore environments and contain rhythmic layering of thin- to medium-bedded shales and silt- to sandstone (Fig. 5.12G; Ranger et al., 1984; Harazim et al., 2013). The black shales are laminated micaceous silty shales with abundant carbonaceous material in form of diffuse organic matter and algal fragments (Fig. 5.12H).

5.6 Results

5.6.1 Lithogeochemistry

5.6.1.1 Sampling, methods, quality assurance, and quality control (QA/QC)

Metalliferous mudstones and graphitic shales were sampled from drill core from 12 deposits, prospects, and showings within the Tally Pond belt (excluding the Upper Block Duck Pond mudstones) and from three locations on coastal outcrops on Bell Island.

Detailed sampling procedures are given in Appendix 5.1. Samples for whole-rock lithogeochemical studies were analysed for major and minor elements by lithium metaborate/tetraborate fusion followed by HNO_3 dissolution and analysis by inductively coupled plasma (atomic) – emission spectroscopy (ICP-ES). Carbon (C) and sulphur (S) were analysed by infrared spectroscopy and mercury (Hg) was analysed by the cold vapour flow injection mercury system (Hg-FIMS). All of the former analyses were done by Activation Laboratories Ltd. (Actlabs) in Ancaster, Canada. Additional trace elements, including rare earth elements (REE), high field strength elements (HFSE), trace metals, and many low field strength elements (LFSE) were analysed by inductively coupled plasma-mass spectrometry (ICP-MS) in the Department of Earth Sciences at Memorial University, using screw-top Teflon® bomb (Savillex®) multi-acid dissolution. The multi-acid (HNO_3, HF, HCl, H_3BO_3, and H_2O_2) whole-rock dissolution process was a modified version of that of Jenner et al. (1990) and Longerich et al. (1990) to account for the high amounts of carbonaceous material in the samples; the procedures are described in detail in Appendix 5.1.

Precision and accuracy were determined by using duplicates and the analyses of reference materials following methods described in Jenner (1996) and Piercey (2014). The reference materials utilized in the study included three different organic- and/or sulphide-rich shales (SCO-1, SDO-1 and SGR-1b) and one iron formation (FeR-1). These standards were run every twenty samples in each analytical batch. In addition, blanks were measured during each analytical run to test contamination; none was detected. Precision was determined using the percent relative standard deviation (% RSD) on the replicate analyses of the reference materials, and accuracy was determined using percent

relative difference (% RD) from accepted values. The detailed QA/QC protocol is given in the Appendix 5.1.

5.6.1.2 Alteration – major element systematics: Immediately after precipitation, metalliferous mudstones are subject to hydrothermal and diagenetic alteration processes due to ongoing hydrothermal activity (Gurvich, 2006; Hannington, 2014). Under these conditions major elements are variably mobile, and alkali elements have considerable mobility (Nesbitt and Young, 1982; Nesbitt, 2003). In plots such as the A-CN-K and A-CNK-FM molar diagrams (Fig. 5.13A-B), the immobile Al_2O_3 is compared to the mobile alkali elements (Nesbitt and Young, 1982). In A-CN-K space, the Lemarchant metalliferous mudstones (orange field) lie within the sericite (illite/muscovite) and also in the carbonate-dolomite dominated fields of the diagram. Only one North Moose Pond and one Higher Levels mudstone sample show strong carbonate alteration. The rest of the Tally Pond belt metalliferous mudstones and shales follow the sericite trend similar to the Lemarchant mudstones (Lode et al., 2015). However, two distinct alteration trends are recognizable in the metalliferous mudstones and the graphitic shales of the Old Camp showing. The shales plot around the average shale field, comparable to the Bell Island shales, whereas the metalliferous mudstones are closer to the sericite and carbonate alteration fields (Fig. 5.13A). In A-CNK-FM space, a clear distinction between graphitic shales and metalliferous mudstone of the Tally Pond belt is apparent: the mudstones overlap with the field of the Lemarchant mudstones, whereas graphitic shales lie outside of this field (Fig. 5.13B). The Tally Pond belt metalliferous mudstones plot near the FM-part of the diagram towards the sulphide-oxide apex and the chlorite-smectite trend, and

for the Lemarchant mudstones also towards the calcite-dolomite apex; the shales trend towards muscovite/illite and feldspars. Also trending towards muscovite/illite, with only minor carbonate contribution, are the Bell Island black shales (Fig. 5.13B). A positive correlation between Al_2O_3 and TiO_2 that goes through the origin ($r^2 = 0.802$ without the Duck West outlier; Fig. 5.13C) in the Tally Pond belt shales and mudstones, indicates that both were likely immobile during post-depositional processes, such as diagenesis and alteration (Barrett and MacLean, 1994).

5.6.1.3 Immobile elements and sediment provenance: Homogenization of detritus in sedimentary basins results in basin muds that contain immobile trace element patterns similar to their source regions (Bhatia and Crook, 1986; Nesbitt and Markovics, 1997). Processes such as chemical weathering, diagenesis, hydrothermal alteration, or low-grade metamorphism, do not significantly alter the ratios of immobile elements like the HFSE (e.g., Zr), the REE (e.g., La), and the compatible elements (e.g., Sc). Hence, ratios of these elements are useful for provenance studies and to reconstruct the evolution of the tectonic environments in which the sediments were deposited (Taylor and McLennan, 1985; Kolata et al., 1996; McLennan et al., 2003). In Th/Sc-Zr/Sc space and ternary diagrams like La-Th-Sc and Th-Sc-Zr/10 (Fig. 5.13D-F), the Tally Pond belt metalliferous mudstones and graphitic shales overlap the fields of the Lemarchant mudstones. This indicates that they share similar source rocks, such as upper crustal rocks with predominantly continental island arc and to a lesser extent oceanic island arc characteristics (Fig. 5.13D-F). Samples trending towards the La-apex, suggest potential La-scavenging from seawater during sedimentation (e.g., Bau, 1991; 1993). The data

shown in the ternary Th-Sc-Zr/10 diagram and the Th/Sc versus Zr/Sc plot indicate that the Tally Pond belt source rocks are zirconium depleted, as previously reported by Squires and Moore (2004) and McNicoll et al. (2010).

5.6.1.4 Hydrothermal versus detrital element signatures: Samples from Lemarchant metalliferous mudstones and Bell Island have been plotted on Boström-type diagrams (Fig. 5.14A-B; Boström et al., 1972; Boström, 1973) and are clearly distinct: the Lemarchant metalliferous mudstones predominantly fall within the hydrothermal sediment field with 40 to 80% hydrothermal component, whereas the Bell Island black shales plot in the detrital sediment field. All Tally Pond belt samples that do plot within the hydrothermal sediment field are metalliferous mudstones, whereas those plotting in the detrital sediment field are graphitic shales and/or tuff samples. The two Cookstown samples have intermediate features (Fig. 5.14A-B). Metalliferous mudstones from the Upper Block at the Duck Pond deposit also fall within the hydrothermal fields in the Boström-type diagrams (Piercey et al., 2012). Characteristic for metalliferous mudstones that are stratigraphically immediately associated with massive sulphides of the Lemarchant deposit (within five meters), are elevated Ba- and Hg contents (up to 130,200 ppm Ba and up to 17,700 ppb Hg, ranging from 646 to 130,200 ppm Ba and 2.5 to 17,700 ppb Hg). The Ba in the Lemarchant metalliferous mudstones is predominantly hosted in barite and celsian and minor in hyalophane and witherite. The anomalous Hg-Ba in the Lemarchant mudstones is in part due to the boiling present in Lemarchant hydrothermal system; however, Ba-Hg-enrichment is a feature common in alteration in VMS throughout the Tally Pond belt (e.g., Collins, 1989). Metalliferous mudstones and

graphitic shales from the Tally Pond belt outside Lemarchant have Ba contents that are up to 3792 ppm and Hg contents up to 8790 ppb (Fig. 5.14C). The Bell Island black shales and two Beaver Lake samples (one shale, one mudstone) have very low Hg, close to and/or below the detection limit of 5 ppm (Fig. 5.14C). To distinguish the high Ba and Hg contents that are associated with massive sulphide mineralization in hydrothermal systems from sedimentary-diagenetically-derived Ba, a plot with Ba/Al versus (Zn+Hg)/Al was utilized (Fig. 5.14D). Ba, Zn, and Hg represent hydrothermally derived components of the mineralization, and Al the detrital constituents. In this plot, proximal Lemarchant metalliferous mudstones show trends towards high Ba/Al and (Zn+Hg)/Al ratios, whereas graphitic shales of the Tally Pond belt, as well as the Bell Island black shales have low ratios. Metalliferous mudstones of the Tally Pond belt fall between those two fields defined by Lemarchant mudstones and graphitic shales (Fig. 5.14D). Figure 5.14E delineates that metalliferous mudstones have higher Fe- and S-contents than graphitic shale and tuff samples. The Lemarchant mudstones have $Fe_2O_{3(Total)}$ that ranges from 13 to 55 wt% and 2 to 42 wt% S, with mudstones that are closely associated with the massive sulphides having higher Fe and S contents than those that are located in more distal environments (Lode et al., 2015). The other Tally Pond belt metalliferous mudstones generally range from 8 to 50 wt% $Fe_2O_{3(Total)}$ and 6 to 38 wt% S, whereas the graphitic shales and tuffs have lower Fe- and S-values (6 and 29 wt% $Fe_2O_{3(Total)}$ and 0.03 to 24.7 wt% S). Similarly, metalliferous mudstones of the Tally Pond belt have higher Zn and Pb contents (76 to 33264 ppm Zn and 21 to 4508 ppm Pb) than the graphitic shales (30 to 3254 ppm Zn and 2 to 912 ppm Pb) and partially overlap with the field of the

Lemarchant proximal mudstones (40 to 162,512 ppm Zn and 8 to 25,600 ppm Pb) (Fig. 5.14F).

5.6.1.5 Rare earth element and Y (REY) signatures: The rare earth element and Y (REY) characteristics of the metalliferous mudstones and graphitic shales of the Tally Pond belt, as well as from the Bell Island black shales are shown in Figure 5.15A-F. Data for the Duck Pond mudstones are from Piercey et al. (2012). All measurements are normalized to the post-Archean Australian shale using the data of McLennan (1989). The Lemarchant mudstones are LREE-depleted and have relatively flat HREE patterns, negative Ce anomalies (Ce/Ce*<1), and predominantly positive Eu anomalies (Eu/Eu* up to 3.5) (Fig. 15A). Ce/Ce* and Eu/Eu* were calculated using the equations after McLennan (1989) where $Ce/Ce^* = (Ce_{sample}/79.6)/ \sqrt{((La_{sample}/38.2)*(Pr_{sample}/8.83))}$ and $Eu/Eu^* = (Eu_{sample}/1.08)/ \sqrt{((Sm_{sample}/5.55)*(Gd_{sample}/4.66))}$, respectively. The Duck Pond mudstones also display a negative Ce anomaly, but have a positive Y anomaly, HREE enrichments, and a smaller positive Eu anomaly (Fig. 5.15A). Black shales from Bell Island have flat REY signatures with no significant anomalies. The Cookstown samples have similar REY signatures to the Bell Island shales; however, they do show small Ce anomalies (Ce/Ce* ~0.7) (Fig. 5.15B). All other Tally Pond belt mudstones have intermediate REY patterns with varying Eu anomalies from slightly negative to strongly positive (Eu/Eu* = 0.9-3.1), negative Ce anomalies (Ce/Ce* = 0.5-0.9), and nil to small positive Y anomalies. The Tally Pond belt shales have Eu/Eu* = 0.8-2.0 and negative Ce anomalies (Ce/Ce* = 0.7-0.99), with one mineralized tuff from Duck West having a strong positive Eu anomaly of Eu/Eu* = 6.8, and one sample from South Moose Pond

having a positive Ce anomaly of Ce/Ce* = 1.5. To assess whether the Ce-anomalies are true anomalies or caused by a positive La-anomaly the samples are plotted in the Ce/Ce* versus Pr/Pr* diagram after Webb and Kamber (2000), modified from Bau and Dulski (1996) (Fig. 5.15G). Accordingly, the Ce-anomalies of the Lemarchant samples are true Ce-anomalies.

5.7 Discussion

5.7.1 Evaluating hydrothermal and detrital origins

Sedimentary rocks occurring in the Tally Pond volcanic belt were deposited in a graben/caldera basin related to arc-rifting with active volcanism and hydrothermal activity (Evans and Kean, 2002; Piercey et al., 2014). They have complex geochemical patterns reflecting variable inputs from: 1) hydrothermal-exhalative precipitates; 2) volcaniclastic to epiclastic material; 3) detrital sediments; and 4) hydrogenous elements scavenged from seawater onto hydrothermal particles (Boström and Peterson, 1966; German and Von Damm, 2003; Peter and Goodfellow, 2003). Exhalative metalliferous mudstones form from seafloor hydrothermal plume fallout when hot, reduced, metal- and sulphide-rich (Fe, Mn, Cu, Ni, Pb, Zn, Hg, As, Ba, S) hydrothermal fluids are vented and mixed with the cold, oxidized, sulphate-rich ambient seawater (Boström and Peterson, 1966; Haymon and Kastner, 1981; Gurvich, 2006). Furthermore, detrital input, proxied by Al and Ti, is a negligible component in exhalative sediments (Boström et al., 1969; Gurvich, 2006). As such, hydrothermal metalliferous mudstones have high Fe and base metal contents, and plot within the hydrothermal fields on Boström-type plots (Fig.

5.14A-B; Boström et al., 1972; Boström, 1973; Lode et al., 2015). Accordingly, samples from Higher Levels, Beaver Lake, Boundary, Boundary West, North and South Moose Pond, Keats Pond, Old Camp that overlap the field of the Lemarchant mudstones and Boström's hydrothermal sediment field (~30-80% hydrothermal component) can be identified as metalliferous mudstones with a hydrothermal exhalative origin (Fig. 5.14A-B). A mineralized tuff sample from Duck West also falls within the hydrothermal sediment field (Fig. 5.14A-B), and is likely a mixture of both tuff and hydrothermal material. The Beaver Lake and Duck West prospects, as well as the Boundary West, Old Camp, and South Moose showings have graphitic shales that are either intercalated with the metalliferous mudstones and bimodal volcanic rocks (e.g., Beaver Lake, Boundary West, Figs. 5.3C, 5.7B-C), and/or overlie the volcanic sequences (e.g., Old Camp, North and South Moose Pond, Figs. 5.8B, 5.9C). These Tally Pond belt graphitic shales cluster around Boström's detrital sediment field and thus are not of hydrothermal origin. Nevertheless, the Boundary West shales, the South Moose Pond shale, and some shale samples from Higher Levels have minimal hydrothermal components (up to 20%), which may have been a result of slight contributions of hydrothermal fluids (Fig. 5.14A-B). The Cookstown metalliferous mudstones/shales have intermediate geochemical characteristics (Fig. 5.14A-F). Based on the geochemistry and the petrographic observations, they are interpreted to be non-exhalative graphitic shales that were overprinted by hydrothermal fluids metalliferous that penetrated the semi-consolidated sediment (e.g., Doyle and Allen, 2003). This is reflected by the sulphide-poor matrix and sulphide-rich (pyrrhotite, chalcopyrite, minor galena) cross-cutting veins and patches (Fig. 5.10C-E). Comparable to the Lemarchant mudstones, the other Tally Pond belt metalliferous mudstones also

have noticeably high base and transition metal (Fe, Zn, Pb), and S contents (Fig. 5.14E-F), reflecting the presence of polymetallic sulphides that were precipitated from hydrothermal fluids (Boström, 1973; Gurvich, 2006; Jones et al., 2006). The sulphide mineralogy of the metalliferous mudstones is also consistent with whole rock geochemical results (Figs. 5.10G, 5.11D, 5.11F, 5.11H, 5.12C).

5.7.2 Evaluating indicators for vent proximity

Metalliferous chemical sedimentary (exhalative) rocks generally have a larger footprint than the associated VMS deposits, which are small targets for exploration (Franklin et al., 1981; Doyle and Allen, 2003; Peter, 2003; Gibson et al., 2007). Because of the hydrothermal plume processes, where hydrothermal fluids mix with the ambient seawater, the metalliferous sediments that precipitate from these mixed fluids record the geochemical characteristics of the contributing fluids relative to the distance to the hydrothermal vent site and massive sulphide mineralization (Franklin et al., 1981; Kalogeropoulos and Scott, 1989; Peter, 2003; Gibson et al., 2007; Slack et al., 2009). Accordingly, it is important to identify these geochemical fingerprints and the potential as ore bearing horizons, and to delineate proximal metalliferous mudstones from distal ones and from less prospective graphitic shales (e.g., Spry et al., 2000; Peter, 2003). In particular, a combination of Ba-enrichment, REY-systematics with positive Eu anomalies, high base metal contents, chondritic Y/Ho ratios (~27), as well as high Fe/Ti and low Al/(Al+Fe+Mn) indicate a hydrothermal derivation of the sediment and precipitation from high temperature (T>250°C) fluids (Boström et al., 1972; Boström, 1973; Slack et al., 2009; Lode et al., 2015).

The metalloid Ba is typically enriched in many VMS deposits (Lydon, 1984; Large, 1992; Huston et al., 2010) and is a useful proxy for geochemical fingerprinting (Collins, 1989; Lode et al., 2015). The enrichment of Ba related to VMS systems is a result of thermochemical breakdown of feldspars in the hydrothermal reaction zone that releases Ba^{2+} into the reduced hydrothermal fluids (German and Von Damm, 2003; Hannington et al., 2005; Griffith and Paytan, 2012). The hydrothermally derived Ba^{2+} precipitates as barite when in contact with seawater sulphate at or near the seafloor in proximity to the hydrothermal vent site, because it is highly insoluble in seawater (Ohmoto and Goldhaber, 1997; Huston and Logan, 2004; Griffith and Paytan, 2012). In other deposits, the Ba is incorporated into micas, carbonates, and other clays during fluid-rock reaction of the VMS-hosting sequence (e.g., Collins, 1989; Peter, 2003; Piercey et al., 2014). The presence of barite and generally high Ba-levels in Lemarchant mudstone samples proximal to mineralization strongly favours a hydrothermal origin and a vent proximal location of deposition (Lode et al., 2015). However, a lack of barite does not necessarily indicate a vent distal environment. Replacement style VMS mineralization may have formed from fluids with Ba but no seawater SO_4^{2-} available for barite formation, which results in footwall and hanging wall rocks with Ba-enrichments without exhalative barite occurrences (e.g., Duck Pond and Boundary deposits; Collins, 1989; Piercey et al., 2014).

In contrast to the vent-proximal Lemarchant mudstones, the other Tally Pond belt metalliferous mudstones have no barite. Based on their overall low Ba contents it is proposed that they precipitated in a more vent-distal depositional environment where less Ba from hydrothermal fluids was available (Fig. 5.14C). Interestingly, graphitic shale

samples of prospects and showings in the Tally Pond belt (not including Lemarchant) have no barite, but higher Ba-contents than some of the Tally Pond belt metalliferous mudstones (Fig. 5.14C). This effect may relate to the commonly observed enrichment of Ba in marine sediments that contain abundant carbonates, organic matter, Fe-Mn oxyhydroxides, and detrital matter, or may be due to Ba incorporation into clays due to fluid-rock reaction of the shales (Peter, 2003; Gonneea and Paytan, 2006; Griffith and Paytan, 2012). To differentiate between Ba that is associated with base metal massive sulphide mineralization and Ba related to alteration or non-hydrothermal marine sedimentary processes, a Ba/Al versus (Zn+Hg)/Al diagram was utilized (Fig. 5.14D), where Zn+Hg and Ba represent the hydrothermally derived elements and Al the detrital component. As a consequence, it is possible to distinguish more clearly graphitic shales that are characterized by lower Ba/Al and (Zn+Hg)/Al from vent proximal mudstones. Only a few of the Tally Pond belt metalliferous mudstones overlap with the proximal Lemarchant mudstone field due to lower Ba-contents. Nevertheless, because of the similarly high (Zn+Hg)/Al, it is suggested that the other Tally Pond belt metalliferous mudstones also precipitated from hydrothermal fluids, but in a more vent-distal depositional environments (Fig. 5.14F).

In VMS-forming environments, host rocks, temperature, pH, fO_2, and chlorinity are key factors controlling the concentration of base metals dissolved in the hydrothermal fluids (Lydon, 1988; Von Damm, 1990; Hannington, 2014). The temperature of the hydrothermal fluids from which the metalliferous sediment precipitated can be broadly estimated by the presence (or absence) of a positive Eu anomaly (Sverjensky, 1984; Bau,

1991). Hydrothermal fluids and precipitates that are derived from high temperature fluids have positive Eu^{2+} anomalies, because the Eu^{2+}/Eu^{3+}-redox equilibrium is strongly temperature-dependent (Sverjensky, 1984; Bau, 1991; German and Von Damm, 2003; Peter, 2003). Under high-T (>250°C), acidic and reducing conditions as in VMS hydrothermal fluids, divalent Eu is the predominant species in solution, and/or bound in related complexes (Sverjensky, 1984; Bau, 1991; Peter, 2003). Consequently, metalliferous mudstones that display pronounced positive Eu anomalies are precipitated from high-T (>250°C) hydrothermal fluids and those that display nil positive Eu anomalies, precipitated from fluids at temperatures <250°C (Sverjensky, 1984; Bau, 1991; German and Von Damm, 2003; Peter, 2003). Metalliferous mudstones and graphitic shales sampled from the Tally Pond deposits, prospects, and showings, and black shales from Bell Island, have variable REE-signatures ranging from hydrothermal (Lemarchant mudstone-like signatures) to non-hydrothermal black shales (flat REE-patterns; i.e., Bell Island shales), and to those that have mixed signatures (Fig. 5.15B-F). It is suggested that the hydrothermal fluids contributing to the metalliferous mudstones associated with the Lemarchant and Boundary deposits, and the Boundary West showing had temperatures exceeding 250°C (Fig. 5.15A, E-F). The graphitic shales and mineralized tuff of the Duck West showing also had contributions from high-T (T>250°C) fluids (Fig. 5.15C). Accordingly, the presence of positive Eu anomalies is a useful indicator of reduced, high-T hydrothermal fluids that mixed with oxygenated water. However, a lack of positive Eu anomalies can either imply that the temperatures were below 250°C, or there were reduced ambient seawater conditions (Bau, 1991; Peter, 2003). Reducing conditions increases the stability of Eu^{2+} in complexes and accordingly,

no Eu anomalies occur (Bau, 1991). Furthermore, most detrital sediments, particularly those of felsic/crustal provenance, also have no positive Eu anomalies (Peter and Goodfellow, 2003), a pattern reflected in the overall flat REE patterns of the Bell Island black shales (Fig. 5.15B). Therefore, increased mixing of hydrothermal and detrital sediments can result in a masking of a positive Eu anomaly due to input of abundant detrital material (Peter and Goodfellow, 2003). Similarly, the paleoredox of the ambient environement in which the fluids vented can be determined from the Ce-systematics of the mudstones and shales. The presence of negative Ce anomalies in hydrothermal sediments is inherited from mixing of the vent fluids with Ce-depleted oxygenated seawater (German and Elderfield, 1990; Hannington, 2009). No negative Ce anomalies, as well as flat REE patterns, are expected in reduced vent fluids, as Ce^{3+} will not oxidize to Ce^{4+} in such fluids (Mills et al., 2001; Peter and Goodfellow, 2003; Humphris and Bach, 2005), or when the shale sample is similar in composition to the shale used for normalization of the samples (e.g., post-Archean Australian shales). Larger contributions of detrital material to the hydrothermal matter can mask and flatten hydrothermal signatures, such as positive Eu, Y, and negative Ce anomalies (Peter and Goodfellow, 2003).

Accordingly, those deposits that have metalliferous mudstones samples with predominantly Ce/Ce* <1 and Eu/Eu* >1 were deposited in an a predominantly oxic environment with contributions of high temperature (T>250°C) hydrothermal fluids, i.e., Higher Levels, Beaver Lake, North and South Moose Pond, Duck Pond Upper Block, Boundary, Boundary West (Fig. 5.15C-F). The flat REY pattern of the metalliferous mudstone sample from Keats Pond (Fig. 5.15F) and graphitic shale samples from Old

Camp (Fig. 5.15D) and North Moose Pond (Fig. 5.15F) suggest reduced conditions and/or a strong dilution by detrital material. The presence of bioturbation in samples from Higher Levels, Beaver Lake, and possibly in shales from North and South Moose Pond supports the oxygenated ambient water conditions at the time of formation of the sediment (e.g., Savrda and Bottjer, 1989).

The REE-patterns of the metalliferous mudstones occurring in the Upper Block of Duck Pond indicate that they precipitated from hydrothermal fluids with low to intermediate temperatures, not exceeding 250°C, and that the constituents of the Duck Pond mudstones had longer residence times in the plume and more mixing of hydrothermal fluids with seawater. As a result, more scavenging of elements from seawater onto hydrothermally derived particles, such as Fe oxyhydroxides occured (Rudnicki, 1995; Peter, 2003), resulting in samples with negative Ce anomalies, elevated HREE, and a strongly pronounced positive Y anomaly in the Duck Pond mudstones. Accordingly, the Duck Pond mudstones are suggested to represent distal stratigraphic equivalents to the proximal Lemarchant mudstones (Piercey et al. 2012; Lode et al., 2015).

5.7.3 Sediment provenance – basin setting and tectonic environment

Provenance-related immobile element systematics of the Tally Pond belt metalliferous mudstones and graphitic shales have continental to oceanic island arc signatures (Fig. 5.13D-F). This is consistent with provenance from local host rocks, which are bimodal island arc sequences with transitional to calc-alkalic character (Rogers

et al., 2006; Squires and Moore, 2004). Furthermore, these systematics are expected for sediments deposited in a graben/caldera basin in a rifted continental arc, or an arc proximal to continental crust, which is the suggested tectonic model for the Tally Pond belt (Rogers et al., 2006; McNicoll et al., 2010; Zagorevski et al., 2010; Piercey et al., 2014). A rifted arc environment is also consistent with much of the mineralogy, mineral compositions and paragenetic sequences in the hydrothermal metalliferous mudstones and the graphitic shales and volcaniclastic-epiclastic sediments of the Tally Pond belt.

It is notable, however, that two distinct age populations are found in the Tally Pond volcanic rocks: 513 ± 2 Ma in the Lemarchant area and the Duck Pond Upper Block and 509 ± 3 Ma in the Duck Pond Mineralized Block and equivalents (e.g., Dunning et al. 1991; McNicoll et al. 2010). Even though these ages overlap with a 95 % confidence interval and 2 σ error ellipses (no overlap for 1 σ errors), the reproducibility of these two ages suggests that they represent two separate age clusters (Fig. 16D; G. Dunning, *pers. comm.* 2015). Additionally, the stratigraphy of the Lemarchant area and the Upper Block at Duck Pond share strong similarities and both contain abundant metalliferous mudstones. A duration of up to 4 Ma for a hydrothermal system appears unlikely. Hydrothermal activity generally occurs as episodic pulses and generally exists not longer than <10,000 yrs; only in exceptional cases long-lived hydrothermal systems can last for ~1 Ma (Cathles et al., 1997). Therefore, it is proposed that VMS-forming hydrothermal activity related to the bimodal volcanism in the Tally Pond belt occurred during two rifting phases: at ~513 Ma (Lemarchant) and ~509 Ma (Duck Pond, Boundary) (Fig 5.16A-B). The Lemarchant deposit is interpreted to have formed in shallow water (<1200 m) at temperatures between 250 to ~325°C, and to have undergone fluid phase separation

with a magmatic fluid contribution to the hydrothermal system (Fig. 5.16C; de Ronde et al., 2012; Hannington et al., 2005; Hannington and Scott, 1989). This is supported by the sulphide mineralogy, which includes sulphosalts, Zn-Pb phases, including low Fe sphalerite, and precious metal bearing phases; metal assemblages, including enrichments in epithermal suite elements; and bladed barite and carbonates, features common to epithermal-type deposits (Gill and Piercey, 2014; Lode et al., 2015). The nearby Lemarchant microgranite is suggested to represent the synvolcanic intrusion providing the heat to thrive the hydrothermal circulation (McNicoll et al., 2010; Squires and Moore, 2004) and potentially contributed magmatic fluids and volatiles to the hydrothermal system. In contrast, the Duck Pond Cu-Zn-Pb massive sulphides have very simple mineralogy and are interpreted to have formed at greater depths (>1200 m below seawater level) and higher temperatures (~350°C), where the fluids could not boil and phase separation did not occur (Fig. 5.16C).

The Duck Pond metalliferous mudstones occur within the ~513 Ma Upper Block at the contact of felsic and mafic volcanic rocks of the Bindons Pond and Lake Ambrose formations, respectively (Piercey et al., 2012). This Upper Block correlates in age and stratigraphy with the bimodal volcanic sequence and metalliferous mudstones in the Lemarchant deposit. The Lemarchant massive sulphides and metalliferous mudstones are interpreted to have been deposited in a smaller scale basin during the first rifting phase at ~513 Ma, and were then subsequently covered by mafic volcanic rocks during and/or immediately after deposition of the massive sulphides and metalliferous mudstones. Hydrothermal activity continued during the emplacement of the basalts as indicated by the presence of abundant interflow mudstones at the Lemarchant deposit (Fig. 5.2; Lode

et al., 2015). Second stage rifting and hydrothermal activity is interpreted to have been associated with the formation of the Duck Pond and Boundary deposits, and other prospects at ~509 Ma (e.g., Boundary West, Old Camp, North and South Moose Pond; Fig. 5.16B). Locally, some of the graphitic shales that occur in the northeastern parts of the Tally Pond belt have stratigraphic relationships that correlate with Duck Pond and Boundary and suggest deposition in the basin related to the second phase of rifting. These suggested Mid-Cambrian graphitic shales are more abundant in the northeastern part of this basin than in the southwestern area, which argues that the area of the second phase rifting may have had more space available to accommodate these sediments. The thick succession of sheared graphitic shales (Black Shale Mélange) and volcaniclastic to epiclastic sediments of the Wigwam Pond group/Noel Paul's Brook group that cover the Cambrian Tally Pond volcanic rocks are interpreted to be Mid-Ordovician and in fault contact with the volcanic rocks (Squires and Moore, 2004).

It is proposed that both rifting phases (~513 Ma and ~509 Ma) in the Tally Pond belt are associated with the formation of massive sulphides and exhalative metalliferous mudstones, i.e., two exhaltive mudstone horizons occur. Additionally, during the 509 Ma event deposition of non-hydrothermal graphitic shales gradually increased, which occur predominantly in the northeastern part of the Tally Pond belt. In detail, the first horizon is represented by metalliferous mudstones of the Beaver Lake, Higher Levels, Duck Pond (Upper Block) and is related to the ~513 Ma Lemarchant hydrothermal event, which also caused the hydrothermal overprint of the Cookstown shales. The metalliferous mudstones from Boundary, Boundary West, Old Camp, Keats Pond, and North and South Moose Pond represent the second horizon and are genetically associated with the younger ~509

Ma Duck Pond/Boundary hydrothermal event. Based on intercalated graphitic shales and metalliferous mudstones in the Tally Pond belt (predominantly the northeastern part), it is suggested that deposition of graphitic shales occurred already in the Mid-Cambrian, contemporaneously to and post-VMS formation (e.g., Serendipity and North Moose Pond). The gradual grading of Mid-Cambrian metalliferous mudstones into volcaniclastic-epiclastic sediments and graphitic shales, suggests that the hydrothermal activity eventually decreased (~ <509 Ma) and deposition of graphitic shales prevailed, i.e. at North Moose Pond. This is also supported by the REY patterns of the Tally Pond metalliferous mudstones, which have mixed hydrothermal and non-hydrothermal (detrital and volcaniclastic-epiclastic) signatures (Fig. 5.15B-F). Therefore, the base of the graphitic shales represents a transitional period in the evolution of the basin, when the hydrothermal systems of the second rifting phase were still active, but the contributions of detrital matter continuously increased. It is proposed that a possibly Silurian compressional environment, which may be related to inversion of the Penobscot backarc basin, caused juxtaposition of the older 513 Ma bimodal sequences of the first rifting phase (e.g., Lemarchant, Duck Pond Upper Block) on top of the younger 509 Ma sequence of the second rifting phase (e.g., Duck Pond, Boundary) (Fig. 5.16D; Squires and Moore, 2004; Zagorevski et al., 2010).

5.8 Conclusions

The Tally Pond volcanic belt metalliferous mudstones provide the ability to understand the relationship of exhalative metalliferous mudstones that are genetically

associated with VMS mineralization in bimodal volcanic environments. Hydrothermally derived mudstones are characterized by: 1) elevated Fe and base metals, and plot within the hydrothermal fields on Boström-type plots; 2) an enrichment in base metal sulphides and in Ba/Al and (Zn+Hg)/Al ratios; and 3) REY systematics that are indicative of deposition from high temperature fluids (i.e., Eu/Eu*>1), with or without evidence for mixing with oxygenated seawater (Ce/Ce*<1). Graphitic shales in the Tally Pond belt are locally spatially associated with mineralization, when either intercalated with hydrothermal metalliferous mudstones and/or when intermingled with mineralized tuff or mudstone fragments. The Tally Pond volcanic belt is proposed to have two rifting phases that are associated with VMS-forming hydrothermal systems, at ~513 Ma (Lemarchant) and at ~509 Ma (Duck Pond/Boundary).

5.9 Acknowledgements

This research was funded by the Canadian Mining Research Organization (CAMIRO) and an NSERC CRD grant. Kind support was provided by Christine Devine, Dianne and Charlie Fost, Michael Vande Guchte, Alexandria Marcotte, and Bryan Sparrow from Paragon Minerals Corporation (now Canadian Zinc Corporation), and from Darren Hennessey, and others from Teck Resources Ltd., Duck Pond Operations. This research is also funded by the NSERC-Altius Industrial Research Chair in Mineral Deposits, funded by NSERC, Altius Resources Inc., and the Research and Development Corporation of Newfoundland and Labrador. Furthermore, the help and support from the technical staff of the Earth Sciences department of Memorial University, Lakmali Hewa,

Keir Hiscock, and Pam King. Discussions with Michael Buschette, Jonathan Cloutier, Shannon Guffey, Dario Harazim, and Inês Nobre Silva, are greatly appreciated. Additionally, I would like to thank John Hinchey from the Geological Survey of Newfoundland for his help and support regarding the nomenclature of the central Newfoundland stratigraphic units.

5.10 References

Aur Resources, L., 2007, Duck Pond Mine, Official Ceremony, May 9, 2007. Company brochure. For updated information see Teck Resources website - www.teck.com.

Barrett, T. J., and MacLean, W. H., 1994, Chemostratigraphy and hydrothermal alteration in exploration for VHMS deposits in greenstones and younger rocks, *in* Lentz, D. R., ed., Alteration and Alteration Processes Associated with Ore-Forming Systems, Short Course Notes Volume 11, Geological Association of Canada, p. 433-467.

Bau, M., 1991, Rare-earth element mobility during hydrothermal and metamorphic fluid rock interaction and the significance of the oxidation-state of europium: Chemical Geology, v. 93, p. 219-230.

_____1993, Effects of syn-depositional and postdepositional processes on the rare-earth element distribution in Precambrian iron-formations: European Journal of Mineralogy, v. 5, p. 257-267.

Bau, M., and Dulski, P., 1996, Distribution of yttrium and rare-earth elements in the Penge and Kuruman iron-formations, Transvaal Supergroup, South Africa: Precambrian Research, v. 79, p. 37-55.

Bhatia, M. R., and Crook, K. A. W., 1986, Trace element characteristics of graywackes and tectonic setting discrimination of sedimentary basins: Contributions to Mineralogy and Petrology, v. 92, p. 181-193.

Boström, K., 1973, The Origin and Fate of Ferromanganoan Active Ridge Sediments: Stockholm Contributions In Geology, v. 27, p. 147-243.

Boström, K., Joensuu, O., Valdés, S., and Riera, M., 1972, Geochemical history of South Atlantic Ocean sediments since Late Cretaceous: Marine Geology, v. 12, p. 85-121.

Boström, K., and Peterson, M. N., 1966, Precipitates from hydrothermal exhalations on the East Pacific Rise: Economic Geology, v. 61, p. 1258-1265.

Boström, K., Peterson, M. N., Joensuu, O., and Fisher, D. E., 1969, Aluminum-poor ferromanganoan sediments on active oceanic ridges: Journal of Geophysical Research, v. 74, p. 3261-3270.

Buschette, M., 2015, Hydrothermal alteration and lithogeochemistry of the Boundary

volcanogenic massive sulfide (VMS) deposit, central Newfoundland, Canada: Unpub. MSc thesis, Memorial University of Newfoundland.

Carey, S., and Sigurdson, H., 1984, A model of volcanogenic sedimentation in marginal basins., *in* Kokelaar, B. P., and Howells, M. F., eds., Marginal Basin Geology: Volcanic and Associated Sedimentary and Tectonic Processes in Modern and Ancient Marginal Basins: Geological Society Special Publication, 16(1), p. 37-58.

Cathles, L. M., Erendi, A. H. J., and Barrie, T., 1997, How long can a hydrothermal system be sustained by a single intrusive event?: Economic Geology, v. 92, p. 766-771.

Collins, C. J., 1989, Report on lithogeochemical study of the Tally Pond volcanics and associated alteration and mineralization, Unpublished Report for Noranda Exploration Company Limited (Assessment File 012A/1033 Newfoundland Department of Mines and Energy, Mineral Lands Division): St. John's, Newfoundland, p. 87.

Copeland, D. A., McClenaghan, S. H., and Piercey, S. J., 2008, 9th year assessment report on diamond drilling, lithogeochemistry, Pulse EM Surveying and Linecutting on Licence 8183M, South Tally Pond Property, Rogerson Lake Area, Newfoundland and Labrador, NTS 12A/10 and 12A/07: St. John's, NL, Canada, Newfoundland and Labrador Geological Survey Assessment File 012A/1459, p. 85.

Copeland, D. A., 2009a, Assessment report on prospecting, lithogeochemical sampling and data interpretation on the Harpoon Property (Licenses 7695M, 10461M, 10464M, 10465M, 10607M, 12357M, 12885M, 13583M, 13448M, 13449M and 13667M) and the South Tally Pond Property (Licences 8183M, 9569M and 14158M) Lake Ambrose Area, Newfoundland and Labrador. NTS 12A/10 and 12A/07, Paragon Minerals Corporation.

_____2009b, Assessment Report on Soil Sampling on the Harpoon Property (Licences 7695M, 10464M and 10465), Lake Ambrose Area, Newfoundland and Labrador. NTS 12A/10 and 12A/07.

Copeland, D. A., Toole, R. M., and Piercey, S. J., 2009, 10th Year supplementary assessment report on soil sampling, Linecutting, Titan 24 Geophysical Surveying, Diamond Drilling and Petrography, Licence 8183M, South Tally Pond Property, Rogerson Lake Area, Newfoundland and Labrador, NTS 12A/10 and 12A/07: St. John's, NL, Canada, Newfoundland and Labrador Geological Survey Assessment File, p. 56.

de Ronde, C. E. J., Butterfield, D. A., and Leybourne, M. I., 2012, Metallogenesis and mineralization of intraoceanic arcs I: Kermadec Arc - Introduction: Economic Geology, v. 107, p. 1521-1525.

Doyle, M. G., and Allen, R. L., 2003, Subsea-floor replacement in volcanic-hosted massive sulfide deposits: Ore Geology Reviews, v. 23, p. 183-222.

Dunning, G. R., Kean, B. F., Thurlow, J. G., and Swinden, H. S., 1987, Geochronology of the Buchans, Roberts Arm, and Victoria Lake groups and Mansfield Cove Complex, Newfoundland: Canadian Journal of Earth Sciences, v. 24, p. 1175-1184.

Dunning, G. R., Swinden, H. S., Kean, B. F., Evans, D. T. W., and Jenner, G. A., 1991, A Cambrian island arc in Iapetus; geochronology and geochemistry of the Lake Ambrose volcanic belt, Newfoundland Appalachians: Geological Magazine, v. 128, p. 1-17.

Evans, D. T. W., and Kean, B. F., 2002, The Victoria Lake Supergroup, central Newfoundland - its definition, setting and volcanogenic massive sulphide mineralization, Newfoundland and Labroador Department of Mines and Energy, Geological Survey, Open File NFLD/2790, p. 68.

Evans, D. T. W., Kean, B. F., and Dunning, G. R., 1990, Geological Studies, Victoria Lake Group, Central Newfoundland Current Research Report, Geological Survey Branch, Report: 90-1, p. 131-144.

Franklin, J. M., Lydon, J. W., and Sangster, D. F., 1981, Volcanic-associated massive sulfide deposits, *in* Skinner, B. J., ed., Economic Geology 75th Anniversary Volume, p. 485-627.

Fraser, D., Giroux, G. A., Copeland, D. A., and Devine, C. A., 2012, NI-43-101 Technical Report and Mineral Resource Estimate on the Lemarchant Deposit, South Tally Pond VMS Project, central Newfoundland, Canada for Paragon Minerals Corporation, National Instrument 43-101 Technical Report: Toronto, ON, Canada, National Instrument 43-101 Technical Report, p. 137.

German, C. R., and Von Damm, K. L., 2003, Hydrothermal Processes, Treatise on Geochemistry: Oxford, Pergamon, p. 181-222.

Gibson, H. L., Allen, R. L., Riverin, G., and Lane, T. E., 2007, The VMS model: Advances and application to exploration targeting, *in* Milkereit, B., ed., Proceedings of Exploration '07: Fifth Decennial International Conference on Mineral Exploration: Toronto, ON, p. 717-730.

Gill, S. B., and Piercey, S. J., 2014, Preliminary mineralogy of barite-associated sulphide mineralization in the Ordovician Zn-Pb-Cu-Ag-Au Lemarchant volcanogenic massive sulphide deposit, Newfoundland and Labrador: Current Research - Geological Survey of Canada, v. 2013-17, p. 15.

Gonneea, M. E., and Paytan, A., 2006, Phase associations of barium in marine sediments: Marine Chemistry, v. 100, p. 124-135.

Griffith, E. M., and Paytan, A., 2012, Barite in the ocean - occurrence, geochemistry, and palaeoceanographic applications: Sedimentology, v. 59, p. 1-19.

Gurvich, E. G., 2006, Metalliferous sediments of the World Ocean - Fundamental theory of deep sea hydrothermal sedimentation: Berlin Heidelberg, Springer.

Hannington, M. D., 2009, Modern submarine hydrothermal systems - a global perspective on distribution, size, and tectonic settings, *in* Cousens, B. L., and Piercey, S. J., eds., Submarine Volcanism and Mineralization: Modern through Ancient, Shourt Course 29-30 May 2008, Geological Association of Canada, p. 91-148.

Hannington, M. D., 2014, Volcanogenic massive sulfide deposits, *in* Holland, H. D., and Turekian, K.K., ed., Treatise on Geochemistry 2nd Edition, 8. Reviews in Economic Geology, Elsevier Ltd, p. 319-350.

Hannington, M. D., de Ronde, C. E. J., and Petersen, S., 2005, Sea floor tectonics and submarine hydrothermal systems, *in* Hedenquist, J. W., Thompson, J. F. H., Goldfarb, R. J., and Richards, J. P., eds., Economic Geology: One Hundredth

Anniversary Volume, 1905-2005: Littleton, CO, USA, Society of Economic Geologists, p. 111-142.
Hannington, M. D., and Scott, S. D., 1989, Gold mineralization in volcanogenic massive sulfides; implications of data from active hydrothermal vents on the modern sea floor: Economic Geology Monographs, v. 6, p. 491-507.
Harazim, D., Callow, R. H. T., and McIlroy, D., 2013, Microbial mats implicated in the generation of intrastratal shrinkage ('synaeresis') cracks: Sedimentology, v. 6, p. 1621-1638.
Haymon, R. M., and Kastner, M., 1981, Hot spring deposits on the Eas Pacific Rise 21°N: preliminary description of mineralogy and genesis: Earth and Planetary Science Letters, v. 53, p. 363-381.
Hinchey, J. G., 2011, The Tulks Volcanic Belt, Victoria Lake Supergroup, Central Newfoundland - Geology, Tectonic Setting, and Volcanogenic Massive Sulfide Mineralization, Report 2011-02: St. John's, NL, Canada, Newfoundland and Labrador Department of Natural Resources, Geological Survey, p. 167.
Hinchey, J. G., and McNicoll, V., 2009, Tectonostratigraphic architecture and VMS mineralization of the southern Tulks Volcanic Belt: New insights from U-Pb geochronology and lithogeochemistry, *in* Pereira, C. P. G., and Walsh, D. G., eds., Current Research, Report 09-01: St. John's, NL, Canada, Geological Survey Branch, p. 13-42.
Humphris, S. E., and Bach, W., 2005, On the Sr isotope and REE compositions of anhydrites from the TAG seafloor hydrothermal system: Geochimica et Cosmochimica Acta, v. 69, p. 1511-1525.
Huston, D. L., and Logan, G. A., 2004, Barite, BIFs and bugs; evidence for the evolution of the Earth's early hydrosphere: Earth and Planetary Science Letters, v. 220, p. 41-55.
Huston, D. L., Pehrsson, S., Eglington, B. M., and Zaw, K., 2010, The geology and metallogeny of volcanic-hosted massive sulfide deposits: Variations through geologic time and with tectonic setting: Economic Geology, v. 105, p. 571-591.
Jenner, G. A., 1996, Trace element geochemistry of igneous rocks: Geochemical nomenclature and analytical geochemistry, *in* Wyman, D. A., ed., Trace Element Geochemistry of Volcanic Rocks: Applications for Massive Sulfide Exploration. , 12, Geological Association of Canada, Short Course Notes, p. 51-77.
Jenner, G. A., Longerich, H. P., Jackson, S. E., and Fryer, B. J., 1990, ICP-MS - A powerful tool for high-precision trace element analysis in Earth sciences: Evidence from analysis of selected U.S.G.S. reference samples: Chemical Geology, v. 83, p. 133-148.
Jones, S., Gemmell, J. B., and Davidson, G. J., 2006, Petrographic, geochemical, and fluid inclusion evidence for the origin of siliceous cap rocks above volcanic-hosted massive sulfide deposits at Myra Falls, Vancouver Island, British Columbia, Canada: Economic Geology, v. 101, p. 555-584.
Kalogeropoulos, S. I., and Scott, S. D., 1989, Mineralogy and geochemistry of an Archean tuffaceous exhalite; the Main Contact Tuff, Millenbach Mine area, Noranda, Quebec: Canadian Journal of Earth Sciences, v. 26, p. 88-105.

Kolata, D. R., Huff, W. D., and Bergström, S. M., 1996, Ordovician K-bentonites of eastern North America: Geological Society of America Special Paper, v. 313, p. 1-89.

Large, R. R., 1992, Australian volcanic-hosted massive sulfide deposits; features, styles, and genetic models: Economic Geology, v. 87, p. 471-510.

Lode, S., Piercey, J. S., and Devine, C. A., 2015, Geology, Mineralogy, and Lithogeochemistry of Metalliferous Mudstones Associated with the Lemarchant Volcanogenic Massive Sulfide Deposit, Tally Pond Belt, Central Newfoundland: Economic Geology, v. 110, p. 1835-1859.

Longerich, H. P., Jenner, G. A., Fryer, B. J., and Jackson, S. E., 1990, Inductively coupled plasma-mass spectrometric analysis of geological samples: A critical evaluation based on case studies: Chemical Geology, v. 83, p. 105-118.

Lydon, J. W., 1984, Ore deposit models; 8, Volcanogenic sulphide deposits; Part I, A descriptive model: Geoscience Canada, v. 11, p. 195-202.

_____1988, Ore deposit models #14; Volcanogenic massive sulphide deposits; Part 2, Genetic models: Geoscience Canada, v. 15, p. 43-65.

McLennan, S. M., 1989, Rare earth elements in sedimentary rocks; influence of provenance and sedimentary processes: Reviews in Mineralogy, v. 21, p. 169-200.

McLennan, S. M., Bock, B., Hemming, S. R., Hurowitz, J. A., Lev, S. M., and McDaniel, D. K., 2003, The roles of provenance and sedimentary processes in the geochemistry of sedimentary rocks, *in* Lentz, D. R., ed., Geochemistry of Sediments and Sedimentary Rocks: Evolutionary Considerations to Mineral Deposit-Forming Environments, GEOText 4: St. John's, NL, Canada, Geological Association of Canada, p. 7-38.

McNicoll, V., Squires, G., Kerr, A., and Moore, P., 2010, The Duck Pond and Boundary Cu-Zn deposits, Newfoundland: new insights into the ages of host rocks and the timing of VHMS mineralization: Canadian Journal of Earth Sciences, v. 47, p. 1481-1506.

McPhie, J., Doyle, M. G., and Allen, C. R., 1993, Volcanic Textures - A guide to the interpretation of textures in volcanic rocks: University of Tasmania, Centre for Ore Deposit and Exploration Studies.

Mills, R. A., and Elderfield, H., 1995, Hydrothermal activity and the geochemistry of metallliferous sediment: Geophysical Monograph, v. 91, p. 392-407.

Moore, P. J., 2003, Stratigraphic implications for mineralization; preliminary findings of a metallogenic investigation of the Tally Pond Volcanics, central Newfoundland, *in* Pereira, C. P. G., Walsh, D. G., and Kean, B. F., eds., Current Research, Report 03-1: St. John's, NL, Geological Survey Branch, p. 241-257.

Nesbitt, H. W., 2003, Petrogenesis of siliciclastic sediments and sedimentary rocks, *in* Lentz, D. R., ed., Geochemistry of Sediments and Sedimentary Rocks: Evolutionary Considerations to Mineral Deposit-Forming Environments, GEOText 4: St. John's, NL, Canada, Geological Association of Canada, p. 39-52.

Nesbitt, H. W., and Markovics, G., 1997, Weathering of granodioritic crust, long-term storage of elements in weathering profiles, and petrogenesis of siliciclastic sediments: Geochimica et Cosmochimica Acta, v. 61, p. 1653-1670.

Nesbitt, H. W., and Young, G. M., 1982, Early Proterozoic climates and plate motions inferred from major element chemistry of luitites: Nature, v. 299, p. 715-717.

Ohmoto, H., and Goldhaber, M. B., 1997, Sulfur and carbon isotopes, *in* Barnes, H. L., ed., Geochemistry of Hydrothermal Ore Deposits, Third Edition, John Wiley and Sons, p. 517-611.

Peter, J. M., 2003, Ancient iron formations: their genesis and use in the exploration for stratiform base metal sulphide deposits, with examples from the Bathurst Mining Camp, *in* Lentz, D. R., ed., Geochemistry of Sediments and Sedimentary Rocks: Secular Evolutionary Considerations to Mineral Deposit-Forming Environments, GEOtext v.4., Geological Association of Canada, p. 145-176.

Peter, J. M., and Goodfellow, W. D., 2003, Hydrothermal sedimentary rocks of the Heath Steele Belt, Bathurst mining camp, New Brunswick; Part 3, Application of mineralogy and mineral and bulk compositions to massive sulfide exploration: Economic Geology Monographs, v. 11, p. 417-433.

Piercey, S. J., 2007, Volcanogenic massive sulphide (VMS) deposits of the Newfoundland Appalachians: An overview of their setting, classification, grade-tonnage data, and unresolved questions, *in* Pereira, C. P. G., and Walsh, D. G., eds., Current Research, Report 07-01: St. John's, NL, Geological Survey Branch, p. 169-178.

_____2014, Modern Analytical Facilities 2. A Review of Quality Assurance and Quality Control (QA/QC) Procedures for Lithogeochemical Data: 2014, v. 41.

Piercey, S. J., Squires, G. C., Brace, T., and Lode, S., 2012, Initial Report: Hydrothermal mudstones from the Duck Pond volcanogenic massive sulfide (VMS) deposit, Central Mobile Belt Newfoundland and Labrador, Canada: Part 1 – Geology and Lithogeochemistry, CAMIRO Project 08E04 2012 Annual Report, The Geochemistry of Shales as Vectors to Ore Deposits, p. 41.

Piercey, S. J., Squires, G. C., and Brace, T. D., 2014, Lithostratigraphic, hydrothermal, and tectonic setting of the Boundary volcanogenic massive sulfide deposit, Newfoundland Appalachians, Canada: Formation by subseafloor replacement in a Cambrian rifted arc: Economic Geology, v. 109, p. 661-687.

Pollock, J., 2004, Geology and Paletectonic History of the Tally Pond Group, Dunnage Zone, Newfoundland Appalachians: An Integrated Geochemical, Geochronological, Metallogenic and Isotopic Study of a Cambrian Island Arc Along the Peri-Gondwanan Margin of Iapetus, Memorial University, 420 p.

Ranger, M. J., Pickerill, R. K., and Fillion, D., 1984, Lithostratigraphy of the Cambrian? - Lower Ordovician Bell Island and Wabana groups of Bell, Little Bell, and Kellys islands, Conception Bay, eastern Newfoundland: Canadian Journal of Earth Sciences = Journal Canadien des Sciences de la Terre, v. 21, p. 1245-1261.

Rogers, N., van Staal, C., Zagorevski, A., Skulski, T., Piercey, S. J., and McNicoll, V., 2007, Timing and tectonic setting of volcanogenic massive sulphide bearing terranes within the Central Mobile Belt of the Canadian Appalachians, *in* Milkereit, B., ed., Proceedings of Exploration '07: Fifth Decennial International Conference on Mineral Exploration: Toronto, ON, p. 1199-1205.

Rogers, N., van Staal, C. R., McNicoll, V., Pollock, J., Zagorevski, A., and Whalen, J., 2006, Neoproterozoic and Cambrian arc magmatism along the eastern margin of

the Victoria Lake Supergroup: A remnant of Ganderian basement in central Newfoundland?: Precambrian Research, v. 147, p. 320-341.

Rudnicki, M. D., 1995, Particle formation, fallout and cycling within the buoyant and non-buoyant plume above the TAG vent field: Geological Society, London, Special Publications, v. 87, p. 387-396.

Sáez, R., Moreno, C., González, F., and Almodóvar, G., 2011, Black shales and massive sulfide deposits: causal or casual relationships? Insights from Rammelsberg, Tharsis, and Draa Sfar: Mineralium Deposita, v. 46, p. 585-614.

Savrda, C. E., and Bottjer, D. J., 1989, Anatomy and implications of bioturbated beds in "black shale" sequences: Examples from the Jurassic Posidonienschiefer (Southern Germany): PALAIOS, v. 4, p. 330-342.

Slack, J. F., Grenne, T., and Bekker, A., 2009, Seafloor-hydrothermal Si-Fe-Mn exhalites in the Pecos greenstone belt, New Mexico, and the redox state of ca. 1720 Ma deep seawater: Geosphere, v. 5, p. 302-314.

Sparkes, B. A., 2005, Assessment Report of Prospecting, Compilation, Trenching, Basal Till Sampling and Geochemical Investigations on Licences 7695M (Fifth Year) and 10607M (First Year), Harpoon Brook Property, (Rubicon Minerals Corporation Project NF442), Lake Ambrose (NTS 12A/10), Newfoundland. Rubicon Minerals Corporation. 24 pages plus appendices.

Spry, P. G., Peter, J. M., and Slack, J. F., 2000, Meta-exhalites as exploration guides to ore, *in* Spry, P. G., Marshall, B., and Vokes, F. M., eds., Metamorphosed and metamorphogenic ore deposits, Reviews in Economic Geology 11: Littleton, CO, Society of Economic Geologists, p. 163-201.

Squires, G. C., MacKenzie, A. C., and MacInnis, D., 1991, Geology and genesis of the Duck Pond volcanogenic massive sulfide deposit, *in* Swinden, H. S., Evans, D. T. W., and Kean, B. F., eds., Metallogenic Framework of Base and Precious Metal Deposits, Central and Western Newfoundland, Geological Survey of Canada Open File 2156: Ottawa, ON, Canada, Geological Survey of Canada, p. 56-64.

Squires, G. C., and Moore, P. J., 2004, Volcanogenic massive sulphide environments of the Tally Pond Volcanics and adjacent area; geological, lithogeochemical and geochronological results, *in* Pereira, C. P. G., Walsh, D. G., and Kean, B. F., eds., Current Research, Report 04-1: St. John's, NL, Geological Survey Branch, p. 63-91.

Squires, G.C., and Hinchey, J.G. 2006. Geology of the Tally Pond Volcanic Belt and Adjacent Areas (parts of NTS 12A/09 & 12A/10). Map 2006-01. Government of Newfoundland and Labrador, Department of Natural Resources, Geological Survey, Map 2006-01, Open File 012A/1202.

Sverjensky, D. A., 1984, Europium Redox Equilibria in Aqueous-Solution: Earth and Planetary Science Letters, v. 67, p. 70-78.

Swinden, H. S., 1988, Introduction to volcanogenic sulphide deposits in Newfoundland, *in* Swinden, H. S., and Kean, B. F., eds., The volcanogenic sulphide districts of central Newfoundland, Geological Association of Canada, p. 1-26.

_____1991, Paleotectonic settings of volcanogenic massive sulphide deposits in the Dunnage Zone, Newfoundland Appalachians: Canadian Institute of Mining and Metallurgy Bulletin, v. 84, p. 59-89.

Swinden, H. S., and Kean, B. F., 1988, Volcanogenic Sulphide Districts of Central Newfoundland, Mineral Deposits Division, Geological Association of Canada, 250 p.

Swinden, H. S., Jenner, G. A., Kean, B. F., and Evans, D. T. W., 1989, Volcanic rock geochemistry as a guide for massive sulphide exploration in central Newfoundland, Current Research, Report 89-1, Newfoundland Department of Mines, p. 201-219.

Taylor, S. R., and McLennan, S. M., 1985, The continental crust: its composition and evolution: Oxford, Blackwell Scientific Publications, 312 p.

van Staal, C. R., and Barr, S. M., 2011, Lithospheric architecture and tectonic evolution of the Canadian Appalachians and associated Atlantic margin, *in* Percival, J. A., Cook, F. A., and Clowes, R. M., eds., Chapter 2 Tectonic Styles in Canada: the LITHOPROBE Perspective, Special Paper 49, Geological Association of Canada, p. 3-55.

Von Damm, K. L., 1990, Seafloor hydrothermal activity; black smoker chemistry and chimneys: Annual Review of Earth and Planetary Sciences, v. 18, p. 173-204.

Wagner, D. W., 1993, Volcanic stratigraphy and hydrothermal alteration associated with the Duck Pond and Boundary volcanogenic massive sulphide deposits, Central Newfoundland: Unpub. M.Sc. thesis, Carleton University, 430 p.

Webb, G. E., and Kamber, B. S., 2000, Rare earth elements in Holocene reefal microbialites; a new shallow seawater proxy: Geochimica et Cosmochimica Acta, v. 64, p. 1557-1565.

Williams, H., 1979, Appalachian Orogen in Canada: Canadian Journal of Earth Sciences, v. 16, p. 792-807.

Williams, H., Colman-Sadd, S. P., and Swinden, H. S., 1988, Tectonostratigraphic subdivisions of central Newfoundland., Current Research, Part B, Paper 88-1B: Ottawa, ON, Canada, Geological Survey of Canada, p. 91-98.

Zagorevski, A., van Staal, C. R., and McNicoll, V. J., 2007, Distinct Taconic, Salinic, and Acadian deformation along the Iapetus suture zone, Newfoundland Appalachians: Canadian Journal of Earth Sciences = Revue Canadienne des Sciences de la Terre, v. 44, p. 1567-1585.

Zagorevski, A., van Staal, C. R., Rogers, N., McNicoll, V. J., and Pollock, J., 2010, Middle Cambrian to Ordovician arc-backarc development on the leading edge of Ganderia, Newfoundland Appalachians: Geological Society of America Memoirs, v. 206, p. 367-396.

Table 5.1

Summary table of deposits, prospects, and showings and mudstone/shale associations in the Tally Pond volcanic belt

Table 5.1 Summary table of deposits, prospects, and showings and mudstone/shale associations in the Tally Pond volcanic belt

	Location	Type if Unit	Associated rocks	Dominant signature	Paleoredox	Other features
1	**Lemarchant deposit Zn-Pb-Cu-Ba-(Au-Ag) VMS**	- Exhalative metalliferous mudstones	- At contact between felsic and overlying mafic volcanic rocks, with or without close association with massive sulphides - As interflow mudstones within the hanging wall mafic volcanic rocks	Hydrothermal, vent proximal: - Elevated Fe/Al and base-metal values - Positive Eu anomalies and chondritic Y/Ho	Oxygenated - Presence of barite associated with mudstones and massive sulphides - Presence of Ce anomalies	- Shallow (for VMS) depositional environment (<1200 m, T: >250°C; pos. Eu anomalies) - Ba-Hg-enrichment due to epithermal input to VMS
2	**Cookstown Showing**	- Graphitic shales	Intercalated with felsic and mafic volcanic rocks	Non-hydrothermal: - Overall flat REE patterns, but: - Sulphide-poor shales cross-cut by sulphide-rich veins (hydrothermal input) ⇒ Non-hydrothermal shales overprinted by hydrothermal fluids	(Partially) oxygenated - Presence of bioturbation - Presence of small neg. Ce anomalies	T <250°C - No pos. Eu anomalies
3	**Higher Levels prospect**	- Exhalative metalliferous mudstones - Minor graphitic shales	- Metalliferous mudstones host mineralization - Mudstones occur within mafic volcanic rocks that overlie felsic volcanic rocks	Hydrothermal, vent distal: - Elevated Fe/Al and base-metal values - Predominantly no positive Eu anomalies, one exception - Small Ce anomalies - Low Ba-levels	(Partially) oxygenated - Presence of bioturbation - Presence of small to large Ce anomalies To reduced - Presence of abundant graphite	If oxygenated: - T predominantly <250°C - No pos. Eu anomalies, except one sample with a strong pos. Eu anomaly If reduced: - T >250°C possible
4	**Beaver Lake prospect**	- Exhalative metalliferous mudstones - Graphitic shales	Metalliferous mudstones and graphitic shales intercalated with felsic and mafic volcanic rocks	Metalliferous mudstones with hydrothermal signatures - Elevated Fe/Al and base-metal values - Positive Eu anomalies Graphitic shales - Overall flat REE patterns (non-hydrothermal)	(Partially) oxygenated - Presence of bioturbation - Presence of Ce and Eu anomalies To reduced - Presence of abundant graphite - Flat REE patterns	If oxygenated: - T predominantly <250°C - No pos. Eu anomalies, except one sample with a pos. Eu anomaly If reduced: - T >250°C possible
5	**Duck West showing**	- Graphitic shales -Mineralized tuff	Jig-saw fit altered felsic volcanic rocks intercalated with graphitic shales and mineralized tuff	- Graphitic shale non-hydrothermal, but hydrothermally overprinted - Tuff with replacement-style mineralization	(Partially) oxygenated - Presence of Eu, but no Ce anomalies	T: >250°C - Pos. Eu anomalies
6	**Duck Pond deposit** From Piercey et al. (2012)	- Exhalative metalliferous mudstones	- At contact between felsic and mafic volcanic rocks and as interflow mudstones	Hydrothermal, vent proximal: - Elevated Fe/Al and base-metal values - Small ositive Eu anomalies and chondritic to seawater-like Y/Ho	Oxygenated - Presence of Ce anomalies	T >250°C
7	**Boundary deposit**	- Exhalative metalliferous mudstones -Mineralized tuff	Mineralized tuff that is intercalated with metalliferous mudstones in lateral extension from massive sulphides	Metalliferous mudstones with hydrothermal signatures - Elevated Fe/Al and base-metal values - Positive Eu anomalies	(Partially) oxygenated - Presence of Eu, but no Ce anomalies	T: at least partially >250°C - Small pos. Eu anomalies
8	**Boundary West showing**	- Exhalative metalliferous mudstones - Graphitic shales	- Metalliferous mudstones associated with felsic tuffs and overlain by mafic flows - Graphitic shales intercalated with felsic volcanic rocks and metalliferous mudstones	Metalliferous mudstones with hydrothermal signatures - Elevated Fe/Al and base-metal values - Positive Eu anomalies Graphitic shales - Overall flat REE patterns (non-hydrothermal)	(Partially) oxygenated - Presence of Eu, but no Ce anomalies	T: >250°C - Pos. Eu anomalies
9	**Old Camp showing**	- Exhalative metalliferous mudstones - Graphitic shales	- Metalliferous mudstones associated with felsic and mafic volcanic rocks - Graphitic shales overlying felsic volcanic rocks	Metalliferous mudstones with hydrothermal signatures - Elevated Fe/Al and base-metal values - But predominantly no or small positive Eu anomalies Graphitic shales - Overall flat REE patterns (non-hydrothermal)	Reduced - Flat REE patters - Graphite-rich - Organic matter-rich to (partially) oxygenated - Small pos. Eu and neg. Ce anomalies	- No pos. Eu anomalies), except one sample If reduced: - T >250°C possible If oxygenated: - T predominantly <250°C (only small Eu anomalies)
10	**Keats Pond showing**	- Predominantly graphitic shales - Minor exhalative metalliferous mudstones	- Metalliferous mudstones associated with andesitic volcanic rocks and intercalated with graphitic shales	Metalliferous mudstones with hydrothermal signatures - Elevated Fe/Al and base-metal values - But predominantly no positive Eu anomalies	Reduced - Flat REE patters - Graphite-rich - Organic matter-rich	- No pos. Eu anomalies) If reduced: - T >250°C possible
11	**North Moose Pond showing**	- Predominantly metalliferous mudstones - Graphitic shales	- Metalliferous mudstones associated with felsic and mafic volcanic rocks - Graphitic shales overlying felsic volcanic rocks	Metalliferous mudstones with hydrothermal signatures - Elevated Fe/Al and base-metal values - Small pos. Eu anomalies Graphitic shales - Overall flat REE patterns (non-hydrothermal)	(Partially) oxygenated - Presence of Ce and Eu anomalies - Potentially presence of bioturbation To reduced - Presence of abundant graphite - Flat REE patterns	((If oxygenated: - T predominantly < or ~250°C - Small pos. Eu anomalies If reduced: - T >250°C possible
12	**South Moose Pond showing**	- Predominantly metalliferous mudstones - Graphitic shales	- Metalliferous mudstones associated with mafic volcanic rocks - Graphitic shales overlying mafic volcanic rocks	Metalliferous mudstones with hydrothermal signatures - Elevated Fe/Al and base-metal values - Small pos. Eu anomalies Graphitic shales - Overall flat REE patterns (non-hydrothermal)	(Partially) oxygenated - Presence of small Eu anomalies - Potentially presence of bioturbation To reduced - Presence of abundant graphite	((If oxygenated: - T predominantly < or ~250°C - Small pos. Eu anomalies If reduced: - T >250°C possible

Table 5.2

Whole-rock lithogeochemical data for the Tally Pond belt mudstones and shales

Sample #			**CNF36588**	**CNF36589**	**CNF36591**	**CNF36592**	**CNF36594**	**CNF36595**	**CNF36599**	**CNF36600**	**CNF36601**	**CNF36581**	**CNF25036**	**CNF25034**	**CNF25040**
Drill Hole			BL11-01	BL11-01	BL11-01	BL11-01	BL11-02	BL11-02	BL11-03	BL11-03	BL11-03	BD10-09	TP88-01	TP88-01	BW10-09
Section N			Beaver Lake	Beaver Lake	Beaver Lake	Beaver Lake	Beaver Lake	Beaver Lake	Beaver Lake	Beaver Lake	Beaver Lake	Boundary	Boundary W	Boundary W	Boundary W
Northing (UTM)			5380677	5380677	5380677	5380677	5380970	5380970	5380996	5380996	5380996	5389274.98	5389441	5389441	5389436.895
Easting (UTM)			522791	522791	522791	522791	523064	523064	523195	523195	523195	540915.52	540068	540068	540070.376
Sample Drill Hole Depth (m)			33.1	133.18	177.27	208.45	245.75	248.91	156.32	165.2	213.8	11.64	70.3	131.18	25.24
Description			IFS	MM	GS	MM	MM	GS	MM	GS	GS	MM	MM	T	GS
C(total)	%	IR	0.28	9.04	2.77	4.69	1.50	1.49	2.74	3.30	14.00	1.31	1.12	0.55	4.81
S(total)	%	IR	0.03	30.70	5.53	13.50	18.00	7.66	10.20	4.05	5.90	29.10	8.06	5.61	6.59
Hg	ppb	FIMS	2.50	2.50	66.00	291.00	299.00	75.00	191.00	162.00	339.00	6440.00	8790.00	683.00	480.00
SiO2	%	ICP-ES	55.16	25.78	61.96	55.88	45.32	40.78	61.30	63.93	52.76	26.83	75.39	70.94	57.72
Al2O3	%	ICP-ES	21.39	4.66	13.09	7.06	9.51	24.56	9.28	8.75	10.31	6.17	2.79	9.12	10.45
Fe(total)[1]	%	ICP-ES	10.23	35.21	7.99	17.09	23.07	10.92	12.71	7.11	8.19	34.92	7.56	6.73	9.85
MnO	%	ICP-ES	0.03	0.02	0.02	0.02	0.03	0.05	0.02	0.12	0.02	0.13	0.01	0.17	0.07
MgO	%	ICP-ES	0.32	0.46	1.09	0.57	0.88	1.70	0.50	1.42	0.75	1.79	0.14	1.56	1.45
CaO	%	ICP-ES	1.14	1.04	1.04	0.85	1.54	1.86	0.40	3.61	1.22	0.03	0.08	0.37	2.62
Na2O	%	ICP-ES	3.42	0.29	0.73	0.25	0.17	1.30	0.50	0.88	0.16	0.07	0.04	0.05	1.07
K2O	%	ICP-ES	1.33	0.97	3.01	1.61	2.78	7.08	2.23	1.73	3.30	1.27	0.86	3.35	2.94
TiO2	%	ICP-ES	1.58	0.22	0.32	0.29	0.48	1.06	0.27	0.31	0.45	0.11	0.10	0.13	0.37
P2O5	%	ICP-ES	0.25	0.13	0.06	0.30	0.78	0.07	0.11	0.08	0.63	0.02	0.01	0.02	0.04
LOI	%	ICP-ES	4.02	29.80	10.51	14.66	14.70	10.65	10.64	10.44	20.33	20.08	6.76	6.50	12.84
Total	%	ICP-ES	98.88	98.55	99.82	98.58	99.26	100.00	97.95	98.37	98.10	91.43	93.73	98.94	99.42
Ba	ppm	ICP-ES	420.00	1269.00	1098.00	3204.00	2060.00	3792.00	590.00	2421.00	463.00	782.00	395.00	651.00	1882.00
Sc	ppm	ICP-ES	41.00	5.00	10.00	7.00	12.00	38.00	9.00	9.00	10.00	9.00	4.00	9.00	20.00
Be	ppm	ICP-ES	2.00	0.50	2.00	2.00	2.00	3.00	1.00	2.00	2.00	0.50	0.50	1.00	1.00
V	ppm	ICP-ES	759.00	772.00	792.00	1025.00	548.00	464.00	991.00	1052.00	6011.00	88.00	132.00	37.00	1021.00
Li	ppm	ICP-MS	20.87	2.17	5.25	2.42	2.87	6.91	3.47	2.88	0.98	8.87	1.60	8.39	5.10
Sr	ppm	ICP-MS	124.46	36.33	41.93	27.75	49.39	66.69	34.81	70.83	31.81	7.31	7.16	12.18	74.92
Y	ppm	ICP-MS	4.89	8.18	15.92	11.01	19.99	11.07	11.50	9.46	20.68	12.37	2.46	11.63	9.40
Zr	ppm	ICP-MS	15.56	48.48	101.59	67.70	84.80	187.51	86.66	69.42	84.68	78.56	21.04	97.81	53.91
Nb	ppm	ICP-MS	1.73	3.08	6.33	3.85	4.58	7.43	3.02	2.79	6.47	0.78	1.52	2.46	1.59
Cs	ppm	ICP-MS	1.65	0.94	1.90	1.09	1.54	2.74	1.18	0.96	2.51	0.81	0.42	1.58	1.97
Ba_2	ppm	ICP-MS	419.16	903.88	1046.57	1657.78	1638.41	2626.80	571.23	2263.67	420.08	676.10	405.86	582.72	2167.38
La	ppm	ICP-MS	8.58	10.92	41.52	13.92	26.14	3.58	15.08	12.89	27.60	10.19	3.98	16.56	5.43
Ce	ppm	ICP-MS	18.29	17.10	78.67	23.28	42.28	7.47	27.14	24.76	45.88	20.74	7.14	33.61	9.93
Pr	ppm	ICP-MS	2.45	2.86	10.05	3.61	6.85	1.13	3.99	3.26	6.96	2.81	1.01	4.52	1.57
Nd	ppm	ICP-MS	11.20	11.06	36.93	13.90	28.32	4.69	15.35	12.41	27.52	11.61	3.62	17.64	6.04
Sm	ppm	ICP-MS	3.26	2.02	7.53	2.56	7.05	1.35	3.22	2.45	6.27	2.74	0.82	3.95	1.45
Eu	ppm	ICP-MS	0.98	0.39	1.07	0.64	2.86	0.35	0.58	0.60	1.34	0.91	0.39	0.90	0.51
Gd	ppm	ICP-MS	2.55	1.48	5.22	2.27	6.32	1.37	2.53	1.94	6.01	2.56	0.59	2.85	1.36
Tb	ppm	ICP-MS	0.33	0.23	0.65	0.32	0.80	0.22	0.35	0.29	0.78	0.37	0.08	0.32	0.23
Dy	ppm	ICP-MS	1.51	1.39	3.20	1.92	3.92	1.63	2.05	1.73	4.13	2.42	0.47	1.85	1.50
Ho	ppm	ICP-MS	0.26	0.31	0.63	0.39	0.75	0.43	0.43	0.38	0.80	0.49	0.10	0.46	0.35
Er	ppm	ICP-MS	0.58	1.03	1.85	1.21	2.03	1.66	1.42	1.26	2.07	1.51	0.31	1.56	1.14
Tm	ppm	ICP-MS	0.09	0.19	0.34	0.27	0.34	0.39	0.29	0.25	0.30	0.31	0.05	0.30	0.24
Yb	ppm	ICP-MS	0.52	1.34	2.50	1.64	2.14	2.65	1.84	1.71	2.10	1.76	0.39	2.27	1.37
Lu	ppm	ICP-MS	0.08	0.20	0.43	0.27	0.36	0.48	0.34	0.29	0.35	0.32	0.08	0.47	0.24
Hf	ppm	ICP-MS	5.68	1.71	6.97	2.87	4.63	9.26	3.76	3.15	5.55	3.50	2.98	4.70	2.68
Ta	ppm	ICP-MS	0.17	0.16	0.56	0.30	0.28	0.42	0.39	0.23	0.63	0.05	0.13	0.20	0.15
Tl	ppm	ICP-MS	0.15	3.81	2.02	4.89	2.98	2.69	2.96	1.84	3.60	17.53	2.18	3.07	3.20
Pb	ppm	ICP-MS	16.27	310.90	37.19	301.23	465.84	73.99	184.82	69.22	112.08	4569.15	2124.15	775.50	71.21
Bi	ppm	ICP-MS	0.13	0.82	0.31	0.68	0.86	2.16	0.54	0.35	0.93	63.59	6.49	0.78	0.42
Th	ppm	ICP-MS	2.96	5.00	8.84	5.44	6.52	7.67	5.17	4.76	9.68	3.38	1.65	4.69	3.98
U	ppm	ICP-MS	0.88	24.30	15.52	12.53	15.02	11.04	16.95	8.21	30.17	10.66	2.95	1.77	6.64
Cr	ppm	ICP-MS	6.58	36.52	32.40	77.99	70.34	42.79	45.32	44.01	126.59	9.90	10.57	5.60	70.62
Fe	ppm	ICP-MS	52398.26	183645.68	41580.40	93708.54	104642.71	57838.51	76059.17	43477.05	47939.66	208325.75	50988.42	50046.40	60578.27
Mn	ppm	ICP-MS	194.88	102.48	121.69	163.40	190.64	343.24	93.52	823.08	128.30	928.98	65.81	1174.01	482.94
Co	ppm	ICP-MS	2.53	14.88	8.49	11.22	16.92	37.05	8.38	8.78	16.98	118.65	3.49	4.63	18.84
Ni	ppm	ICP-MS	3.08	245.68	200.45	214.81	123.52	74.64	222.99	176.62	1164.98	65.21	29.71	21.32	129.50
Cu	ppm	ICP-MS	13.76	528.82	195.45	409.73	346.86	69.90	198.75	155.38	723.80	16271.66	1204.36	180.13	321.82
Zn	ppm	ICP-MS	29.52	1525.44	673.05	1325.68	629.72	44.15	969.84	1376.41	880.59	33264.13	32204.31	1367.74	1699.49
As	ppm	ICP-MS	6.11	1118.42	112.84	402.72	618.16	98.61	418.55	234.87	1789.71	1038.30	286.71	219.47	239.19
Se	ppm	ICP-MS	4.37	22.79	12.40	22.53	5.61	8.26	15.13	22.86	88.58	46.83	3.57	0.52	10.40
Br	ppm	ICP-MS	108.91	113.83	119.97	114.25	114.98	115.96	120.92	126.67	121.58	108.06	100.20	118.16	100.82
Mo	ppm	ICP-MS	1.00	222.46	97.16	82.07	47.19	51.73	110.06	34.81	252.64	131.88	49.08	12.50	17.48
Ag	ppm	ICP-MS	0.12	7.01	1.35	4.97	7.11	1.83	3.91	4.02	6.99	38.55	24.29	4.27	2.76
Cd	ppm	ICP-MS	0.07	11.69	8.29	10.58	2.16	0.46	10.28	17.81	3.59	99.52	121.83	4.99	17.38
Sn	ppm	ICP-MS	3.27	2.95	4.95	3.46	3.44	4.29	3.40	3.60	4.40	16.25	3.93	4.92	3.52
Sb	ppm	ICP-MS	6.14	374.49	12.04	68.58	123.84	45.83	72.81	36.28	136.18	147.89	59.20	33.41	88.61
Te	ppm	ICP-MS	0.04	0.23	0.37	1.01	0.64	0.87	0.28	0.33	1.07	33.47	1.06	0.16	0.45
I	ppm	ICP-MS	1.62	1.62	1.62	1.62	1.62	1.62	1.62	1.62	1.62	1.62	4.94	4.94	4.94
W	ppm	ICP-MS	1.00	3.59	3.59	4.49	7.97	15.28	2.93	1.82	6.07	2.05	4.42	2.35	2.78
Ce/Ce*			0.02	0.02	0.03	0.02	0.02	0.01	0.03	0.01	0.05	0.02	0.02	0.03	0.01
Eu/Eu*			4.62	4.56	5.63	4.03	3.69	4.99	5.06	4.22	4.86	3.97	3.26	4.68	3.89
Y/Ho			48.96	116.25	26.45	230.11	78.81	1059.19	39.14	187.81	16.78	76.77	99.18	39.31	346.73

[1]Fe(total) = (Fe_2O_3+FeO)

MM: Metalliferous mudstone
IFM: Interflow metalliferous mudstone
IFS: Interflow shale
GS: Graphitic shale
T: Tuff
GS/MM: Graphitic shale with hydrothermal overprint

Data table for Lemarchant mudstones in Lode et al. (2015)

Sample #			**CNF25037**	**CNF25038**	**CNF25039**	**CNF25046**	**CNF25045**	**CNF25041**	**CNF25042**	**CNF25043**	**CNF25049**	**CNF25048**	**CNF36597**	**CNF36598**	**CNF25029**
Drill Hole			BW10-10	BW10-11	BW10-11	BW10-12	BW10-12	BW10-14	BW10-15	BW10-15	BW11-20	BW11-24	CT11-01	CT11-01	DP11-284
Section N			Boundary W	Boundary W	Boundary W	Boundary W	Boundary W	Boundary W	Boundary W	Boundary W	Boundary W	Boundary W	Cookstown	Cookstown	Duck West
Northing (UTM)			5389438	5389402	5389402	5389475	5389475	5389475			5389513		5377300	5377300	5386612.49
Easting (UTM)			540071	540035	540035	540104	540104	540104			540062		521075	521075	537083.93
Sample Drill Hole Depth (m)			56.09	3.8	12.97	95.36	101.51	39.11	142.36	142.8	23.72	44.89	22.31	22.09	636.78
Description			MM	MM	MM	IFM	GS	MM	MM	MM	GS	MM	GS/MM	GS/MM	GS
C(total)	%	IR	4.58	8.11	3.23	2.98	3.43	2.09	5.69	5.45	0.49	2.05	0.71	2.77	0.02
S(total)	%	IR	10.10	26.30	13.80	11.50	6.05	12.80	15.00	24.30	11.80	6.22	6.55	7.82	4.94
Hg	ppb	FIMS	545.00	235.00	1080.00	525.00	302.00	2590.00	857.00	70.00	102.00	314.00	105.00	248.00	109.00
SiO2	%	ICP-ES	52.64	22.19	65.14	62.46	48.83	51.09	55.06	42.03	38.10	78.29	50.31	46.23	53.53
Al2O3	%	ICP-ES	9.99	7.82	2.55	4.42	13.62	10.31	4.04	3.79	19.07	2.34	14.53	14.71	23.77
Fe(total)[1]	%	ICP-ES	13.09	30.23	15.94	15.53	10.05	15.42	18.67	29.95	16.52	8.80	16.81	18.88	6.24
MnO	%	ICP-ES	0.13	0.05	0.04	0.03	0.09	0.07	0.04	0.03	0.11	0.05	0.24	0.17	0.02
MgO	%	ICP-ES	1.37	0.96	0.49	1.53	2.24	1.35	0.76	0.44	4.07	0.73	3.13	3.48	1.35
CaO	%	ICP-ES	2.35	1.55	0.80	1.34	4.55	3.16	1.70	0.66	0.75	0.90	1.25	1.11	0.05
Na2O	%	ICP-ES	0.19	0.23	0.02	0.54	1.34	0.51	0.31	0.15	0.10	0.23	4.34	3.02	0.36
K2O	%	ICP-ES	2.89	2.50	0.86	0.78	3.76	3.11	1.14	1.14	6.10	0.56	1.72	2.69	6.86
TiO2	%	ICP-ES	0.28	0.33	0.10	0.15	0.63	0.43	0.16	0.19	0.80	0.10	0.50	0.65	0.36
P2O5	%	ICP-ES	0.08	0.06	0.02	0.04	0.03	0.18	0.03	0.04	0.05	0.02	0.50	0.57	0.02
LOI	%	ICP-ES	15.36	28.30	13.00	12.06	13.35	13.30	17.24	21.46	11.97	7.64	5.22	7.80	6.68
Total	%	ICP-ES	98.37	94.23	98.97	98.88	98.47	98.93	99.16	99.86	97.64	99.66	98.54	99.30	99.25
Ba	ppm	ICP-ES	1040.00	1176.00	423.00	282.00	1471.00	2335.00	391.00	377.00	3275.00	368.00	585.00	627.00	3642.00
Sc	ppm	ICP-ES	14.00	12.00	3.00	8.00	34.00	21.00	7.00	4.00	53.00	3.00	19.00	22.00	27.00
Be	ppm	ICP-ES	1.00	1.00	0.50	0.50	1.00	1.00	0.50	0.50	1.00	0.50	2.00	3.00	2.00
V	ppm	ICP-ES	598.00	825.00	353.00	225.00	684.00	385.00	289.00	594.00	402.00	161.00	522.00	1332.00	9.00
Li	ppm	ICP-MS	3.85	3.36	1.18	9.40	4.92	5.31	1.55	1.40	21.40	2.41	8.34	9.91	8.57
Sr	ppm	ICP-MS	45.18	52.38	19.80	27.59	69.80	56.51	28.01	17.22	22.31	24.60	70.59	51.51	23.11
Y	ppm	ICP-MS	12.76	12.30	3.71	3.44	6.34	15.04	4.09	5.08	4.73	12.54	32.73	52.60	12.24
Zr	ppm	ICP-MS	88.19	68.56	28.34	30.74	50.59	77.16	33.89	40.37	45.17	26.71	75.91	110.95	269.35
Nb	ppm	ICP-MS	2.33	2.59	1.46	0.51	0.50	1.57	1.32	2.37	0.22	3.21	3.62	7.17	2.11
Cs	ppm	ICP-MS	1.86	2.44	0.52	0.62	2.02	1.62	0.84	1.14	2.95	0.47	0.61	1.58	4.42
Ba_2	ppm	ICP-MS	1004.07	1077.89	404.70	274.74	1423.83	2298.56	352.77	405.92	2170.70	354.29	531.46	610.46	3630.26
La	ppm	ICP-MS	13.30	16.03	4.00	1.80	3.29	6.80	6.37	6.61	5.47	4.18	18.94	35.44	8.04
Ce	ppm	ICP-MS	25.54	26.63	7.62	3.46	6.04	14.57	12.29	12.52	12.72	8.28	31.06	51.00	20.47
Pr	ppm	ICP-MS	3.76	4.04	1.04	0.49	1.03	2.34	1.80	1.94	1.96	1.11	5.11	8.93	2.81
Nd	ppm	ICP-MS	14.90	15.47	3.97	2.19	4.17	10.48	6.71	7.17	8.50	4.18	20.93	35.48	11.66
Sm	ppm	ICP-MS	3.71	3.12	0.88	0.59	1.10	3.34	1.39	1.45	2.15	1.05	4.83	7.78	3.16
Eu	ppm	ICP-MS	0.90	0.75	0.24	0.19	0.38	2.36	0.36	0.32	0.76	0.21	1.06	1.78	1.25
Gd	ppm	ICP-MS	3.13	2.45	0.68	0.60	1.04	3.76	1.10	1.05	1.44	1.10	5.20	8.10	2.77
Tb	ppm	ICP-MS	0.40	0.32	0.11	0.10	0.17	0.53	0.14	0.16	0.18	0.25	0.81	1.32	0.50
Dy	ppm	ICP-MS	2.28	2.02	0.68	0.55	1.13	2.98	0.80	0.95	1.01	1.91	5.20	8.29	3.23
Ho	ppm	ICP-MS	0.50	0.47	0.15	0.13	0.24	0.58	0.18	0.20	0.20	0.47	1.13	1.78	0.68
Er	ppm	ICP-MS	1.58	1.57	0.48	0.44	0.80	1.81	0.55	0.70	0.67	1.57	3.12	5.08	1.96
Tm	ppm	ICP-MS	0.31	0.26	0.09	0.09	0.18	0.32	0.11	0.18	0.15	0.28	0.50	0.77	0.32
Yb	ppm	ICP-MS	1.95	1.80	0.72	0.57	1.16	2.12	0.74	0.91	0.94	1.93	2.95	4.75	2.06
Lu	ppm	ICP-MS	0.38	0.34	0.12	0.10	0.19	0.36	0.14	0.17	0.14	0.31	0.43	0.69	0.29
Hf	ppm	ICP-MS	4.36	2.90	2.18	2.67	2.55	3.34	2.52	1.55	2.64	1.14	3.71	6.86	13.97
Ta	ppm	ICP-MS	0.28	0.30	0.12	0.04	0.03	0.18	0.12	0.19	0.02	0.12	0.28	0.55	0.16
Tl	ppm	ICP-MS	4.21	6.46	7.82	3.24	2.30	36.34	5.56	5.77	5.65	1.74	0.68	1.46	8.81
Pb	ppm	ICP-MS	277.96	412.98	162.55	173.60	37.45	270.66	436.19	669.97	83.24	142.45	140.06	85.42	30.08
Bi	ppm	ICP-MS	0.47	0.93	0.33	0.55	0.31	0.25	0.57	0.46	0.11	0.22	1.22	0.38	0.14
Th	ppm	ICP-MS	6.31	7.32	2.53	2.51	2.71	3.39	3.76	4.09	1.43	2.03	4.17	8.45	9.42
U	ppm	ICP-MS	13.10	31.93	8.00	1.62	4.73	5.92	31.01	12.49	1.86	3.05	13.29	36.55	3.76
Cr	ppm	ICP-MS	46.45	45.65	16.62	22.51	55.05	32.03	21.17	24.34	66.13	19.68	42.46	83.30	1.20
Fe	ppm	ICP-MS	83912.02	174453.96	97069.37	85637.59	60684.23	85265.57	101519.44	159325.37	80825.93	49814.77	90354.82	100348.66	41629.32
Mn	ppm	ICP-MS	966.90	389.75	274.21	225.33	620.49	513.23	291.05	155.05	704.06	328.11	1770.43	1262.91	113.90
Co	ppm	ICP-MS	12.61	17.27	6.48	61.62	36.24	37.39	35.62	11.93	54.07	4.25	14.42	20.70	0.76
Ni	ppm	ICP-MS	207.10	203.95	150.69	175.04	75.59	60.31	125.54	232.65	59.36	74.47	134.18	240.34	1.66
Cu	ppm	ICP-MS	207.65	345.59	248.52	248.03	161.77	137.19	227.89	291.39	91.35	180.63	154.19	202.26	26.68
Zn	ppm	ICP-MS	1387.87	945.88	749.16	209.69	487.90	344.46	90.57	147.45	150.46	316.68	525.47	1191.89	34.31
As	ppm	ICP-MS	520.74	908.29	677.37	413.80	122.28	1087.25	617.83	947.72	47.12	222.54	15.31	1.70	319.08
Se	ppm	ICP-MS	14.17	19.39	14.02	16.58	8.56	7.19	15.37	16.02	1.67	4.06	7.68	15.11	14.61
Br	ppm	ICP-MS	96.30	104.45	102.35	118.27	103.63	101.43	96.73	91.24	98.48	104.89	115.22	127.24	152.42
Mo	ppm	ICP-MS	145.77	235.86	169.74	26.73	5.37	28.86	185.28	126.01	8.44	24.54	63.71	128.29	10.88
Ag	ppm	ICP-MS	8.02	27.11	7.87	1.69	1.12	41.36	7.68	12.62	3.43	2.97	1.29	1.66	1.63
Cd	ppm	ICP-MS	7.72	8.85	7.14	3.88	4.32	1.30	0.38	1.06	0.52	1.74	3.01	13.56	0.25
Sn	ppm	ICP-MS	3.62	3.43	2.87	2.63	3.44	3.03	2.90	2.97	2.73	2.84	2.91	3.78	4.63
Sb	ppm	ICP-MS	113.91	273.76	152.01	98.00	31.40	126.65	158.69	223.68	18.23	67.73	2.11	8.39	5.29
Te	ppm	ICP-MS	0.10	0.80	0.55	1.37	0.79	0.05	0.08	1.57	0.55	0.65	0.27	0.66	0.23
I	ppm	ICP-MS	4.94	4.94	4.94	4.94	4.94	4.94	4.94	4.94	4.94	4.94	1.62	1.62	3.39
W	ppm	ICP-MS	4.77	4.71	3.26	0.85	2.59	9.30	3.15	6.00	3.68	3.62	3.27	5.55	4.20
Ce/Ce*			0.02	0.02	0.02	0.01	0.01	0.01	0.02	0.02	0.01	0.02	0.03	0.05	0.01
Eu/Eu*			4.76	4.32	4.22	4.31	4.10	3.16	4.22	4.49	3.97	5.29	4.83	4.61	3.90
Y/Ho			78.20	73.38	105.69	156.66	447.41	343.53	61.43	57.07	598.74	88.03	30.89	17.69	452.83

[1]Fe(total) = (Fe_2O_3+FeO)

MM: Metalliferous mudstone
IFM: Interflow metalliferous mudstone
IFS: Interflow shale
GS: Graphitic shale
T: Tuff
GS/MM: Graphitic shale with hydrothermal overprint

Data table for Lemarchant mudstones in Lode et al. (2015)

Sample #			CNF25028	CNF25060	CNF25076	CNF25059	CNF25058	CNF25057	CNF25017	CNF25087	CNF25086	CNF25088	CNF25089	CNF25092	CNF25021
Drill Hole			DP11-284	HL91-01	HL91-01	HL91-01	HL91-01	HL91-01	374-64	NM01-05	NM01-05	NM00-01	NM00-01	NM00-01	OC11-01
Section N			Duck West	Higher Levels	Higher Levels	Higher Levels	Higher Levels	Higher Levels	Keats Pond	North Moose	North Moose	North Moose	North Moose	North Moose	Old Camp
Northing (UTM)			5386612.49	5377398	5377398	5377398	5377398	5377398							5388111
Easting (UTM)			537083.93	523016	523016	523016	523016	523016							540995
Sample Drill Hole Depth (m)			639.76	11.1	16	18.41	22.7	25.05	47.95	48.42	39.24	171.48	172.17	176.85	29
Description			T	MM	MM	MM	MM	MM	MM	GS	MM	MM	MM	MM	GS
C(total)	%	IR	0.07	3.03	3.42	3.03	1.79	1.98	8.06	2.14	3.76	2.54	2.57	2.72	1.78
S(total)	%	IR	24.70	31.30	33.10	37.50	26.90	23.60	11.50	1.06	13.10	18.20	17.90	14.70	0.21
Hg	ppb	FIMS	2090.00	95.00	92.00	61.00	66.00	101.00	510.00	34.00	217.00	195.00	263.00	129.00	52.00
SiO2	%	ICP-ES	37.01	17.98	15.25	15.22	23.09	36.69	40.92	53.53	55.72	55.15	42.59	40.06	56.99
Al2O3	%	ICP-ES	8.79	5.16	3.63	3.13	2.70	5.74	9.23	17.86	2.85	2.92	9.09	11.56	15.59
Fe(total)[1]	%	ICP-ES	29.15	47.01	49.85	49.74	38.36	33.28	17.22	7.04	18.37	22.61	25.36	22.47	9.36
MnO	%	ICP-ES	0.13	0.09	0.10	0.03	0.06	0.04	0.07	0.12	0.08	0.04	0.06	0.09	0.15
MgO	%	ICP-ES	1.12	0.25	0.50	0.36	0.63	0.65	1.28	2.96	2.07	0.64	1.85	1.65	3.37
CaO	%	ICP-ES	0.03	0.18	0.72	0.31	7.99	0.20	1.63	2.37	4.15	1.04	1.56	2.58	0.58
Na2O	%	ICP-ES	0.16	0.20	0.04	0.05	0.02	0.13	0.40	0.16	0.11	0.37	0.82	1.20	1.45
K2O	%	ICP-ES	2.23	0.49	0.24	0.30	0.08	1.09	2.67	5.19	0.75	0.53	1.64	2.41	3.19
TiO2	%	ICP-ES	0.14	0.20	0.17	0.15	0.09	0.25	0.52	0.87	0.12	0.12	0.23	0.43	0.96
P2O5	%	ICP-ES	0.01	0.08	0.03	0.06	4.40	0.09	0.87	0.20	0.02	0.12	0.12	0.72	0.19
LOI	%	ICP-ES	17.19	26.17	27.56	28.51	21.19	19.16	24.60	8.70	15.82	15.07	16.16	15.86	7.23
Total	%	ICP-ES	95.95	97.82	98.09	97.88	98.60	97.32	99.42	99.00	100.10	98.60	99.47	99.03	99.05
Ba	ppm	ICP-ES	1054.00	59.00	30.00	39.00	19.00	186.00	585.00	959.00	210.00	79.00	244.00	371.00	400.00
Sc	ppm	ICP-ES	12.00	10.00	6.00	6.00	6.00	13.00	10.00	18.00	4.00	3.00	11.00	16.00	24.00
Be	ppm	ICP-ES	0.50	2.00	1.00	1.00	0.50	1.00	2.00	3.00	0.50	0.50	1.00	2.00	2.00
V	ppm	ICP-ES	2.50	343.00	505.00	433.00	578.00	1717.00	537.00	240.00	464.00	185.00	617.00	670.00	251.00
Li	ppm	ICP-MS	8.22	13.56	16.70	7.84	8.97	7.09	15.35	15.75	2.79	1.94	8.50	6.18	59.28
Sr	ppm	ICP-MS	10.25	32.40	15.36	14.81	110.24	16.58	64.75	79.55	61.92	22.10	35.77	66.68	46.68
Y	ppm	ICP-MS	2.64	7.04	4.91	3.97	48.34	5.69	21.80	13.87	3.94	7.15	15.72	38.72	12.10
Zr	ppm	ICP-MS	109.76	29.21	27.89	24.52	22.70	43.64	81.93	114.10	20.34	24.51	113.09	107.01	117.31
Nb	ppm	ICP-MS	0.56	0.66	0.64	0.75	0.28	1.59	6.59	8.43	0.50	1.33	4.13	3.13	5.84
Cs	ppm	ICP-MS	5.76	0.61	0.49	0.36	0.14	1.10	3.91	5.58	1.09	0.45	1.15	1.60	5.19
Ba_2	ppm	ICP-MS	978.12	57.45	29.34	36.65	23.11	185.78	578.91	948.57	193.28	74.47	238.74	347.42	396.47
La	ppm	ICP-MS	0.72	5.24	5.18	5.52	28.08	5.99	28.68	42.49	4.37	9.85	8.67	34.71	33.76
Ce	ppm	ICP-MS	1.90	9.85	9.11	8.69	25.24	9.63	58.70	77.81	6.33	15.67	13.56	51.90	68.43
Pr	ppm	ICP-MS	0.32	1.82	1.62	1.55	5.34	1.66	7.87	9.99	0.99	2.43	2.38	8.63	8.29
Nd	ppm	ICP-MS	1.37	7.32	6.05	6.06	23.81	6.47	30.93	36.62	3.70	9.96	9.95	36.56	30.10
Sm	ppm	ICP-MS	0.49	1.63	1.19	1.26	5.34	1.18	6.21	6.60	0.78	2.21	2.17	8.02	5.69
Eu	ppm	ICP-MS	0.79	0.30	0.24	0.23	2.75	0.20	1.42	1.27	0.27	0.48	0.70	1.93	1.10
Gd	ppm	ICP-MS	0.62	1.51	1.01	0.98	7.61	1.04	6.00	4.67	0.82	1.89	2.15	7.95	4.06
Tb	ppm	ICP-MS	0.11	0.19	0.15	0.12	0.91	0.14	0.76	0.55	0.11	0.23	0.33	1.11	0.48
Dy	ppm	ICP-MS	0.64	1.19	0.82	0.64	5.53	0.84	4.18	3.02	0.68	1.38	2.29	6.62	2.62
Ho	ppm	ICP-MS	0.11	0.25	0.16	0.14	1.20	0.19	0.82	0.55	0.15	0.27	0.53	1.34	0.51
Er	ppm	ICP-MS	0.30	0.78	0.54	0.41	3.07	0.66	2.18	1.65	0.52	0.84	1.81	3.81	1.53
Tm	ppm	ICP-MS	0.07	0.15	0.11	0.07	0.41	0.12	0.36	0.30	0.13	0.18	0.33	0.61	0.27
Yb	ppm	ICP-MS	0.32	1.00	0.72	0.58	2.28	0.84	2.07	1.89	0.62	0.78	2.64	3.62	1.75
Lu	ppm	ICP-MS	0.04	0.19	0.13	0.11	0.38	0.15	0.32	0.34	0.12	0.12	0.47	0.58	0.30
Hf	ppm	ICP-MS	4.60	1.46	1.17	1.21	2.31	1.76	3.57	5.77	1.08	0.90	6.35	4.11	5.78
Ta	ppm	ICP-MS	0.04	0.06	0.04	0.08	0.02	0.15	0.64	0.79	0.05	0.09	0.38	0.29	0.60
Tl	ppm	ICP-MS	115.42	4.77	5.32	4.20	0.54	2.28	2.43	1.04	3.03	1.42	2.68	1.56	0.66
Pb	ppm	ICP-MS	337.86	151.57	256.05	243.96	82.53	137.09	214.16	18.24	210.32	163.64	116.06	128.96	914.99
Bi	ppm	ICP-MS	0.34	0.24	0.42	0.22	0.20	0.35	0.50	0.30	0.16	0.28	0.34	2.42	0.50
Th	ppm	ICP-MS	4.10	2.56	2.30	2.34	1.56	3.36	11.84	16.15	1.61	2.02	5.57	7.34	14.88
U	ppm	ICP-MS	2.32	21.24	15.11	14.27	12.47	5.37	18.06	6.19	3.06	5.01	10.41	14.82	4.41
Cr	ppm	ICP-MS	4.75	41.31	32.40	28.17	40.43	67.68	91.68	101.52	34.51	17.95	35.67	79.63	91.96
Fe	ppm	ICP-MS	161024.81	276538.00	266621.81	287540.06	219476.95	189757.20	96756.64	49498.53	123216.84	152104.85	172093.49	143233.56	60948.96
Mn	ppm	ICP-MS	859.59	633.69	598.77	222.85	427.63	167.20	513.48	875.35	592.59	296.51	442.91	620.33	1049.09
Co	ppm	ICP-MS	0.68	18.34	14.13	15.70	47.94	27.57	21.01	19.52	20.55	6.28	8.15	17.44	22.46
Ni	ppm	ICP-MS	12.09	244.72	345.17	405.98	437.21	552.41	131.87	58.94	187.35	85.79	163.93	148.46	50.89
Cu	ppm	ICP-MS	731.76	304.57	421.38	422.83	184.84	243.37	323.05	75.82	137.26	270.48	217.61	101.44	63.85
Zn	ppm	ICP-MS	599.43	1244.04	566.37	643.37	924.11	4633.18	810.95	135.31	834.64	357.19	1297.61	940.23	132.82
As	ppm	ICP-MS	4811.45	1067.27	1128.74	1386.34	621.85	901.56	333.93	51.28	399.85	479.69	507.23	323.66	17.17
Se	ppm	ICP-MS	281.86	7.63	355.16	22.17	23.73	30.14	13.15	4.10	13.19	4.87	9.09	11.40	1.55
Br	ppm	ICP-MS	419.35	88.15	481.11	91.05	103.16	97.98	113.01	124.29	116.50	124.30	132.87	134.04	105.66
Mo	ppm	ICP-MS	47.28	257.20	215.57	207.99	27.84	44.91	81.92	9.66	26.72	71.53	59.02	22.96	1.45
Ag	ppm	ICP-MS	43.14	4.06	3.38	3.53	1.64	3.58	3.16	0.53	2.48	3.36	3.68	1.77	0.44
Cd	ppm	ICP-MS	1.77	4.90	2.55	3.97	7.89	40.48	3.80	0.75	9.35	2.51	8.27	4.69	0.02
Sn	ppm	ICP-MS	3.56	2.65	3.25	3.16	2.79	3.12	3.12	4.53	2.52	2.79	3.56	3.48	4.31
Sb	ppm	ICP-MS	48.64	98.93	112.27	117.49	34.91	70.74	124.14	7.26	127.77	71.57	81.95	24.25	2.64
Te	ppm	ICP-MS	0.55	0.27	0.98	0.26	0.84	0.84	0.69	0.25	0.18	0.21	0.54	6.03	0.55
I	ppm	ICP-MS	2.71	1.59	1.91	1.59	1.59	1.59	3.36	1.62	0.01	1.62	1.62	1.62	4.13
W	ppm	ICP-MS	1.61	1.79	1.70	1.83	3.35	1.44	3.65	3.47	0.46	0.37	1.10	1.51	2.95
Ce/Ce*			0.00	0.05	0.07	0.07	0.27	0.03	0.04	0.04	0.03	0.07	0.04	0.06	0.05
Eu/Eu*			2.22	5.22	4.62	4.98	3.11	4.85	4.41	4.56	3.68	4.76	3.88	4.50	4.65
Y/Ho			1467.53	11.26	5.79	7.06	0.68	31.04	20.40	22.57	48.10	8.02	28.15	10.69	11.85

[1]Fe(total) = (Fe_2O_3+FeO)

MM: Metalliferous mudstone
IFM: Interflow metalliferous mudstone
IFS: Interflow shale
GS: Graphitic shale
T: Tuff
GS/MM: Graphitic shale with hydrothermal overprint

Data table for Lemarchant mudstones in Lode et al. (2015)

Sample #			**CNF25022**	**CNF25023**	**CNF25024**	**CNF25025**	**CNF25018**	**CNF25033**	**CNF25032**	**CNF25031**	**CNF25030**	**CNF25019**	**CNF25012**	**CNF25055**	**CNF25054**
Drill Hole			OC11-01	OC11-01	OC11-01	OC11-01	OC11-03	OC01-03	OC01-03	OC01-03	OC01-03	OC11-03	OC11-07	OC11-08	OC11-08
Section N			Old Camp	Old Camp	Old Camp	Old Camp	Old Camp	Old Camp	Old Camp	Old Camp	Old Camp	Old Camp	Old Camp	Old Camp	Old Camp
Northing (UTM)			5388111	5388111	5388111	5388111	5387989	5387989	5387989	5387989	5387989	5387989	5387678	5387690	5387690
Easting (UTM)			540995	540995	540995	540995	540581	540581	540581	540581	540581	540581	540308	540521	540521
Sample Drill Hole Depth (m)			34.38	129.9	130.93	132.1	20	28.82	37.39	91.97	103.45	122.41	196.91	73.9	202.27
Description			T	MM	MM	GS	GS	GS	GS	MM	MM	MM	GS	GS	MM
C(total)	%	IR	2.64	4.87	4.83	3.41	4.66	8.83	1.72	3.23	2.56	2.73	1.59	4.84	2.80
S(total)	%	IR	0.33	24.60	18.50	5.20	2.01	2.79	0.13	10.70	11.20	7.95	4.55	3.16	13.10
Hg	ppb	FIMS	43.00	335.00	1590.00	1370.00	319.00	335.00	29.00	512.00	937.00	772.00	457.00	250.00	1410.00
SiO2	%	ICP-ES	52.83	40.73	44.37	70.06	57.82	60.83	55.76	61.38	67.21	71.18	60.27	54.41	64.09
Al2O3	%	ICP-ES	12.89	4.26	5.38	7.62	15.17	12.16	15.77	2.88	3.93	4.24	15.91	14.88	3.14
Fe(total)[1]	%	ICP-ES	9.42	29.62	22.28	7.26	6.49	6.67	10.72	12.61	14.30	10.55	7.40	7.86	16.36
MnO	%	ICP-ES	0.39	0.02	0.02	0.02	0.12	0.06	0.15	0.02	0.01	0.02	0.02	0.08	0.02
MgO	%	ICP-ES	3.87	0.36	0.59	0.96	1.75	1.42	3.92	0.70	0.70	0.63	1.53	1.80	0.62
CaO	%	ICP-ES	4.45	0.40	3.55	0.72	1.27	0.69	1.51	1.01	0.48	1.28	1.03	1.79	0.67
Na2O	%	ICP-ES	2.83	0.36	0.39	0.50	1.03	0.80	1.83	0.17	0.33	1.14	1.02	0.77	0.58
K2O	%	ICP-ES	1.82	0.90	1.12	1.42	3.76	2.94	2.37	0.49	0.51	0.45	2.60	4.06	0.25
TiO2	%	ICP-ES	1.08	0.18	0.28	0.30	0.89	0.63	1.11	0.08	0.08	0.16	0.22	0.78	0.06
P2O5	%	ICP-ES	0.16	0.02	2.23	0.08	0.11	0.13	0.11	0.02	0.01	0.27	0.06	0.08	0.06
LOI	%	ICP-ES	10.83	21.00	17.43	8.49	10.01	14.53	7.44	11.69	10.73	9.10	7.63	11.73	11.87
Total	%	ICP-ES	100.60	97.84	97.66	97.44	98.42	100.90	100.70	91.02	98.30	99.04	97.69	98.24	97.72
Ba	ppm	ICP-ES	221.00	347.00	414.00	563.00	492.00	367.00	331.00	127.00	128.00	128.00	664.00	514.00	84.00
Sc	ppm	ICP-ES	20.00	6.00	7.00	10.00	18.00	11.00	19.00	2.00	3.00	6.00	15.00	16.00	4.00
Be	ppm	ICP-ES	1.00	1.00	2.00	2.00	3.00	3.00	2.00	0.50	0.50	0.50	2.00	3.00	0.50
V	ppm	ICP-ES	207.00	321.00	905.00	1536.00	346.00	426.00	126.00	504.00	350.00	208.00	172.00	308.00	117.00
Li	ppm	ICP-MS	40.18	4.08	7.70	13.90	32.69	39.49	113.62	3.17	6.37	5.77	38.89	24.71	1.59
Sr	ppm	ICP-MS	237.09	30.04	79.81	38.41	64.77	42.68	70.83	30.38	28.74	50.95	118.71	87.42	46.24
Y	ppm	ICP-MS	9.49	7.22	75.13	15.71	11.95	11.86	11.79	8.78	15.10	19.35	15.22	13.99	8.17
Zr	ppm	ICP-MS	60.47	44.16	54.93	59.88	138.07	103.38	128.83	29.84	36.13	42.75	176.89	134.33	33.69
Nb	ppm	ICP-MS	0.86	0.88	1.45	1.82	11.23	7.68	10.60	2.67	2.61	1.78	2.02	12.10	0.86
Cs	ppm	ICP-MS	2.19	1.77	2.38	2.75	7.16	5.41	4.21	0.96	0.93	0.63	3.89	7.52	0.47
Ba_2	ppm	ICP-MS	218.62	370.90	428.95	561.96	445.19	359.05	328.41	133.54	141.94	121.35	619.11	581.48	87.33
La	ppm	ICP-MS	12.45	7.01	37.92	11.85	42.29	35.59	35.58	3.30	5.16	10.18	15.81	54.19	3.37
Ce	ppm	ICP-MS	27.69	11.10	52.29	17.66	83.12	67.47	77.67	6.99	12.21	19.66	31.61	106.74	7.47
Pr	ppm	ICP-MS	3.90	1.70	9.35	2.89	9.77	8.42	9.14	0.97	1.75	2.85	4.34	11.80	1.13
Nd	ppm	ICP-MS	16.34	6.01	39.24	10.20	33.40	30.37	34.60	3.90	7.36	12.37	17.61	41.64	4.67
Sm	ppm	ICP-MS	3.82	1.18	8.57	1.95	5.85	5.45	6.65	0.96	1.77	3.11	3.76	6.82	1.16
Eu	ppm	ICP-MS	0.91	0.30	2.24	0.45	1.05	1.06	1.30	0.18	0.32	0.81	0.53	1.42	0.27
Gd	ppm	ICP-MS	2.89	1.05	9.53	1.80	3.96	4.12	4.66	0.93	1.58	3.67	2.70	4.51	0.98
Tb	ppm	ICP-MS	0.36	0.16	1.31	0.27	0.49	0.49	0.50	0.18	0.29	0.52	0.39	0.60	0.18
Dy	ppm	ICP-MS	1.99	1.10	8.36	1.88	2.69	2.64	2.70	1.27	2.10	3.17	2.44	3.18	1.27
Ho	ppm	ICP-MS	0.38	0.25	1.87	0.46	0.51	0.49	0.51	0.31	0.52	0.68	0.55	0.59	0.30
Er	ppm	ICP-MS	1.13	0.88	5.63	1.53	1.59	1.45	1.56	1.07	1.82	1.85	1.84	1.82	1.10
Tm	ppm	ICP-MS	0.21	0.16	0.81	0.29	0.28	0.23	0.23	0.20	0.33	0.31	0.38	0.32	0.19
Yb	ppm	ICP-MS	1.22	1.09	4.60	1.79	1.89	1.65	1.96	1.34	2.05	1.90	2.76	2.09	1.43
Lu	ppm	ICP-MS	0.20	0.21	0.70	0.30	0.30	0.28	0.34	0.25	0.34	0.31	0.49	0.34	0.26
Hf	ppm	ICP-MS	3.10	3.10	2.48	2.79	6.30	5.00	8.95	1.16	1.25	3.51	8.40	6.16	2.73
Ta	ppm	ICP-MS	0.08	0.08	0.14	0.17	1.11	0.82	1.05	0.11	0.13	0.13	0.20	1.09	0.06
Tl	ppm	ICP-MS	0.35	3.07	4.44	1.72	0.92	1.05	0.48	3.38	5.21	1.71	2.33	0.91	5.23
Pb	ppm	ICP-MS	15.21	519.42	184.42	52.11	195.94	58.65	5.97	206.79	290.62	199.63	276.78	53.06	360.74
Bi	ppm	ICP-MS	0.18	0.29	0.51	0.38	1.85	1.24	0.11	1.37	0.88	0.28	1.03	0.96	1.56
Th	ppm	ICP-MS	4.20	4.20	6.32	6.82	20.82	15.04	13.48	1.88	2.17	3.47	7.72	19.50	2.09
U	ppm	ICP-MS	1.40	9.60	40.10	33.23	11.07	14.07	2.16	1.71	2.77	6.50	3.75	12.64	2.02
Cr	ppm	ICP-MS	6.02	17.81	47.89	136.35	94.95	94.57	63.17	2.66	13.45	19.21	15.52	180.96	8.39
Fe	ppm	ICP-MS	5956.21	163261.01	122087.39	45343.34	39692.27	44155.34	69676.26	8708.04	92369.47	65987.96	39831.02	51330.24	97046.67
Mn	ppm	ICP-MS	275.04	136.99	147.31	142.87	834.36	456.26	1072.25	11.44	60.58	167.80	113.93	558.74	126.51
Co	ppm	ICP-MS	1.90	10.51	13.87	7.38	50.85	44.23	13.53	0.27	9.77	21.54	4.69	42.85	7.71
Ni	ppm	ICP-MS	6.84	74.03	375.48	147.61	75.88	122.51	42.52	10.63	418.70	71.56	68.23	79.66	201.06
Cu	ppm	ICP-MS	5.05	291.44	322.01	395.00	338.05	165.32	53.80	27.85	302.48	112.26	166.80	186.61	206.77
Zn	ppm	ICP-MS	30.37	411.51	1817.92	3253.67	82.96	187.19	197.11	186.08	1333.25	326.82	1074.16	132.15	1533.45
As	ppm	ICP-MS	1.10	862.81	766.53	225.87	79.36	128.67	16.54	33.00	791.48	337.55	198.79	85.60	766.73
Se	ppm	ICP-MS	1.55	13.52	16.55	23.99	4.78	5.75	3.79	1.65	11.84	3.62	8.54	5.14	5.90
Br	ppm	ICP-MS	10.78	94.96	97.46	100.64	103.15	109.63	108.79	10.53	117.83	110.69	109.20	99.89	99.48
Mo	ppm	ICP-MS	0.27	128.57	113.55	25.91	31.05	43.31	0.91	1.00	39.06	28.37	16.42	13.49	37.38
Ag	ppm	ICP-MS	0.03	16.46	7.92	2.66	1.15	1.34	0.51	0.38	1.89	2.07	3.64	0.82	4.77
Cd	ppm	ICP-MS	0.01	2.89	14.74	32.51	0.56	1.43	0.37	1.33	8.80	2.67	6.14	1.02	7.48
Sn	ppm	ICP-MS	0.35	3.22	3.24	3.75	5.27	4.09	4.39	0.28	2.76	2.78	4.23	5.18	2.49
Sb	ppm	ICP-MS	0.13	280.94	282.01	62.11	13.58	32.66	2.63	10.64	288.47	88.06	42.79	15.91	167.97
Te	ppm	ICP-MS	0.55	0.43	0.55	0.55	0.25	1.04	0.01	0.12	0.49	0.55	0.40	0.71	1.77
I	ppm	ICP-MS	0.58	5.63	3.90	2.98	4.36	4.94	4.94	4.94	4.94	5.50	5.93	1.59	1.59
W	ppm	ICP-MS	0.12	1.13	2.93	1.71	5.75	4.15	3.91	0.13	1.31	2.99	1.07	3.92	0.78
Ce/Ce*			0.04	0.03	0.06	0.03	0.05	0.05	0.05	0.02	0.03	0.05	0.03	0.05	0.03
Eu/Eu*			4.66	4.16	4.31	4.30	4.65	4.53	4.67	5.41	5.40	4.64	5.77	4.17	4.90
Y/Ho			17.75	49.51	10.92	47.53	11.63	10.31	9.30	38.43	24.81	12.57	41.99	9.49	24.89

[1]Fe(total) = (Fe_2O_3+FeO)

MM: Metalliferous mudstone
IFM: Interflow metalliferous mudstone
IFS: Interflow shale
GS: Graphitic shale
T: Tuff
GS/MM: Graphitic shale with hydrothermal overprint

Data table for Lemarchant mudstones in Lode et al. (2015)

Sample #			**CNF25053**	**CNF25052**	**CNF25051**	**CNF25015**	**CNF25026**	**CNF25027**	**CNF25077**	**CNF25078**	**CNF25079**	**CNF25083**	**CNF25084**
Drill Hole			OC11-08	OC11-08	OC11-08	SM97-06	SM97-08	SM97-08	Bell Island	Bell Island	Bell Island	Bell Island	Bell Island
Section N			Old Camp	Old Camp	Old Camp	South Moose	South Moose	South Moose	The Beach	The Beach	Lance Cove	Powersteps	Powersteps
Northing (UTM)			5387690	5387690	5387690		5392441	5392441	Beach Fm.	Beach Fm.	Beach Fm.	Powerst. Fm.	Powerst. Fm.
Easting (UTM)			540521	540521	540521		544510	544510					
Sample Drill Hole Depth (m)			204.81	208.3	253.11	145.49	121.3	122.82					
Description			MM	MM	GS	GS	IFM	IFM	Brown shale	Gray shale	Dark gray shale	Siltic mudstone	Dark gray shale
C(total)	%	IR	2.41	3.97	8.29	2.75	0.14	0.10	0.12	0.17	0.39	0.32	0.36
S(total)	%	IR	11.60	17.60	3.62	2.99	28.80	27.30	0.06	0.05	0.12	0.32	0.10
Hg	ppb	FIMS	1350.00	1550.00	992.00	162.00	94.00	74.00	2.50	2.50	7.00	10.00	5.00
SiO2	%	ICP-ES	70.12	57.96	64.30	54.28	18.94	36.49	71.91	57.17	54.92	49.30	54.55
Al2O3	%	ICP-ES	1.66	3.51	10.14	15.16	8.35	4.47	12.66	20.53	21.78	18.83	22.46
Fe(total)[1]	%	ICP-ES	14.73	21.29	5.79	11.07	44.15	37.12	6.86	8.72	8.47	19.20	8.83
MnO	%	ICP-ES	0.03	0.01	0.03	0.20	0.08	0.05	0.04	0.04	0.07	0.06	0.07
MgO	%	ICP-ES	0.59	0.44	0.77	2.44	4.02	2.09	1.01	1.79	1.79	2.27	1.93
CaO	%	ICP-ES	0.94	0.07	0.43	1.56	0.24	0.15	0.28	0.43	0.34	0.53	0.24
Na2O	%	ICP-ES	0.19	0.27	1.26	1.07	0.12	0.11	1.31	1.28	0.95	0.84	1.03
K2O	%	ICP-ES	0.21	0.40	2.17	2.79	0.40	0.30	2.08	4.29	3.67	2.27	3.98
TiO2	%	ICP-ES	0.05	0.13	0.51	0.62	0.31	0.22	0.87	1.23	1.09	1.09	1.17
P2O5	%	ICP-ES	0.04	0.05	0.09	0.16	0.08	0.10	0.10	0.24	0.15	0.29	0.13
LOI	%	ICP-ES	10.73	15.35	12.66	9.18	21.42	18.43	3.14	4.97	6.48	5.97	6.26
Total	%	ICP-ES	99.29	99.48	98.16	98.53	98.12	99.52	100.20	100.70	99.71	100.70	100.60
Ba	ppm	ICP-ES	70.00	122.00	501.00	501.00	123.00	82.00	416.00	725.00	748.00	391.00	786.00
Sc	ppm	ICP-ES	2.00	7.00	12.00	19.00	14.00	7.00	11.00	21.00	22.00	24.00	23.00
Be	ppm	ICP-ES	0.50	0.50	2.00	2.00	0.50	0.50	2.00	3.00	3.00	6.00	4.00
V	ppm	ICP-ES	94.00	564.00	689.00	366.00	239.00	147.00	75.00	141.00	147.00	164.00	155.00
Li	ppm	ICP-MS	2.21	3.00	19.86	76.48	18.73	9.08	65.70	83.37	127.82	165.51	119.26
Sr	ppm	ICP-MS	37.45	19.36	47.53	54.91	7.64	5.23	82.35	126.67	181.85	109.68	139.08
Y	ppm	ICP-MS	5.24	14.91	13.58	14.63	5.86	7.46	14.20	32.82	21.82	22.83	18.88
Zr	ppm	ICP-MS	17.49	36.88	96.08	128.30	56.71	41.25	104.62	130.53	114.71	83.94	121.30
Nb	ppm	ICP-MS	0.65	0.86	3.53	2.33	1.08	0.67	13.65	21.34	20.28	16.01	20.35
Cs	ppm	ICP-MS	0.45	0.90	4.03	4.21	0.38	0.30	2.54	8.16	8.11	6.32	8.08
Ba_2	ppm	ICP-MS	75.45	128.55	432.72	533.47	119.36	80.61	364.19	710.18	731.77	398.01	763.41
La	ppm	ICP-MS	2.56	4.82	14.89	57.93	4.11	9.45	32.84	47.45	45.14	36.86	47.15
Ce	ppm	ICP-MS	4.78	9.08	30.14	183.97	8.44	19.20	69.72	101.01	87.77	76.26	88.08
Pr	ppm	ICP-MS	0.67	1.49	3.62	13.66	1.31	3.12	8.25	12.55	10.75	9.49	11.04
Nd	ppm	ICP-MS	2.55	5.54	13.48	45.97	5.69	12.68	31.24	49.25	40.46	36.25	40.64
Sm	ppm	ICP-MS	0.64	1.23	2.63	6.86	1.25	2.88	5.89	10.58	7.69	7.20	7.39
Eu	ppm	ICP-MS	0.14	0.28	0.62	1.74	0.32	0.61	1.29	2.56	1.63	1.50	1.49
Gd	ppm	ICP-MS	0.64	1.22	2.37	4.24	1.27	1.87	4.77	10.18	5.96	6.16	5.35
Tb	ppm	ICP-MS	0.12	0.24	0.37	0.53	0.17	0.21	0.61	1.36	0.81	0.87	0.68
Dy	ppm	ICP-MS	0.75	1.85	2.39	2.83	1.02	1.34	3.30	7.54	4.52	5.10	3.85
Ho	ppm	ICP-MS	0.19	0.48	0.51	0.54	0.24	0.28	0.59	1.35	0.89	0.96	0.75
Er	ppm	ICP-MS	0.66	1.78	1.65	1.62	0.70	0.91	1.62	3.45	2.56	2.62	2.24
Tm	ppm	ICP-MS	0.10	0.35	0.27	0.30	0.12	0.20	0.27	0.49	0.44	0.43	0.40
Yb	ppm	ICP-MS	0.84	2.35	1.97	2.15	1.01	1.01	1.54	2.93	2.49	2.51	2.49
Lu	ppm	ICP-MS	0.14	0.41	0.31	0.39	0.17	0.17	0.25	0.46	0.38	0.38	0.41
Hf	ppm	ICP-MS	0.87	1.06	5.22	7.69	4.17	1.76	5.26	10.21	6.58	4.32	10.16
Ta	ppm	ICP-MS	0.05	0.04	0.33	0.23	0.16	0.08	1.32	1.86	1.81	1.41	1.99
Tl	ppm	ICP-MS	2.94	4.14	2.72	0.87	0.19	0.14	0.39	0.74	0.79	0.51	0.72
Pb	ppm	ICP-MS	384.26	410.35	66.42	80.29	204.41	184.89	29.28	12.09	21.71	11.68	17.09
Bi	ppm	ICP-MS	0.30	0.32	0.65	0.27	24.48	10.72	0.11	0.24	0.37	0.22	0.33
Th	ppm	ICP-MS	1.39	2.73	11.02	17.33	5.33	4.75	11.42	16.28	15.92	14.92	16.50
U	ppm	ICP-MS	3.59	14.73	18.80	6.16	10.56	14.01	2.08	2.71	3.00	2.70	3.28
Cr	ppm	ICP-MS	7.45	19.03	204.87	395.85	32.26	22.29	65.85	118.62	105.94	115.87	114.66
Fe	ppm	ICP-MS	92553.50	109232.69	34305.02	66477.37	222782.77	193240.74	41638.51	52520.45	47099.61	122904.06	55719.75
Mn	ppm	ICP-MS	165.86	42.41	207.15	1428.21	509.27	324.81	234.80	258.45	450.09	409.15	473.84
Co	ppm	ICP-MS	4.67	12.39	14.72	26.46	125.17	72.41	11.84	21.42	21.63	31.67	22.20
Ni	ppm	ICP-MS	51.49	192.68	251.63	54.65	238.82	181.26	30.90	52.34	51.99	61.95	53.74
Cu	ppm	ICP-MS	169.79	239.23	368.43	69.52	540.23	536.07	17.56	34.94	42.80	57.59	42.13
Zn	ppm	ICP-MS	530.19	1082.91	1592.62	134.99	105.57	75.54	89.08	99.54	114.32	115.12	96.58
As	ppm	ICP-MS	616.82	847.27	381.59	63.85	27.85	133.79	6.01	5.54	8.14	107.53	9.50
Se	ppm	ICP-MS	3.42	9.85	18.71	1.69	34.07	37.43	4.37	2.93	4.37	4.37	4.37
Br	ppm	ICP-MS	101.10	99.80	108.91	103.17	96.93	90.64	129.97	130.92	113.87	134.13	128.52
Mo	ppm	ICP-MS	61.22	107.66	55.77	4.40	108.81	209.99	1.48	0.83	0.77	5.40	0.79
Ag	ppm	ICP-MS	6.43	5.77	1.94	1.05	2.47	2.42	0.30	0.36	0.25	0.28	0.30
Cd	ppm	ICP-MS	2.71	8.32	20.59	0.40	0.18	0.61	0.11	0.11	0.11	0.07	0.06
Sn	ppm	ICP-MS	3.08	2.95	4.40	3.00	2.78	2.59	3.74	4.63	4.48	4.43	4.77
Sb	ppm	ICP-MS	132.18	254.41	50.63	12.28	4.36	3.92	0.27	0.27	0.23	0.21	0.24
Te	ppm	ICP-MS	2.11	0.55	0.19	0.55	13.13	5.37	0.18	0.11	0.18	0.18	0.18
I	ppm	ICP-MS	1.59	4.94	4.94	8.13	1.78	2.73	1.62	1.62	1.62	1.62	1.62
W	ppm	ICP-MS	0.61	1.01	2.84	1.45	2.29	0.74	2.67	4.47	4.13	6.04	4.38
Ce/Ce*			0.03	0.03	0.03	0.04	0.03	0.06	0.05	0.04	0.04	0.05	0.04
Eu/Eu*			5.09	4.70	4.31	3.61	4.40	4.85	4.37	4.44	4.46	4.59	4.48
Y/Ho			27.34	25.31	33.64	8.65	29.96	8.67	12.67	15.28	16.57	10.61	16.67

[1]Fe(total) = (Fe_2O_3+FeO)

MM: Metalliferous mudstone
IFM: Interflow metalliferous mudstone
IFS: Interflow shale
GS: Graphitic shale

Data table for Lemarchant mudstones in Lode et al. (2015)

Fig. 5.1 A-C

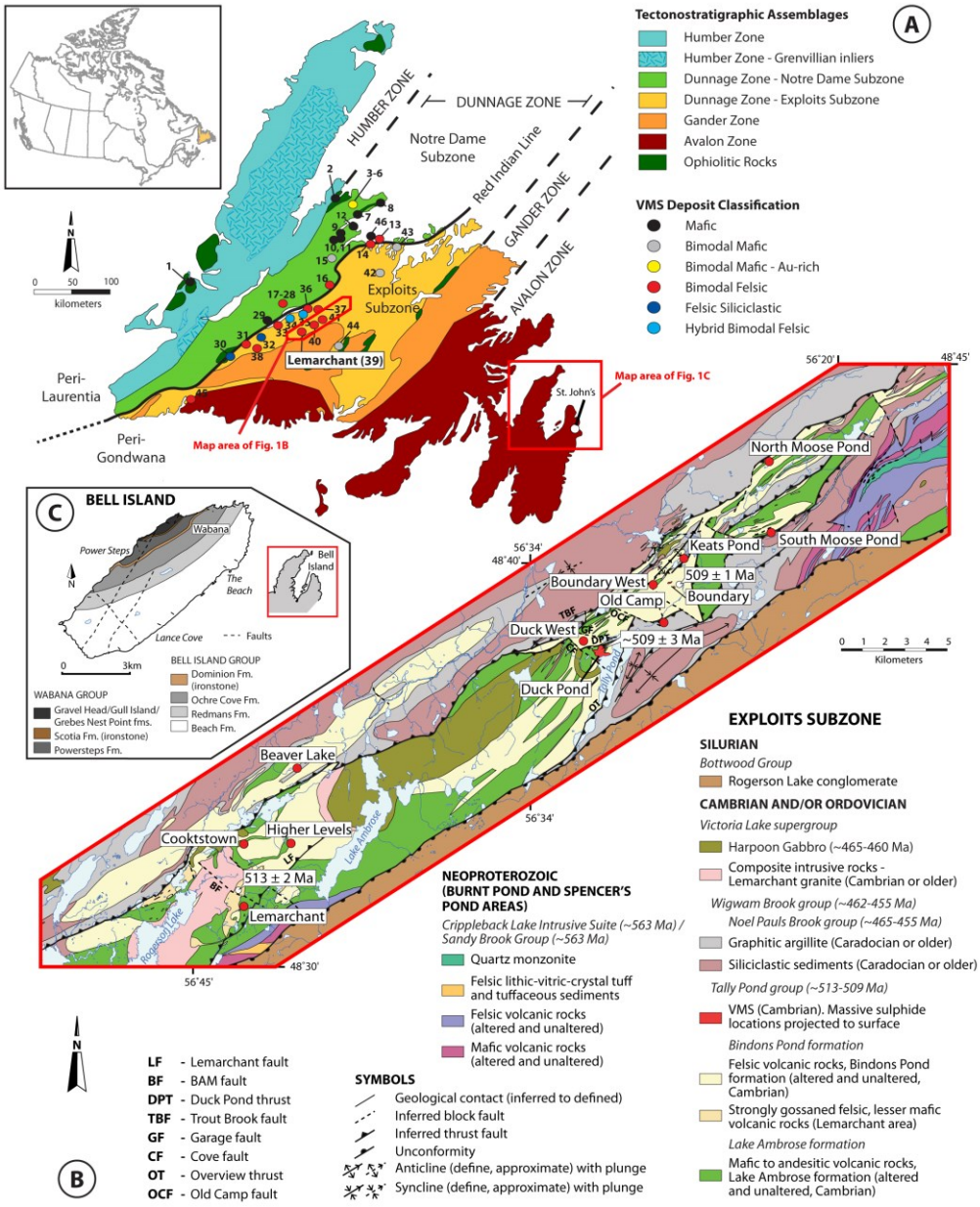

Figure 5.1 *A) Overview map showing the tectonostratigraphic assemblages with the main zones of the Newfoundland Appalachians (Avalon, Gander, Dunnage, and Humber zones) and VMS occurrences within the Notre Dame and Exploits subzones (modified after Swinden 1991; Piercey 2007). Notre Dame Subzone VMS: 1 – York Harbour; 2 – 8 - Baie Verte belt deposits; 9 – 12, 46 – Springdale belt deposits; 13 – 29 Buchans-Roberts Arm deposits. Exploits Subzone VMS: 30 – 37 - Tulks belt deposits; Tally Pond belt deposits: 39 – Lemarchant; 40 – Duck Pond; 41 – Boundary; 42 – 45 – Point Leamington belt deposits. B) Geological map of the Tally Pond volcanic belt and adjacent areas (parts of NTS 12A/09 & 12A/10. Map modified after Map 2006-1 from G.C. Squires and J.G. Hinchey, and Copeland, 2009-012A-1486. C) Overview map of Bell Island. Outcrops from Lance Cove, The Beach, and Powersteps were sampled. Map modified after Ranger et al. (1984) and Harazim et al. (2013).*

Fig. 5.2

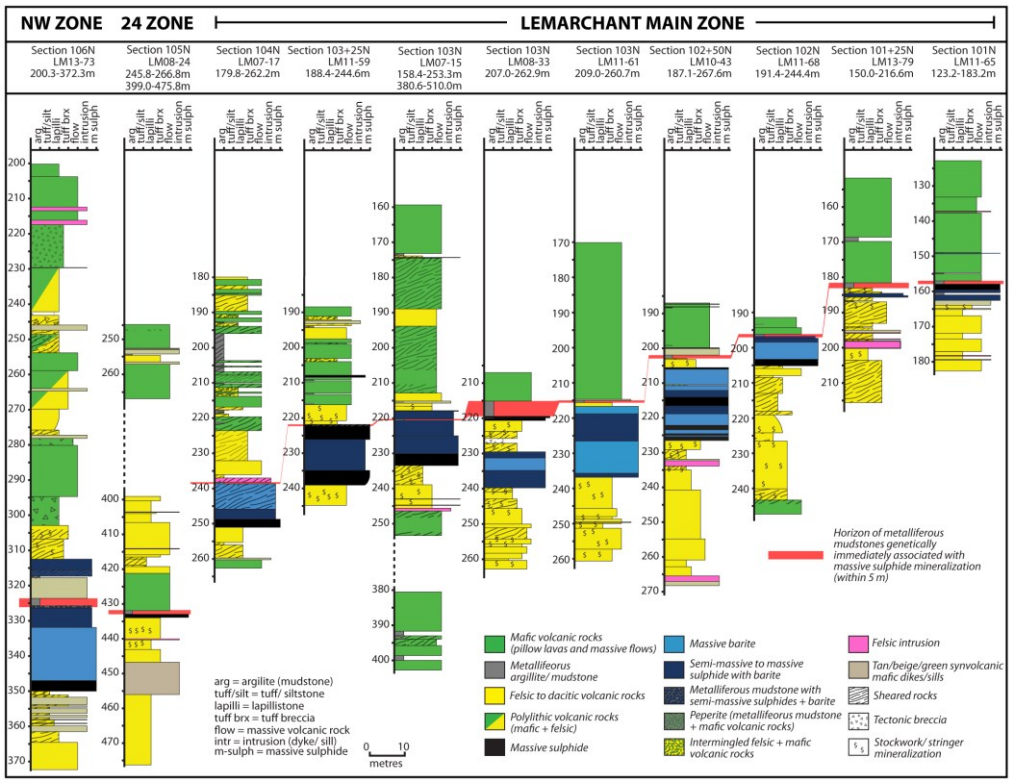

Figure 5.2 *North-south long-section with graphic logs of the Lemarchant deposit and its three mineralized zones: the Lemarchant Main Zone, the 24 Zone, and the Northwest Zone.*

Fig. 5.3 A-C

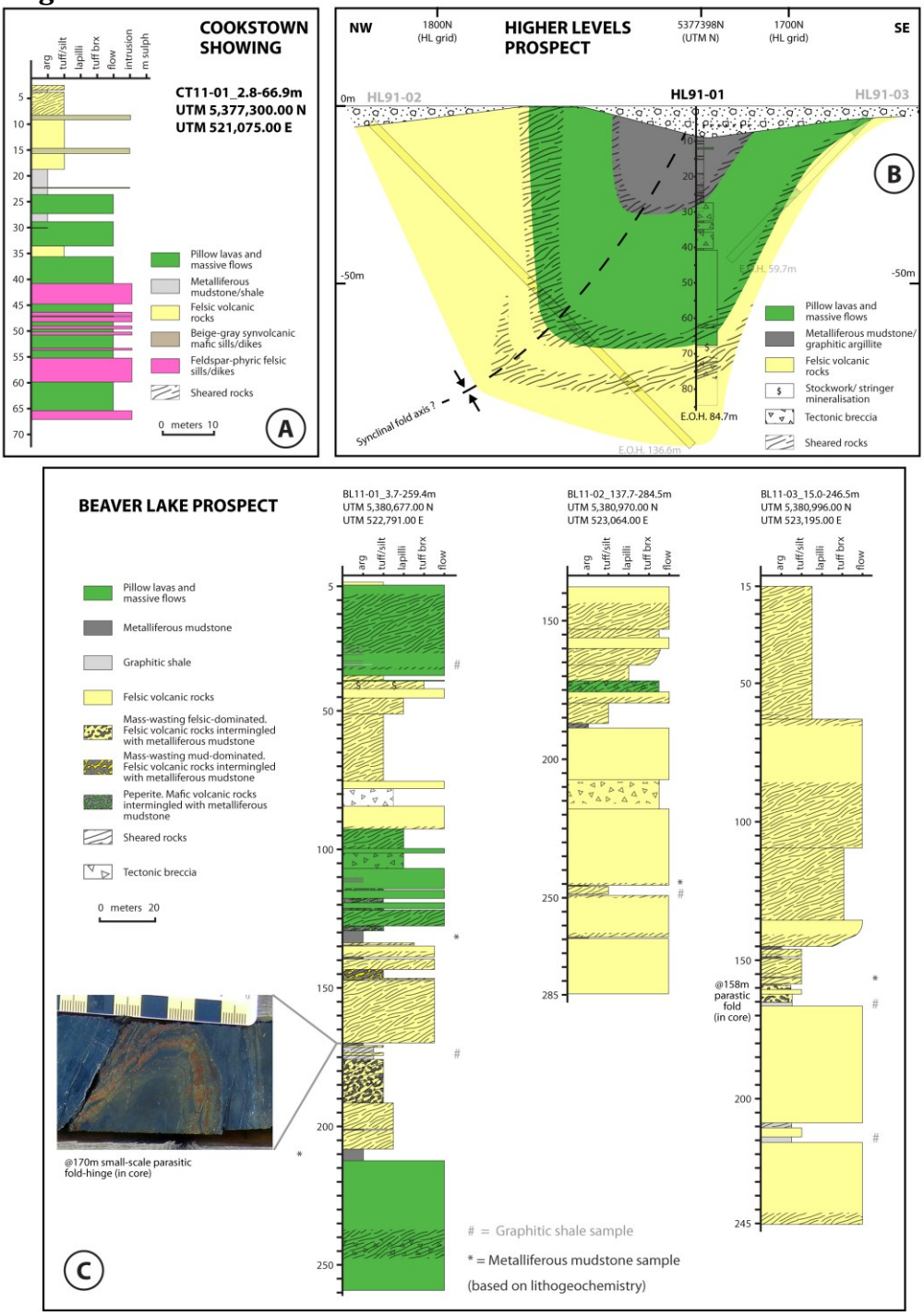

Figure 5.3 *A) Graphic log of the drill hole CT11-01 of the Cookstown showing, B) Northwest-southeast cross-section of the synclinal structure of the Higher Levels prospect with superimposed graphic log of drill hole HL91-01 (this study), and drill holes HL91-02 and -03. Modified after Squires and Moore (2004), C) Graphic logs of the drill holes BL11-01, BL11-02, and BL11-03 of the Beaver Lake prospect.*

Fig. 5.4

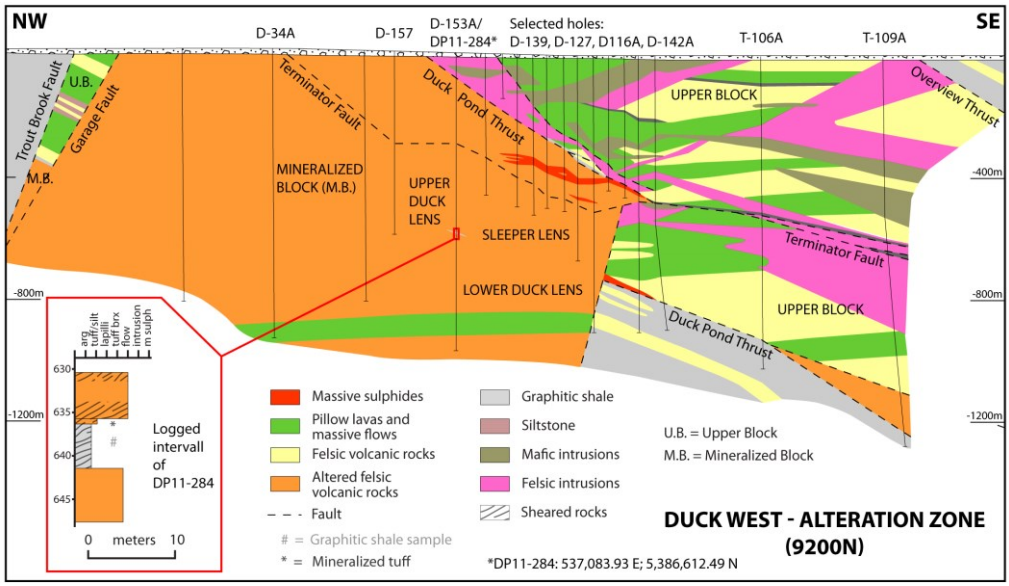

Figure 5.4 *Northwest-southeast cross-section of the Duck West alteration zone, Duck West showing. Close-up section of the graphic log of drill hole DP11-284 that contains a graphitic shale and mineralized tuff horizon is represented as graphic log. Modified after unpublished draft from Teck Resources Ltd. and G. Squires, pers. comm. 2014.*

Fig. 5.5

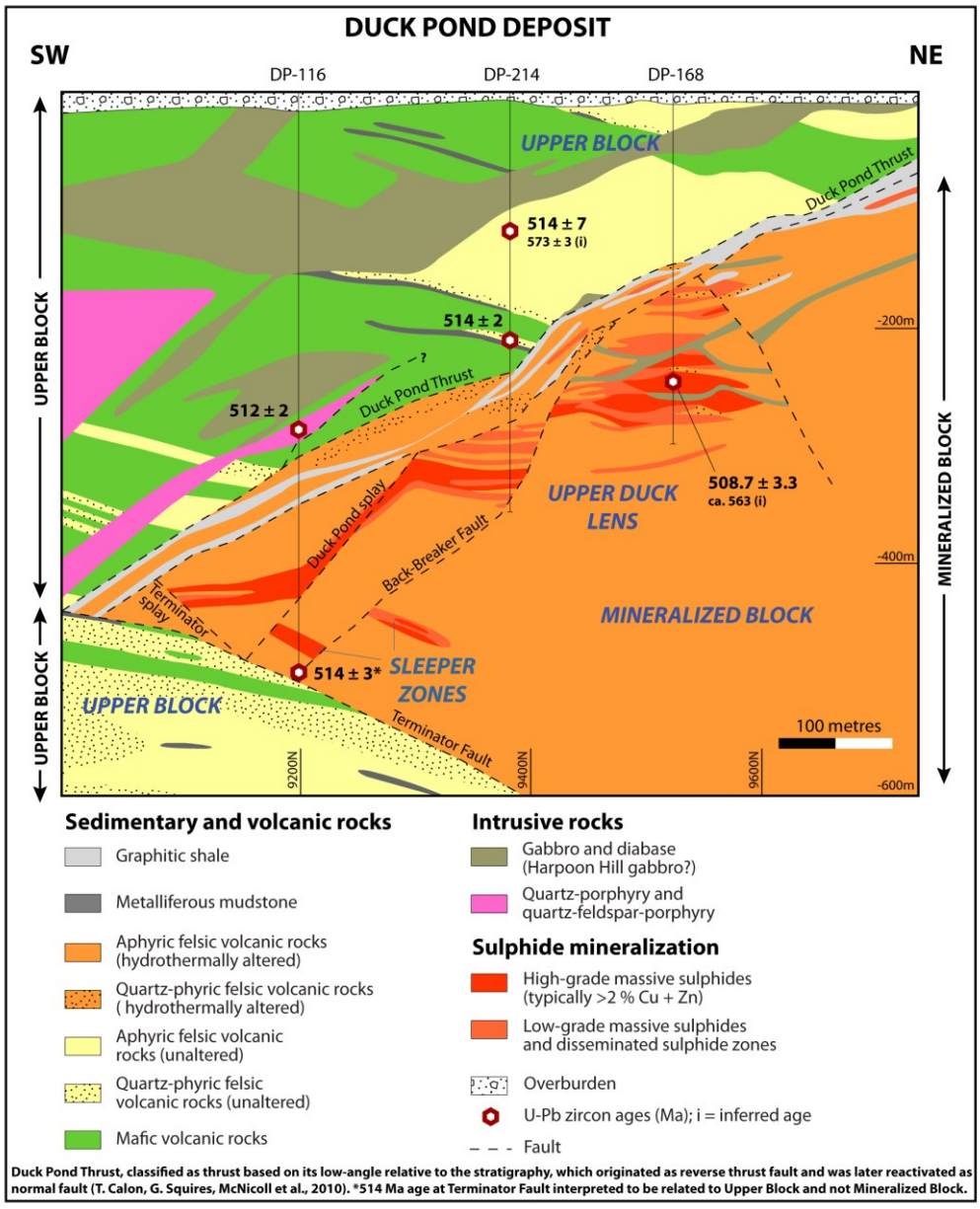

Figure 5.5 *Southwest-northeast cross-section of the Mineralized Block (Block below the Duck Pond) with the main Duck Pond ore body (Upper Duck lens) with locations of the geochronological samples. The unmineralized Upper Block is tectonically juxtaposed on top of the Mineralized Block. Modified after Squires and Moore (2004) and McNicoll et al. (2010) and references therein.*

Fig. 5.6

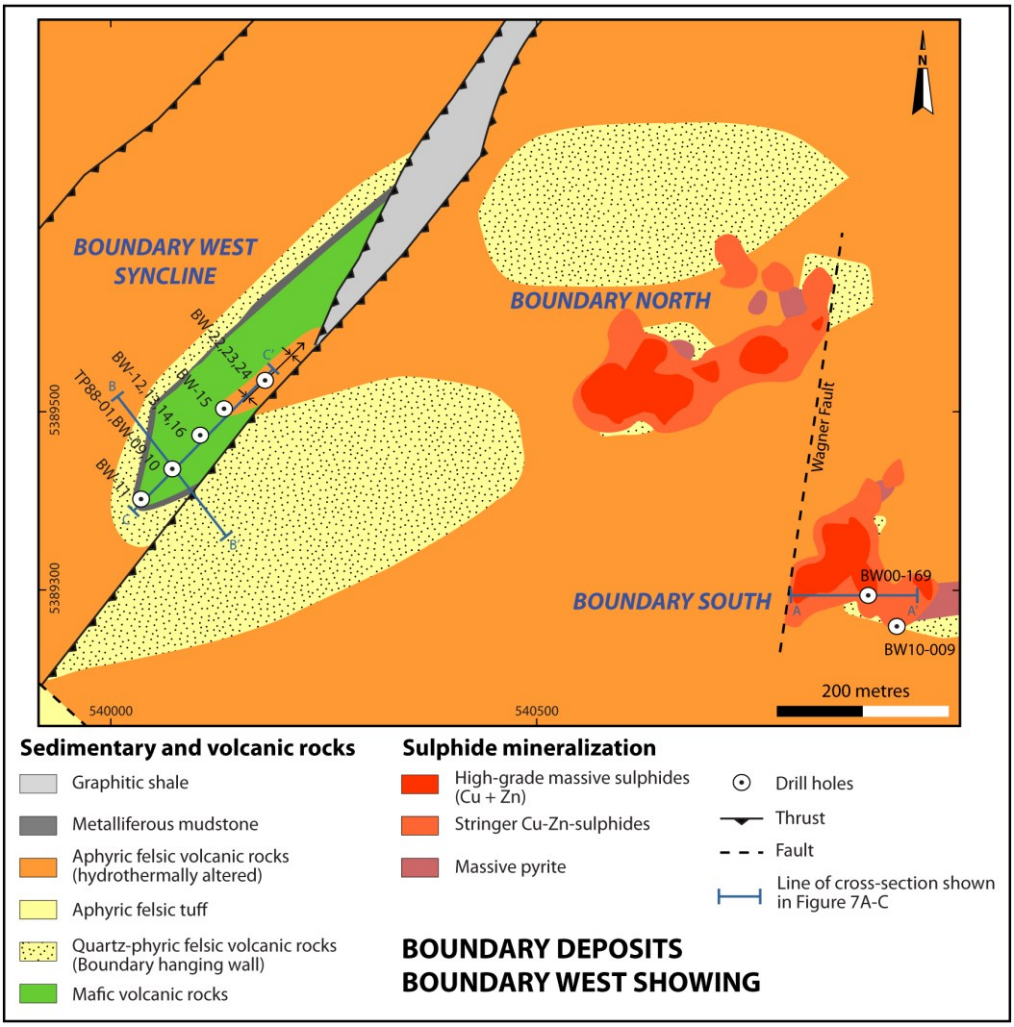

Figure 5.6 *Map area of the Boundary deposits and the synclinal structure of the Boundary West showing. Massive sulphides of the Boundary North and South zones are projected to surface. Not shown: Boundary Southeast Zone, which is located 200 m southeast of the South Zone. Modified after unpublished drafts of G. Squires and Darren Hennessey, Teck Resources Ltd., and Buschette (2015).*

Fig. 5.7 A-C

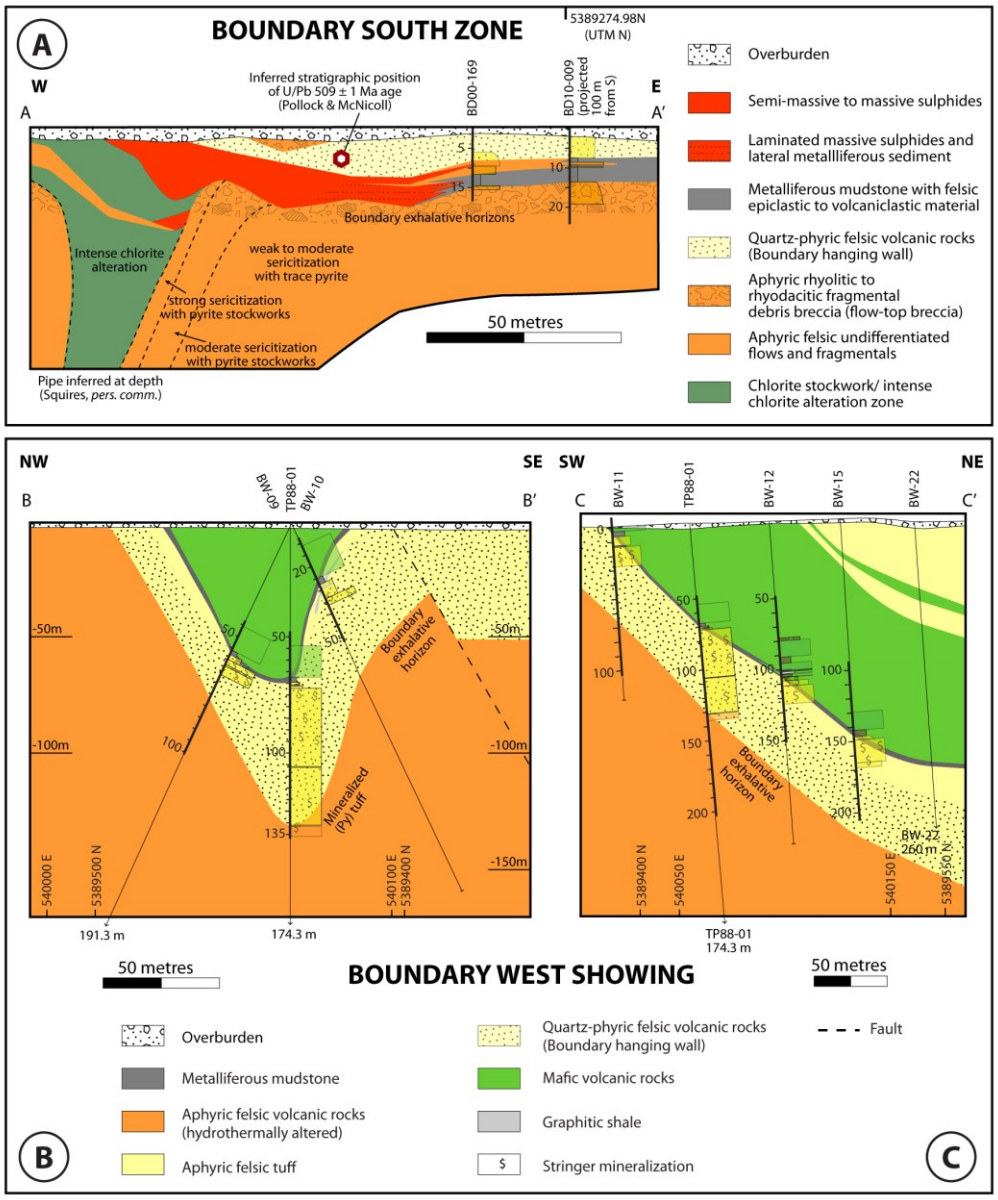

Figure 5.7 *A) West-east cross-section of the Boundary South Zone and superimposed graphic logs (this study) of the drill holes BD00-169 and BD10-009 showing the relationship of the massive sulphides with the associated metalliferous mudstones. Modified after interpretation of P. Moore (2003) and McNicoll et al. (2010), B) Northwest-southeast cross-section of the Boundary West syncline and superimposed graphic logs (this study) of sections containing metalliferous mudstones and/or graphitic shales of drill holes BW10-09, TP88-01, and BW10-10. Modified after unpublished drafts of G. Squires, Teck Resources Ltd., C) Southwest-northeast long-section of the Boundary West syncline and superimposed graphic logs (this study) of sections containing metalliferous mudstones and/or graphitic shales of drill holes BW10-11, TP88-01, BW10-12, and BW10-15. Modified after unpublished drafts of G. Squires, Teck Resources Ltd.*

Fig. 5.8 A-B

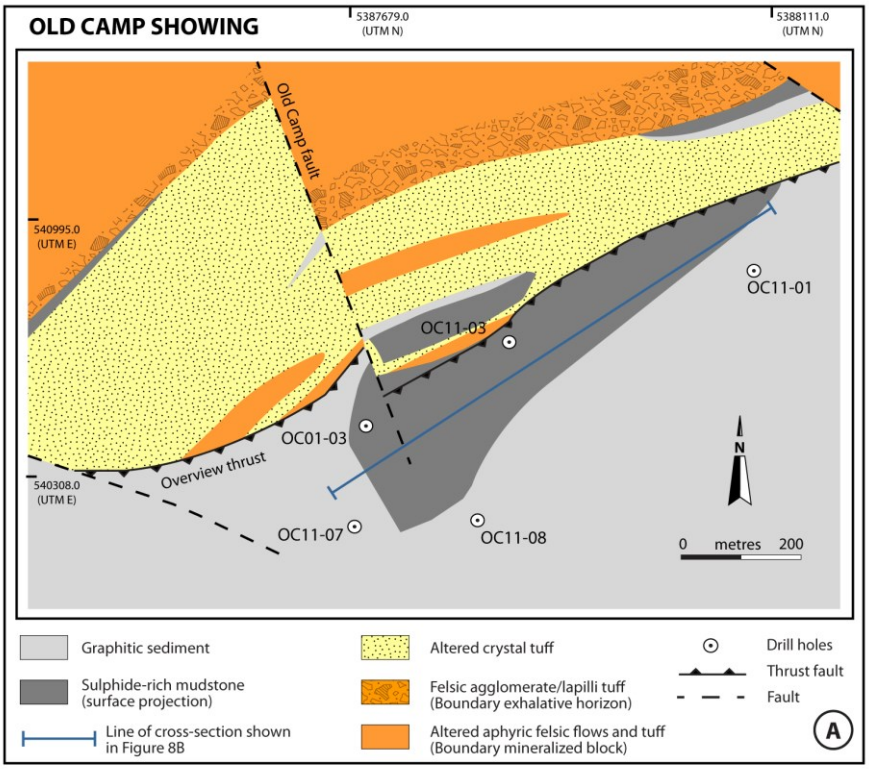
OLD CAMP SHOWING
5387679.0 (UTM N)
5388111.0 (UTM N)
Old Camp fault
540995.0 (UTM E)
OC11-01
OC11-03
OC01-03
Overview thrust
540308.0 (UTM E)
OC11-07
OC11-08
N
0 metres 200
Graphitic sediment
Sulphide-rich mudstone (surface projection)
Line of cross-section shown in Figure 8B
Altered crystal tuff
Felsic agglomerate/lapilli tuff (Boundary exhalative horizon)
Altered aphyric felsic flows and tuff (Boundary mineralized block)
Drill holes
Thrust fault
Fault
A

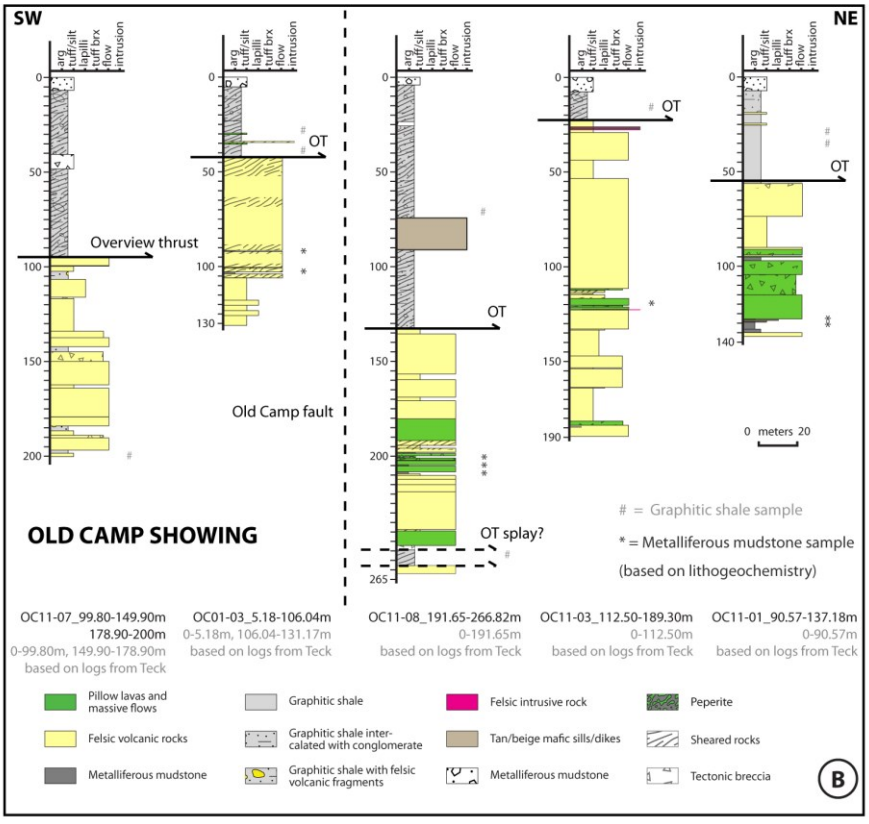
SW
NE
arg
tuff/silt
lapilli
tuff brx
flow
intrusion
Overview thrust
OT
Old Camp fault
OT splay?
0 meters 20
= Graphitic shale sample
* = Metalliferous mudstone sample
(based on lithogeochemistry)
OLD CAMP SHOWING
OC11-07_99.80-149.90m
178.90-200m
0-99.80m, 149.90-178.90m
based on logs from Teck
OC01-03_5.18-106.04m
0-5.18m, 106.04-131.17m
based on logs from Teck
OC11-08_191.65-266.82m
0-191.65m
based on logs from Teck
OC11-03_112.50-189.30m
0-112.50m
based on logs from Teck
OC11-01_90.57-137.18m
0-90.57m
based on logs from Teck
Pillow lavas and massive flows
Felsic volcanic rocks
Metalliferous mudstone
Graphitic shale
Graphitic shale inter-calated with conglomerate
Graphitic shale with felsic volcanic fragments
Felsic intrusive rock
Tan/beige mafic sills/dikes
Metalliferous mudstone
Peperite
Sheared rocks
Tectonic breccia
B

Figure 5.8 *A) Map area of the Old camp showing. Metalliferous mudstone horizons are projected to surface. Modified after unpublished drafts of D. Hennessey, Teck Resources Ltd., B) Section of southwest-northeast oriented graphic logs of the Old Camp showing that contain metalliferous mudstones and/or graphitic shales.*

Figure 5.9 *A) Northwest-southeast cross-section of the Keats Pond showing with drill holes 374-3-79 and 374-4-79 and superimposed graphic log of drill hole 374-64 (this study). Section modified after draft from Price – Norex Joint Venture, 1979 and G. Squires, pers. comm., B) Map area of the North Moose Pond and South Moose Pond showings. Modified after unpublished drafts of Teck Resources Ltd., C) Graphic logs of sections that contain metalliferous mudstones and/or graphitic shales of drill holes NM00-01 and NM01-05 from the North Moose Pond showing and of SM97-06 and SM97-08 from the South Moose Pond showing.*

Figure 5.10 *A) Core photograph of a finely laminated metalliferous mudstone from the Lemarchant deposit. Sulphide-rich veins are cross-cutting the lamination. Drill hole LM13-79, 181.9 m, B) Reflected light microscope image of a framboid-rich metalliferous mudstone from the Lemarchant deposit with a precious metal-bearing sulphide-rich vein. Py = pyrite, Ccp = chalcopyrite, Gn = galena, Ank = ankerite, Chl = chlorite, and Qz = quartz. Drill hole LM13-76, 163.8 m, C) Core photograph of a dark gray pyrrhotite-rich shale from the Cookstown showing. Pyrrhotite occurs parallel lamination and as patches. Drill hole CT11-01, 22.10 m, D) Reflected light microscope image of a patchy pyrrhotite vein with interstitial chalcopyrite and minor galena. Cookstown showing. Po = pyrrhotite, Ccp = chalcopyrite, and Gn = Galena. CT11-01, 22.30 m, E) Reflected light microscope image of a pyrrhotite halo around a vein, extending into the sulphide-poor matrix. CT11-01, 22.10 m, F) Core photograph of a finely laminated metalliferous mudstone from the Higher Levels prospect. Sulfide-rich veins cross-cut the lamination. Drill hole HL91-01, 18.4 m, G) Reflected light microscope image of a framboid-rich mudstone with euhedral pyrite (Py), chalcopyrite (Ccp), quartz (Qz), ankerite (Ank), dolomite (Dol), and chlorite (Chl) occurring in vein. Chalcopyrite displays a supergene covellite rim. HL91-01, 18.4 m. H) Reflected light microscope image of subhedral graphite (Gr)- and pyrite (Py)-rich vein with quartz (Qz), ankerite (Ank)-dolomite (Dol), and chlorite (Chl) as gangue. HL91-01, 18.4 m, I) Core photograph of a finely laminated sulphide-rich shale from the Beaver Lake prospect. Sulphide-rich veins are cross-cutting the lamination. Drill hole BL11-03, 165.2m, and J) Reflected light microscope image of a sulphide patch in a shale with euhedral pyrite, chalcopyrite, and sphalerite with quartz (Qz), ankerite, dolomite (Dol), and chlorite (Chl) as gangue. BL11-01, 177.3 m.*

Fig. 5.9 A-B

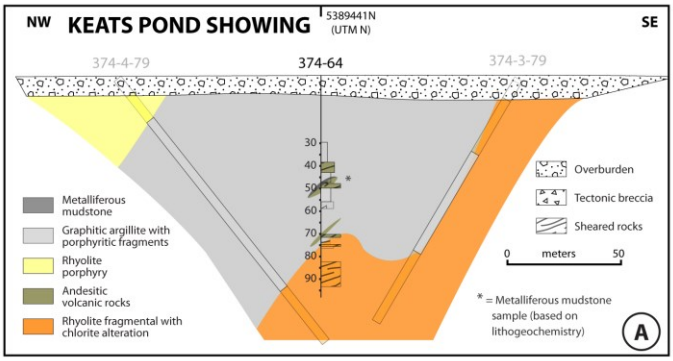
NW
KEATS POND SHOWING
5389441N
(UTM N)
SE
374-4-79
374-64
374-3-79
30
40
50
60
70
80
90
Metalliferous mudstone
Graphitic argillite with porphyritic fragments
Rhyolite porphyry
Andesitic volcanic rocks
Rhyolite fragmental with chlorite alteration
Overburden
Tectonic breccia
Sheared rocks
0 meters 50
* = Metalliferous mudstone sample (based on lithogeochemistry)
A

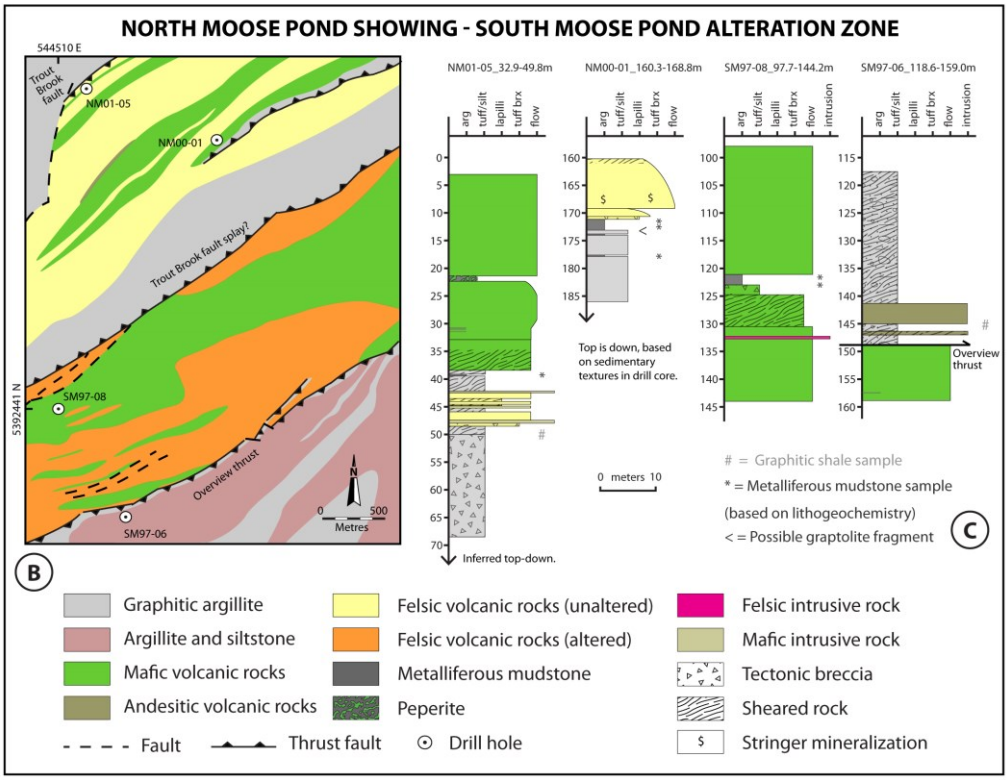
NORTH MOOSE POND SHOWING - SOUTH MOOSE POND ALTERATION ZONE
544510 E
5392441 N
Trout Brook fault
NM01-05
NM00-01
Trout Brook fault splay?
SM97-08
Overview thrust
SM97-06
N
0 500
Metres
B
NM01-05_32.9-49.8m
NM00-01_160.3-168.8m
SM97-08_97.7-144.2m
SM97-06_118.6-159.0m
arg
tuff/silt
lapilli
tuff brx
flow
intrusion
Top is down, based on sedimentary textures in drill core.
Inferred top-down.
0 meters 10
Overview thrust
= Graphitic shale sample
* = Metalliferous mudstone sample (based on lithogeochemistry)
< = Possible graptolite fragment
C
Graphitic argillite
Argillite and siltstone
Mafic volcanic rocks
Andesitic volcanic rocks
Fault
Felsic volcanic rocks (unaltered)
Felsic volcanic rocks (altered)
Metalliferous mudstone
Peperite
Thrust fault
Drill hole
Felsic intrusive rock
Mafic intrusive rock
Tectonic breccia
Sheared rock
Stringer mineralization

Fig. 5.10 A-J

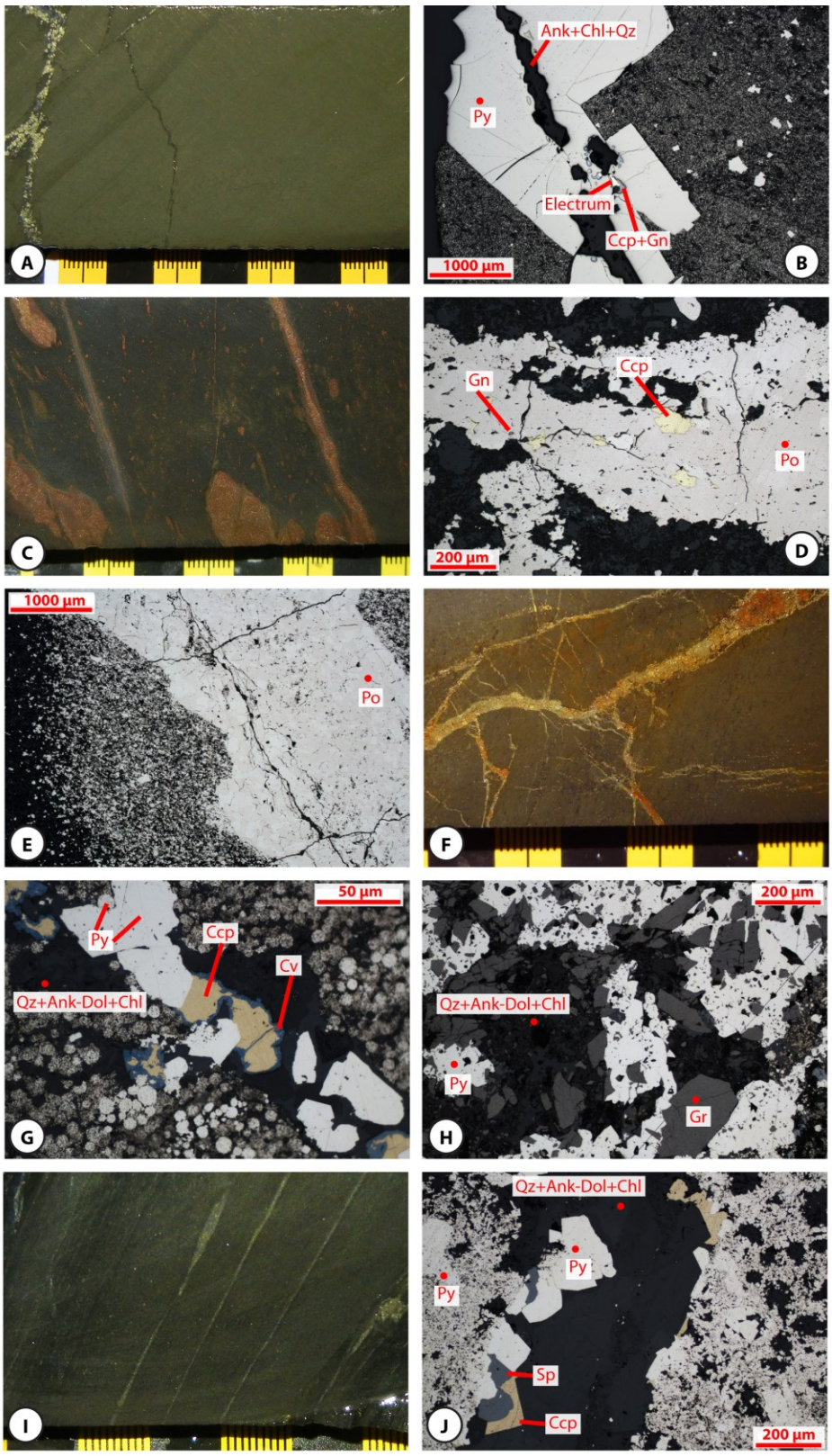
A
Ank+Chl+Qz
Py
Electrum
Ccp+Gn
1000 µm
B
C
Gn
Ccp
Po
200 µm
D
1000 µm
Po
E
F
50 µm
Py
Ccp
Cv
Qz+Ank-Dol+Chl
G
200 µm
Qz+Ank-Dol+Chl
Py
Gr
H
I
Qz+Ank-Dol+Chl
Py
Py
Sp
Ccp
J
200 µm

Fig. 5.11 A-J

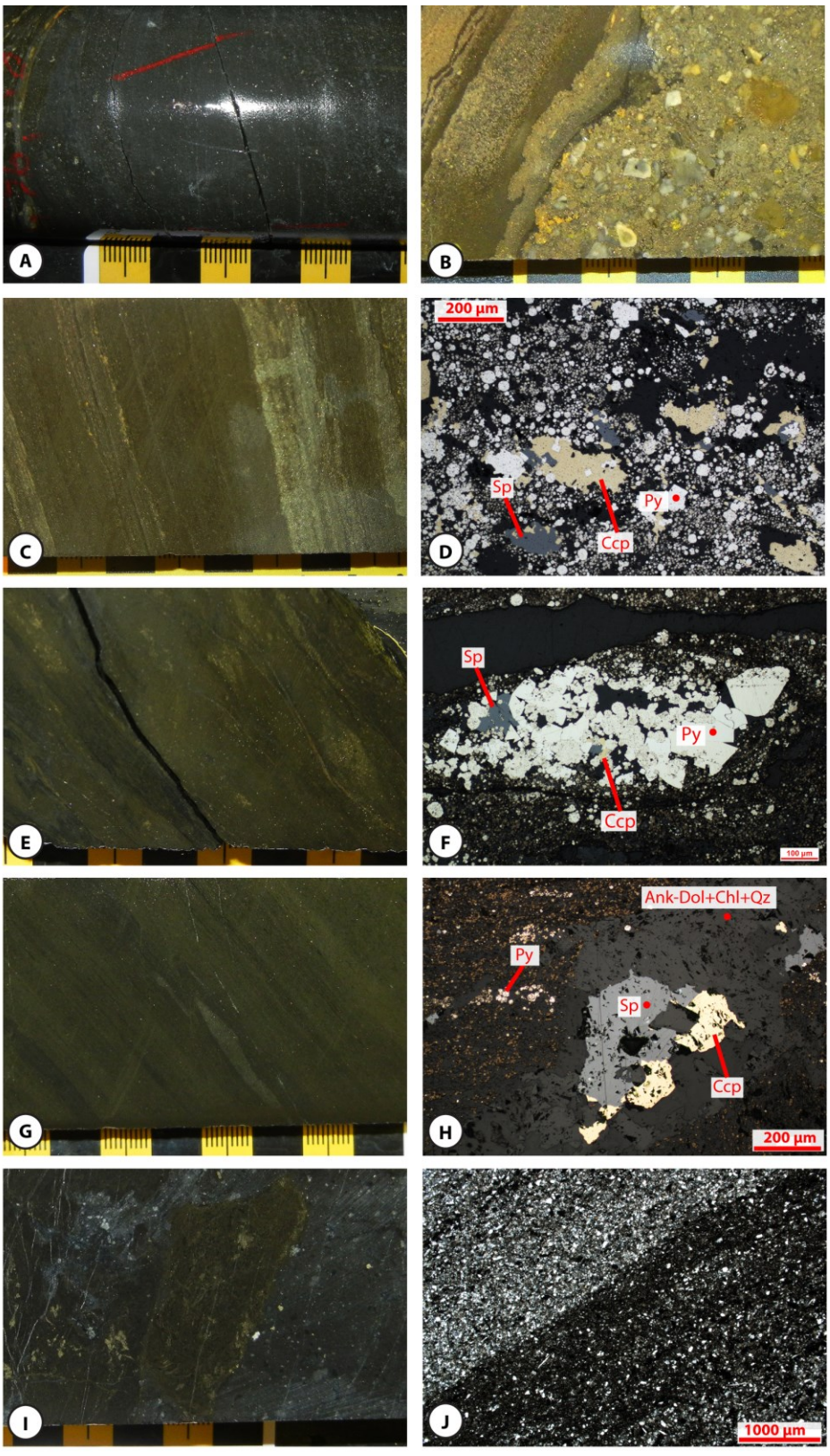
A
B
200 µm
Sp
Py
Ccp
C
D
Sp
Py
Ccp
100 µm
E
F
Ank-Dol+Chl+Qz
Py
Sp
Ccp
200 µm
G
H
1000 µm
I
J

Figure 5.11 *A) Core photograph of a dark grey-brown siltic shale that is intercalated between altered felsic volcanic rocks. Duck West, DP11-284, 636.8 m, B) Core photograph of a brown laminated metalliferous mudstone with intercalated mineralized tuff to lapilli tuff layers. Mineralized tuff layers formed via replacement-style mineralization. Boundary, BD00-169, 14.13 m, C) Core photograph of a brown laminated metalliferous mudstone with minor intercalated mineralized tuff layers. Boundary, BD10-009, 11.6 m, D) Reflected light image of a thin-section of a finely laminated metalliferous framboid-rich mudstone with euhedral pyrite (Py), interstitial chalcopyrite (Ccp), and sphalerite (Sp). Boundary, BD10-009, CNF36581, 11.6 m, E) Core photograph of a brown laminated to reworked metalliferous mudstone. Boundary West, BW10-11, 3.8 m. F) Reflected light image of a thin-section of graphite- and framboid-rich mudstone. Framboids locally overgrown by euhedral pyrite (Py). Sphalerite (Sp) and chalcopyrite (Ccp) occur interstitially between euhedral and framboidal pyrite. Sphalerite displays chalcopyrite disease. Boundary West, BW10-10, 3.8 m, G) Core photograph of a brown finely laminated metalliferous mudstone. Old Camp, OC11-01, 129.9 m, H) Reflected light image of a thin-section of a framboid-rich metallifeorus mudstone with a cross-cutting sulphide-rich vein. Vein filled with sphalerite (Sp), chalcopyrite (Ccp), euhedral pyrite (Py), and ankerite-dolomite (Ank-Dol), Fe-Mg-chlorite (Chl), and quartz (Qz) as gangue. OC11-01, Old Camp, 129.9 m, I) Core photograph of a gray graphitic shale intermingled with brown metalliferous mudstone fragments. Old Camp, OC01-03, 91.9 m, and J) Transmitted light image (II polars) of a thin-section of a finely laminated siltic shale with intercalated graphite-rich layers. Sediment matrix predominantly consists of quartz, clay, sericite, chlorite, and K-feldspar, with accessory apatite, rutile, zircon, and pyrite, chalcopyrite and galena. Old Camp, OC11-01, 29.0 m.*

Figure 5.12 *A) Core photograph of a dark brown finely laminated metalliferous mudstone with a sulphide-rich cross-cutting vein. Keats Pond, 374-64, 47.9 m, B) Core photograph of a brown finely laminated metalliferous mudstone. North Moose Pond, NM00-01, 172.2 m, C) Reflected light image of a finely laminated framboid-rich metalliferous mudstone with thick carbonate-quartz-sulphide veins cross-cutting the lamination. Sulphides in veins are predominantly euhedral pyrite (Py), interstial chalcopyrite (Ccp) and sphalerite (Sp), and pyrrhotite. Sphalerite displays chalcopyrite disease. North Moose Pond, NM00-01, 171.5 m, D) Synaeresis cracks/dewatering structures in a volcaniclastic silt- to sandstone. North Moose Pond, NM00-01, 173.3 m, E) Graphitic shale with mineralized tuff fragments. South Moose Pond, SM97-06, 145.8 m, F) Reflected light image of a locally reworked graphite-rich metalliferous mudstone. Lamination cross-cut by quartz (Qz)-carbonate veins. Carbonates consist of ferroan dolomite to Mg-Mn-bearing ankerite (Dol-Ank). Sulphides in veins are euhedral pyrite (Py), chalcopyrite (Ccp), and minor galena. Contact of vein to framboidal mudstone lined by hematite (Hem). Carbonate alteration extends into mudstone matrix. South Moose Pond, SM97-06, 145.5 m, G) Rhythmic layering of black shales and siltstones. Bell Island, The Beach, Beach Formation, and H) Transmitted light image (II polars) of a thin-section of a laminated siltic black shale with finely disseminated organic matter (OM) and possible algal remnants (Alg). Sediment matrix predominantly consists of quartz, K-feldspar, albite, chlorite, clay, and muscovite (Ms), with accessory apatite, rutile, and zircon. Bell Island, The Beach, Beach Formation.*

Fig. 5.12 A-H

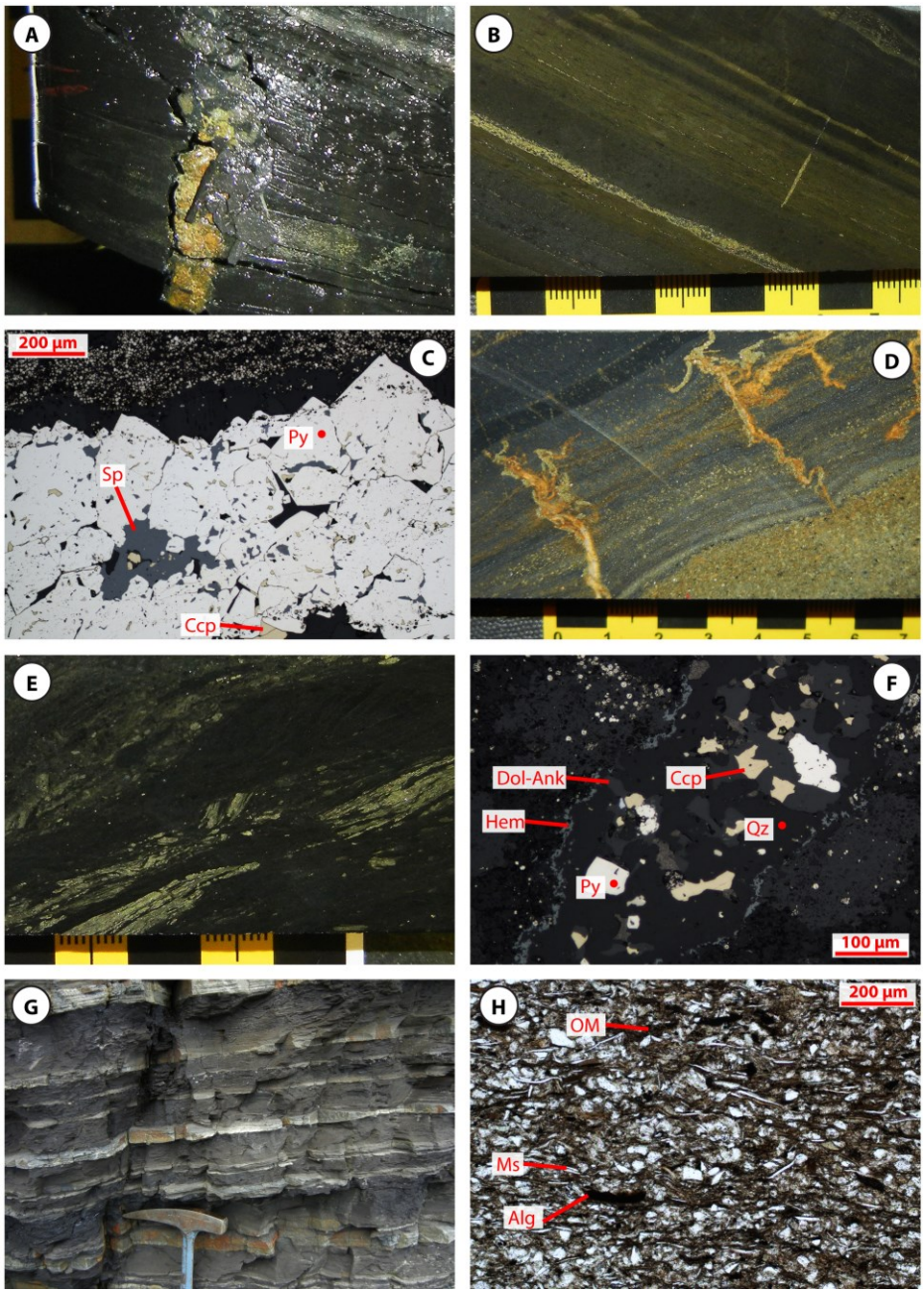
A
B
200 µm
C
Py
Sp
Ccp
D
E
F
Dol-Ank
Ccp
Hem
Qz
Py
100 µm
G
H
200 µm
OM
Ms
Alg

Fig. 5.13 A-F

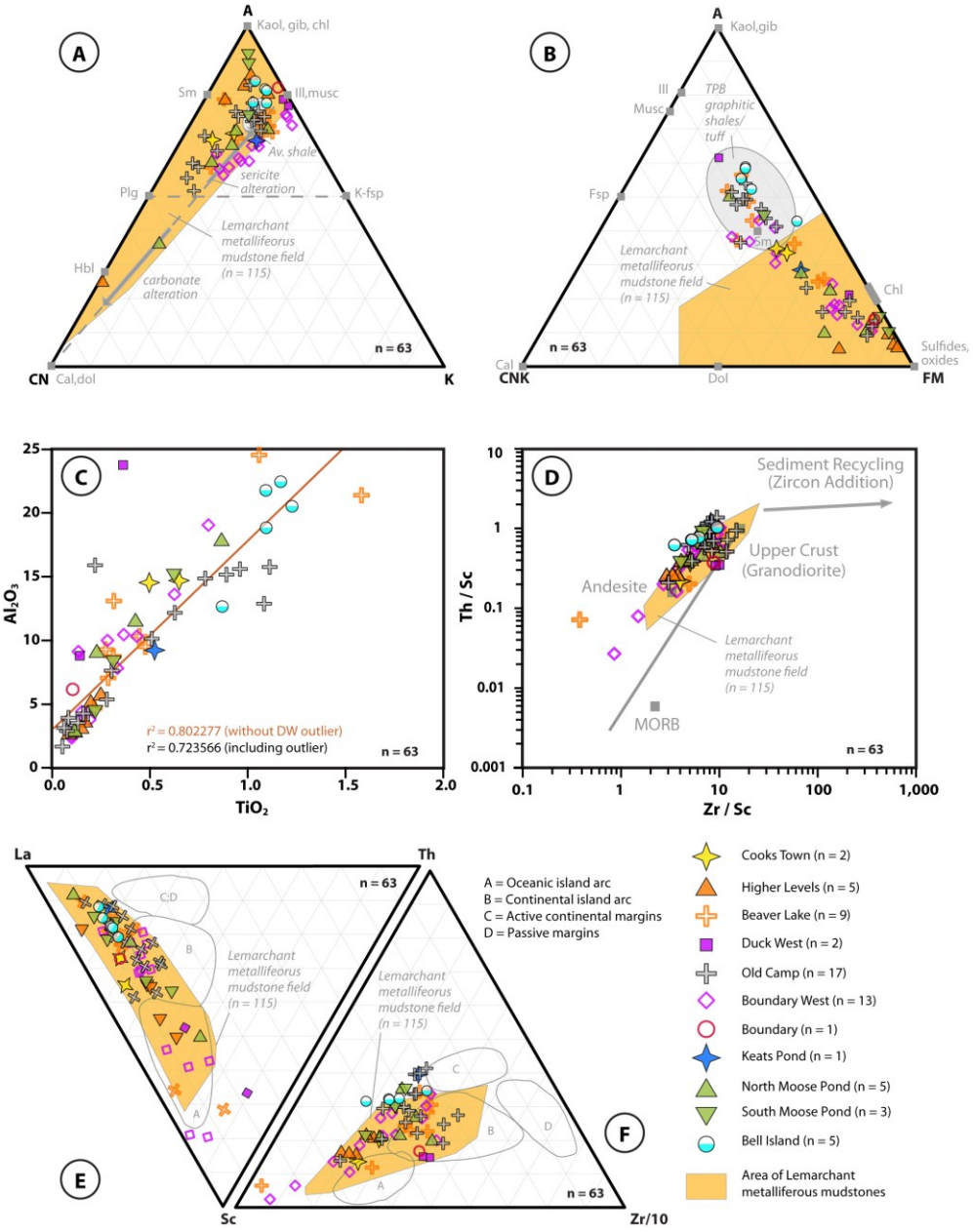

Figure 5.13 *A) Ternary A-CN-K diagram A = Al_2O_3, CN = $CaO+Na_2O$, and K = K_2O, B) Ternary A-CNK-FM diagram. A = Al_2O_3, CNK = $CaO+Na_2O+K_2O$, and FM = $(FeO+Fe_2O_3)$ +MgO. Cal = Calcite, Dol = Dolomite, Fsp = feldspar, Musc = Muscovite, Ill = Illite, Kaol = Kaolinite, Gib = Gibbsite, Chl = Chlorite, Hbl = Hornblende, Plg = Plagioclase, Sm = Smectite, C) Al_2O_3 versus TiO_2, D) The Th/Sc versus Zr/Sc diagram, E) and F) La-Th-Sc and Th-Sc-Zr/10 plots. Orange fields represent areas of data of Lemarchant metalliferous mudstones (Lode et al. in press). Diagrams A) and B) are after Nesbitt (2003), C) after Barrett and MacLean (1994), and D) to F) Immobile element plots after Bhatia and Crook (1986).*

Fig. 5.14 A-F

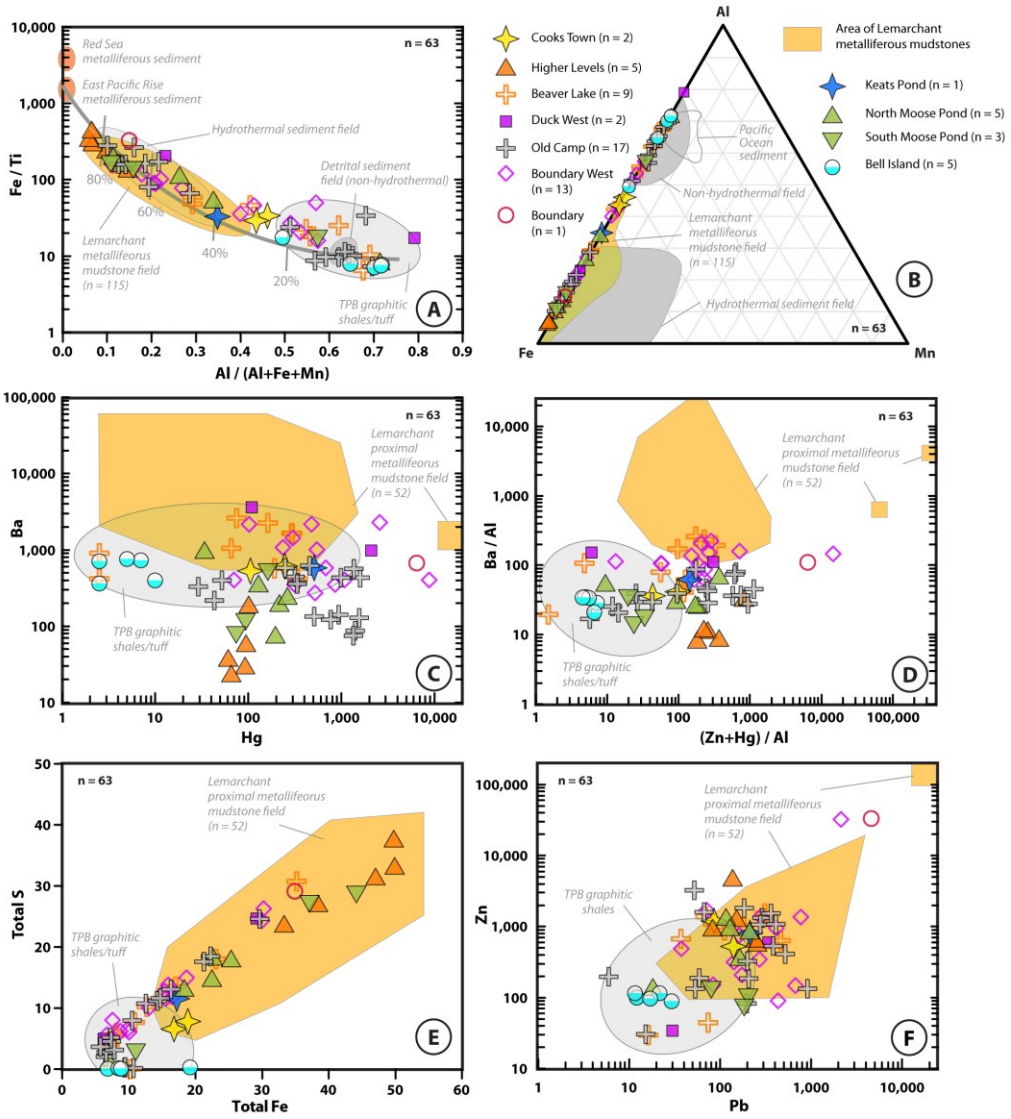

Figure 5.14 *Fe-Ti/Al-Fe-Mn (A) and Fe-Al-Mn (B) discrimination diagrams after Boström et al. (1972, 1973). Selected base metal, transition element, and hydrothermal element plots: C) Ba versus Hg (after Piercey et al., 2012), D) Ba/Al versus (Zn+Hg)/Al, where Ba, Zn, and Hg represent the hydrothermally derived components of the mineralization, and Al is a detrital constituent, E) Total S versus Fe_2O_3 (T), and F) Zn versus Pb.*

Fig. 5.15 A-G

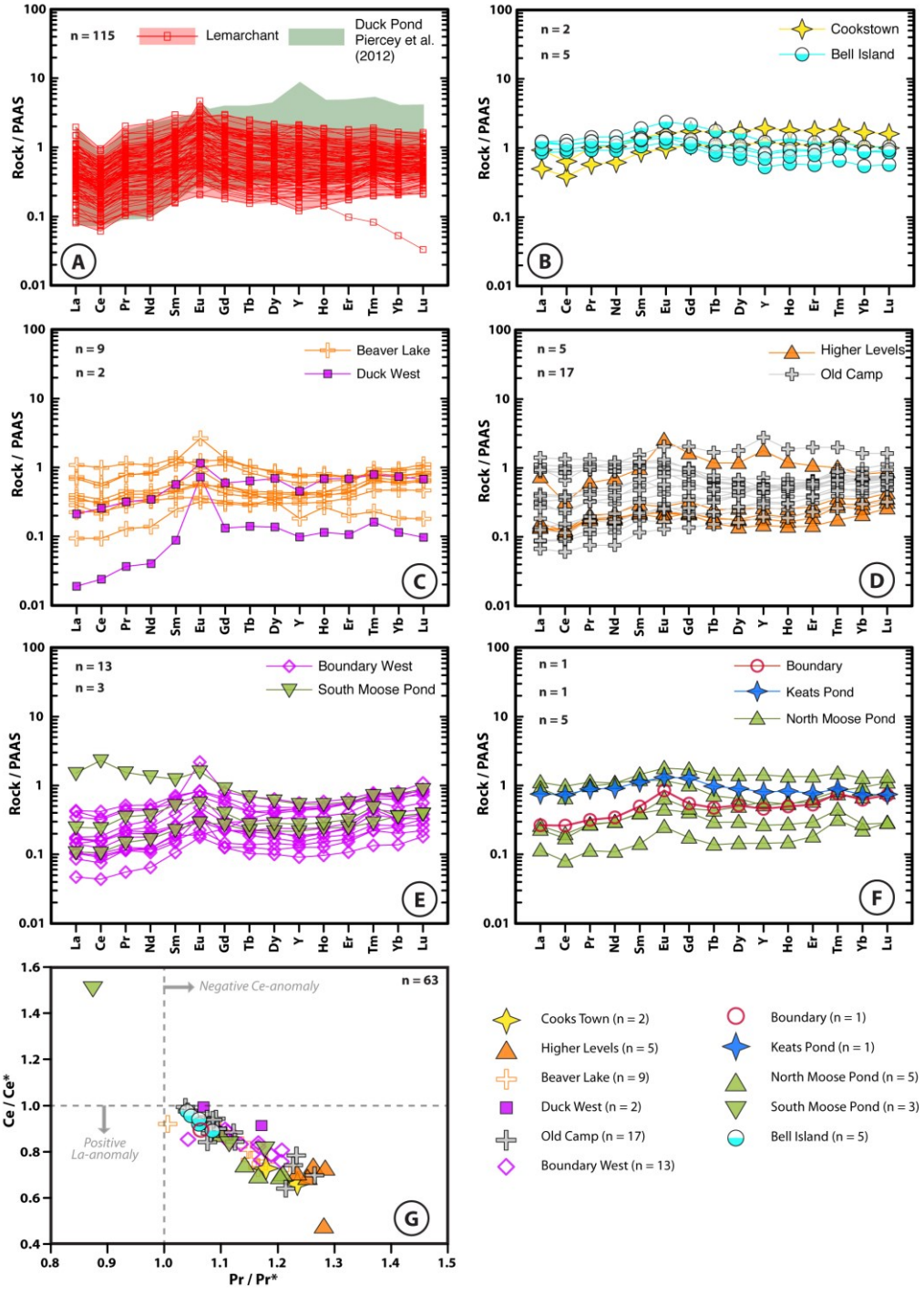
n = 115
Lemarchant
Duck Pond
Piercey et al.
(2012)
A
n = 2
n = 5
Cookstown
Bell Island
B
n = 9
n = 2
Beaver Lake
Duck West
C
n = 5
n = 17
Higher Levels
Old Camp
D
n = 13
n = 3
Boundary West
South Moose Pond
E
n = 1
n = 1
n = 5
Boundary
Keats Pond
North Moose Pond
F
Rock / PAAS
La Ce Pr Nd Sm Eu Gd Tb Dy Y Ho Er Tm Yb Lu
n = 63
Negative Ce-anomaly
Positive
La-anomaly
Ce / Ce*
Pr / Pr*
G
Cooks Town (n = 2)
Higher Levels (n = 5)
Beaver Lake (n = 9)
Duck West (n = 2)
Old Camp (n = 17)
Boundary West (n = 13)
Boundary (n = 1)
Keats Pond (n = 1)
North Moose Pond (n = 5)
South Moose Pond (n = 3)
Bell Island (n = 5)

Figure 5.15 *REE plus Y geospider plots of the Tally Pond belt metalliferous mudstones and graphitic shales: A) Lemarchant (red) and Duck Pond (green) metalliferous mudstones, B) Bell Island and Cookstown mudstones and shales, C) Beaver Lake and Duck West mudstones, shales, and mineralized tuff, D) Higher Levels and Old Camp mudstones and shales E) Boundary West and South Moose Pond mudstones and shales, and F) Boundary, Keats Pond, and North Moose Pond mudstones and shales. All samples are normalized to the post-Archean Australian shale of McLennan (1989). G) Ce/Ce* versus Pr/Pr* diagram to determine whether Ce anomalies are true anomalies or caused by positive La-anomalies. Accordingly, the positive Ce anomalies in the Lemarchant samples are true Ce anomalies. Ce/Ce* and Pr/Pr* values are calculated based on McLennan (1989) and the equation* $Pr/Pr^* = (Pr_{sample}/8.83)/SQRT((Ce_{sample}/79.6)*(Nd_{sample}/3.39))$*. Diagrams are after Webb and Kamber (2000).*

Fig. 5.16 A-D

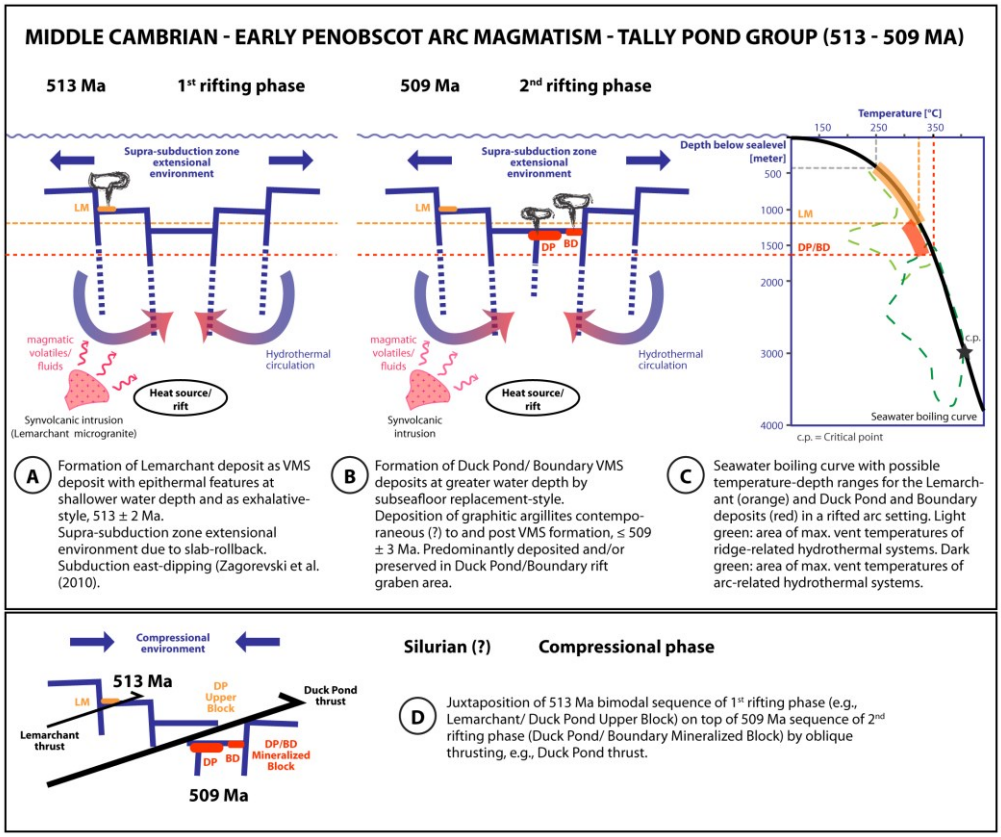

Figure 5.16 *A-B) Simplified two phase rifting model for the Middle Cambrian, early Penobscot arc magmatism of the Tally Pond group (513 - 509 Ma). C) Diagram of the two-phase curve for seawater and areas of maximum vent temperatures for modern hydrothermal systems with conditions for the Lemarchant and Duck Pond/Boundary hydrothermal systems. Light green dashed outlined area: depth-temperature ranges of maximum vent temperatures for selected ridge-related hydrothermal systems (Indian Ocean, East Pacific Rise, Mid-Atlantic Ridge, and NE Pacific ridges, and sediment covered ridges). Dark green dashed outlined area: depth-temperature ranges of maximum vent temperatures for selected arc-related hydrothermal systems (backarc, arc volcano). Orange stripe: possible temperature/water depth range for the Lemarchant hydrothermal system in a rifted arc setting. Red stripe: possible temperature/water depth range for the Duck Pond/Boundary hydrothermal system in a rifted arc setting. Modified after Hannington et al. (2005). D) Simplified diagram of the, possibly Silurian, compressional phase juxtaposing the older 513 Ma sequence (Lemarchant, Upper Duck Pond Block), over the younger 509 Ma sequence (Duck Pond/Boundary).*

Appendix 5.1

5.1.1 Lithogeochemistry methods

During fieldwork 80 drill holes that contain metalliferous mudstones and graphitic shales from twelve locations in the Tally Pond volcanic belt were logged and selected mudstones and shales sampled for thin-section preparation and whole-rock analyses. Petrographic studies were undertaken on 253 thin-sections, which predominantly represent various types of mudstone, shales, and tuff. Three locations were sampled on coastal outcrops on Bell Island and from these, five shale samples prepared for thin-section and whole-rock lithogeochemical studies. From the Lemarchant deposit a detailed sampling was undertaking. The Lemarchant mudstones include those that: 1) are immediately associated with or occur within five meters of massive sulphides and represent the main stratigraphic marker between the felsic and mafic volcanic rocks (Bindons Pond formation and Lake Ambrose formation, respectively); 2) do not have an obvious spatial and possibly genetic relation with mineralization, but occur along the same stratigraphic contact between the Bindons Pond and Lake Ambrose formations; 3) occur within the Bindons Pond felsic volcanic rocks; and 4) occur as interflow mudstones in the hanging wall Lake Ambrose basalts. Tuff is intercalated with all types of mudstones, and if the tuff had a sufficient thickness they were sampled for whole-rock geochemistry as well. Detailed analyses are presented in Lode et al. (2015). Metalliferous mudstones associated with the Upper Block of the Duck Pond deposit were sampled and studied in detailed by Piercey et al. (2012).

High resolution backscattered electron (BSE) images were obtained using a FEI Quanta 400 scanning electron microscope (SEM) at Memorial University, which is equipped with an energy dispersive x-ray (EDX) analytical system from Bruker. Samples for whole-rock lithogeochemical studies (n = 189) were analyzed for major and minor elements by lithium metaborate/tetraborate fusion followed by HNO_3 dissolution and analysis by inductively coupled plasma (atomic) – emission spectroscopy (ICP-ES). Carbon (C) and sulphur (S) were obtained by infrared spectroscopy and mercury (Hg) was obtained by the cold vapour flow injection mercury system (Hg-FIMS). All of the former analyses were obtained at Activation Laboratories Ltd. (Actlabs) in Ancaster, Canada. Additional trace elements, including rare earth elements (REE), high field strength elements (HFSE), trace metals, and many low field strength elements (LFSE) were analyzed in the Department of Earth Sciences at Memorial University, using screw-top Teflon® bomb (Savillex®) multi-acid dissolution with a finish by inductively coupled plasma-mass spectrometry (ICP-MS). The whole-rock dissolution process was a modified version of that of Jenner et al. (1990) and Longerich et al. (1990) to account for the high amounts of carbonaceous material in the samples, as outlined below.

Powdered sample equivalent to 0.1000 g was put into a clean and dry screw-top Teflon® bomb (Savillex®) with 2 ml of 8N nitric acid (HNO_3) and 1 ml of hydrofluoric acid (HF) and placed on a hot plate at ~70 °C for three days. If the sample was not completely dissolved after that time, the cap was carefully removed and the condensed sample liquid on the cap rinsed into the jar with 8N HNO_3, and the bomb was left uncovered on the hot plate at about 80-100 °C to evaporate until dry. When dry, another 2 ml of 8N HNO_3 and 2 ml of hydrochloric acid (HCl) were added, the lid closed, and the

sample left for a further day on a hot plate to reflux at ~70°C. After this additional step, or if the sample was already completely dissolved after the initial three days, the sample was evaporated until dry. When dry, 2 ml of 8N HNO_3 and 1 ml of boric acid (0.453M) were added to the sample liquid and then evaporated to dryness. To the dried sample a further 2 ml of 8N HNO_3 and 2 ml HCl were added, the cap was placed back on the jar and the sample left for 2 hours on the hot plate at ~70°C. After 2 hours, the cap was removed and the sample liquid evaporated to dryness. When dry, 2 ml of 8N HNO_3 and 1.3 ml oxalic acid (0.22M) were added, the cap placed back on, and the sample left for 2 hours on the hot plate at ~70°C. Subsequently, an additional 1 ml of H_2O_2 was added, the cap placed back on again, and the sample left for another 2 hours on the hot plate at ~70°C. Since many of the samples contain abundant carbonaceous material it is noted that each additional 1 ml of HCl and 1 ml of H_2O_2 added above reduced the amount of visible residual carbonaceous material quite significantly.

Solution material from the latter step above was transferred into 120 ml snap seal container. For this, the caps are rinsed with nanopure water into the snap seal jar, 0.665 ml HF/boric solution (0.113M HF/ 0.453 boric acid) is added, and the weight made up to a final weight of 60 g with nanopure water. If visible residues still remained, the sample was filtered before the final sample dissolution preparation.

Two tubes were prepared for the ICP-MS, one with the sample dissolution and one with the sample dissolution plus a trace spike solution. To each 11 ml test tubes 0.5 g of sample solution were added with one tube having 9.5 g of 0.2N HNO_3 added, whereas the second tube contained 4.5 g of 0.2N HNO_3 and 5 g of trace spike solution; both tubes were capped, shaken and mixed prior to analysis by ICP-MS.

The residues left behind in the filter paper were checked at Memorial University via scanning electron microscope - energy dispersive X-ray spectroscopy (SEM-EDX) to ascertain that no elements of interest, particularly the HFSE and REE, remained. For this, the residues were mounted on a holder with double-sided carbon tape and semi-quantitatively analyzed by EDX under low-vacuum conditions to avoid carbon-coating. The analyses of the residues yielded, with one exception, purely carbonaceous material, and hence, no important trace elements were present in the residues. One residue consisted of predominantly carbonaceous material with traces of barite. Accordingly, to avoid interferences of organic matter with Ba, Ba-values of the fusion method (ICP-ES) were used, instead of ICP-MS. To correct for a possible mass spectral interference of the isobaric phases $^{135}Ba^{16}O$ and ^{151}Eu, two standard solutions were utilized and the interference factor calculated accordingly (Jenner et al, 1990).

5.1.2 Quality assurance and quality control (QA/QC)

Precision and accuracy of the analyses were determined using duplicates and reference materials following methods described in Jenner (1996) and Piercey (2014). The reference materials utilized in the study included three different organic- and/or sulfide-rich shales (SCO-1, SDO-1 and SGR-1b) and one iron formation (FeR-1). These standards were run every twenty samples and with each analytical batch. In addition, blanks were utilized during each analytical run to test contamination; none was detected. Precision was determined using the percent relative standard deviation (% RSD) on the replicate analyses of the reference materials, and accuracy was determined using percent

relative difference (% RD) from accepted values. Analyses from Actlabs of the major and some minor elements, and C, S, and Hg have following % RSD precision values: major elements range between 0.7-4.5% RSD; P_2O_5. Ba, Sr, Y, Zr, Sc, V have % RSD values between 0.6-8.2% RSD; and 0.7-1.8% RSD for C, S, and Hg. Accuracy of the Actlabs analyzed major and minor elements ranges from 0.1-11.8% RD, from 1.8-4.8% RD for C and S, and 0.7-7.7% RD for Hg.

Analytical precision calculated for samples analyzed at Memorial University yielded the following values: low field strength elements (LFSE) range between 3.7-12.5% RSD (except Rb), and high field strength elements HFSE had 4.5-11.1% RSD. The REE (La to Lu) % RSD values range from 4.8-8.6 and base and transitional metals have a precision between 3.3-11.9% RSD.

Determination of accuracy is dependent on and limited to the quality and amount of published and certified values. For many sediment-rich samples the range of certified values is limited and/or results were obtained by methods not utilized in this study (e.g., Instrumental Neutron Activation Analysis - INAA). Therefore, accuracy values in the analyses outlined below are provided for where published data were available. Accuracies for elements in standard FeR-1 range from 1.32-8.79% RD for most of the REE except Tm. Tm yields less an accurate value of 15.3% RD. The standard SCO-1 has an accuracy of 2.0-6.5% RD for La, Pr and Nd, 12.8% RD for Ce, and 1.9% RD for Pb. Accuracies for standard SDO-1 range from 1.9-9.1% RD for La to Gd, and Tm, 11.0-23.6% RD for Tb to Er, Yb, and Lu. Base metal and transition elements have accuracy values ranging between 3.0-13.7% RD, and Zn of 22.8% RD. SGR-1b yields accuracy values between

1.6-15.3% RD base metal and transition elements, and 0.01 to 17.6% RD for REE (La to Yb, except, Pr and Tb).

CHAPTER 6

Summary uniting the material presented in the individual chapters and outlines for future research

6.1 Summary

6.1.1 Whole-rock lithogeochemistry/exploration implications

This thesis was aimed at understanding the stratigraphic and textural relationships between hydrothermal metalliferous mudstones and graphitic shales to volcanogenic massive sulphide (VMS) mineralization and to determine the depositional environment and basin redox conditions. The importance of metalliferous sediments as stratigraphic marker horizon due to their temporal and spatial association with ancient economically valuable VMS deposits is generally recognized (e.g., Kalogeropoulos and Scott, 1989; Large, 1992; Hannington, et al., 1995; Peter and Goodfellow, 1996; Spry et al., 2000); yet, the understanding of the relationship of VMS mineralization and genesis to the hydrothermal sediments is incomplete. In central Newfoundland this is especially acute, as apart from the preliminary studies of Piercey (2008, 2010, 2012), there has been no detailed research undertaken regarding the setting and genesis of hydrothermal sediments associated with VMS deposits. Therefore, results herein will contribute to a greater understanding of the hydrothermal ore-forming systems within the Central Mobil Belt, Newfoundland.

The Tally Pond volcanic belt is an excellent location to approach this problem, since it contains economically significant VMS deposits (including the Duck Pond and Boundary mines, as well as the Lemarchant deposit) and numerous other prospects, and showings, which are locally genetically and/or spatially associated with metalliferous mudstones and/or graphitic shales. The Cambrian precious metal-bearing bimodal felsic Lemarchant Zn-Pb-Cu-Ba VMS deposit is closely genetically associated with metalliferous mudstones in various spatial and stratigraphic relations to the ore and the main stratigraphy is generally well preserved. Hence, the Lemarchant deposit provided the opportunity to investigate lithogeochemical proxies that are useful in vectoring towards VMS-style mineralization. Based on the lateral extension of these sediments and the generally small size of VMS deposits, the metalliferous mudstones represent important stratigraphic horizons in the location of VMS-style mineralization. Thus, the lithogeochemical criteria that were determined on the Lemarchant mudstones could be used to evaluate a possible prospectivity of the other mudstone and shale occurrences in the Tally Pond volcanic belt.

The lithogeochemical fingerprinting used in this study is based on the principle that metalliferous sediments precipitate from black smoker plume fallout, after mixing of hot, reduced and metal-rich vent fluids with cold, oxidized, sulphate-rich ambient seawater. The polymetallic (Fe, Cu, Zn, Pb) sulphides precipitate together with barite, anhydrite, amorphous silica, and Al-poor clays in proximity to the hydrothermal vent at the mount flanks and in adjacent depressions in the seafloor. Due to the mixing of the physico-chemically distinct fluids (hydrothermal fluids and seawater), the precipitating particles gain geochemical signatures, which can indicate residence times within the

hydrothermal plume (e.g., more mixing with seawater = longer residence time = more distal environment). Accordingly, it is important in ancient metalliferous mudstones to identify lithogeochemical proxies that can confirm a hydrothermal origin and short residence times in the plumes, i.e. proximity to the massive sulphides.

Within the scope of this PhD project, productive hydrothermal mudstones have specific lithogeochemical signatures, including: 1) elevated Fe and base metal contents, and plot within the hydrothermal fields on Boström-type plots; 2) high Ba/Al and (Zn+Hg)/Al ratios; 3) REY systematics that are indicative of deposition from high temperature fluids (>250°C and Eu/Eu*>1), and that are rock buffered (i.e., Y/Ho~27 and unlike seawater with Y/Ho>44). Furthermore, a presence of barite within the mudstones and/or massive sulphides, as at the Lemarchant deposit, indicates vent proximal positioning and deposition in oxygenated bottom waters. The latter is also supported by occurrences of marcasite in the Lemarchant mudstones and the presence of negative Ce anomalies (Ce/Ce*<1) in the mudstones. The Lemarchant mudstones have also, as well as the Lemarchant massive sulphides, enrichments in base metal sulphides and epithermal suite elements, namely Hg-Sb-As, which is unique to the Lemarchant deposit in the Tally Pond belt, but is similar to other VMS-epithermal hybrids in comparable settings.

At Lemarchant, all metalliferous mudstones are of hydrothermal origin and deposited in vent proximity from high temperature fluids (>250°C) under oxygenated conditions. Due to the general similarity of the REY-patterns between the mudstones of various stratigraphic levels, it is suggested here that they were all derived from the same hydrothermal fluids. Nevertheless, the above lithogeochemical proxies differentiate metalliferous mudstones that occur either immediately on top, or laterally along strike,

from massive sulphide mineralization, or as interflow mudstones within hanging wall basaltic rocks (i.e., were deposited vent proximal vs. distal). In a like manner these lithogeochemical fingerprints were used to evaluate metalliferous mudstones and graphitic shales (other than Lemarchant) occurring in the Tally Pond belt and some of these mudstones are of hydrothermal origin. Outside of Lemarchant, however, the Tally Pond belt mudstones and shales have more variable signatures ranging from hydrothermal (signatures as above) to non-hydrothermal black shales (no positive Eu-anomalies, flat REE-patterns), to those with mixed lithogeochemical signatures. Based on smaller or no Eu anomalies, and less pronounced elevated base metal contents, it is proposed that those Tally Pond belt metalliferous mudstones (other than Lemarchant) precipitated from fluids with temperatures below 250°C, in a more vent distal depositional environment. Studies by Piercey et al. (2012) indicate that the metalliferous mudstones occurring in the Upper Block of the Duck Pond deposit are similarly to the Lemarchant mudstones in regard to stratigraphy and textures, but lithogeochemical data (small Eu-anomalies, enriched REYs, higher Y/Ho ratios) indicate that the Duck Pond mudstones were deposited in a more vent distal environment. The volcanic rocks of the Upper Block at Duck Pond also correlate in age (~513 Ma) with those adjacent to the Lemarchant deposit and hence, it is proposed that the Duck Pond hydrothermal mudstones represent distal equivalents to the vent proximal Lemarchant mudstones.

In essence, it is suggested that the metalliferous mudstones of the Beaver Lake, Higher Levels, Duck Pond (Upper Block) are related to the Lemarchant hydrothermal system, which also caused a hydrothermal overprint of the Cookstown shales. The metalliferous mudstones from Boundary, Boundary West, Keats Pond, North and South

Moose Pond, and Old Camp are genetically associated with the Duck Pond/Boundary hydrothermal system. The lowermost part of the graphitic shale sequences that occur predominantly in the northeastern part of the Tally Pond belt, are proposed to be contemporaneous with the Duck Pond/Boundary mineralizing event and hence, locally may have a spatial association to massive sulphide mineralization and may represent a second prospective sedimentary horizon. Accordingly, mudstones from those areas with more Lemarchant-like hydrothermal signature and hence, vent-proximal character, might be better exploration targets than those mudstones and black shales that seem to have predominantly detrital and less hydrothermal contributions.

6.1.2 Sulphur and Pb isotopic compositions of polymetallic sulphides hosted within the Lemarchant hydrothermal mudstones

Because of the exquisite textural and paragenetic preservation of polymetallic sulphides (euhedral, framboidal, tube-like, and spheroidal pyrite; pyrrhotite; chalcopyrite; arsenopyrite; and galena) in the Lemarchant metalliferous mudstones, they provided an opportunity to evaluate changing sources of sulphur and lead in both space, and as a function of the VMS deposit evolution. The analyses were undertaken by in situ secondary ion mass spectroscopy (SIMS) and yielded $\delta^{34}S$ values ranging from -38.8 ‰ to +14.4 ‰, with an average of ~ -12 ‰. The $\delta^{34}S$ systematics indicate that S was predominantly biogenically-derived. The most common known biogenic process is the biogenic/microbial sulphate reduction of seawater sulphate (BSR), which has maximum fractionation factors $\Delta^{34}S_{\text{Seawater sulphate-}H_2S}$ of ~45 ‰. However, BSR alone cannot explain

the strongly ^{34}S-depletion (i.e., negative $\delta^{34}S$ values <25 ‰) and large $\Delta^{34}S_{Seawater\ sulphate\text{-}H_2S}$ fractionation factors up to 73.3 ‰. This study found that the biogenic sources and processes consist of BSR, coupled with biogenic/microbial sulphide oxidation (BSO), and microbial disproportionation of intermediate S compounds. A combination of these can explain the large negative extent of $\delta^{34}S$ values in the Lemarchant mudstone sulphides. The total S budget of the Lemarchant mudstone involves not only organic, but also inorganic sources and processes. These inorganic processes or sources include thermochemical sulphate reduction (TSR) of seawater sulphate and igneous S that also contributed to the S budget in the hydrothermal mudstones. Especially, mudstones that are closely associated with massive sulphides have greater TSR-derived S (+/- igneous/magmatic S) contributions than interflow mudstones and mudstones that have no immediate association with mineralization.

Galena from the same mudstones have Pb isotopic compositions that suggest both juvenile and more evolved Pb sources contributed to the Lemarchant hydrothermal system. The mixed Pb is consistent with derivation from underlying basement rocks. Proximal Lemarchant mudstones also have lower radiogenic $^{206}Pb/^{204}Pb$ ratios and more positive $\delta^{34}S$ values within the range of both TSR and/or magmatic S. The more radiogenic $^{206}Pb/^{204}Pb$ ratios in the more distal mudstones indicate that they have additional contributions of a more radiogenic, detritally derived, Pb source. The correspondence of juvenile Pb and igneous $\delta^{34}S$ may be represent another vector for proximity to mineralization in hydrothermal mudstones, and may also be a potential

mechanism to record magmatic contributions to VMS hydrothermal systems in similar exhalative environments globally.

6.1.3 Neodymium isotopic provenance studies on exhalative hydrothermal Lemarchant mudstones

Lithogeochemical and Nd isotopic provenance studies indicate that the detrital/volcaniclastic/epiclastic component in the Lemarchant mudstones has arc affinities and a crustal component, derived from the underlying Ediacaran age peri-Ganderian basement (Sandy Brook Group, Crippleback Intrusive Suite). This rifted arc environment is consistent with existing Pb data from the Duck Pond, Boundary, and Lemarchant deposits, and other prospects in the Tally Pond volcanic belt (Swinden and Thorpe, 1984; Pollock and Wilton, 2001; Rogers et al., 2006; McNicoll et al., 2010, Piercey, *unpublished data*).

6.2 Outlook

6.2.1 Micro (and macro?) fauna in Cambro-Ordovician metalliferous mudstones and graphitic shales of the Tally Pond volcanic belt – potential for Cambrian hydrothermal vent communities

Within the scope of this PhD project, the metalliferous mudstones and graphitic shales of the Tally Pond volcanic belt have been studied in detail in regard to their petrography, stratigraphy, and lithogeochemistry. However, the role of bacteria (i.e.,

microbial activity) and a possible presence of hydrothermal micro (and macro?) vent communities in the Cambrian Lemarchant hydrothermal metalliferous mudstones and Cambro-Ordovician graphitic shales has only been discussed concerning biogenic sulphur sources and processes that contributed to the polymetallic sulphides hosted in the Lemarchant mudstones (Chapter 3).

Modern hydrothermal systems are known to be highly diverse, and the utilization of bacteria that provide energy to the hydrothermal vent fauna via chemosynthesis was already reported in the late 1970s by Corliss et al. (1979). Despite such knowledge on the modern seafloor fauna, little is known about preserved ancient hydrothermal vent communities (e.g., Little, 1997; Little et al., 2002, Herrington et al., 2011). One of the oldest proven vent community macrofauna that are associated with massive sulphide deposits are e.g., the Ordovician to Devonian oceanic arc sequences of the Uralides, the Mesozoic Tethyan ophiolite belt, and the Jurassic of North America. They consist of fossil hydrothermal vent tube worms, molluscs and brachiopods, as well as bacterial remnants (Little 2002, 2004; Herrington et al., 2011). Bacterial filamentous textures were reported in the Early Ordovician (~490 Ma) jasper that are associated with the Løkken and Høydal VMS deposits (Grenne and Slack, 2003; Little et al. 2004). Studies on fauna related to hydrothermal vents in Newfoundland are even scarcer and include reports of microbial low-temperature hydrothermal vent communities that use chemosynthetic processes in Early Carboniferous carbonate mounds, Big Cove Formation, reported by von Bitter et al. (1990). Early Cambrian sponges from the Forteau Formation (shale, siltstone, sandstone, and carbonate) Newfoundland, are reported from Harvey, (2010).

The Cambro-Ordovician Lemarchant mudstones and graphitic shales of the Tally Pond volcanic belt show a variety of textures and structures that are suggested to be of biogenic origin that may indicate the presence of microfauna (e.g., microbial mats, radiolaria) and potentially macrofauna (e.g., sponge spiculae, graptolites, ichnofabrics). Accordingly, a detailed study of the various biogenic textures in the Lemarchant mudstones and other Tally Pond belt shales and mudstones, can contribute to a better understanding of the Early Phanerozoic evolution of hydrothermal vent communities and other fauna in the Tally Pond rift basin and globally.

6.2.2 Hyperspectral reflectance analyses of exhalative metalliferous mudstones of the Lemarchant volcanogenic massive sulphide deposit, Tally Pond volcanic belt, central Newfoundland, Canada

Exhalative metalliferous mudstones are precipitated pre-, syn-, and post –ore formation and form a semipermeable layer capping the massive sulphides (Haymon and Kastner, 1981; Peter, 2003; Hannington, 2014). They are formed as black smoker plume fall out, when Fe, Zn, Pb, and Cu-sulphides co-precipitate with sulphates (barite, anhydrite), and other phases (e.g., amorphous silica, nontronite, and Fe-oxyhydroxides), after mixing of hydrothermal fluids with ambient seawater (Campbell et al., 1984; Hekinian et al., 1993; German and Von Damm, 2003; Gurvich, 2006). Subsequent hydrothermal alteration of VMS deposits and associated sedimentary rocks typically consists of clays, chlorite, sericite (white mica) and carbonates (Franklin et al., 1981; Large et al., 2001). With hyperspectral reflectance, such as near visible infrared (NIR)

and short-wave infrared (SWIR), it is possible to detect minerals containing chemical bonds like OH, CO_3, SO_4, NH_4, and Al, Fe, and Mg (Clark et al., 1990; Herrmann et al., 2001; Cloutier et al., in prep.). Accordingly, NIR-SWIR is an excellent tool to study mineral assemblages occurring within the metalliferous mudstones as primary constituents and those that are a result of hydrothermal alteration (e.g., Herrmann et al., 2001; van Ruitenbeek et al., 2005; Cloutier et al., *unpublished data*). The advantage of hyperspectral analysis is that it is fast, non-destructive, requires little or no sample preparation, and can be performed directly on fresh core or outcrop (Herrmann et al., 2001; Bowtiz and Ehling, 2008; Buschette, 2015; Cloutier et al., *unpublished data*).

Mineral assemblages occurring within the metalliferous mudstones associated with the Cambrian precious metal-bearing Lemarchant Zn-Pb-Cu-Au-Ag-Ba VMS deposit record the processes associated with the hydrothermal VMS forming event, as well as of the epithermal one, which is overprinting VMS-style mineralization (Gill, 2015; Lode et al., 2015; Lode et al., *in press*). Hyperspectral analyses of the Lemarchant mudstones could be used to identify different types of carbonates, such as calcite, ankerite, dolomite, and possibly Fe-Ca-Mg-Mn-carbonates (and maybe witherite?), which occur disseminated in the mudstone matrix, but also in up to several mm-thick veins. The thickness of veins may be sufficient to distinguish the overlapping peaks of carbonates and phyllosilicates (e.g., Cloutier et al., *unpublished data*). These different carbonate species are of interest, because they may help to distinguish hydrothermal versus epithermal mineral phases, e.g., bladed calcite occurs in association with bladed barite, potentially indicating boiling, whereas the Fe-Ca-Mg-Mn-carbonates may be related to

the hydrothermal fluids. Other minerals of interests in the mudstones are nontronite, an Al-poor smectite, Fe-Mg-chlorite, as well as kaolinite.

In essence, hyperspectral analyses of the mudstones obtained from mudstones with a wide spatial and vertical distribution around the main mineralized zones of the Lemarchant mudstones may help textures related to hydrothermal versus the epithermal event, may help to identify different mudstones at Lemarchant, and accordingly, may help to better predict prospective stratigraphy.

6.3 References

Bowtiz, J., and Ehling, A., 2008, Non-destructive infrared analyses: a method for provenance analyses of sandstones: Environmental Geology, v. 56, p. 623-630.

Buschette, M., 2015, Hydrothermal alteration and lithogeochemistry of the Boundary volcanogenic massive sulfide (VMS) deposit, central Newfoundland, Canada: Unpub. MSc thesis, Memorial University of Newfoundland.

Campbell, I. H., McDougall, T. J., and Turner, J. S., 1984, A note on fluid dynamic processes which can influence the deposition of massive sulfides: Economic Geology, v. 79, p. 1905-1913.

Clark, R. N., King, T. V. V., Kleijwa, M., and Swayze, G. A., 1990, High spectral resolution reflectance spectroscopy of minerals: Journal of Geophysical Research, v. 95, p. 12,653-12,680.

Corliss, J. B., Dymond, J., Gordon, L. I., Edmond, J. M., von Herzen, R. P., Ballard, R. D., Green, K., Williams, D., Bainbridge, A., Crane, K., and van Andel, T. H., 1979, Submarine thermal springs on the Galápagos Rift: Science, v. 203, p. 1073-1083.

Franklin, J. M., Sangster, D. M., and Lydon, J. W., 1981, Volcanic-associated massive sulfide deposits, *in* Skinner, B. J., ed., Economic Geology Seventy-Fifth Anniversary Volume, Society of Economic Geologists, p. 485-627.

German, C. R., and Von Damm, K. L., 2003, Hydrothermal Processes, Treatise on Geochemistry: Oxford, Pergamon, p. 181-222.

Gill, S. B., 2015, Mineralogy, metal zoning, and genesis of the Zn-Pb-Ba-Ag-Au Lemarchant volcanogenic massive sulfide (VMS) deposit, Memorial University of Newfoundland.

Grenne, T., and Slack, J. F., 2003, Bedded jaspers of the Ordovician Lokken Ophiolite, Norway; seafloor deposition and diagenetic maturation of hydrothermal plume-derived silica-iron gels: Mineralium Deposita, v. 38, p. 625-639.

Gurvich, E. G., 2006, Metalliferous sediments of the World Ocean - Fundamental theory of deep sea hydrothermal sedimentation: Berlin Heidelberg, Springer.

Hannington, M. D., 2014, Volcanogenic massive sulfide deposits, *in* Holland, H. D., and Turekian, K.K., ed., Treatise on Geochemistry 2nd Edition, 8. Reviews in Economic Geology, Elsevier Ltd, p. 319-350.

Hannington, M. D., Jonasson, I. R., Herzig, P. M., and Petersen, S., 1995, Physical and chemical processes of seafloor mineralization at mid-ocean ridges: Geophysical Monograph, v. 91, p. 115-157.

Harvey, T. H. P., 2010, Carbonaceous preservation of Cambrian hexactinellid sponge spicules: Biology Letters, v. 6, p. 834-837.

Haymon, R. M., and Kastner, M., 1981, Hot spring deposits on the East Pacific Rise 21°N: preliminary description of mineralogy and genesis: Earth and Planetary Science Letters, v. 53, p. 363-381.

Hekinian, R., Hoffert, M., Larqué, P., Cheminée, J. L., Stoffers, P., and Bideau, D., 1993, Hydrothermal Fe and Si oxyhydroxide deposits from South Pacific intraplate volcanoes and East Pacific Rise axial and off-axial regions: Economic Geology, v. 88, p. 2099-2121.

Herrington, R., Little, C. T. S., and Maslennikov, V., 2011, The fossil record of VMS associated vent fauna assemblages, Geological Association of Canada-Mineralogical Association of Canada-Society of Economic Geologists-Society of Geology Applied to Ore Deposits Joint Annual Meeting, 34: Ottawa, ON (May 25-27), Geological Association of Canada, p. 91.

Herrmann, W., Blake, M., Doyle, M., Huston, D., Kamprad, J., Merry, N., and Pontual, S., 2001, Short wavelength infrared (SWIR) spectral analysis of hydrothermal alteration zones associated with base metal sulfide deposits at Rosebery and Western Tharsis, Tasmania, and Highway-Reward, Queensland: Economic Geology, v. 96, p. 939-955.

Huston, D. L., Pehrsson, S., Eglington, B. M., and Zaw, K., 2010, The geology and metallogeny of volcanic-hosted massive sulfide deposits: variations through geologic time and with tectonic setting: Economic Geology, v. 105, p. 571-591.

Jørgensen, B. B., Isaksen, M. F., and Jannasch, H. W., 1992, Bacterial Sulfate Reduction Above 100°C in Deep-Sea Hydrothermal Vent Sediments: Science, v. 258, p. 1756-1757.

Kalogeropoulos, S. I., and Scott, S. D., 1989, Mineralogy and geochemistry of an Archean tuffaceous exhalite; the Main Contact Tuff, Millenbach Mine area, Noranda, Quebec: Canadian Journal of Earth Sciences = Journal Canadien des Sciences de la Terre, v. 26, p. 88-105.

Kampschulte, A., and Strauss, H., 2004, The sulfur isotopic evolution of Phanerozoic seawater based on the analysis of structurally substituted sulfate in carbonates: Chemical Geology, v. 204, p. 255-286.

Konhauser, K. O., 2007, Introduction to Geomicrobiology, Blackwell Publishing Ltd, 440 p.

Large, R. R., 1992, Australian volcanic-hosted massive sulfide deposits; features, styles, and genetic models: Economic Geology, v. 87, p. 471-510.

Large, R. R., Allen, R. L., Blake, M. D., and Herrmann, W., 2001, Hydrothermal alteration and volatile element haloes for the Rosebery K Lens volcanic-hosted massive sulfide deposit, western Tasmania: Economic Geology, v. 96, p. 1055-1072.

Little, C. T. S., 1997, Fossil hydrothermal vent communities: an update: RIDGE Newsletter, v. 13, p. 34-37.

_____2002, The fossil record of hydrothermal vent communities: Cahiers de Biologie Marine, v. 43, p. 313-316.

Little, C. T. S., Glynn, S. E., and Mills, R. A., 2004, Four hundred and ninety million year record of bacteriogenic iron oxide precipitation at sea-floor hydrothermal vents: Geomicrobiology Journal, v. 21, p. 415-429.

Lode, S., Piercey, J. S., and Devine, C. A., 2015, Geology, mineralogy, and lithogeochemistry of metalliferous mudstones associated with the Lemarchant volcanogenic massive sulfide deposit, Tally Pond belt, Central Newfoundland: Economic Geology.

Lode, S., Piercey, S. J., Layne, G. D., Piercey, G., and Cloutier, J., *in press*, Multiple sulphur and lead sources recorded in hydrothermal exhalites associated with the Lemarchant volcanogenic massive sulphide deposit, central Newfoundland, Canada: Mineralium Deposita.

McNicoll, V., Squires, G., Kerr, A., and Moore, P., 2010, The Duck Pond and Boundary Cu-Zn deposits, Newfoundland: new insights into the ages of host rocks and the timing of VHMS mineralization: Canadian Journal of Earth Sciences, v. 47, p. 1481-1506.

Peter, J. M., 2003, Ancient iron formations: their genesis and use in the exploration for stratiform base metal sulphide deposits, with examples from the Bathurst Mining Camp, *in* Lentz, D. R., ed., Geochemistry of Sediments and Sedimentary Rocks: Secular Evolutionary Considerations to Mineral Deposit-Forming Environments, GEOtext v.4., Geological Association of Canada, p. 145-176.

Peter, J. M., and Goodfellow, W. D., 1996, Mineralogy, bulk and rare earth element geochemistry of massive sulphide-associated hydrothermal sediments of the Brunswick horizon, Bathurst mining camp, New Brunswick: Canadian Journal of Earth Sciences, v. 33, p. 252-283.

Piercey, S. J., Squires, G. C., Brace, T., and Lode, S., 2012, Initial Report: Hydrothermal mudstones from the Duck Pond volcanogenic massive sulfide (VMS) deposit, Central Mobile Belt Newfoundland and Labrador, Canada: Part 1 – Geology and Lithogeochemistry, CAMIRO Project 08E04 2012 Annual Report, The Geochemistry of Shales as Vectors to Ore Deposits, p. 41.

Piercey, S.J., 2008, Report on the sulfide mineralogy and petrology of massive sulfide from the Lemarchant volcanogenic massive sulfide (VMS) prospect, Central Newfoundland. Report to Paragon Minerals Corporation. SJPGeo Consulting.

_____2010, Update on hydrothermal sedimentary rocks from the Duck Pond VMS deposit, Tally Pond VMS Belt, central Newfoundland. Keystone_Masterslides.

Pollock, J. C., and Wilton, D. H. C., 2001, Metallogenic studies of the Tally Pond Belt, Victoria Lake Group; trace-element geochemistry and lead-isotope data from the Exploits Subzone, Newfoundland: Report - Government of Newfoundland and Labrador. Dept. of Mines and Energy, Geological Survey, Report: 2001-1, pp.247-266, Mar 2001.

Rogers, N., van Staal, C. R., McNicoll, V., Pollock, J., Zagorevski, A., and Whalen, J., 2006, Neoproterozoic and Cambrian arc magmatism along the eastern margin of the Victoria Lake Supergroup: A remnant of Ganderian basement in central Newfoundland?: Precambrian Research, v. 147, p. 320-341.

Spry, P. G., Peter, J. M., and Slack, J. F., 2000, Meta-exhalites as exploration guides to ore, *in* Spry, P. G., Marshall, B., and Vokes, F. M., eds., Metamorphosed and metamorphogenic ore deposits, Reviews in Economic Geology 11: Littleton, CO, Society of Economic Geologists, p. 163-201.

Swinden, H. S., and Thorpe, R. I., 1984, Variations in style of volcanism and massive sulfide deposition in Early to Middle Ordovician island-arc sequences of the Newfoundland Central Mobile Belt: Economic Geology, v. 79, p. 1596-1619.

van Ruitenbeek, F. J. A., Cudahy, T., Hale, M., and van der Meer, F. D., 2005, Tracing fluid pathways in fossil hydrothermal systems with near-infrared spectroscopy: Geology, v. 33, p. 597-600.

von Bitter, P. H., Scott, S. D., and Schenk, P. E., 1990, Early Carboniferous low-temperature hydrothermal vent communities from Newfoundland: Nature, v. 344, p. 145-148.